Advances in Materials Science and Engineering

Sustainable Building Materials and Technologies 2018

Lead Guest Editor: Nadezda Stevulova
Guest Editors: Kestutys Baltakys, Estokova Adriana, and Sverak Tomas

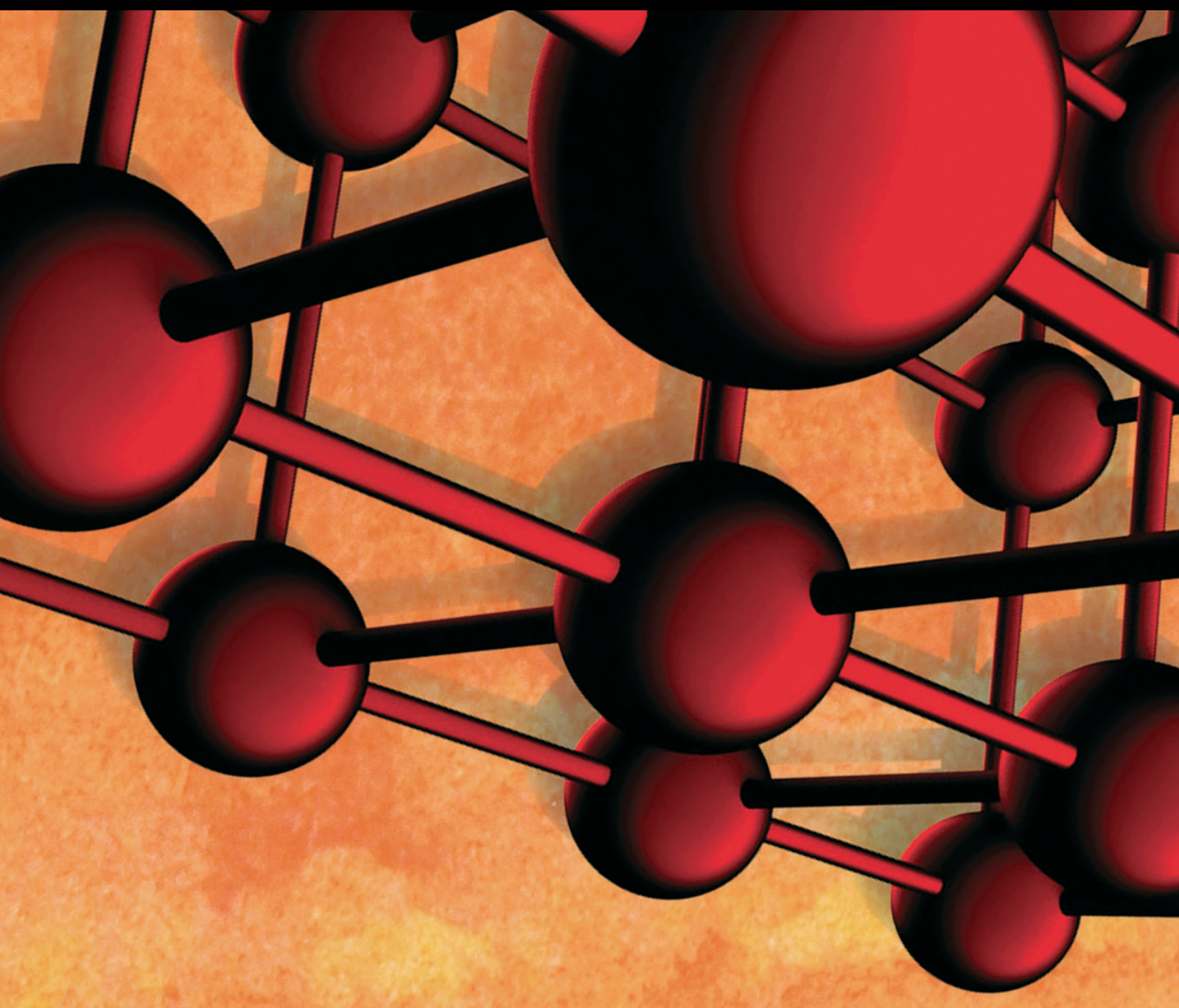

Sustainable Building Materials and Technologies 2018

Advances in Materials Science and Engineering

Sustainable Building Materials and Technologies 2018

Lead Guest Editor: Nadezda Stevulova
Guest Editors: Kestutys Baltakys, Estokova Adriana, and Sverak Tomas

Editorial Board

Contents

Hindawi
Advances in Materials Science and Engineering
Volume 2018, Article ID 9491813, 2 pages
https://doi.org/10.1155/2018/9491813

Editorial
Sustainable Building Materials and Technologies 2018

Nadezda Stevulova[1], **Kestutis Baltakys**[2], **Adriana Estokova**[1] and **Tomas Sverak**[3]

[1]*Department of Material Engineering, Institute of Environmental Engineering, Faculty of Civil Engineering, Technical University of Kosice, Slovakia*
[2]*Department of Silicate Technology, Faculty of Chemical Technology, Kaunas University of Technology, Kaunas, Lithuania*
[3]*Institute of Materials Chemistry, Faculty of Chemistry, Brno University of Technology, Brno, Czech Republic*

Correspondence should be addressed to Nadezda Stevulova; nadezda.stevulova@tuke.sk

Received 1 October 2018; Accepted 1 October 2018; Published 4 November 2018

The annual special issue *Sustainable Building Materials and Technologies* seeks to collect a coherent whole of studies aimed at increasing the sustainability in construction industry. It covers several topics oriented on the innovative technologies of key building materials production with lower energy and natural raw material consumption and controlled minimization of the total generation of greenhouse gases, development of new environmentally friendly materials and agents, characterization of the properties of construction materials, and methodologies applied in building of structures as core issues of the sustainable development in the field of construction in integration with environmental, social, and economic factors in changing climate conditions.

In this special issue, the papers are addressed to advances in sustainable strategies of the development of building structures with environmentally friendly building materials with improved properties and innovative integrated solutions to key building materials.

The generation of large amounts of industrial inorganic by-products as well waste originating from renewable resources is becoming a drive to their utilization in cement and concrete material and a contribution to waste disposal. The use of waste materials in production of traditional building materials and the applicability of developed new environmentally friendly admixtures improving cement mixture workability, concrete performance, and ensuring economic feasibility are investigated in some papers. The utilization of waste from coal power plants (circulating fluidized bed combustion desulfurization slag) in mortars and their expansion and strength characteristics are evaluated by Z. Cheng et al. The influence of grinding time of slag and amount of added ground slag and sodium sulphate on the expansion rate and compressive strength of cured mortars is studied. Similarly, Y. Li et al. aim at exploring the performances of concrete blended with ultrafine ground granulated blast-furnace slag in the form of slurry.

K. H. Younis et al. examine the feasibility of nanosilica used for improvement of the performance of concrete containing recycled aggregates derived from processing construction and demolition concrete waste of buildings in terms of microstructure, strength properties, and water absorption of concrete.

H. Liu and coworkers focus on the design of the conductive graphite tailing concrete and optimization of its composition due to key parameters affecting the compressive strength of concrete such as water to cement ratio, sand quantity, graphite tailings content, and carbon fibre content. The electrical characteristics of the graphite tailing concrete with optimal contents of graphite tailings and carbon fibre for electrical resistivity prediction are investigated.

The contribution of H. Liu et al. deals with an experimental study on modification of the asphalt binder using crumb rubber from end-of-life tyres and diatomite. Results reveal that asphalt with the addition of crumb rubber can improve the high temperature susceptibility, viscosity, and elastic recovery ability of binder.

In the paper by F. Wu et al., the influences of incorporating two types of fibre (polypropylene and glass) and different volume fraction on the mechanical properties of peach shell lightweight concrete are investigated.

The paper by Y. Guo et al. reports on the utilization of wheat straw as biomass raw material in the preparation of polycarboxylate superplasticizer. The attention is paid to optimizing the preparation conditions of graft copolymerization of the large cellulose molecules of straw fibre and superplasticizer to improve the performance of the water-reducing agent as well as to reduce its production cost.

J. Zhou et al. study the mechanical behaviour of embedding strength of designed construction material—parallel strand bamboo perpendicular to grain. The feasibility for this material is assessed.

X. Lin et al. use a multifunctional smart composite material prepared by dispersing soft magnetic particles into a Silly Putty matrix for the design of a novel shear thickening magnetorheological damper with rate-sensitive characteristic (speed locking) and semiactive controlling properties for large civil engineering structures. A multiparameter and symmetry model is established for description of the dynamic hysteretic behaviour of this damper.

Another group of authors focus their research on the durability and resistivity of the materials. Z. Guo et al. report on the basalt fibre reinforced concrete in China with an emphasis on alkali resistance of fibres and static mechanical properties of composites such as the strength and toughness. In this paper, six research topics related to alkali resistance and static mechanical properties of three-dimensional, randomly distributed basalt fibre-reinforced concrete are proposed.

W. Zhang et al. pay the attention to the research of the degradation of roller compacted concrete samples cured for 28 days during the freeze-thaw cyclic process in potassium acetate solution. The weight loss, the dynamic elastic modulus, the mechanical properties, and the residual strain of concrete samples are evaluated.

H. Min et al. investigate the sulfuric acid corrosion mechanism for concrete in a soaking environment. Based on the theory of reaction boundary layer, this paper presents a sulfuric acid corrosion model for concrete usable for prediction of the mechanism in practical engineering and providing the foundation for steel corrosion prediction.

B. Cui et al. study the effects of different concentrations of sodium sulphate and immersion time on the strength and the structure of hydration products. The fly ash-based coal mine filling paste test blocks were evaluated in comparison to the referential filling paste.

The paper related to using cement-solidified contaminated soil as road subgrade material is presented by Y. Zhou et al. Carbonation effects on strength and the settlement of this solidified soil are evaluated.

The advanced construction technology is of the interest in the following papers: W. Drozd et al. concentrate on an innovative alternative construction technology applying in low-impact buildings. A comparative study of three type of walls made of locally sourced materials with biomass component in terms of construction time is presented.

The paper by D. Zhang et al. presents a new type of joint for connecting steel beams with a concrete-filled double-skin steel tubular column and the examined failure modes and hysteretic behaviours. A finite element analysis model of the joint was also established and validated by comparing its predictions with experimental results.

In the paper by J. Yue, the seismic responses of a large-space vertical hybrid structure and the mechanical behaviour of the Y-type-steel steel reinforced concrete column are analysed. A local-fine finite element model is proposed, and a large-space vertical hybrid structure is numerical simulated.

The environmental, social, and economic indicators for measuring sustainable construction materials are analysed in the paper by H. Danso. Based on the statistical evaluation of data collected from structured questionnaires including 25 indicators, 12 key indicators are identified.

Conflicts of Interest

Nadezda Stevulova, Kestutis Baltakys, Adriana Estokova, and Tomas Sverak as Guest Editors of the annual special issue *Sustainable Building Materials and Technologies* hereby declare no conflicts of interest.

Nadezda Stevulova
Kestutis Baltakys
Adriana Estokova
Tomas Sverak

Hindawi
Advances in Materials Science and Engineering
Volume 2018, Article ID 4315345, 12 pages
https://doi.org/10.1155/2018/4315345

Research Article

Experimental Study on the Durability of Fly Ash-Based Filling Paste in Environments with Different Concentrations of Sulfates

Boqiang Cui,[1] Yin Liu ,[1,2] Hao Guo,[1] Zhanxin Liu,[1] and Yao Lu[1]

[1]*State Key Laboratory of Mining Disaster Prevention and Control Co-founded by Shandong Province and the Ministry of Science and Technology, Shandong University of Science and Technology, Qingdao 266590, China*
[2]*Henan Key Laboratory for Green and Efficient Mining and Comprehensive Utilization of Mineral Resources, Henan Polytechnic University, Jiaozuo 454000, China*

Correspondence should be addressed to Yin Liu; liuyin-73@163.com

Received 18 January 2018; Revised 3 April 2018; Accepted 17 July 2018; Published 19 August 2018

Academic Editor: Estokova Adriana

In order to study the effects of different concentrations of sulfate on the strength of fly ash-based coal mine filling paste, using variable control, mechanical analysis, and other means, the changes in the uniaxial compressive strengths of filling paste blocks soaked in different concentrations of sodium sulfate solution for different durations are studied, and their stress-strain curves are discussed. The hydrated products of each block are analyzed at different stages by XRD, and the results indicate that different concentrations of sodium sulfate solution have different effects on the strength of the filling paste after soaking for different durations. A sodium sulfate solution with a concentration of 5% had an activator effect on the fly ash-based filling paste and enhanced the strength of the filling paste. A sodium sulfate solution with a concentration of 10% and 15% increased the early strength of the paste test block faster, but after 60 d, the strength decreased. The stress-strain curves for these blocks show that the elastic moduli of the filling paste test blocks change irregularly, and it was found that with the increase in soaking time, the blocks soaked in the 10% and 15% sodium sulfate solutions developed fissures in the later stage that adversely affected the strength of the filling paste. The XRD results show that the filling paste test block hydration products are hydrated calcium silicate (C-S-H) based and that ettringite (AFt), beneficial to strength of the filling paste in proper quantities, appeared in the main product of the filling paste test blocks that were soaked in the sodium sulfate solution. With the increase in the concentration of the sodium sulfate solution, the AFt is generated in larger quantities, and gypsum crystals begin to appear, which is not conducive to the filling paste block strength.

1. Introduction

Coal mine paste filling technology is an important part of green coal mining: it not only plays a significant role in supporting the overlying strata, preventing or reducing surface subsidence of the coal mine [1–5], but also provides an effective solution the problem of "three under, one above" mining (mining under a building, under a railway, under a water body, or above confined water) [6, 7]. As a result of its usefulness, paste filling technology has been widely applied and practiced in the field of mine filling. As a core component of filling technology, filling materials have always been the focus of research, with particular focus in recent years on how to both reduce the cost of filling and ensure the safety of mine production [8–11]. Paste filling materials consist of aggregates and cementitious materials. The use of fly ash in filling paste offers many potential benefits. Fly ash has the potential for cementitious activity, is cheap and easily sourced, and its use reduces the pollution of fly ash in the environment, thus more and more scientists have been interested in its potential applications. Much research has been conducted on the effects of fly ash content, particle size, activity, and conveyance performance on the performance of coal filling paste [12–17].

After entering the goaf, the filling paste is often in a complex mine environment. The coupling of different properties such as temperature, chemistry, and pressure has a certain influence on the long-term stability of the filling

paste [18–21]. Most of the mine water contains sulfate, chlorine salt, and other substances; the filling paste is soaked in the mine water for a long time, and it can interact with these salts, thus causing the change of performance. Among them, the influence of sulfate on filling paste properties cannot be ignored [22, 23]. Some studies have shown that a proper amount of sulfate can stimulate the activity of the fly ash in the filling paste, promoting early paste strength. Feng et al. [24] used the lime absorption method to explore the excitation effect of different activators on fly ash activity and concluded that the effect of sulfate excitation was superior to that of chlorine salt excitation, and the higher the sodium sulfate concentration, the more obvious the excitation effect. Guo et al. [25] investigated the microstructures of gypsum and fly ash adhesives by using X-ray diffraction, scanning electron microscopy, and pore structure analysis, and it is proved that desulfurization gypsum can effectively destroy Si-O and Al-O bonds in fly ash particles and produce AFt and other substances, so as to improve the compressive strength and tensile bond strength of fly ash-cemented material. He and Wei [26] studied the effect of sulfate on the performance of fly ash-cement adhesives with different fly ash contents using strength tests, and the results show that in a certain sulfate range, the greater the amount of activator is, the better the effect of fly ash will be. Ke et al. [27] theoretically analyzed the mechanisms of the effects of desulfurization gypsum on the activity of a cement-fly ash material; it is believed that the activation mechanism of sulfate to fly ash is mainly SO_4^{2-} under the action of Ca^{2+} reacting with AlO_2^- on the surface of fly ash particles to generate AFt.

However, excessive sulfate can corrode the filling paste, which is unfavorable to the long-term stability of the hardened paste. Fall and Benzaazoua [28] analyzed the strength change trend of the filling paste in a sulfate environment by establishing mathematical models and proved that when the sulfate concentration is too high, the later strength of the filling paste will be adversely affected. Through strength tests and microanalysis, Pokharel and Fall [29] and Fall and Pokharel [30] explored the coupling effect of sulfate and temperature on the durability of the filling paste. Liu et al. [31] analyzed the corrosion and degradation mechanisms of filling materials in an acidic environment by means of intensity detection, scanning electron microscopy, and X-ray diffraction and studied the products generated by filling bodies subjected to a sulfate environment over time, indicating that excessive production of Aft and other substances is a key factor in reducing the strength of the filling paste. Sun et al. [32] studied the creep characteristics of the filling paste after sulfate attack by mechanical analysis and determined the one-dimensional and three-dimensional constitutive creep equations; the studies show that the accelerated creep of paste is filled in the later stage of sulfate attack, which affects the filling effect. Li and Fall [33] used thermogravimetric analysis and X-ray diffractometry to examine the compositional changes of the filling paste under sulfate attack and explored the influence mechanisms of sulfate on early filling paste performance.

Many studies have demonstrated that although an appropriate amount of sulfate can improve the performance of a fly ash, it also has a certain effect on the durability of the filling paste. However, at present, research into fly ash-based filling pastes is mostly focused on the properties of the paste itself and the principle of coal ash stimulation. Little attention has been paid to the influence of the filling environment on the properties of a fly ash-based filling paste. Fly ash-based filling paste contains a large amount of fly ash, and the influences of multiple factors on the behavior of fly ash filling paste when injected into the goaf are different depending on the conditions. Due to the different sulfate content of different mines, the effect of sulfate on the filling paste is also different, and the durability of the filling paste in a sulfate environment directly affects the filling effect. If the sulfate in the filling environment can be effectively used to improve the long-term stability of the filling material, this would represent a significant development in coal mine paste filling technology.

In this paper, to provide theoretical support for the study of the durability of fly ash-based filling pastes in different sulfate environments, the influence of different sulfate concentrations on the strength of a fly ash-based filling paste was analyzed using strength tests. Microstructural and compositional changes in the fly ash-based filling paste after sulfate attack were then investigated using micro-XRD analysis.

2. Experimental Program

2.1. Materials

2.1.1. Fly Ash. A grade III fly ash from a power plant in Huangdao District, Qingdao, Shandong Province, was selected. The appearance of the fly ash was grey brown, and the main chemical composition is shown in Table 1.

2.1.2. Cement. The cement used in these experiments was 32.5 ordinary Portland cement produced by Shandong Shanshui Cement Group Limited. The chemical composition of the clinker is shown in Table 2.

2.1.3. Sodium Sulfate. The sodium sulfate used in these experiments was of analytical purity, produced by Tianjin Feng Boat Chemical Reagent Technology Co., Ltd., and its sodium sulfate content was more than 99%.

2.2. Selection of Material Ratio. The filling paste is made up of cementitious material and aggregate. In order to minimize the cost of filling, the optimization ratio of this mix has always been given careful attention. Coal mine safety regulations require that the initial setting time of the filling paste be 3-4 h, the final setting time be less than 8 h, the bleeding rate be less than 3%, and the slump be in the range of 18–24 cm. Taking the Zibo Mining Group Daizhuang Coal Mine as an example to provide an engineering background, Zhang et al. [34] determined that the ideal ratio of fly ash to cement was between 2 and 8, and the ideal ratio of gangue to cement was between 4 and 10. They also pointed out that when the ratio of cement, fly ash, and aggregate was

Table 1: Chemical contents of fly ash.

Loss	SiO_2	Al_2O_3	Fe_2O_3	CaO	MgO
11.62	52.35	32.60	2.51	8.13	0.95

Table 2: Chemical components and mineral composition of ordinary silicate cement.

Chemical composition	CaO	SiO_2	Al_2O_3	Fe_2O_3	MgO	SO_3	f-CaO
Mass ratio	62.58	22.95	5.32	3.90	2.06	2.33	0.86

1 : 4 : 6, the mass concentration was 74% and the filling paste exhibited the best performance as well as good application in the field. Liu et al. [35] studied the performance of urban waste paste filling materials and also found that this ratio provided the best effect. The influence of the aggregate on the filler paste body is mainly accounted for by its particle size distribution. From a chemical point of view, the minerals in the aggregate are mostly inert, and the effect of sulfate on the performance of the aggregate is insignificant [8]. Taking into account that the impact of the groundwater environment on a filling paste is mainly on the hydration products of its cementitious material, in this study, a slurry test was used, and the ratio of cement to fly ash was set at 1 : 4. The composition of tested mixtures is shown in Table 3.

2.3. Experimental Design. Filling pastes produce different hydration products in different environments, and the quantity of generated hydration products varies significantly. As the hydration products vary, the strength of the test block will be affected to varying degrees. In this study, filling paste blocks were prepared with cement and fly ash. The strength, stress-strain curves, and hydration components of the specimens immersed in clean water and in sodium sulfate concentrations of 5%, 10%, and 15% were analyzed to determine the mechanism of their effect on the paste strength. The test blocks were soaked in 4 sets of 12 blocks, one set soaked in each solution, for a total of 48 blocks. Within each set of twelve blocks, three blocks each were soaked for 30 d, 60 d, 90 d, and 120 d. In order to eliminate the influence of temperature and humidity on the strength of the test blocks, the blocks were cured under a constant relative humidity of 90% and a temperature of 25°C. Once the blocks were demoulded, they were placed into the different solutions for soaking. The experimental design of this study is shown in Table 4.

2.4. Experimental Steps. According to the experimental scheme, the proportion of cement to fly ash was evenly mixed at a ratio of 1 : 4, adding an appropriate amount of water to provide a mass concentration of 74%. With reference to the "Standard Test Method for Long-Term Performance and Durability of Ordinary Concrete" (GB/T 50082-2009), the paste slurry was tamped into 100 × 100 × 100 mm molds, and bubbles were discharged using a shaking table. Prior to destructive specimen testing, the blocks were divided into four groups: each group of test blocks was completely soaked in clean water, a 5%, a 10%, or a 15% sodium sulfate solution, under constant temperature conditions, until reaching the specified soaking duration of 30 d, 60 d, 90 d, or 120 d. The specimens were then removed from the solutions and tested for uniaxial compressive strength and analyzed by XRD. The basic operational flow chart of the experiment is shown in Figure 1.

Table 3: The composition of tested mixtures.

Filling materials	Cement	Fly ash	Water
Ratio	14.8%	59.2%	26%

2.4.1. Uniaxial Compressive Strength Test. The paste test blocks were placed on an AG-X250 Shimadzu testing machine for uniaxial compression testing. The loading method used was displacement control, with the loading speed set to 0.01 mm/s. A camera was used to record the changes in the paste block during the testing process. Each test was repeated three times, and the average result was taken as the strength of the tested block. The compressive test loading process is shown in Figure 2.

2.4.2. XRD Experiment. After the uniaxial compression test was completed, samples were taken from the damaged test specimen and placed in pure ethanol to stop all hydration. After 24 h, the sample was removed and dried at 40 centigrade in a vacuum to avoid destroying the molecular structure of the sample. The samples were ground after the drying and then passed through a 74 μm sieve. The passing portion of the ground sample (i.e. the portion smaller than 74 μm) was analyzed by XRD using the instrument shown in Figure 3.

3. Results and Discussion

3.1. Results and Analysis of Uniaxial Compression Tests. Fly ash-based filling paste soaked in different concentrations of sulfate solution exhibited significant differences in strength. By examining the uniaxial compression strength results shown in Table 5, the changes in the strength of the filling paste specimens subjected to different conditions can be clearly seen.

As can be seen in Table 5, specimens subjected to the same conditions exhibit very similar strengths: the standard deviation in all groups was less than 0.4 MPa. Therefore, the average of the three tests of each specimen condition was taken as the uniaxial compressive strength for the given condition. For ease of comparison, one test block from each group was taken for stress-strain analysis.

3.1.1. Effect of Different Sulfate Concentrations on the Strength of the Filling Paste. As can be seen from Figure 4, with the increase in soaking time, the strength of the test blocks subjected to different soaking environments clearly

Table 4: Experimental design to determine the effect of sulfate on the durability of filling paste.

Solid ratio (cement : fly ash)	Test type	Sample specifications	Concentration of sodium sulfate solution	Curing temperature (°C)	Relative humidity (%)
1 : 4	Uniaxial compression test XRD experiment	100 × 100 mm <74 μm	0%, 5%, 10%, 15%	25	90

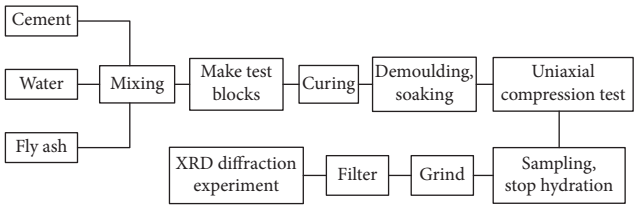

Figure 1: Experimental operation flow chart.

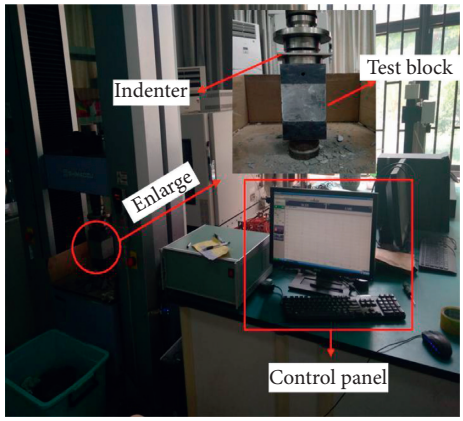

Figure 2: Uniaxial compression test.

Figure 3: XRD analysis.

changes. With the increase in soaking time, the uniaxial compressive strength of the filling paste blocks soaked in clean water and 5% sodium sulfate solution increased. After soaking for 30 d, the strength of the test blocks soaked in clean water were the weakest, while the strength of the test blocks soaked in the 10% sodium sulfate solution were the strongest; the average value was 11.34 MPa. After soaking for 60 d, the strength of the test blocks soaked in the 10% sodium sulfate solution increased significantly by 37.1%. The strength of the test blocks soaked in the 5% sodium sulfate solution was higher than that of the test blocks soaked in the 15% sodium sulfate solution, and the strength of test blocks soaked in clean water remained the lowest of the four soaking conditions. After soaking for 90 d, the strength of the test blocks soaked in the 10% and 15% sodium sulfate solutions decreased, while the strength of the test blocks soaked in the 5% sodium sulfate solution increased significantly, showing a 15.6% improvement over the strength of the blocks after 60 d of soaking, and the strength of the test blocks soaked in clean water continued to slowly increase. After soaking for 120 d, the strength of the test blocks soaked in clean water and in the 5% sodium sulfate tended to be steady, while that of the test blocks soaked in the 10% and 15% sodium sulfate solution continued to decrease. At this time, the strength of the test blocks soaked in the 5% sodium sulfate solution was the highest, followed by the test blocks soaked in the clean water, and then the test blocks soaked in the 10% sodium sulfate solution, while the test blocks soaked in the 15% sodium sulfate solution exhibited the lowest strength.

The active ingredients in the filling paste that was soaked in clean water are certain; under the action of water molecules, the yield of hydrated calcium silicate and other hydration products slowly increases, therefore, the strength of the material also gradually increases, tending to slow down after the active material has completely reacted. Due to the different concentrations of sodium sulfate in the other three solutions in which the test blocks were soaked, different materials were generated. The appropriate concentration of sulfate can fully stimulate the fly ash reaction with cement clinker in the active substance, generating ettringite (AFt), which fills in the voids in the test blocks, increasing their strength. The test blocks that were soaked in the 5% sodium sulfate solution showed an increase in strength with the increase in immersion time, showing that in this material, the sodium sulfate plays the role of an activator. When the concentration of sulfate is too high, it can accelerate the formation of AFt in the specimen at an early stage, such that the strength of the filling paste test blocks increases rapidly. With the increase in soaking time and the accompanying continuation of the reaction, the filling paste not only produces a large amount of AFt, but the expansion of the filling paste body increases, resulting in an accompanying stress increase, reducing the strength of the filling paste, and causing the precipitation of gypsum crystals. Because of this behavior, the strengths of the test blocks soaked in the 10% and 15% sodium sulfate solutions increased more in the early soaking time than the other two groups, but their strength gradually decreased after 60 d of soaking.

Table 5: Uniaxial compressive strength of filling paste after immersion in different concentrations of sulfate solution.

Sulfate concentration		Uniaxial compressive strength (MPa)											
		30 d soaking time			60 d soaking time			90 d soaking time			120 d soaking time		
Clean water	Test results	10.27	9.98	10.08	12.51	12.67	13.1	13.92	13.51	13.76	14.37	14.66	14.53
	Mean value		10.11			12.76			13.73			14.52	
	Standard deviation		0.14			0.31			0.21			0.15	
5%	Test results	10.32	10.61	10.81	13.42	13.56	13.82	15.92	15.51	15.73	15.95	16.32	16.11
	Mean value		10.58			13.60			15.72			16.13	
	Standard deviation		0.25			0.29			0.21			0.19	
10%	Test results	10.97	11.55	11.5	15.31	15.97	15.37	14.52	14.91	15.24	12.96	13.89	14.04
	Mean value		11.34			15.55			14.89			13.63	
	Standard deviation		0.32			0.36			0.36			0.34	
15%	Test results	10.57	10.88	11.07	13.31	13.67	13.64	12.92	12.51	12.31	12.16	11.62	11.41
	Mean value		10.84			13.54			12.58			11.73	
	Standard deviation		0.25			0.20			0.31			0.39	

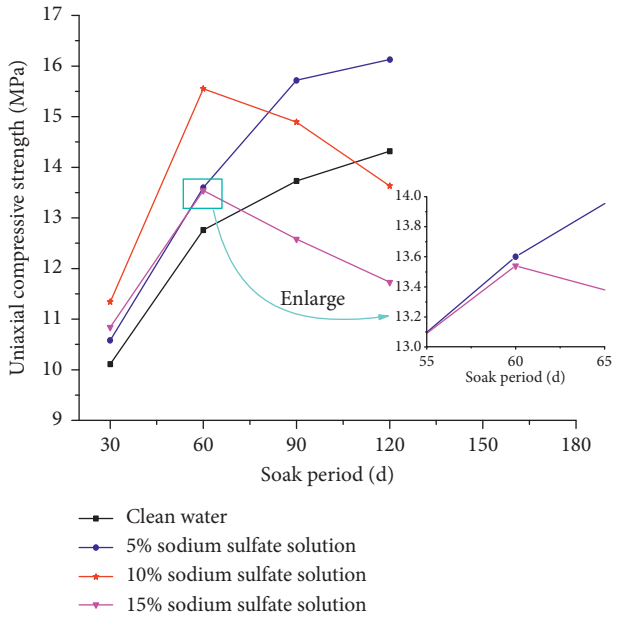

Figure 4: Effect of different concentrations of sulfate solution on the strength of filling paste.

3.1.2. Stress-Strain Analysis of Test Blocks in Different Soaking Time. It can be seen in Figure 5 that after soaking for 30 d, the peak stress in the filling paste test blocks soaked in the 15% sodium sulfate solution was larger than for the other three groups, while the elastic modulus was the smallest. After soaking for 60 d, the peak stress in each group increased, and the peak stress in test blocks soaked in clean water remained the lowest. At this time, the peak stress and stiffness of the filling paste test blocks soaked in the 10% sodium sulfate solution reached their maximum, indicating an elastic modulus of nearly 1000 MPa. The test block soaked in the 15% sodium sulfate solution exhibited delayed damage after reaching a strain of 1.7%, while the stress was still rising. After soaking for 90 d, the peak stress in the test blocks soaked in clean water and in the 5% sodium sulfate solution showed significant increase, while the peak stresses in the other two groups decreased relatively. The filling paste blocks soaked in 10% sodium sulfate solution also exhibited delayed failure phenomenon at 90 d, but at a failure stress, it was lower than that of the filling paste blocks soaked in the 15% sodium sulfate solution. After soaking for 120 d, the peak stress in the test blocks soaked in the 5% sodium sulfate solution was the highest (about 10% higher than the test blocks soaked in clean water), while the peak stress in the test blocks soaked in the other two solutions was significantly reduced. The test blocks soaked in the 10% sodium sulfate solution exhibited delayed failure at a strain of 2.60%, after which the stress continued to rise. The test blocks soaked in the 15% sodium sulfate solution reached their peak at a strain of 1.75% and then maintained a certain residual strength as the stress slowly decreased.

Under different soaking times and different concentrations of sulfate solution, the stress and strain characteristics of the filling paste test blocks are obviously different, and the elastic modulus is irregular. After peak stress, all filling paste test blocks maintained a certain residual strength. This is because the filling paste test blocks contain plain concrete. Before damage, the test blocks first undergo a compaction strengthening stage before entering the elastic stage. The cracks produced after the rupture then appear in alternately staggered rows, with shards flaking around the test block core (Figure 6). Because of this behavior, the stress continues to be borne by the core of the block, and thus will not fall as sharply as it does when rock is subjected to similar damage.

The filling paste test blocks produce different substances at different stages of soaking. The early absorption of sodium sulfate provides sufficient SO_4^{2-} for the filling paste, generating AFt to fill the internal voids in the test block matrix. This indicates that for sulfate concentrations in a certain range, the filling paste block strength increases with the increase in sulfate concentration. After peak stress is achieved, there remains a certain residual strength, and the stress decreases slowly. The presence of excessive AFt can cause the internal stress in the filling paste test block to increase, resulting in microcracks, leading to a decrease in the strength of the test blocks. Therefore, when subjected to uniaxial compression, the test blocks soaked in a solution

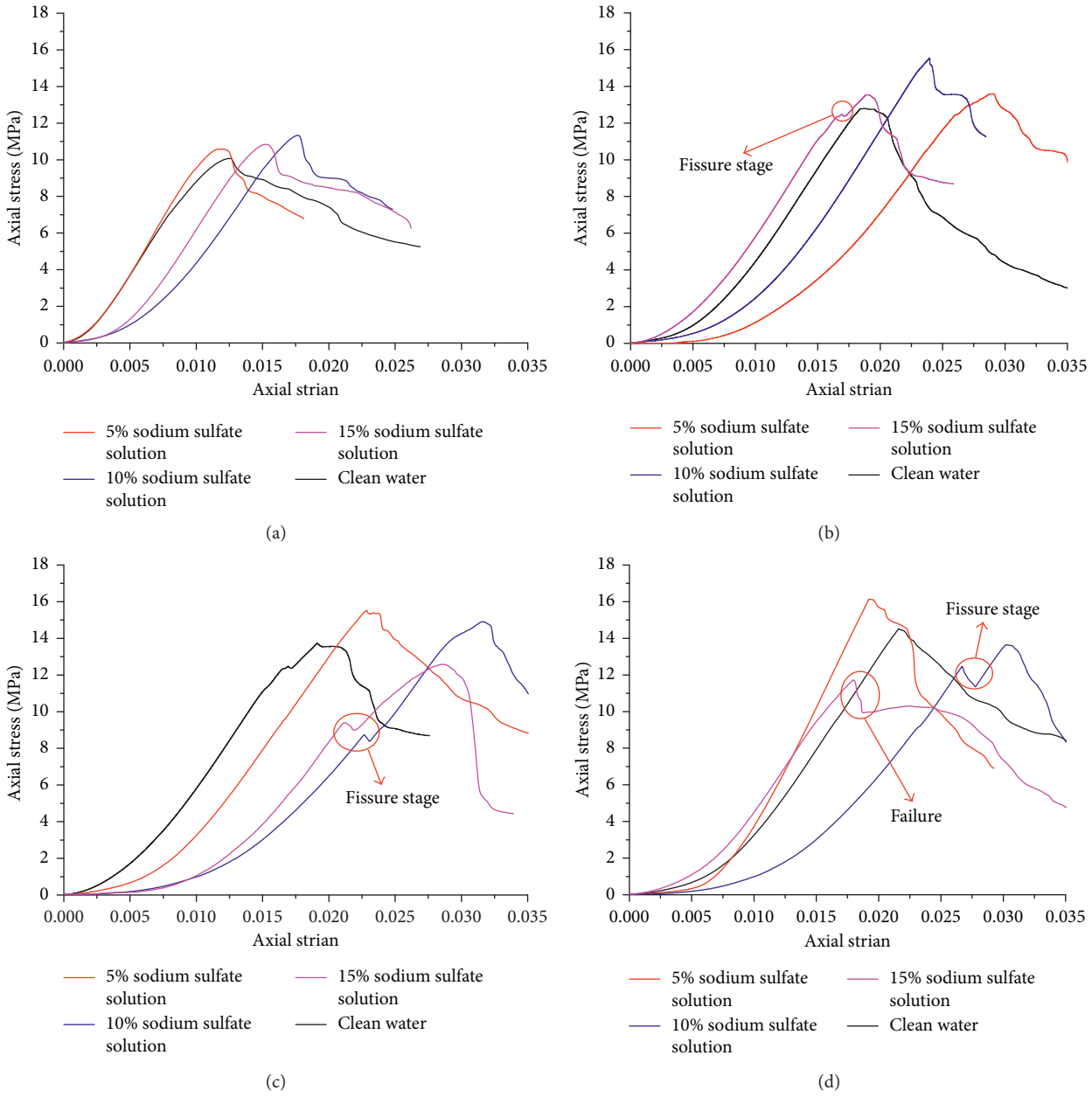

Figure 5: Stress-strain curves of each group for each soaking period: (a) 30 d; (b) 60 d; (c) 90 d; (d) 120 d.

with a high concentration of sulfate will first manifest a cracking stage, indicating strain energy release, and then enter into a compaction stage before finally reaching the peak stress and destroying the test block.

3.2. Results of XRD Analysis. Through the results of the strength testing of the test blocks soaked in varying sodium sulfate solutions, it was found that the differences in the solution concentration and soaking time had a significant effect on the filling paste test block strengths. To better understand these effects, XRD was used to analyze the hydration products and explore the regularity of the paste changes. Figure 7 shows the XRD pattern of the hydrated products in the filling paste soaked in different solutions for different periods of time.

As shown in Figure 7(a), after soaking in the four different solutions for 30 d, the strongest peak in the XRD analysis of the test samples is observed for SiO_2, indicating that there is still a great deal of cement and fly ash that has not yet been hydrated in the filling paste. At this time, the main products in the test blocks soaked in clean water are $Ca(OH)_2$, hydrated calcium silicate (C-S-H), hydrated calcium aluminate (C-A-H), and hydrated calcium aluminosilicate (C-A-S-H). With the addition of sodium sulfate in the soaking solution and with the increase in its concentration, the peak value of SiO_2 and C-A-H in the test blocks gradually decreased and $Ca(OH)_2$ disappeared, accompanied by

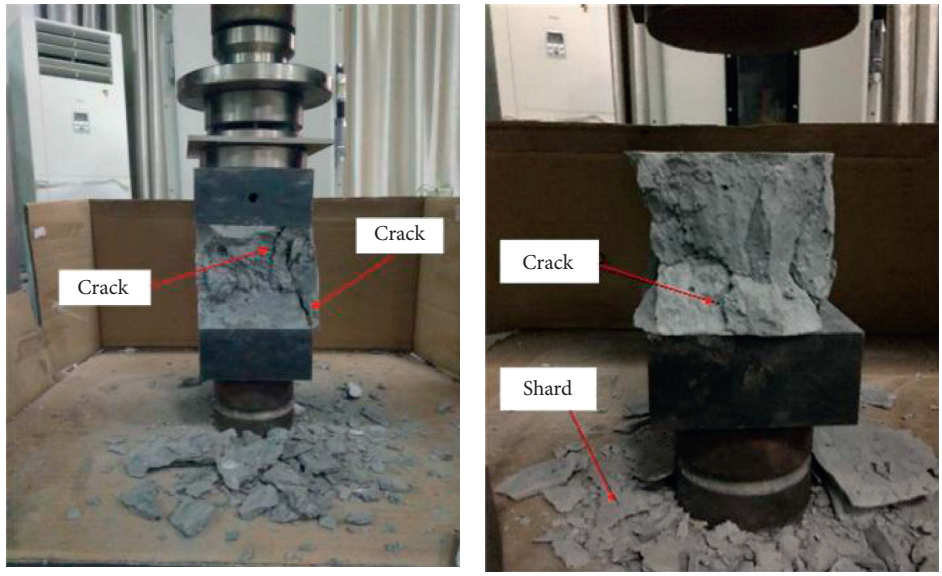

(a) (b)

Figure 6: Typical condition of a test block after destruction: (a) cracking; (b) flaking and peeling.

the formation of AFt. These changes are mainly due to the addition of the sodium sulfate, providing SO_4^{2-} for the production of AFt and consuming a large quantity of products such as $Ca(OH)_2$ and C-A-H. It can be inferred that in the early stages of soaking in sodium sulfate, AFt was produced inside the filling paste test blocks and filled in the internal voids, making the test blocks denser and thus stronger. This inference is supported by the fact that for a soaking time of 30 d, the strength of the test blocks soaked in the clean water was lower than that of the test blocks soaked in the sulfate solution, and within a certain sulfate range, the strength of the filling paste blocks increased with the increase in sulfate concentration.

In Figure 7(b), it can be seen that when the filling paste test blocks were soaked for 60 d, the diffraction peaks of the samples of each test set obviously grew in number, and the peak value of SiO_2 exhibited a downward trend. Compared with the samples soaked for 30 d, the number of C-S-H peaks of the samples soaked in clean water increased significantly, indicating that a large amount of hydrated calcium silicate was already produced in the filling paste to provide strength. A significant AFt peak appeared in the filling pastes soaked in sodium sulfate solutions. With the increase in sulfate concentration, the intensity of the AFt peak increased. At 60 d, the intensity of the AFt peak of the test blocks soaked in the 10% sodium sulfate solution was the largest, as was the uniaxial compressive strength, indicating that a proper amount of AFt can enhance the strength of the filling paste. However, gypsum began to appear in the test blocks that were soaked in the 15% sodium sulfate solution, and these blocks exhibited the lowest uniaxial compressive strength of all test blocks soaked for this duration, indicating that excessive SO_4^{2-} leads to the creation of expansive gypsum inside the filling paste, reducing its strength.

After soaking for 90 d, the uniaxial compressive strength of the test blocks decreased for larger concentrations of sulfate in the soaking solution. At this time, the strength of the test blocks soaked in the 5% sodium sulfate solution was the greatest. As can be seen from Figure 7(c), the larger the sulfate concentration, the higher the AFt peak exhibited in the XRD pattern of the hydration products in the test blocks. This means that the filling paste has generated a large amount of AFt by this time, which increases the internal stress in the test blocks while filling the voids in the block matrix. As this process continues, more microcracks are generated, thereby reducing the strength of the filling paste. The quantity of gypsum in the test blocks that were soaked in the 15% sodium sulfate solution showed a relative increase, and the test blocks soaked in the 10% sodium sulfate solution also indicated that gypsum was generated. This phenomenon suggests that a high concentration of sulfate can produce a large amount of gypsum in the filling paste, reducing its strength. The strength of the test blocks soaked in clean water was relatively improved after 90 d, and the peak value of SiO_2 in the XRD pattern was reduced. However, the diffraction peaks of gelling materials such as hydrated calcium silicate, hydrated calcium aluminate, and hydrated calcium aluminosilicate showed a significant increase, indicating that, as the hydration reaction progresses, large amounts of the SiO_2 in the filling paste are consumed to form hydrated calcium silicate and other gelling substances, which enhance the strength of the filling paste blocks.

After soaking for 120 days, the strength of the test blocks soaked in water and the 5% sodium sulfate solution still indicated a slow increase in strength. However, the uniaxial compressive strength of the test blocks soaked in the 10% and 15% sodium sulfate solutions decreased significantly. As can be seen from Figure 7(d), the XRD pattern of the test blocks soaked in the 10% and 15% sodium sulfate solutions shows significant increases in the AFt and gypsum peaks. This indicates that the mass production of AFt and gypsum affects the strength of the filling paste test blocks, and as such

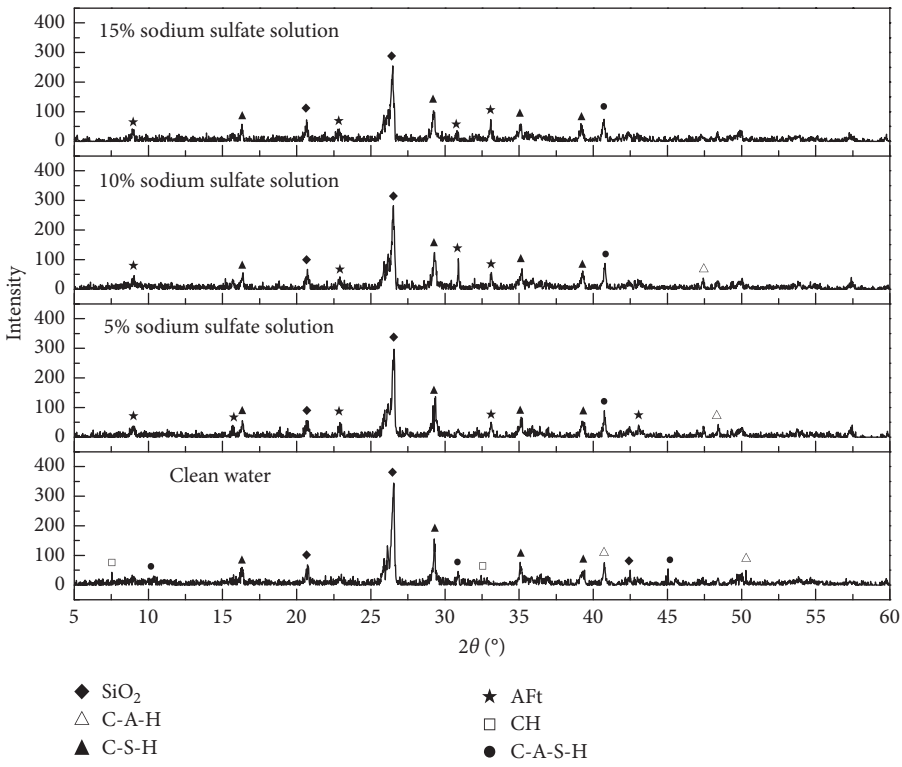

(a)

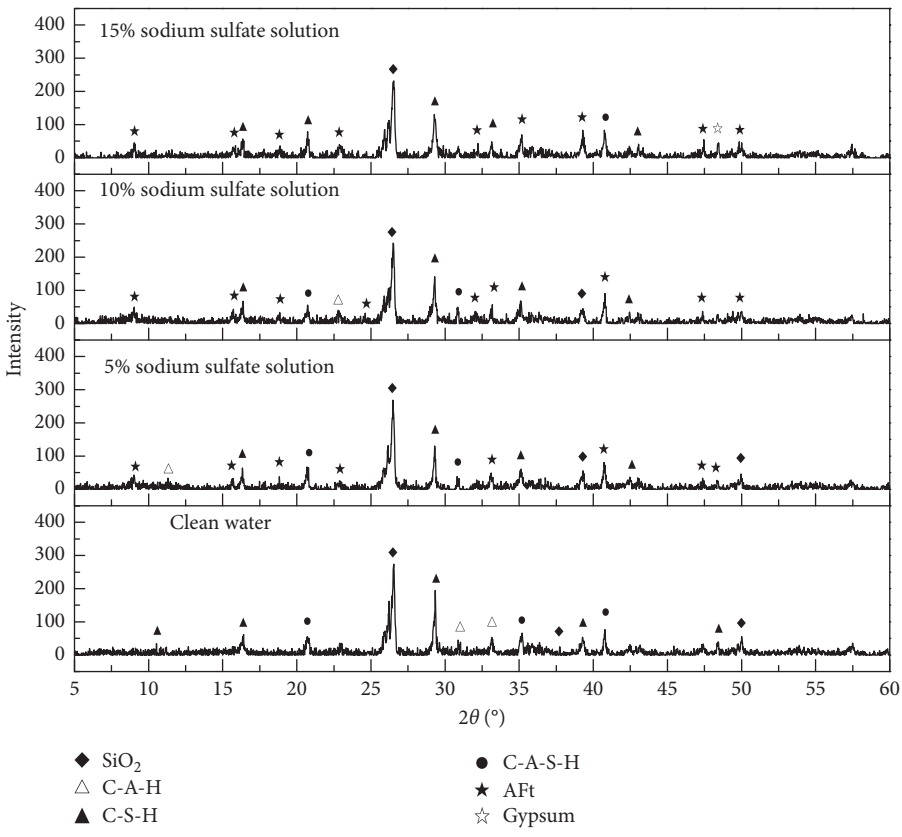

(b)

Figure 7: Continued.

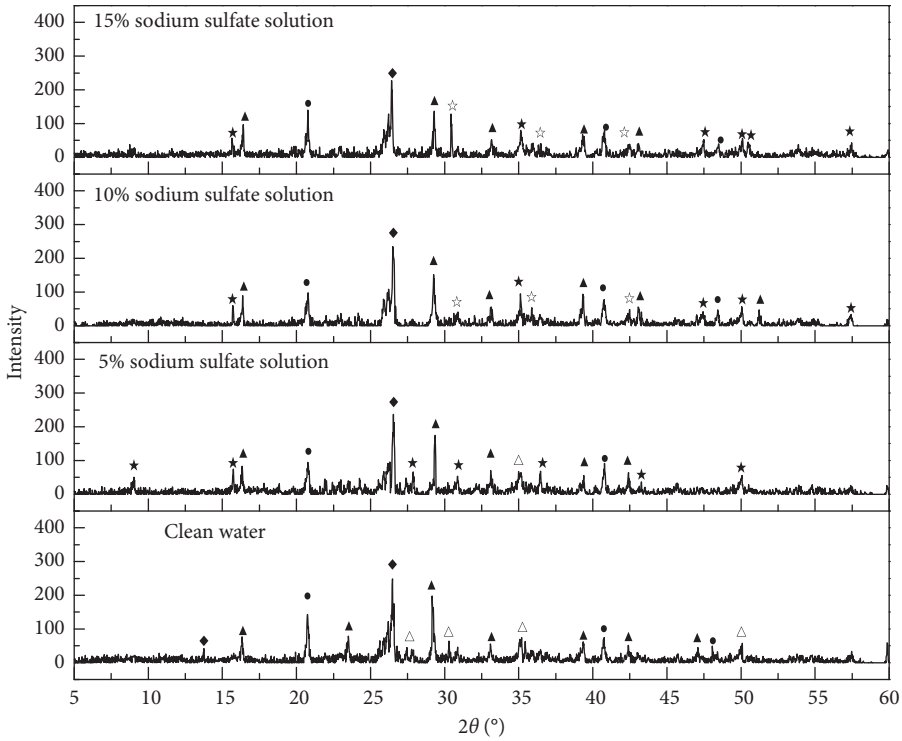

(c)

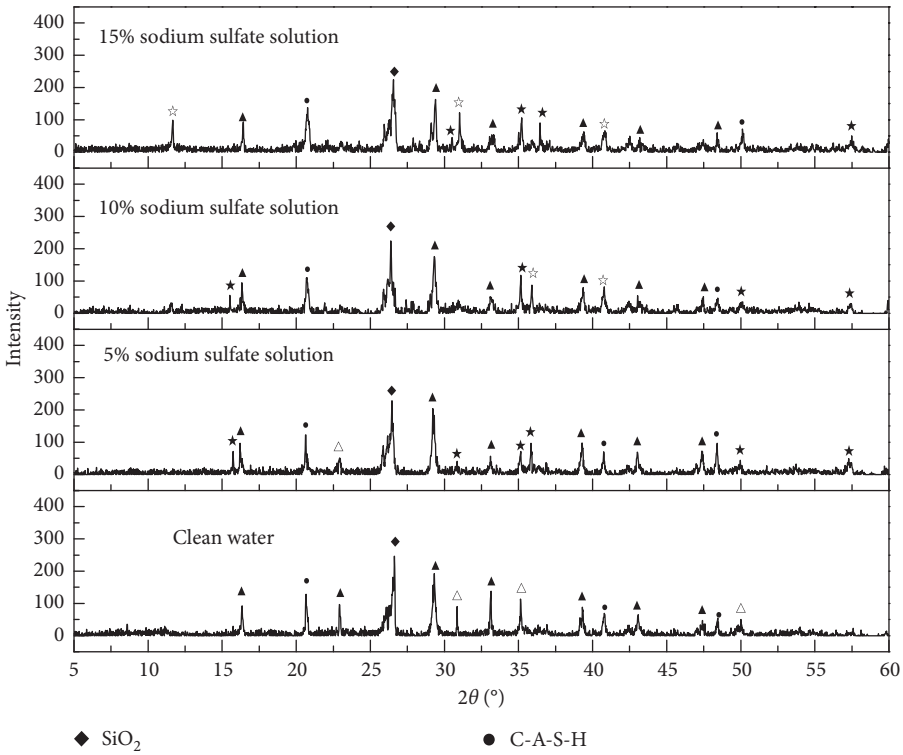

(d)

Figure 7: XRD patterns of hydrated products of filling paste in each immersion solution for each soaking period: (a) 30 d; (b) 60 d; (c) 90 d; (d) 120 d.

it is not conducive to the filling of mines. However, when the filling paste was soaked in the 5% sodium sulfate solution, there was no gypsum formed in the filling paste, and there was a small amount of C-A-H. This formation of the appropriate amount of AFt provides a higher strength than the other two sulfate-soaked test blocks. The test blocks soaked in clean water indicated that the hydrated calcium silicate, hydrated calcium aluminate, and hydrated calcium aluminate peaks had been enhanced but not to a significant degree. This suggests that because the change in product intensity is so gentle, the internal filling paste hydration is nearing saturation.

Figure 7 demonstrates that, for the same soaking period, the XRD patterns of the hydration products of filling pastes soaked in different solutions were similar, but the quantities of hydration products were different. For the same soaking solution and different soaking periods, the same XRD peaks for hydration products exhibited larger differences. The differences in the quantity of these hydration products have a significant effect on the strength of the filling pastes during each soaking period.

3.3. Action Mechanism of Sulfate in Fly Ash-Based Filling Paste. The influence of sulfate on the strength of fly ash-based filling paste is mainly determined by the hydration products. A large number of active SiO_2 and Al_2O_3 exist in fly ash, which only have potential cementitious activity. Without an activator, these substances do not generally produce gelling.

In an environment without sulfate, the $Ca(OH)_2$ generated by the hydration of the cement clinker provides an alkaline environment for the fly ash. The Si-O and Al-O bonds in the components are broken, and the glass phase is gradually dissolved. The silicon oxides in the vitreous body begin to hydrate, forming a large amount of C-S-H and C-A-H, providing strength for the cementing system. The chemical equation of this process is given as follows [26]:

$$\begin{aligned} SiO_2 + Ca(OH)_2 + H_2O &\longrightarrow CaO \cdot SiO_2 \cdot xH_2O \\ Al_2O_3 + Ca(OH)_2 + H_2O &\longrightarrow CaO \cdot Al_2O_3 \\ &\quad \cdot xH_2O \\ Al_2O_3 + Ca(OH)_2 + 2SiO_2 + 3H_2O &\longrightarrow CaO \cdot Al_2O_3 \\ &\quad \cdot 2SiO_3 \cdot 4H_2O \end{aligned} \tag{1}$$

The XRD analysis indicated that with the increase in soaking time, the C-S-H and C-A-H diffraction peaks increased, which has an inevitable connection to the increase in strength. Compared to the test blocks soaked in clean water, there are many more AFt formations in the hydration products of the paste test blocks soaked in sodium sulfate solutions, and the amount of AFt produced also affects the strength of the paste. After the sulfate ions enter the interior of the filling paste, they can react with the unreacted $Ca(OH)_2$ to generate calcium sulfate, then calcium sulfate reacts with hydrated calcium aluminate ($4CaO{\cdot}Al_2O_3{\cdot}13H_2O$) in the fly ash and cement to form hydrated calcium sulfoaluminate, that is, AFt. The reaction equation is as follows [36]:

$$\begin{aligned} 4CaO \cdot Al_2O_3 \cdot 13H_2O + 3(CaSO_4 \cdot 2H_2O) + 14H_2O \\ \longrightarrow 3CaO \cdot Al_2O_3 \cdot 3CaSO_4 \cdot 32H_2O + Ca(OH)_2 \end{aligned} \tag{2}$$

Because AFt can be stably present and exhibits expandability, a small amount of sulfate ion-generated AFt can fill the gaps in the interior of the paste, increasing the strength of the paste. However, the excessive formation of AFt expands the filling paste, increasing the internal stress and reducing strength. Therefore, in the early stages of soaking, the strengths of the paste blocks soaked in sodium sulfate solutions are relatively high. With the increase in soaking time, the strength of the test blocks soaked in high-concentration sodium sulfate solutions decreases, indicating that when the SO_4^{2-} is too high in the groundwater environment in which the filling paste is applied, gypsum crystals will be precipitated. The reaction equation is as follows [37]:

$$Ca(OH)_2 + SO_4^{2-} + 2H_2O \longrightarrow CaSO_4 \cdot 2H_2O + 2OH^- \tag{3}$$

Filling pastes soaked in the 10% and 15% sodium sulfate solutions will produce gypsum in the later stages of soaking, and their strengths will decrease accordingly. This demonstrates that the production of gypsum has a negative influence on the strength of the filling paste. The formation of gypsum increases the volume of the filling paste, and internal expansion stress is produced in the filling body, leading to damage of the test blocks. At the same time, the consumption of $Ca(OH)_2$ inside the filling paste decomposes the gelling substances generated within the paste, further reducing its strength.

4. Conclusions

A series of filling paste test blocks were soaked in varying concentrations of sodium sulfate solutions for varying durations. The uniaxial compressive strengths of the blocks were then determined, and XRD analyses of the constituent materials of the pastes were conducted to identify the products present in the paste material. The testing program resulted in the following conclusions:

(1) In the early stages of immersion, the uniaxial compressive strength of the filling paste test blocks soaked in 10% sodium sulfate solution was the highest. With the increase in soaking time, the uniaxial compressive strengths of the test blocks soaked in clean water and the 5% sodium sulfate solution were improved, while the strength of the filled paste test blocks soaked in the 10% and 15% sodium sulfate solutions decreased after soaking for 60 d.

(2) After soaking for 120 d, the uniaxial compressive strength of the filling paste test blocks soaked in the 5% sodium sulfate solution was the highest, indicating that an appropriate concentration of sodium sulfate in the soaking solution acts as an activator for the fly ash in the filling paste.

(3) The stress-strain curves indicate that the elastic moduli of the filling paste test blocks change irregularly. After soaking for 60 d, the strength of the filling pastes soaked in a higher concentration than the 5% sodium sulfate solution began to display microcracks, affecting the strength of the test blocks.

(4) It can be seen from the XRD patterns that the main hydration product generated in the filling paste was C-S-H. The main product generated in the filling paste test blocks soaked in the sodium sulfate solution was initially AFt, though with the increase in the concentration of sodium sulfate and soaking time, gypsum crystals appeared in the filling paste, which are detrimental to the strength of the test blocks.

(5) A concentration of 5% sodium sulfate is helpful for improving the strength of a fly ash-based filling paste. Sodium sulfate solutions with concentrations of 10% and 15% increased the early strength of the filling paste faster, but with the continued increase in AFt and gypsum crystals after longer soaking durations, the strength decreased, and thus sulfate concentrations of this intensity are not conducive to the durability of a fly ash-based filling paste.

This research has determined that the presence of sulfate in mine water can be useful to the properties of filling pastes containing fly ash. However, the concentrations of sulfates in the subject mine must be carefully determined, as excessive concentrations of sulfates can lead to detrimental effects of the strength of the filling paste. By quantifying the behaviors of fly ash-based filling pastes in sulfate environments, this research has defined how this material can be successfully applied to coal mine filling.

Data Availability

All data are available within the article or from the corresponding author upon request.

Conflicts of Interest

The authors declare that they have no conflicts of interest.

Acknowledgments

This research was supported by China Coal Industry Association Science and Technology Research Guidance Project (MTKJ2016-277) and received grants from the Natural Science Foundation of Shandong Province (ZR2017MEE055), Key Project of Green and High Efficiency Mining and Comprehensive Utilization of Mineral Resources in Henan Province (s201609).

References

[1] Q. L. Chang, H. Q. Zhou, J. B. Bai et al., "Study and practice of overburden stability of paste filling and mining," *Journal of Mining and Safety Engineering*, vol. 28, no. 2, pp. 279–282, 2011.

[2] S. J. Chen, D. W. Yin, F. W. Cao, Y. Liu, and K. Ren, "An overview of integrated surface subsidence-reducing technology in mining areas of China," *Natural Hazards*, vol. 81, no. 2, pp. 1129–1145, 2016.

[3] J. L. Xu, Q. You, W. B. Zhu, X. S. Li, and W. Q. Lai, "The theoretical study of strip filling control mining subsidence," *Journal of China Coal Society*, vol. 32, no. 2, pp. 119–122, 2007.

[4] H. J. Zhao, F. S. Ma, Y. M. Zhang, and J. Guo, "Monitoring and mechanisms of ground deformation and ground fissures induced by cut-and-fill mining in the Jinchuan Mine 2, China," *Environmental Earth Sciences*, vol. 68, no. 7, pp. 1903–1911, 2013.

[5] W. B. Zhu, J. M. Xu, J. L. Xu, D. Y. Chen, and J. X. Shi, "Pier-column backfill mining technology for controlling surface subsidence," *International Journal of Rock Mechanics and Mining Sciences*, vol. 96, pp. 58–65, 2017.

[6] Y. Liu, Y. Lu, H. Guo, and B. Q. Cui, "Experimental study on proportion optimization of construction waste paste filling materials," *Safety in Coal Mines*, vol. 48, no. 6, pp. 65–68, 2017.

[7] M. G. Qian, J. L. Xu, and X. X. Miu, "Coal mine green mining technology," *Journal of China University of Mining and Technology*, vol. 32, no. 4, pp. 343–348, 2003.

[8] W. C. Li, *Characteristics and mechanism of sulphate effect on the early age properties of cemented paste backfill*, Ph.D. dissertation, China University of Mining & Technology, Beijing, China, 2016.

[9] H. Q. Zhang, Y. Liu, and Q. F. Wang, "Study on performance of filling with urban construction waste," *Mining Research and Development*, vol. 34, no. 4, pp. 37–39, 2014.

[10] W. M. Cheng, X. M. Hu, J. Xie, and Y. Y. Zhao, "An intelligent gel designed to control the spontaneous combustion of coal: fire prevention and extinguishing properties," *Fuel*, vol. 210, pp. 826–835, 2017.

[11] Z. D. Cui and H. H. Sun, "The preparation and properties of coal gangue based sialite paste-like backfill material," *Journal of China Coal Society*, vol. 35, no. 6, pp. 896–899, 2010.

[12] O. Nasir and M. Fall, "Shear behavior of cemented pastefill–rock interfaces," *Engineering Geology*, vol. 101, no. 3–4, pp. 146–153, 2008.

[13] T. Y. Qi, G. R. Feng, Y. X. Guo et al., "Experimental study on the changes of coal paste backfilling material performance during hydration process," *Journal of Mining and Safety Engineering*, vol. 32, no. 1, pp. 42–48, 2015.

[14] Z. C. Wang, H. C. Xia, and H. F. Wang, "Analysis of hydration mechanism and microstructure of composite cementitious materials for filling mining," *Journal of Wuhan University of Technology*, vol. 32, no. 4, pp. 910–913, 2017.

[15] Y. Li, R. J. Wang, F. Yan, X. He, and Y. Sun, "Effect of fly ash on frost resistance and sulfate resistance of concrete," *Journal of Northwest A and F University*, vol. 45, no. 2, pp. 219–226, 2017.

[16] M. Fall, J. Célestin, and F. Han, "Suitability of bentonite-paste tailings mixtures as engineering barrier material for mine waste containment facilities," *Minerals Engineering*, vol. 22, no. 9-10, pp. 840–848, 2009.

[17] A. Ren, G. R. Feng, Y. X. Guo et al., "Influence on performance of coal mine filling paste with fly ash," *Journal of China Coal Society*, vol. 39, no. 12, pp. 2374–2380, 2014.

[18] R. Rani and M. K. Jain, "Effect of bottom ash at different ratios on hydraulic transportation of fly ash during mine fill," *Powder Technology*, vol. 315, no. 4, pp. 309–317, 2017.

[19] M. Fall and S.S. Samb, "Effect of high temperature on strength and microstructural properties of cemented paste backfill," *Fire Safety Journal*, vol. 44, no. 4, pp. 642–651, 2009.

[20] D. Wu, Y. B. Hou, T. F. Deng, Y. Z. Chen, and X. L. Zhao, "Thermal, hydraulic and mechanical performances of cemented coal gangue-fly ash backfill," *International Journal of Mineral Processing*, vol. 162, no. 3, pp. 12–18, 2017.

[21] Q. F. Wang, Y. Liu, H. Q. Zhang, and N. Jiang, "Durability test of gangue paste stowing material," *Coal Mining Technology*, vol. 19, no. 1, pp. 3–6, 2014.

[22] M. Gao, *Study on deterioration mechanism of cement-based rich-water material in corrosive environment*, Ph.D. dissertation, University of Science and Technology, Beijing, China, 2017.

[23] Q. Sun, X. L. Li, X. Wei, and Q.W. Mu, "Experimental study on the influence of mine water corrosion over filling paste strength," *Bulletin of the Chinese Ceramic Society*, vol. 34, no. 5, pp. 1246–1251, 2015.

[24] G. R. Feng, Y. F. Ren, X. Y. Zhang et al., "The activating experimental research of fly ash for mining filling material in Tashan Mine," *Journal of China Coal Society*, vol. 36, no. 5, pp. 732–737, 2011.

[25] X. L. Guo, H. S. Shi, and W. A. Dick, "Utilization of thermally treated flue gas desulfurization (FGD) gypsum and class-C Fly Ash (CFA) to prepare CFA-based geopolymer," *Journal of Wuhan University of Technology*, vol. 28, no. 1, pp. 132–138, 2013.

[26] T. S. He and G. Q. Wei, "Effect of activators excitated cement specimen with different amount of fly ash on strength," *Concrete*, vol. 235, no. 5, pp. 62–64, 2009.

[27] G. J. Ke, X. F. Yang, H. Peng et al., "Progress of research on chemical activating mechanisms of fly ash," *Journal of China Coal Society*, vol. 30, no. 3, pp. 366–370, 2005.

[28] M. Fall and M. Benzaazoua, "Modeling the effect of sulphate on strength development of paste backfill and binder mixture optimization," *Cement and Concrete Research*, vol. 35, no. 2, pp. 301–314, 2005.

[29] M. Pokharel and M. Fall, "Combined influence of sulphate and temperature on the saturated hydraulic conductivity of hardened cemented paste backfill," *Cement and Concrete Composites*, vol. 38, no. 3, pp. 21–28, 2013.

[30] M. Fall and M. Pokharel, "Coupled effects of sulphate and temperature on the strength development of cemented tailings backfills: Portland cement-paste backfill," *Cement and Concrete Composites*, vol. 32, no. 10, pp. 819–828, 2010.

[31] J. H. Liu, M. Gao, and A. X. Wu, "Corrosion and deterioration mechanism of water-rich filling materials in acid solution," *Chinese Journal of Engineering*, vol. 38, no. 9, pp. 1212–1220, 2016.

[32] Q. Sun, X. L. Li, and X. Wei, "Study on creep property of paste filling material under sulfate corrosion," *Journal of Safety Science and Technology*, vol. 11, no. 3, pp. 12–18, 2015.

[33] W. C. Li and M. Fall, "Sulphate effect on the early age strength and self-desiccation of cemented paste backfill," *Construction and Building Materials*, vol. 106, no. 12, pp. 296–304, 2016.

[34] X. G. Zhang, J. Lin, J. X. Liu, F. Li, and Z. Z. Pang, "Investigation of hydraulic-mechanical properties of paste backfill containing coal gangue-fly ash and its application in an underground coal mine," *Energies*, vol. 10, no. 9, p. 1309, 2017.

[35] Y. Liu, *Experimental study on the performance of paste backfilling materials with construction waste recycled aggregate*, Ph.D. dissertation, University of Science and Technology, Shandong, China, 2013.

[36] G. S. Li, "Sulfate resistance of fly ash concrete (English)," *Journal of the Chinese Ceramic Society*, vol. 40, no. 1, pp. 39–48, 2012.

[37] F. G. Leng, Y. X. Zhou, and J. Wang, *Inspection and assessment of concrete durability*, Building Materials Press, Beijing, China, 2012.

Hindawi
Advances in Materials Science and Engineering
Volume 2018, Article ID 9297628, 9 pages
https://doi.org/10.1155/2018/9297628

Research Article

Mechanical and Electrical Characteristics of Graphite Tailing Concrete

Hongbo Liu,[1] Kun Liu ,[2,3] Zhu Lan,[1] and Dashuang Zhang[1]

[1]*School of Civil Engineering and Architecture, Heilongjiang University, Harbin 150080, China*
[2]*Key Lab of Structures Dynamics Behavior and Control of the Ministry of Education, Harbin Institute of Technology, Harbin 150080, China*
[3]*Key Lab of Smart Prevention and Mitigation of Civil Engineering Disasters of the Ministry of Industry and Information Technology, Harbin Institute of Technology, Harbin 150080, China*

Correspondence should be addressed to Kun Liu; kun.liu@hit.edu.cn

Received 21 February 2018; Revised 11 July 2018; Accepted 25 July 2018; Published 14 August 2018

Academic Editor: Estokova Adriana

The graphite tailing causes serious environmental pollution, and the pollution problem becomes worse and worse with the increase in graphite demands. This paper focuses on the graphite tailing concrete, which can alleviate the environment problem through utilizing graphite tailings. With the orthogonal experimental design, 16 groups of specimens were designed to investigate the compressive strength of the graphite tailing concrete, and each group had 6 specimens. The significance sequence of the influencing factors for the compressive strength was studied, including the ratio of water to cement, sand ratio, graphite tailings content, and carbon fiber content. The optimal contents of graphite tailings and carbon fiber were obtained from the further experimental study on the electrical characteristics of the graphite tailing concrete, and a regression analysis was conducted to develop the predictive mixture design relationships for the electrical resistivity of the conductive graphite tailing concrete. The experimental results show that the conductive concrete mixture containing graphite tailings and carbon fiber has satisfactory mechanical strength along with well electrical conductivity. With the increase in graphite tailings content, the compressive strength decreases slowly, but the electrical resistivity decreases much more obviously. Predictions with the proposed relationship are in reasonable agreement with experimental results. This study provides references for the graphite tailing utilization alleviating the environment problems.

1. Introduction

Graphite tailings are derived from froth flotation process of graphite ores [1]. With the increase in graphite production, the massive tailings containing hydrocarbon oil, diesel oil, and heavy metals have been generated during the past years in China, which pollute environment and occupy a large amount of land. The tailing dust flies with the wind, which causes serious air contamination. Most of the previous researches on graphite tailing mainly focused on the vanadium extraction, the evaluation of heavy metal pollution, and the preparation of foam concrete [2, 3]. It has been pointed out that the graphite tailings so far have not been effectively developed and utilized [4]. In this paper, the graphite tailing conductive concrete will be studied, which can utilize the graphite and alleviate environment problems.

Conductive concrete is a kind of heterogeneous material that is composited by binding and conductive materials, dielectric aggregates, and water [5]. The usage of electrically conductive concrete for deicing is a relatively new material technology, and the conductive concrete could pave way to heat roads [5], bridges [6], and airport [7, 8]. Paving a bridge deck with the electrically conductive concrete could also provide cathodic protection for the reinforcing steel [9]. In conductive concrete, conductive materials [10–12] that replace ordinary concrete aggregates provide with high electrical conductivity, and conductive materials usually include graphite, steel fiber, and carbon fiber [13]. Graphite has good

electrical conductivity and pressure-sensitive characteristics, and it can be easily obtained in powder form [1]. Concrete added graphite powder will perform well conductivity, but former studies indicate that the strength of concrete will reduce rapidly with increasing graphite powder dosage [14]. When the graphite dosage is greater than 15%, the increase of the conductivity is not obvious, but the compressive strength decreases remarkably [15]. There is some graphite left in the graphite tailings, so the graphite tailings can provide conductive materials for the conductive concrete [1]. The additions of graphite tailings can reduce the electrical resistivity of concrete, and the tailings have less effect on the strength of concrete than pure graphite because the graphite fuses with rock. But the graphite content in tailings is limited, so another conductive material is needed to be added in the concrete to increase the conductivity.

Steel fiber and carbon fiber are other two conductive materials used in concrete usually [13]. The steel fiber-reinforced concrete is in many ways a well-known construction material, and its use has gradually increased over the last decades [16]. Yet the resistivity of steel fiber conductive concrete is not stable and changes with ages and environment. The alkaline environment in the concrete causes the steel fiber to produce a layer of passive film, which leads to the increase in resistivity, so steel fiber alone is unstable as conductive material [17]. The resistivity of carbon fiber is stable at high and low temperatures, and carbon fiber possesses a satisfactory corrosion resistance. In recent years, carbon fiber-reinforced polymer (FRP) materials in the form of fabrics and laminates have been motivated to use for retrofitting these corrosion-damaged reinforced concrete components [18]. The resistivity will be different with same carbon fiber if the uniform dispersal in concrete cannot be ensured, so the uniform dispersal of the carbon fiber is a key factor of using it as conductive material in concrete [13]. The use of a dispersive agent is necessary to disperse carbon fiber evenly in concrete [13, 19], but the carbon fiber as conductive material is stable. The tailings are easy to disperse in concrete, because graphite tailing size composition is even and the average particle size is 0.10 mm, which also will improve the uniform dispersal of the carbon fiber. Based on the above discussion, the steel fiber is not considered and the carbon fiber is adopted in the graphite tailing concrete as additional conductive material in this study, because the stability is a key issue for construction material.

Graphite tailing concrete can be applied as conductive concrete if the electrical resistivity is good enough [20], but mechanical properties of the graphite tailing concrete are the important factors in civil engineering. So the compressive strength should be studied at first. The orthogonal experimental design method has been adopted widely in civil engineering, such as construction material [21, 22] and structural optimization [23]. Orthogonal experimental design is the study of multifactor and level of design method, through the part of the test to find out the optimal level combination [24]. In this study, there are four key factors affecting the compressive strength of the conductive concrete including the ratio of water to cement, sand ratio, graphite tailings content, and carbon fiber content. It would require too many specimens with the full factorial design, so the orthogonal experimental design will be adopted for the compressive strength experimental study to reduce the required experimental specimens [25]. For the electrical characteristic experiment study, the four-electrode method will be adopted, which has been proved that it can provide more accurate measured results [26] than those with other measured methods.

In order to alleviate the environment problem through utilizing graphite tailings, the following studies are performed. Graphite tailings are added to the conventional concrete to make the conductive graphite tailing concrete, and carbon fibers are added to further improve the electrical conductivity. The effects of the ratio of water to cement, sand ratio, graphite tailings content, and carbon fiber content on mechanical characteristics are studied experimentally based on the orthogonal experimental design, and then, the electrical characteristics are studied with the four-electrode method. The optimal contents of graphite tailings and carbon fiber are studied, and the mixture design relationships for the electrical resistivity are predicted by regression analysis.

2. Experimental Materials

2.1. The Composition of the Graphite Tailings. The graphite tailing sample on experiment is obtained from a graphite mine in Jixi City, China. The chemical composition is analyzed with X-ray fluorescence, and the results are shown in Table 1.

The mineral composition of tailings was analyzed with X-ray diffraction mineral identification. The main mineral compositions of the tailings are quartz, grossular, lead bismuth vanadium oxide, graphite, and so on. Table 1 shows that the main composition of tailings is SiO_2, and there are also high levels of Al_2O_3 and CaO in the graphite tailing samples. From the chemical composition, it meets the basic requirements of concrete aggregate.

2.2. Other Experimental Materials. The cement used was Portland cement PI 42.5 provided by Harbin Swan cement factory, China. Standard river sand was used as fine aggregates. Crushed stone was used as coarse aggregates, and the particle size was no more than 20 mm. Chopped carbon fibers of 7 μm in diameter and 6 mm in nominal length were used as the additional conductive filler, and hydroxyethyl cellulose was used as the dispersive agent of carbon fiber. Defoamer was added to accompany hydroxyethyl, and the defoamer-cement ratio was 0.15% (by volume). The ratio of naphthalene superplasticizer to cement was 1% (by weight).

3. Compressive Strength

3.1. Orthogonal Experiment Design. There are four factors that affect the concrete mechanical and electrical properties to be investigated in this study: (A) water/cement material (W/C) ratio, (B) sand ratio, (C) tailings content, and (D) chopped carbon fiber content, and each factor has four

Table 1: Chemical composition of graphite tailings.

Composition	Fe_2O_3	MgO	Al_2O_3	SiO_2	CaO	K_2O	C	V_2O_5	Loss
Content (%)	5.073	2.326	10.205	62.498	15.547	2.26	1.13	0.308	0.653

different levels. Since the full factorial design requires 256 mixes, the orthogonal experimental design was adopted to reduce the number of mixes.

Orthogonal experimental design is based on the probability theory, the mathematical statistics, and the standardized orthogonal table. Orthogonal experimental design can select the right amount of representative samples from a large number of experimental designs to arrange experiments reasonably. To design an optimal test, it should have reasonable indicator and reference for selecting factor and the corresponding level. In this test, all the factors and corresponding levels are shown in Table 2.

The foundation of the orthogonal experimental design is the orthogonal table, and it forms as

$$\mathbf{L}_n\left(m^k\right), \tag{1}$$

where $\mathbf{L}$ is the symbol of the orthogonal table, n is the number of trials arranged by the orthogonal table (it is 16 in this study), m is the most number of factors arranged in the orthogonal table (it is selected to be 4 in this study), and k is the each factor level number to get the largest number in each single factor (it is selected to be 5 in this study).

According to the orthogonal experimental design table of $\mathbf{L}_{16}(4^5)$, a total of 16 mixes were tested. Tailings content was calculated by total weight. Carbon fiber content was calculated by total volume, and the density of carbon fiber is $1.76 \times 103\,\text{kg/m}^3$. The details of the tested mixture composition per cubic metre are listed in Table 3. The target compressive strength is $40\,\text{N/mm}^2$ when W/C is 0.49, the target compressive strength is $35\,\text{N/mm}^2$ when W/C is 0.54, the target compressive strength is $30\,\text{N/mm}^2$ when W/C is 0.60, and the target compressive strength is $25\,\text{N/mm}^2$ when W/C is 0.49.

Hydroxyethyl was first added into water and left for 20 minutes letting it dissolve completely, and then carbon fibers and defoamer were added into water and stirred gently. The rest of the mixing water was poured into the mixer followed by the superplasticizer. Then, the cement was added and stirred by a rotary mixer for 3 minutes. The mixer was stopped, and the carbon fibers were poured into the mixer. When the mixer was run for 1 minute, the sand and the tailings were added and stirred for 3 minutes. Finally, the crushed stones were added and stirred for 3 minutes. After the mixture was poured into an oiled mold, the electrode (if applicable) was laid in fresh concrete. Then an external vibrator was used to facilitate compaction and decrease the amount of air bubbles. The samples were demolded after 24 hours and then cured under the standard condition at a temperature of 20°C and a relative humidity of 100% for 28 days [27].

The size of the concrete specimens for compressive strength tests was $150\,\text{mm} \times 150\,\text{mm} \times 150\,\text{mm}$, and each group with same mix proportion had 6 specimens for compressive strength tests as shown in Figure 1(a). Compressive strength was tested according to Standard for Test Method of Mechanical Properties on Ordinary Concrete (by Chinese Standard GB/T 50081-2002), and a servo-controlled hydraulic testing machine as shown in Figure 1(b) was used to apply a constant stress rate of 300 kPa/s.

Table 2: Factors and levels.

Level	W/C	Sand ratio (%)	Tailings content (%)	Carbon fiber content (%)
Level 1	0.49	30	0	0
Level 2	0.54	33	5	0.15
Level 3	0.60	36	10	0.30
Level 4	0.68	39	15	0.45

3.2. Result Analysis. The compressive strengths are listed in Table 4, and the orthogonal experimental analysis is employed to obtain the optimal concrete mix [28]. The range analysis is conducted to evaluate the significance levels of all the influencing factors and select the optimal level of each factor. For range analysis, the Kam value and range value (R) are calculated as listed in Table 5. The Kam value for each level of a parameter is the arithmetic mean of four values of samples with the same level. For example, for concrete strength, the Kam 1 for parameter A is the arithmetic mean of concrete strength of samples with W/C of 0.49. The range value for each factor is the difference between the maximal and minimal values of the four levels, and the most significant factor has the highest R value. According to the R value, the most significant factor is tailings content, followed by W/C, and they have similar degree of influence. However, for sand ratio and carbon fiber content, the strength changes are insignificant (5.1% and 2.0% changes, resp.) as the parameter level changed.

Figure 2(a) shows the relationship between arithmetic mean of compressive strength and W/C. It shows that the arithmetic mean of compressive strength reduces 32.3% when the W/C increases from 0.49 to 0.68, which is consistent with target compressive strength and present researches [29, 30].

Figure 2(a) shows the relationship between arithmetic mean of compressive strength and W/C. It shows that the arithmetic mean of compressive strength reduces 32.3% when the W/C increases from 0.49 to 0.68, which is consistent with target compressive strength and present researches [29, 30].

Adopted sand ratio in the tests derives from the rational range of Standard for Test Method of Mechanical Properties on Ordinary Concrete, and the variations among levels are not very large as shown in Figure 2(b). It shows that the compressive strength decreases with the increase in sand ratio, but the differences are very small. It is consistent with

Table 3: The composition of the tested mixture per cubic metre.

Specimen	Water (kg/m^3)	Cement (kg/m^3)	Sand (kg/m^3)	Crushed stone (kg/m^3)	Graphite tailings (kg/m^3)	Carbon fiber (kg/m^3)
1	195	397.96	542.11	1264.93	0	0
2	195	397.96	556.72	1130.32	120	2.64
3	195	397.96	564.13	1002.91	240	5.28
4	195	397.96	564.35	882.69	360	7.92
5	195	361.11	517.17	1206.72	120	5.28
6	195	361.11	608.48	1235.41	0	7.92
7	195	361.11	534.2	949.69	360	0
8	195	361.11	625.52	978.37	240	2.64
9	195	325	492	1148	240	7.92
10	195	325	501.6	1018.4	360	5.28
11	195	325	676.8	1203.2	0	2.64
12	195	325	686.4	1073.6	120	0
13	195	286.76	467.47	1090.76	360	2.64
14	195	286.76	553.82	1124.42	240	0
15	195	286.76	647.36	1150.87	120	7.92
16	195	286.76	748.11	1170.12	0	5.28

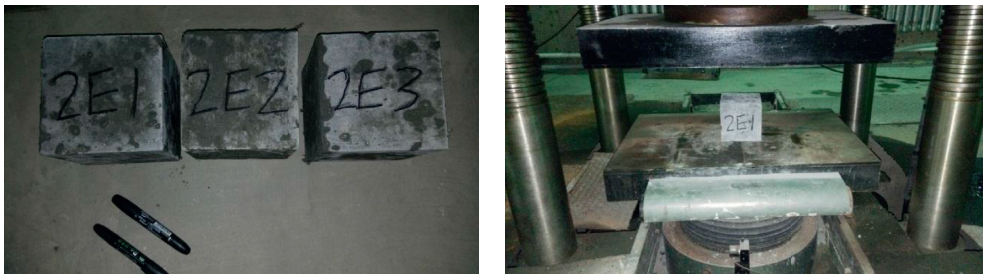

(a) (b)

Figure 1: Compressive strength test. (a) Test specimen and (b) servo-controlled hydraulic testing machine.

Table 4: Compressive strength.

Specimen	W/C	Sand ratio (%)	Tailings content (%)	Carbon fiber content (%)	Compressive strength (N/mm^2)	Standard deviation of compressive strength
1	0.49	30	0	0	43.7	1.315
2	0.49	33	5	0.15	41.2	0.834
3	0.49	36	10	0.30	39.6	0.942
4	0.49	39	15	0.45	31.2	0.994
5	0.54	30	5	0.30	38.5	0.529
6	0.54	33	0	0.45	42.6	1.227
7	0.54	36	15	0	24.9	1.058
8	0.54	39	10	0.15	34.3	0.962
9	0.60	30	10	0.45	32.9	1.183
10	0.60	33	15	0.30	24.3	0.752
11	0.60	36	0	0.15	35	0.617
12	0.60	39	5	0	31.6	0.897
13	0.68	30	15	0.15	20.4	0.825
14	0.68	33	10	0	22.8	0.529
15	0.68	36	5	0.45	30.9	0.776
16	0.68	39	0	0.30	31.3	1.269

the present common results of study that sand ratio mainly has effect on the workability of concrete and has little effect on compressive strength. The graphite tailings can also serve as part action of fine aggregates, so it leads to that the sand ratio is near 30% in the experiment which makes the compressive strength to be higher with enough workability.

Table 5: Range analysis on compressive strength (N/mm^2).

Factors	*W*/*C*	Sand ratio	Tailings content	Carbon fiber content
Kam 1	38.925	33.875	38.15	30.75
Kam 2	35.075	32.725	35.55	32.725
Kam 3	30.95	32.6	32.4	33.425
Kam 4	26.35	32.1	25.2	34.4
R	12.575	1.775	12.95	3.65

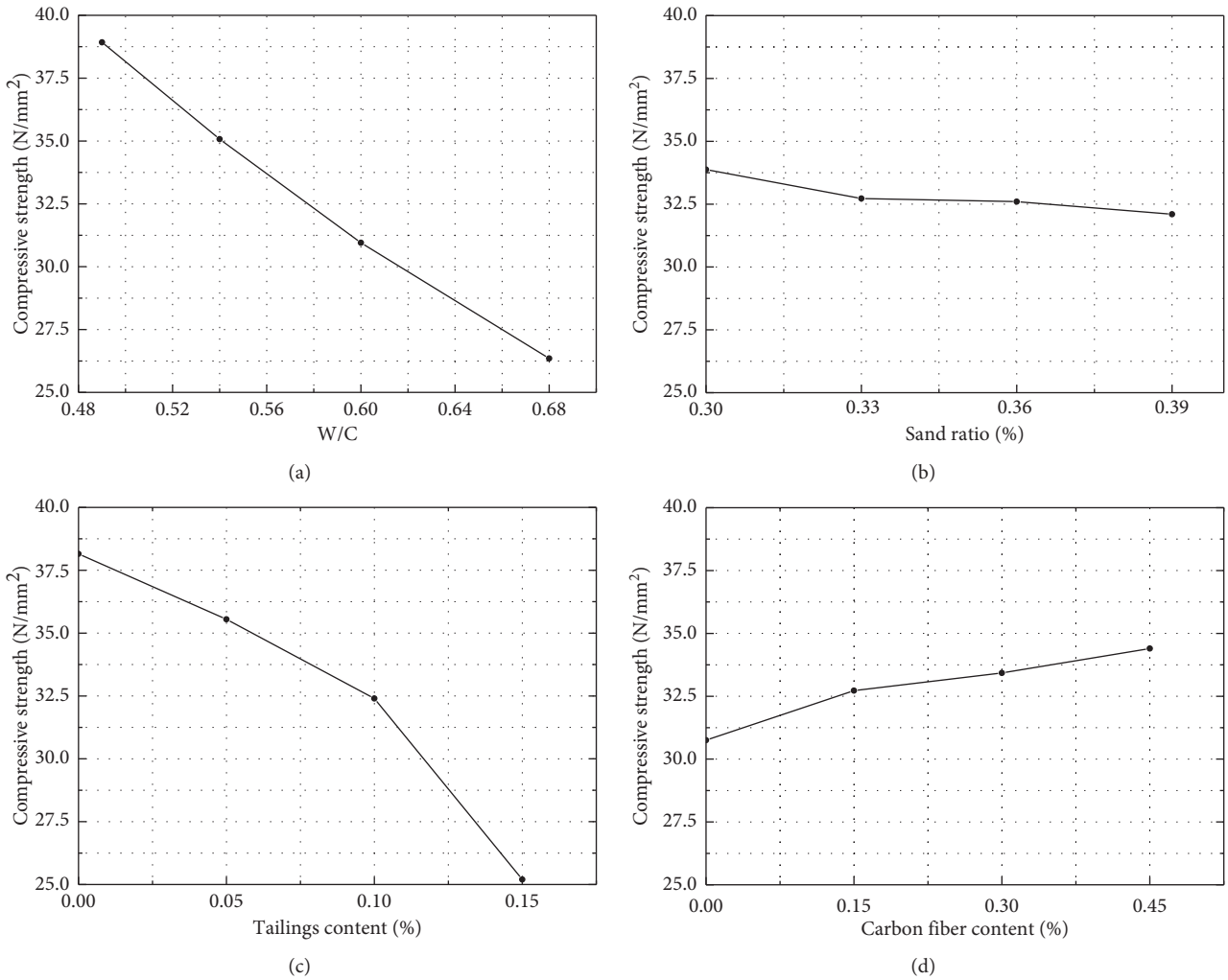

Figure 2: Relationship between compressive strength and affecting factors. (a) *W*/*C*; (b) sand ratio; (c) tailings content; (d) carbon fiber content.

The arithmetic mean of compressive strength decreases with the increase of graphite tailings content as shown in Figure 2(c). In the beginning, the degradation of compressive strength is not very fast. The strength of concrete will reduce rapidly if the graphite tailings content is greater than 10%. Graphite tailings also contain some free graphite and hydrocarbon oil which will lead to degradation of strength rapidly. When tailings content is 10%, the relationship between compressive strength and target strength is listed in Table 6, which is extracted from Table 4. The compressive strength does not reduce too much with respect to the target strength because compressive strength can be slightly improved by carbon fiber.

The chopped carbon fibers have a little reinforcing effect on compressive strength as shown in Figure 2(d). It is rod-like or mesh-like long carbon fibers that have been heretofore used for a carbon fiber-reinforced concrete, and short carbon fibers are used only for mortar containing no coarse aggregate or spraying repair material. One reason is that the carbon fibers are damaged when the carbon fibers are incorporated in the form of short fiber into a concrete containing a coarse aggregate. Even if the chopped carbon fibers are used, the

Table 6: Compressive strength and target strength.

Specimen	W/C	Tailings content (%)	Compressive strength	Target strength	Compressive strength (%)
3	0.49	10	39.6	40	−1.0
8	0.54	10	34.3	35	−2.0
9	0.60	10	32.9	30	9.7
14	0.68	10	22.8	25	−8.8

mechanical effect is only to prevent development of cracking that already occurred. The other reason is that the bonding between the carbon fibers and the cement matrix is not strong enough. In order to improve strength, it is important to have good bonding between the carbon fibers and the cement matrix. The carbon fiber surface is coated with a layer of epoxy resin. The layer of epoxy resin makes the chopped carbon fibers to easily slip out from a cement matrix.

4. Electrical Characteristics

4.1. Experiment Design of Four-Electrode Method. The size of the specimens for electrical properties was 150 mm × 150 mm × 300 mm. Each group with the same mix proportion had 3 specimens for electrical property tests. The effect of W/C and sand ratio on the resistivity of conductive concrete is very limited and complex relative to conductive materials. According to the previous study and target compressive strength of 30 N/mm^2, W/C and sand content were 0.6 and 30%, respectively. Carbon fiber volume was from 0.0 to 0.45%, and tailings content was from 0 to 15%.

The selection and arrangement of electrodes significantly affect the experiment on conductive properties. There are several test methods for measuring the electrical resistivity of concrete such as two-electrode method [13] and four-electrode method [28]. The two-electrode method includes posted outside methods (sticking graphite cloth or outer sticky copper electrodes) and embedded methods (embedded stainless steel sheet or steel mesh electrodes). The four-electrode method embeds four stainless steel sheets or steel mesh electrodes in parallel within the concrete. The four-electrode method can eliminate contact resistance and is recognized as a suitable and reliable method for testing resistivity [31]. The four-electrode technique was selected for this study to measure the electrical resistivity of specimens.

The electrical schematic of the four-electrode method is shown in Figure 3(a), and the electrical resistivity measurement in the lab is shown in Figure 3(b). Four parallel steel mesh electrodes are installed into the specimens as electrodes, and the mesh size is 25 mm × 25 mm to fit the coarse aggregate as shown in Figure 3(b). The distance between the electrode and the edge of the mold ranges from 15 mm to 20 mm, and the length of the electrode out of the concrete is 30 mm. Two electrodes (C and D) in the two sides of the specimen deliver current I_{AB} into the system, whereas the other two electrodes (A and B) detect the voltage U_{CD}. The ratio between voltage U_{CD} and current I_{AB} can be used to determine the electrical resistivity of specimens.

4.2. Result Analysis. As shown in Figure 4, the increase of graphite tailings can obviously decrease the electrical resistivity of specimens. The decrease of resistivity will slow down when carbon fiber content is more than 0.3% if the graphite tailings content is held constant. The addition of conductive components in the concrete, such as carbon fiber and graphite tailings, can significantly improve the electrical conductivity of concrete while maintaining good mechanical properties. The increase in conductive materials facilitates the formation of conductive networks, which overlap with one another to decrease concrete resistivity. In concrete, current is conducted by electrons or holes in the conductive network and tunnels over the substrate barrier. As the dosage of the conductive component increases to a critical value, the conductive networks expand to a certain range to form conductive paths, thus decreasing the resistivity of conductive concrete. When the dosage of conductive materials exceeds the threshold, the amplitude of reduction significantly diminishes although the resistivity of the conductive concrete continues to decrease [13].

From an economic view, the optimum dosage of conductive materials should approach the percolation threshold. So, an appropriate percentage of carbon fiber is 0.3% if the requirement for electrical resistivity is not very high. To get better conductivity, graphite tailings can be added more to the concrete if the concrete can satisfy the demand for strength. This experimental study shows that the appropriate percentage for tailings is 10% for good enough strength.

The electrical resistivity can be lower than 1 kΩ·cm as shown in Table 7, and graphite tailing concrete can be used in deicing or snow melting [32]. If the electrical resistivity is high, it will not generate heat effectively. A regression analysis of measured resistivity data in Table 7 is conducted to predict electrical resistivity of concrete. Two variables are examined, including tailings content and carbon fiber content. W/C and sand content keep constant and are 0.6 and 30%, respectively. The fitted equation is shown as follows:

$$R = 20.72 + 0.9452\left(\operatorname{arccot}\left(7.86 - 40.94C_{cf}\right)\right)^3 + \frac{419100}{\left(C_{gt} + 34.79\right)^{2.5}} + 0.01377C_{gt}^2 - 37.75C_{cf} + 0.523\left(C_{cf}C_{gt}\right)^{1.6}, \quad (2)$$

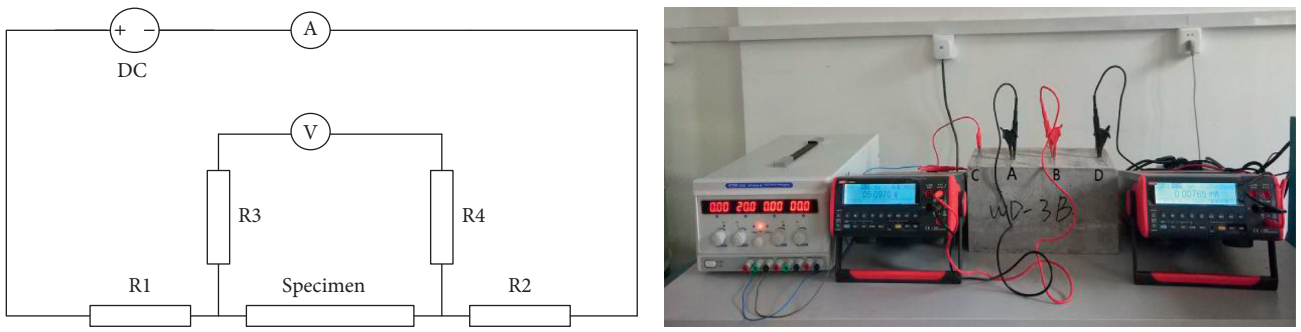

Figure 3: The measurement circuit of the four-electrode method. (a) Electrical schematic with electrical connections and (b) electrical resistivity measurement with the four-electrode method.

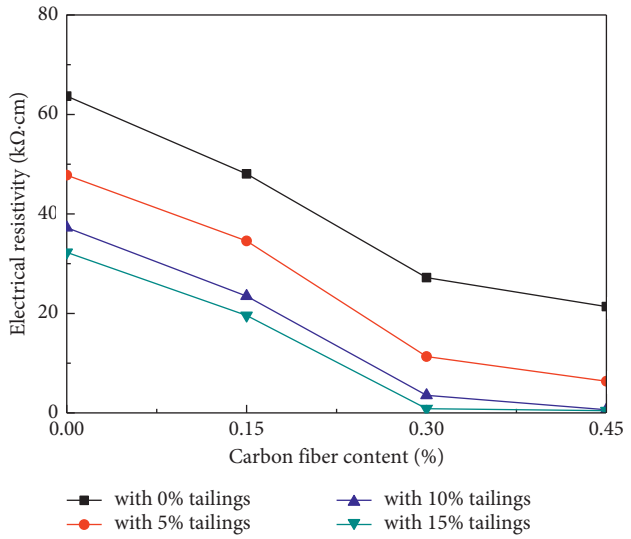

Figure 4: Electrical resistivity with different tailings content and carbon fiber content.

Table 7: Measured resistivity and estimated resistivity.

Specimen	Tailings (%)	Carbon fiber (%)	Measured resistivity (kΩ·cm)	Estimated resistivity (kΩ·cm)	Relative error (%)
1	0	0	63.68	63.805	−0.20
2	5	0	47.8	47.408	0.82
3	10	0	37.24	37.692	−1.21
4	15	0	32.28	32.156	0.38
5	0	0.15	48.04	49.163	−2.34
6	5	0.15	34.56	33.096	4.23
7	10	0.15	23.48	24.050	−2.43
8	15	0.15	19.6	19.429	0.87
9	0	0.3	27.2	26.672	1.94
10	5	0.3	11.32	11.276	0.39
11	10	0.3	3.53	3.591	−1.74
12	15	0.3	0.837	0.826	1.32
13	0	0.45	21.36	21.000	1.69
14	5	0.45	6.36	6.517	−2.47
15	10	0.45	0.643	0.689	−7.16
16	15	0.45	0.435	0.453	−4.06

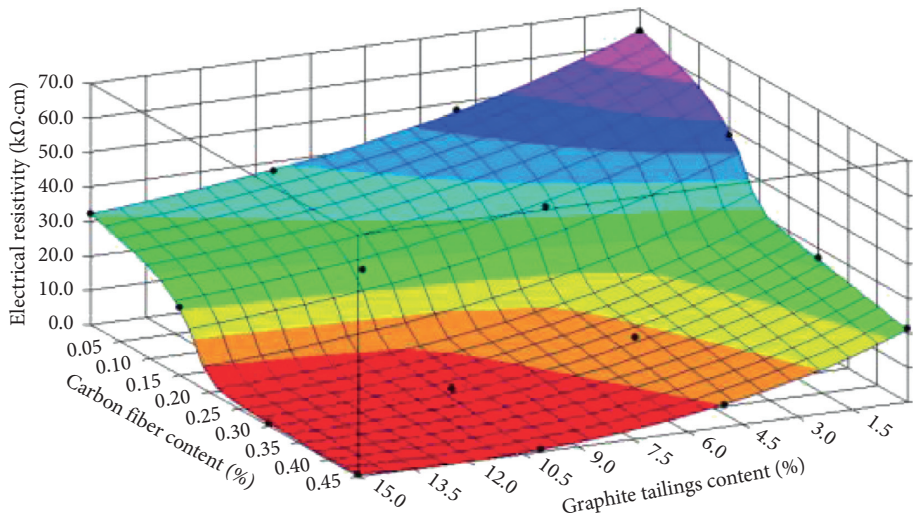

Figure 5: Electrical resistivity results with proposed regression equation.

where R is the electrical resistivity (kΩ·cm), C_{gt} is the graphite tailings content (%), and C_{cf} is the carbon fiber content (%).

An inverse trigonometric function is used to simulate threshold effect of electrical resistivity. The comparison between measured resistivity and estimated resistivity is shown in Table 7 and Figure 5. The maximum of relative errors is 7.16%.

Predictions with the proposed relationship are in reasonable agreement with experimental results measured by the four-electrode method. Fitting curved surface is rational and acceptable at not only experimental points but also transitional regions.

5. Conclusions

This paper proposed the method of the graphite tailing utilization for conductive concrete, and the compressive strength and electrical conductivity of the conductive concrete are investigated by test. The conductive concrete mixture containing graphite tailings and carbon fiber shows a good electrical conductivity and an enough mechanical strength. Some of the conclusions from the study are as follows:

(1) For graphite tailing concrete, it is more reasonable that the sand ratio is near 30% so that compressive strength is high enough with good workability.

(2) The compressive strength decreases with the increasing graphite tailings content. When tailings content is 10%, the compressive strength does not reduce too much with respect to the target strength because compressive strength can be slightly improved by carbon fiber.

(3) The increase of graphite tailings can obviously decrease the electrical resistivity of specimens. Graphite tailing concrete can be used in deicing or snow melting. From an economic view, an appropriate percentage for carbon fiber is 0.3% if the requirement for electrical resistivity is not very high.

(4) Predictions with the proposed relationship are in reasonable agreement with experimental results measured by the four-electrode method. Fitting curved surface is rational and acceptable at not only experimental points but also transitional regions.

Data Availability

The data used to support the findings of this study are available from the corresponding author upon request.

Disclosure

The founding sponsors had no role in the design of the study; in the collection, analyses, or interpretation of data; in the writing of the manuscript; and in the decision to publish the results.

Conflicts of Interest

The authors declare no conflicts of interest.

Acknowledgments

This work was supported by the National Natural Science Foundation of China (Grant nos. 51008094 and 51678221) and Heilongjiang Natural Science Foundation (Grant no. LC2017025).

References

[1] N. Vasumathi, T. V. Vijaya Kumar, S. Ratchambigai, R. S. Subba, and R. G. Bhaskar, "Flotation studies on low grade graphite ore from eastern India," *International Journal of Mining Science and Technology*, vol. 25, no. 3, pp. 415–420, 2015.

[2] J. Sun, X. Wang, C. Liu, and Y. Zhao, "Correlation and change between soil nutrient and heavy metal in graphite tailings wasteland during vegetation restoration," *Journal of Soil and Water Conservation*, vol. 23, no. 3, pp. 102–106, 2009.

[3] S. Wang, "Preparation of foam concrete from graphite tailing," *Advanced Materials Research*, vol. 356–360, pp. 1994–1997, 2012.

[4] B. Cuiping, G. Wenqi, F. Dexin et al., "Natural graphite tailings as heterogeneous Fenton catalyst for the decolorization of rhodamine B," *Chemical Engineering Journal*, vol. 197, pp. 306–313, 2012.

[5] P. Xie and J. J. Beaudoin, "Electrically conductive concrete and its application in deicing," *International Concrete Abstracts Portal*, vol. 154, pp. 399–418, 1995.

[6] S. Yehia and Y. T. Christopher, "Conductive concrete overlay for bridge deck deicing," *ACI Materials Journal*, vol. 96, no. 3, pp. 399–418, 1999.

[7] Y. Lai, Y. Liu, and D. Ma, "Automatically melting snow on airport cement concrete pavement with carbon fiber grille," *Cold Regions Science and Technology*, vol. 103, pp. 57–62, 2014.

[8] J. Gomis, O. Galao, V. Gomis, E. Zornoza, and P. Garcés, "Self-heating and deicing conductive cement: experimental study and modeling," *Construction and Building Materials*, vol. 75, pp. 442–449, 2015.

[9] R. F. Stratfull, "Experimental cathodic protection of a bridge deck," *Transportation Research Record*, vol. 500, pp. 1–15, 1974.

[10] L. Bertolini, F. Bolzoni, T. Pastore, and P Pedeferri, "Effectiveness of a conductive cementitious mortar anode for cathodic protection of steel in concrete," *Cement and Concrete Research*, vol. 34, no. 4, pp. 681–694, 2004.

[11] A. Pérez, M. A. Climent, and P. Garcés, "Electrochemical extraction of chlorides from reinforced concrete using a conductive cement paste as the anode," *Corrosion Science*, vol. 52, no. 5, pp. 1576–1581, 2010.

[12] J. Xu and W. Yao, "Current distribution in reinforced concrete cathodic protection system with conductive mortar overlay anode," *Construction and Building Materials*, vol. 23, no. 6, pp. 2220–2226, 2009.

[13] J. Wu, J. Liu, and F. Yang, "Three-phase composite conductive concrete for pavement deicing," *Construction and Building Materials*, vol. 75, pp. 129–135, 2015.

[14] X. Liu and S. Wu, "Study on the graphite and carbon fiber modified asphalt concrete," *Construction and Building Materials*, vol. 25, no. 4, pp. 1807–1811, 2011.

[15] C. Y. Tuan and S. Yehia, "Evaluation of electrically conductive concrete containing carbon products for Deicing," *ACI Materials Journal*, vol. 101, no. 4, pp. 287–293, 2004.

[16] P. S. Song and S. Hwang, "Mechanical properties of high-strength steel fiber-reinforced concrete," *Construction and Building Materials*, vol. 18, no. 9, pp. 669–673, 2004.

[17] A. O. S. Solgaard, M. Geiker, C. Edvardsen, and A. Kuter, "Observations on the electrical resistivity of steel fibre reinforced concrete," *Materials and Structures*, vol. 47, no. 1-2, pp. 335–350, 2014.

[18] J. Xie and R. Hu, "Experimental study on rehabilitation of corrosion-damaged reinforced concrete beams with carbon fiber reinforced polymer," *Construction and Building Materials*, vol. 38, no. 1, pp. 708–716, 2012.

[19] S. Vaidya and E. N. Allouche, "Strain sensing of carbon fiber reinforced geopolymer concrete," *Materials and Structures*, vol. 44, no. 8, pp. 1467–1475, 2011.

[20] B. Han, K. Zhang, X. Yu, E. Kwon, and J. Ou, "Electrical characteristics and pressure-sensitive response measurements of carboxyl MWNT/cement composites," *Cement and Concrete Composites*, vol. 34, no. 6, pp. 794–800, 2012.

[21] X. Li and J. Hao, "Orthogonal test design for optimization of synthesis of super early strength anchoring material," *Construction and Building Materials*, vol. 181, pp. 42–48, 2018.

[22] G. Zou, J. Xu, and C. Wu, "Evaluation of factors that affect rutting resistance of asphalt mixes by orthogonal experiment design," *International Journal of Pavement Research and Technology*, vol. 10, no. 3, pp. 282–288, 2017.

[23] E. Jiaqiang, D. Han, A. Qiu et al., "Orthogonal experimental design of liquid-cooling structure on the cooling effect of a liquid-cooled battery thermal management system," *Applied Thermal Engineering*, vol. 132, pp. 508–520, 2018.

[24] L. Franek and X. Jiang, "Orthogonal design of experiments for parameter learning in image segmentation," *Signal Processing*, vol. 93, no. 6, pp. 1694–1704, 2013.

[25] Z. Ge, Z. Gao, R. Sun, and L. Zheng, "Mix design of concrete with recycled clay-brick-powder using the orthogonal design method," *Construction and Building Materials*, vol. 31, no. 1, pp. 289–293, 2012.

[26] T. Liu, R. Huang, F. Li et al., "Study on the measurement accuracy of circular transmission line model for low-resistance Ohmic contacts on III-V wide band-gap semiconductors," *Current Applied Physics*, vol. 18, no. 7, pp. 853–858, 2018.

[27] B. Chen, K. Wu, and W. Yao, "Conductivity of carbon fiber reinforced cement-based composites," *Cement and Concrete Composites*, vol. 26, no. 4, pp. 291–297, 2004.

[28] A. A. Saad, "Effect of concrete mixing parameters on propagation of ultrasonic waves," *Construction and Building Materials*, vol. 19, no. 4, pp. 257–263, 2005.

[29] X. H. Vu, Y. Malecot, L. Daudeville, and E. Buzaud, "Effect of the water/cement ratio on concrete behavior under extreme loading," *International Journal for Numerical and Analytical Methods in Geomechanics*, vol. 33, no. 17, pp. 1867–1888, 2009.

[30] M. Kawamura and Y. Kasai, "Mix design and strength of soil–cement concrete based on the effective water concept," *Materials and Structures*, vol. 44, no. 2, pp. 529–540, 2011.

[31] O. Sengul and O. E. Gjorv, "Electrical resistivity measurements for quality control during concrete construction," *ACI Materials Journal*, vol. 105, no. 6, pp. 541–547, 2008.

[32] S. Yehia, C. Y. Tuan, D. Ferdon, and B. Chen, "Conductive concrete overlay for bridge deck deicing: mixture proportioning, optimization and properties," *ACI Materials Journal*, vol. 97, no. 2, pp. 172–181, 2000.

Hindawi
Advances in Materials Science and Engineering
Volume 2018, Article ID 6514025, 13 pages
https://doi.org/10.1155/2018/6514025

Research Article

Experimental and Numerical Investigation of Concrete-Filled Double-Skin Steel Tubular Column for Steel Beam Joints

Dongfang Zhang,[1] **Junhai Zhao**,[1] **and Yufen Zhang**[2]

[1]*School of Civil Engineering, Chang'an University, Xi'an, Shaanxi 710061, China*
[2]*School of Civil and Transportation Engineering, Hebei University of Technology, Tianjin 300401, China*

Correspondence should be addressed to Dongfang Zhang; zhangdongfang_2008@163.com

Received 28 February 2018; Accepted 17 July 2018; Published 5 August 2018

Academic Editor: Nadezda Stevulova

This paper presents a new type of joint for connecting steel beams with a concrete-filled double-skin steel tubular (CFDST) column. Four half-scale specimens of the joint with different specifications were constructed and tested under a constant axially compressive force with vertical low-reversal loads applied to the beam ends to examine their failure modes and hysteretic behaviors. The beam hinging mechanism of the joint was observed in the radian area of the horizontal end plates. The proposed connection was found to exhibit good energy dissipation capabilities with its limit rotation in the failure state reaching 0.05 rad, thus satisfying the FEMA-350 ductility requirement of ≥0.03 rad for seismic resistance. A finite element analysis (FEA) model of the joint was also established and validated by comparing its predictions with experimental results. The FEA model was used to investigate the effects of different parameters such as the stiffened height of the web anchorage plate, axial load level, steel and concrete strengths, steel ratio on the moment-rotation relationship, and initial stiffness of the connection. This paper presents some important design considerations of the connection, as well as aspects requiring further study.

1. Introduction

Concrete-filled steel tubular (CFST) columns exhibit excellent static behavior and seismic resistance and are widely used in construction projects in seismic areas. A recently developed type of CFST column referred to as a concrete-filled double-skin steel tubular (CFDST) column has attracted much attention in the civil engineering community in recent times. A CFDST column is composed of double concentric steel tubes with the internal space fully or partly filled with concrete. Comparing with the conventional CFST column, the bending stiffness, ductility, and seismic performance of the CFDST column are significantly increased because of the inner steel tube [1–4]. CFDST columns may also be effective for dealing with the requirement for large-profile columns in some engineering projects. When used in buildings, CFDST columns are usually connected to steel beams. There have, however, been few studies on such connections, which tend to be complex owing to the double-skin tubes. This, as well as the nonexistence of applicable standard codes and practices, has hampered the application of CFDST columns in high-rise buildings in seismic regions.

There have been previous experimental and numerical studies on the connection of ordinary CFST column to steel beams. Through experiments and simulations, Han and Li [5, 6] investigated the seismic performance of connections between CFST columns and steel beams with external diaphragms. Both the beam and column failures were observed, and a series of numerical parametric investigations were also used to examine the effects of the joint parameters on the initial stiffness, bending capacity, and failure modes of the joints. Jianguo et al. [7] conducted experimental and numerical analyses of the seismic behavior of composite frames with concrete-filled rectangular steel tubular columns (CFRSTCs). The results obtained by an FEA model fitted well with those of model tests in terms of the stiffness, strength, hysteretic behavior, and component deformation. Wang and Spencer [8] experimentally and numerically

investigated a blind bolted end plate joint between a CFST column and a steel beam. Parametric analyses based on a finite element analysis (FEA) model validated by experimental results were used to investigate the behavior of the joint. Based on the findings, they recommended a reasonable bolt anchorage length ratio for this type of joint. Kang et al. [9] numerically investigated the shear bearing capacity of the connection between an internal diaphragm and a concrete-filled steel tube (CFT) column. Based on their findings and previous theory, they proposed relationships between the shear force and the deformation of the modified joint. Rezaifar and Younesi [10] developed a new connection between a CFST column and a steel beam using trapezoidal external stiffeners and horizontal bar mats, and used FEA to investigate its seismic performance. The results indicated that the connection was potentially applicable to constructions in seismic areas, affording a good alternative for connection using continuity plates. Through experiments and simulations, Tao et al. [11] investigated the seismic behavior of the connection between a steel beam and a CFST column using high strength through column bolts and extended end plates. The effects of the yield stress and thickness of the end plate on the rotation stiffness and moment capacity of the joint were examined for integration of the joint in engineering designs. Liu et al. [12] experimentally and numerically investigated the seismic behavior of the connection between a specially shaped CFST column and a steel beam joint. They introduced an exterior diaphragm and a vertical rib as joint stiffeners and analyzed the failure mode, stiffness, and seismic performance index based on the load deformation and strain curves. They proposed a shear resistance formula of the joint based on the internal load transmission for engineering application.

However, there has been very little recent research on the connection of a CFDST column. Zhang et al. [13, 14] presented a ring beam joint between a CFDST column and reinforced concrete (RC) beams. Experimental and numerical analyses were used to investigate the seismic behavior of the joint. Nevertheless, to enable broad application of the CFDST column, it is necessary to design a joint for connecting it to a steel beam. Zhang et al. [15] proposed a joint for connecting a CFDST column to a steel beam based on the idea of the vertical stiffener joint. Experiments were performed to evaluate the seismic behavior of the joint, which was found to exhibit high strength, stiffness, ductility, and energy dissipation capability.

In the present study, the mechanical behavior of a progressive joint for connecting a CFDST column to a steel beam was investigated experimentally and numerically. An experimental program for investigating the composite joint was first developed. An FEA model of the joint was subsequently established, taking into consideration the concrete confinement effect, concrete damage characteristic, and interaction between the concrete and the steel tube. The FEA model was validated by comparing its predictions with the experimental results. A parametric analysis based on the FEA model was also conducted to investigate the effects of different parameters such as the stiffness height, axial load level, material strength, and steel ratio on the joint behavior.

2. Experimental Program

2.1. Design of Test Specimens. The prototypes of the steel beam and the CFDST column of the test specimens were designed in accordance with GB 50936-2014 [16]. To achieve an excellent behavior of the CFDST column, a web anchorage plate was attached to the inner steel tube for connection to the steel beam through the outer steel tube, as shown in Figure 1. A horizontal end plate with a reduced section was also welded to the outer tube wall and the web anchorage plate, for welding to the flange of the steel beam. Finally, a vertical plate was welded around the connection region to strengthen the stability of the composite joint. The detailed construction information and parameters of the tested joint specimens are presented in Figure 2 and Table 1, respectively.

The section of each column consisted of an outer square tube and an inner circular tube of seamless steel, with the internal space filled with concrete, as shown in Figure 3(a). The section of the square tube measured $250 \times 250 \times 8$ mm (side length × side length × thickness), and that of the circular tube measured 133×6 mm (diameter × thickness). The H-shaped section of each steel beam measured $244 \times 175 \times 7 \times 11$ mm (height × flange width × web thickness × flange thickness), as shown in Figure 3(b). The size of the horizontal end plate is shown in Figure 3(c). The main parameters of the composite joint included the type of the two web anchorage plates and the extension length of the vertical plate, as shown in Figures 3 (d)–3(f).

2.2. Test Setup and Loading Program. The purpose of the experimental study was to simulate the mechanical properties of the tested joints under earthquake action. The boundary conditions of a model of the cruciform beam-to-column joint were reproduced in the test setup, as shown in Figure 4(a). A 2000 kN vertical hydraulic jack was placed at the top of the column and used to apply a constant vertical force to simulate the effect of the upper floors of a multistorey building. The vertical actuator was glidingly attached to the reaction frame, and a spherical hinge was placed between the actuator and the column to simulate the inflection point of the joint specimen. The column end was restrained by a rigid transverse beam connected to the reaction wall, but allowed to freely rotate in the loading plane. A vertical low-reversal cyclic load was applied to each end of the beam by an MTS hydraulic actuator to simulate the seismic loading effect. Four specially designed out-of-plane lateral braces were used to avoid torsion of the joint specimen during the loading process, as shown in Figure 4(b).

During the test of all the specimens, after calibration of all the instrumentation, the vertical hydraulic jack was first used to apply a constant axial load of 1514 kN to the top of the column. A vertical low-reversal load was then applied to each end of the two-segment beam under displacement control, as depicted in Figure 5. The loading profile in the figure is based on the recommendations of the Chinese standard JGJ/T 101-2015 [17]. For convenience of description of the testing process, the pushing and pulling

actions of the vertical actuator of the right beam segment were defined as positive (+) and negative (−), respectively. The loading process began with one cycle of each of ±6, ±12, and ±18 lateral displacements. Subsequently, sets of three cycles with progressively increasing lateral displacement amplitudes of ±24, ±30, ±36, ±42, ... were implemented until failure of the specimen or reduction of the load below 85%.

2.3. Material Properties. The strength and elastic modulus of the steel were measured in accordance with the GB/T 228.1-2010 standard [18]. The same type of steel was used to fabricate the web anchorage plates and the outer square tubes, whereas another type was used to fabricate the horizontal end plates and vertical plates. The detailed mechanical properties of all the steel components are presented in Table 2. Nine concrete cubes with a side length of 150 mm were molded and their compressive strength was measured using the standard test method. The average compressive strength f_{cu} was determined to be 59.5 MPa.

3. Finite Element Modelling

The finite element program ABAQUS was used to conduct some pertinent parametric investigations on the tested composite joint. The principal modelling factors of the joint included the element types, meshes, connections between elements, material models, boundary conditions, and calculation method.

3.1. Element Types and Meshes. The steel and concrete components were modeled by solid elements (C3D8R) of an eight-node reduction integral format in ABAQUS/CAE 6.11. The calculation precision is even more precise when the grid is distorted. In addition, under a bending moment, the occurrence probability of the shear self-locking phenomenon is low. The calculation can still be continued with relative accuracy under a larger model deformation.

The structured adaptive grid meshing technique was used to achieve an appropriate element shape. A relatively fine mesh was applied to the core concrete and steel beam because of their complex stress distribution and obvious deformation. The FEA model of the SBJ2-2 specimen is shown in Figure 6.

3.2. Material Models

3.2.1. Material Modelling of Steel. A nonlinear combined (isotropic/kinematic) hardening plasticity model was applied to the steel components including the steel tubes, steel beams, and all the construction plates of the joint model. The well-known Bauschinger effect under cyclic loading was considered in the steel model.

The multilinear stress-strain relationship model presented by Abdel-Rahman and Sivakumaran [19] was applied to the square and circular steel tubes to approximate the real performance of steel tubes under seismic action. A square steel tube section in the model was divided into the corner zone and the flat zone, as shown in Figure 7. The stress-stain relationship of the flat zone was also applied to the circular steel tube in the analysis. The equation of the five stages of the elastic-plastic stress-strain model is available in [20].

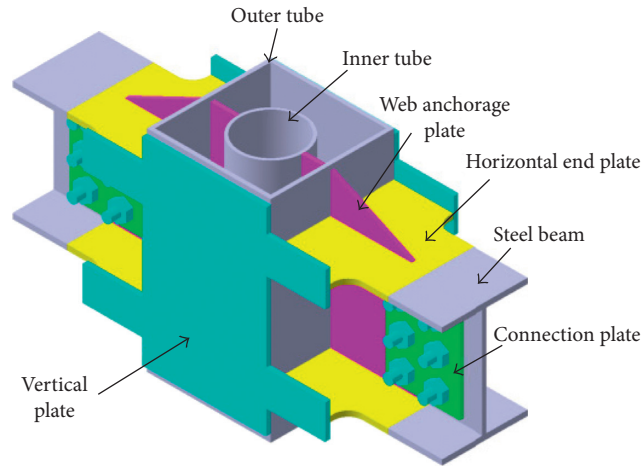

Figure 1: Construction of joint specimen.

A trilinear stress-strain elastic-plastic model was applied to the steel beams, construction plates, and bolts for better simulation of the descending branch of the force-deformation curve of the joint model under cyclic loading. The three stages of the constitutive model are shown in Figure 8, where $\varepsilon_A = f_y/E_s$, $\varepsilon_B = (f_u - f_y)/0.1E_s$, $\varepsilon_C = 0.03$, and f_y, f_u, and E_s are listed in Table 2.

3.2.2. Material Modelling of Concrete. Concrete is a discrete material and more complex than steel. A concrete damage plasticity (CDP) model was applied to the concrete in the present analysis. The model is based on an elastic-plastic model, includes the damage variable factor D, and well simulates the stiffness degradations of concrete under cyclic loading, according to Lubliner et al. [21] and Lee and Fenves [22]. Under axial loading, the core concrete was subjected to the double-side constraints of the internal and external steel tubes. Owing to the interactions between the steel tubes and the concrete, the mechanical properties of the core concrete were more complex than usual. The confined concrete stress-strain relationship proposed by Han et al. [23] was used to analyze the core concrete of the CFST in compression, while the core concrete constitutive model was applied to the tensile state in accordance with the Chinese code GB 50010-2010 [24]. The compressive stress-strain curves are shown in Figure 9.

The parameters of the CDP model included a dilation angle of 30°, plastic potential eccentricity of 0.1, ratio of the ultimate compressive strength to the biaxial compressive strength of 1.16, ratio between the second stress invariants on the meridional plane and the compression meridian of 2/3, and viscosity coefficient of 0.0005. There is no stipulated method for determining the damage variable factor (D) in the relevant standards and regulations. The following equation is used to determine the compression damage factor d_c and the tension damage factor d_t [25]:

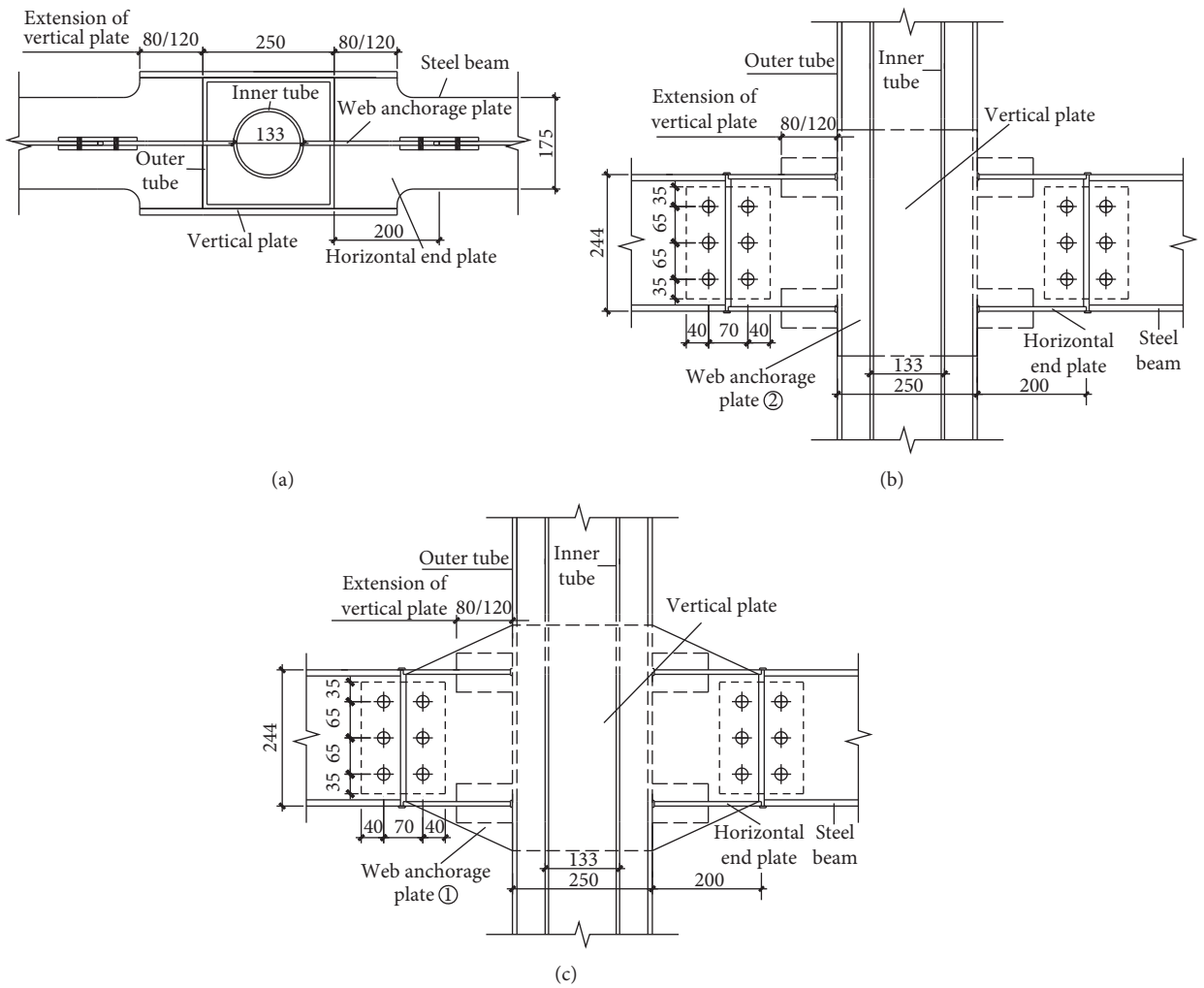

Figure 2: Details of the joint specimens. (a) Plan view of a specimen. (b) Elevation view of the SBJ1-1 and SBJ1-2 specimens. (c) Elevation view of the SBJ2-1 and SBJ2-2 specimens.

$$d_k = \frac{(1-\beta)\varepsilon^{\text{in}} E_c}{\sigma_k + (1-\beta)\varepsilon^{\text{in}} E_c} \quad (k = t, c), \tag{1}$$

where the subscript k ($k = t, c$) represents the tensile or compressive stress state, β is the ratio of the plastic strain to the inelastic strain (β is within 0.35–0.7 when the concrete is in the compressive state and 0.50–0.95 when in the tensile state), ε^{in} is the inelastic strain of the concrete (given by (2)), σ_k ($k = t, c$) is the tensile or compressive stress of the concrete corresponding to the strain ε, and E_c is the elastic modulus of the concrete (3.6×10^4 MPa according to GB 50010-2010) [24].

$$\varepsilon^{\text{in}} = \varepsilon - \sigma_k E_c^{-1}. \tag{2}$$

3.3. Interaction between Concrete and Steel Tubes. The contact relationship between the steel tubes and the concrete was defined by considering the slippages in the normal and tangential directions on the surfaces of the two materials. The contacting surfaces were allowed to transfer the pressure in the tangential direction, but penetration in the normal direction was not allowed. Hard contact was applied in the normal direction to simulate the surfaces of the steel tubes and core concrete, while the Mohr–Coulomb friction model was applied in the tangential direction. In the present analysis, the friction coefficient in the tangential direction was considered to be 0.25 in accordance with [26]. The tangential bond shear stresses between the surfaces of the steel tubes and the concrete were as detailed by Roeder et al. [27].

Table 1: Details of the test specimens.

Specimen	Web anchorage plate	Extension of vertical plate
SBJ1-1	Nonstiffening	80 mm
SBJ1-2	Nonstiffening	120 mm
SBJ2-1	Stiffening	80 mm
SBJ2-2	Stiffening	120 mm

3.4. Finite Element Model Description. The FEA model of the representative SBJ2-2 specimen is illustrated in Figure 6. The model considers the material and geometric nonlinearities

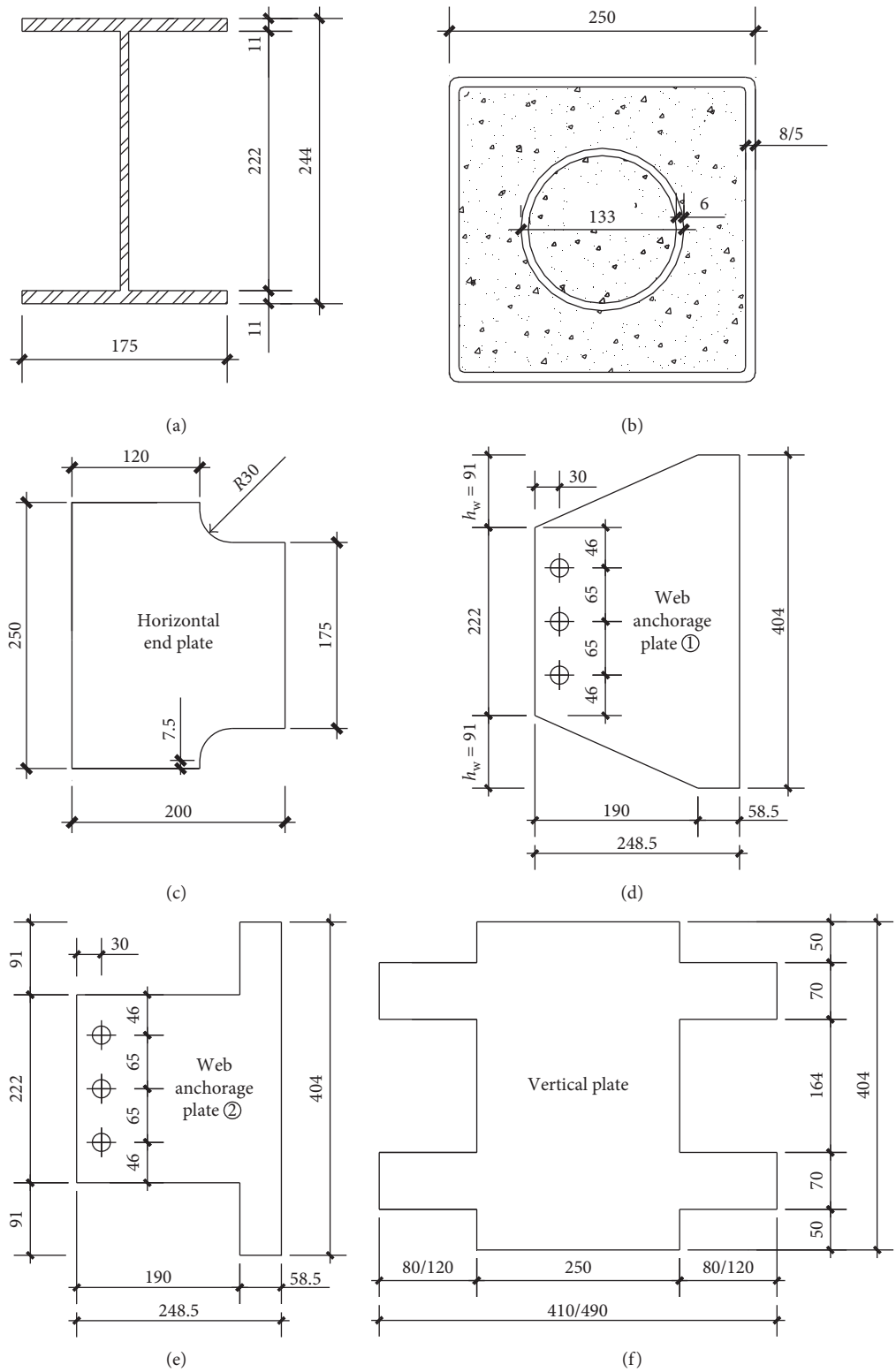

Figure 3: Details of the beam, column, and construction plates. (a) Beam. (b) Column. (c) Horizontal end plate. (d) Stiffening type. (e) Nonstiffening type. (f) Vertical plate.

and the boundary conditions. Two reference points were established on the top and bottom of the column, respectively. The test boundary conditions were reproduced in the FEA model. An axial load N_0 was applied to the top of the CFDST column in the first step, and a cyclic displacement load was subsequently applied to the beam trips. The Newton–Raphson method in the ABAQUS/Standard implicit calculation module was used to solve the model.

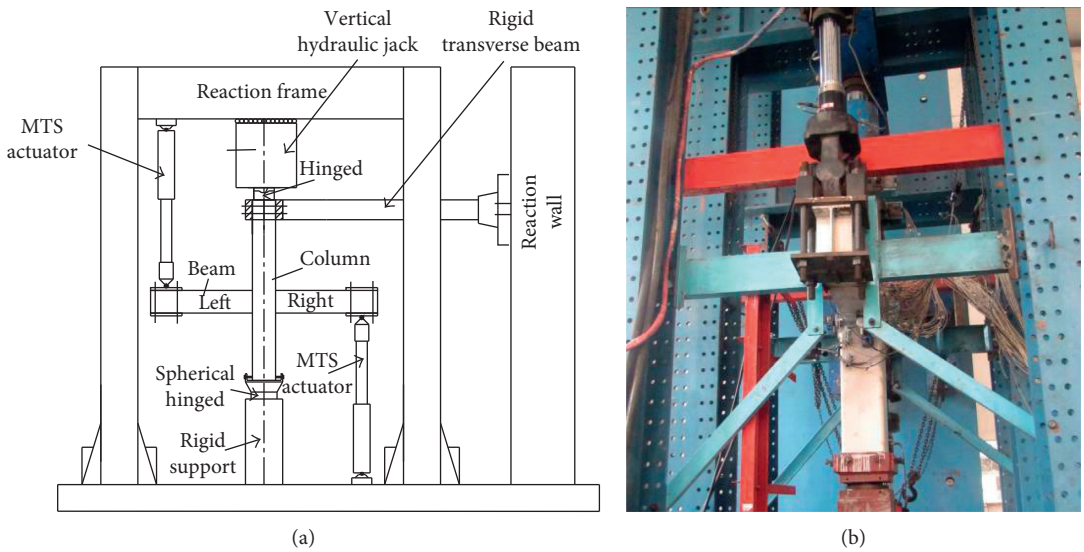

Figure 4: Test setup. (a) Diagram of the loading device. (b) Lateral brace of the steel beams.

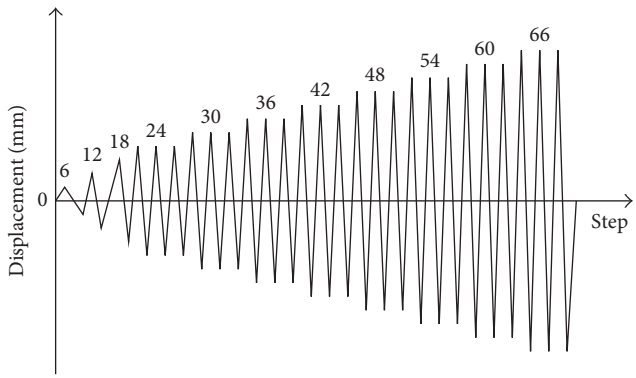

Figure 5: Loading history.

3.5. Verification

3.5.1. Failure Mode. Figures 10–13 compare the failure modes determined by tests and FEAs, from which rough agreement can be observed. The indicated large deformation of the steel is approximatively attributed to fracturing. The radian areas of the horizontal end plates of both the left and right segments of the beam of the SBJ1-1 specimen tore during the test, as shown in Figures 10(a) and 10(c), respectively, and the FEA results reveal obvious buckling at the same locations, as can be observed from Figure 10(b). The two results are thus in good agreement. In contrast to the SBJ1-1 specimen with the extension 80 mm of the vertical plate, the extension length of the vertical plate in the SBJ1-2 specimen was 120 mm. The failure positions in the latter specimen observed in the test and simulation were away from the joint core region, as shown in Figure 11. Conversely, the SBJ2-1 specimen with extension 80 mm failed starting from the break at the radians of the horizontal end plate, with slight buckling of its stiffening web anchorage plate observed in both the test and simulation results, causing a small fracture of the steel tube wall, as shown in Figure 12. Comparing with the SBJ2-1 specimen, the phenomenon of fracture on the steel tube did not happen for the SBJ2-2 specimen with extension 120 mm, as shown in Figure 13. The test and simulation results for the SBJ2-2 specimen indicated that the plastic hinge obviously moved away from the steel tube face due to the longer extension length of the vertical plate.

The failure modes of a composite joint are affected by the formation of the web anchorage plate and the extension length of the vertical plate. The joint construction details can be modified to adjust the beam failure modes to satisfy the design requirements of "strong column, weak beam" and "strong joint, weak component" for seismic resistance.

3.5.2. Moment-Rotation Hysteresis Curves. The hysteresis curve is an important indication of the seismic performance of a structure. The moment-rotation (M-θ) hysteresis curves of the different specimens of the considered composite joint are shown in Figure 14. Generally, good agreement can be observed between the M-θ hysteresis curves obtained from the test and FEA results, with the pinching phenomenon particularly well reproduced by the FEA model. The reloading and unloading stiffness predicted by FEA are also close to those determined by testing. The real mechanical behavior of the joint can thus be investigated using the present FEA model. However, the numerical simulation results are not entirely consistent with those of the tests. This is mainly because of the double stress complexity factors in the heat zone generated by the welding of the steel and the differing weld qualities, which cannot be precisely simulated by the FEA model.

Figure 14 shows that the composite joint has a shuttle-shaped hysteresis curve and possesses good energy dissipation capabilities, as indicated by the area of the envelope. The limit rotation of the joint also reaches 0.05 rad in the failure state, satisfying the FEMA-350 ductility requirement of no less than 0.03 rad for seismic resistance [28].

Table 2: Material properties of the steel components.

Item	Thickness t (mm)	Yield strength f_y (MPa)	Tensile strength f_u (MPa)	Elastic modulus E_s (MPa)
Square tube	8	338.12	481.70	2.27×10^5
Circular tube	6	323.08	491.39	2.19×10^5
Beam flange	11	272.41	447.40	2.23×10^5
Beam web	7	291.00	457.23	2.22×10^5
Horizontal end plate	12	272.61	445.86	2.18×10^5

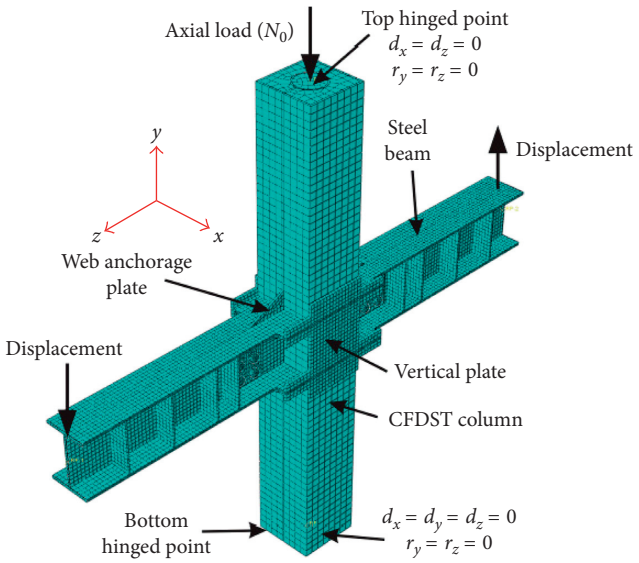

Figure 6: General view of the FEA model of the SBJ2-2 specimen.

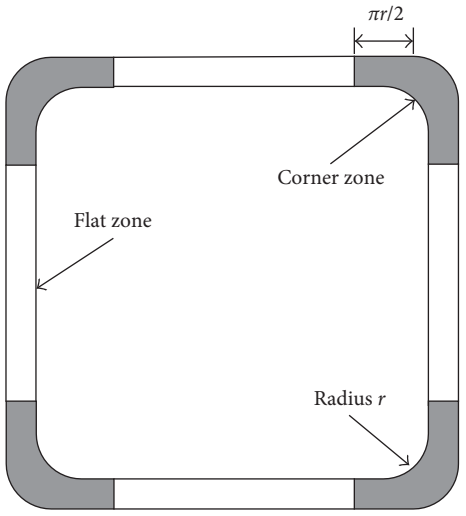

Figure 7: Flat and corner zones of the section of a cold-formed square steel tube.

The forgoing shows that the failure pattern, hysteresis curve, bearing capacity, and stiffness predicted by the FEA model are in good agreement with the test results. The FEA model thus adequately simulates the nonlinear mechanical properties of the composite joint and can be used for further parametric analysis.

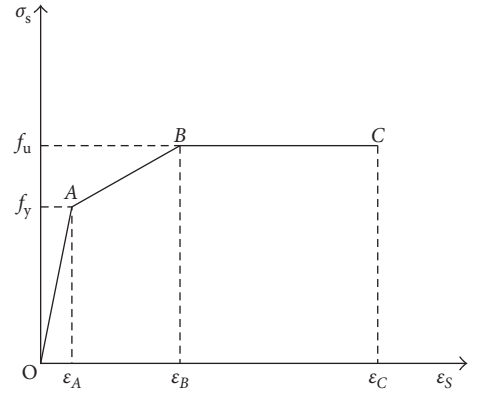

Figure 8: Constitutive trilinear stress-strain relationship.

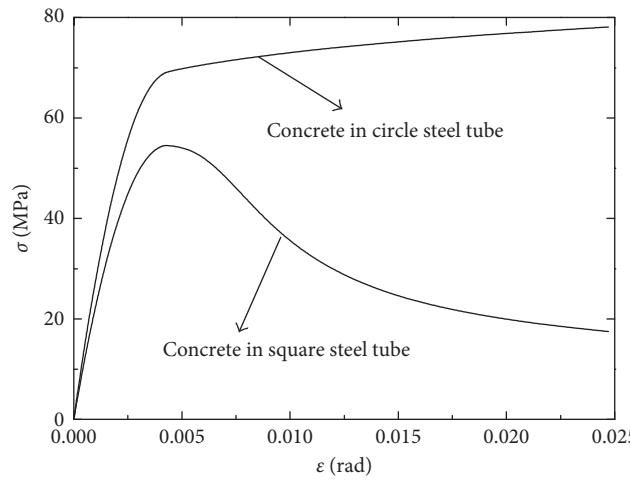

Figure 9: Compressive stress-strain curves of the core concrete.

4. Parametric Investigation

The proposed FEA model was used to conduct a parametric investigation to determine the effects of the joint parameters on its moment-rotation relationship. The main parameters included the height of the stiffening of the web anchorage plate (h_w), axial load level (n), material strength, steel ratio of the column (α), beam-to-column linear stiffness ratio (k_i), and beam-to-column bending capacity ratio (k_m).

The axial load level (n) was defined in this study as N_0/N_u, where N_0 and N_u are, respectively, the axial load applied to the CFDST column and the compressive bearing capacity of the

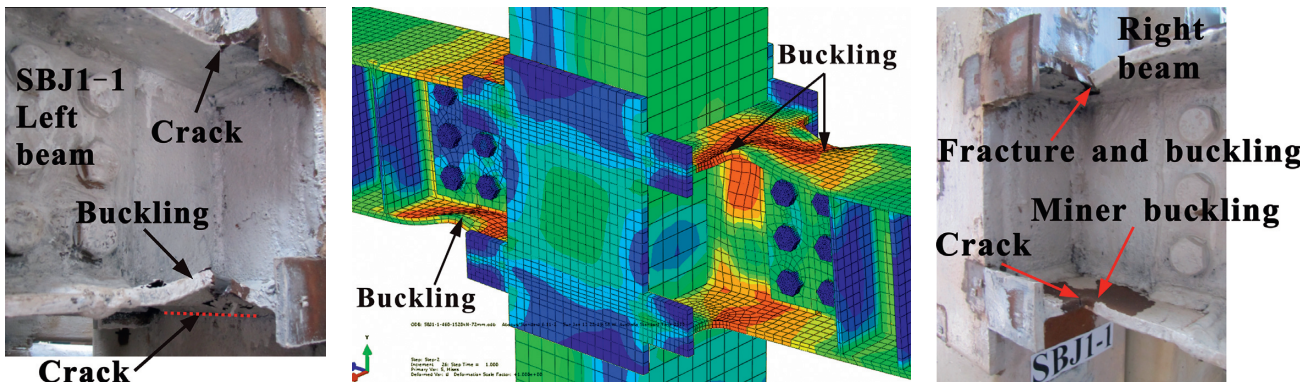

(a) (b) (c)

Figure 10: Comparison of the failure modes of the SBJ1-1 specimen determined by test and FEA. (a) Test: left beam segment. (b) FEA. (c) Test: right beam segment.

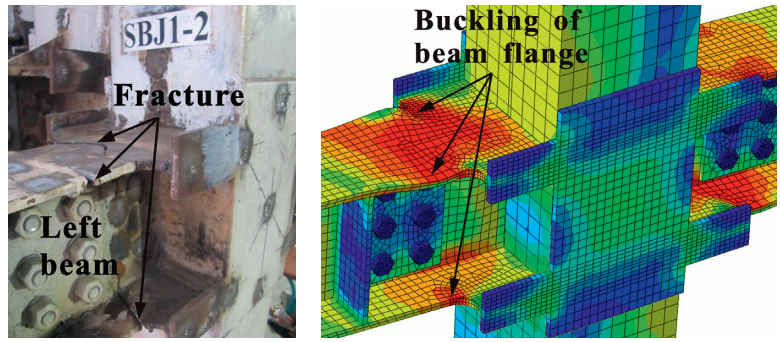

(a) (b)

Figure 11: Comparison of the failure modes of the SBJ1-2 specimen determined by test and FEA. (a) Test. (b) FEA.

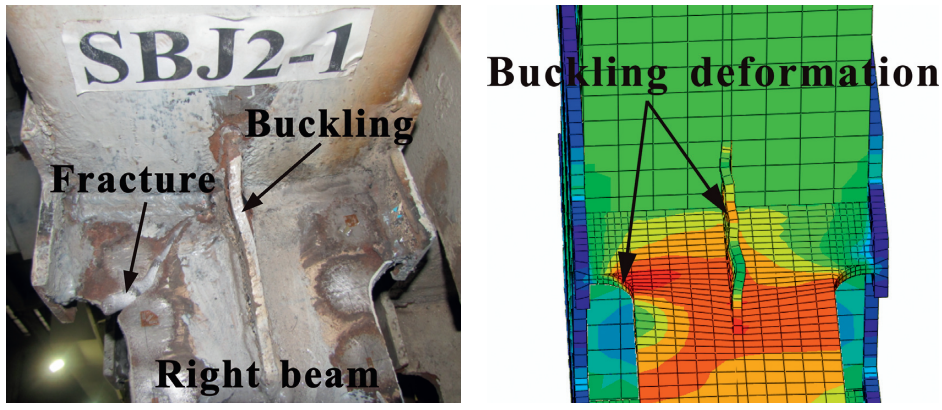

(a) (b)

Figure 12: Comparison of the failure modes of the SBJ2-1 specimen determined by test and FEA. (a) Test. (b) FEA.

CFDST column, as calculated by Zhang et al. [29]. The steel ratio of the column (α) was defined as A_s/A_c, where A_s and A_c are, respectively, the cross-sectional areas of steel tubes and the concrete filled into the column. The beam-to-column linear stiffness ratio (k_i) was defined as i_b/i_c, where i_b and i_c are, respectively, the linear stiffness of the steel beam and the CFDST column. The beam-to-column bending capacity ratio (k_m) was defined as M_b/M_c, where M_b and M_c are, respectively, the bending capacities of the steel beam and the CFDST column calculated according to CECS 159: 2004 [30].

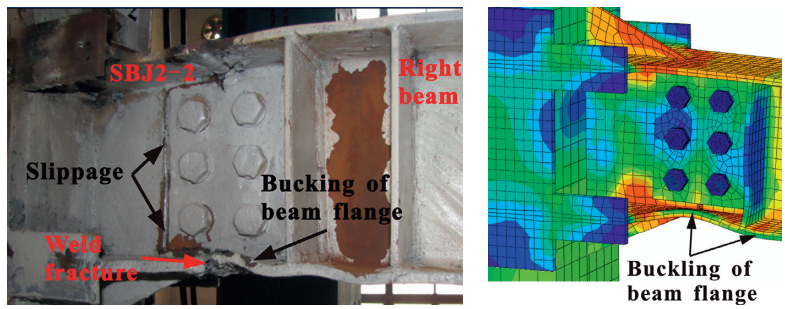

Figure 13: Comparison of the failure modes of the SBJ2-2 specimen determined by test and FEA. (a) Test. (b) FEA.

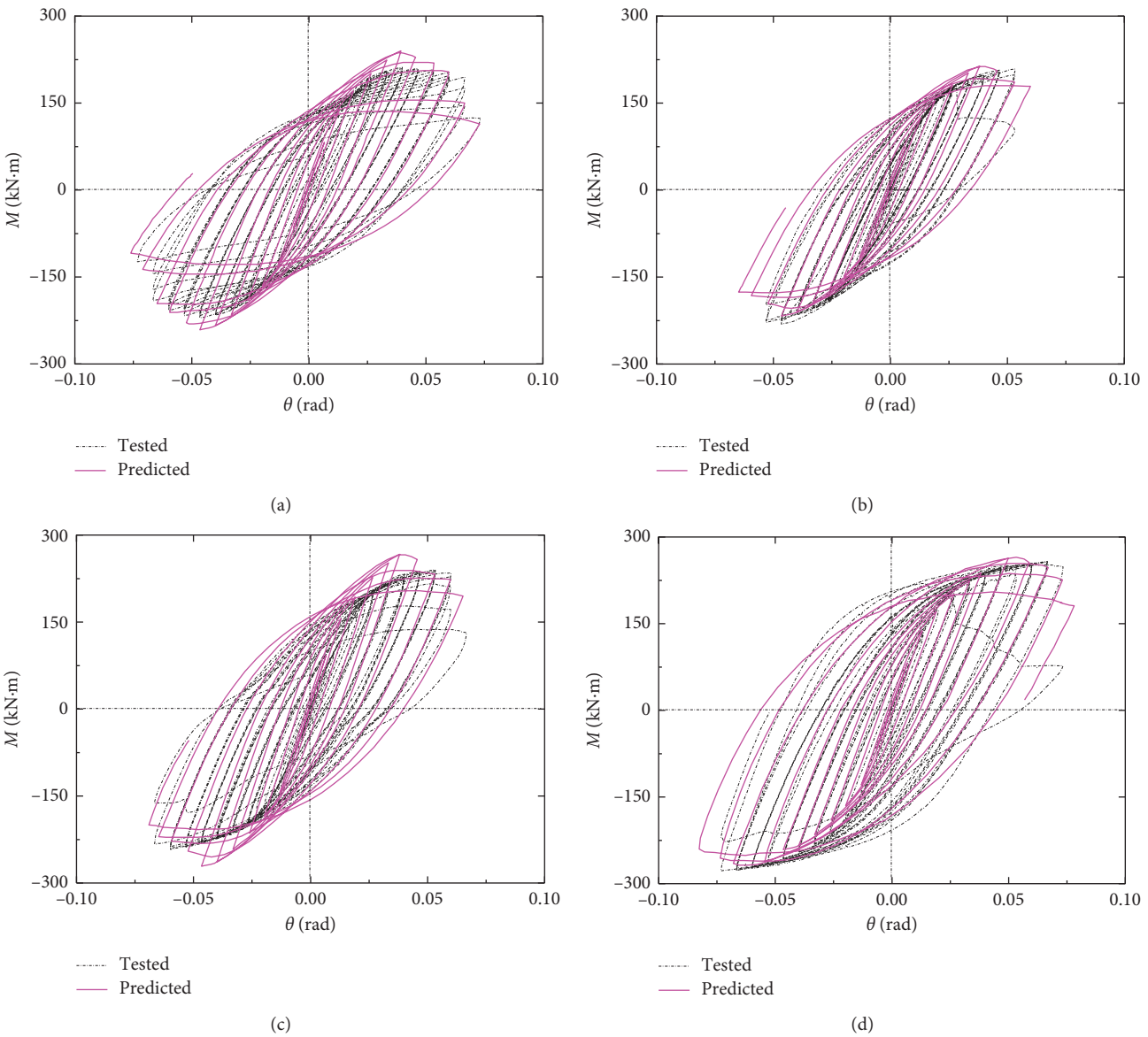

Figure 14: Comparison of the hysteresis curves obtained from the test and FEA results. (a) SBJ1-1. (b) SBJ1-2. (c) SBJ2-1. (d) SBJ2-2.

The basic parameter values used for the calculation examples are as follows:

(i) Joint type: cruciform joint with stiffening of the web anchorage plate, $h_w = 100$ mm

(ii) CFDST column: section as shown in Figure 3(a), height = 2.1 m, $f_y = 345$ MPa, $f_{cu} = 60$ MPa, and $N_0 = 2633$ kN ($n = 0.4$)

(iii) Steel beam: H-244 × 175 × 7 × 11 mm, span length- = 2.5 m, and $f_y = 345$ MPa

(iv) Other parameters: $\alpha = 0.194$, $k_i = 0.434$, and $k_m = 0.592$.

4.1. Effect of Stiffened Height of Web Anchorage Plate (h_w). The effect of the stiffened height was investigated by varying its value as $h_w = 0$, 40, 80, and 100 mm. Figure 15(a) shows the effect on the M-θ relationship of the composite joint. It can be observed that the initial stiffness and ultimate bending capacity of the joint are enhanced with increasing stiffened height (h_w). The stiffened height of the web anchorage plate (h_w) is evidently an important determinant of the M-θ relationship of the considered composite joint. In addition, a stiffened height of 100 mm can be observed to optimize the behavior of the joint for the sizes of the beam and column in the present example. In practical engineering applications, the space utilization rate of a building structure is affected by the stiffened height of the web anchorage plate (h_w).

4.2. Effect of Column Axial Load Level (n). Figure 15(b) shows the effect of the column axial load level (n) on the M-θ relationship, as n is varied as 0, 0.2, 0.4, 0.6, and 0.8. It can be seen that the ultimate bending capacity is only slightly affected by the variation, whereas the initial stiffness is significantly enhanced with increasing n. The composite joint thus exhibits a good bearing capacity under a high axial load level, as well as under a high axial compression ratio ($n = 0.6$; $N_0 = 3950$ kN).

4.3. Effect of Strength of Steel Beam (f_{y1}). The effect of the strength of the steel beam (f_{y1}) on the M-θ relationship was investigated by varying f_{y1} as 235, 345, 390, and 420 MPa, as shown in Figure 15(c). It can be observed from the figure that the bending moment bearing capacity of the joint increases with increasing yield strength of the steel beam, but the initial stiffness is hardly affected by the varying f_{y1}. Because the elastic modulus of the steel beam (E) is minimally affected by the variation of the yield strength, the initial stiffness of the joint is thus not enhanced by an increase in the strength of the steel beam.

4.4. Effect of Strength of Steel Tubes (f_{y2}). Figure 15(d) shows the effect of the strength of the steel tubes (f_{y2}) on the M-θ relationship, with the variation of f_{y2} as 235, 345, 390, and 420 MPa. It can be seen from the figure that the bearing bending capacity at the failure stage of the composite joint increases with increasing f_{y2}, whereas there is only a slight effect on the initial stiffness of the joint.

4.5. Effect of Concrete Strength (f_{cu}). The effect of the strength of the concrete filled into the steel tubes (f_{cu}) on the M-θ relationship was also investigated. For this purpose, f_{cu} was varied as 30, 40, 60, and 80 MPa, as shown in Figure 15(e). An axial load level (n) of 0.6 was used for this parameter analysis to verify the excellent behavior of a CFDST column under heavy compressive loading. It was found that the composite joint exhibited good bending resistance under axial loading (load level $n = 0.6$), despite the C30 concrete filled into the steel tubes of the column. The ultimate bending capacity and initial stiffness of the joint were slightly enhanced with increasing concrete strength (f_{cu}).

4.6. Effect of Steel Ratio (α). To examine the effect of the steel ratio (α), a finite element analysis was performed in which α was varied as 0.109, 0.132, 0.194, and 0.237. The results are shown in Figure 15(f), from which it can be observed that the bending moment capacity and initial stiffness of the joint are significantly enhanced with increasing α of the CFDST column. The variation of α was achieved by varying the wall thickness of the outer steel tube. The increase of the tube wall thickness used to achieve a higher α increased the constraint on the filling concrete, as well as the flexural rigidity of the column. The steel ratio α was found to be the main impacting factor of the bending moment capacity and initial stiffness of the composite joint.

4.7. Effect of Beam-to-Column Linear Stiffness Ratio (k_i). Figure 15(g) shows the effect of the beam-to-column linear stiffness ratio (k_i) on the M-θ relationship. The variation of k_i was achieved by varying the length of the beam. It can be seen from the figure that the bending moment capacity and initial stiffness of the joint are obviously affected by k_i. However, the flexural capacity of the joint is significantly lower for a k_i value of 0.764 compared with other values. This is mainly because the relative beam-to-column rotation for $k_i = 0.764$ is larger for a given vertical displacement of the beam ends, resulting in an earlier damage of the beam. The beam-to-column linear stiffness ratio is a principal factor of the behavior of the composite joint, with a value of 0.5 being optimal.

4.8. Effect of Beam-to-Column Bending Capacity Ratio (k_m). The effect of the beam-to-column bending capacity ratio (k_m) on the M-θ relationship was examined by varying it as 0.436, 0.592, 0.664, and 0.721. As indicated by Figure 15(h), the bending moment capacity and initial stiffness of the joint significantly increase with increasing k_m, especially when k_m increases from 0.436 to 0.592. The variation of k_m was achieved by varying the size of the beam section. A beam-to-column bending capacity ratio of 0.6 is suggested for optimization of the composite joint. Nevertheless, in practical engineering applications, it is necessary to take both

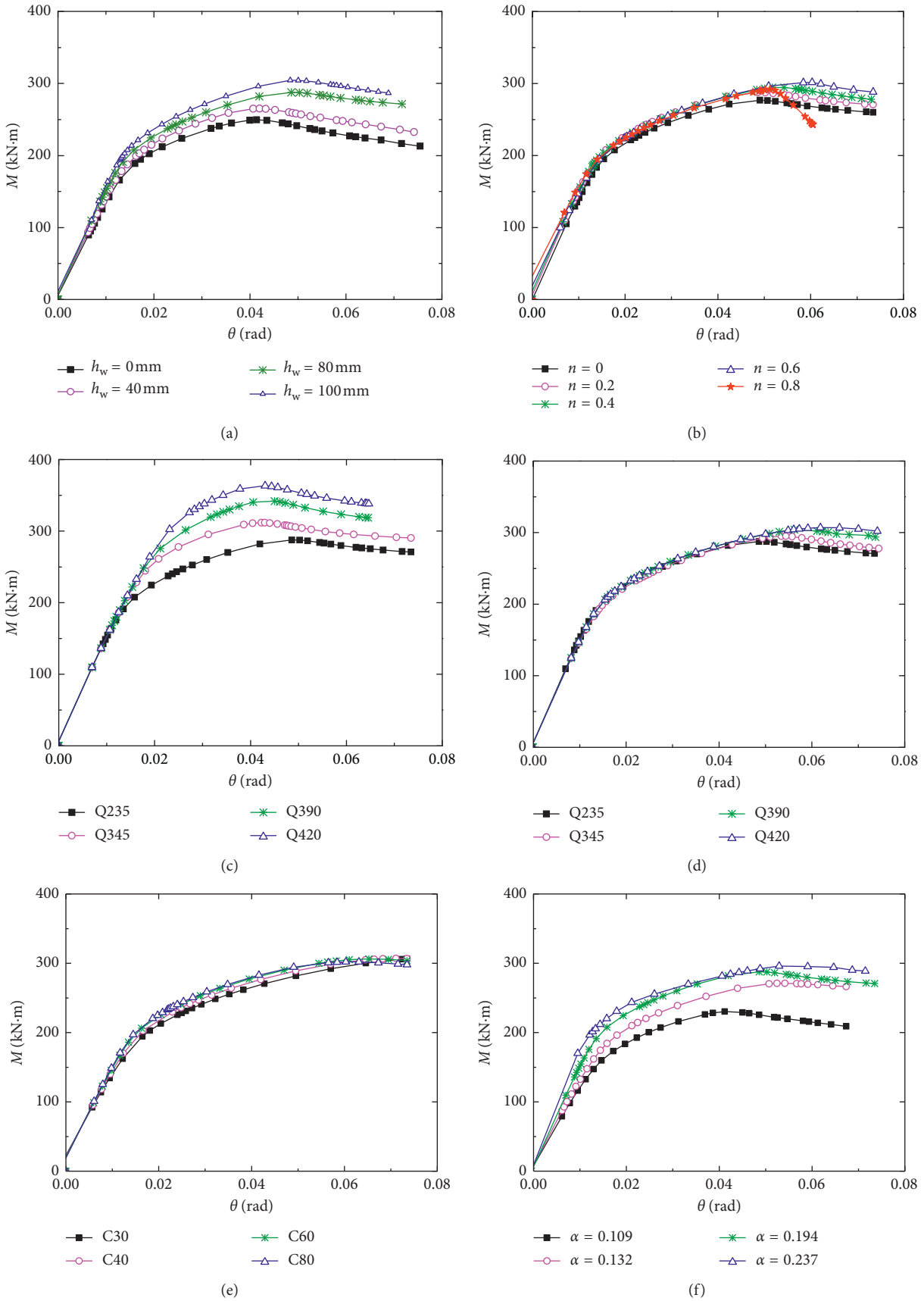

Figure 15: Continued.

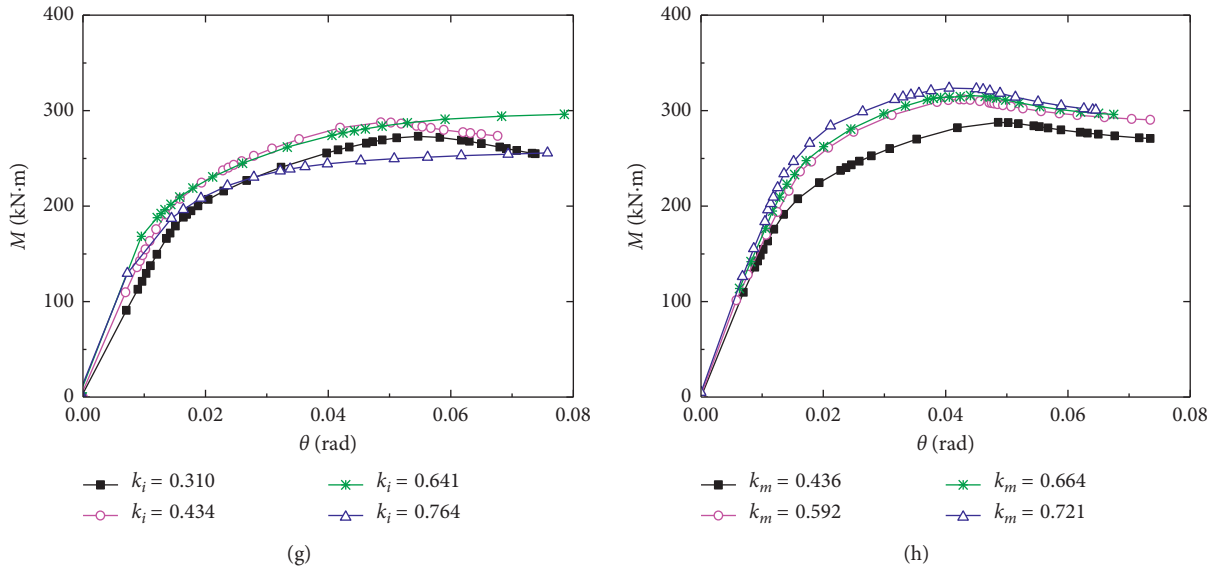

FIGURE 15: Effect of various parameters on the M-θ relationship of the CFDST column-beam joint. (a) Stiffened height (h_w). (b) Column axial load level (n). (c) Strength of beam steel (f_{y1}). (d) Strength of tube steel (f_{y2}). (e) Concrete strength (f_{cu}). (f) Steel ratio (α). (g) Beam-to-column linear stiffness ratio (k_i). (h) Beam-to-column bending capacity ratio (k_m).

economy and mechanical effectiveness into consideration in setting the beam-to-column bending moment ratio.

5. Conclusions

Based on the results of the experimental and numerical investigations of the steel-beam-CFDST-column joint in the present study, the following conclusions and design suggestions are presented:

(1) The plastic hinge of the joint under cyclic loading occurs at the beam ends. The extension of the vertical plate can be used to move the plastic hinge away from the face of the column to protect the core regions of the joints. The joint satisfies the design principles of "strong column, weak beam" and "strong joint, weak component" for seismic resistance.

(2) All the obtained moment-rotation hysteretic curves are plump, indicating an excellent energy dissipation capacity of the joint. The web anchorage plate with stiffening enhances the stiffness, bearing capacity, and energy dissipation capacity of the joint, enabling effective transfer of tensile stress from the beam segments to the column. The limit rotation of the joint reaches 0.05 rad in the failure state, satisfying the FEMA-350 ductility requirement of ≥0.03 rad for seismic resistance.

(3) The proposed FEA model of the steel-beam-CFDST-column composite joint is effective for predicting the behavior of the joint and can be used for further parametric analysis.

(4) Based on the results of parametric investigations, the stiffened height of the anchorage web plate and the strength of the steel beam significantly affect the bearing moment capacity of the joint, while the strengths of the concrete and steel tubes minimally affect that. The level of the axial load on the CFDST column moderately affects the bearing moment capacity of the joint. The joint still behaves well under a high axial load level of 0.6.

(5) The bending moment capacity and initial stiffness of the composite joint are significantly enhanced with increasing steel ratio of the CFDST column, beam-to-column bending capacity ratio, and beam-to-column linear stiffness. A beam-to-column bending capacity ratio of 0.6 and beam-to-column linear stiffness ratio of 0.5 are suggested for optimality of the composite joint.

Further theoretical investigation of the proposed mechanical model of the composite joint based on the conclusions of the present study is planned by the authors.

Data Availability

The data used to support the findings of this study are available from the corresponding author upon request.

Conflicts of Interest

The authors declare that there are no conflicts of interest related to this study.

Acknowledgments

This study was financially supported by the National Natural Science Foundation of China (NSFC) (Grant no. 51508028), the Natural Science Foundation of Shaanxi Province (Grant no. 2018JQ5119), the China Postdoctoral Science Foundation (Grant nos. 2014M562357 and 2015M580803), the

Special Fund for Basic Scientific Research of the Central Colleges (Grant nos. 300102288112 and 310828173402), and the Postdoctoral Research Project of Shaanxi Province.

References

[1] B. McKinley and L.-F. Boswell, "Behaviour of double skin composite construction," *Journal of Constructional Steel Research*, vol. 58, no. 10, pp. 1347–1359, 2002.

[2] L.-H. Han, H. Huang, and X.-L. Zhao, "Analytical behaviour of concrete-filled double skin steel tubular (CFDST) beam-columns under cyclic loading," *Thin-Walled Structure*, vol. 47, no. 6-7, pp. 668–680, 2009.

[3] L.-H. Han, W. Li, and R. Bjorhovde, "Developments and advanced applications of concrete-filled steel tubular (CFST) structures: members," *Journal of Constructional Steel Research*, vol. 100, pp. 211–228, 2014.

[4] Q.-Q. Liang, "Nonlinear analysis of circular double-skin concrete-filled steel tubular columns under axial compression," *Engineering Structure*, vol. 131, pp. 639–650, 2017.

[5] L.-H. Han and W. Li, "Seismic performance of CFST column to steel beam joint with RC slab: experiments," *Journal of Constructional Steel Research*, vol. 66, no. 11, pp. 1374–1386, 2010.

[6] W. Li and L.-H. Han, "Seismic performance of CFST column to steel beam joints with RC slab: analysis," *Journal of Constructional Steel Research*, vol. 67, no. 1, pp. 127–139, 2010.

[7] N. Jianguo, H. Yuan, Y. Weijian, and F. Jiansheng, "Seismic behavior of CFRSTC composite frames considering slab effects," *Journal of Constructional Steel Research*, vol. 68, no. 1, pp. 165–175, 2012.

[8] J.-F. Wang and B.-F. Spencer, "Experimental and analytical behavior of blind bolted moment connections," *Journal of Constructional Steel Research*, vol. 82, no. 1, pp. 33–47, 2013.

[9] L.-P. Kang, R.-T. Leon, and X.-L. Lu, "Shear strength analyses of internal diaphragm connections to CFT columns," *Steel and Composite Structures*, vol. 18, no. 5, pp. 1083–1101, 2015.

[10] O. Rezaifar and A. Younesi, "Finite element study the seismic behavior of connection to replace the continuity plates in (NFT/CFT) steel columns," *Steel and Composite Structures*, vol. 21, no. 1, pp. 73–91, 2016.

[11] Z. Tao, W. Li, B.-L. Shi, and L. H. Han, "Behaviour of bolted end-plate connections to concrete-filled steel columns," *Journal of Constructional Steel Research*, vol. 134, pp. 194–208, 2017.

[12] J.-C. Liu, Y.-L. Yang, J.-P. Liu, and X. Zhou, "Experimental investigation of special-shaped concrete-filled steel tubular column to steel beam connections under cyclic loading," *Engineering Structures*, vol. 151, pp. 68–84, 2017.

[13] Y.-F. Zhang, J.-H. Zhao, and C.-S. Cai, "Seismic behavior of ring beam joints between concrete-filled twin steel tubes columns and reinforced concrete beams," *Engineering Structures*, vol. 39, pp. 1–10, 2012.

[14] D.-F. Zhang, Y.-F. Zhang, and J.-H. Zhao, "Finite element analysis on the ring beam joint with discontinuous outer tube between composite CFST and RC beams," *Building Structures*, vol. 43, no. 5, pp. 39–44, 2013, in Chinese.

[15] Y.-F. Zhang, D.-F. Zhang, and J.-H. Zhao, "Experimental study on seismic behavior of the connection between composite CFST column and H-shape steel beam," *Journal of Building Structure*, vol. 34, no. 9, pp. 40–48, 2013, in Chinese.

[16] GB 50936-2014, *Technical Code for Concrete Filled Steel Tubular Structures*, China Architecture & Industry Press, Beijing, China, 2014, in Chinese.

[17] JGJ/T 101-2015, *Specification for Seismic Test of Buildings*, China Architecture & Building Press, Beijing, China, 2015, in Chinese.

[18] GB/T 228.1-2010, *Metallic Materials-Tensile Testing-Part I: Method of Test at Room Temperature*, China Standard Press, Beijing, China, 2010, in Chinese.

[19] N. Abdel-Rahman and K. Sivakumaran, "Material properties models for analysis of cold-formed steel members," *Journal of Structural Engineering*, vol. 123, no. 9, pp. 1135–1143, 1997.

[20] L.-H. Han, Z. Tao, and W.-D. Wang, *Advanced Composite and Mixed Structure-Testing, Theory and Design Approach*, China Science Press, Beijing, China, 2009, in Chinese.

[21] J. Lubliner, J. Oliver, S. Oller, and E. Oñate, "A plastic-damage model for concrete," *International Journal of Solids and Structures*, vol. 25, no. 3, pp. 299–326, 1989.

[22] J. Lee and G. Fenves, "Plastic-damage model for cyclic loading of concrete structures," *Journal of Engineering Mechanics*, vol. 124, no. 8, pp. 892–900, 1998.

[23] L.-H. Han, G.-H. Yao, and Z. Tao, "Performance of concrete-filled thin-walled steel tubes under pure torsion," *Thin-Walled Structure*, vol. 45, no. 1, pp. 24–36, 2007.

[24] GB 50011-2010, *Code for Seismic Design of Buildings*, China Architecture & Industry Press, Beijing, China, 2010, in Chinese.

[25] J. Zhang, Q.-Y. Wang, S.-Y. Hu et al., "Parameters verification of concrete damaged plastic model of ABAQUS," *Building Structure*, vol. 38, no. 8, pp. 127–130, 2008, in Chinese.

[26] S. Schneider, "Axially loaded concrete-filled steel tubes," *Journal of Structural Engineering*, vol. 124, no. 10, pp. 1125–1138, 1998.

[27] C. Roeder, B. Cameron, and C. Brown, "Composite action in concrete filled tubes," *Journal of Structural Engineering*, vol. 125, no. 5, pp. 477–484, 1999.

[28] FEMA-350, *Recommended Seismic Design Moment-Frame Buildings*, Federal Emergency Management Agency, Washington, DC, USA, 2000.

[29] Y.-F. Zhang, J.-H. Zhao, and Y.-Y. Liu, "Calculation of compressive bearing capacity of concrete-filled twin steel tubes based on twin shear unified strength theory," *Mechanics in Engineering*, vol. 34, no. 3, pp. 36–42, 2012, in Chinese.

[30] CECS 159: 2004, *Technical Specification for Structures With Concrete-Filled Rectangular Steel Tube Members*, China Planning Press, Beijing, China, 2004, in Chinese.

Hindawi
Advances in Materials Science and Engineering
Volume 2018, Article ID 4150145, 11 pages
https://doi.org/10.1155/2018/4150145

Research Article

Research on the Expansion Characteristics and Compressive Strength of Mortars Containing Circulating Fluidized Bed Combustion Desulfurization Slag

Zhi Cheng,[1,2] **Zhijun Cheng**,[2] **Hua Hou**,[1] **Tao Han**,[1] **and Lan Liu**[2]

[1]*School of Materials Science and Engineering, North University of China, Taiyuan 030051, China*
[2]*School of Science, North University of China, Taiyuan 030051, China*

Correspondence should be addressed to Zhi Cheng; chengzhi@nuc.edu.cn

Received 28 February 2018; Revised 4 May 2018; Accepted 20 May 2018; Published 4 July 2018

Academic Editor: Kestutys Baltakys

Circulating fluidized bed combustion (CFBC) desulfurization slag is a waste residue discharged from coal power plants. In this article, expansion characteristics and compressive strength of mortars containing CFBC desulfurization slag were evaluated, subjected to mechanical grinding time, the amount of additive, and chemical activation. Correlations between the linear expansion rate and compressive strength were investigated. The hydration products of cement-slag cementitious system were analyzed by X-ray diffraction (XRD) and scanning electron microscopy (SEM). The results show that mechanical grinding can increase both the expansion and compressive strength of mortars containing CFBC desulfurization slag, and the compressive strength and linear expansion can develop in coordination. While increasing the amount of the fine desulfurization slag, the linear expansion rate increases, and the compressive strength reaches to the maximum when the amount is 30%. Moderate sodium sulfate as an activator can both promote the compressive strength and increase the expansion of mortars.

1. Introduction

In 2012, coal accounted for about 30% of primary energy sources available and played a role in 41% of the world's electricity generation. As the largest country in terms of coal consumption in the world, China consumed 2.943 billion tons of standard coal equivalent in 2013, accounting for more than half of the global total. It is estimated that global coal consumption will increase by more than 50%, as compared with 97% in developing countries, by 2030 [1, 2]. Circulating fluidized bed combustion (CFBC) technology is an environmentally friendly, efficient, and clean coal-fired technology, which can use common bituminous coal, anthracite, lignite, peat, and coal gangue as fuels [3–6]. CFBC was popularized rapidly in the last two decades. Because limestone is added to CFBC as a desulfurizer, the discharged ash and slag of CFBC are 30%–40% more than those of pulverized coal combustion. Most of them cannot be utilized and stacked directly in storage sites, which not only occupied the land and polluted the environment but also wasted. The comprehensive utilization of CFBC ash and slag has aroused much attention.

CFBC desulfurization slag is the waste residue discharged from the bottom of CFBC [7]. CFBC desulfurized slag is produced at 850~900°C, which is different from pulverized coal combustion ashes. The physical and chemical properties of CFBC desulfurization slag are also different from pulverized coal combustion ashes [8, 9]. Previous researches have shown that CFBC desulfurization slag has pozzolanic activity, self-hardening property, large water absorption, and high expansibility. A higher content of $CaSO_4$ and f-CaO leads to larger volume expansion, which has adverse effects on the properties of products prepared with CFBC desulfurization slag and limits its use in building materials [10].

Some researchers [9, 11, 12] have performed investigations on the expansion characteristics and mechanical properties of CFBC desulfurized slag. They concluded that the expansibility is closely related to the content of SO_3

Table 1: The chemical composition of CFBC desulfurization slag (wt.%).

SiO_2	Al_2O_3	CaO	SO_3	Fe_2O_3	MgO	TiO_2	K_2O	P_2O_5	Na_2O	MnO	Cl	ZnO
42.19	25.9	10.99	5.91	3.10	1.35	0.84	0.79	0.12	0.06	0.03	0.02	0.01

(usually anhydrite) and f-CaO, and mechanical grinding and chemical activation can increase CFBC desulfurized slag's strength. However, CFBC desulfurization slags from different regions or different types of coals have different chemical composition content, which results in significant disparities in activity and expansibility. Mechanical grinding, especially ultrafine grinding, can improve the activity of desulfurization slag, but the influence mechanism of grinding on expansion is not clear. The use of chemical activators such as sulfate and other materials can improve the activity of desulfurization slag but increase volume expansion. The expansion in late hydration may cause the strength to be reduced or even eliminated [13–15]. Moreover, there is seldom report on study of CFBC desulfurization slag in mortar or concrete as an additive. It is necessary to research on desulfurization slag as additive so as to verify the possibility of CFBC desulfurization slag as an additive in mortar or concrete.

In this paper, mortars containing CFBC desulfurization slag were prepared, the linear expansion rate and compressive strength of the mortars were tested, the influence mechanism of grinding time, amount of CFBC desulfurization slag and sodium sulfate on the expansion characteristics, and compressive strength of mortars were investigated, and furthermore, the correlation between the expansion characteristics and compressive strength of the mortar was analyzed.

2. Experiments

2.1. Materials and Sample Preparation. Raw CFBC desulfurization slag was from Pingshuo Coal Gangue Power Plant of Shanxi Province in China. It was ground by a standard ball mill for 13 minutes, 25 minutes, 39 minutes, 55 minutes, and 72 minutes, respectively. After grinding, the samples were sent through an 80 μm square hole sieve. Samples were labeled as T1, T2, T3, T4, and T5 and then used in this experiment. The physical and chemical properties of CFBC desulfurization slag were determined by an ARL 9800XP plus X-ray fluorescence (XRD), and the results are given in Table 1 and Figure 1.

The specific surface area and particle size distribution of CFBC desulfurized slag under different grinding times were tested using the HELOS-RODOS (Sympatec GmbH Co., Ltd., Clausthal-Zellerfeld, Germany), as shown in Table 2. Differential and cumulative particle size distribution curves are shown in Figure 2. With grinding time increasing, the specific surface area also increases. However, when grinding time is more than 55 minutes and the powder was ground until 72 minutes, the specific surface area decreases. This is due to the "agglomeration" phenomenon [16].

The morphology of raw slag and ground slags was characterized by field emission scanning electron microscopy

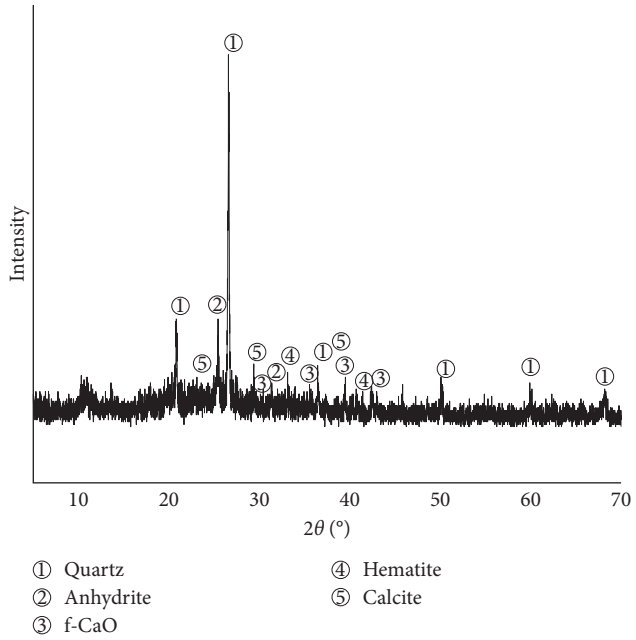

Figure 1: XRD patterns of CFBC desulfurized slag.

(FE-SEM, Hitachi S4800), as shown in Figure 3. Through scanning electron microscopy (SEM) observation, it can be observed that the surface of the raw desulfurization slag is loose and porous. Although the particle size becomes smaller after grinding, the surface is still loose and porous [15, 16].

The cement of Grade PO 42.5 from Chihoi cement plant was used in this experiment. The fine aggregate was China ISO Standard sand, produced by Xiamen ISO Standard Sand Co., Ltd. Solid sodium sulfate was produced by Tianjin Guangfu Technology Development Co., Ltd. Polycarboxylate superplasticizer was used as the water-reducing admixture.

2.2. Mixture Proportions of Mortars. The mixture proportions of mortars are shown in Table 3. Cementitious materials included cement and ground CFBC desulfurization slag. The ratio of cementitious materials and standard sand was 1:2 (mass ratio), the water-to-binder ratio (W/B) was 0.3, and the ground slags were used from T1 to T5. The dosages of ground desulfurization slag were 10%, 20%, 30%, 40%, and 50% of the total cementitious materials. The dosages of sodium sulfate were 1%, 1.5%, and 2% of the total cementitious materials. Thirteen types of mortars (SJ1~SJ13) were created, referring to JC/T 603–2004, "standard test method for drying shrinkage of mortar."

2.3. Test Methods. The compressive strength of mortars was tested according to the Chinese Standard GBT 17671–1999,

Table 2: Particle size distribution with grinding time of CFBC desulfurization slag.

Grinding time (min)	Specific surface area (m^2/kg)	Particle size distribution (%)							
		0–3 μm	3–10 μm	10–18 μm	18–25 μm	25–36 μm	36–50 μm	50–102 μm	>102 μm
13	260	13.67	12.22	9.46	5.72	7.87	8.61	23.53	18.92
25	330	17.49	15.79	12.17	7.18	9.91	10.68	21.52	5.26
39	400	21.33	18.97	14.08	8.09	10.7	10.37	12.87	3.59
55	650	32.89	22.66	13.89	8.81	9.44	7.55	4.76	0
72	630	31.21	22.93	14.65	8.73	8.87	6.9	6.71	0

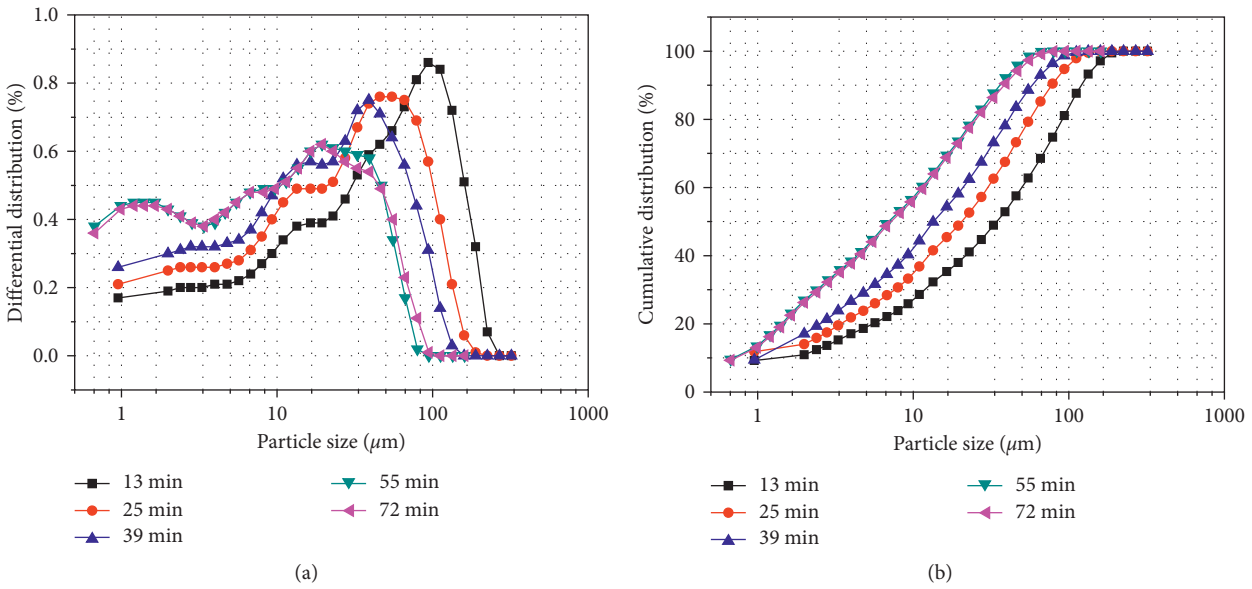

Figure 2: Differential and cumulative particle size distribution of CFBC desulfurization slag.

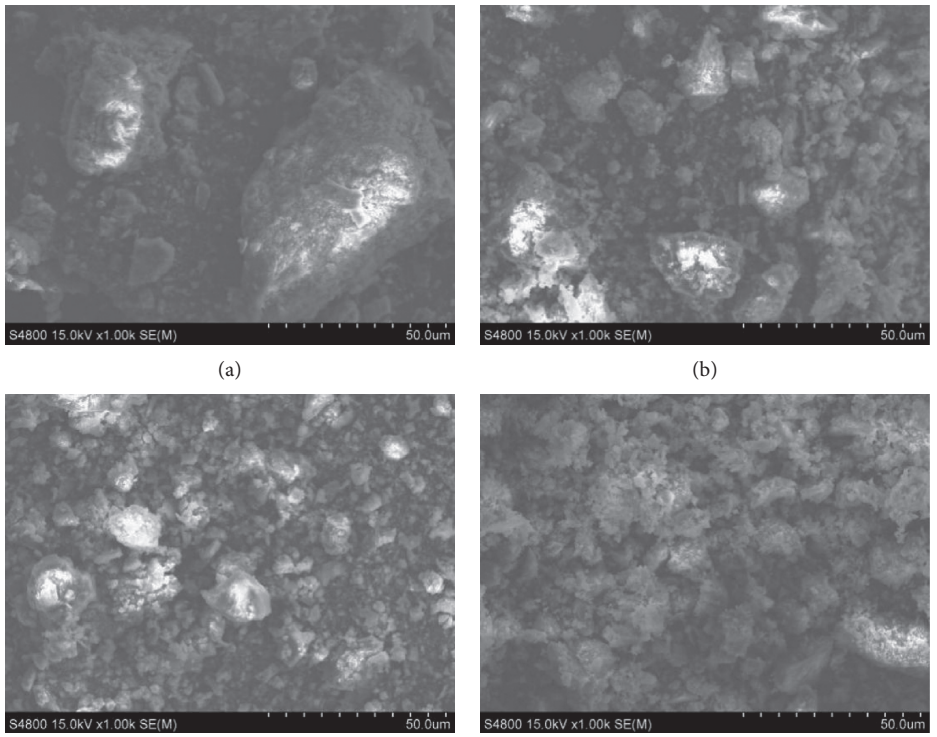

Figure 3: SEM images of CFBC desulfurization slag particles. (a) Raw slag; (b) T1 (13 min); (c) T3 (39 min); (d) T5 (72 min).

Table 3: Mixture proportions of mortars.

Number	Fineness	Cementitious materials	Cement	Desulfurization slag	Sodium sulfate	Standard sand	Water	Water-reducing admixtures
SJ1	T1 (13 min)	500	350	150	0	1000	150	1.0%
SJ2	T2 (25 min)	500	350	150	0	1000	150	0.9%
SJ3	T3 (39 min)	500	350	150	0	1000	150	1.0%
SJ4	T4 (55 min)	500	350	150	0	1000	150	0.9%
SJ5	T5 (72 min)	500	350	150	0	1000	150	0.8%
SJ6	—	500	500	0	0	1000	150	0.5%
SJ7	T3 (39 min)	500	450	50	0	1000	150	0.8%
SJ8	T3 (39 min)	500	400	100	0	1000	150	0.8%
SJ9	T3 (39 min)	500	300	200	0	1000	150	1.1%
SJ10	T3 (39 min)	500	250	250	0	1000	150	1.2%
SJ11	T3 (39 min)	500	350	150	5	1000	150	1.2%
SJ12	T3 (39 min)	500	350	150	7.5	1000	150	1.4%
SJ13	T3 (39 min)	500	350	150	10	1000	150	1.6%

"inspection method for the strength of the cement sand mortar (ISO method)." The specimens were put in a standard curing box after pouring. The mold was removed after 24 hours and then cured in water.

The linear expansion rate test was carried out according to the Chinese Industry Standard JC/T 603-2004, "standard test method for drying shrinkage of mortar." The curing condition was same as compressive strength specimens'. After demoulding, the initial length values of specimens were measured as L_0, and the length values at any age were measured as L_1. The expression $(L_1 - L_0)/L_0 \times 100\%$ can be used to calculate the linear expansion rate of mortar at each age.

Mineralogical compositions and the hydrated products were identified via X-ray diffraction (XRD) using the D/max-RB X-ray diffraction system (Japan Rigaku Corporation, Tokyo, Japan). The microstructures of the hydrated products were detected using SEM (Hitachi S4800; Hitachi, Ltd., Tokyo, Japan).

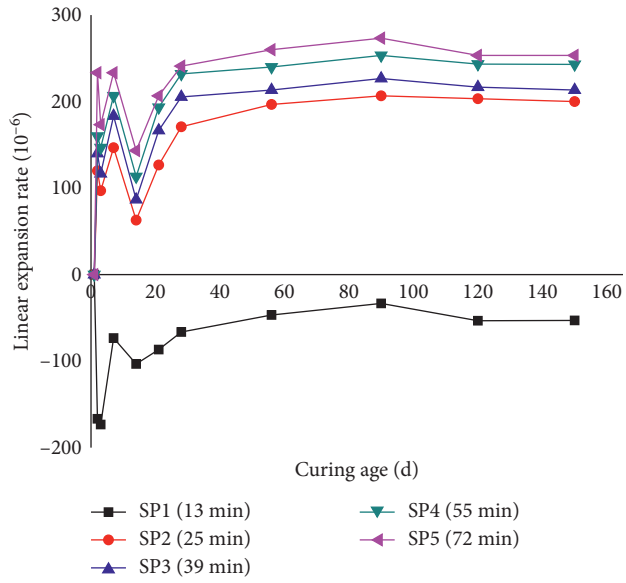

Figure 4: Linear expansion rate of the mortars with different grinding times.

3. Results and Discussion

3.1. Influences of Grinding Time on Mortars. Linear expansion rate curves of the mortars with different grinding times are shown in Figure 4. The linear expansion rate of the mortars has a large fluctuation in the early age. After removal of the mold, there is a period of controlled expansion or shrinkage from the first 7 days to 14 days. After 14 days, the mortars continue to expand or shrink and become stable after 28 days. SP1 shows shrinkage characteristics, while SP2, SP3, SP4, and SP5 show expansion characteristics. The longer the slag's grinding time, the bigger the mortar's linear expansion rate.

The existence of anhydrite and f-CaO in desulfurization slag is the main reason why mortars expand. In contact with water, anhydrite produces gypsum and f-CaO produces Ca$(OH)_2$, and then, hydration products continue to react to form ettringite. These reactions all lead to volume expansion [17–19]. In desulfurization slag, the anhydrite is wrapped by f-CaO. On the one hand, grinding can increase the content of f-CaO and improve the alkalinity, which will help to produce Ca$(OH)_2$ and accelerate the hydration of the anhydrite; on the other hand, grinding can destruct the wrapping structure and release anhydrite, which will help to produce gypsum. The longer the grinding time is, the more the anhydrite and f-CaO will be. Therefore, the larger the linear expansion rate will be.

The compressive strengths of mortars with different grinding times are shown in Figure 5. While curing age increases, the compressive strengths of mortars containing desulfurization slag with various grinding times all increase. At each age, the longer the grinding time is, the bigger the compressive strength will be.

The hydration products of desulfurization slag mainly are calcium silicate hydrate (C–S–H) gel, hydrated calcium aluminate, gypsum, calcium hydroxide, ettringite, etc. Among them, C–S–H gel and ettringite are the main

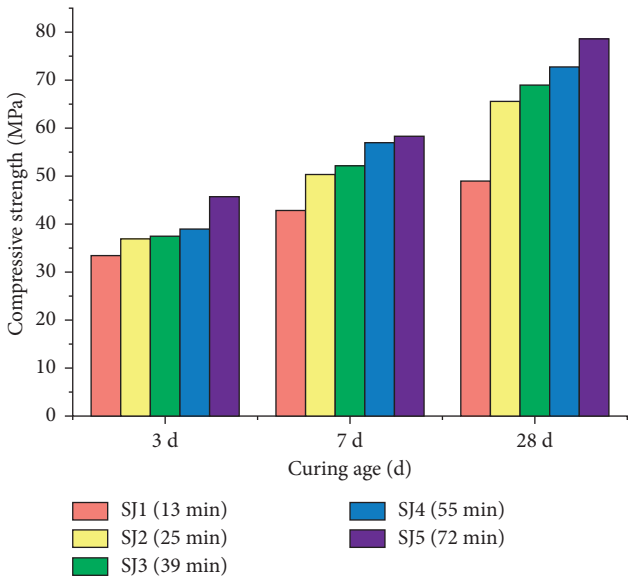

Figure 5: Compressive strength of the mortars with different grinding times.

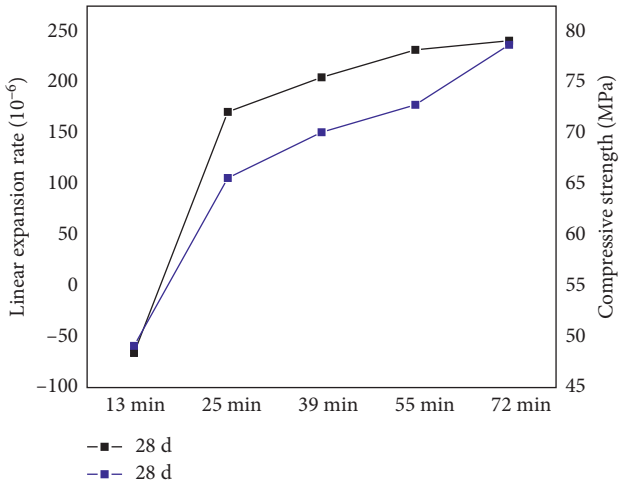

Figure 6: Correlation between the linear expansion rate and compressive strength.

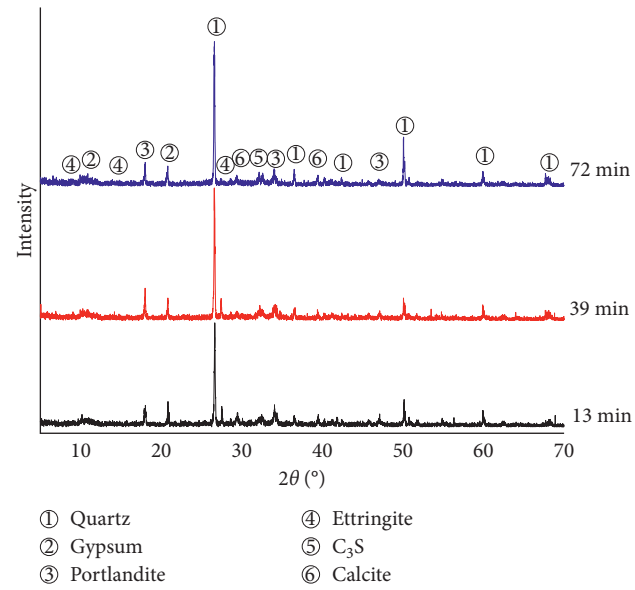

Figure 7: XRD patterns of the mortars with different grinding times at 3 d age.

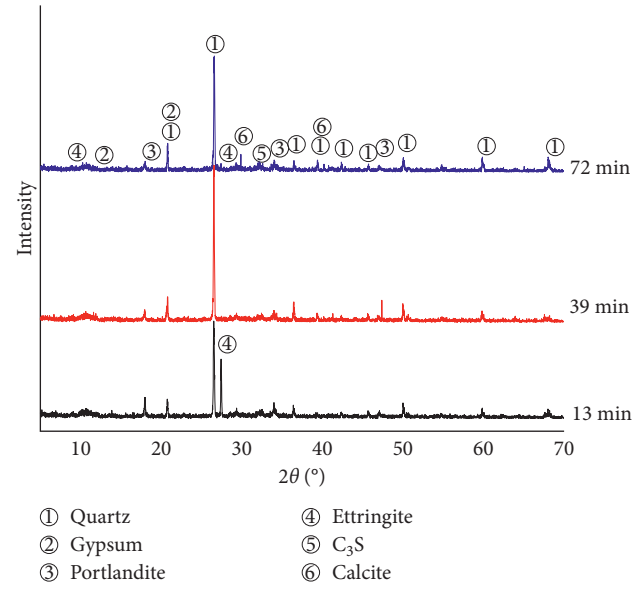

Figure 8: XRD patterns of the mortars with different grinding times at 28 d age.

materials forming cementitious system strength. Grinding can increase the surface area of the desulfurization slag, improve the activity of active components such as SiO_2 and Al_2O_3, and make the hydration process fast [20]. The longer the grinding time is, the quicker and better the hydration will be, and the more the C–S–H gel and ettringite will produce. Meanwhile, the hydration of anhydrite is also faster, which can fill the voids and improve strength.

The correlation curve of linear expansion rate and compressive strength under different grinding times of desulfurization slag at 28 d age is shown in Figure 6. The linear expansion rate and compressive strength of mortars all increase while grinding time increases. So we can conclude that the linear expansion rate is positively correlated with the compressive strength under different grinding times. This indicates that mechanical grinding can improve both the linear expansion rate and the compressive strength of the mortars, and the compressive strength and linear expansion can develop in coordination.

XRD patterns of the mortars with different grinding times at different ages are shown in Figures 7 and 8. We can find that, as grinding time increases, X-ray diffraction peak intensity of $Ca(OH)_2$ and gypsum has little difference at 3 d age, while X-ray diffraction peak intensity of $Ca(OH)_2$ decreases, and X-ray diffraction peak intensity of gypsum increases at 28 d age. This indicates that the longer the grinding time is, the faster and greater the $Ca(OH)_2$ reacts with other substances, and the more the anhydrite hydrates,

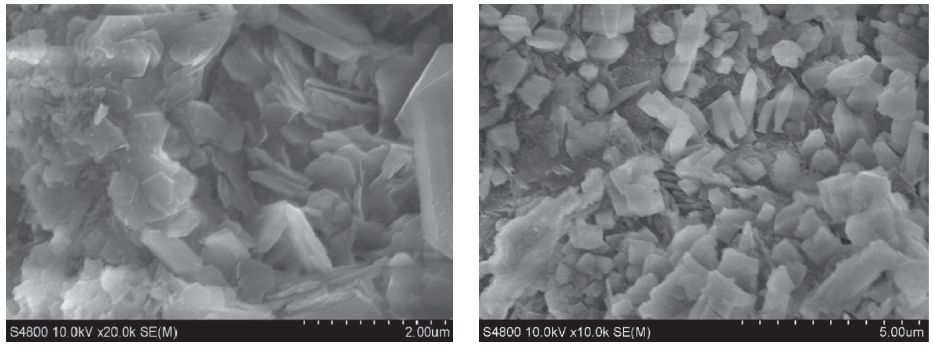

(a) (b)

Figure 9: SEM of mortars with different grinding times at 28 d age. (a) SJ1; (b) SJ5; $Ca(OH)_2$ is hexagonal plate; gypsum is clavate.

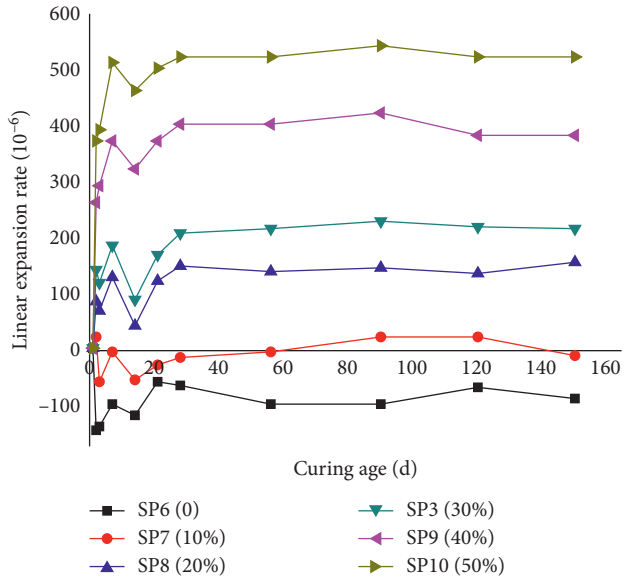

Figure 10: Linear expansion rate of mortars with different amounts of slag.

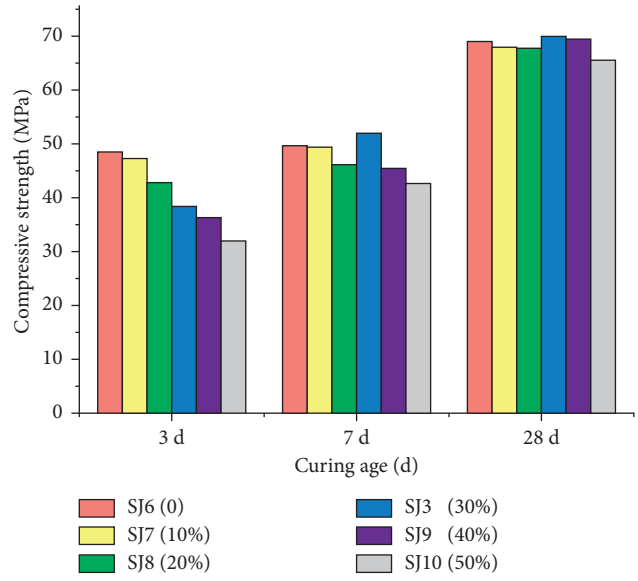

Figure 11: Compressive strength of mortars with different amounts of slag.

and then, the more the C–S–H gel and ettringite produce. This is the reason why longer grinding time of desulfurization slag leads to larger volume expansion and bigger compressive strength. By SEM, we can find that there is a large amount of hexagonal plate $Ca(OH)_2$ in SJ1 and a large amount of clavate gypsum in SJ5 at 28 d age, as shown in Figure 9.

3.2. Influences of Desulfurization Slag's Amount on Mortars. As shown in Figure 10, comparing with SJ6, SJ1~SJ5 containing fine desulfurization slag show clear expansion characteristics. The specimens release expansion intensively for 7 days, then shrink from 7 days to 14 days, and after that, continue to expand and essentially stabilize after 28 days. The linear expansion rate is closely related to the amount of the fine desulfurization slag. The linear expansion rate increases with the amount of the fine desulfurization slag, which shows a positive correlation. That is because that the larger the amount of fine desulfurization slag, the more the expansion component such as anhydrite and f-CaO, and then the larger the expansion rate.

It can be seen from Figure 11 that all the compressive strengths of SJ1~SJ5 at 3 d age decrease when fine desulfurization slag is added. The bigger the amount of fine desulfurization slag, the bigger the decline. At 7 d age, the compressive strength of SJ3 with the content of 30% is higher than that of SJ6. The compressive strengths of SJ9 and SJ10 also increase significantly, which reduce the gap with SJ6. At 28 d age, SJ3 gains the highest compressive strength, SJ9 also gains higher compression strength than SJ6, and SJ10 has the lowest compressive strength but is down by only 4.8% in comparison with SJ6. The results indicate that the fine desulfurization slag has a negative effect on the early strengths of the mortars. The greater adverse effect occurs with a greater amount of additive. Meanwhile, the fine desulfurization slag can promote the growth speed of the mortars' compressive strength in later stage, and the compressive strength can be raised by a reasonable amount of fine desulfurization slag.

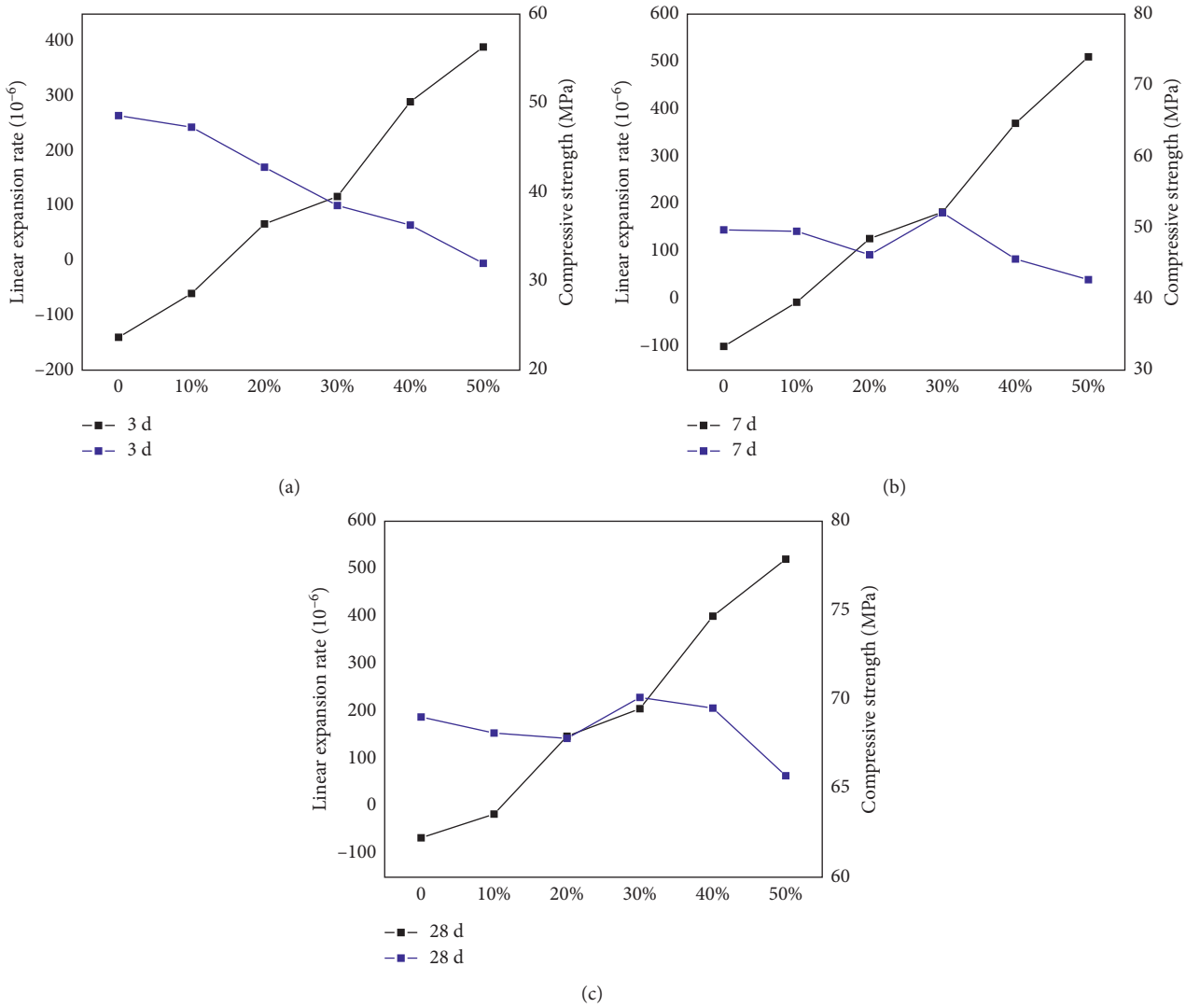

Figure 12: Correlation between the linear expansion rate and compressive strength.

The fine desulfurization slag contains active compositions such as SiO_2, Al_2O_3, and CaO. The activity has been further improved after mechanical grinding [21], so the slag has good activity. But the fine desulfurization slag also contains anhydrite, which hydrates slowly in the early age. So its hydration and hardening are slower than those of cement in the early age [22–24]. Therefore, in the early age, the higher the amount of fine desulfurization slag, the lower the activity, the slower the hardening speed, and the lower the strength. While curing age continues to increase, more anhydrite hydrates and more gypsum is produced. Gypsum can continue to react with $Ca(OH)_2$ and hydrated calcium aluminate and then produce ettringite. The ettringite can fill the pores and improve the compactness of mortars [25], so the compressive strength increases rapidly. But too much fine desulfurization slag can lead to great expansion and anhydrite cannot hydrate completely, which decrease the compressive strength of the mortar. So there exists a reasonable amount of fine desulfurization slag. When the amount is 30%, the compressive strengths at 7 d age and 28 d age gain the maximum compressive strength.

As shown in Figure 12, at 3 d age, with the increase of the desulfurization slag's amount, the linear expansion rate of the mortars increases gradually, while the compressive strength of the mortars decreases. The linear expansion rate and the compressive strength are negatively correlated. At the age of 7 d and 28 d, with an increase of desulfurization slag's amount, the linear expansion rate increases gradually, but the compressive strength gradually increases only when the amount is 20%~30%. It indicates that expansion and compressive strength of the mortars develop in coordination only when the amount is 20%~30%. When the amount is 30%, the compressive strength reaches to the maximum.

As shown in Figure 13, at 3 d age, the diffraction peak intensity of gypsum increases with the increase of amount, while $Ca(OH)_2$ is not very different. This indicates that, in the early age, the higher the amount of the desulfurization slag, the more the dissolved anhydrite, and the more the gypsum. The $Ca(OH)_2$ generated by calcium oxide and the

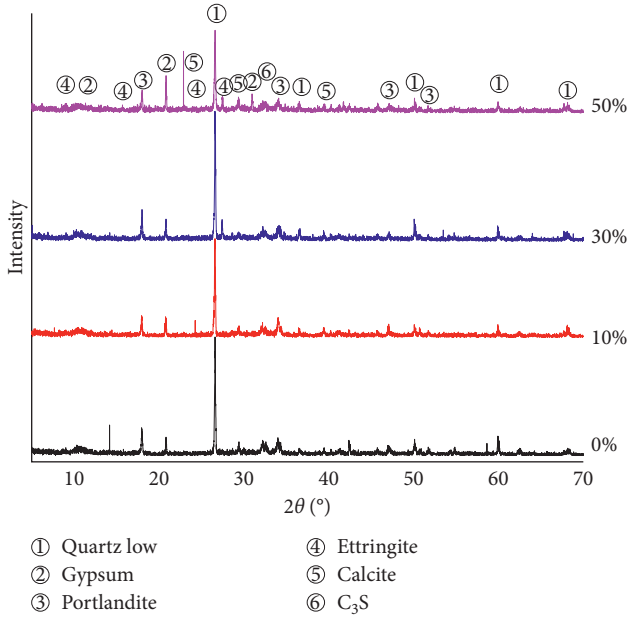

Figure 13: XRD patterns of mortars with different amounts at 3 d age.

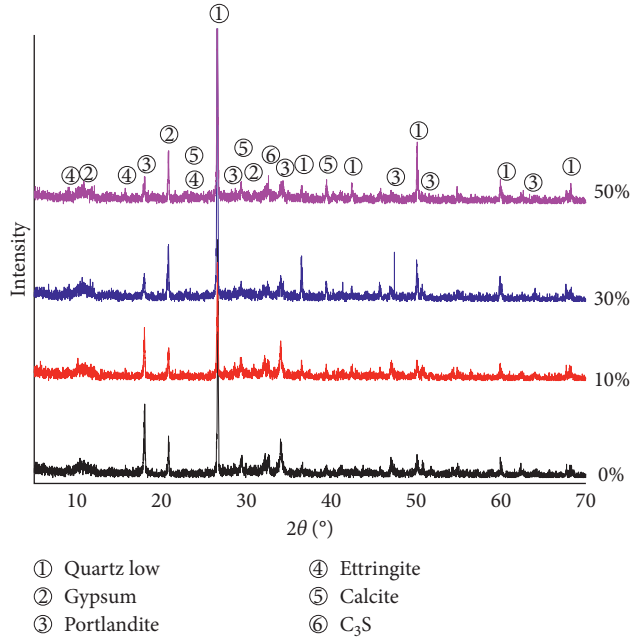

Figure 14: XRD patterns of mortars with different amounts at 28 d age.

$Ca(OH)_2$ participated in hydration reaction are nearly equal in number. As shown in Figure 14, at 28 d age, with the increase of the amount, the diffraction peak intensity of the $Ca(OH)_2$ is smaller and smaller, while the diffraction peak intensity of the gypsum is bigger and bigger. This indicates that the higher the amount is, the more the $Ca(OH)_2$ was consumed and the more the anhydrite hydrated to gypsum, which means that the more the C–S–H and ettringite produce.

When the amount of the desulfurization slag is too much, anhydrite cannot hydrate entirely. As shown in Figure 15, a large number of blocky anhydrite can be found, which means that there still exists unhydrated anhydrite. Figure 15 also shows that no cracks exist in SJ10, indicating that expansion did not cause damage to the specimen.

3.3. Influences of Sodium Sulfate on Mortars. As shown in Figure 16, the linear expansion rate of SP11, SP12, and SP13 is larger than that of SP3. The larger the amount of sodium sulfate, the larger the linear expansion rate. This indicates that sodium sulfate can increase the expansion of mortars. As seen from Figure 17, sodium sulfate can also increase the compressive strengths of mortars, especially the early compressive strength. As shown in Figure 18, with an increase in the amount of sodium sulfate, the linear expansion rate and the compressive strength both increase, which means that the linear expansion rate and compressive strength were positively correlated under different amounts of sodium sulfate. We can conclude that the linear expansion and compressive strength can develop in coordination with the addition of sodium sulfate.

The desulfurization slag contains SO_3 in a form of anhydrite, and anhydrite hydrates very slowly [26–29]. Researches have shown that alkali and sulfate can improve the activity of modified desulfurization ash [30, 31]. In this work, we used sodium sulfate as an activator.

Previous research has shown that moderate sodium sulfate can improve the early hydration rate of the anhydrite and increase its set and hardening speed greatly, but it has little effect on the later stage [32]. Anhydrite hydrates to gypsum, and then to produce ettringite, all can lead to volume expansion. So the linear expansion rate of mortar increases. Sodium sulfate can also raise the early compressive strength of mortar because of the production of more ettringite.

As shown in Figures 19 and 20, comparing with the mortar without sodium sulfate, the diffraction intensity of $Ca(OH)_2$ and gypsum is weaker, while the diffraction intensity of ettringite is stronger in the mortar with 1.5% sodium sulfate. This indicates that the hydration consumed more $Ca(OH)_2$ and gypsum and produced more ettringite. Therefore, the compressive strength and expansion rate of mortars are both raised. Through SEM as shown in Figure 21, a large number of clavate gypsum and acicular ettringite were found in the mortar with 1.5% sodium sulfate at 3 d age.

4. Conclusions

In this work, a series of mortars containing ground desulfurization slag from circulating fluidized bed combustion were prepared. Linear expansion rate and compressive strength were tested to evaluate expansion characteristics and mechanical property. XRD and SEM were used to verify mechanism analysis along with linear expansion rate and compressive strength tests. Several conclusions can be drawn based on the investigation; they are as follows:

Mechanical grinding can improve both the linear expansion rate and the compressive strength of the mortars. The longer the grinding time is, the bigger the linear

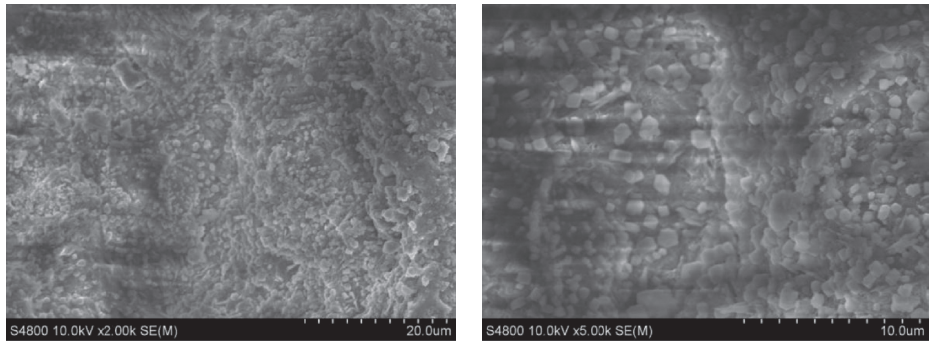

(a) (b)

Figure 15: SEM of SJ10 (50%). Note: anhydrite is blocky.

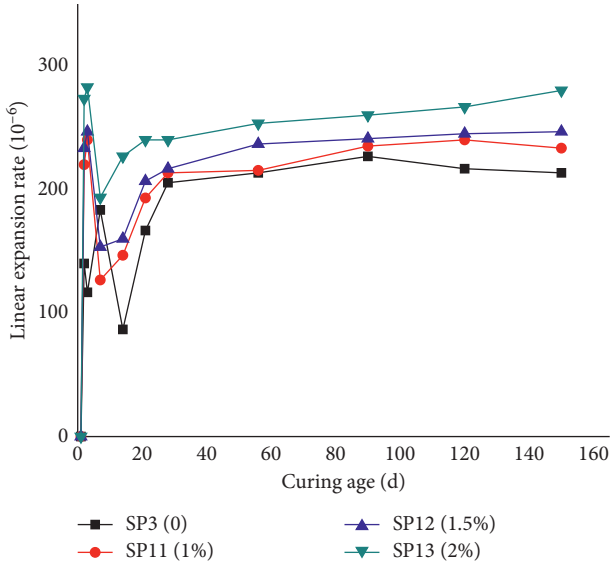

Figure 16: Linear expansion rate of mortars with different amounts of sodium sulfate.

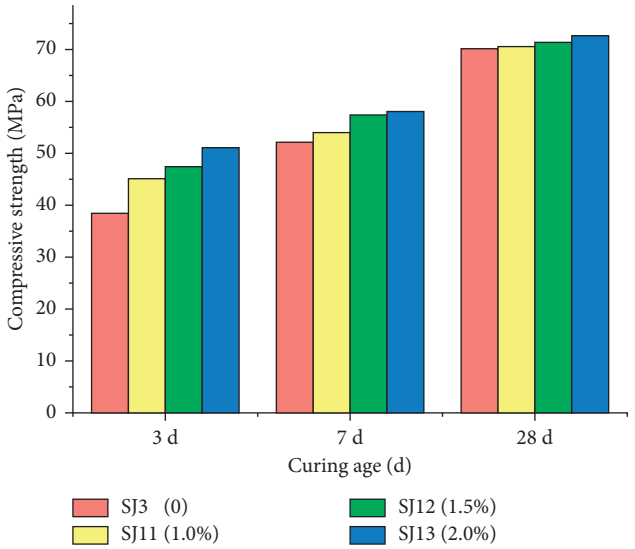

Figure 17: Compressive strength of mortars with different amounts of sodium sulfate.

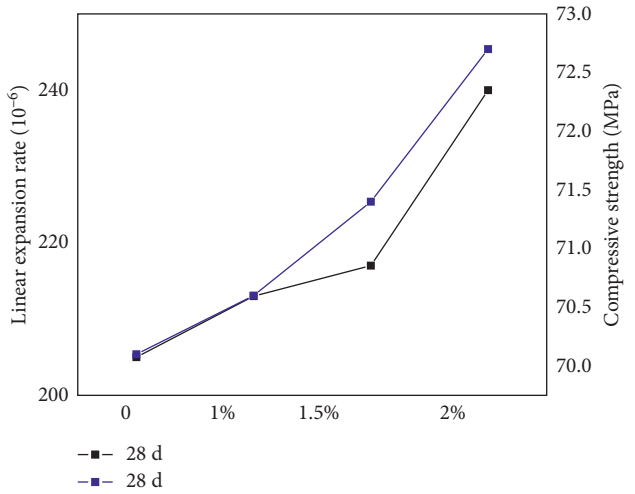

Figure 18: Correlation between the linear expansion rate and compressive strength.

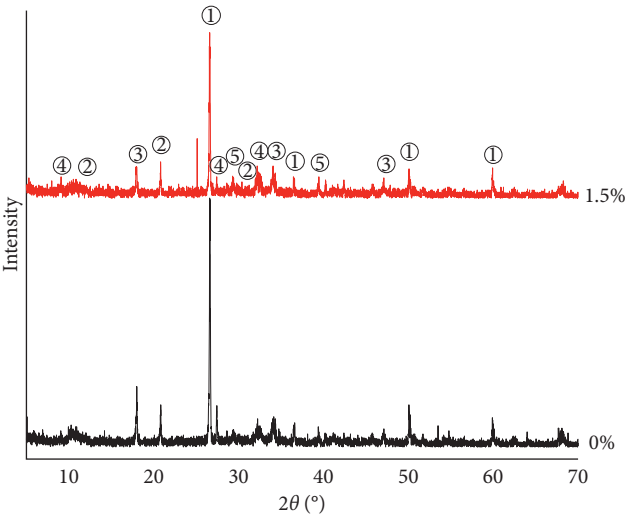

Figure 19: XRD patterns of mortars with different amounts of sodium sulfate at 3 d age.

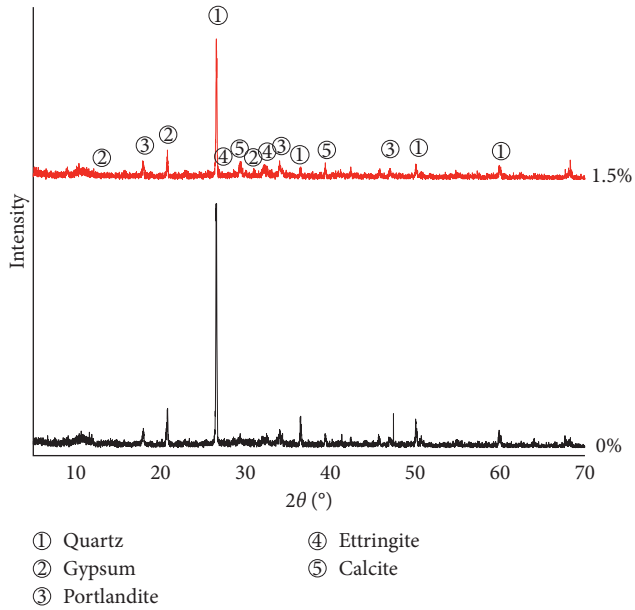

Figure 20: XRD patterns of mortars with different amounts of sodium sulfate at 28 d age.

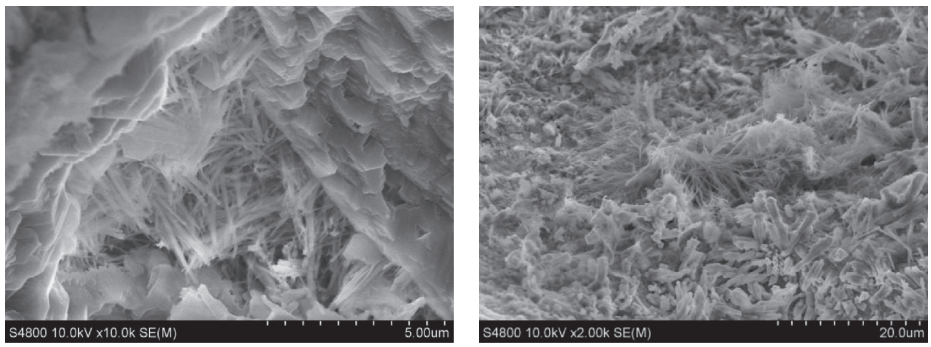

(a) (b)

Figure 21: SEM of the mortar (SJ12). Note: AFt is acicular; gypsum is clavate.

expansion rate and the compressive strength are. The linear expansion rate is positively correlated with the compressive strength under different grinding times.

The linear expansion rate increases with the amount of the fine desulfurization slag. At 3d age, all the compressive strengths of SJ1~SJ5 added fine desulfurization slag decline. The linear expansion rate and the compressive strength are negatively correlated. At 28 d age, the compressive strength gradually increases only when the amount is 20%~30%, and the mortar with 30% amount gains the highest compressive strength. There exists a reasonable amount of fine desulfurization slag for the compressive strength of mortar.

Sodium sulfate has an active excitation effect on the hydration of anhydrite in desulfurization slag with a moderate amount, which can promote the compressive strength and increase the expansion of mortars. With an increase in the amount of sodium sulfate, the linear expansion rate and the compressive strength both increase, and they showed a positive correlation.

Data Availability

The data used to support the findings of this study are available from the corresponding author upon request.

Conflicts of Interest

The authors declare that they have no conflicts of interest.

Acknowledgments

This work was financially supported by the Graduate Student Education Innovation Projects of Shanxi Province (no. 2016163) and Science Fundamental Research Projects of Shanxi Province (no. 201601D202048).

Supplementary Materials

The supplementary materials include images (Figure S1) of the linear expansion rate and compressive strength tests, as

well as the raw data of the compressive strength (Table S1) and the linear expansion rate (Table S2) of mortars. (*Supplementary Materials*)

References

[1] S. Naganathan, A. Yousef Omer Mohamed, and K. Mustapha, "Performance of bricks made using fly ash and bottom ash," *Construction and Building Materials*, vol. 96, pp. 576–580, 2015.

[2] J. Yuan, "The future of coal in China," *Resources, Conservation and Recycling*, vol. 129, pp. 290–292, 2018.

[3] J. Zhao, D. Wang, and S. Liao, "Effect of mechanical grinding on physical and chemical characteristics of circulating fluidized bed fly ash from coal Gangue power plant," *Construction and Building Materials*, vol. 101, pp. 851–860, 2015.

[4] S. Bae and K. Lee, "Carbonation behavior of fly ash with circulating fluidized bed combustion (CFBC)," *Journal of the Korean Ceramic Society*, vol. 52, no. 2, pp. 154–158, 2015.

[5] H. Nguyen, T. Chang, J. Shih, C. Chen, and T. Nguyen, "Influence of circulating fluidized bed combustion (CFBC) fly ash on properties of modified high volume low calcium fly ash (HVFA) cement paste," *Construction and Building Materials*, vol. 91, pp. 208–215, 2015.

[6] T. Wu, M. Chi, and R. Huang, "Characteristics of CFBC fly ash and properties of cement-based composites with CFBC fly ash and coal-fired fly ash," *Construction and Building Materials*, vol. 66, pp. 172–180, 2014.

[7] J. Koornneef, M. Junginger, and A. Faaij, "Development of fluidized bed combustion—an overview of trends, performance and cost," *Progress in Energy and Combustion Science*, vol. 33, no. 1, pp. 19–55, 2007.

[8] S. Rajaram, "Next generation CFBC," *Chemical Engineering Science*, vol. 54, no. 22, pp. 5565–5571, 1999.

[9] X. Li, Q. Chen, K. Huang, B. Ma, and B. Wu, "Cementitious properties and hydration mechanism of circulating fluidized bed combustion (CFBC) desulfurization ashes," *Construction and Building Materials*, vol. 36, pp. 182–187, 2012.

[10] W. Kuo, H. Wang, and C. Shu, "Engineering properties of cementless concrete produced from GGBFS and recycled desulfurization slag," *Construction and Building Materials*, vol. 63, pp. 189–196, 2014.

[11] Y. Chen, M. Ko, J. Chang, and C. Lin, "Recycling of desulfurization slag for the production of autoclaved aerated concrete," *Construction and Building Materials*, vol. 158, pp. 132–140, 2018.

[12] N. Dung, T. Chang, and C. Chen, "Engineering and sulfate resistance properties of slag-CFBC fly ash paste and mortar," *Construction and Building Materials*, vol. 63, pp. 40–48, 2014.

[13] X. Fu, Q. Li, J. Zhai, G. Sheng, and F. Li, "The physical–chemical characterization of mechanically-treated CFBC fly ash," *Cement and Concrete Composites*, vol. 30, no. 3, pp. 220–226, 2008.

[14] M. Chi and R. Huang, "Effect of circulating fluidized bed combustion ash on the properties of roller compacted concrete," *Cement and Concrete Composites*, vol. 45, pp. 148–156, 2014.

[15] X. Li, Q. Chen, B. Ma, J. Huang, S. Jian, and B. Wu, "Utilization of modified CFBC desulfurization ash as an admixture in blended cements: physico-mechanical and hydration characteristics," *Fuel*, vol. 102, pp. 674–680, 2012.

[16] Y. Xia, Y. Yan, and Z. Hu, "Utilization of circulating fluidized bed fly ash in preparing non-autoclaved aerated concrete production," *Construction and Building Materials*, vol. 47, pp. 1461–1467, 2013.

[17] E. J. Anthony and D. L. Granatstein, "Sulfation phenomena in fluidized bed combustion systems," *Progress in Energy and Combustion Science*, vol. 27, no. 2, pp. 215–236, 2001.

[18] E. Anthony, L. Jia, and Y. Wu, "CFBC ash hydration studies," *Fuel*, vol. 84, no. 11, pp. 1393–1397, 2005.

[19] E. J. Anthony, E. M. Bulewicz, K. Dudek, and A. Kozak, "The long term behaviour of CFBC ash–water systems," *Waste Management*, vol. 22, no. 1, pp. 99–111, 2002.

[20] P. Pourghahramani and E. Forssberg, "Microstructure characterization of mechanically activated hematite using XRD line broadening," *International Journal of Mineral Processing*, vol. 79, no. 2, pp. 106–119, 2006.

[21] Z. Zhang, J. Qian, C. You, and C. Hu, "Use of circulating fluidized bed combustion fly ash and slag in autoclaved brick," *Construction and Building Materials*, vol. 35, pp. 109–116, 2012.

[22] C. Freidin, "Influence of variability of oil shale fly ash on compressive strength of cementless building compounds," *Construction and Building Materials*, vol. 19, no. 2, pp. 127–133, 2005.

[23] L. Junfu, Z. Jiansheng, Z. Hai, L. Qing, and Y. Guangxi, "Performance evaluation of a 220t/H CFB boiler with water-cooled square cyclones," *Fuel Processing Technology*, vol. 88, no. 2, pp. 129–135, 2007.

[24] G. Sheng, J. Zhai, Q. Li, and F. Li, "Utilization of fly ash coming from a CFBC boiler co-firing coal and petroleum coke in Portland cement," *Fuel*, vol. 86, no. 16, pp. 2625–2631, 2007.

[25] G. Sheng, Q. Li, J. Zhai, and F. Li, "Self-cementitious properties of fly ashes from CFBC boilers co-firing coal and high-sulphur petroleum coke," *Cement and Concrete Research*, vol. 37, no. 6, pp. 871–876, 2007.

[26] N. Menad, J. N. Ayala, F. Garcia-Carcedo, E. Ruiz-Ayúcar, and A. Hernández, "Study of the presence of fluorine in the recycled fractions during carbothermal treatment of EAF dust," *Waste Management*, vol. 23, no. 6, pp. 483–491, 2003.

[27] Y. Song, J. Qian, Z. Wang, and Z. Wang, "Self-cementing mechanism of CFBC coal ashes at early ages," *Journal of Wuhan University of Technology-Mater*, vol. 23, no. 3, pp. 338–341, 2008.

[28] Y. Shen, J. Qian, and Z. Zhang, "Investigations of anhydrite in CFBC fly ash as cement retarders," *Construction and Building Materials*, vol. 40, pp. 672–678, 2013.

[29] G. Sheng, Q. Li, and J. Zhai, "Investigation on the hydration of CFBC fly ash," *Fuel*, vol. 98, pp. 61–66, 2012.

[30] J. Temuujin, R. P. Williams, and A. van Riessen, "Effect of mechanical activation of fly ash on the properties of geopolymer cured at ambient temperature," *Journal of Materials Processing Technology*, vol. 209, no. 12-13, pp. 5276–5280, 2009.

[31] P. Chindaprasirt, U. Rattanasak, and C. Jaturapitakkul, "Utilization of fly ash blends from pulverized coal and fluidized bed combustions in geopolymeric materials," *Cement and Concrete Composites*, vol. 33, no. 1, pp. 55–60, 2011.

[32] P. Jiahui, Z. Jianxin, Q. Jindong, B. Leng, and W. Tizhi, "Influence of sodium sulfate on anhydrite hydration process and morphology of its dihydrate products," *Journal of the Chinese Ceramic Society*, vol. 36, no. 10, pp. 1356–1361, 2008.

Hindawi
Advances in Materials Science and Engineering
Volume 2018, Article ID 2092383, 7 pages
https://doi.org/10.1155/2018/2092383

Research Article

Research on Wheat Straw Application in the Preparation of Superplasticizer

Yiping Guo,[1] **Weiyong Zhu**,[2] **Ruqin Gao**,[1] **and Guoting Li**[1]

[1]*Department of Environmental and Municipal Engineering, North China University of Water Resources and Electric Power, Zhengzhou 450046, China*
[2]*Powerchina Water Environment Governance, Shenzhen, Guangdong 518102, China*

Correspondence should be addressed to Yiping Guo; 82275113@qq.com

Received 3 March 2018; Revised 24 April 2018; Accepted 2 May 2018; Published 3 July 2018

Academic Editor: Nadezda Stevulova

Wheat straw was utilized in the preparation of polycarboxylate superplasticizer (PCS) to improve its performance as well as to reduce the production cost in this paper. The addition time and pretreatment time of wheat straw in the production of PCS were detected. Orthogonal experimental design was adopted to optimize the components of reactants, and the adding time of the initiator was also examined. The PCS produced with wheat straw in this paper kept a rather high water-reducing rate. In addition, the results of some physical characteristics showed there were no obvious differences between the PCS produced with and without wheat straw, while the PCS produced with wheat straw had the longer time of coagulation. At the same time, infrared spectrum implied that the addition of wheat straw made the side chain more abundant and had little influence on the main chain of the large molecules.

1. Introduction

Polycarboxylate superplasticizer (PCS) is recognized as vital admixtures in the utilization of modern concrete technology because they could improve the workability of concrete by dispersing agglomerated hydrating cement particles present in the paste, and they could result in the highly flowable concrete or reduce the water to cement ratio of concrete [1]. There are three generations of water-reducing mixtures used in concrete. The first generation is generally manufactured from lignosulfonates and is usually called the ordinary water-reducing agent. The second one is made from sulfonated naphthalene formaldehyde or sulfonated melamine formaldehyde which belongs to the superplasticizer. Polycarboxylate superplasticizer (PCS) was introduced as the third and latest generation of concrete admixtures in the 1980s which definitely has the superior performances [2, 3]. The ordinary water-reducing lignosulfonate-based mixture has the low production cost and excellent retarding effect. However, if their additive dosages exceeded the recommended dosages in concrete, it would result in the noncondensation of concrete for several days and delay the project. And under the limited recommended dosages, the water-reducing rate is just between 6% and 12%, which cannot meet the construction requirement. The second generation of superplasticizers has better performance and acceptable production cost; however, formaldehydes are used in large quantities in their production processes, which lead to the serious environmental pollutions. The latest polycarboxylate superplasticizer (PCS) could satisfy both the construction and environment requirements; however, the production costs are pretty high [4, 5]. With the development of sustainable strategy around the world, green chemistry has become a core part of the international chemistry discipline. From the perspective of material process engineering, which is the full utilization of renewable resources, it is imperative to develop new water-reducing agents that are environmentally friendly, meet the standard of performance, and have economic feasibility [6, 7].

Cellulosic biomass as the primary product of photosynthesis exists widely in terrestrial environments, and there are a large number of active groups such as hydroxyl groups consisted in the polymer structure of cellulose, which could easily occur derivatization through esterification and etherification reaction under certain conditions and at the

same time, some water-soluble cellulose derivatives show some prominent properties such as thickening, dispersion, emulsification, solubilization, and protective colloid. This derivative process has the features of extensive raw material sources and is environmental friendly, so it is widely used in many areas [8, 9]. In the field of building materials, research about cellulose derivatives such as water-reducing agent has also been attracted the attention and it has been reported that the main raw materials for the preparation of the water-reducing agent is based on biomass including cellulose, hemicelluloses, and starch and the modification methods including carboxymethylated, carboxyethyl, alkyl sulfonic acid, and sulfuric acid esterification. For example, the researchers from the United States and Japan used starch as the raw material to produce the polysaccharide water-reducing agent [10, 11]. In China, besides starch, there are researches utilizing cotton fiber, cotton linter, and bagasse as raw materials for the production of the water-reducing agent. These measures could reduce the production cost as well as reinforce the performance of concrete [12–14]. These researches show that, for all the polysaccharides such as starch, cellulose, and so on, through rational molecular design and the appropriate reaction conditions, they are probably prepared into water-reducing agents with high efficiency in concrete [15–18]. However, the systematic preparation process of the cellulose-based water-reducing agent is rarely reported.

Straws and stalks are the main part of crops, and a large number of straw and stalk wastes would be generated every year. If they are not handled properly, the serious resource wastes and environmental pollution would happen. The utilization of crop residues such as straws and stalks has been as a major strategic industry in the area of the renewable resources development in the 21st century of the world. And the resources' utilization is mainly focused on the development of chemical industry and building materials [19–21]. According to current reports, the raw materials used for the production of the water-reducing agent are mostly cellulose products. At the same time, the research on the utilization of straws and stalks directly to prepare the water-reducing agent has not been reported yet.

In this paper, wheat straw waste was joined in the preparation of polycarboxylate superplasticizer (PCS), through the graft copolymerization of the large molecules of straw fiber and PCS to improve the performance of the water-reducing agent as well as to reduce its production cost. The proper addition time of wheat straw was obtained. And the orthogonal experiment was utilized to optimize every ingredient ratio. At the same time, the addition speed of the initiator was also examined. The differences between the application performances and production cost of the PCS with and without the modification of wheat straw were compared. In addition, an infrared analysis was made to distinguish the mechanism.

2. Materials and Methods

2.1. Materials. Wheat straw was collected from the suburb of Zhengzhou, China. Before using, it was washed and soaked with deionized water and then fried at 80°C for 24 h. After that, they were ground and passed through an 80-mesh screen. Part of the sieved wheat straw was immersed in the solution of NaOH for 24 h, and the product was washed with 1% HCl and deionized water until the eluent reached neutral followed by drying at 80°C for 24 h by passing through the 80-mesh screen again. The final product was stored in a desiccator for further use in all the experiments.

Methyl allyl polyoxyethylene (TPEG) 2400 and 1000, schistose and waxy white solids, respectively, of industrial grade, were supplied by Jiangsu Haian Petroleum Chemical Factory. Maleic anhydride (MAN), flaky, white solid, was of analytical grade and purchased from Tianjin Kemiou Chemical Reagent Co., Ltd. Sodium methallyl sulfonate (SMAS), crystalline powder, was purchased from Shanghai Macklin Company. Acrylamide (AM), white solid, was of analytical grade and purchased from Tianjin Kemiou Chemical Reagent Co., Ltd. Ammonium persulfate, white, crystalline solid, was of analytical grade and also purchased from Tianjin Kemiou Chemical Reagent Co., Ltd. Sodium hydroxide, white, uniform grain, was purchased from Yantai Shuangshuang Chemical Industry Co., Ltd. The cement P.O. 42.5 was supplied by China United Cement Zhengzhou Co., Ltd.

2.2. Synthesis of PCS. TPEG-1000, TPEG-2400, maleic anhydride (MAN), sodium methallyl sulfonate (MAS), acrylamide (AM), and distilled water were added according to some proportion into a 500 ml four-neck round-bottom flask with a stirrer, a water separator with a condenser and a thermometer. The device was kept in a constant temperature water bath at a constant temperature of 80°C. When the reactants dissolved and reached the temperature of 80°C, the initiator was added through the constant pressure drop funnel. Then, the system was kept in the same temperature for several hours. When the reaction finished, it was naturally cooled to room temperature, followed by adjusting pH to 7.0 using sodium hydroxide solution. Finally, the water-reducing agent products of brown transparent liquid was obtained.

2.3. Performance Measurements. The cement fluidity of the water-reducing agent products was tested by the standard test method of the concrete additive uniformity test of China (GB/T 8077-2000), and the water cement ratio was 0.29.

The water-reducing rate determination method was according to the concrete admixture standard of China (GB8076-2008), and the calculation formula is as follows:

$$W_R = \left[\frac{(W_0 - W_1)}{W_0}\right] \times 100\%, \quad (1)$$

where W_R (%) is the water-reducing rate, W_0 (kg/m^3) is the water consumption of the benchmark concrete unit, and W_1 (kg/m^3) is the water consumption of the mineral admixture concrete unit.

Solid content determination and concrete slump tests were according to the concrete admixture standards of China (GB8076-2008); the errors were kept no more than 0.3%, and the calculation formula is as follows:

$$X_s = \left[\frac{(M_2 - M_0)}{(M_1 - M_0)}\right] \times 100\%, \quad (2)$$

where X_s (%) represents the solid content, M_0 (g) is the quality of the weighing bottle, and M_1 (g) is the quality of the original sample, while M_2 (g) is the quality of the weighing bottle and the dried sample.

In the determination of compressive strength, all the processes such as concrete mixing, molding, measurement, and data processing were in accordance with the ordinary concrete mechanics performance standard test method of China (GB/T50081-2002). The concrete was prepared according to the concrete admixture standard of China (GB/8076-2008), where the specified ratio of C (cement) : S (stone) : G (sand) : W (water) in the concrete mixture was 1 : 2.11 : 3.5 : 0.48 and the cement type was P.O 42.5 R, which was purchased from China United Cement Group Co., Ltd, in Henan Dengfeng. The sand and stone were produced in Jiayu town, Zhengzhou, Henan Province, China.

3. Results and Discussion

3.1. Addition of Wheat Straw in the Production of PCS

3.1.1. Effect of Different Addition Periods of Wheat Straw on Cement Fluidity. A mature technology of the preparation of PCS was selected through experimental comparison. The effect of different addition periods of wheat straw on cement fluidity was firstly examined, and the result is shown in Figure 1, where A represents the original process without wheat straw (WS), B represents that the wheat straw (WS) was initially added with other reactants, C represents that the wheat straw (WS) was added with the initiator, and D represents that the wheat straw (WS) was added after the addition of the initiator. It is clearly seen that the cement fluidity increased along with the addition of wheat straw, and the results implied that the performance of PCS could be improved through the addition of wheat straw. It could be seen that the maximum cement fluidity was obtained when the wheat straw was joined at the beginning of the reactions, and the cement fluidity increased a little when the wheat straw was added after the addition of the initiator. However, there was no change observed when the wheat straw added with the initiator. The results meant that wheat straw improved the fluidity performance of PCS maybe through graft copolymerization to the main chain macromolecules, and the mechanism should not be the free-radical polymerization, because the radical initiator could inactivate the effect of wheat straw. The better and feasible way was to add the wheat straw in the beginning with other reagents.

3.1.2. Effect of Pretreatment Time of Wheat Straw on Cement Fluidity. As is well known, wheat straw is composed of macromolecules such as cellulose, hemicelluloses, and lignin. In order to make the wheat straw to react sufficiently, pretreatment of wheat straw was utilized. On the basis of references and work experiences, hydrochloric acid with the concentration of 0.5 mol/L was selected to immerse wheat straw, and then, the mixture was kept at room temperature for different periods of time; after that, the mixture was suction filtered through the Büchner funnel and rinsed with distilled water at the same time in order to reduce the acidity of wheat straw; finally, it was dried and reserved for use. Figure 2 shows the effect of different pretreatment time periods of wheat straw on cement fluidity, where the pretreatment wheat straw of different time periods was added in the same quality at the beginning with other reactants. It can be seen from Figure 2 that when the pretreatment time of wheat straw was 0 and 12 h, the cement fluidity remained around 32 cm. However, when the pretreatment time increased to 18 h, the cement fluidity decreased a little. When the pretreatment time continued to extend, the cement fluidity decreased more. The results implied that the pretreatment was not in favor of the reactions because the improvement of the fluidity of PCS produced with wheat straw should be attributed to the graft copolymerization of

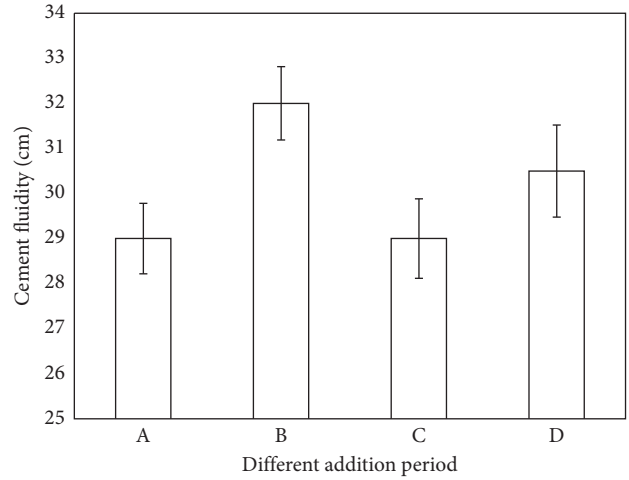

Figure 1: Effect of different addition periods of wheat straw (WS) on cement fluidity. A: no WS, B: WS added initially, C: WS added with the initiator, D: WS added after the initiator.

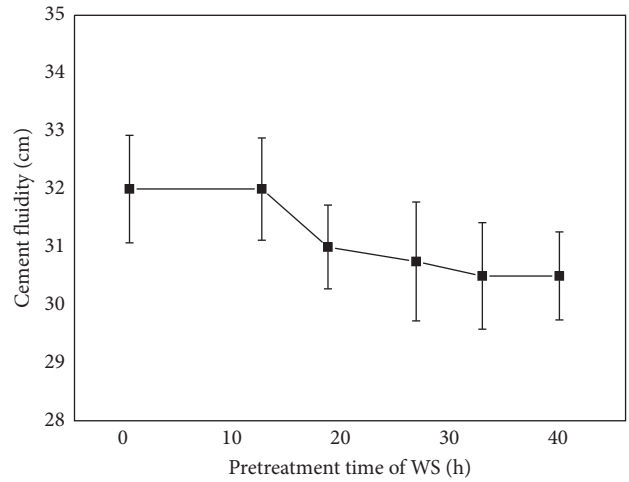

Figure 2: Effect of different pretreatment time periods of wheat straw (WS) on cement fluidity.

Table 1: Orthogonal experimental design for nine trials with three levels of concentrations for each reactant components' variable and corresponding cement fluidity.

Run	TPEG-2400	TPEG-1000	MAS	WS	Cement fluidity (cm)
1	1	1	1	1	27.5
2	1	2	2	2	28.75
3	1	3	3	3	29.75
4	2	1	2	3	31
5	2	2	3	1	28.25
6	2	3	1	2	31.5
7	3	1	3	2	32.25
8	3	2	1	3	30.75
9	3	3	2	1	32
MV 1	28.67	30.25	29.92	29.29	—
MV 2	30.25	29.25	30.92	30.83	—
MV 3	31.67	31.08	30.08	30.5	—
EV	3	1.83	1	1.58	—

the large molecules of wheat straw, while the pretreatment reduced the molecular weight of the wheat straw, which resulted in the decrease of the fluidity. So in the following experiments, the wheat straw without pretreatment was used directly in the reactions.

3.2. Optimization of Reactions for PCS Production with Wheat Straw

3.2.1. Optimization of Reactants for PCS Production. Orthogonal experimental design was adopted to find the optimal reactant components. Four reactants such as TPEG-2400, TPEG-1000, MAS, and wheat straw were chosen to optimize the components because they were the main ingredients that affect the product performance as well as the cost [22, 23]. Table 1 describes the orthogonal experimental design for nine trials with three levels of concentrations for each reactant components' variable and corresponding cement fluidity. At the same time, the mean values (MVs) and orthogonal extreme values (EVs) are also shown in Table 1, while Table 2 illustrates the levels of the four factors used in the experimental design. It could be seen from Table 1 that all the four factors influenced the cement fluidity of PCS directly, and the orthogonal extreme values of TPEG-2400, TPEG-1000, MAS, and wheat straw (WS) were 3, 1.83, 1, and 1.58, respectively. So, the sequence according to the effects of reactant on the cement fluidity of PCS was TPEG-2400, TPEG-1000, wheat straw (WS), and MAS. The results also verified that the performance of PCS depended on the amounts of macromolecules. In addition, it could be found that, in the orthogonal experiment design, the effect trends of TPEG-2400 and TPEG-1000 on the cement fluidity of PCS are still rising, which meant that if their dosages increased continually, the cement fluidity of PCS could improve; however, the product cost would also increase. In order to satisfy both the performance and the cost, the dosages of TPEG-2400 and TPEG-1000 were chosen to be 30 g and 18.75 g, respectively. And when the dosage for both MAS and wheat straw was 2 g, the cement fluidity of PCS had the optimal values.

Table 2: Levels of variables used in the experimental design.

Variable	Low level (1)	Middle level (2)	High level (3)
TPEG-2400 (g)	15	22.5	30
TPEG-1000 (g)	6.25	12.5	18.75
MAS (g)	1	2	3
WS (g)	1	2	3

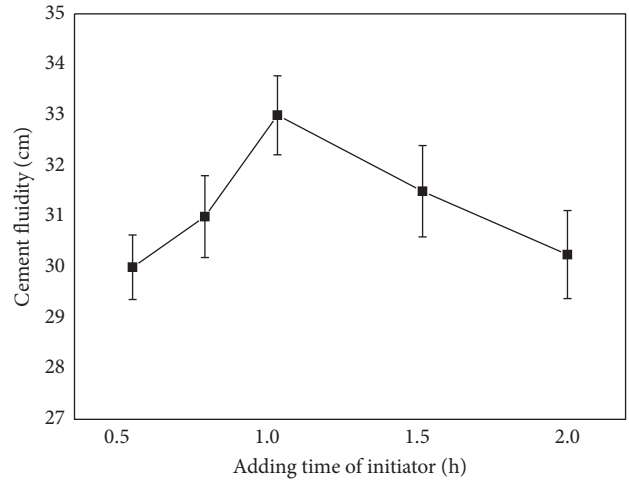

Figure 3: Effect of different adding time periods of the initiator on cement fluidity.

3.2.2. Optimization of Reaction Time for PCS Production with Wheat Straw. Considering the reaction characteristics of slow initiate, fast growth, and speed termination for free-radical polymerization, the adding time of the initiator is vital for the reactions. Temperature has a great influence on the decomposition of the initiator, and the higher the temperature is, the faster the initiator spreads; at the same time, more free radicals will be produced, and the polymerization speed is accelerated. Hence, the initiator is usually added when the reaction temperature gets the proper point, which is beneficial to the polymerization reaction. In this experiment, the proper temperature for the initiator added was 80°C, and the adding time was examined in order to obtain the optimal reaction condition. Figure 3 shows the effect of different adding time periods of the initiator on cement fluidity. The adding time was set as 0.5 h, 0.75 h, 1 h, 1.5 h, and 2 h, respectively, which meant the different adding speed of the initiator into the reaction system. It is clearly seen that the cement fluidity appeared in the parabolic trend along with the increase of adding time, and when the adding time was 1h, the maximal cement fluidity was obtained, which showed the optimal reaction condition, so the best adding time of the initiator was 1 h for this experiment.

3.3. Characteristics of the PCS Produced with Wheat Straw

3.3.1. Some Physical Properties. All the PCS produced with wheat straw appeared brown and without obvious odor with the pH around 7.0. In addition, some physical properties were also detected to better understand the characteristics of PCS produced with wheat straw in this experiment. Table 3

Table 3: Changes of density, viscosity, and solid content along with the variation in cement fluidity using the PCS produced with wheat straw.

Cement fluidity (cm)	ρ (g/ml)	μ (MPa·s)	Solid content (%)
27.5	1.182	62.3	39.2
28.75	1.190	60.0	39.5
31.5	1.193	61.6	40.2
32.25	1.192	66.8	40.5
33	1.195	65.7	40.7

shows the changes of solid content, density, and viscosity along with the variation in cement fluidity. It is clearly seen that both the solid content and density rose along with the increase of cement fluidity. At the same time, the viscosity also improved when wheat straw was utilized in the production of PCS. The viscosity of PCS without wheat straw was around 50 MPa·s, while the values of PCS with wheat straw were between 60 and 67 MPa·s. It was known that viscosity is related to the degree of molecular polymerization to some extent, so the molecular mass of PCS with wheat straw was bigger than the one without wheat straw. However, it could be seen from the table that the viscosity was not much related with the cement fluidity because the values were close and had no obvious rules.

3.3.2. Cement Fluidity under Different Dosages of PCS Produced with Wheat Straw. It is well known that the dosages of PCS have great effects on cement fluidity, so the dosages of PCS with wheat straw were tested to find the optimal dosage. Figure 4 exhibits the values of cement fluidity under different dosages of PCS produced with wheat straw. The obvious difference was observed with and without PCS, and along with the increase of dosages, the cement fluidity showed significant improvements. When the dosage was 0.5%, the cement fluidity reached the highest value, and when the dosage rose continually, the cement fluidity had no much changes. Considering the product cost, the dosage of 0.5% was chosen as the optimal one.

3.3.3. Comparison of Concrete Slump and Compressive Strength of PCS Produced with and without Wheat Straw. The concrete slump mainly refers to whether the mixing concrete is easy to be used in the construction for the workers and whether the concrete is uniformly dense. The concrete slump also reflects the properties of the concrete's fluidity, cohesion, and water retention, and all of these characteristics of concrete are affected by the performance of the water-reducing agent, so the concrete slump could be used to validate the performance of the water-reducing agent. When the concrete slump is smaller and the compressive strength is bigger, the performance of the water-reducing agent is better. Table 4 lists out the values of water-reducing rate, concrete slump, and compressive strength of the PCS samples produced with and without wheat straw. The results showed that there were no obvious differences between the two technologies, and the utilization of wheat straw in the production of PCS could maintain the high performance of PCS. And in the experiments, it was found that the PCS produced with wheat straw had longer time of coagulation, which is more beneficial for the construction. At the same time, the production costs were compared between the two technologies, and the production cost of the new technology could be reduced around 2 dollars per kilogram compared with the one without wheat straw.

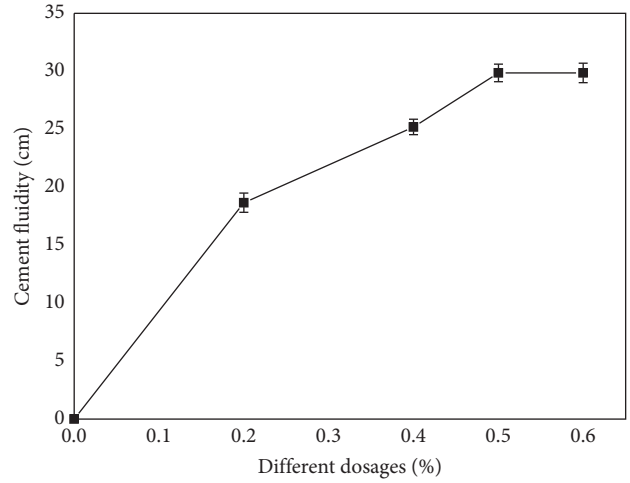

Figure 4: Cement fluidity under different dosages of PCS produced with wheat straw.

Table 4: Values of water-reducing rate, concrete slump, and compressive strength of PCS samples produced with and without wheat straw (WS).

PCS sample	Water-reducing rate (%)	Concrete slump (mm)	Compressive strength (MPa)		
			3d	7d	28d
Without WS	28.1	195	35.8	41.2	53.7
With WS	29.6	180	36.9	41.9	54.8

3.3.4. Infrared Spectrum Analysis. In order to obtain a deeper cognition of the new technology, infrared spectrum was adopted. The infrared spectrograms of PCS produced with and without wheat straw are plotted in Figures 5(a) and 5(b). It could be seen clearly that there were nine obvious peaks such as 3422.86 cm^{-1}, 2923.32 cm^{-1}, 2126.73 cm^{-1}, 1650.97 cm^{-1}, 1455.28 cm^{-1}, 1351.55 cm^{-1}, 1252.96 cm^{-1}, 1097.84 cm^{-1}, and 960.06 cm^{-1} in Figure 5(b), while there were just five obvious peaks such as 3383.15 cm^{-1}, 2110.79 cm^{-1}, 1642.52 cm^{-1}, 1350.78 cm^{-1}, and 1083.60 cm^{-1} in Figure 5(a).

These peaks indicated there were carboxyl and sulfonic groups and ether bond existed in the two products, while the hydroxyl group peak, carbon-hydrogen bond bending vibration peak, and stretching vibration peak of carbon-carbon bonds were not obvious in the product produced with wheat straw, which could be speculated that there were reactions between functional groups in wheat straw and hydroxyl group on the original chain; at the same time, the grafting reaction happened on the side chain restricted the vibration of the main chain.

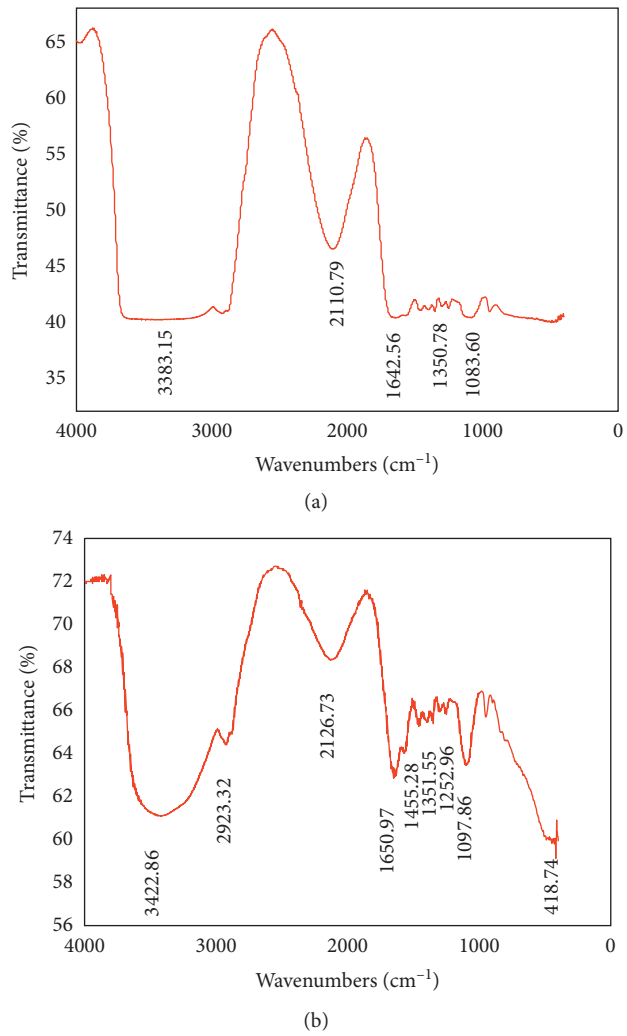

Figure 5: Infrared spectrograms of PCS produced (a) with wheat straw and (b) without wheat straw.

4. Conclusion

Experiment results showed that the utilization of wheat straw in the preparation of PCS could reduce its production cost as well as improve the performance. The optimal experimental conditions were that the wheat straw without additional chemical pretreatment was added with other reagents in the beginning of the reactions, and the mole ratios of methallyl polyoxyethylene (TPEG) 1000: methallyl polyoxyethylene (TPEG) 2400: maleic anhydride (MAN): acrylamide (AM): sodium methallyl sulfonate (SMAS) were 3 : 2 : 12 : 7 : 2. Meanwhile, the quality ratio of added wheat straw to methallyl polyoxyethylene (TPEG) 2400 was 1 : 15, and the initiator of ammonium sulfate dosage was 0.3% of the total mass fraction of monomer. The initiator concentration was 40% while the initiator adding time was 1 h, and the reaction system was kept at 80°C for 4 h at last. The rather high cement fluidity of 33 cm and the longer time of coagulation were obtained, which is more beneficial for the construction. At the same time, the production cost could be reduced around 2 dollars per kilogram product when using wheat straw. In addition, infrared spectrum revealed that the wheat straw could be grafted on to the main chain. The following research should focus on designing more rational reactions in view of molecular structure to fully develop the potential of wheat straw in the preparation of high-efficient water-reducing agents.

Data Availability

The data used to support the findings of this study are available from the corresponding author upon request.

Conflicts of Interest

The authors declare that they have no conflicts of interest.

Acknowledgments

The authors are thankful to the Foundation for University Key Youth Teacher of Henan Province of China (2013GGJS-088) and Science and Technology Research Project of Henan Province (152102210323 and 2017754).

References

[1] P. Gao, M. Deng, and N. Feng, "The influence of superplasticizer and superfine mineral power on the flexibility, strength and durability of HPC," *Cement and Concrete Research*, vol. 31, no. 5, pp. 703–706, 2011.

[2] C. A. Pierre, "Cements of yesterday and today, concrete of tomorrow," *Cement and Concrete Research*, vol. 20, no. 9, pp. 1349–1359, 2000.

[3] L. Lei and J. Plank, "A concept for a polycarboxylate superplasticizer possessing enhanced clay tolerance," *Cement and Concrete Research*, vol. 42, no. 10, pp. 1299–1306, 2012.

[4] J. Plank, Z. M. Dai, and H. Keller, "Fundamental mechanisms for polycarboxylate intercalation into C_3A hydrate phases and the role of sulfate present in cement," *Cement and Concrete Research*, vol. 40, no. 1, pp. 45–57, 2010.

[5] L. Lei and J. Plank, "Synthesis, working mechanism and effectiveness of a novel cycloaliphatic superplasticizer for concrete," *Cement and Concrete Research*, vol. 42, no. 1, pp. 118–123, 2012.

[6] F. Y. Zhou, *Synthetic Biology Sulfonate/Sulfate and Applied Research as Water Reducer*, Southwest University, Chongqing, China, 2015.

[7] H. F. Wu, *Study on Preparation and Performance of Bio-Superplasticizer*, Master's thesis, Changchun University of Technology, Changchun, China, 2012.

[8] C. M. Saric, K. H. Khayat, and H. A. Tagnit, "Performance characteristics of cement grouts made with various combinations of high-range water reducer and cellulose-based viscosity modifier," *Cement and Concrete Research*, vol. 33, no. 12, pp. 1999–2008, 2003.

[9] G. K. Byung, S. P. Jiang, and J. Carmel, "The adsorption behavior of PNS superplasticizer and its relation to fluidity of cement paste," *Cement and Concrete Research*, vol. 30, no. 6, pp. 887–893, 2000.

[10] M. C. Vieira, D. Klemm, and L. Einfeldt, "Dispersing agents for cement based on modified polysaccharides," *Cement and Concrete Research*, vol. 35, no. 5, pp. 883–890, 2005.

[11] L. Einfeldt, G. Albrecht, and A. Kem, "Use of water-soluble polysaccharide derivatives as dispersing agents for mineral binder suspensions," US Patent 20040103824AI, 2004.
[12] F. Y. Huang, *Synthesis and Application of Concrete Water Reducers Based on Natural Polymers*, Dalian University of Technology, Dalian, China, 2008.
[13] W. Q. Liu and G. J. Luo, "Preparation of concrete additive from lint cellulose," *Chemical Materials for Construction*, vol. 12, no. 3, pp. 118–120, 1996.
[14] F. Z. Gong, S. X. Cheng, and C. H. Li, "Preparation of water soluble dispersant agent from cane dregs," *Guangxi Chemical Industries*, vol. 30, no. 2, pp. 6–8, 2001.
[15] W. F. Hagen, W. Hohn, and W. G. Hildebrandt, "Cement-based systems using plastification/extrusion auxiliaries prepared from raw cotton linters," US Patent 20050241543, 2005.
[16] D. F. Zhang, B. Z. Ju, and S. F. Zhang, "Dispersing mechanism of carboxymethyl starch as water-reducing agent," *Journal of Applied Polymer Science*, vol. 105, no. 2, pp. 486–491, 2007.
[17] A. Peschard, A. Govina, J. Pourchez et al., "Effect of polysaccharides on the hydration of cement suspension," *Journal of the European Ceramic Society*, vol. 26, no. 8, pp. 1439–1445, 2006.
[18] D. F. Zhang, B. Z. Ju, and S. F. Zhang, "The study on the synthesis and action mechanism of starch succinate half ester as water-reducing agent with super retarding performance," *Carbohydrate Polymers*, vol. 70, no. 4, pp. 363–368, 2007.
[19] A. J. Ragauskas, "The path forward for biofuels and biomaterials," *Science*, vol. 311, no. 5760, pp. 484–489, 2006.
[20] R. Sindhu, P. Biond, and A. Pandey, "Biological pretreatment of lignocellulosic biomass-an overview," *Bioresource Technology*, vol. 199, pp. 76–82, 2016.
[21] Y. Meng, C. Jost, J. Mumme, K. J. Wang, and B. LInke, "An analysis of single and two stage, mesophilic and thermophilic high rate systems for anaerobic digestion of corn stalk," *Chemical Engineering Journal*, vol. 288, pp. 78–86, 2016.
[22] X. S. Ming, *Synthesis and Properties of Polycarboxylate Type Superplasticizer*, Master's thesis, Wuhan University of Technology, Wuhan, China, 2012.
[23] X. Liu, J. N. Guan, and H. H. Lai, "Performances and working mechanism of a novel polycarboxylate superplasticizer synthesized through changing molecular topological structure," *Journal of Colloid and Interface Science*, vol. 504, pp. 12–24, 2017.

Hindawi
Advances in Materials Science and Engineering
Volume 2018, Article ID 2681461, 15 pages
https://doi.org/10.1155/2018/2681461

Research Article

The Mechanical Properties of a Novel STMR Damper Based on Magnetorheological Silly Putty

Xiao-Guo Lin,[1,2] Fei Guo,[3] Cheng-Bin Du,[1] and Guo-Jun Yu[4]

[1]*Department of Engineering Mechanics, Hohai University, Nanjing 211100, China*
[2]*School of Civil and Transportation Engineering, Ningbo University of Technology, Ningbo 315211, China*
[3]*MCC Huatian Engineering & Technology Corporation, Nanjing 210019, China*
[4]*Faculty of Civil Engineering and Mechanics, Jiangsu University, Zhenjiang 212013, China*

Correspondence should be addressed to Cheng-Bin Du; cbdu@hhu.edu.cn

Received 6 February 2018; Accepted 10 April 2018; Published 25 June 2018

Academic Editor: Kestutys Baltakys

A novel shear thickening magnetorheological (STMR) damper with both speed locking and semiactive controlling properties was designed and fabricated based on multifunctional smart composite materials which was defined as magnetorheological Silly Putty (MRSP). The rate sensitive property and magnetorheological effect of MRSP samples were analyzed by using a rheometer to select the best filler for the STMR damper. The mechanical properties of the STMR damper were investigated through slow, fast, and dynamic experiments. The experimental results indicate that the STMR damper exhibits an obvious rate sensitive characteristic and semiactive control property. On one hand, when the STMR damper is simulated fast enough, it can realize the "speed switch" function, which enables it to instantly lock up and act as a shock transmission unit (STU). On the other hand, when the STMR damper is applied with current, the damping force can be adjusted by magnetic field strength to realize its semiactive controlling property. In addition, a multiparameter and symmetry model was established to describe the dynamic hysteretic behavior of the STMR damper, which is consistent with the experimental data.

1. Introduction

Magnetorheological Silly Putty (MRSP) is a smart multifunctional composite prepared by dispersing soft magnetic particles into a Silly Putty matrix with shear stiffening property [1]. This new kind of smart material is the solid state of the magnetorheological shear thickening fluid (MRSTF) proposed by Zhang et al. and Peng et al. [2, 3]. Subsequently, Wang et al. [4, 5] first developed a magnetically responsive shear-stiffening gel with excellent shear stiffening performance and magnetorheological effect. This novel magnetically responsive shear-stiffening gel can provide credible tunability with external stimuli.

At this stage, the vibration damper based on a single magnetorheological material requires an external magnetic field, which belongs to the active device. Magnetorheological materials are widely used in all kinds of MR dampers, and the technology is relatively mature. Lord Company of USA and BASF Company of Germany have developed many commercialized MR dampers. For example, the RD-1005-type MR damper produced by Lord Company is the earliest application of the international commercialized MR damper with damping force over 2200 N [6]. MR dampers designed for large civil engineering structures show greater structure size and damping force output. Qu et al. developed a full-scale MR damper output of up to 500 kN, carried out a study on the key technologies of the leakproof design of the magnetic field and built-in butterfly spring, and finally applied the full size MR damper to a highway railway cable-stayed bridge with semiactive vibration control [7–10]. Yu et al. developed the self-decoupled magnetorheological (SDMR) damper, which produced the largest output of 360 kN. The displacement decoupling mechanism was set up in the damper, and permanent magnets were arranged to provide the function of self-protection. The SDMR damper was mainly applied to the semiactive vibration control of frame and grid structures [11–14].

The single shear thickening material is used as energy dissipation fillers for small passive ST dampers. Zhang et al. developed a speed-driven damper based on the shear thickening fluid and studied the dynamic performance of the ST damper through both experiment and theory methods [15]. These results confirm that the ST damper presents higher stiffness and damping at high-speed dynamic loading than those at low-speed loading and absorbs more energy. Zhou et al. developed a double-out rod-type ST damper filled by shear thickening fluid of a high-concentration polystyrene-ethyl acrylate nanometer particle suspension. The dynamical experiment results reveal that with the increase in excitation frequency, the storage modulus and energy dissipation modulus rapidly increase, and the output of the ST damper dramatically boosts, exhibiting great absorption and energy dissipation capacity; the maximum energy dissipation modulus reached up to 21 kPa [16]. The most common application of shear thickening materials in civil engineering structures is the shock transmission unit (STU), which is a device resembling a speed switch. It is basically approximating to a general damper in appearance and internal structure, which is composed of a piston and cylinder and regarded as a special damper. Silly Putty has become a promising material for the special damper of STU, which is widely used in the multispan bridge [17].

The MR damper is the most mature energy dissipation device in the field of magnetorheological vibration damping. From the point of energy, the principle of the work is to change the energy spectrum of the vibration source's excitation to the system and reduce the passed energy to suppress the vibration. However, in the face of huge incentive loads, the vibration damping, which the MR damper depends on, does not slow down the deformation or even destruction of civil engineering structures due to insufficient stiffness; besides, the mechanism of damping is relatively simple. In addition, these MR dampers all belong to active devices, which means that in the event of a circuit failure that cannot be controlled by a magnetic field, the damper loses the significance of the semiactive vibration control. The current solutions include setting a permanent magnet to make the magnetorheological fluid in the MR damper produce certain yield strength, but the scheme makes the design of the damper more complex. Furthermore, commonly used permanent magnets are made of NdFeB material with strong temperature instability, meaning that the higher the temperature, the faster the demagnetization. The shear thickening material is mainly used in caging devices, including all kinds of speed locking devices, in order to improve the overall stiffness of the structure and achieve the purpose of seismic resistance and vibration reduction. At the moment, researchers of the world only focus on the study of the mechanisms of magnetorheological damping and shear thickening damping respectively, and there is no intersection between each other. However, there are no relevant studies that combine the characteristics of two kinds of intelligent materials as a whole to explore new intelligent dampers with double vibration damping mechanisms.

In this work, a novel shear thickening magnetorheological (STMR) damper was designed and fabricated based on MRSPs. Compared with traditional MR dampers, the STMR damper not only exhibited controllable characteristics of damping force under the adjustment of the magnetic field but also provided a "locking" function under an unexpected sudden rare load, which was more suitable for the vibration control of large civil engineering structures. In order to verify the dual vibration damping characteristics of the STMR damper, slow, fast, and dynamic mechanical property experiments were carried out. Finally, a multiparameter and symmetry model was established and deduced to describe the dynamic hysteretic behavior of the STMR damper.

Table 1: Composition of the Silly Putty matrix.

Composition	Weight percentage
Polydimethylsiloxane (PDMS)	65
Silica	17
Thixotrol	9
Boric acid	4
Glycerine	1
Titanium dioxide	1
Dimethyl cyclosiloxane	1

2. Experimental Section of MRSPs

2.1. Materials. The Dow Corning 3179 dilatant compound, which was purchased from Dow Corning Co., Ltd., was used as the Silly Putty matrix. The composition of the Silly Putty matrix is outlined in Table 1. Polydimethylsiloxane (PDMS) as a commonly used organic silicon material is the major constituent of the composition. The soft magnetic particles of the carbonyl iron (CI) with an average size of 3.5 μm were purchased from Jiangsu Tianyi Ultra-fine metal powder Co. Ltd. (Xuyi, China).

2.2. Preparation and Testing of MRSPs. The dilatant compound as matrix and the different volume fractions of CI as fillers were homogeneously mixed using a two-roll mill (Nantong Hailite Rubber Machinery Inc., China, XK-160 model) at room temperature. For the mechanical mixing method, up to six different volume fractions were considered for the present study: 0, 6.98, 10.11, 15.84, 20.80, and 27.29%. The prepared samples were marked as MRSP 0, MRSP 1, MRSP 2, MRSP 3, MRSP 4, and MRSP 5, in sequence. In this work, the dynamic rheological properties of the MRSP samples were carried out using a commercial rheometer (Physica MCR 302, Anton Paar Co., Austria). During the testing procedure, a parallel plate PP20 with a diameter of approximately 20 mm was used, and a gap of 1 mm was maintained at all times. At the same time, a controllable magnetic field was generated by an external coil. Besides, all the samples for the experiment were maintained at an approximately same volume value. The MRSP sample and MCR 302 rheometer are displayed in Figure 1.

3. Experimental Section of the STMR Damper

3.1. Designing of STMR Damper. The structure of the STMR damper is shown in Figure 2, with its appearance

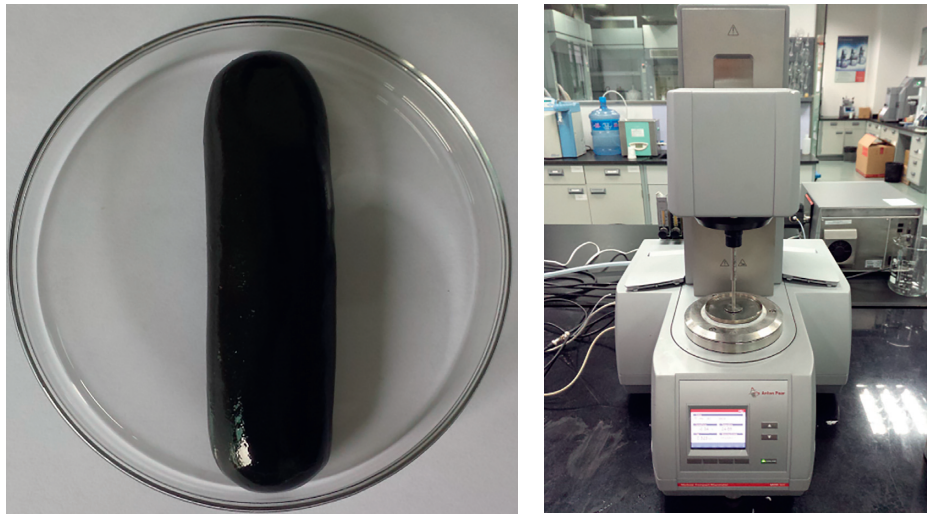

(a) (b)

Figure 1: Preparation of (a) the MRSP sample and (b) the MCR 302 rheometer.

approximating to a traditional MR damper, mainly consisting of the main cylinder tube, accessory cylinder tube, auxiliary cylinder, main piston, accessory piston, and piston rod. The filling material in the main cylinder exhibits high-MR effect, while the inner filling material of the auxiliary cylinder presents a higher shear stiffening effect to improve the overall safety reserve. So, both the main cylinder and auxiliary cylinder are combined together into a cooperative cylinder. The main piston and auxiliary piston are arranged on the piston rod, the main piston and piston rod are connected with the method of a rigid threaded connection, and two circular excitation coils are detoured in two opposite directions on the main piston. Each of the two excitation coils connects one wire to the external power supply through the traverse channel, and the power mode is in the paralleling way. The accessory piston is connected with the piston rod through the butterfly spring and allows it to move along the piston rod within the maximum compression amount of the spring, in order to realize the decoupling function. The filling materials in the main and auxiliary cylinders generate flow and deformation in their own working gaps.

The STMR damper mainly consists of the main cylinder controlled by magnetorheology and the accessory cylinder with displacement decoupling characteristic. This novel damper not only maintains the performance of an adjustable damping force by magnetic field, but also possesses obvious rate sensitive characteristic which provides the function of locking structure to disperse loading under high frequency or impaction. The basic structural parameters of the STMR damper are listed in Table 2.

3.2. Testing of the STMR Damper. The physical object of the STMR damper is displayed in Figure 3. The energy dissipation of the STMR damper is mainly triggered by the flow and deformation of the filling materials. The rate sensitive characteristic and magnetorheological effect of MRSPs are the internal reasons for the damper to adapt to environmental incentives and directional intelligent controllability. In order to verify the rate sensitivity and magnetic control characteristics of the STMR damper, the mechanical properties were investigated by the SDS-300 electrohydraulic servostatic and dynamic testing machine. The main contents of the testing included the following: (1) the influence of different rates on the mechanical properties of the damper under slow and fast axial tension conditions; (2) the influence of different frequencies and different current excitations on the dynamic hysteretic properties of the damper under large and small displacements. The installation of the testing machine for the STMR damper is displayed in Figure 4. In the testing procedure, a current excitation with an adjustable DC-regulated power supply was adopted, and the maximum input current was 3 A. In each experiment, the piston carried on the reciprocating movement from the balance position, which was mainly located in the middle position between the main and accessory cylinder tubes. In the damper structure diagram, the limit stroke of the piston was 65 mm, and in the present experiment of dynamic mechanical properties, the amplitude of the large displacement was 55 mm.

4. Results and Discussion

4.1. Rate Sensitive Characteristic of MRSPs. In the earlier research, when there was no external magnetic field applied, the soft magnetic particles of CI were evenly dispersed in the Silly Putty matrix to form isotropic viscoelastic materials [1]. From this point, the CI powder was considered as a general particle filling, which played a role in strengthening the matrix material. The larger the volume fraction of the CI particle is, the greater the shear storage modulus of the sample becomes, which is in consistent with the

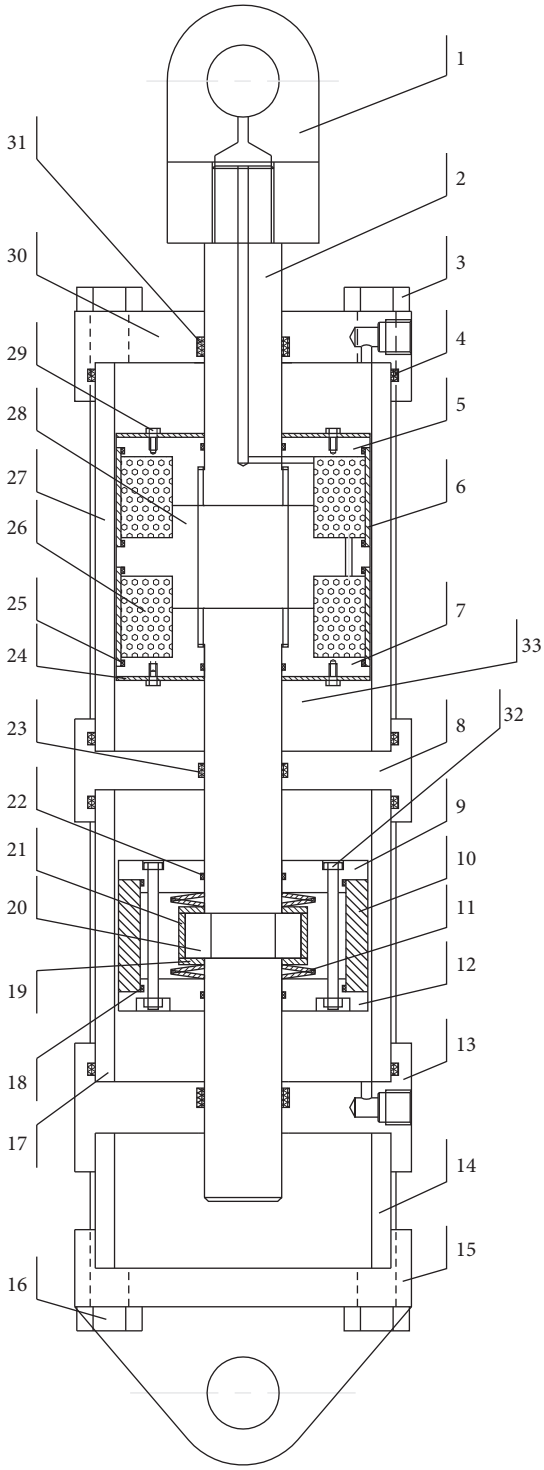

Assembly drawing of STMR damper		
Serial Number	Name	Quantity
1	Single earring for axial use	1
2	Piston rod	1
3	Pull rod bolt 1	4
4	Seal ring of type O	4
5	Main piston 1	1
6	Coil sleeve	1
7	Main piston 2	1
8	Connecting cylinder cover 1	1
9	Accessory piston 1	1
10	Accessory piston sleeve	1
11	Butterfly spring	4
12	Accessory piston 2	1
13	Connecting cylinder cover 2	1
14	Auxiliary cylinder tube	1
15	Back end cover	1
16	Pull rod bolt 2	4
17	Accessory cylinder tube	1
18	Seal ring of type O	2
19	Sleeve baffle	2
20	Semiring	2
21	Semiring sleeve	1
22	Seal ring of type O	2
23	Seal ring of type O	1
24	Magnetically isolated copper piece	2
25	Seal ring of type O	4
26	Coil	1
27	Main cylinder tube	1
28	Main piston 3	1
29	Screw	8
30	Front end cover	1
31	Seal ring of type Yx	2
32	Hexagon head bolt	4
33	Filling materials	2

Figure 2: Basic structure of the STMR damper.

empirical formula (1). This formula explains the rule of shear modulus varying with the volume fraction of rigid particles randomly filled in the rubber matrix [18]. The addition of rigid particles leads to the decrease in internal motion space within the matrix, which further promotes the interaction between the molecular chains. Simultaneously, more obvious obstacles are encountered in solving the entanglement of the molecular chains, which shows the escalation in shear storage modulus on a macroscopic point of view [5]:

$$G_{\text{ran}} = G_0\left(1 + 2.5\phi + 14.1\phi^2\right), \quad (1)$$

where G_{ran} refers to the shear modulus of composites filled with rigid particle composites, G_0 is the shear modulus of the

Table 2: Main structure parameter of the STMR damper.

Working gap of the main cylinder tube	2 mm	Working gap of the accessory cylinder	2 mm
External diameter of the main piston	156 mm	External diameter of the accessory piston	156 mm
Wall thickness of steel tube of the main cylinder tube	15 mm	Wall thickness of steel tube of the accessory cylinder tube	15 mm
Piston's stroke limit of the main cylinder tube	65 mm	Piston's stroke limit of the accessory cylinder tube	65 mm
Length of working gap of the main cylinder tube	206 mm	Length of working gap of the accessory cylinder tube	117 mm
Piston's number of windings of the main cylinder tube	980	Effective stroke of decoupling spring	7 mm
Diameter of piston rod	50 mm	Maximum power	<120 W
Piston's current range of the main cylinder tube	0~3 A	Designed damping force	300 kN

Figure 3: Entity of the STMR damper.

Figure 4: The experimental setup of the STMR damper.

matrix material without the filling of rigid particles, and ϕ means the volume fraction of rigid particles.

Besides, from the earlier research, in order to compare the shear stiffening degree of the MRSP samples, the absolute shear stiffening effect (ASTe) and relative shear stiffening effect (RSTe) are defined as the index of measurement [1], as shown specifically in the following formula:

$$\begin{aligned} \text{ASTe} &= G'_{\max} - G'_{\min}, \\ \text{RSTe}\% &= \frac{G'_{\max} - G'_{\min}}{G'_{\min}} \times 100\%, \end{aligned} \tag{2}$$

where $G'_{\max}$ stands for the maximum shear storage modulus excited by the loading frequency and $G'_{\min}$ refers to the initial shear storage modulus. When the angular frequency increases, the MRSP samples exhibit an obvious rate sensitive characteristic and a sharply increased storage modulus, together with the demonstration that the sample "hardens." Furthermore, the higher the content of the CI powder is, the more beneficial it is to the absolute shear stiffening effect of the material. In earlier research [1], for the MRSP 5 sample, under normal temperatures, the absolute modulus change is 0.6145 MPa, which equals to approximately twice the pure shear stiffening matrix MRSP 0, while the relative shear stiffening effect is 1412.64%, which is far less than 77584.21% of the pure shear stiffening matrix MRSP 0.

However, under the condition of an external magnetic field, the soft magnetic particles of the CI powder were arranged into chain-like ordered structures along the direction of the magnetic flux line in the interior of the shear stiffening matrix, forming the anisotropic structure. The pure shear stiffening matrix MRSP 0 sample was not influenced by the magnetic field due to the absence of soft magnetic particle fillings. Figure 5 illustrates the relationship between shear storage modulus of the MRSP samples with different contents of soft magnetic particles and the angular frequencies separately under different external magnetic fields, in which the angular frequency is 1–100 rad/s with continuous change. It is observed from the diagram that with the strength of the exerted magnetic field enhancing, the shear storage modulus of the sample increases as well. For the MRSP 5 sample, the maximum storage modulus after shear stiffening is approximately 0.5 MPa under the condition of zero magnetic field. Nonetheless, under the constant magnetic flux density of 0.627 T, the maximum storage modulus after shear stiffening is up to 2.3 MPa, and the magneto-induced modulus caused by the magnetic field equals to approximately 1.8 MPa. For the transverse comparison between different samples, when the content of the CI powder rises up, the storage modulus at the same magnetic flux density keeps an upward tendency. The maximum storage modulus of the MRSP 1 sample under a magnetic flux density of 0.627 T is 0.6 MPa, while the particle mass fraction of MRSP 5 reaches twice as much as that of MRSP 1, but the maximum modulus equals to approximately four times as that of MRSP 1. On one hand, no matter how the soft magnetic particles are randomly filled or arranged in the matrix with a certain ordered structure, under the situation that the content of soft magnetic particles grows up, the reinforcement effect of the material increases. On the other hand, previous studies expose that the higher the

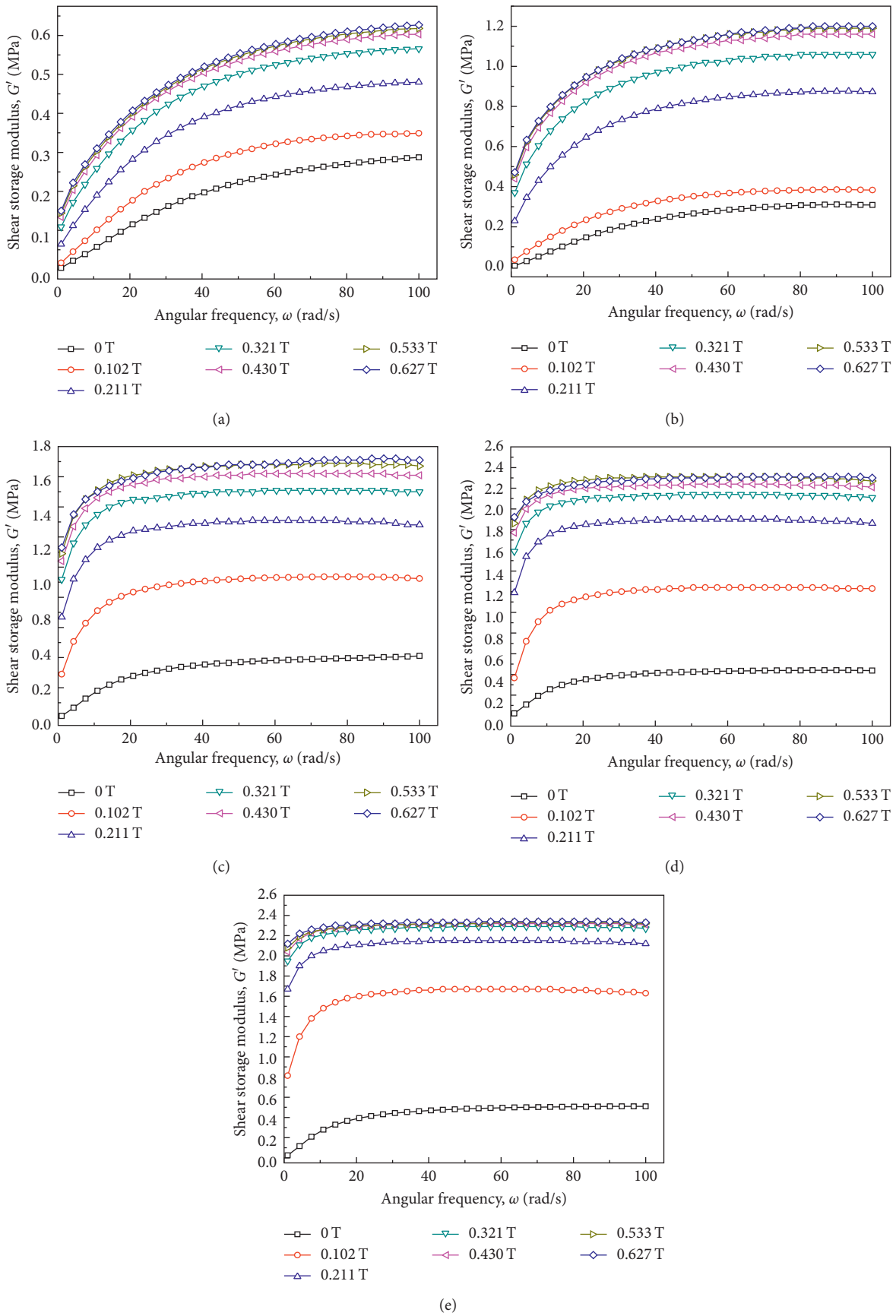

Figure 5: The shear storage modulus of MRSP samples as a function of angular frequency at different magnetic flux densities. (a) MRSP 1, (b) MRSP 2, (c) MRSP 3, (d) MRSP 4, and (e) MRSP 5.

Table 3: G'_{max}, G'_{min}, ASTe, and RSTe of the MRSP samples.

Samples	Magnetic flux density, B (T)	G'_{max} (MPa)	G'_{min} (MPa)	ASTe (MPa)	RSTe (%)
MRSP 1	0	0.287	0.00346	0.28354	8194.80
	0.102	0.349	0.01620	0.33280	2054.32
	0.211	0.480	0.06410	0.41590	648.83
	0.321	0.566	0.10900	0.45700	419.27
	0.430	0.603	0.13400	0.46900	350
	0.533	0.618	0.14400	0.47400	329.17
	0.627	0.627	0.15000	0.47700	318
MRSP 2	0	0.309	0.00531	0.30369	5719.21
	0.102	0.383	0.03550	0.34750	978.87
	0.211	0.873	0.22900	0.64400	281.22
	0.321	1.060	0.37000	0.69000	186.49
	0.430	1.160	0.44000	0.72000	163.64
	0.533	1.190	0.45900	0.73100	159.26
	0.627	1.200	0.47100	0.72900	154.78
MRSP 3	0	0.411	0.0131	0.39790	3037.40
	0.102	0.924	0.2900	0.63400	218.62
	0.211	1.280	0.6690	0.61100	91.33
	0.321	1.500	0.9190	0.58100	63.22
	0.430	1.610	1.0400	0.57000	54.81
	0.533	1.670	1.0900	0.58000	53.21
	0.627	1.710	1.1300	0.58000	51.33
MRSP 4	0	0.44	0.0228	0.41720	1829.82
	0.102	1.24	0.366	0.87400	238.80
	0.211	1.90	1.19	0.71	59.66
	0.321	2.14	1.59	0.55	34.59
	0.430	2.24	1.77	0.47	26.55
	0.533	2.31	1.86	0.45	24.19
	0.627	2.31	1.92	0.39	20.31
MRSP 5	0	0.51	0.0239	0.4861	2033.89
	0.102	1.67	0.814	0.8560	105.16
	0.211	2.15	1.67	0.48	28.74
	0.321	2.29	1.95	0.34	17.44
	0.430	2.32	2.04	0.28	13.73
	0.533	2.33	2.08	0.25	12.02
	0.627	2.34	2.12	0.22	10.38

volume fraction of particles, the denser the chain-like ordered structures form under the same magnetic field condition, which leads to the increasing of the magneto-induced modulus.

Similarly, the ASTe and RSTe indexes are implemented to illustrate the influence of magnetic flux density on the shear stiffening effect of the MRSP samples, and the relevant parameters are listed in Table 3. It is perceived that for samples with low content of soft magnetic particles, such as MRSP 1 and MRSP 2, the magnetic flux density is conducive to the promotion of the shear stiffening effect of the MRSP samples. The greater the magnetic flux density is, the more superior the value of the ASTe becomes. For samples with volume fraction of soft magnetic particle up to 15%, such as MRSP 3, MRSP 4, and MRSP 5, the influence of magnetic flux density on absolute shear stiffening effect is relatively complex. With the increase of magnetic flux density, ASTe presents a tendency of falling down after ascending first, which demonstrates that only under weak magnetic field conditions (no more than 0.1 T), it becomes conducive to the absolute shear stiffening effect of high particle content samples. Besides, with the increase of magnetic flux density, the initial shear storage modulus of the samples significantly intensifies, while the relative shear stiffening effect of samples declines, and the RSTe value decreases. However, for the transverse comparison between different samples, under the zero magnetic field conditions, the higher the particle content of the sample becomes, the greater the absolute shear stiffening effect it achieves, which is in line with the previous description. As the intensity of the magnetic field increases for the samples with the higher particle content, the ASTe value becomes smaller. When the magnetic flux density is 0.627 T, the change in the absolute modulus of MRSP 2 is 0.729 MPa. Nevertheless, with the increase of particle content, the ASTe value of the sample subsequently declines, and in addition, the absolute modulus of MRSP 5 drops to only 0.22 MPa. Under zero magnetic field condition, the filling of soft magnetic particles plays a certain positive role in the absolute modulus change in the MRSP samples. As the magnetic flux density increases, the ordered structure of the soft magnetic particles in the interior of the matrix becomes more complex. The larger the volume fraction is, the closer the connections

become between particles and particles and between chain and chain, thereby providing partial support for the macroscopic shear modulus. However, the movement of the matrix molecular chains is greatly hindered due to the decrease of internal motion space within the matrix. From the viscoelastic aspect, it is not beneficial to the relaxation and rebalance process of the high molecular polymer, which leads to the reduction of the absolute shear stiffening effect of the samples. Therefore, for the MRSP samples with a high content of soft magnetic particles, in order to give full play to the characteristic of shear stiffening, the external magnetic field in its working environment should not be too large.

4.2. Magnetorheological Effect of MRSPs. Under a continuously changing magnetic field, the soft magnetic particles are rapidly magnetized into dipoles and are arranged into chain-like ordered structures within the interior of the matrix until the magnetic saturation is achieved. Macroscopically, the continuous variation of the shear modulus of the MRSPs eventually reaches a steady state of saturation. The magnetorheological effect determines the directional controllable performance of the MRSPs, which is usually measured by the change of modulus. Currently, the research results indicated that the lower the loading frequency was, the higher the magnetorheological effect became, and the more the conducive it was to the adjustment of the magnetic field. However, the loading frequency was higher, the matrix modulus of MRSP became larger, the chain-like resistance of soft magnetic particles in the interior of the matrix became greater, and the magnetorheological effect tended to be lower [1]. Figure 6 reveals the varied relationship between the shear storage modulus and magnetic flux density of different samples under the conditions of different shear strain, low load frequency ($\omega = 1$ rad/s), and magnetic flux density continuous changing from 0 to 0.894 T. Correspondingly, the larger the shear strain is, the smaller the storage modulus of the sample becomes. As the magnetic flux density enhances, the shear storage modulus rapidly increases before 0.4 T and gradually tends to magnetic saturation after 0.4 T. Likewise, the absolute magnetorheological effect (AMRe) and relative magnetorheological effect (RMRe) are adopted as the indexes for the performance of magnetic field adjustment, as shown in the following equation:

$$\begin{aligned} \mathrm{AMRe} &= G'_{\max} - G'_{\min}, \\ \mathrm{RMRe}\% &= \frac{G'_{\max} - G'_{\min}}{G'_{\min}} \times 100\%, \end{aligned} \tag{3}$$

where $G'_{\max}$ means the maximum shear storage modulus when reaching magnetic saturation, while $G'_{\min}$ is the initial shear storage modulus under zero magnetic field. The correlated results of all the curves in Figure 6, which are calculated according to (3), are listed in Table 4.

For the transverse comparison of the samples with different contents of soft magnetic particles, the larger the volume fraction of soft magnetic particles is, the greater the magneto-induced modulus becomes, and the more obvious the absolute magnetorheological effect tends to be. For MRSP 5 with the highest particle content, the magneto-induced modulus is up to 1.5 MPa at the strain of 0.5%. The relative magnetorheological effect is mainly determined by the initial shear storage modulus, from which it can be observed that, for loading conditions at small strains of 0.5% and 1%, the relative magnetorheological effect produced by the same sample varies with no obvious difference from each other. This is for the reason that within the strain of 1%, each group of MRSP sample is in the linear viscoelastic region, which displays no obvious difference of initial modulus. However, when the strain continues to climb up to 5% and 10%, respectively, the initial modulus sharply decreases outside the linear viscoelastic region, and in turn, the magnetorheological effect becomes quite different. Besides, the relative magnetorheological effect with strain of 10% is higher than that with the strain of 5%. With the increase in the content of CI powder, the relative magnetorheological effect tends to enhance. When the strain is 0.5%, the relative magnetorheological effect of MRSP 5 reaches 352% at most; nevertheless, if the shear strain increases to 10%, the relative magnetorheological effect of MRSP 4 reaches as high as 617%, and the adjustable range of the magnetic field is relatively wide. Consequently, it is beneficial to obtain great magnetorheological effect when the volume fraction of the soft magnetic particle is high.

4.3. Slow and Fast Mechanical Properties of the STMR Damper. By comparing the rate sensitive characteristic and magnetorheological effect of each MRSP samples, the MRSP 5 sample with high magnetorheological effect was finally selected as the filling material in the main cylinder tube of the STMR damper. Since there was no soft magnetic particles filled in MRSP 0 sample, due to its higher relative shear stiffening effect, it was regarded as the filling materials for the accessory cylinder tube of the STMR damper. For the STMR damper with the locking function, when the relative speed rate of the piston to the cylinder is slower than 1 mm/s, it is considered as a slow testing, but when the speed rate is greater than 1 mm/s, it is regarded as a fast testing. Firstly, in order to meet the requirements of the slow testing, the control rates were set constantly as 0.033 mm/s, 0.083 mm/s, 0.166 mm/s, 0.33 mm/s, 0.66 mm/s, and 0.83 mm/s, respectively. Figure 7 is the force-displacement curve of the STMR damper when the control rate is 0.033 mm/s, from which it is clear that the whole region is approximately divided into three parts: elastic region, viscoelastic region, and viscous region. The force-displacement curve displays a linear relationship in the elastic region, a nonlinear relationship in the viscoelastic region, and gradually reaches stability in the viscous region, which tends to a certain value. According to the force-displacement curve of the elastic region and Hooke's law, the elastic stiffness K of the STMR damper at different tensile rates is calculated. Figure 8 shows the relationship between the elastic stiffness of the STMR damper and the

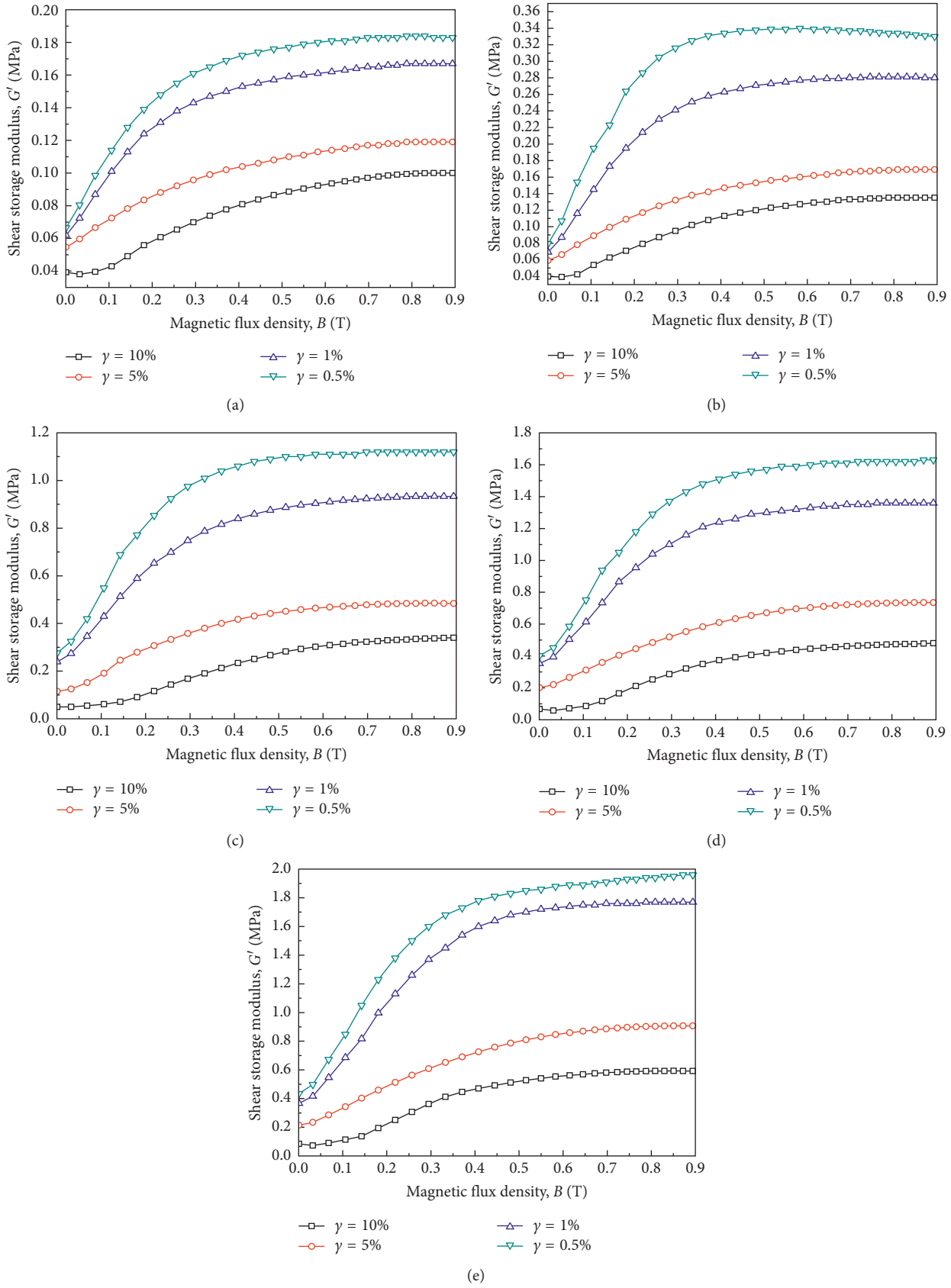

Figure 6: The shear storage modulus of MRSP samples as a function of magnetic flux density at different shear strains. (a) MRSP 1, (b) MRSP 2, (c) MRSP 3, (d) MRSP 4, and (e) MRSP 5.

Table 4: G'_{max}, G'_{min}, AMRe, and RMRe of the MRSP samples.

Samples	Shear strain, γ	G'_{max} (MPa)	G'_{min} (MPa)	AMRe (MPa)	RMRe (%)
MRSP 1	0.5%	0.184	0.0666	0.1174	176.28
	1%	0.167	0.0619	0.1051	169.79
	5%	0.119	0.0547	0.0643	117.55
	10%	0.100	0.0393	0.0607	154.45
MRSP 2	0.5%	0.340	0.0796	0.2604	327.14
	1%	0.281	0.0692	0.2118	306.07
	5%	0.169	0.0590	0.1100	186.44
	10%	0.135	0.0398	0.0952	239.20
MRSP 3	0.5%	1.120	0.2770	0.8430	304.33
	1%	0.934	0.2390	0.6950	290.79
	5%	0.484	0.1150	0.3690	320.87
	10%	0.340	0.0498	0.2902	582.73
MRSP 4	0.5%	1.630	0.4020	1.2280	305.47
	1%	1.360	0.3530	1.0070	285.27
	5%	0.735	0.2010	0.5340	265.67
	10%	0.480	0.0669	0.4131	617.49
MRSP 5	0.5%	1.960	0.4340	1.5260	351.61
	1%	1.770	0.3660	1.4040	383.61
	5%	0.907	0.2140	0.6930	323.83
	10%	0.592	0.0843	0.5077	602.25

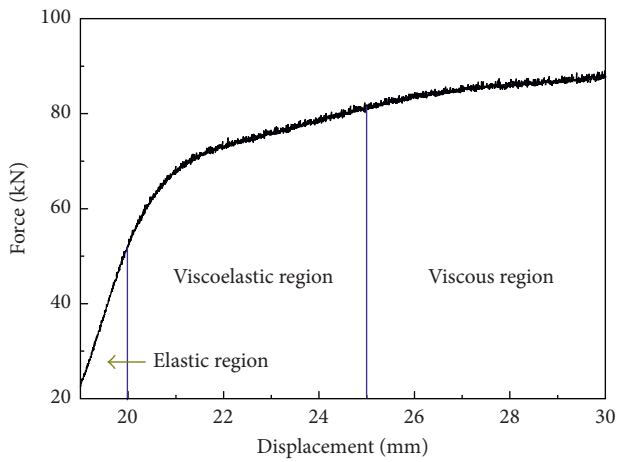

Figure 7: Division of the displacement-resistance region.

control rate, from which it is detected that the greater the control rate is, the greater the elastic stiffness of the STMR damper becomes. When the set control rate equals to 0.033 mm/s, elastic stiffness tends to be less than 30 kN/mm; however, when the control rate is up to 0.83 mm/s, the elastic stiffness exceeds 65 kN/mm, which is twice as much as that of the former. Accordingly, it proves that under the condition of a slow testing, the STMR damper exhibits a certain rate sensitive characteristic.

The fast testing displays that the STMR damper can be instantaneously locked at a certain rate to transfer the designed load. According to AASHTO, when a fast testing is carried out, the locking distance should be within 12 mm [19]. Figure 9 shows the force-displacement curves with

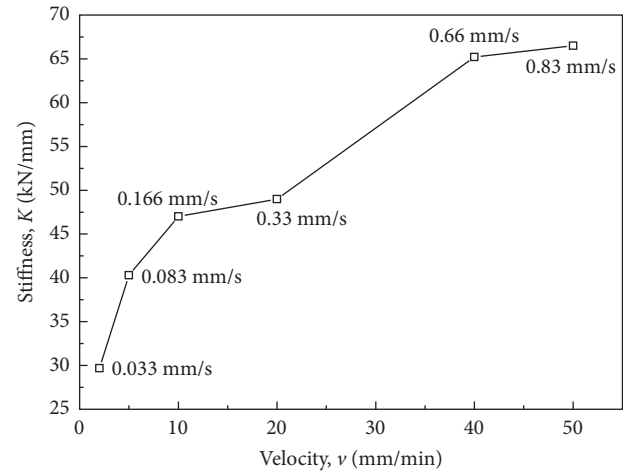

Figure 8: Relationship between velocity and spring stiffness.

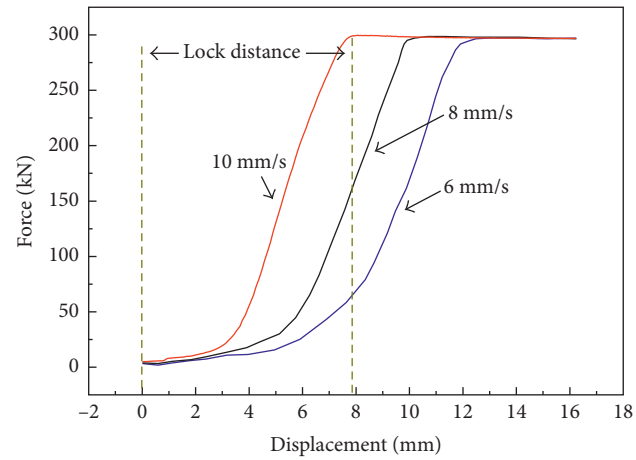

Figure 9: The relationship between displacement and resistance force.

a constant control rate of 6 mm/s, 8 mm/s and 10 mm/s, respectively. It is observed that when the force is loaded from 0 to 300 kN, the locking distances under the three control rates are all less than 12 mm, which is in full compliance with the provisions of AASHTO. Nevertheless, when the control rate increases, the lock distance and locking time tend to shorten. The locking distance under the control rate of 10 mm/s is approximately 8 mm, and the locking time is only 0.8 s, which achieves instant locking, while on the other hand, the lock times of the other two groups under the control rates are both more than one second. Therefore, combined with these experimental results, the developed STMR damper accomplishes the locking function within a short time and distance, which reveals that the STMR damper can be simplified as a "rate switch" with a locking rate of 10 mm/s, meaning that instant locking happens when this rate is exceeded.

4.4. Dynamic Mechanical Properties of the STMR Damper. When the amplitude is within the range of the maximum compression of the butterfly spring, only the main piston of

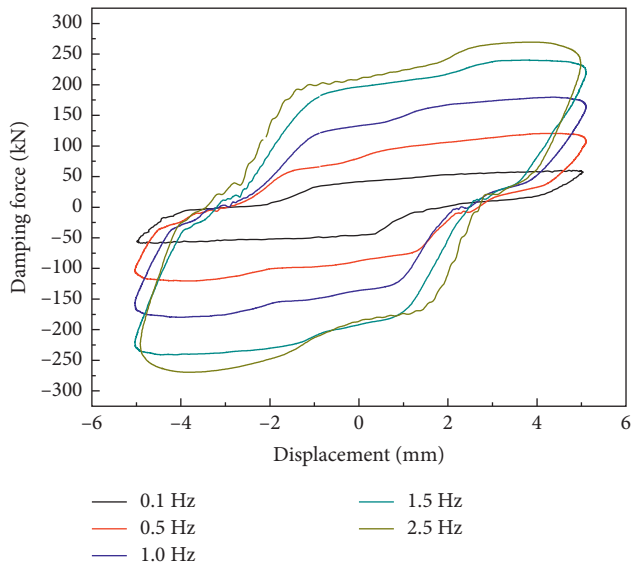

Figure 10: Relationship between the damping force and displacement for the STMR damper.

the STMR damper works. When the amplitude exceeds the maximum compression of the butterfly spring, the main and accessory pistons work together, resulting in a greater output of damping force. Since the interior of the STMR damper is filled by MRSPs with the rate sensitive characteristic, it is necessary to confirm the dynamic rate sensitive performance. So, the excitation frequency of 0.1 Hz, 0.5 Hz, 1.0 Hz, 1.5 Hz, and 2.5 Hz were, respectively, applied under a displacement of 5 mm. The experimental results are displayed in Figure 10. From the experimental curve, it is sensed that under the condition of small displacement, within a frequency range of 0.1 Hz–2.5 Hz, the damping force changes from 60.3 to 269.5 kN. The higher the excitation frequency is, the greater the shear rate of materials in the interior of the damper comes to be, the larger the damping force becomes, and the more apparent the rate sensitive characteristic turns out to be. Besides, the ratio between the maximum and minimum damping force is 4.5, showing that when the excitation frequency is more than 1.5 Hz, the damping force gradually tends to saturation, and the change range is limited, which is consistent with the rate sensitive performance of the MRSP samples. When the excitation frequency enhances, the envelope area of the damping force-displacement curve inclines to enlarge, indicating that the energy dissipation capacity of the STMR damper becomes stronger, and the frequency directly affects the energy dissipation capacity of the STMR damper. The force of the butterfly spring is superimposed on the STMR damper, which leads to the slant of the hysteresis curve.

In order to validate the adjustable characteristic of the mechanical properties for the STMR damper under the effect of the magnetic field, the dynamic mechanical properties were investigated under different currents, during which the same displacement control was adopted, and each working condition was circulated for 10 times. The testing conditions were as follows: the displacement was 5 mm, the frequencies were 0.1 Hz, 0.5 Hz, 1.0 Hz, and 1.5 Hz, and a current of 0 A, 1 A, 2 A, and 3 A was applied in each case, respectively. When the displacement was 55 mm and the frequency was 0.1 Hz, a current of 0 A, 1 A, 2 A, and 3 A was similarly applied; nevertheless, when the input current increased in sequence, the magnetic flux density in the working gap of the STMR damper also enhanced and the damping force of the damper also correspondingly magnified as well. Figure 11 presents the experimental results under the above testing conditions, showing from the damping force-displacement curves that whether it is under the condition of small displacement or large displacement, and the STMR damper exhibits certain mechanical property of magnetic field controllability.

As shown in Figure 11, frequency is an important factor that affects the adjustable range of the damping force of the STMR damper under a small displacement of 5 mm. In Figure 11(a), the excitation frequency is 0.1 Hz, presenting that when the input current changes from 0 to 3 A, the variation range of the damping force is 60.3–189.3 kN, and the ratio between the maximum and minimum damping force is approximately 3.1. In Figures 11(b)–11(d), the excitation frequencies are 0.5 Hz, 1.0 Hz, and 1.5 Hz, respectively, revealing the fact that when the current changes from 0 to 3 A, the ratio between the maximum and minimum damping force becomes 2.0, 1.4, and 1.2, respectively. Accordingly, the increase of frequency directly affects the adjustable range of the damper under the excitation of the magnetic field, which demonstrates that the higher the frequency is, the narrower the adjustable range turns out to be. This is for the reason that the high excitation frequency makes the filling materials to stiffen, and the soft magnetic particles in the magnetic field are chain blocked, which is not advantageous to stimulate the magnetorheological effect, and thereby makes the adjustable range of the damper under magnetic field narrow down. In Figure 11(e), under the condition of a displacement of 55 mm with low frequency and large displacement, the damper presents the obvious characteristic of magnetic field controllability. When the input current changes from 0 to 3 A, the variation range of the damping force is 212.8–272.1 kN, and the ratio between the maximum and minimum damping force is approximately 1.3. When the damper is under the condition of large displacement, since the butterfly spring works together with the main and accessory cylinder tubes after the compression limit, the hysteresis curve displays a certain sag in the positive and negative strokes.

In the structural vibration control, as the external excitation frequency is not enough to make the STMR damper induce the speed locking, it is given full play to the adjustment ability of the damper in the magnetic field, which indicates that the STMR damper can be simplified to a larger traditional MR damper.

4.5. Dynamic Hysteretic Mechanical Model for the STMR Damper. The dynamic damping force of the STMR damper can be decomposed into a superposition of three components of force: the first component of force refers to applied

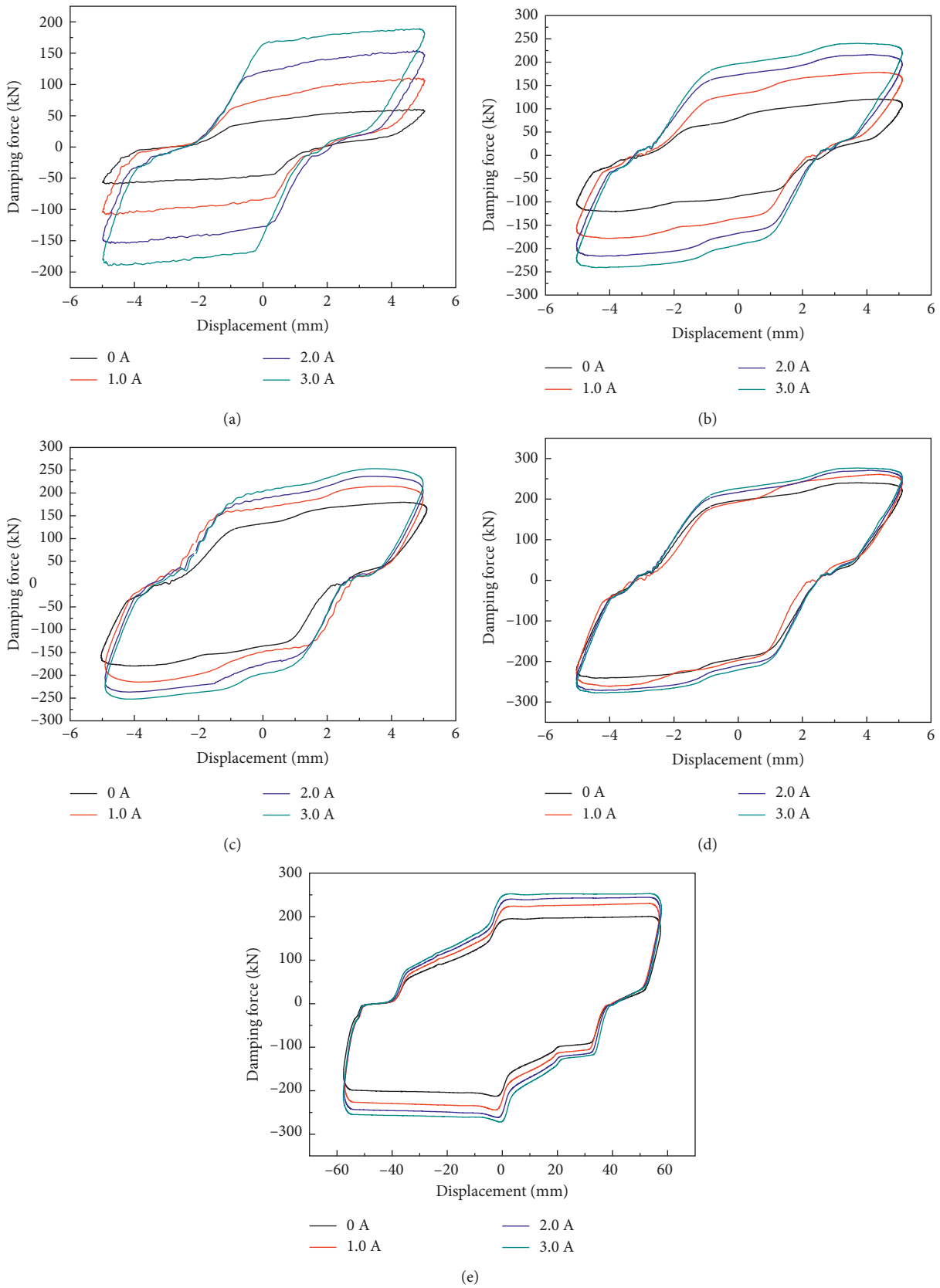

Figure 11: Relationship between damping force and displacement for the STMR damper at different frequencies and displacements: (a) 0.1 Hz, 5 mm; (b) 0.5 Hz, 5 mm; (c) 1.0 Hz, 5 mm; (d) 1.5 Hz, 5 mm; (e) 0.1 Hz, 55 mm.

force f_{mr}, which is produced by the magnetorheological effect of the material, which is related to the current or exerted magnetic field strength; the second component of force f_{pm} stands for the applied force to describe the characterization of polymer properties, which is connected with external excitation rate or strain rate; as for f_{bs}, it means the additional force of the butterfly spring, which satisfies with Hooke's Law.

The first component of force f_{mr} can be expressed as

$$f_{mr} = k'_1 u + c'\dot{u} + f_p, \tag{4}$$

where k'_1 and c' are the stiffness and damping coefficients depending on the magnetic field strength, respectively; u and $\dot{u}$ stand for the displacement and speed rate; f_p is the hysteretic subitem, which is controlled by the following Bouc–Wen differential equation:

$$\begin{aligned} f'_p &= \alpha\dot{u} - \beta\dot{u}\left|f_p\right|^n - \gamma|\dot{u}|f_p\left|f_p\right|^{n-1} \\ &= \left\{\alpha - \left[\beta + \gamma\ \mathrm{sgn}\left(\dot{u}f_p\right)\right]\left|f_p\right|^n\right\}\dot{u}, \end{aligned} \tag{5}$$

where α, β, γ, and n are all the parameters to control the shape of the hysteretic curve.

The second component of force f_{pm} refers to the material viscoelasticity or nonlinear stiffness characteristic, which can be expressed as

$$f_{pm} = k''_1 u + k''_3 u + c''\dot{u}, \tag{6}$$

where k''_1, k''_3, and c'' are the stiffness and damping coefficients depending on the speed rate or the strain rate, respectively.

The third component of force f_{bs} means the additional force of the butterfly spring, when under the situation that the excitation amplitude is less than the maximum compression of the butterfly spring; according to Hooke's law, it is expressed as

$$f_{bs} = k_{bs} u, \tag{7}$$

where k_{bs} stands for the stiffness of the butterfly spring.

Based on (4), (6), and (7), the damping force of the STMR damper can be expressed as

$$f = f_{mr} + f_{pm} + f_{bs} = (k_1 + k_{bs})u + k_3 u^3 + c\dot{u} + \lambda f_p, \tag{8}$$

where $k_1 = k'_1 + k''_1$; $k_3 = k''_3$; $c = c' + c''$; and λ represents the proportional coefficient between the hysteretic and nonhysteretic force. All the stiffness and damping coefficients depend on the strain rate and magnetic field density.

For the dynamic mechanical properties of the STMR damper, it can be considered that the shear storage modulus of the MRSPs contributes to the stiffness part of the device structure, whereas the damping characteristic of the material contributes to the damping part of the device structure. Consequently, in (8), the stiffness coefficients k_1 and k_3, damping coefficient c, and ratio coefficient λ can be rewritten into functions of magnetic field and speed rate as below, respectively. Furthermore, related studies revealed that stiffness and damping are almost linearly dependent on the external magnetic field and strain rate [20]:

$$k_1 = k_{10}(H_e) + k_{11}(H_e)|\dot{u}| + k_{12}(H_e)|\dot{u}|^2, \tag{9}$$

$$k_3 = k_{30}(H_e) + k_{31}(H_e)|\dot{u}|, \tag{10}$$

$$c = c_0(H_e) + c_1(H_e)|\dot{u}|, \tag{11}$$

$$\lambda = \lambda_0(H_e) + \lambda_1(H_e)|\dot{u}|, \tag{12}$$

where k_{10}, k_{11}, k_{12}, k_{30}, k_{31}, c_0, c_1, λ_0, and λ_1 are approximated as the linear equation of the external magnetic field H_e.

The displacement hysteresis phenomenon of the STMR damper is caused by the subitem f_p of the hysteretic force; therefore, in combination with (5), the hysteretic force can be expressed as

$$\begin{aligned} &F_1(f_p) = u - u_+ \\ &F_2(f_p) = u - u_+ \\ &F_3(f_p) = u - u_- \\ &F_3(f_p) = u - u_- \\ &\text{or } f_p = F_1^{-1}(u - u_+), \quad \dot{u} \geq 0, \quad f_p \geq 0 \\ &\quad f_p = F_2^{-1}(u - u_+), \quad \dot{u} \geq 0, \quad f_p \leq 0 \\ &\quad f_p = F_3^{-1}(u - u_-), \quad \dot{u} \leq 0, \quad f_p \geq 0 \\ &\quad f_p = F_4^{-1}(u - u_-), \quad \dot{u} \leq 0, \quad f_p \leq 0, \end{aligned} \tag{13}$$

where $F_i(f_p)$ $(i = 1, 2, 3, 4)$ represents the function of f_p and $F_i^{-1}(f_p)$ means the inverse function of $F_i(f_p)$. Furthermore, u_+ and u_-, respectively, refer to the lagging displacement produced in the positive and negative directions of the equilibrium position. In the testing process, the upward of the balanced position is positive, while the downward of the balanced position is negative. In a cycle, once the peak and valley values of the displacement are equal and the lagging displacement of the positive and negative directions reaches equivalence, the hysteresis curve presents the symmetric characteristic. Besides, when $n = 1$ and $\beta = \gamma$, (5) can be simplified to

$$f_p = \begin{cases} \dfrac{\alpha}{\beta+\gamma}\left[1 - e^{-(\beta+\gamma)(u-u_+)}\right], & \dot{u} \geq 0, \quad f_p \geq 0 \\ \alpha(u - u_+), & \dot{u} \geq 0, \quad f_p \leq 0 \\ \alpha(u - u_-), & \dot{u} \leq 0, \quad f_p \geq 0 \\ \dfrac{-\alpha}{\beta+\gamma}\left[1 - e^{(\beta+\gamma)(u-u_-)}\right], & \dot{u} \leq 0, \quad f_p \leq 0, \end{cases} \tag{14}$$

Therefore, according to (8) and (14), the damping force of the STMR damper can be ultimately expressed as

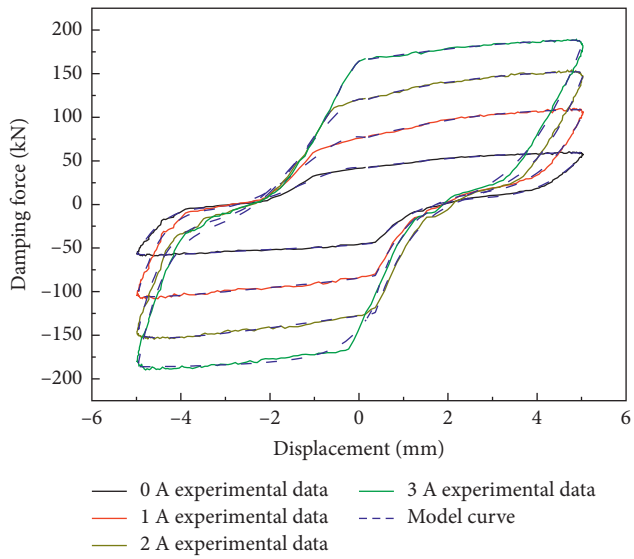

Figure 12: The relationship between the model curve and experimental data of the STMR damper.

Table 5: Results of the parameter identification.

Parameters	$I = 0$ A	$I = 1$ A	$I = 2$ A	$I = 3$ A
k_{10}	−0.15	−0.00049	5.35	−48.87
k_{11}	33.59	5.85	−13.03	29.70
k_{12}	−57.71	−82.02	14.16	−1.03
k_{30}	0.45	0.022	0.25	−0.14
k_{31}	−0.43	0.027	−0.34	0.09
c_0	−45.23	238.50	61.14	307.36
c_1	143.15	0.31	65.55	−93.70
λ_0	0.00083	0.94	2.01	−1.45
λ_1	23.20	60.74	2.55	26.09
α	1.23	1.35	0.38	1.02
β	0.033	0.022	0.50	0.01
λ	0.033	0.022	0.50	0.01
n	1	1	1	1
k_{bs}	0.40	0.40	0.40	0.40

$$f = \begin{cases} (k_1 + k_{bs})u + k_3u^3 + c\dot{u} + \lambda\dfrac{\alpha}{\beta+\gamma}\left[1 - e^{-(\beta+\gamma)(u-u_+)}\right], & \dot{u} \geq 0, \quad f_p \geq 0 \\ (k_1 + k_{bs})u + k_3u^3 + c\dot{u} + \lambda\alpha(u - u_+), & \dot{u} \geq 0, \quad f_p \leq 0 \\ (k_1 + k_{bs})u + k_3u^3 + c\dot{u} + \lambda\alpha(u - u_-), & \dot{u} \leq 0, \quad f_p \geq 0 \\ (k_1 + k_{bs})u + k_3u^3 + c\dot{u} + \lambda\dfrac{-\alpha}{\beta+\gamma}\left[1 - e^{(\beta+\gamma)(u-u_-)}\right], & \dot{u} \leq 0, \quad f_p \leq 0, \end{cases} \tag{15}$$

As a result, the stiffness coefficients k_1 and k_3, the damping coefficient c, and the ratio coefficient λ are expanded from (9)–(12), respectively.

Marquardt algorithm was adopted to carry out the parameter identification on the damping mechanical model of the STMR damper. Low frequency and small displacement experimental data were selected, among which the excitation frequency was 0.1 Hz, the amplitude was 5 mm, and the current input was 0 A, 1 A, 2 A, and 3 A, respectively. From the experimental data, it can be perceived that the lagging displacement in both positive and negative directions is 2 mm, whereas 14 parameters based on the symmetric dynamic hysteretic mechanical model were identified. The identification results are listed in Table 5. Figure 12 displays the comparison between the dynamic hysteresis experimental curves of the STMR damper and the model hysteresis curve acquired by parameter identification, presenting that the model curve stands in good agreement with the experimental data, which further validates the correctness of the multiparameter and symmetric dynamic hysteretic model, and indicates that the method of parameter identification is effective.

5. Conclusions

In this work, a novel STMR damper with rate sensitive characteristic (speed locking) and semiactive controlling property was designed and fabricated based on multifunctional composite MRSPs. Both the mechanical properties of MRSPs and the STMR damper were experimentally investigated. Firstly, the MRSP 5 and MRSP 0 samples exhibited the best magnetorheological effect and relative shear stiffening effect, respectively, which were chosen as the fillers of the main cylinder and accessory cylinder. Secondly, through slow and fast experiments, the STMR damper presented an obvious rate sensitive property and realized the speed locking function in a short time and distance when external excitation rate was fast enough. Besides, dynamic experiment results indicated that the damping force of the STMR damper could be controlled by the excitation frequency and the applied magnetic field. Finally, a multiparameter and symmetry hysteretic model was proposed to describe the dynamic hysteretic behavior of the STMR damper, which agreed well with the experimental data.

Conflicts of Interest

The authors declare that there are no conflicts of interest regarding the publication of this paper.

Acknowledgments

This work was supported by Primary Research and Development Plan of Jiangsu Province (Grant no. BE2017167); Natural Science Foundation of Zhejiang Province (Grant no. LY15E080015); National Natural Science Foundation of China (Grant no. 51508237); Natural Science Foundation of Jiangsu Province (Grant no. BK20140560); and Research Foundation for Advanced Talents of Jiangsu University (Grant no. 14JDG161).

References

[1] F. Guo, C. B. Du, G. J. Yu, and R. P. Li, "The static and dynamic mechanical properties of magnetorheological silly putty," *Advances in Materials Science and Engineering*, vol. 2016, Article ID 7079698, 11 pages, 2016.

[2] X. Z. Zhang, W. H. Li, and X. L. Gong, "Study on magnetorheological shear stiffening fluid," *Smart Materials and Structures*, vol. 17, no. 1, p. 015051, 2008.

[3] G. R. Peng, W. H. Li, T. F. Tian, J. Ding, and M. Nakano, "Experimental and modeling study of viscoelastic behaviors of magneto-rheological shear stiffening fluids," *Korea-Australia Rheology Journal*, vol. 26, no. 2, pp. 149–158, 2014.

[4] S. Wang, W. Jiang, W. Jiang et al., "Multifunctional polymer composite with excellent shear stiffening performance and magnetorheological effect," *Journal of Materials Chemistry C*, vol. 2, no. 34, pp. 7133–7140, 2014.

[5] Y. Wang, S. Wang, C. Xu, S. Xuan, W. Jiang, and X. Gong, "Dynamic behavior of magnetically responsive shear-stiffening gel under high strain rate," *Composites Science and Technology*, vol. 127, pp. 169–176, 2016.

[6] B. Sapiński, "Parametric identification of MR linear automotive size damper," *Journal of Theoretical and Applied Mechanics*, vol. 40, no. 3, pp. 703–722, 2002.

[7] W. L. Qu, S. Q. Qin, J. W. Tu et al., "Intelligent control for braking-induced longitudinal vibration responses of floating-type railway bridges," *Smart Materials and Structures*, vol. 18, no. 12, p. 125003, 2009.

[8] W. L. Qu, J. Liu, J. W. Tu, M. Run, and H. Cheng, "Crucial techniques for design of 500 kN large-scale MR damper," *Earthquake Engineering and Engineering Vibration*, vol. 27, no. 2, pp. 124–130, 2007, in Chinese.

[9] W. L. Qu, M. Run, and J. W. Tu, "Design and simulation of a new full scale MR damper," *Journal of Wuhan University of Technology*, vol. 29, no. 2, pp. 87–90, 2007, in Chinese.

[10] W. L. Qu, S. Q. Qin, J. W. Tu, J. Liu, and Q. Zhou, "Theory and crucial technologies of intelligent control for response in deck and towers of Wuhan Tianxingzhou cable-stayed bridge subjected to train braking," *China Civil Engineering Journal*, vol. 43, no. 8, pp. 63–72, 2010, in Chinese.

[11] G. J. Yu, C. B. Du, and T. Sun, "Thermodynamic behaviors of a kind of self-decoupling magnetorheological damper," *Shock and Vibration*, vol. 2015, Article ID 502747, 9 pages, 2015.

[12] G. J. Yu, C. B. Du, and F. X. Wan, "Design and experimental studies on self-decoupling magneto-rheological damper," *Journal of Vibration, Measurement and Diagnosis*, vol. 32, no. 3, pp. 426–431, 2012, in Chinese.

[13] G. J. Yu and C. B. Du, "Design and experimental studies on composite magneto-rheological damper," *Chinese Quarterly of Mechanics*, vol. 35, no. 1, pp. 131–138, 2014, in Chinese.

[14] G. J. Yu, T. Sun, B. Su et al., "Research of architectural structures semi-active control based on SDMR damper," *Journal of Chongqing University of Technology (Nature Science)*, vol. 29, no. 11, pp. 42–50, 2015, in Chinese.

[15] X. Z. Zhang, W. H. Li, and X. L. Gong, "The rheology of shear stiffening fluid (STF) and the dynamic performance of an STF-filled damper," *Smart Materials and Structures*, vol. 17, no. 3, p. 035027, 2008.

[16] H. Zhou, C. Y. Guo, L. H. Zong et al., "Performance of shear stiffening fluid and a damper as its application," *Journal of Vibration and Shock*, vol. 32, no. 18, pp. 15–20, 2013, in Chinese.

[17] J. Liang and X. H. Zhang, "Rheological properties of SP in shock transmission application," *Journal of Materials in Civil Engineering*, vol. 27, no. 9, p. 04014250, 2015.

[18] L. C. Davis, "Model of magnetorheological elastomers," *Journal of Applied Physics*, vol. 85, no. 6, pp. 3348–3351, 1999.

[19] AASHTO, *AASHTO LRFD Bridge Construction Specifications*, American Association of State Highway and Transportation Officials, Washington, DC, USA, 2012.

[20] C. Collette, G. Kroll, G. Saive, V. Guillemier, and M. Avraam, "On magnetorheologic elastomers for vibration isolation, damping, and stress reduction in mass-varying structures," *Journal of Intelligent Material Systems and Structures*, vol. 21, no. 15, pp. 1463–1469, 2010.

Hindawi
Advances in Materials Science and Engineering
Volume 2018, Article ID 9198656, 11 pages
https://doi.org/10.1155/2018/9198656

Review Article

Review of Basalt Fiber-Reinforced Concrete in China: Alkali Resistance of Fibers and Static Mechanical Properties of Composites

Zhensheng Guo, Chunfeng Wan, Mengye Xu, and Jinxiang Chen

Key Laboratory of Concrete and Pre-Stressed Concrete Structures of the Ministry of Education, Southeast University, Nanjing 210096, China

Correspondence should be addressed to Chunfeng Wan; wan@seu.edu.cn

Received 12 February 2018; Revised 22 April 2018; Accepted 10 May 2018; Published 21 June 2018

Academic Editor: Nadezda Stevulova

Research on three-dimensional, randomly distributed BFRC in China is analyzed and summarized in relative depth in this study. The results indicate that the effect of the fiber component and alkali corrosion temperature on the alkali resistance of BF is significant; the BF has little effect on the compressive strength of the concrete; the tensile and flexural strengths of the composites significantly increase compared with plain concrete, and the fiber content has a significant effect on the strength. In light of some problems in the current research, six possible research topics are suggested: (1) investigating the alkali resistance of the BF under dynamic temperatures, lower alkali concentrations, and longer alkali corrosion times; (2) improving the alkali resistance of the BF by increasing its hydrophobicity; (3) determining the optimal fiber distribution orientation of the BF with various characteristic parameters; (4) establishing the calculation formulas for the critical content and critical aspect ratio of various types of BF; (5) determining the optimal mixture ratio of two or more fibers in the FRC while studying the complementary mechanisms between each other; and (6) improving the dispersion of the BF and the BF/matrix interfacial properties.

1. Introduction

Concrete, which is the most widely used material in civil engineering, has the advantages of high compressive strength and good durability. However, it also has the disadvantages of high dead weight, low tensile strength, poor toughness, low fracture energy, and poor impact resistance [1–3]. Concrete needs to be used in conjunction with other materials, which complement its properties, and thus, the application space will be expanded. Reinforced concrete and FRC are two of the most common building materials. The fibers used in such composites include steel fiber, carbon fiber, glass fiber, BF, synthetic fiber, and plant fiber [4]. Among them, as a new material in the 21st century [5], BF has a wide range of raw material sources, good thermal stability (the end-use temperature range is −263 to 900°C), thermal insulation (the thermal conductivity is approximately 0.04 W/(m·K)), good environmental compatibility, high tensile strength, and high elastic modulus [6–9]. Due to the mixing of BF, the internal structure of the concrete can be optimized; it can be reinforced and toughened, and its thermal insulation and durability can be improved, among other effects [10–13].

The Czech Republic began testing basalt wool as a substitute for asbestos at the end of the 1950s. The erosion resistance of the fiber and the bonding between the fiber and the cement were found to be effectively improved by adding alkali resistance components into the fiber and treating the surface with a polymer [14, 15]. The former Soviet Union made a step forward in their BF research and set out to investigate it in the 1960s. However, the publication of numerous patents and papers related to BF and large-scale production did not begin until the 1990s [16, 17]. The study of BF in Europe, the United States, Japan, and other countries started in the 1970s, and the production process was inferior to those in the former Soviet Union [5]. However, in recent years, in-depth research on BFRC has

been reported in Europe, the United States, and Japan, specifically reports on the alkali resistance of BF by Sim et al. [18] and Lipatov et al. [19]; the strength, heat resistance, high-temperature resistance, and inflaming retarding of BF glass aggregate concrete by Borhan et al. [20–22]; the thermal deformation of BF-aerated concrete by Sinica et al. [23]; the conventional mechanical properties of concrete with a high BF content by Ayub et al. [24]; and the wear-corrosion resistance of BFRC by Kabay [25], among others.

In China, in 1978, the Nanjing Glass Fiber Institute [26] first proposed the use of basalt to produce alkali-resistant fiber and enhance concrete. In the same year, Shen [27] conducted an experimental study on the alkali resistance of BF. In 1980, Du [28] summarized a report in the former Soviet Union's *Building Materials* about the advantages and engineering application prospects of BF. In 1990, Zhao [29] translated a brief report from the former Soviet Union entitled "Basalt Fiber Reinforced Concrete," which first introduced the concept of BFRC components. However, systematic reports on BFRC began in the early 21st century with the reports on the performance of BF, the research progress abroad, the wide application prospects of BF in the field of concrete, and other aspects of BF by Hu et al. [5, 30], Ye [31], and Wang and Zhang [32], among others.

Enabled by continuous improvements in the production process, BF has been incorporated into three-dimensional, randomly distributed FRC, fiber-reinforced polymer bars, fiber cloth, fiber grille, and other composite forms to address practical engineering needs. It has significantly improved the various properties of concrete. This paper mainly reviews the research progress that has been published in Chinese journals concerning the alkali resistance of BF and the basic mechanical properties of the three-dimensional, randomly distributed BFRC. The existing problems are noted and some are detailed, and specific research strategies are put forward, pointing out the direction to improve the aforementioned properties of BFRC. Due to space limitations, the impact mechanical properties, crack resistance, and durability of BFRC will be reported in another paper.

2. The Alkali Resistance of BF

Because concrete is alkaline, the alkali corrosion resistance of BF directly affects the adaptability and the properties of BF in the material. The literature [33] stipulates the alkali resistance of BF and requires that the filament-breaking strength retention rate of the BF used for concrete is not less than 75% after being exposed in the saturated $Ca(OH)_2$ solution at 100°C for 4 h [34]. Therefore, studies of the alkali resistance of BF in terms of the properties of BFRC are both necessary and meaningful.

2.1. Research Progress. The alkali resistance of BF is mainly affected by factors such as the alkali concentration of the application environment, the alkali corrosion temperature, the alkali corrosion time, the properties of the fiber itself, and the pretreatment conditions, among others. In the nearly 40 years since Shen first studied BF in 1978 [27], experimental studies on the alkali resistance of BF have mainly been focused around the aforementioned aspects. Because the physical and mechanical properties of current BF are much better than 20 years ago, research since 2000 is the primary body of work elaborated on in the following sections.

In 2004, Wang et al. [6] studied the chemical composition of BF and its surface modification with alkali solutions. Their results showed that the main chemical components of BF were SiO_2, CaO, and Al_2O_3, which played important roles in determining the chemical stability, mechanical strength, and thermal stability of the BF. After treatment with a 0.1 mol/L NaOH solution, the surface of the BF exhibited some defects, such as a tumor-like substance and corrosion pits, increasing the roughness and surface area. This effect led to a decrease in the fiber strength but improved the interfacial bond between the fiber and the matrix. In 2010 and 2015, Wei et al. [35] and Li et al. [36] analyzed the mechanism of the alkali corrosion of BF. The network skeleton structure of the fiber was mainly composed of Si and Al. In the alkaline solution, a substitution reaction occurred between the OH^- and ≡Si–O–Si≡ in the fiber, resulting in dissolution of the Si element, cleavage of the silicate ion skeleton network, and destruction of other components in the framework. The OH^- diffused into the internal structure of the fiber, leading to lamellar spalling of the surface layer.

In 2006, Wang et al. [37] studied the alkali resistance of BF, which was produced by Heilongjiang Jingpo Lake Basalt Fiber Company, in an alkali corrosion environment of boiling 2 mol/L NaOH solution. Their results showed that the BF was mainly composed of Si, O, Fe, Ca, and other elements. After boiling for 3 h, the mass retention rate of the raw yarn and the strength retention rate of the fiber tow after dipping and curing were approximately 96% and 82%, respectively, indicating high alkali corrosion resistance capacity. The authors attributed this high capacity to the presence of alkali metal oxides in the BF.

In 2007, Huo et al. [38] investigated the alkali resistance of the BF filament and tow in an alkaline corrosion environment of 2 mol/L NaOH solution at 80°C. The model of the fiber, which was produced by the Shanghai Russian Basalt Fiber Co. Ltd., differed from that investigated by Wang et al. The tow was prepared by dipping in 648 gum epoxy. The results (Figure 1(a)) showed that the mass of the fiber decreased slowly with increasing alkaline corrosion time after soaking in an alkali solution. The mass retention rate after 24 h was approximately 88%. The fracture strength of the filament and tow after plying gum treatment rapidly decreased; their strength retention rate after 3 h was approximately 60%. These results indicated that the plying gum treatment could not improve the alkali resistance of the fiber over a short time. The microscopic appearance of the fiber after alkali corrosion exhibited significant pits due to surface spalling (Figures 1(b) and 1(c)). In addition, compared with the conditions used by Wang et al. [37], the experiment had a lower alkali corrosion temperature, and the reaction rate was correspondingly lower; however, the strength retention rate of the tow was lower, which might be related to the fiber component.

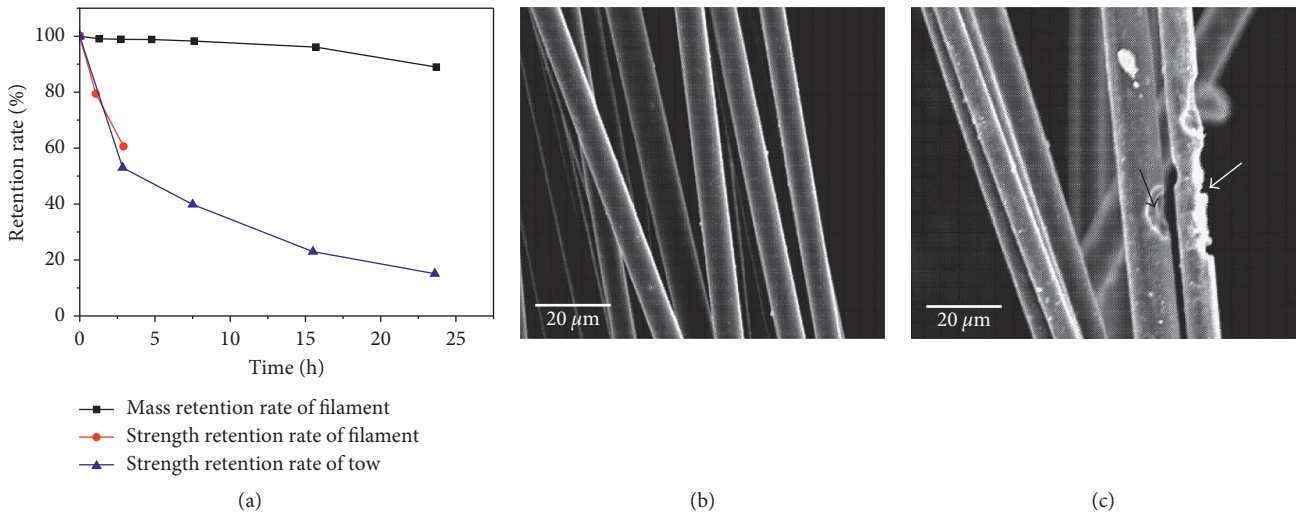

FIGURE 1: The alkali resistance of BF in 2 mol/L NaOH solution at 80°C: (a) curves showing the variation of the mass and strength of the fiber with increasing alkali corrosion time and SEM images of the fibers (b) before and (c) after the alkali corrosion [38].

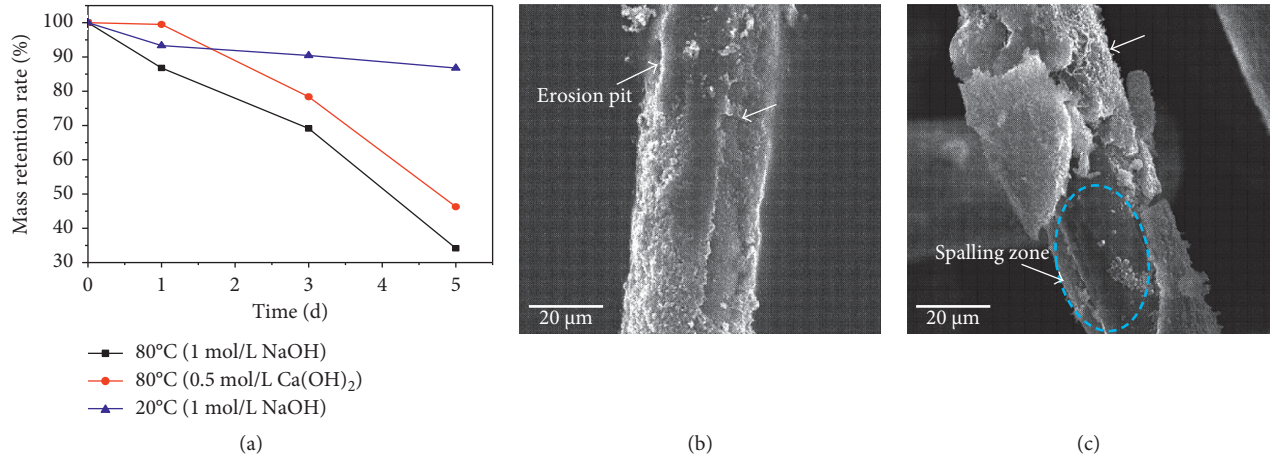

FIGURE 2: The effect of alkali corrosion temperature on BF. (a) The mass retention rate-alkali corrosion time curves at different temperatures and the alkali corrosion damage at (b) 20°C and (c) 80°C [39].

In 2010, Huang and Deng [39] studied the alkali resistance of BF at different alkali corrosion temperatures and longer corrosion times. They found that after being soaked in a 1 mol/L NaOH solution for 5 d (Figure 2(a)), the BF exhibited a mass retention rate of 87% when the temperature was 20°C; in addition, the corrosion degree was lower. However, the mass retention rate was only 33% at 80°C, showing significant corrosion and spalling (Figures 2(b) and 2(c)). The temperature strongly affects the alkali resistance of BF. In addition, compared with the results of Huo et al. [38], those of Huang and Deng [39] were obtained at the same alkali corrosion temperature (80°C) but at different concentrations of the alkali solution (1 mol/L and 2 mol/L), which gave mass retention rates of 87% and 89%, respectively; thus, the concentration of the solution had little effect on the mass of the BF under higher alkali concentrations.

In 2012, Wu et al. [40] studied the effect of alkali concentrations on the tensile strength of twisted BF with a single diameter of 8 μm. The concentrations of NaOH solution ranged between 0.5 and 2 mol/L, and the alkali corrosion time and temperature were 3 h and 100°C, respectively. Tensile strength retention rate of fiber was determined according to GB/T 7690.3-2001, and the results (Figure 3) showed that the damage of alkali solution to fiber intensified with the increase in concentration, resulting in the fibrous weak surface and the sharp decline in strength. The strength retention rate of fiber was only 53.67% when the concentration was 2 mol/L, which was quite different from that of 82% obtained by Wang et al. [37] under the same condition. The distinction might result from the twisting treatment in addition to the different fiber contents.

In conclusion, the results in the aforementioned studies show that the influence of the fiber component, internal microstructure, alkali corrosion temperature, and alkali corrosion time on the alkali resistance of BF is significant. However, the effects of the fiber pretreatment and the increase in the alkali solution concentration under higher

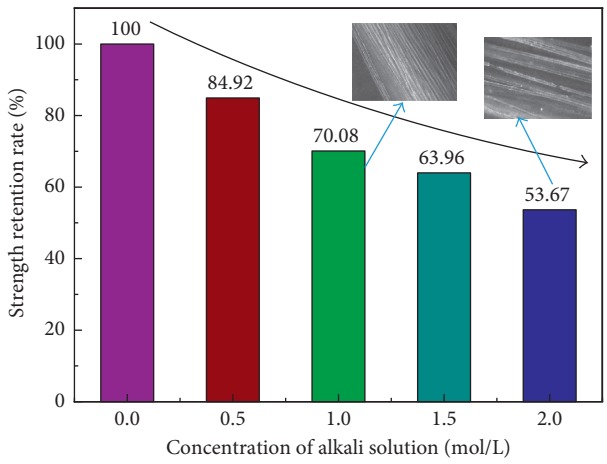

Figure 3: The effect of alkali concentration on the twisted BF [40].

alkali conditions have a limited impact on the alkali resistance. Therefore, in future research, well-directed studies are needed on the alkali resistance of BF and its adaptability based on the characteristics of the concrete. The aforementioned performance of BF can be improved through the fiber performance and the alkali corrosion environment.

2.2. Analysis and Prospects. On the basis of the review of the antecedent research results concerning the alkali resistance of BF and the application working conditions of BF in concrete, the following four research directions are put forward:

(1) On the basis of the temperature variation curve as a function of the age of the concrete structure under the actual working conditions, the alkali resistance of BF needs to be measured and studied at the dynamic alkali corrosion temperature. Such a study will enable the mechanism of influence on the properties of the BFRC to be concurrently examined. In the current study, the alkali resistance of BF is studied at a constant temperature. However, in the course of hardening of the concrete, factors such as the concrete material properties, hydration heat, and casting temperature indicate that the temperature parabolically changes and tends to become stable with age. Moreover, different concrete structures with different measurement point locations show distinctly different temperature changes (Figure 4). In addition, the temperature will affect the alkali corrosion reaction rate and the alkalinity of the environment surrounding the fiber, which are important factors in studies of the alkali resistance of BF. Therefore, investigations of the corrosion resistance of BF under dynamic temperature are necessary to simulate the environment of concrete and to explore the mechanism by which BF modifies the mechanics, durability, and other properties of BFRC.

(2) To study the adaptability of BF in the concrete, the alkali resistance of BF in a simulated alkali solution with a pH of 10.5–13.5 should be evaluated. Some authors [41] have shown that the pH value of well-hydrated Portland cement was between 12.5 and 13.5, and the pH value of sulfoaluminate low-alkali cement was between 10.5 and 11.5. As a result, the pH value of concrete is lower than that. In the aforementioned studies, NaOH solutions with a concentration of 1 mol/L or higher were mostly used; the alkalinity of these solutions is significantly higher than that of Portland cement paste. Otherwise, the alkali corrosion rate exhibits a high correlation with the concentration of the alkali solution [42]. Therefore, the alkali resistance of the current BF in a solution with alkalinity equal to that of the concrete material should be studied.

(3) The alkali corrosion time of BF in the simulated alkali solution should be properly extended according to the specific concrete structure. As Figure 4 shows, the temperature of the raft foundation nearly returns to its normal temperature after 10 d; however, the dam needs 25 d to reach its initial temperature, which is considerably longer than the time required for the raft foundation. However, most of the alkali corrosion times in the aforementioned research were only a few hours and certainly not more than 7 d. Even in the case of accelerated alkali corrosion experiments at a higher temperatures and shorter times, the extent to which these test results reflect the actual conditions of BF in the concrete requires further study. Therefore, the alkali corrosion time of BF should be extended appropriately according to the actual expected working conditions.

(4) The hydrophobicity of BF needs be measured, and the moisture transport mechanism should be determined. The alkali resistance of the BF and the overall properties of the composites are improved by increasing its hydrophobicity. As previously mentioned, the long-term alkali resistance of BF needs to be improved. The existing methods for improving the hydrophobicity mainly include BF surface modification by plying gum, the addition of ZrO_2 into the BF [19], and the use of low-alkaline cement. However, many factors must be considered, such as the limited improvement, delaying alkali corrosion instead of stopping it, increasing the cost of the project, and the lack of supply, among others. However, through the determination of the zeta potential, Hu et al. [43–45] showed that although the BF was an inorganic material made from rock through melting and wire drawing, its surface was inert, and the elements on the surface of BF could form hydrogen bonds with hydrophilic polar groups. Meanwhile, the surface of BF contained many Si atoms, which would chemically react with the surrounding active groups under certain conditions. Therefore, the alkali corrosion reaction can readily occur. On the other hand, water is a transmission medium of various ions. If the hydrophobicity of BF is good, the alkaline corrosion ions cannot easily enter the fiber because of the lack of the transmission medium, and it is difficult to destroy the

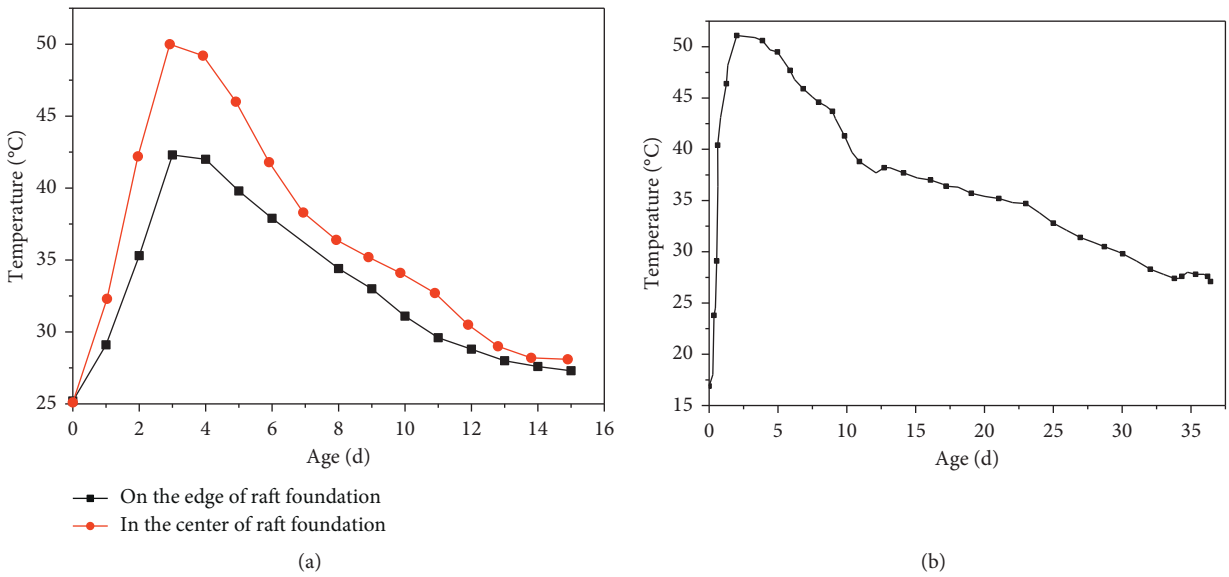

FIGURE 4: Curves showing the variation of temperature with increasing age of the concrete. (a) The measured values of the temperature field of the concrete at different points of a raft foundation and (b) the measured temperature field value of the concrete at the center of the base of an arch dam [46, 47].

BF. By contrast, BF can not only absorb the surrounding water used for the cement hydration reaction, which adversely affects the hardening of the concrete and the properties of the fiber/matrix interface, but also provide the carrier for the transmission of the alkali corrosion ions. Therefore, improvements in the hydrophobicity of BF and in the ability to block moisture are beneficial for improving the alkali resistance as well as the mechanical properties and durability of the BFRC. The hydrophobic and moisture transmission of BF has rarely been reported in depth in the literature. The next step should be to improve the alkali resistance of BF and the overall performance of the composite by measuring the hydrophobicity and elucidating the moisture transmission mechanism. From these two aspects of the BF and the concrete, through fiber surface modification and by adding mineral admixtures into the matrix, the dispersion of the BF in the matrix and the BF/matrix interfacial properties would be improved and the mechanical properties of the composite would be enhanced.

3. Static Mechanical Properties of BFRC

Similar to conventional concrete members, BFRC members have been subjected to various loads under different working conditions. Research on the static mechanical properties has also mainly focused on the strength, flexural toughness, and fracture mechanical properties, which are elaborated below.

3.1. Strength of BFRC. In recent years, researchers have studied the change rule for the mechanical properties of various concretes, including ordinary concrete, self-compacting concrete, concrete with high mineral-admixture contents, shotcrete, and concrete-filled steel tubes. This work consisted of measuring the compressive, tensile, and flexural strengths of BFRC with different fiber contents under different conditions, such as different ages and mineral admixtures. The fiber content has typically been on the order of 0.5–8.5 kg/m^3, the investigated aging times have mostly been 3 d, 7 d, and 28 d, and the mineral admixtures have mainly included fly ash and silica fume. We will describe these below.

In 2008, Li et al. [48] studied the 28 d cubic compression, axial compression, splitting tensile, and flexural strengths of BF-reinforced self-compacting concrete (BFRSCC) (Figure 5) with a fiber content of 0.8–4.8 kg/m^3, a length of 10–25 mm, and a diameter of 7–15 μm in accordance with CECS13:89. The results showed that with increasing fiber content, compared with that of plain self-compacting concrete (PSCC), the cubic compressive strength of the BFRSCC decreased by 3–10%. The overall trend of the axial compressive strength of BFRSCC first decreased and then increased before finally reaching strength slightly greater than that of PSCC. The splitting tensile strength gradually increased after an initial slight reduction, whereas the flexural strength decreased after initially slowly increasing. Both the tensile and flexural strengths showed peak values, where the maximum increase was 17% and 24%, respectively, and the corresponding optimal fiber content is 3.2 kg/m^3. These results were attributed to the BF [48], which is soft and fine, forming a weak honeycomb-like or pore-like structure in the concrete and resulting in poor dispersion or a clustering phenomenon in the process of concrete mixing. These features reduced the density of the concrete and the cubic compressive strength. For the axial compressive strength, in addition to the aforementioned discussion, the increasing BF had a lateral restraint effect similar to that of stirrups, which improved the

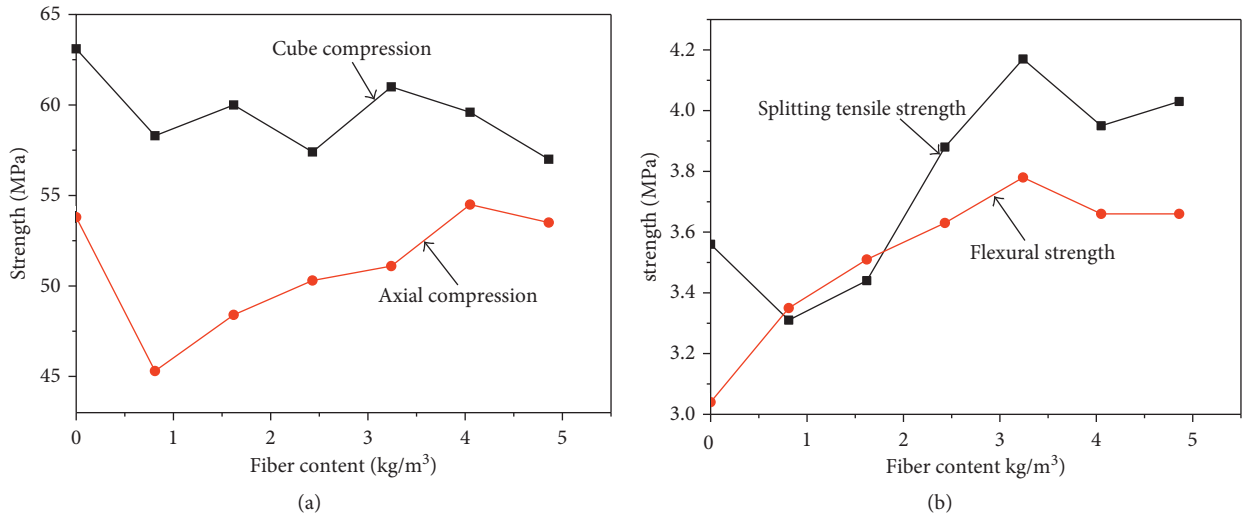

Figure 5: The effects of fiber content on (a) the cubic and axial compressive strengths and (b) the splitting tensile and flexural strengths of BFRSCC [48].

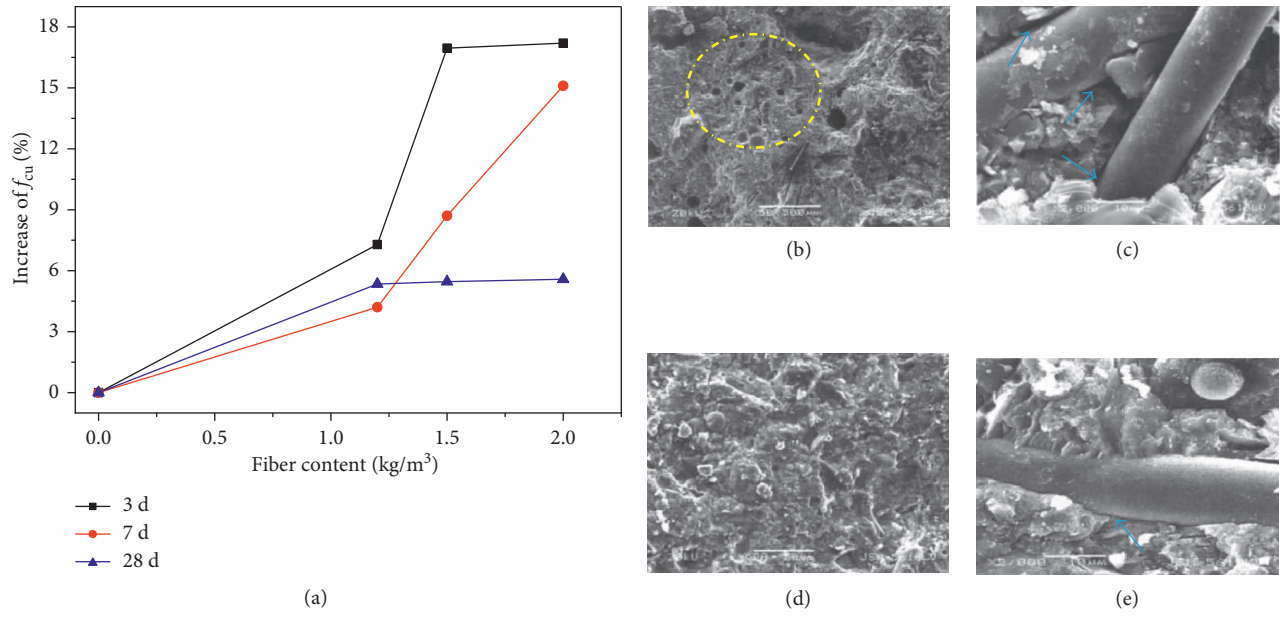

Figure 6: The effect of the pretreatment of BF on BFRC: (a) the change of the cubic compressive strength (f_{cu}) at different ages with the fiber content, (b) the section of matrix without pretreatment, (c) the interface between BF and matrix without pretreatment, (d) the section of matrix with pretreatment, and (e) the interface between BF and matrix with pretreatment [51].

compressive strength of the matrix. Under the influence of two plus-minus factors, the axial compressive strength exhibited a parabolic variation. The research concerning the axial compressive strength of the BFRC-filled steel tubular short columns, reported by Wang et al. [49] in 2013, also demonstrated this point. The splitting tensile and flexural strengths could be used as indexes to evaluate the tensile strength of the material. According to composite theory [50], the ultimate tensile strength of the BFRC was directly related to the ultimate tensile strength of the fiber and its content; otherwise, the tensile strength of BF is higher. Consequently, a reasonable amount of BF could improve the two mechanical indexes without affecting the workability of the self-compacting concrete.

In 2009, by pretreating BF via wrapping up it with cement paste before mixing, Wu et al. [51] investigated the compressive strength of the BFRC standard cubic specimens with a fiber content of 1.2–2.0 kg/m^3, a length of 12 mm, and a radius of 15 μm according to the standard GB/T 50081-2002. The results showed that (Figure 6(a)) with increasing fiber content, the biggest growth of 28 d and early cubic compression strength (f_{cu}) of BFRC was about 5% and 17%, respectively. Compared with the results of Li et al. [48], the pretreatment had improved the compressive properties of

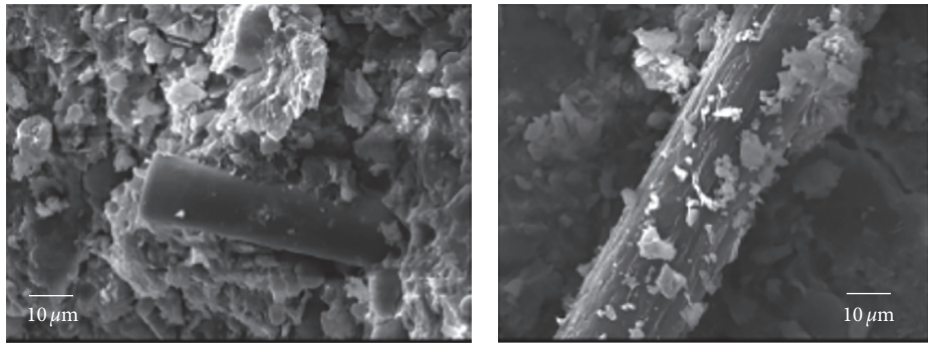

(a) (b)

Figure 7: The micromorphology of the (a) BF and (b) PPF fibers in concrete [53].

BFRC to some extent. The reason was that the cement paste provided a lubricating effect between fibers and aggregates and made them fully contact with each other, thus effectively reducing the porosity of the matrix and enhancing the interfacial bond between fibers and matrix (Figures 6(b)–6(e)). In addition, the fibers wrapped with cement paste had better fluidity in the matrix, which increased its distribution uniformity.

In 2011, Ye et al. [52] studied the flexural tensile strength of high-strength BFRC with a relatively large amount of fly ash and silica fume with a fiber content of 8.4 kg/m^3 and a length of 6 mm, 18 mm, and 30 mm. The fiber was pretreated in three ways: direct shortcutting, plying gum, and twisting and plying gum. The results showed that compared with the PC, the maximum increase at 3 d, 7 d, and 28 d for the flexural tensile strength of BFRC was 20%, 27%, and 18%, respectively. The corresponding optimum fiber length and pretreatment method were 18 mm with direct shortcutting fiber. On the basis of the changing rate of the increase in strength with age, no apparent weakening of the fiber reinforcement with age was observed in the experiments, which might be related to the improvement in the alkali resistance.

In 2012, Luo and Bi [53] studied the influence of BF and hybrid fibers composed of BF and polypropylene fiber (PPF) on the cubic compressive strength of self-compacting concrete from the perspective of its pore structure. The BF contents were 1.3 kg/m^3 and 2.7 kg/m^3, while the PPF content was 0.05–0.3 kg/m^3. In the case of concrete reinforced only by BF, the results suggested that the compressive strength was reduced compared with that of PSCC, similar to the results of a study by Li et al. [48]. This strength reduction was attributed to three factors. First, according to the four levels of pore size in the concrete proposed by Wu and Lian [54], the reduction of harmless or less harmful pores and the increase of harmful or more harmful pores in the BFRC would result in reduced density and strength. Second, from the perspective of micromorphology (Figure 7), BF was quite smooth compared to PPF. Thus, a very few hydration products would adhere to it, leading to weakening of the BF/matrix interface, which in turn diminished the effective advantages of the fiber properties. The third factor was the failure mode. Only cracks appeared during the compressive failure of BFRC; no fragments were observed to burst apart. The failure mode of the BFRC was integrated, which suggested that the toughness of the specimen increased. For the hybrid fiber-reinforced self-compacting concrete, the 28 d strengths were improved by various degrees, and the greatest increase was approximately 38%. The corresponding contents of BF and PPF were 2.7 kg/m^3 and 0.1 kg/m^3, respectively. The existence of PPF decreased the density and pore size, and the elasticity modulus and tensile strength of PPF were smaller than those of BF by an order of magnitude; the PPF thereby became a complementary support material to the BF, significantly increasing the strength.

In 2016, Zhou et al. [55] studied the splitting tensile and flexural strengths of BF-reinforced shotcrete under tunnel dry heat working conditions simulated using a stove and analyzed the structural mechanisms from the perspective of the anticrack functionality of the BF in the matrix. The ratio of raw materials was determined according to JGJ55-2000 and GB50086-2001. Their results suggested that the mechanical properties of the BF-reinforced shotcrete under dry heat conditions were significantly reduced compared with those measured under standard conditions. The existence of the BF could not appreciably improve the tensile and flexural strengths of the shotcrete, and the results even indicated a slight decrease in the mechanical properties at some fiber contents. The likely reasons for this behavior were related to the lower orientation coefficient of the three-dimensional, randomly distributed BF [50], the insufficient alkali resistance and dispersion of the BF used in the experiment, and the poor bond performance between the fiber and the matrix.

In 2016, based on the uniaxial compression test of BF-reinforced resin concrete cylinder and the theory of damage mechanics, Yu et al. [56] built the uniaxial compression constitutive model of the structure according to the generalized Hooke's law and the theory of Weibull strength distribution:

$$\sigma = 4.6 \times 10^4 \varepsilon \exp\left[-\left(\frac{\varepsilon}{0.006}\right)^{2.5}\right]. \quad (1)$$

The results indicated that the model agreed well with the experimental results, and the trend of change of model was

similar to that of plain concrete, but the strain during the rising section was obviously bigger than that of the latter [57]. This study made a theoretical contribution to the research on the mechanical properties of the material.

In short, research into the strength of the BFRC resulted in discrete or even opposite results because the strength was affected by the fiber characteristic parameters, fiber content, material properties of the matrix, preparation method, and the composite age, among other factors. However, the existence of BF in general had little effect on the compressive strength of the concrete but could nonetheless result in apparent improvements in the tensile and flexural strengths. The fiber content influenced the strength of the material, and an optimal content value existed. The adulteration of mineral admixtures and PPF was beneficial to the BF's enhancement of the concrete. On the basis of the aforementioned studies, further research can be conducted on the optimal mixture ratio and to complement the reinforcement mechanism from BF and other fibers with different properties, such as PPF, on the basis of different matrix materials and requirements.

3.2. Flexural Toughness and Fracture Mechanics. A few published works exist on the flexural toughness and fracture mechanics of BFRC. Scholars have mainly studied the influence of the characteristic parameters, such as the content and aspect ratio of the fiber, on the flexural toughness index, fracture toughness, and fracture energy. They have also discussed improvements in the toughness and fracture properties of the concrete as a result of the fiber. These results are illustrated and analyzed below.

He and Lu [58] and Ye et al. [52] reported on the flexure toughness of a B2010 beam in 2009 and 2011, respectively. The index used to measure the flexure toughness was the JSCEG552 standard proposed by the Japan Social of Civil Engineers. The flexure toughness of the BFRC was 5.6 times that of PC, as reported by He and Lu [58]. However, in the latter study, Ye et al. [52] noted that the BFRC, which was influenced by the fiber length, twisting treatment, and surface modification, exhibited a flexure toughness only 1.2–2.1 times of that of PC, as evaluated under different experimental conditions. Because the roughness of the fiber increased after the twisting treatment, which improved the bonding properties between the fiber and the matrix, the load-displacement curve of the concrete reinforced by twisted fiber was much flatter. The twisted fiber could substantially improve the toughness of the concrete. In consideration of the data in the latter report was much more sufficient, the results were closer to practical situations. Nonetheless, the presence of BF could clearly improve the flexure toughness of concrete.

In 2016, according to ASTM E647-11 and RILEM three-point bending test method, Xue et al. [59] studied the influence of the BF content and aspect ratio on three performance parameters: the fracture energy, fracture toughness, and the ductility index, which defined the fracture mechanics properties of concrete, and thoroughly analyzed the impact mechanism. The BF content in their study was approximately 6.6–40 kg/m^3, the diameter was 15 μm, and the length was 5–25 mm. Their results suggested the following:

(1) There were three stages during the occurrence and development of cracks in BFRC: (i) the no-cracks expanding stage when the fiber and concrete worked together; (ii) the crack stable growth stage, where the bridge stress of the fiber had delayed effects; and (iii) the crack unstable growth stage after the net stress of the crack tip reached the ultimate stress.

(2) The presence of the BF could improve the fracture mechanics of the concrete to some extent. The amplifications were 37% in the fracture energy, 44% in the fracture toughness, and 19% in the ductility index. The variation tendencies of all of the three fracture mechanical parameters first increased and then decreased with increasing fiber content and increasing aspect ratio. Thus, a corresponding BF optimal content or aspect ratio existed.

(3) The mechanism by which the BF influenced the fracture mechanics of the concrete was as follows:

  (i) The BF filament is too soft, fine, and smooth to induce surface modification [6] and anchorage, and its tensile strength is high. Therefore, the interfacial bonding stress might be less than the tensile strength of the fiber, and the main cause of failure was that the fibers being withdrawn during the process of fracture failure. However, the nonmain crack resistance increased when the cracks propagate and the fracture performance was improved by benefiting from the interfacial debonding, frictional slip, and obliquity effect. However, the remaining pores would accelerate the unstable propagation of cracks as the composite reached its ultimate strength.

On the basis of the aforementioned research, one conclusion was that the BF would substantially improve the toughness and fracture mechanics of the concrete if the mixing and characteristic parameters of the fiber were properly selected.

3.3. Analysis and Prospects. After organizing and summarizing the studies regarding the strength, toughness, and fracture mechanics of the BFRC, we identify the following issues that require further research:

(1) On the basis of the pullout test of a single (or single-bundle) BF with different distributions and orientations in the concrete, the coupling among the tensile strength, fiber/matrix interfacial bonding strength, and the lateral shear strength of the fiber as well as the optimal distribution of the fiber corresponding to different types of characteristic parameters can be determined. When the orientation of BF is consistent with the pullout force, the fiber will be easily pulled out. By contrast, if the included angle between the fiber and the pullout force is too large, lateral shear failure will most likely occur for the

fiber. In both circumstances, the tensile strength of the fiber cannot be efficiently utilized. Thus, if the coupling among them could be realized and an optimal orientation distribution of diverse types of fibers could be obtained, the mechanical properties (e.g., the tensile, flexure, and fracture performance) of the BFRC can be significantly improved.

(2) The formula concerning the critical content and aspect ratio of the BF in concrete can be established with respect to the bonding properties between the BF and the concrete and the random distribution characteristics of the fiber in the matrix. In the current research body, only the influence of the fiber content and aspect ratio on the mechanical properties is reported, whereas experimental studies and theoretical analyses of the critical content and aspect ratio remain obscured. However, according to the theory of the compound function between a fiber and a concrete [50], the ultimate tensile strength could only be significantly improved when the fiber content was larger than the critical value. The relationship between the actual aspect ratio and the critical aspect ratio of the fiber directly influenced the failure mode and the realization of fiber enhancement. Therefore, additional research on this aspect is needed.

(3) The mechanical model of BFRC needs an in-depth study in order to fully reveal its mechanical behavior mechanism. Based on the above analysis, it is found that the number of model research about BFRC is very limited in China. Compared with the uniaxial compression constitutive model of high-strength BFRC proposed by Ayub et al. [60], these models still have some defects such as the inadequate reflection of the fiber content and the single expression of stress-strain full process, and they need further modifications and perfections. In addition, the static mechanics model research of BFRC such as shear and bending mechanics is still rare. Therefore, it will be an important area for future research.

4. Conclusion

In summary, the studies reported in China in this century described the alkali resistance of fibers under different alkali corrosion environments and pretreatment methods, and the static mechanical properties, such as the strength and toughness, of the BFRC under different characteristic parameters and content. The main results were illustrated as follows: the composition and temperature strongly influenced the alkali resistance of the BF, whereas the pretreatment had limited effects; the BF had almost no effect on the compressive strength but could significantly improve the tensile and flexural strengths; in addition, the fiber content could notably influence the strength.

Hereby, we propose the following six research topics related to alkali resistance and static mechanical properties of three-dimensional, randomly distributed BFRC:

(1) The alkali resistance and adaptability in the concrete with BF under the conditions of dynamic alkali corrosion temperature, lower concentration of alkali, and longer alkali corrosion times should be measured and investigated. In addition, its mechanism of influence on the mechanical properties of the BFRC should be investigated.

(2) On the basis of the determination of the hydrophobicity and moisture transmission mechanism of the fiber, the alkali resistance of BF and the integral performance of composites can be improved via the BF's hydrophobicity and moisture transmission.

(3) On the basis of the pullout test of a single (or single-bundle) BF with different distributions and orientations in the concrete, the optimal orientation of the BF with different characteristic parameters should be investigated to achieve the maximum enhancement to the matrix.

(4) A formula for the critical content and aspect ratio for various kinds of BFs in concrete should be established, and the mechanism of influence of the BF with different contents and aspect ratios on the mechanical properties of the matrix (e.g., tensile, flexure, and fracture performance) should be explored, and the aforementioned properties should be optimized.

(5) With the objective of varying the material characteristics and applications of the matrix, the optimal mixture ratio and the complementary mechanism between the BF and other types of fibers with different properties, such as PPF, in the concrete should be studied.

(6) From the perspective of BF and the concrete, the dispersion of the BF and BF/matrix interfacial properties should be improved through surface modification of the fiber and the addition of mineral admixtures to the matrix, thereby improving the mechanical properties of the composites.

Conflicts of Interest

The authors declare that they have no conflicts of interest.

Acknowledgments

This study was supported by the National Natural Science Foundation of China (Grant no. 51578140).

References

[1] Y. Gong, R. X. Shen, and H. Q. Li, *Application of Dura Fiber in Civil Engineering*, China Machine Press, Beijing, China, 2002, in Chinese.

[2] L. H. Xu, D. T. Xia, G. Z. Xia, and Y. Chi, "Effect of steel fiber and polypropylene fiber on the strength of high strength concrete," *Journal of Wuhan University of Technology*, vol. 29, no. 4, pp. 58–60, 2007.

[3] S. L. Xu and H. D. Li, "A review on the development of research and application of ultr a high toughness cementitious

composites," *China Civil Engineering Journal*, vol. 41, no. 6, pp. 45–60, 2008.

[4] J. Y. Sun, "Frost resistance characteristics of fiber concrete," *Journal of Building Materials*, vol. 16, no. 3, pp. 437–440, 2013.

[5] X. Q. Hu, Y. F. Luo, and T. N. Shen, "Basalt continuous fiber and its reinforcing composite material," *Hi-Tech Fiber and Application*, vol. 27, no. 2, pp. 1–11, 2002.

[6] G. J. Wang, D. K. Shang, L. N. Hu, K. L. Zhang, Z. H. Guo, and Y. J. Guo, "Investigation of modification of basalt fibers and preparation of ecocomposites thereof," *Acta Materiae Compositae Sinica*, vol. 21, no. 1, pp. 38–44, 2004.

[7] L. A. Shi, H. Y. Ma, and Z. D. Rong, "Influence of basalt fiber and its geotextile on mechanical performance of ultra-high performance cement composites," *Journal of Nanjing University of Aeronautics and Astronautics*, vol. 44, no. 3, pp. 415–419, 2012.

[8] D. Zhang, Q. Xu, and Y. Guo, "Experiments on strength and shrinkage of expansive soil with basalt fiber reinforcement," *Journal of Southeast University*, vol. 42, no. 5, pp. 975–980, 2012.

[9] L. J. Ouyang, B. Ding, Z. D. Lu, and J. T. Yu, "Experimental study on seismic performance of short columns strengthened with BFRP and CFRP," *Journal of Tongji University*, vol. 41, no. 2, pp. 166–172, 2013.

[10] J. F. Mao, W. G. Dong, and S. Z. Cong, "Characteristics and application prospect of basalt fiber," *Technical Textiles*, vol. 10, pp. 38–40, 2007.

[11] R. Yang and Z. Wang, "Research on physical and mechanical properties of basalt fiber reinforced concrete," *Yangtza River*, vol. 46, no. 13, pp. 78–81, 2015.

[12] L. Zhao, "The influences of basalt fiber on mechanical properties of cement-based materials," *China Concrete and Cement Products*, vol. 9, pp. 46–48, 2012.

[13] Y. C. Zhang, Q. N. Li, and C. Z. Fang, "Study of the mechanical properties and durability of fiber reinforced concrete based on meso analysis," *Concrete*, vol. 8, pp. 48–50, 2016.

[14] D. X. Hao, "The progress of basalt fiber and its product technology abroad," *China Building Materials Science and Technology*, vol. 3, pp. 84-85, 1990.

[15] Y. H. Gu, "Alkali resistant mineral fiber," *Fiber Glass*, vol. 4, pp. 32–42, 1978.

[16] L. Wang, Y. Chen, and Z. W. Li, "Properties of continuous basalt fiber and composites," *Fiber Reinforced Plastics/Composites*, vol. 6, pp. 22–24, 2000.

[17] Y. Chen, L. Wang, and Z. W. Li, "Properties and application of basalt fiber," *New Building Materials*, vol. 8, pp. 28–31, 2000.

[18] J. Sim, C. Park, and D. Y. Moon, "Characteristics of basalt fiber as a strengthening material for concrete structures," *Composites Part B: Engineering*, vol. 36, no. 6-7, pp. 504–512, 2005.

[19] Y. V. Lipatov, S. I. Gutnikov, M. S. Manylov, E. S. Zhukovskaya, and B. I. Lazoryak, "High alkali-resistant basalt fiber for reinforcing concrete," *Materials and Design*, vol. 73, pp. 60–66, 2015.

[20] T. M. Borhan, "Properties of glass concrete reinforced with short basalt fibre," *Materials and Design*, vol. 42, pp. 265–271, 2012.

[21] T. M. Borhan and C. G. Bailey, "Modelling basalt fibre reinforced glass concrete slabs at ambient and elevated temperatures," *Materials and Structures*, vol. 47, no. 6, pp. 999–1009, 2014.

[22] T. M. Borhan and C. G. Bailey, "Structural behaviour of basalt fibre reinforced glass concrete slabs," *Materials and Structures*, vol. 47, no. 1-2, pp. 77–87, 2014.

[23] M. Sinica, G. A. Sezeman, D. Mikulskis, M. Kligys, and V. Česnauskas, "Impact of complex additive consisting of continuous basalt fibres and SiO_2 microdust on strength and heat resistance properties of autoclaved aerated concrete," *Construction and Building Materials*, vol. 50, pp. 718–726, 2014.

[24] T. Ayub, N. Shafiq, and M. F. Nuruddin, "Effect of chopped basalt fibers on the mechanical properties and microstructure of high performance fiber reinforced concrete," *Advances in Materials Science and Engineering*, vol. 2014, Article ID 587686, 14 pages, 2014.

[25] N. Kabay, "Abrasion resistance and fracture energy of concretes with basalt fiber," *Construction and Building Materials*, vol. 50, pp. 95–101, 2014.

[26] Nanjing Fiberglass Research and Design Institute, "Melt mineral wool slag with containing titania," *Fiberglass*, vol. 1, p. 6, 1978.

[27] R. X. Shen, "Improving durability of glass fiber in cement-base materials," *Journal of the Chinese Ceramic Society*, vol. 6, no. 3, pp. 199–213, 1978.

[28] S. Q. Du, "Prospects for development and applied range of basalt fiber," *Fiberglass*, vol. 4, p. 49, 1980.

[29] X. W. Zhao, "Basalt fiber reinforced concrete," *Journal of Water Resources and Water Engineering*, vol. 3, p. 75, 1990.

[30] X. Q. Hu and S. N. Hu, "The applications of the CBF in war industry & civil fields," *Hi-Tech Fiber and Application*, vol. 30, no. 6, pp. 7–13, 2005.

[31] D. Q. Ye, "Continuous basalt fiber-new materials in twenty-first Century," *Building Materials Industry Information*, vol. 6, p. 5, 2002.

[32] B. P. Wang and W. Zhang, "Properties and applications of basalt fiber," *Research and Application of Building Materials*, vol. 4, pp. 17-18, 2002.

[33] GB/T 23265-2009, *Chopped Basalt Fiber for Cement, Cement Mortar and Concrete*, Standards Press of China, Beijing, China, 2009.

[34] JCT 572-94, *Alkali-Resistant Glass Fiber Twistless Roving*, Standards Press of China, Beijing, China, 1978.

[35] B. Wei, H. L. Cao, and S. H. Song, "Tensile behavior contrast of basalt and glass fibers after chemical treatment," *Material Design*, vol. 31, no. 9, pp. 4244–4250, 2010.

[36] F. Z. Li, G. C. Li, H. M. Wang, and Q. Tong, "Effect of acid/alkali corrosion on properties of basalt fiber yarn," *Materials Review B*, vol. 29, no. 1, pp. 110–113, 2015.

[37] M. C. Wang, Z. G. Zhang, Z. J. Sun, and M. Li, "Corrosion resistance characteristic of continuous basalt fiber and its reinforcing composites," *Journal of Beijing University of Aeronautics and Astronautics*, vol. 32, no. 10, pp. 1255–1258, 2006.

[38] W. J. Huo, Z. G. Zhang, M. C. Wang, M. Li, and Z. J. Sun, "Experimental study on acid and alkali resistance of basalt fiber used for composites," *Acta Materiae Compositae Sinica*, vol. 24, no. 6, pp. 77–82, 2007.

[39] K. J. Huang and M. Deng, "Stability of basalt fibers in alkaline solution and its effect on the mechanical property of concrete," *Acta Materiae Compositae Sinica*, vol. 27, no. 1, pp. 150–154, 2010.

[40] X. Wu, W. L. Chen, Z. Y. Wang, and C. F. Yu, "Experimental study on the properties of basalt fiber yarn," *Journal of Zhejiang Sci-Tech University*, vol. 29, no. 5, pp. 660–663, 2012.

[41] P. K. Mehta and P. J. M. Monteiro, *Concrete: Microstructure, Properties, and Materials*, China Electric Power Press, Beijing, China, 2008, in Chinese.

[42] Z. Li, T. L. Xiao, Q. Y. Pan, J. M. Cheng, and S. G. Zhao, "Corrosion behaviour and mechanism of basalt fibres in

acidic and alkaline environments," *Corrosion Science*, vol. 110, pp. 15–22, 2016.

[43] M. F. Fang and H. Huang, "Study and application of wood plastic composites," *Modern Agricultural Science and Technology*, vol. 3, pp. 8–14, 2009.

[44] L. N. Hu, D. K. Shang, S. J. Li, W. H. Chen, and B. J. Song, "Study on the interfacial functionary mechanism of plant fiber/basalt fiber composite material," *Polymer Materials Science and Engineering*, vol. 20, no. 6, pp. 29–32, 2004.

[45] S. Nachtigall, A. Felix, and R. Mauler, "Blend compatibilizers based on silane- and maleic anhydride–modified polyolefins," *Journal of Applied Polymer Science*, vol. 88, no. 10, pp. 2492–2498, 2003.

[46] J. Wang, S. Yan, and J. L. Wang, "Numerical simulation and real-time survey of temperature fields of mass concrete in raft-foundation," *Journal of Liaoning Technical University*, vol. 34, no. 3, pp. 364–368, 2015.

[47] W. M. He and J. M. Guo, "Monitoring and measurement of core temperature of mass concrete," *Journal of Railway Engineering Society*, vol. 6, pp. 64–67, 2011.

[48] R. Li, Z. Bi, Y. Wang, and H. Y. Liu, "Experimental study on mechanical properties of short basalt fiber self-compacting concrete," *China Concrete and Cement Products*, vol. 2, pp. 48–50, 2008.

[49] H. L. Wang, H. Li, X. L. Yang, Q. C. Ren, and P. Dong, "Experimental research on basalt fibre reinforced concrete filled steel tubular short columns subjected to axial compression load," *Building Structure*, vol. 43, no. 22, pp. 22–25, 2013.

[50] J. Z. Xu, *Technology and Application of Fiber Reinforced Concrete*, China Architecture and Building Press, Beijing, China, 2003, in Chinese.

[51] Z. X. Wu, H. Q. Yuan, Z. A. Lu, and X. C. Fan, "Experimental research on mechanical properties of basalt fiber reinforced concrete," *Concrete*, vol. 9, pp. 67–78, 2009.

[52] B. T. Ye, J. Y. Jiang, W. Sun, C. H. Wang, and J. Hu, "Experimental study on reinforcing HSC with large volume mineral admixtures basalt fibers," *Journal of Southeast University*, vol. 41, no. 3, pp. 611–615, 2011.

[53] B. B. Luo and Q. W. Bi, "Experimental study on the influence of pore structure of hybrid fibers self-compacting concrete on compressive strength," *Bulletin of the Chinese Ceramic Society*, vol. 31, no. 3, pp. 626–630, 2012.

[54] Z. W. Wu and H. Z. Lian, *High Performance Concrete*, China Railway Press, Beijing, China, 1999, in Chinese.

[55] P. Zhou, Z. J. Wang, Y. Yang, and X. F. Ji, "Experimental study of the performance of basalt fiber shotcrete under heat damage," *Journal of Civil, Architectural and Environmental Engineering*, vol. 38, no. 1, pp. 69–76, 2016.

[56] Y. H. Yu, R. F. Wu, Y. M. Chen, and P. Xu, "Uniaxial compression constitutive model of basalt fiber nesin concrete," *Concrete*, vol. 9, pp. 69–71, 2016.

[57] GB 50010-2010, *Code for Design of Concrete Structures*, China Architecture and Building Press, Beijing, China, 2010.

[58] D. Q. He and Z. A. Lu, "Experimental study on mechanical properties of chopped basalt fiber reinforced concrete," *Journal of Henan University*, vol. 39, no. 3, pp. 320–322, 2009.

[59] Q. C. Xue, J. C. Zhang, J. He, and T. J. Ramze, "Experimental study of fracture properties for basalt-fiber-reinforced concrete," *Journal of Harbin Engineering University*, vol. 37, no. 8, pp. 1027–1033, 2016.

[60] T. Ayub, N. Shafiq, and S. U. Khan, "Compressive stress-strain behavior of HSFRC reinforced with basalt fibers," *Journal of Materials in Civil Engineering*, vol. 28, no. 4, article 06015014, 2016.

Hindawi
Advances in Materials Science and Engineering
Volume 2018, Article ID 7812674, 9 pages
https://doi.org/10.1155/2018/7812674

Research Article

Influences of Ultrafine Slag Slurry Prepared by Wet Ball Milling on the Properties of Concrete

Yubo Li,[1] **Shaobin Dai**,[1] **Xingyang He**,[2] **and Ying Su**[2]

[1]*Wuhan University of Technology, Wuhan 430070, China*
[2]*Hubei University of Technology, Wuhan 430070, China*

Correspondence should be addressed to Xingyang He; lunwenhe2017@sina.com

Received 27 December 2017; Accepted 23 April 2018; Published 4 June 2018

Academic Editor: Sverak Tomas

The application of ultrafine ground-granulated blast-furnace slag (GGBFS) in concrete becomes widely used for high performance and environmental sustainability. The form of ultrafine slag (UFS) used in concrete is powder for convenience of transport and store. Drying-grinding-drying processes are needed before the application for wet emission. This paper aims at exploring the performances of concrete blended with GGBFS in form of slurry. The ultrafine slag slurry (UFSS) was obtained by the process of grinding the original slag in a wet ball mill, which was mixed in concrete directly. The durations of grinding were 20 min, 40 min, and 60 min which were used to replace Portland cement with different percentages, namely, 20, 35, and 50, and were designed to compare cement with original slag concrete. The workability was investigated in terms of fluidity. Microstructure and pore structure were evaluated by X-ray diffraction (XRD), scanning electron microscopy (SEM), and mercury intrusion porosimetry (MIP). The fluidity of concrete mixed with UFSS is deteriorated slightly. The microstructure and early strength were obviously improved with the grind duration extended.

1. Introduction

Cement, the main cementitious material used in the concrete, is the base material of construction. Cement manufacture is a highly energy-intensive process. The total energy consumption of the global cement industry is estimated at 2% of global primary energy use, which accounts for approximately 7% of all global carbon dioxide emissions [1, 2]. The development of ecofriendly concrete in the construction industry is gaining deep concern and intensive research worldwide.

Ground-granulated blast-furnace slag (GGBFS) is a by-product of steel making [3]. GGBFS has been found to exhibit excellent cementitious properties when it was finely powdered [4]. The use of GGBFS as supplementary cementitious material not only reduces the usage of cement [5] but also improves the porosity performance of OPC concrete [6]. In addition, GGBFS is one of the major precursor materials used in the production of alkali-activated materials (AAMs) [7]. As a kind of alternative cementitious material, GGBFS shows comparable mechanical performance to blended slag cement and similar or even lower global warming potential compared with the best available concrete technology [8]. The reactivity of GGBFS is considered an important parameter to assess the effectiveness of GGBFS in concrete composites, which varies greatly with the source of slag, types of raw material used, methods of cooling, and the duration of milling [9]. Pal et al. [10] investigated the relationship between the hydraulic index (HI) of slag and the influencing factors of slag, including glass content, fineness, and chemical composition. Zhao et al. [11] studied the particle characteristics and hydration activity of GGBFS containing industrial crude glycerol-based milling aids. The result indicated that means and milling aids strongly affect the activity of GGBFS.

Wet milling is a method of producing powder slurry by milling materials with mediums together, with advantages of uniformity, high milling efficiency, and small noise contrast with dry milling. It is widely used in cement and ceramics industries [12] and rarely in the field of slag powder. Nowadays, the main milling methods of slag are dry milling processes and need to go through drying-milling-drying

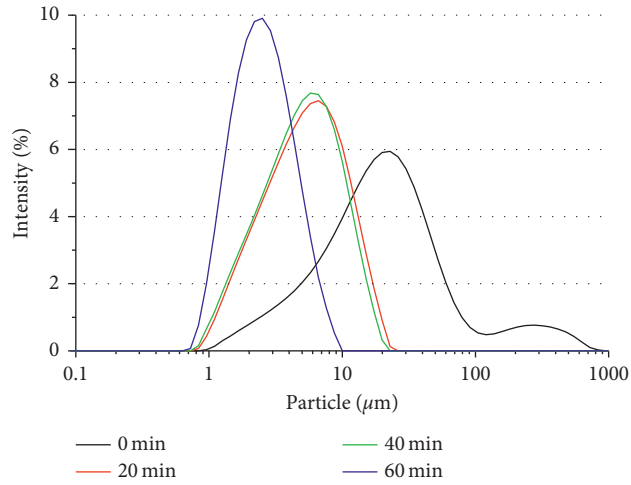

Figure 1: Different particle size distributions of slag particles at different wet milling durations.

processes before application for wet emissions. If the dry milling process is replaced by the wet milling process, the drying process can be omitted and be applied to concrete directly.

In this paper, the feasibility of UFSS prepared by the wet ball mill process applied in concrete was investigated. The properties of concrete were tested by kinds of test methods and analysis methods.

2. Materials and Experimental Details

2.1. Materials

2.1.1. Ground-Granulated Blast-Furnace Slag (GGBFS). The GGBFS was from the Capital Iron and Steel Company in the state of Beijing (China). Specific gravity of GGBFS was 2.92. The particle size distribution and microstructure of slag slurry/powder for different wet milling durations and the original slag (0 min) are shown in Figure 1, Table 1, and Figure 2. The chemical composition and physical properties of slag are shown in Table 2. Compared with the original slag, the size range of UFSS was reduced and the morphology was smooth.

2.1.2. Cement. Cement was from Jidong Cement Co., Ltd, the state of Hebei province (China), Portland cement 42.5, and the specific surface area is 316 m^2/kg. The physical and mechanical properties of cements are shown in Table 2.

2.1.3. Other Materials. The fine aggregates and coarse aggregates used were natural river sand and broken stones. Maximum particle size of fine aggregates and coarse aggregates was 2.36 mm and 20 mm, respectively. Fineness modulus of fine aggregates was 2.7. Table 3 shows the properties of coarse and fine aggregates of concrete. The indicator test methods were carried out according to the Chinese national standards GB14684-2011 and GB14685-2011.

Table 1: The main integral distribution of slag powder at different wet grinding times.

Sample	d (0.1) (μm)	d (0.5) (μm)	d (0.9) (μm)
0 min	4.32	18.18	70.47
20 min	1.82	5.01	11.41
40 min	1.734	4.73	10.59
60 min	1.21	2.32	4.62

2.2. Experimental Details

2.2.1. Experimental Design. The durations of grinding were 20 min (UFSS20), 40 min (UFSS40), and 60 min (UFSS60) which were used to replace Portland cement with different percentages, namely, 20, 35, and 50, and were designed to compare portland cement with original slag concrete (from B1 to E3, Table 4). Consulting the literature [13–16], 10–60% of slag replace cement in concrete displays good performance, and the fineness of slag can also make a difference. In this study, the specimens of compressive strength and workability were concrete, and that of microstructure tests were corresponding paste. The designations of mixtures are shown in Table 4; the concrete mix proportion is cement : water : sand : stone = 1 : 0.5 : 1.57 : 2.36. The mixture codes in Table 4 are the percentage figures, which indicated the weight percentage between different raw materials.

2.2.2. Wet Ball Milling Details. The ball crusher is YXQM-2L, the grinding speed is 400 r/min, the ratio of water to solid is 0.5, the ratio of ball to materials is 4, and the milling media are Φ8 mm agate ball and Φ3 mm zirconia ball.

2.2.3. Specimen Preparation. GGBFS and water were mixed and ground. Firstly, different UFSS were obtained through controlled grinding duration based on the milling curve. Then, the UFSS was mixed with the remaining water during the preparation of the specimen, and the other conventional steps were carried out according to the Chinese national standard GB/T 50081-2002.

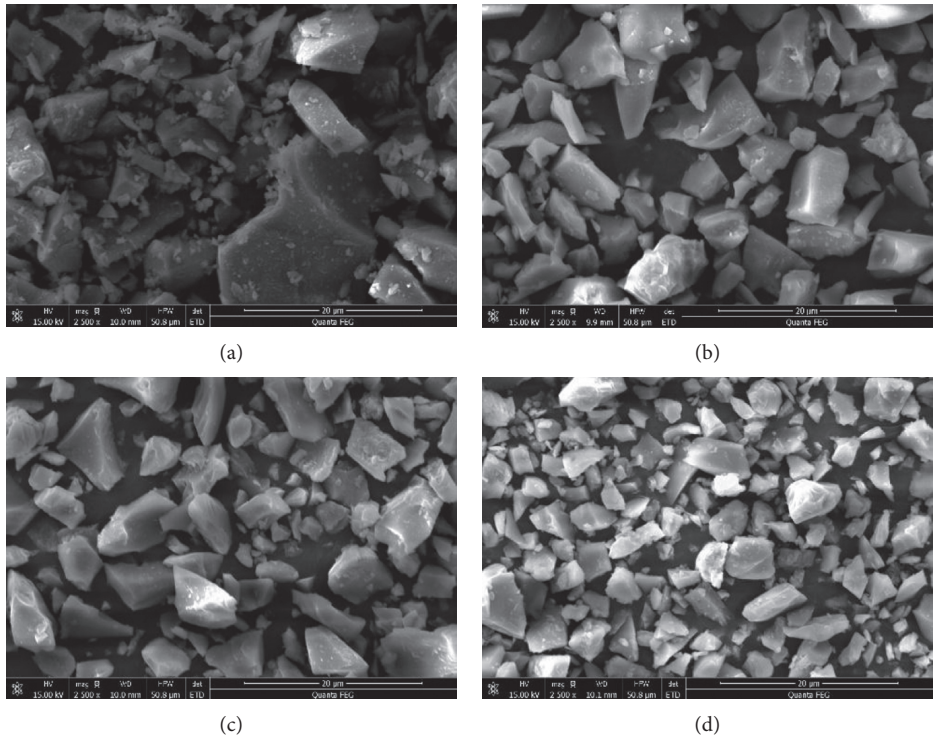

(a) (b) (c) (d)

Figure 2: SEM images of slag powder at different wet grinding times: (a) raw slag and wet grinding for (b) 20 min, (c) 40 min, and (d) 60 min.

Table 2: Chemical composition of GGBFS and cement.

	Oxide composition of GGBFS (wt.%)	Oxide composition of cement (wt.%)
SiO_2	33.50	23.03
Al_2O_3	12.52	5.11
Fe_2O_3	1.10	3.34
CaO	37.90	63.33
MgO	9.29	2.06
SO_3	2.51	2.33

Table 3: The properties index of coarse and fine aggregates of concrete.

	Grading	Mud content (%)	Apparent density (kg/m^3)	Bulk density (kg/m^3)
Coarse	Continuous	0.4	2773	1458
Sand	II level	1.6	2659	1463

2.3. Testing Methods

2.3.1. Flowability. The flowability tests of the fresh mixed concrete were performed in conformity with the Chinese national standard GB/T 2419-2005.

2.3.2. Compressive Strength. The compressive strength tests were performed in conformity with the Chinese national standard GB/T 17671-2005, and the ages were 3 days, 7 days, 28 days, and 90 days.

2.3.3. Scanning Electron Microscopy (SEM). The microstructure of specimens of 28 days was tested by scanning electron microscopy (FEI Quanta 450FEG), with the magnification of ×2000 and ×10000.

2.3.4. X-Ray Diffraction (XRD). The model of laboratory X-ray diffraction used was D/MAX-RB (RIGAKU Corporation, Japan). The test angle range was 5–70°, and the test error was controlled within 0.02° ($\Delta 2\theta \leq \pm 0.02°$). The age of specimens was 28 days.

2.3.5. Mercury Intrusion Porosimetry (MIP). The microporous structure of specimens at 28 days was tested by mercury intrusion porosimetry complying ISO 15901-1:2005. The porosity, median pore diameter of area, and the average pore diameter of hydration production were analyzed using Demo windows 9400 series software.

3. Results and Discussion

3.1. Workability. The workability is the ease of working with a freshly mixed concrete in the stages of handing, placing, compacting, and finishing. Slump is always regarded as an indicator of the workability of concrete [14]. To explore the feasibility of UFSS replace cement in concrete, the slump was tested and is depicted in Figure 3.

The content and grinding duration of UFSS reduced slump. Mixing E3 with 50% UFSS60 showed a slump value of 169 mm as compared to 180 mm and 174 mm showed by mixtures E1 and E2 which had 20% and 35% UFSS60.

Table 4: Designations of mixtures in this research.

Number		GGBFS		Cement (wt.%)	Sand (wt.%)	Coarse (wt.%)	Water (wt.%)
		Content (wt.%)	Milling duration (min)				
A	A1	0	—	100	157	236	50
B	B1	20	0	80	157	236	50
	B2	35	0	65	157	236	50
	B3	50	0	50	157	236	50
C	C1	20	20	80	157	236	50
	C2	35	20	65	157	236	50
	C3	50	20	50	157	236	50
D	D1	20	40	80	157	236	50
	D2	35	40	65	157	236	50
	D3	50	40	50	157	236	50
E	E1	20	60	80	157	236	50
	E2	35	60	65	157	236	50
	E3	50	60	50	157	236	50

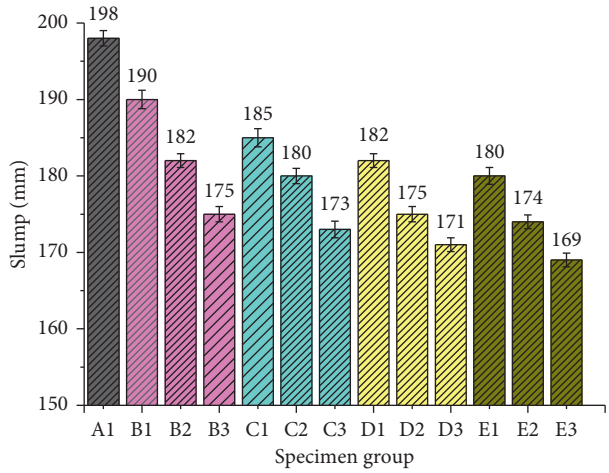

Figure 3: Slump of mixture with different contents and milling durations.

Similarly discipline was observed in series A, B, C, and D. The increase of content of slag decreased the fluidity, which confirmed the trend obtained by Deb et al. [14]. Under the condition of same dosage of slag, take 35% as an example, the slump of C2, D2, and E2 were reduced by 5.3%, 7.9%, and 8.4%, respectively, compared to B2. Similarly discipline was observed in 20% and 50% series.

The slump was decreased slightly with the increase of content and milling duration extended for slag. The results of this part were similar to the results of literatures [17, 18]. The reasons for that were that the increases of surface of slag powder led to increased water demand. What is more, the slag was contacted with the aqueous medium directly, and the vitreous network of slag particles is more easily to be dissolved in the process of wet ball milling. The surface of the slag particles becomes rough, leading to poor workability. This may be a further reason for the above results.

3.2. Compressive Strength. The results of compressive strength tests of specimens at different ages are depicted in Figure 4. UFSS could accelerate the development of compressive strength at the early age of concrete. For E3 with 50% of UFSS60, the 3-day strength reached 60.1% of that of 28 days, while the values of B3, C3 and, D3 were found to be 48.1%, 56%, and 58.7%, respectively. For 50%, the ratios of 7 and 28 days strength of original slag, UFSS20, UFSS40, and UFSS60 were found to be 63.7%, 65.7%, 69.3%, and 74.2%, respectively.

The above results confirmed the trend obtained in dry ground slag by Yan Shi and Arash Aghaeipour [19, 20]. The reasons for the above results may be the disparity of activity and particle size of slag. The average diameter (d (0.5)) of UFSS20, UFSS40, and UFSS60 was 5.01 μm, 4.73 μm, and 2.32 μm, respectively, while that of original slag was 18.18 μm. The compactness of concrete was improved, and the large pores were reduced effectively (specification in Section 3.3 specifically). Sharmila and Dhinakaran [21] studied the compressive strength of commercially available ultrafine slag applied to the concrete. They found that the performance of concrete was improved. The study [22] showed that the activity of slag was lower than that of cement and failed to exhibit considerable reaction in the early age.

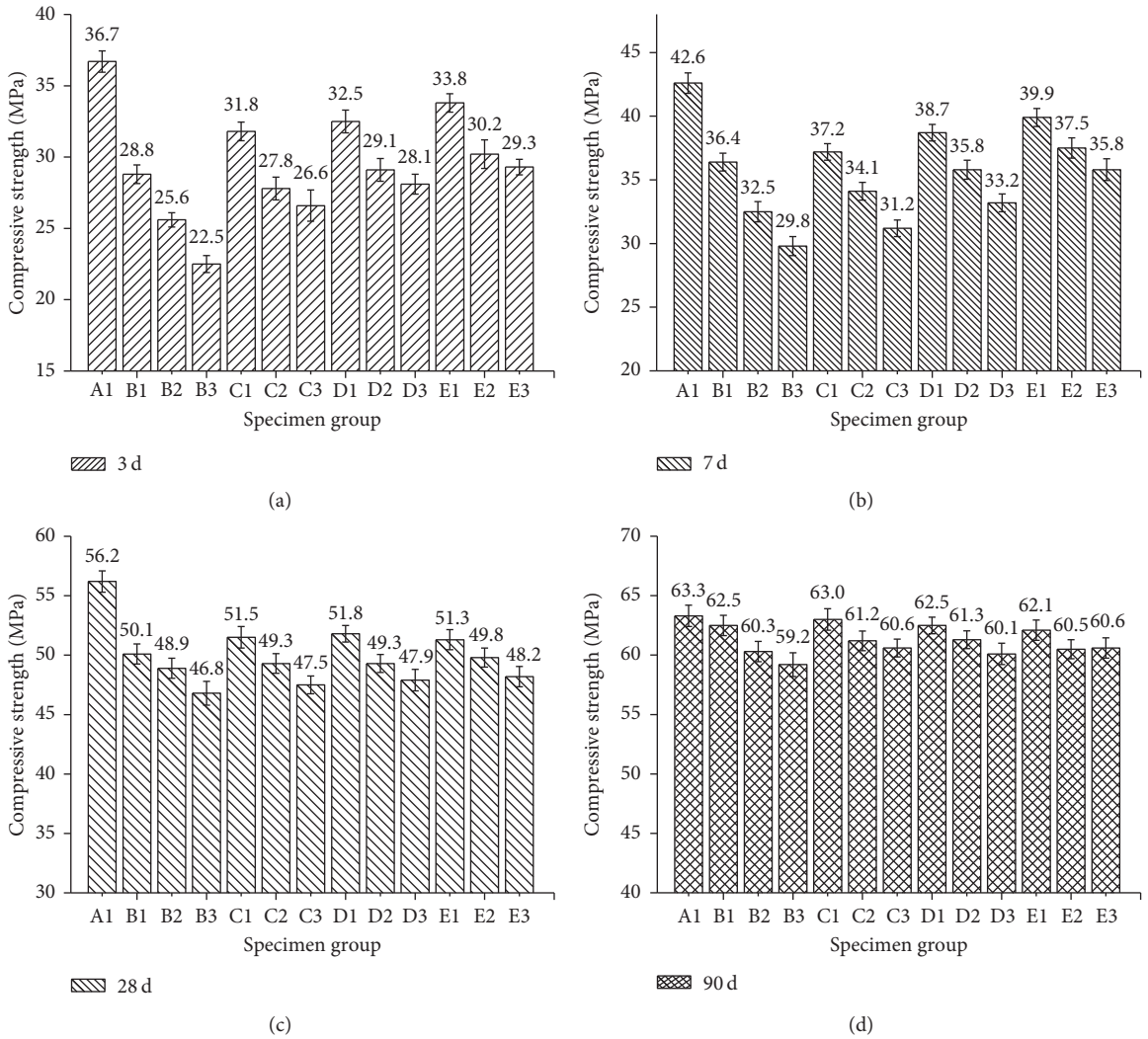

Figure 4: Compressive strength of specimens at different ages.

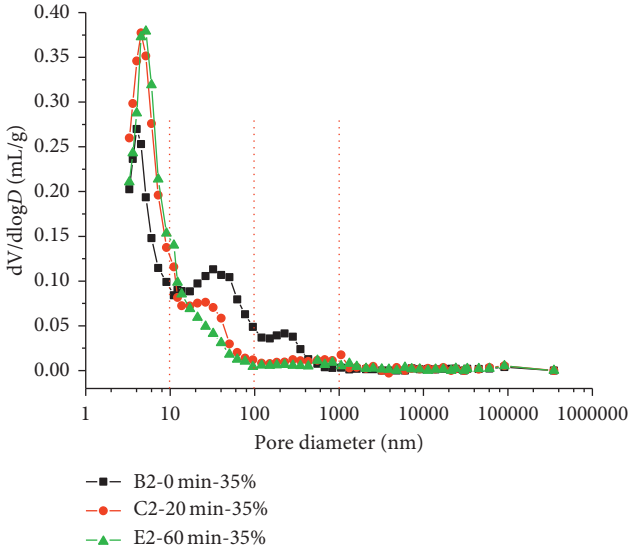

Figure 5: Pore size distribution curves of specimens with 35% of UFSS at 28 days.

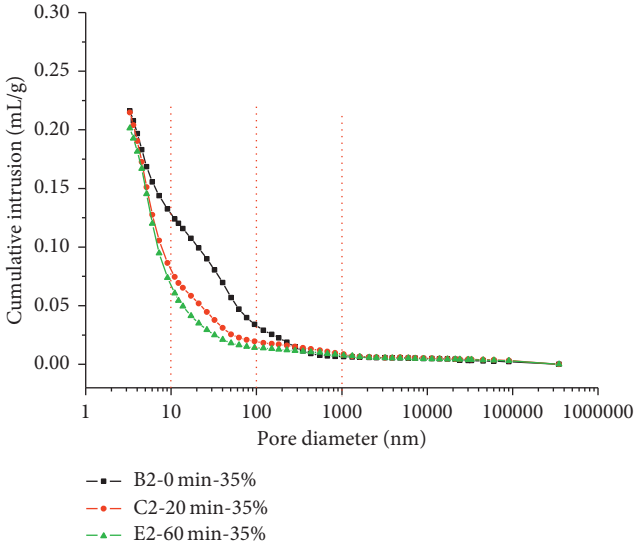

Figure 6: Cumulative pore volumes of specimens with 35% of slag cured for 28 days.

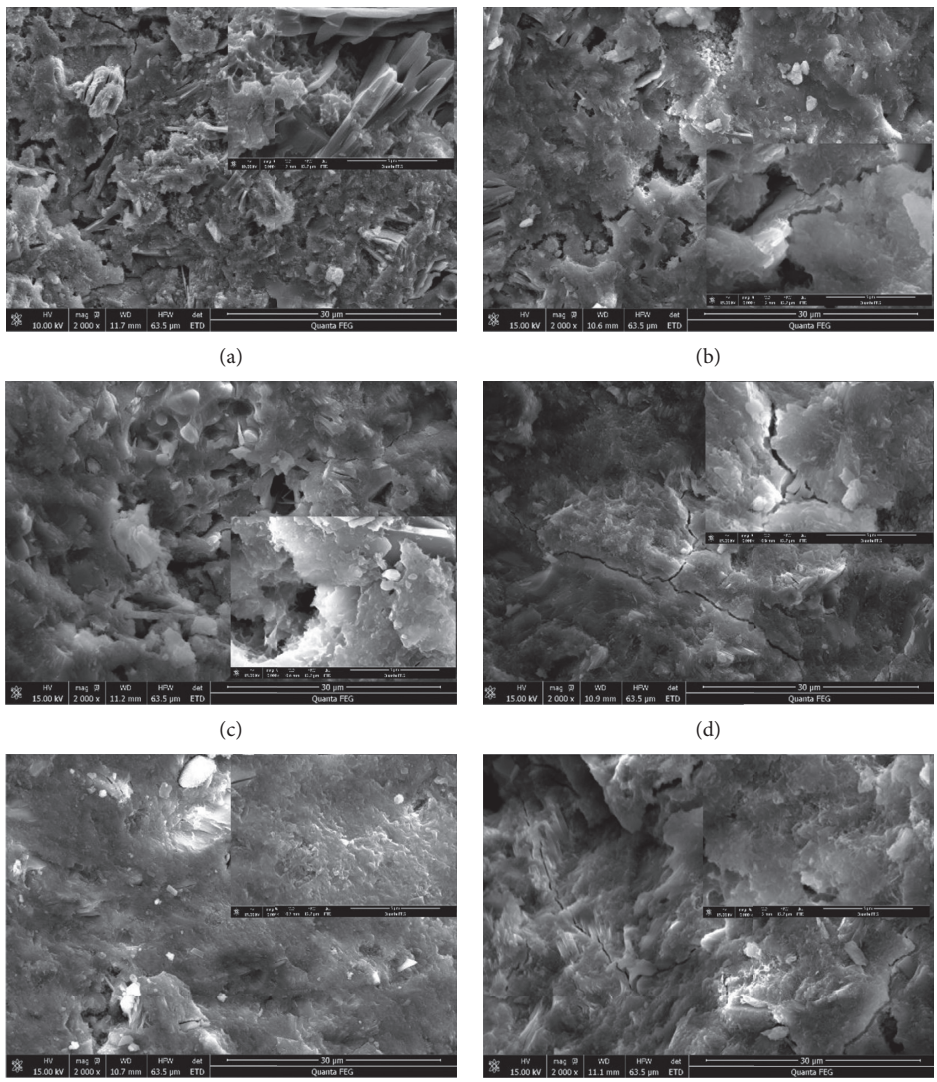

Figure 7: SEM images of specimens cured for 28 days: (a) B2-0 min-35%, (b) C2-20 min-35%, (c) D1-40 min-20%, (d) D2-40 min-35%, (e) D3-40 min–50%, and (f) E2-60 min-35%.

The activity of slag disposed by the milling process was improved, which was beneficial for the improvement of compressive strength especially in early ages.

The results of compressive strength at ages 28 days and 90 days showed that the compressive strength of specimens decreased with the increase of slag content and increased with the duration of grinding extend. The gaps of compressive strength of specimens become smaller with the extension of age. Sharmila and Dhinakaran [23] found that the compressive strength of concrete was reduced when the content of ultrafine slag exceeded 15%. The aggregation of fine particles leads to a higher porosity. However, this phenomenon was not observed with slag of 50% in this study. The wet ball mill was carried out in aqueous media, the surface of the particles formed hydrated films under the effect of aqueous media, and the surface energy of particles was relatively lower to the dry ball mill. What is more, the UFSS was mixed with water first and then mixed together with other raw materials; the particles get a good dispersion in the concrete.

3.3. Pore Structure. The results of pore size distribution (PSD) of B2, C2, and E2 at 28 days are shown in Figure 5. UFSS refined the pores and created a distribution peak for the pore range within 100 nm, and the trend was clearly observed in the specimens with UFSS60. Three characteristic ranges of pore sizes were divided: <10 nm (Part I), 10 nm–100 nm (Part II), and >100 nm (Part III), with various peaks in each range, which represent small pores, middle capillary pores, and larger capillary pores [24].

For specimens incorporating 35% of UFSS, the pattern of PSD curves was significantly different for different grinding durations. B2 samples (original slag, 35%) present triplet

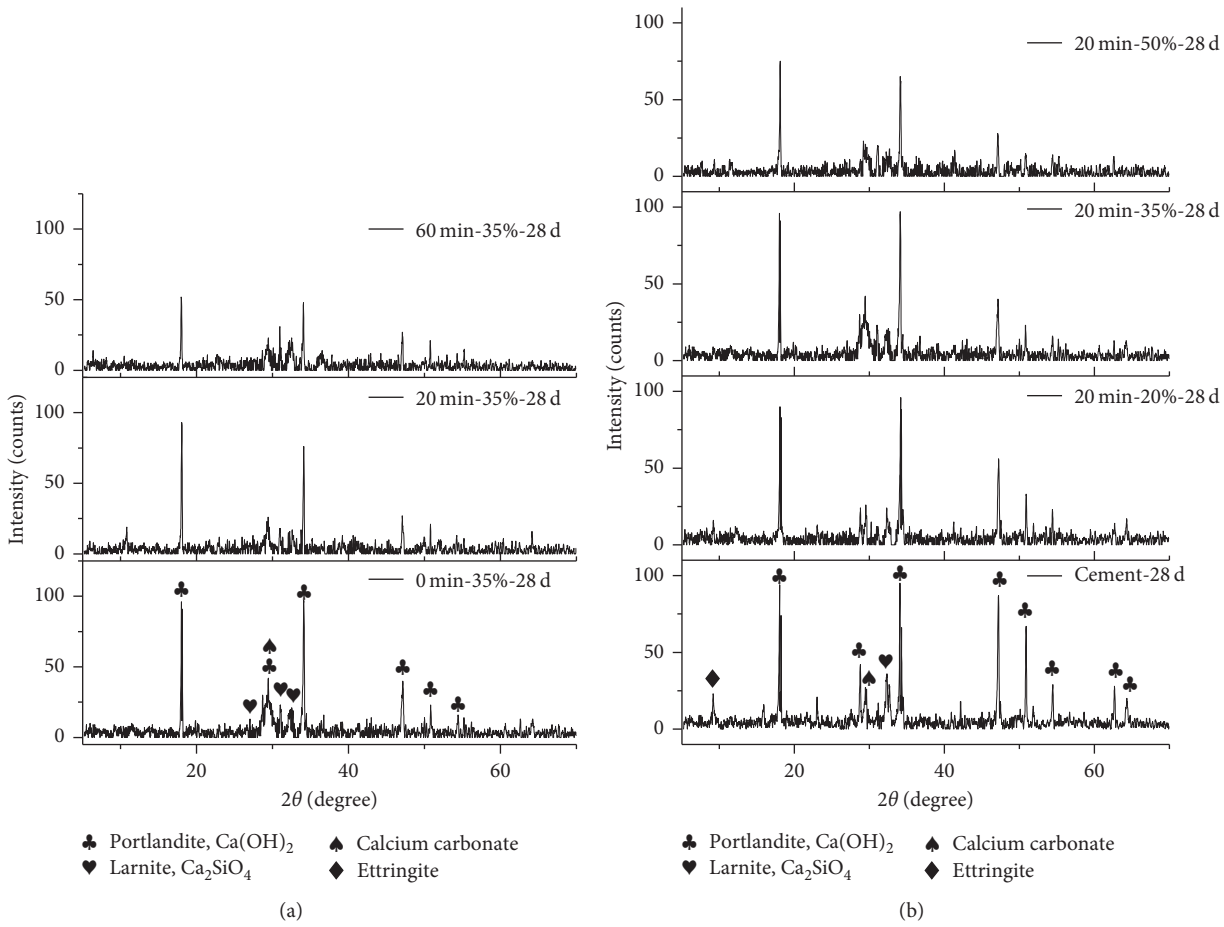

Figure 8: XRD of the specimens cured for 28 days.

peak characteristics in Part I, Part II, and III. The pores consisted of small pores, middle capillary pores, and larger capillary pores. C2 samples (UFSS20, 35%) present dual peak characteristics in Part I and Part II. The pores were refined and mainly consisted of small pores and middle capillary pores. E2 samples (UFSS20, 35%) present single peak characteristics in Part I, which mainly consists of small pores.

For the range of Part I, the formation of small pores was mainly the hydration of cementitious materials [24, 25]. The hydration extent of B2 was limited compared to the other two groups. The values of C2 and E2 were close, indicating that the extents of hydration reaction were similar with an age of 28 days. For the range of Part II, the pores >10 nm were formed by the filling effect of particles in concrete [26]. The peak of the PSD curve of B2 was obvious; the compactness of hardened body was poor relatively. The peak of the PSD curve of C2 exits and is weaker than B2, indicating that UFSS20 could improve the compactness of concrete compared to original slag. E2 showed a smooth curve in this part, indicating that the compactness of concrete could be improved obviously. For the range of Part III, only the curves of B2 exit a peak. UFSS obtained from wet milling could improve the compactness of concrete effectively.

Figure 6 shows the cumulative pore volumes of the specimens corresponding to Figure 5. As the particle size of slag reduces, the pore volume decreased. The porosities of B2, C2, and E2 were 24.7986%, 24.0260%, and 23.7765%, respectively. The porosities decreased with the reduction of sizes of particles. The slag slurry reduced the distribution of larger pores and optimized the porosity distribution. The compactness and compressive strength of concrete were optimized.

3.4. Microstructure Tests. Figure 7 shows the SEM images of specimens incorporating UFSS at 28 days. The larger capillary pores were easily observed in B2. From the images of D1, D2, and D3, the compactness of specimens was improved with the increasing of slag content. Ultrafine slag particles played an important role in the compactness performance of harden body. The compactness of pates was improved with the grind duration extending, which was consistent with the results of MIP tests. This further explained the increase of compressive strength of concrete with ultrafine slag.

The cement particles were wrapped by slag particles, causing delay of the reaction process for cement particles, and the hydrated products of cement particles were not easily observed. However, the activity of slag particles was lower than that of cement particles even through the milling process. This was why the compressive strength decreased with the increased content of slag, even if the porosity was improved.

3.5. X-Ray Diffraction Analysis. XRD analysis was carried out to examine the influences of the content and fineness of slag on hydration and phase. XRD images are shown in Figure 8. From XRD analysis, mineral phases of portlandite, calcium carbonate, larnite, and ettringite were found.

In the cement paste blended with slag, three structure reactions were involved: cement hydration, the pozzolanic reaction of slag, and hydration reaction of slag [27, 28]. However, slag exhibits a pozzolanic reaction in the presence of calcium hydroxide ($Ca(OH)_2$) formed upon cement hydration [20]. The extent of slag involved in the reaction could be reflected by the amount of calcium hydroxide under same content conditions. It could be seen from the XRD images (Figure 8(a)) that the content of calcium hydroxide decreased with the decrease of particle size. The results illustrated that the activity slag treated through wet milling was increased, which accounted for the increase of compressive strength. With different slag dosages, the test results of various contents of slag (Figure 8(b)) complied with the above regularity: the amount of calcium hydroxide reduced with the increase in content.

4. Conclusion

This study investigated the influences of ultrafine slag slurry (UFSS) prepared by the wet ball mill on the properties of cement and concrete. The results obtained were summarized as follows:

(i) Wet ball mill could improve the size distribution of slag particles effectively. The slag decreased the slump of concrete slightly.

(ii) Use of UFSS as a substitute to cement improved the compressive strength of concrete especially at early ages.

(iii) UFSS optimized the pore size distribution of the plaster. The amount of large pores (10–100 nm) were decreased notably and created distribution in the range of small pores (<10 nm).

Conflicts of Interest

The authors declare that there are no conflicts of interest regarding the publication of this article.

Acknowledgments

The authors gratefully acknowledge the support of the National Key Research and Development Plan (no. 2017YFB0310003) and the Science and Technology Support Program of Hubei Province (no. 2017ACA178) for funding this project.

References

[1] G. Tesema and E. Worrell, "Energy efficiency improvement potentials for the cement industry in Ethiopia," *Energy*, vol. 93, no. 2, pp. 2042–2052, 2015.

[2] J. Li, P. Tharakan, D. Macdonald, and X. Liang, "Technological, economic and financial prospects of carbon dioxide capture in the cement industry," *Energy Policy*, vol. 61, no. 10, pp. 1377–1387, 2013.

[3] C. L. H Wang and C. Y. Lin, "Strength development of blended blast furnace slag cement mortars," *Journal of the Chinese Institute of Engineers*, vol. 9, no. 3, pp. 233–239, 1986.

[4] M. C. G. Juenger and R. Siddique, "Recent advances in understanding the role of supplementary cementitious materials in concrete," *Cement and Concrete Research*, vol. 78, pp. 71–80, 2015.

[5] A. A. Ramezanianpour, "Effect of curing on the compressive strength, resistance to chloride-ion penetration and porosity of concretes incorporating slag, fly ash or silica fume," *Cement and Concrete Composites*, vol. 17, no. 2, pp. 125–133, 1995.

[6] M. Mahoutian, Y. Shao, A. Mucci, and B. Fournier, "Carbonation and hydration behavior of EAF and BOF steel slag binders," *Materials and Structures*, vol. 48, no. 9, pp. 3075–3085, 2015.

[7] M. Iqbal Khan, G. Fares, and S. Mourad, "Optimized fresh and hardened properties of strain hardening cementitious composites: effect of mineral admixtures, cementitious composition, size, and type of aggregates," *Journal of Materials in Civil Engineering*, vol. 29, no. 10, p. 04017178, 2017.

[8] F. Puertas and A. Fernández-Jiménez, "Mineralogical and microstructural characterization of alkali-activated fly ash/slag pastes," *Cement and Concrete Composites*, vol. 25, no. 3, pp. 287–292, 2003.

[9] S. Kumar, R. Kumar, A. Bandopadhyay et al., "Mechanical activation of granulated blast furnace slag and its effect on the properties and structure of portland slag cement," *Cement and Concrete Composites*, vol. 30, no. 8, pp. 679–685, 2008.

[10] S. C. Pal, A. Mukherjee, and S. R. Pathak, "Investigation of hydraulic activity of ground granulated blast furnace slag in concrete," *Cement and Concrete Research*, vol. 33, no. 9, pp. 1481–1486, 2003.

[11] J. Zhao, D. Wangb, and P. Yana, "Particle characteristics and hydration activity of ground granulated blast furnace slag powder containing industrial crude glycerol-based grinding aids," *Construction and Building Materials*, vol. 104, pp. 134–141, 2016.

[12] H. Goudarzi and S. Baghshahi, "PZT ceramics prepared through a combined method of B-site precursor and wet mechanically activated calcinate in a planetary ball mill," *Ceramics International*, vol. 43, no. 4, pp. 3873–3878, 2017.

[13] A. Nazari, M. H. Rafieipour, and S. Riahi, "The effects of CuO nanoparticles on properties of self compacting concrete with GGBFS as binder," *Materials Research*, vol. 14, no. 3, pp. 307–316, 2011.

[14] P. S. Deb, P. Nath, and P. K. Sarker, "The effects of ground granulated blast-furnace slag blending with fly ash and activator content on the workability and strength properties of geopolymer concrete cured at ambient temperature," *Materials and Design*, vol. 62, pp. 32–39, 2014.

[15] J. Qiu, H. S. Tan, and E.-H. Yang, "Coupled effects of crack width, slag content, and conditioning alkalinity on autogenous healing of engineered cementitious composites," *Cement and Concrete Composites*, vol. 73, pp. 203–212, 2016.

[16] A. Allahverdi and M. Mahinroosta, "Mechanical activation of chemically activated high phosphorous slag content cement," *Powder Technology*, vol. 245, pp. 182–188, 2013.

[17] Y. Tang, X. Zuo, S. He, O. Ayinde, and G. Yin, "Influence of slag content and water-binder ratio on leaching behavior of cement pastes," *Construction and Building Materials*, vol. 129, pp. 61–69, 2016.

[18] P. Nath and P. K. Sarke, "Effect of GGBFS on setting, workability and early strength properties of fly ash geopolymer concrete cured in ambient condition," *Construction and Building Material*, vol. 66, pp. 163–171, 2016.

[19] A. Aghaeipour and M. Madhkhan, "Effect of ground granulated blast furnace slag (GGBFS) on RCCP durability," *Construction and Building Materials*, vol. 141, pp. 533–541, 2017.

[20] Y. Shi, H. Chen, J. Wang, and Q. Feng, "Preliminary investigation on the pozzolanic activity of superfine steel slag," *Construction and Building Materials*, vol. 82, pp. 227–234, 2015.

[21] P. Sharmila and G. Dhinakaran, "Compressive strength, porosity and sorptivity of ultra fine slag based high strength concrete," *Construction and Building Materials*, vol. 120, pp. 48–53, 2016.

[22] A. Karimpour, "Effect of time span between mixing and compacting on roller compacted concrete (RCC) containing ground granulated blast furnace slag (GGBFS)," *Construction and Building Materials*, vol. 24, no. 11, pp. 2079–2083, 2010.

[23] P. Sharmila and G. Dhinakaran, "Strength and durability of ultra fine slag based high strength concrete," *Structural Engineering and Mechanics*, vol. 55, no. 3, pp. 675–686, 2015.

[24] K. Li, Q. Zeng, M. Luo, and X. Pang, "Effect of self-desiccation on the pore structure of paste and mortar incorporating 70% GGBS," *Construction and Building Materials*, vol. 51, pp. 329–337, 2014.

[25] Q. Zeng, K. Li, T. Fen-Chong, and P. Dangla, "Pore structure characterization of cement pastes blended with high-volume fly ash," *Cement and Concrete Research*, vol. 42, no. 1, pp. 194–204, 2012.

[26] Y. C. Choi, J. Kim, and S. Choi, "Mercury intrusion porosimetry characterization of micropore structures of high-strength cement pastes incorporating high volume ground granulated blast-furnace slag," *Construction and Building Materials*, vol. 137, pp. 96–103, 2017.

[27] X. Feng, E. J. Garboczi, D. P. Bentz, P. E. Stutzman, and T. O. Mason, "Estimation of the degree of hydration of blended cement pastes by a scanning electron microscope point-counting procedure," *Cement and Concrete Research*, vol. 34, no. 10, pp. 1787–1793, 2004.

[28] Y. C. Ding, T. W. Cheng, P. C. Liu, and W. H. Lee, "Study on the treatment of BOF slag to replace fine aggregate in concrete," *Construction and Building Materials*, vol. 146, pp. 644–651, 2017.

Hindawi
Advances in Materials Science and Engineering
Volume 2018, Article ID 1512830, 11 pages
https://doi.org/10.1155/2018/1512830

Research Article

Feasibility of Using Nanoparticles of SiO_2 to Improve the Performance of Recycled Aggregate Concrete

Khaleel H. Younis[1,2,3] **and Shelan M. Mustafa**[1]

[1]*Erbil Technology Institute, Erbil Polytechnic University Erbil, Kurdistan Region, Iraq*
[2]*Environmental Engineering, Knowledge University Erbil, Kurdistan Region, Iraq*
[3]*Civil Engineering, Ishik University, Erbil, Kurdistan Region, Iraq*

Correspondence should be addressed to Khaleel H. Younis; khaleelyounis@epu.edu.krd

Received 14 February 2018; Accepted 9 May 2018; Published 24 May 2018

Academic Editor: Sverak Tomas

The aim of this paper was to examine the feasibility of using nanoparticles of SiO_2 (nanosilica) to improve the performance of recycled aggregate concrete (RAC) containing recycled aggregate (RA) derived from processing construction and demolition waste of concrete buildings. The examined properties include compressive strength, splitting tensile strength, and water absorption. The study also includes examining the microstructure of RA and RAC with and without nanoparticles of SiO_2. In total, nine mixes were investigated. Two mixes with RA contents of 50% and 100% were investigated and for each RA content; three mixes were prepared with three different nanoparticles dosages 0.4%, 0.8%, and 1.2% (by mass of cement). A control mix with natural aggregate (NA) was also prepared for comparison reasons. The results show that nanoparticles of silica can improve the compressive strength, tensile strength, reduce the water absorption, and modify the microstructure of RAC.

1. Introduction

The world is currently facing a global sustainability and environmental issue due to the increasing generation of massive quantities of waste by construction and demolition activities. The construction and demolition activities are necessary due to the expansion of urbanization which increases the demand for constructing more infrastructures such as housing, roads, bridges, and tunnels. Also, natural disasters such as earthquakes and wars lead to the destruction and devastation of many buildings, bridges, and roads, generating huge amounts of construction material rubbles. For example, vast quantities of building rubbles have been generated in Iraq over the last decades as a result of conflicts and terrorist attacks. At the global level, more than 500 million tons of construction and demolition waste (CDW) and building rubbles are generated worldwide annually [1]. Such a huge quantity of CDW requires substantial areas of land to dispose of, causing serious environmental issues. Also, depletion of natural resources of natural aggregates used in the production of concrete contributes to other environmental and sustainability concerns. These environmental issues and concerns have led the researchers worldwide to examine methods to mitigate the impact of these issues on the environment. One way is recycling the CDW and reusing them as aggregate and as an alternative to the natural aggregate in concrete. The utilization of recycled aggregate (RA) derived from processing CDW in concrete can save the environment through conserving the scarce landfill areas and reduce the consumption rate of the natural resources of aggregates [1, 2].

The use of the RA generated from processing CDW of concrete elements in new concrete has been investigated for decades. Nonetheless, the properties of the recycled aggregate concrete (RAC), as reported by the researchers, are inferior to that of the natural aggregate concrete (NAC). RAC exhibits low compressive, tensile, and flexural strength as well as high water absorption, porosity, and shrinkage [1, 3–5]. For these reasons, most codes of practice allow the natural aggregate in concrete to be only partially (20–30%) replaced by RA, especially in structural applications [6]. Many researchers have attributed this performance of RAC

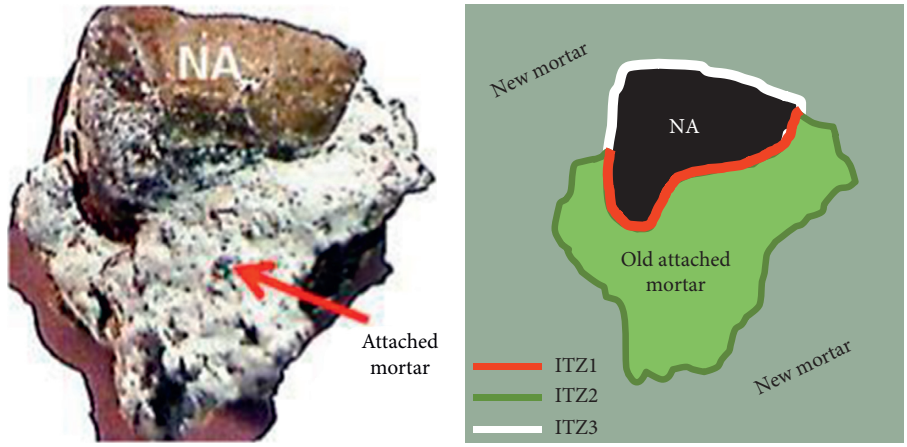

(a) (b)

Figure 1: (a) Recycled aggregate (RA) particle. (b) Schematic of the RA particle in RAC showing all ITZs.

to the heterogeneous nature of the RA caused by the attached mortar exist on its surface [7, 8]. The attached mortar is characterized by high porosity, microcracks, and flaws which make the RA particle weak and its microstructure loose. Weak interfacial transition zone (ITZ) between the recycled concrete aggregate (RCA) and the cement matrix has also been identified [1, 9, 10]. Moreover, the presence of more than one ITZ in the RAC is another reason for the low quality of the RAC [1, 9, 11]. In RAC, there are three ITZs : ITZ1 which is between the old attached mortar and the natural aggregate, ITZ2 which is between the natural aggregate and the new cement mortar, and ITZ3 is between the old and new cement mortars [1] (Figure 1). It is reported by Ryu [11] that the relative quality of old ITZ and new ITZs in RAC plays a key role in determining the compressive strength of the RAC.

Therefore, researchers have tried various approaches to improve the properties of RA and RAC. Several studies focused on developing approaches to enhance the properties of the RA particles, whereas many other studies tried to improve the RAC properties through focusing on the technology of concrete production [1, 10], for example, separating the mortar that is attached to the natural aggregate from its surface using different approaches [7, 8, 10]. Despite the fact that the properties of the RA particles were improved using these approaches, they resulted in several drawbacks such as energy consumption, compromising durability aspects, and high cost [1, 8].

Aiming at improving the performance of RAC, other researchers have examined the utilization of fine and ultrafine reactive cementitious materials such as fly ash, ground granulated blast furnace slag, and silica fume in RAC [1, 5, 10, 12–14]. It is reported that these materials help to improve the performance of RAC due to the pozzolanic reaction and the filling ability resulting in a dense microstructure and strong ITZ [1, 9, 10]. However, the use of these materials in RAC does not always lead to a performance comparable to that of NAC. Hence, the need for investigating the use of other materials is vital. Nanomaterials are promising in this regard. The mechanical properties and the microstructure of RAC can be enhanced by the use of materials with reactive nanoparticles.

Over the last decade, the use of nanomaterials has emerged in the construction materials field. Many researchers in this field have explored the use of nanomaterials in concrete aiming at producing constructional materials (such as concrete) with superior performance and novel applications. Nanomaterials are characterized by nanoscale size particles. They have particles with the diameter of less than 100 nm [15]. In previous studies, several types of materials with nanoparticles have been used to improve the mechanical properties, durability behavior, and microstructure of cement paste, mortar, and concrete, for example, nano-SiO_2 [16–18], nano-TiO_2 [15, 19], nano-Al_2O_3 [20, 21], nano-Fe_2O_3 [21], carbon nanotubes [22], nanoclay [15], and nanolimestone [18]. However, among these nanoparticles, nano-SiO_2 (nanosilica) can be considered as the most frequently used one in improving the performance of concrete [15, 17]. Owing to its very small size (in the range of nanometers) and the pozzolanic reaction, nanosilica particles are very effective in enhancing the performance of concrete [23]. Nanomaterial, particularly nano-SiO_2, has the ability to improve the strength [23, 24] and the durability of concrete [17, 25] through accelerating the hydration reaction and filling the micropores in the cement paste structure, thus decreasing the porosity of concrete which in turn results in strength enhancement. Nanosilica can not only reduce the porosity of the cement paste, but also helps to densify the ITZ between the aggregate particle and the cement paste [23]. Studies [18, 24, 25] have shown that the addition of nanosilica results in increased compressive, tensile, and flexural strength of conventional concrete.

Studies on the use of nanosilica to upgrade the performance of RAC are very limited [26]. Hosseini et al. [27, 28] found that the compressive strength of RAC increased to reach a similar strength to that of NAC, when 3% (by mass of cement) of nano-SiO_2 is added to the RAC mixture. Also, Li et al. [29] reported that the static compressive strength of modified RAC with 2% (by mass of cement) of nanosilica was higher than that of the RAC without nanosilica by 21.6%. The addition of 2% of nanosilica also improved the dynamic compressive strength of RAC [29].

Since only few studies have tackled improving the performance of RAC using nanoparticles of SiO_2, this study aims at investigating the effect of using nano-SiO_2 to improve the mechanical properties and modify the microstructure of RAC. In this study, nano-SiO_2 at different dosages was added to RAC to enhance its performance. Compressive strength and splitting tensile strength of RAC with and without nanoparticles of SiO_2 were determined to assess the effect of these nanoparticles on the mechanical performance of RAC mixtures. Furthermore, the effect of these nanoparticles on the water absorption of RAC was also measured to assess its durability. Moreover, the microstructure of RAC mixtures with and without nanoparticles of silica was also evaluated through microscopic and scanning electron microscopy (SEM) observations. The obtained results can help promote the use of RAC in different civil engineering applications and enrich the literature of the research field of methods to improve the performance RAC.

2. Materials and Experimental Program

2.1. Materials

2.1.1. Cement. Portland cement (CEM I type) was used in this study meeting the requirements of Iraqi specifications [9]. The cement is manufactured by Mas company located in Sulymania, Iraq. Table 1 presents the chemical analysis of the cement (as given by the supplier).

2.1.2. Aggregates. Two types of coarse aggregates were used, natural, and recycled. The natural gravel was rounded river aggregate with a maximum size of 20 mm, water absorption of 1%, and specific gravity of 2.6. The coarse RA was recycled concrete aggregate produced by crushing old concrete portions generated by demolishing old concrete buildings. The water absorption and the specific gravity of the RA were 3.3% and 2.45, respectively. The fine aggregate used in this study was sand with a maximum size of 5 mm.

2.1.3. Nanomaterials. The material used in this study was nanosilica supplied by HWNANO Company in China. The nano-SiO_2 was in the form of powder (Figure 2(a)) with a purity of 99% SiO_2 (Figure 2). The average particle size of the nanosilica was between 20 and 30 nm with a surface area of 125 m^2/g. The X-ray diffraction (XRD) analysis of the powder sample of the SiO_2 nanoparticles is shown in Figure 2(b), while Figure 2(c) shows an SEM image of the nanoparticles of the nano-SiO_2.

2.1.4. Superplasticizers. Superplasticizers were used to ensure a uniform dispersion of the nanoparticles as explained in Section 2.3. The superplasticizer was an aqueous solution containing polycarboxylate ether (PCE) polymers.

2.2. Variables and Mix Proportions. In total, nine different concrete mixes were prepared. The code of mixes and the variables of the study are shown in Table 2. The mixes are divided into three groups according to the type of coarse aggregate, the content of coarse recycled aggregate, and the content of nanoparticles of SiO_2. The study includes one control mix made with natural coarse aggregate NCA (R0) and two mixes made with recycled coarse aggregate RCA in which the NA is replaced by RA at contents of 50% and 100% and six mixes (three for each RA content) made with three contents (0.4%, 0.8%, and 1.2% by cement mass) of nano-SiO_2. All mixes had the same quantity of cement (400 kg/m^3), water (192 kg/m^3), and fine aggregate (719 kg/m^3), whilst the quantity of coarse aggregate used was 1125 kg/m3. All mixes were made with the same water/cement (w/c) ratio (0.48). For the mixes incorporating RA, the water quantity was adjusted (100% water absorption of the RA was compensated during mixing) to account for the water absorption of the RA to ensure that all mixes have the same effective water to cement ratio.

Table 1: Chemical analysis of OPC.

SiO_2	Al_2O_3	Fe_2O_3	CaO	MgO	SO_3	Na_2O	K_2O	Na_2O_{eq}
20.98	4.95	2.85	65.9	0.79	2.8	0.24	0.43	0.52

2.3. Mixing, Preparation of Specimens, and Curing. A pan mixer with a capacity of 0.1 m^3 was used to mix the ingredients and prepare all concrete mixtures. For the mixes containing nano-SiO_2, the nanosilica powder was added to one liter of water and an amount of superplasticizer (0.5% by mass of cement) to form an aqueous solution. The solution was mixed using a high-speed blender to ensure a uniform distribution of the nanoparticles and avoiding the agglomeration of these particles due to the strong attractive forces of van der Waals.

The procedure of mixing the ingredients of the concrete is as follows: Firstly, the coarse aggregate was added and mixed with the aqueous solution of nano-SiO_2 and part of the mixing water for 1 minute. Then, the ingredients were left in the mixer pan for 10 minutes to allow the recycled coarse aggregate to absorb the nanoparticles and form a coating layer on their surfaces. Secondly, the fine aggregate, cement, and the rest of the mixing water were added and mixed for 3 minutes.

After the completion of mixing the ingredients, for each mix, six (100 mm) cubes and three (100 × 200 mm) cylinders were cast. The concrete was mixed using a pan mixer and compacted using a vibrating table. After casting, the specimens were then covered by plastic sheets and allowed to cure for 24 hours before being demoulded. Then, the specimens were kept in water tanks for 27 days for further curing.

2.4. Tests

2.4.1. Compressive Strength Test. The compressive strength was obtained at the age of 28 days using the 100 mm cubes and BS EN 12390-3 [30].

2.4.2. Splitting Tensile Strength Test. The splitting tensile strength was obtained at the age of 28 days using the 100 × 200 mm cylinders and BS EN 12390-6 [31].

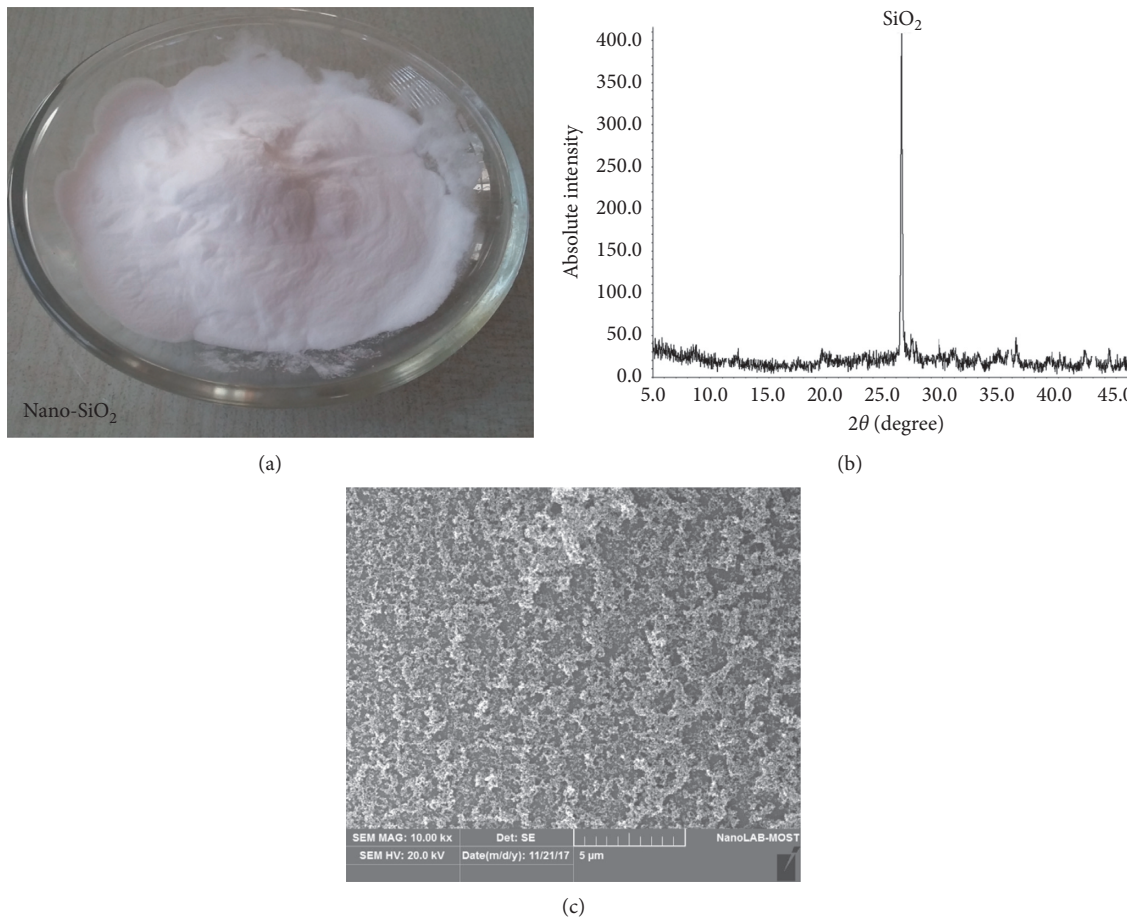

Figure 2: (a) Nano-SiO_2 in powder form; (b) XRD analysis of SiO_2 nanoparticles used in the study; (c) SEM image of the nano-SiO_2.

Table 2: Code of mixes and variables of study.

Mix number	Mix code	Type of coarse aggregate	Nano-SiO_2 content (%)[a]	Coarse recycled aggregate content (%)
1	R0	Natural	0	0
2	R50	Natural + recycled	0	50
3	R100	Recycled	0	100
4	R50N0.4	Natural + recycled	0.4	50
5	R50N0.8	Natural + recycled	0.8	50
6	R50N1.2	Natural + recycled	1.2	50
7	R100N0.4	Recycled	0.4	100
8	R100N0.8	Recycled	0.8	100
9	R100N1.2	Recycled	1.2	100

[a]By cement mass.

2.4.3. Water Absorption (WA) Test. The water absorption of all concrete mixtures in this study was determined by following the procedure described in the standard test of ASTM C642-13 [32]. For each mix, three specimens (cubes) of concrete with dimensions of (100 ∗ 100 ∗ 100 mm) were used in the WA test. The specimens were tested at the age of 28 days. After 28 days of water curing, the specimens were dried in an oven with a temperature of 100–110°C for 24 hours. The dried specimens were then weighed, and the dry mass of the specimens were recorded when a constant dry mass was reached. The constant dry mass means when the difference of two successive dry mass readings is equal or less than 0.5% of the lowest mass reading (value). After that, the specimens were fully immersed in water for 24 hours. The specimens, then, were taken out, and the surface moisture was removed using a dry and absorbent cloth. Finally, the mass of the specimens (after immersing in water) were recorded. The WA (%) was calculated as the difference between the saturated mass and the dry mass with respect of the dry mass of the specimen.

2.4.4. Microstructure Observations. Individual particles of recycled coarse aggregate were investigated using a digital microscope. Scanning electron microscopy (SEM) was also

Table 3: Results of compressive strength test.

Mix	Compressive strength			
	Strength (MPa)	Normalized strength to control mix R0	Normalized strength to mix R50	Normalized strength to mix R100
R0	40.6	1.00	—	—
R50	34.1	0.84	1.00	—
R100	30.2	0.74	—	1.00
R50N0.4	37.5	0.92	1.10	—
R50N0.8	40.3	0.99	1.18	—
R50N1.2	41.0	1.00	1.20	—
R100N0.4	32.0	0.79	—	1.06
R100N0.8	34.2	0.84	—	1.13
R100N1.2	35.1	0.86	—	1.16

used to assess the microstructure of the RA particles and concrete samples with and without nanoparticles of SiO_2.

3. Results and Discussion

3.1. Compressive Strength. The results of the compressive strength at the age of 28 days for all mixes are presented in Table 3. The result of each mix is the average of three specimens. The table also shows the normalized strength (with respect to the control mix R0, mix made with 50% RA, mix R50 and mix made with 100% RA, mix R100). It is worth to mention that the addition of nanoparticles of SiO_2 reduced the workability of concrete mixes. However, the workability of all mixes represented by slump test values was equal to or higher than the target value of the mix design which is 50 mm. The values of the slump test ranged between 100 mm for Mix R0 to 50 mm for mix R100N1.2.

As expected, the compressive strength of the RAC mixes without nanosilica (R50 and R100) is lower than that of the control mix (R0), as can be seen in Table 3 and Figure 3. The compressive strength of RAC decreases by 16% and 26% when the natural coarse aggregate is replaced by 50% and 100%, respectively. Similar behavior was reported in [1, 33]. This is mainly due to the heterogeneous nature of the recycled aggregate which is characterized by a weak and cracked surface resulted from the adhered mortar and the crushing process of demolished concrete [9, 10]. In addition, the inferior properties of RA such as low strength and high porosity and water absorption in comparison to natural aggregate (NA) could be another reason for the decline in compressive strength of concrete when NA is replaced by RA [1, 9].

Figure 4 represents the compressive strength of RAC mixes made with 50% and 100% of RA at different nano-SiO_2 contents. The compressive strength of the control mix (R0) is also shown in Figure 4. The figure shows that the addition of nano-SiO_2 enhances the compressive strength of the mixes containing recycled aggregate. It is clear that the content of nanoparticles affects the degree of strength enhancement. It can be seen that the compressive strength increases with the increase of content of nanosilica regardless of the recycled aggregate content. For example, when the nanosilica is added at contents of 0.4%, 0.8%, and 1.2%, the compressive strength increases by 10%, 18%, and

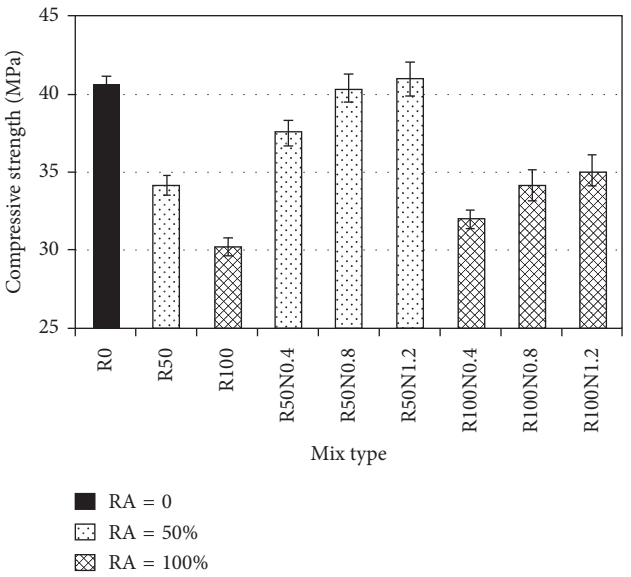

Figure 3: Compressive strength of all mixes.

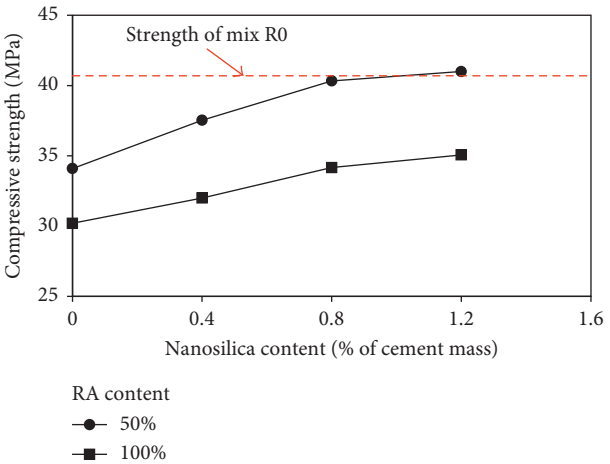

Figure 4: Effect of nanosilica particle content on the compressive strength of RAC mixes.

22% for mixes containing 50% RA and by 6%, 13%, and 16% for mixes made with 100% RA. The results also show that the increase in strength for mixes containing 50% RA is higher

Table 4: Results of splitting tensile strength test.

Mix	Splitting tensile strength			
	Strength (MPa)	Normalized strength to control mix R0	Normalized strength to mix R50	Normalized strength to mix R100
R0	3.65	1.00	—	—
R50	3.40	0.93	1.00	—
R100	3.31	0.91	—	1.00
R50N0.4	3.56	0.98	1.05	—
R50N0.8	3.74	1.03	1.10	—
R50N1.2	3.72	1.02	1.09	—
R100N0.4	3.37	0.92	—	1.02
R100N0.8	3.46	0.95	—	1.05
R100N1.2	3.58	0.98	—	1.08

than those with 100% RA in all nanosilica contents. It seems that the addition of nanosilica in contents up to 0.8% (by mass of cement) to the RAC mixes is very beneficial and can result in comparable strength to that of the control mix R0 (mix with natural coarse aggregate), in particular at RA content of 50% [34]. Similar compressive strength enhancements were observed by [26, 28, 29] but at different dosages of nanoparticles of SiO_2. The strength enhancement could be attributed to the reduced porosity and modified microstructure of the RA particles and RAC due to the addition of the nanoparticles of SiO_2 [34]. The mechanisms leading to this strength improvement is explained in Section 3.4 where the effect of adding the nanoparticles on the microstructure of the RAC is discussed.

3.2. Splitting Tensile Strength. The results of the splitting tensile strength at the age of 28 days of all mixes are listed in Table 4 and shown in Figure 5. The result of each mix is the average of three cylindrical specimens. The table also shows the normalized strength (with respect to the strength of the control mix R0). The percentage of strength enhancement due to adding nanoparticles of SiO_2 (compared to mixes R50 and R100) is also presented.

Similar to the results of the compressive strength, the splitting tensile strength of RAC mixes is lower than that of the control mix. In comparison with the tensile strength of the control mix, the splitting tensile strength of RAC mixes declined by 7% and 9% at RA contents of 50% and 100%, respectively, as can be seen in Table 4 and Figure 5. Previous studies [35–37] also reported reduction in the splitting tensile strength of concrete when the natural coarse aggregate was replaced by RA. Positive effect on the splitting tensile strength of the RAC mixes can be observed when nanoparticles are added to these mixes (Figure 5). The tensile strength of RAC mixes made with 50% of RA improved by up to 10% as a result of the addition of nanoparticles of SiO_2. Tensile strength enhancement up to 8% was also obtained for RAC mixes made with 100% of RA.

Figure 6 shows the variation of the splitting tensile strength of the RAC mixes with respect the nanosilica content. It can be seen that the rate of strength increases due to the addition of nanoparticles is higher in RAC mixes made with 50% RA than mixes made with 100% RA. At 50%

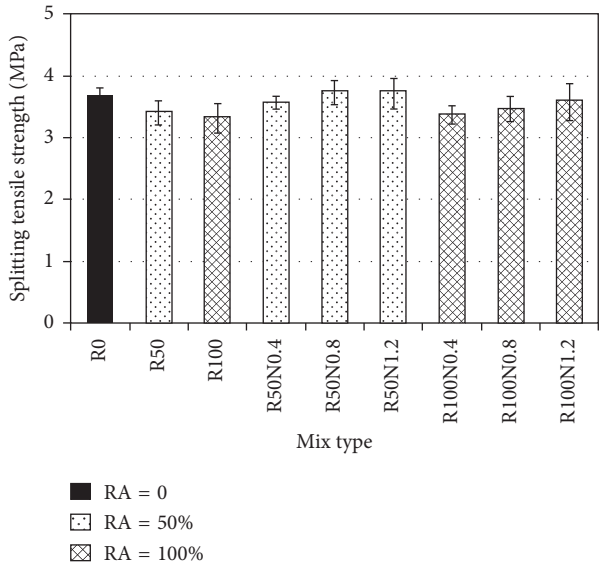

Figure 5: Splitting tensile strength of all mixes.

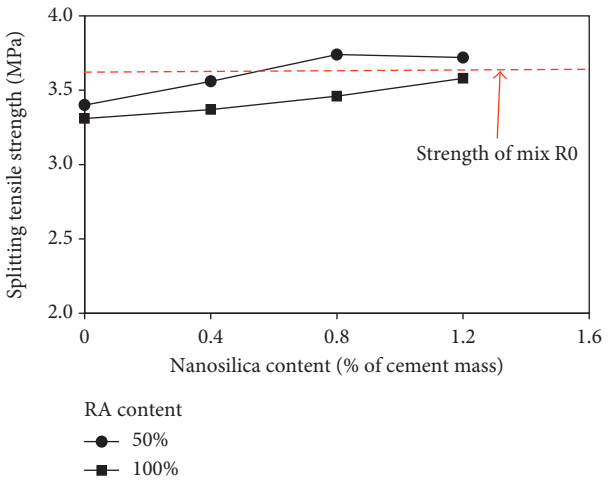

Figure 6: Effect of nanosilica particles content on the splitting tensile strength of RAC mixes.

RA content, the addition of nanoparticles results in comparable splitting tensile strength to that of the control mix at 0.4% nanoparticle content or even higher at 0.8% and 1.2%

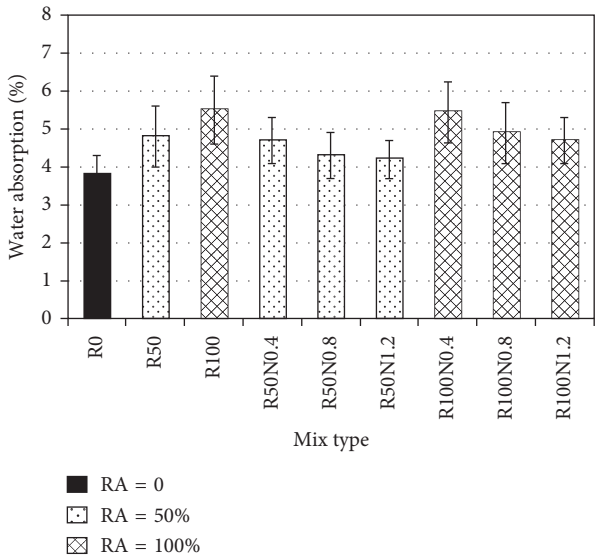

Figure 7: Water absorption (WA) of all mixes.

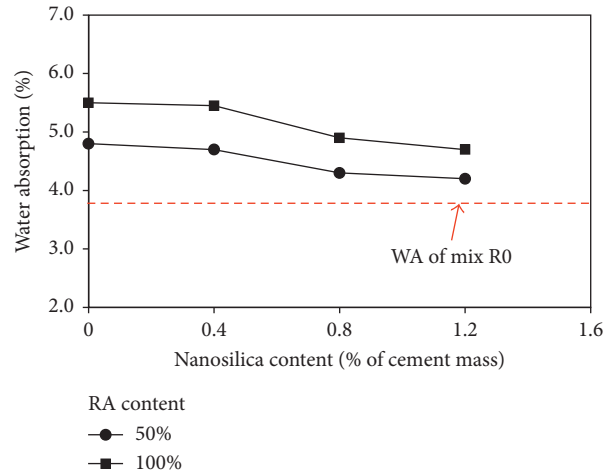

Figure 8: Effect of nanosilica particles content on the WA of RAC mixes.

contents as can be seen in Figure 6. At 100% RA content, the strength increases with the increase of the nanoparticles content to reach just under the strength of the control mix at 1.2% nanoparticles content. Splitting tensile strength improvement due to the addition of nanoparticles of silica was also observed by [28, 38]. This strength improvement of RAC mixes could be attributed to the modification of the microstructure of the RA and the hardened concrete which is explained in detail in Section 3.4.

3.3. Water Absorption. The results of the WA after immersion in water for 24 hours are shown in Figure 7. The age of the specimens at testing was ranged between 28 and 30 days. The results indicate that RAC mixes without nanosilica exhibit higher water absorption than the control mix (R0). The WA of the of the control mix was 3.8%, whereas the WA of the of the RAC mixes with 50% and 100% RA contents were 4.8% and 5.5%, respectively. Water penetrates into concrete because of the ability of the aggregate to absorb water and also due to the presence of micro/macro pores (capillary pores, air voids, and ITZ) in the cement/mortar matrix. The high water absorption of the RAC mixes can be attributed to the inherent nature of the porous microstructure of the RA particles caused by the adhered mortar [1, 3, 4] (as will be explained in Section 3.4).

The influence of adding nanoparticles of SiO_2 with various contents on the WA of RAC mixes is shown in Figure 8 which also shows the WA of the control mix. It can be noticed that although none of the RAC mixes containing nanoparticles of silica shows comparable WA to that of the control mix, the addition of nanoparticles reduces the WA of the RAC mixes. At both contents of RA (50%and 100%), the influence of adding 0.4% of nanoparticles on the WA is insignificant, whilst adding 0.8% of nano-SiO_2 leads to a decline of 10% and 11% in the WA of RAC mixes with 50% and 100% RA contents, respectively. A further slight decrease in WA of the RAC mixes can be observed when the nanosilica content increases to 1.2%. The reduction in WA of the RAC mixes made with nanoparticles of SiO_2 can be mainly attributed to the modification on the RA particles due to the layer of nanoparticles which covers the surface of the RA. This could strengthen the weak, porous, and cracked surface of the RA particles (see Section 3.4) increasing the resistance of the RA against the penetrability of water. The densification of the microstructure of the cement matrix and the ITZ due to the addition of nanosilica particles (as will be explained in next section) could also help in reducing the WA of the RAC mixes.

3.4. Microscopic and Scanning Electron Microscopy Observations. The surface of individual particles of the recycled aggregate with and without nanosilica was observed by a microscope to support and justify the gained enhancement in the compressive strength and tensile strength for the mixes made with recycled coarse aggregate. Also, SEM images for recycled aggregate particles and concrete specimens were taken and studied for the same purpose.

3.4.1. Recycled Aggregate Specimens (Particles). Figure 9(a) shows an image taken by a microscope with a magnification of 20x for the surface of a recycled aggregate particle. Microcracks and voids can be identified on the surface of the RA particle as can be seen in Figure 9(b) which shows part of the surface of the RA particle with higher magnification. These microcracks and voids are the main cause of the weakness of the RA which in turn results in low strength concrete [1, 9, 10]. A weak and cracked zone (ITZ) between the natural aggregate and the attached mortar can be observed. These microcracks and weak ITZ are usually caused by the process of the crushing of the demolished concrete [9]. Similarly, microcracks and weak ITZ can be identified in Figure 4(c) which shows an SEM image for the surface of a RA particle.

To assess the effect of adding the nanosilica as a coat layer around the RA particles on their surfaces, microscopic images were taken for individual particles as can be seen in

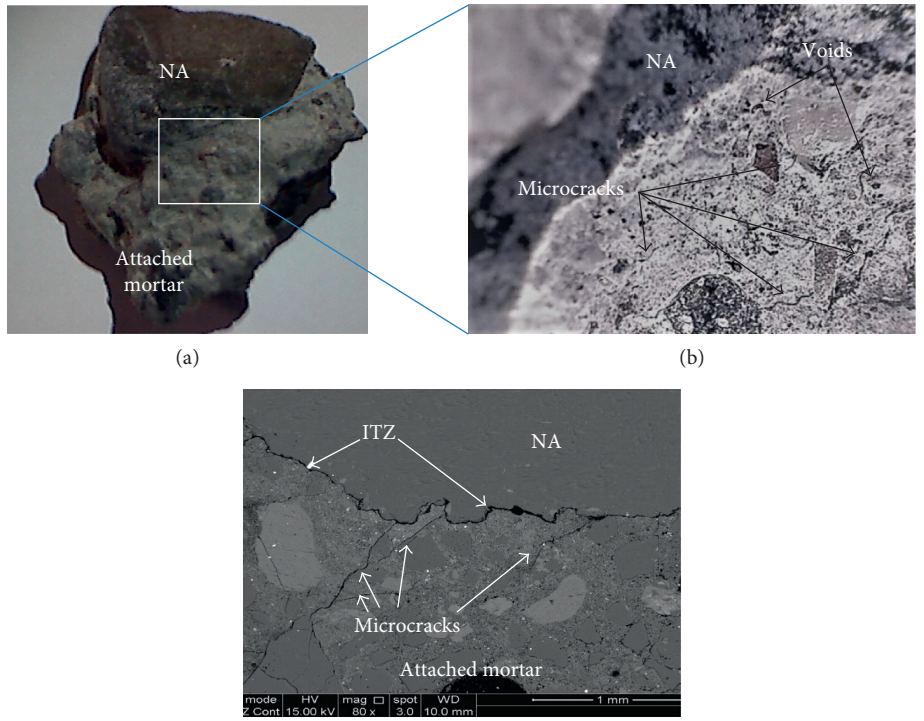

Figure 9: (a) RA particle at 20x magnification. (b) RA surface at 200x magnification. (c) SEM image of the surface of a recycled coarse aggregate particle.

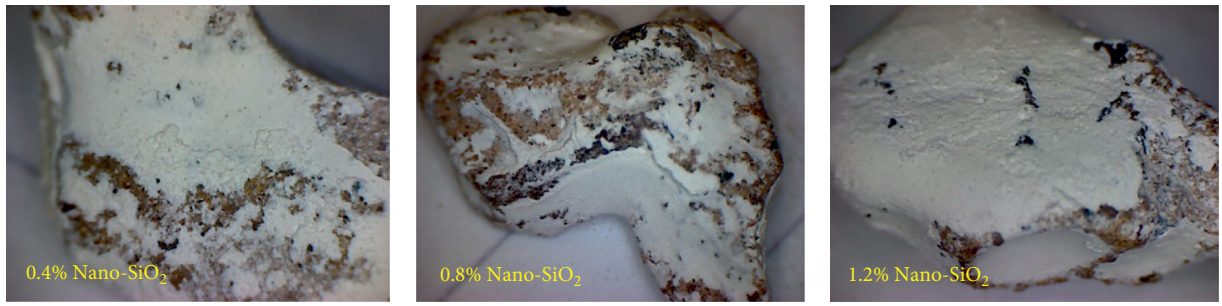

Figure 10: Microscopic images of RA particles with different nanosilica contents: (a) 0.4%; (b) 0.8%; (c) 1.2%.

Figure 10. The effect of nanosilica on the surface of the RA particles is clear. The Nanosilica modifies the surface by sealing all the microcracks and filling all the voids. This modification can partly explain the enhancement in the strength gained by adding nanosilica to the mixes with RA.

3.4.2. Concrete Specimens. The effect of using SiO_2 nanoparticles on the microstructure of RAC was also evaluated through studying concrete specimens with and without nano-SiO_2. The SEM images for the concrete specimens were taken and presented in Figures 11 and 12. Figure 11 shows SEM image for the RAC specimens without silica nanoparticles. The image clearly shows the fact that there are different ITZs in RAC: ITZ1 which exists between the NA particle and the old attached mortar, ITZ2 which lays between the NA particles and the new cement matrix (mortar), and ITZ3 which develops between the new and the old cement mortars. The existence of these ITZs with different microstructures increases the heterogeneous nature of RAC and hence results in a low quality concrete in terms of both strength and durability aspects [34]. Also, the image shows that ITZ3, like the other two ITZs, is porous and can be clearly identified by the very fine black line. The high porosity of this ITZ is due to the high concentration of Ca $(OH)_2$ resulted from the hydration of cement [9, 10].

On the other hand, the ITZ3 in the RAC specimen coated with SiO_2 nanoparticles (Figure 12) cannot be clearly identified with a black line. Although, the old attached mortar and the new mortar can be recognized by their different porosity and microstructure, the two parts seem to be connected very well, and the zone between them

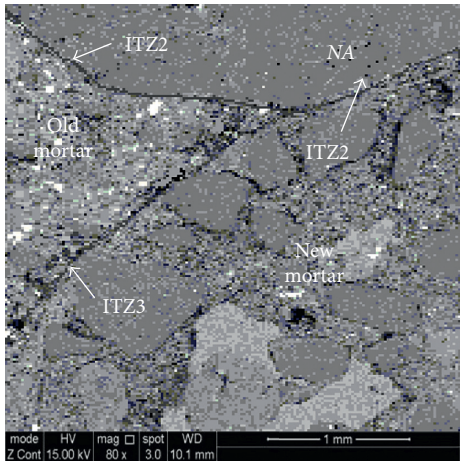

Figure 11: SEM image explains the ITZs in RAC sample without nanosilica.

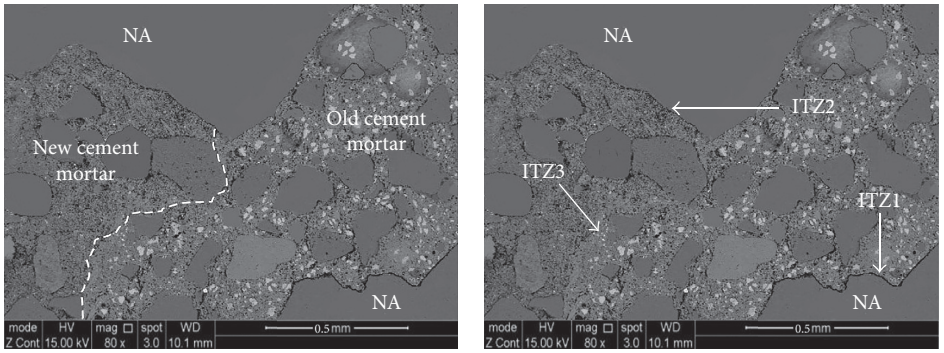

(a) (b)

Figure 12: (a) SEM image of a concrete sample with nanosilica; (b) image of the ITZs of a concrete sample with nanosilica.

(which is the ITZ3) is very dense (Figure 12(b)). The densification of the microstructure of the ITZ3 can be attributed to the effect of adding the nanoparticles of silica. These nanoparticles can result in a dense ITZ through two mechanisms: one is physical and the other one is chemical. The latter is attributed to the chemical ability of the SiO_2 nanoparticles to react with the $Ca(OH)_2$ (one of the cement hydration products) and leading to the formation of more gel product, calcium silicate hydroxide (C-S-H), which is the product responsible of the strength of the concrete and dense microstructure of the ITZ in concrete [23, 39, 40]. The former can be due to large surface area and the super-ultrafine size of the nanoparticles. This small size of these particles helps in filling up all the micropores/nanopores and voids exit in the attached mortar and the ITZ resulting in a more densified microstructure of the cement matrix [34, 38, 40]. Hence, these two mechanisms seem to be the main reasons behind the improvement of the strength of the RAC containing nanoparticles of SiO_2.

4. Conclusions

The following conclusions can be drawn based on the results and discussion.

(i) The addition of nanoparticles of SiO_2 can improve the compressive strength of recycled aggregate concrete regardless of the content of RA.

(ii) The increase in compressive strength depends on the content of the nanoparticles of SiO_2 content.

(iii) The addition of nanoparticles of silica at contents of 0.4%, 0.8%, and 1.2% results in an increase in the compressive strength of 10%, 18%, and 22% for mixes containing 50% RA and of 6%, 13%, and 16% for mixes made with 100% RA, respectively.

(iv) Adding nanoparticles to RAC can result in comparable splitting tensile strength to that of the control mix at 0.4% nanoparticles content or even higher at 0.8%; while at 100% RA content, the splitting tensile strength increases to reach just under the strength of the control mix at 1.2% nanoparticles content.

(v) Regardless of the content of RA, the addition of nanoparticles of SiO_2 resulted in reducing the WA of RAC up to 11% at 0.8% of nanoparticle content compared to RAC mixes without nanoparticles.

(vi) The enhancement in strength and the reduction in the WA of the RAC due to the addition of nanoparticles can be attributed to the modification in the pore structure of the concrete.

(vii) Microscopic and SEM observations revealed the heterogeneous nature of the RA particles, which is characterized by weak and cracked attached mortar and porous ITZ.

(viii) RAC microstructure can be positively modified through the addition of SiO_2 nanoparticles which can help densify the microstructure RAC by physical and chemical mechanisms.

(ix) RAC with nanoparticles of SiO_2 can demonstrate comparable strength to that of NAC; hence, great enhancement in terms of sustainability and environmental impact of RA can be achieved.

Data Availability

The authors state that the data for all tests are available. Please contact the corresponding author for the data and further information.

Disclosure

Part of this research has been presented in the 4th International Engineering Conference on Developments in Civil and Computer Applications IEC 2018, Erbil Polytechnic University and Ishik University, Erbil, Iraq, 2018 [34].

Conflicts of Interest

The authors declare no conflicts of interest.

Acknowledgments

The authors would like to acknowledge the support received from the Erbil Polytechnic University.

References

[1] K. H. Younis and K. Pilakoutas, "Strength prediction model and methods for improving recycled aggregate concrete," *Construction and Building Materials*, vol. 49, pp. 688–701, 2013.

[2] M. Gomes and J. de Brito, "Structural concrete with incorporation of coarse recycled concrete and ceramic aggregates: durability performance," *Materials and Structures*, vol. 42, no. 5, pp. 663–675, 2009.

[3] V. W. Y. Tam and C. M. Tam, "Parameters for assessing recycled aggregate and their correlation," *Waste Management & Research*, vol. 27, no. 1, pp. 52–58, 2009.

[4] S. C. Angulo, P. M. Carrijo, A. D. Figueiredo, A. P. Chaves, and V. M. John, "On the classification of mixed construction and demolition waste aggregate by porosity and its impact on the mechanical performance of concrete," *Materials and Structures*, vol. 43, no. 4, pp. 519–528, 2010.

[5] M. L. Berndt, "Properties of sustainable concrete containing fly ash, slag and recycled concrete aggregate," *Construction and Building Materials*, vol. 23, no. 7, pp. 2606–2613, 2009.

[6] P. Goncalves and J. Brito, "Recycled aggrgate concrete (RAC)-comparative analysis of existing specifications," *Magazine of Concrete Research*, vol. 62, no. 5, pp. 339–346, 2010.

[7] V. W. Y. Tam, C. M. Tam, and K. N. Le, "Removal of cement mortar remains from recycled aggregate using pre-soaking approaches," *Resources Conservation and Recycling*, vol. 50, no. 1, pp. 82–101, 2007.

[8] A. Akbarnezhad, K. C. G. Ong, M. H. Zhang, C. T. Tam, and T. W. J. Foo, "Microwave-assisted beneficiation of recycled concrete aggregates," *Construction and Building Materials*, vol. 25, no. 8, pp. 3469–3479, 2011.

[9] V. W. Y. Tam, X. F. Gao, and C. M. Tam, "Microstructural analysis of recycled aggregate concrete produced from two-stage mixing approach," *Cement and Concrete Research*, vol. 35, no. 6, pp. 1195–1203, 2005.

[10] A. Katz, "Treatments for the improvement of recycled aggregate," *Journal of Materials in Civil Engineering*, vol. 16, no. 6, pp. 597–603, 2004.

[11] J. S. Ryu, "Improvement on strength and impermeability of recycled concrete made from crushed concrete coarse aggregate," *Journal of Materials Science Letters*, vol. 21, no. 20, pp. 1565–1567, 2002.

[12] B. Gonzalez-Fonteboa and F. Martinez-Abella, "Concretes with aggregates from demolition waste and silica fume. Materials and mechanical properties," *Building and Environment*, vol. 43, no. 4, pp. 429–437, 2008.

[13] S. Kou, C. Poon, and D. Chan, "Influence of fly ash as a cement addition on the hardened properties of recycled aggregate concrete," *Materials and Structures*, vol. 41, no. 7, pp. 1191–1201, 2008.

[14] J. S. Li, H. N. Xiao, and Y Zhou, "Influence of coating recycled aggregate surface with pozzolanic powder on properties of recycled aggregate concrete," *Construction and Building Materials*, vol. 23, no. 3, pp. 1287–1291, 2009.

[15] M. Sumesh, U. Johnson Alengaram, M. Z. Jumaat, K. H. Mo, and M. F. Alnahhal, "Incorporation of nano-materials in cement composite and geopolymer based paste and mortar: a review," *Construction and Building Materials*, vol. 148, pp. 62–84, 2017.

[16] J. Bernal, E. Reyes, J. Massana, N. León, and E. Sánchez, "Fresh and mechanical behavior of a self-compacting concrete with additions of nano-silica, silica fume and ternary mixtures," *Construction and Building Materials*, vol. 160, pp. 196–210, 2018.

[17] L. G. Li, J. Zhu, Z. H. Huang, A. K. H. Kwan, and L. J. Li, "Combined effects of micro-silica and nano-silica on durability of mortar," *Construction and Building Materials*, vol. 157, pp. 337–347, 2017.

[18] W. Li, Z. Huang, F. Cao, Z. Sun, and S. P. Shah, "Effects of nano-silica and nano-limestone on flowability and mechanical properties of ultra-high-performance concrete matrix," *Construction and Building Materials*, vol. 95, pp. 366–374, 2015.

[19] E. Mohseni, F. Naseri, R. Amjadi, M. M. Khotbehsara, and M. M. Ranjbar, "Microstructure and durability properties of cement mortars containing nano-TiO_2 and rice husk ash," *Construction and Building Materials*, vol. 114, pp. 656–664, 2016.

[20] N. Leon, J. Massana, F. Alonso, A. Moragues, and E. Sánchez-Espinosa, "Effect of nano-Si_2O and nano-Al_2O_3 on cement mortars for use in agriculture and livestock production," *Biosystems Engineering*, vol. 123, pp. 1–11, 2104.

[21] M. Oltulu and R. Şahin, "Effect of nano-SiO_2, nano-Al_2O_3 and nano-Fe_2O_3 powders on compressive strengths and capillary

water absorption of cement mortar containing fly ash: a comparative study," *Energy and Buildings*, vol. 58, pp. 292–301, 2013.

[22] P. Mondal, "Nanomechanical properties of cementitious materials," Ph.D. thesis, *Civil & Environmental Engineering*, Northwestern University, Evanston, IL, USA, 2008.

[23] F. Sanchez and K Sobolev, "Nanotechnology in concrete: a review," *Construction and Building Materials*, vol. 24, no. 11, pp. 2060–2071, 2010.

[24] F. U. A. Shaikh, S. W. M. Supit, and P. K. Sarker, "A study on the effect of nano silica on compressive strength of high volume fly ash mortars and concretes," *Materials & Design*, vol. 60, pp. 433–442, 2014.

[25] S. P. Shah, P. Hou, and M. S. Konsta-Gdoutos, "Nano-modification of cementitious material: toward a stronger and durable concrete," *Journal of Sustainable Cement-Based Materials*, vol. 5, no. 1-2, pp. 1–22, 2016.

[26] W. Li, C. Long, V. W. Y. Tam, C.-S. Poon, and W. H. Duan, "Effects of nano-particles on failure process and microstructural properties of recycled aggregate concrete," *Construction and Building Materials*, vol. 142, pp. 42–50, 2017.

[27] P. Hosseini, A Booshehrian, and A Madari, "Developing concrete recycling strategies by utilization of nano-SiO_2 particles," *Waste and Biomass Valorization*, vol. 2, no. 3, pp. 347–355, 2014.

[28] B. B. Mukharjee and S. V. Barai, "Influence of nano-silica on the properties of recycled aggregate concrete," *Construction and Building Materials*, vol. 55, pp. 29–37, 2014.

[29] W. Li, Z. Luo, C. Long, C. Wu, W. H. Duan, and S. P. Shah, "Effects of nanoparticle on the dynamic behaviors of recycled aggregate concrete under impact loading," *Materials & Design*, vol. 112, pp. 58–66, 2016.

[30] BS EN 12390-3:2009, *Testing Hardened Concrete Part 3: Compressive Strength of Test Specimens*, British Standards Institution, London, UK, 2009.

[31] BS EN 12390-6:2009, *Testing Hardened Concrete Part 6: Splitting Tensile Strength of Test Specimens*, British Standard Institution, London, UK, 2009.

[32] ASTM C642-13, *Standard Test Method for Density, Absorption, and Voids in Hardened Concrete*, 2103, American Standards for Testing and Materials, ASTM International, West Conshohocken, PA, USA, 2013.

[33] L. Evangelista and J de Brito, "Mechanical behaviour of concrete made with fine recycled concrete aggregates," *Cement & Concrete Composites*, vol. 29, no. 5, pp. 397–401, 2007.

[34] K. H. Younis and S. M. Mustafa, "Application of nano materials to enhance mechanical performance and microstructure of recycled aggregate concrete," in *Proceedings of the 4th International Engineering Conference on Developments in Civil and Computer Applications IEC 2018*, Erbil Ploytechnic University and Ishik University, Erbil, Iraq, 2018.

[35] S-c. Kou, C.-s. Poon, and F. Agrela, "Comparisons of natural and recycled aggregate concretes prepared with the addition of different mineral admixtures," *Cement and Concrete Composites*, vol. 33, no. 8, pp. 788–795, 2011.

[36] Z. H. Duan and C. S. Poon, "Properties of recycled aggregate concrete made with recycled aggregates with different amounts of old adhered mortars," *Materials & Design*, vol. 58, pp. 19–29, 2014.

[37] N. Kisku, H. Joshi, M. Ansari, S. K. Panda, S. Nayak, and S. C. Dutta, "A critical review and assessment for usage of recycled aggregate as sustainable construction material," *Construction and Building Materials*, vol. 131, pp. 721–740, 2017.

[38] F. U. A. Shaikh, H. Odoh, and A. B. Than, "Effect of nano silica on properties of concretes containing recycled coarse aggregates," *Proceedings of the Institution of Civil Engineers-Construction Materials*, vol. 168, no. 2, pp. 68–76, 2015.

[39] H. Zhang, Y. Zhao, T. Meng, and S. P. Shah, "The modification effects of a nano-silica slurry on microstructure, strength, and strain development of recycled aggregate concrete applied in an enlarged structural test," *Construction and Building Materials*, vol. 95, pp. 721–735, 2015.

[40] A. M. Said, M. S. Zeidan, M. T. Bassuoni, and Y. Tian, "Properties of concrete incorporating nano-silica," *Construction and Building Materials*, vol. 36, pp. 838–844, 2012.

Hindawi
Advances in Materials Science and Engineering
Volume 2018, Article ID 3647395, 8 pages
https://doi.org/10.1155/2018/3647395

Research Article

Experimental Investigation on Embedding Strength Perpendicular to Grain of Parallel Strand Bamboo

Junwen Zhou,[1,2] **Dongsheng Huang**,[2] **Yang Song**,[1] **and Chun Ni**[3]

[1]*School of Civil and Architecture Engineering, Changzhou Institute of Technology, Changzhou 213032, China*
[2]*School of Civil Engineering, Nanjing Forestry University, Nanjing 210037, China*
[3]*FPInnovations, Vancouver, BC, Canada V6T 1Z4*

Correspondence should be addressed to Junwen Zhou; zhoujw@czu.cn

Received 7 November 2017; Revised 25 March 2018; Accepted 10 April 2018; Published 13 May 2018

Academic Editor: Nadezda Stevulova

Parallel strand bamboo (PSB) is a latest construction material; to know more about mechanical properties of PSB, 5 groups of specimens with difference only in bolt diameter were designed to study the impact of the fastener diameter on embedding strength perpendicular to grain of PSB. Based on the tested result, the feasibility for PSB of the theoretical equation in the American code and European code on embedding strength predication was assessed. A controlled displacement was used to load till specimen failure, the stress-displacement curve of all specimens was obtained in terms of the tested results, and the yielding tested strength based on 5% bolt diameter offset proposed by the American code was found. The tested results showed that the yielding strength perpendicular to grain of PSB was stable, the variable coefficient was between 5.88% and 13.34%, and the average yielding strength values were 80.84 MPa, 77.40 MPa, 76.52 MPa, 74.20 MPa, and 67.01 MPa, respectively, which decreased with the increase of bolt diameter, and the average yielding strength values are larger than the calculated results using theoretical formula. Therefore, the theoretical equation on embedding yielding strength of wood in the American code and European code applies to PSB.

1. Introduction

Nowadays, timber and bamboo buildings again have started gaining attention because low-carbon and ecological concepts are the new architecture tendency. Also, primary construction materials used in modern timber structures are renewable materials and are better than fossil materials such as steel and concrete in thermal performance, which is in conformity with the sustainable development principle [1, 2]; thus, timber buildings have become a new development trend in recent decades. In northern America, timber buildings are already preferred in low-carbon architecture, and almost 90% of low-rise buildings are timber structures. Nowadays, more and more midrise and tall timber buildings have been constructed in some countries, such as the most famous 18-storey Brock Commons Student Residence with a height of 53 meters in UBC [3]. The growth period of original structural wood from the time of planting to harvesting is longer, about decades, which is indirectly proportional to the existing demand, especially in Asian countries.

In addition, constructed wood is sparse due to cutting of trees in early stage; hence, bamboo is preferred for its short harvesting period and identical excellent mechanical performance compared with traditional wood.

Bamboo, widely planted in Asia, especially in Southeast Asia, is "the second forestry resource" because of the suitable temperature and humidity in lower geographic latitude.

Bamboo was already used as a construction material about thousand years ago [4]. Bamboo has a short harvesting period of about 3–5 years [5–8]. Bamboo is easily available and has higher mechanical strength compared to wood [9]; however, because of its thin wall and hollow and limited sections, large scale use of raw bamboo is restricted in building structures. As a result, raw bamboo is commonly used in rural houses, simple bridges, water channels, and some landscape architecture. With the progress in technology, some new engineered bamboo materials, such as

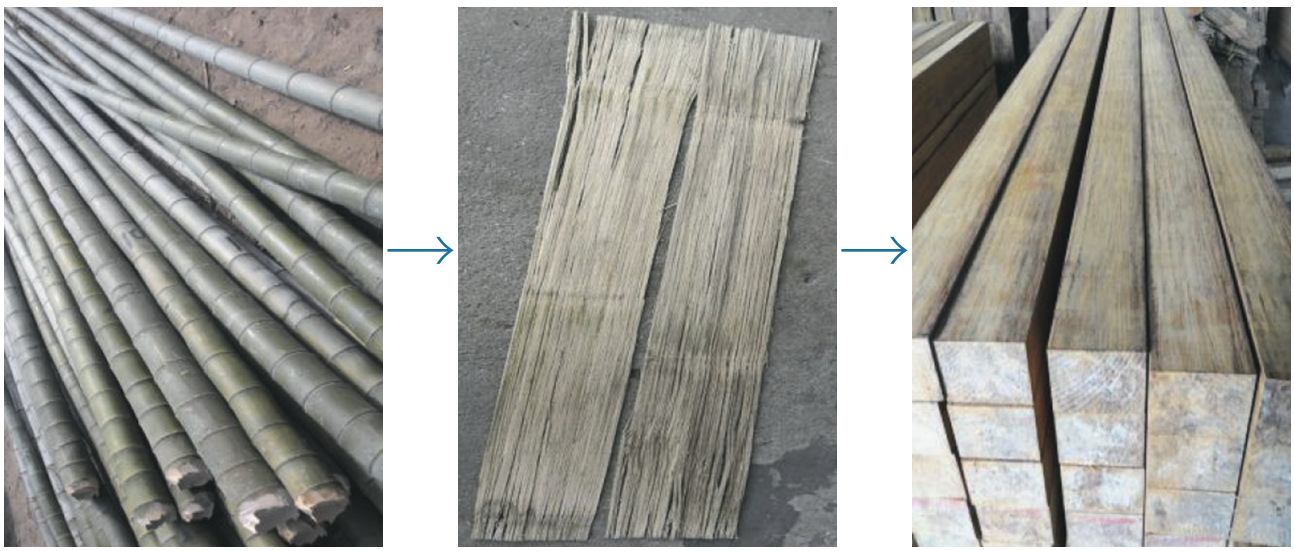

(a) (b) (c)

Figure 1: Manufacturing process of parallel strand bamboo. (a) Raw bamboo. (b) Bamboo fiber bundle. (c) Parallel strand bamboo.

laminated bamboo [10–13] and parallel strand bamboo (PSB) [14–16], have been developed and those materials have a pronounced breakthrough in dimensions and, therefore, have higher load-bearing capacity and posses a better application prospect in building structures.

PSB is a new engineering material made with raw bamboo. At plant, PSB is fabricated in the manufacturing process expressed in Figure 1; first, original bamboo is cut into certain length according to the demand parallel to grain and, then, is rolled into bamboo fiber bundle which is broken in the longitudinal direction and connected in the latitudinal direction, as shown in Figure 1(b). The bamboo fiber bundle is dried to reach a moisture content between 5% and 10%, immersed in glue well, and then put into billet under pressure and heat, and the fiber is aligned to be in parallel with the length of the member. Once the adhesive of phenolic resin is cured, the bamboo fiber is glued together to form a PSB member. Commonly, the shape of PSB is sheet or prism which is actually determined in terms of practical applications. PSB holds the continuity fiber of bamboo and overcomes some defect of section limit and concentration knot, and as a result, PSB owns the outstanding mechanical performances compared to raw bamboo [16]. A two-storey building has been constructed in China using PSB material [14]. The superiority mentioned above indicates that PSB has a good prospect to be an alternative construction material. At present, some studies on PSB mainly deal with the mechanical performance of small-scale specimens and basic components [15–17], showing that PSB has more superior qualities than engineered wood.

Like wooden buildings, bamboo buildings are also prefabricated structure buildings, and the mechanical performance of connection, such as bearing capacity, and stability are very important, concerning the safety of the overall structure. As a basic connection mode, bolted connection has been used widespread in modern wooden structures, and dowel bearing of wood in connection is the main behavior of bolted connection, impacting the mechanical performance of whole connection. Few studies were performed to determine the four important influence factors, fastener diameter, density of wood, moisture content, and load-to-grain angle, on embedding strength of wood.

Rammer [18] investigated the mechanical performance of embedding strength of hardwoods parallel to grain, and three diameters of steel nail and fastener were tested. The results showed that fastener diameter has affinity on embedding stiffness and no affinity on embedding strength; however, the nail diameter has obvious influence on embedding strength and stiffness. Rammer and Winistorfer [19] proposed the calculating formula, including the moisture content for embedding capacity of wood. Sawata and Yasumura [20] tested the dowel-bearing strength with four kinds of fastener diameter parallel to grain and perpendicular to grain, respectively; the embedding strength is decided based on the 5% bolt diameter offset method and 5 mm displacement maximum load, and the result shows that the embedding strength perpendicular to grain increases with the decrease in dowel diameter. Franke and Magnière [21] investigated the embedding behavior of European hardwoods through the testing analysis, and the influence of the load-to-grain angle and fastener diameter was studied. Schweigler et al. [22] studied the embedding performance of fastener with two kinds of diameter on different load-to-grain in the laminated veneer lumber, and the relative mechanical behavior was obtained. Seri et al. [23] concentrated on the embedding performance of glulam with and without glue line wood with two different fastener diameters, and the results show that the fastener diameter and manufacturing method have pronounced influence on the dowel-bearing strength of the specimen.

The dowel-bearing experiment with superiorities of convenience, practicability, and economy is employed to attain some important data; to the author's knowledge, only few studies are available on embedding strength of PSB perpendicular

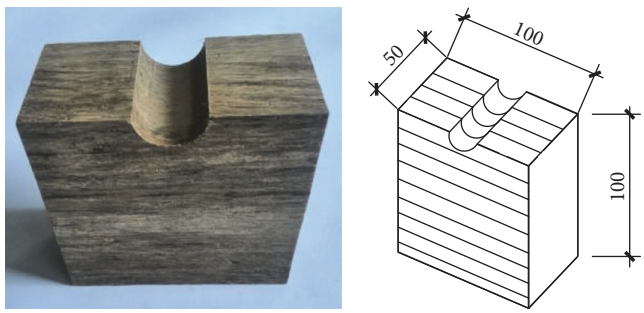

(a) (b)

Figure 2: Drawing details of the specimen.

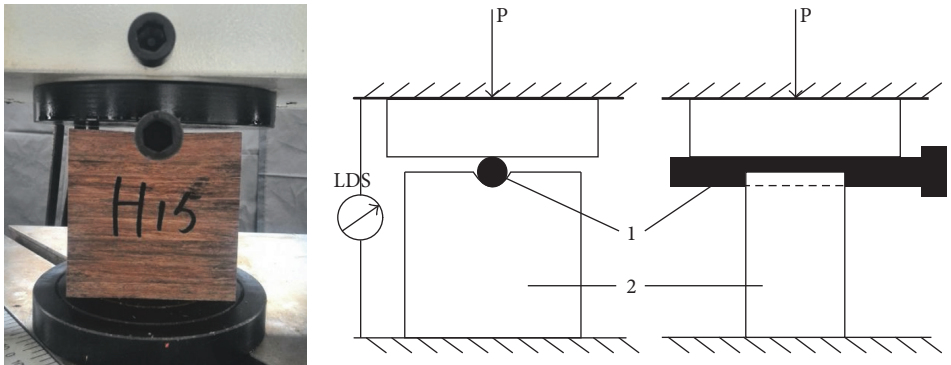

(a) (b)

Figure 3: Experimental setup.

(a) (b)

Figure 4: Typical failure mode of the specimen.

to grain, so more works are needed to be done to know about the mechanical behavior of PSB. To achieve the aim of this study, 40 specimens divided into 5 groups in terms of bolt diameter were tested to investigate the dowel-bearing property of PSB; based on the experiment and computational analysis, the formula for calculating the embedding strength will be proposed for PSB perpendicular to grain.

2. Test Procedure

PSB emerged recently as a new construction material; there are no tested criterion and method for PSB, concerning about similar mechanical performance as engineering wood, and the test method for engineering wood was employed to test the PSB material.

According to ASTM D5764-97a [24], tests were conducted by a square PSB block with a half-circle-hole perpendicular to grain located in the top face and a hole of 1.0 mm larger than the fastener diameter. All the specimens were same in dimension with 100 mm length, 50 mm width, and 100 mm height, except for the magnitude of the circle hole, and a detailed drawing of the specimen is shown in Figure 2. PSB has bigger density because of tremendous pressure in a higher temperature condition during the

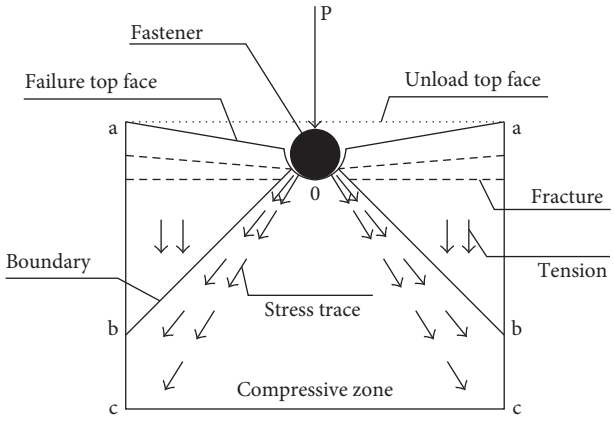

Figure 5: Stress state of the specimen.

manufacturing process, and the average tested value of gravity and moisture content are 1.08 g/cm^3 and 9.0%, respectively, in terms of ASTM D2395 [25], and the average tested value of compression strength perpendicular to grain is 62 N/mm^2 according to ASTM D143-09 [26].

According to the experimental method provided by ASTM D5764-97a [24] for evaluating the embedding strength of wood and wood-based material, a controlled displacement of 1 mm/min was adopted to apply the fastener till the specimen failure which can be defined that the side part PSB of hole meeting the loading plate and fastener embedded in PSB or load reaching 85% of the ultimate load. The laser displacement sensor (LDS) was employed to monitor the overall deformation of the specimen in the vertical direction, which is shown in Figure 3. Before the normal test, a small scale load was applied to check all devices at the start of the test.

3. Test Result

3.1. Failure Mode. When failure occurred, all fasteners were submerged into the specimen and the bearing zone under the fastener sank distinctly; unloaded PSB besides the fastener met the loading plate and cracked in the horizontal direction in all the specimens; PSB under the fastener bulged out of the plane; a vertical crack or a diagonal crack or both were observed in the broken specimen; the typical failure mode is shown in Figure 4.

The stress state of the specimen under loading is shown in Figure 5; the load was transferred though fastener from the loading plate to the specimen, and the bamboo fiber including under fastener and inside the stress dispersal boundary line was subjected to compressive force.

As shown in Figure 5, compression stress cannot reach the left and right zones oab, which is far away from the direct compressive zone o and is out of the stress dispersal boundary line; therefore, vertical deformation in zone oab is little. For zone obccb, especially contacting zone o, obvious deformation occurred on account of direct compression of the fastener; vertical deformation in zone bc brought out tension to bamboo fiber in zone obc; as a result, the horizontal fracture parallel to grain came out in zone ab, mainly near to the top face. Because of concentrated stress under fastener, bamboo fiber had large deformation in the vertical direction out of the grain plane, which results in bulking of bamboo out of the plane. Furthermore, the larger horizontal deformation brought out one or more fractures in bamboo fiber near fastener; with the increase of load, the fracture developed in the direction of two lateral edges and going down or sloping down; at the end, the specimen broke due to fracture which is shown in Figure 4.

Table 1 shows all the tested results. The dowel-bearing strength perpendicular to grain was obtained by the 5% fastener diameter offset method proposed in ASTM D5764-97a [24]. In this way, the load-displacement curve was obtained first in terms of tested data. A straight line fit to the initial linear portion of the load-displacement curve was offset by a deformation of 5% fastener diameter, and the load at which the offset line intersects the load-displacement curve was used as the yield load; finally, the yield load was divided by the bolt diameter and specimen thickness to get the embedding strength, and the method of obtaining yielding strength is shown in Figure 6. Table 1 gives the average value of each group specimen.

3.2. Strength-Displacement Curve. The strength-displacement curve of the 5 group specimens are shown in Figures 7–11. These curves in Figures 7 and 8 are for the bolt diameter of 12 mm and 14 mm, respectively. It was obvious that the curve is similar in tendency and rises as the load increases, and at the end, the load stops due to the meeting between the loading plate and the top face of the specimen.

In two groups specimen of bigger diameter of 20 mm and 24 mm, especially the group of 24 mm diameter, when the curve reached the summit value point, the dowel-bearing capacity started decreasing and obvious discreteness in peak load was observed. The previous phenomenon may be due to the following reasons: for groups H1 and H2 with a small bolt diameter, the interstice in PSB under load started diminishing, before the bolt was immersed into PSB, and the specimen was extruded to be compact; therefore, the embedding capacity increased constantly. Moreover, the loading path is shorter because of small diameter, and the loading will stop when the loading plate meets the top face of the specimen before the specimen was compacted well. This makes that the defect in structure and construction of the specimen did not display during the test.

As for groups H4 and H5 with a bigger bolt diameter, due to the longer loading path, fracture perpendicular to grain because of large deformation of internal bamboo fiber under increasing load comes after the PSB was extruded fully to be dense.

It is also observed that bolts with bigger diameter have larger bearing stiffness, and the bearing stiffness of group H1 is minimum and group H5 is maximum. Because bolts with bigger diameter have larger bearing area, the deformation of the specimens under a larger bolt is less than that of the specimens under a smaller bolt in the same load.

According to the tested results in Table 1, it is shown that even the yielding strength of each group decreased with the

Table 1: Tested result.

Specimen group	Number	Diameter of bolt (mm)	①	②	③	④	⑤	⑥ ①/③	⑦ ①/④	⑧ ⑤/①
H1	8	12	80.84	5.88	72.16	68.42	133.26	1.12	1.18	1.65
H2	8	14	77.40	8.42	68.61	63.34	114.30	1.13	1.22	1.48
H3	8	16	76.52	10.63	65.25	59.26	105.35	1.17	1.29	1.38
H4	8	20	74.20	12.20	59.04	53.00	99.32	1.26	1.40	1.34
H5	8	24	67.01	13.34	53.42	48.38	84.54	1.25	1.39	1.26

Note. ① is the average value of yielding strength based on the 5% bolt diameter offset method (MPa). ② is the variable coefficient of tested yielding strength (%). ③ is the calculating value of formula in BS EN 1995 (MPa). ④ is the calculating value of formula in NDS-2015 (MPa). ⑤ is the average value of ultimate tested strength (MPa).

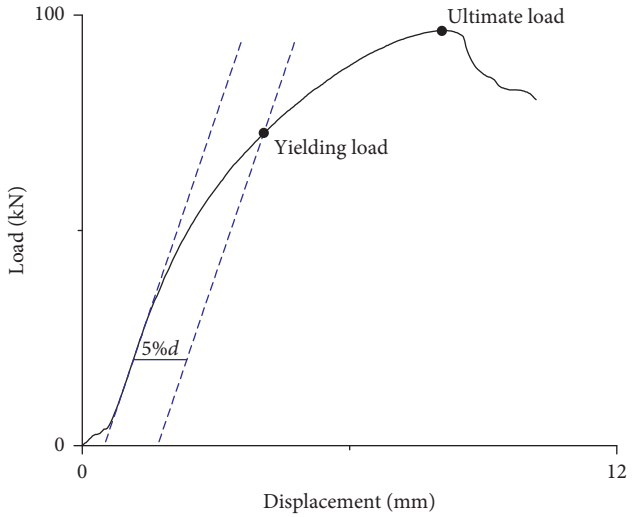

Figure 6: Method to evaluate the yielding load.

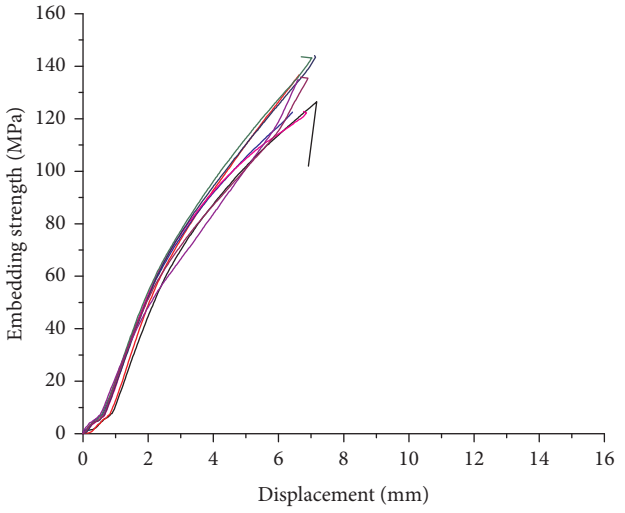

Figure 7: Strength-displacement curve of group H1.

increase in bolt diameter, which demonstrates that the magnitude of bolt has pronounced effect on dowel-bearing strength, which is in agreement with the tested results of Sawata and Yasumura [20]. Furthermore, the variable coefficient enlarges as the bolt diameter increases, which are in agreement with regularities of distribution of strength-displacement of the specimen.

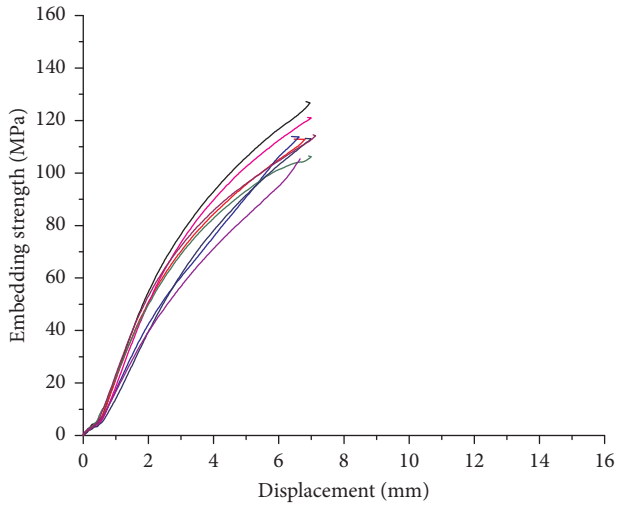

Figure 8: Strength-displacement curve of group H2.

In addition, from Table 1, it is also observed that the ratio between the maximum bearing strength and yielding strength of 5% diameter offset decreased with the increase in bolt diameter, which indicated that bolted connection in small bolt diameter that has larger bearing capacity was calculated with the yielding strength of 5% diameter offset.

3.3. Bearing Capacity Perpendicular to Grain. The strength-displacement curve in Figures 7–11 showed that it is not easy to find the obvious yielding point in the curve; therefore, other approaches were needed to seek the yielding strength for engineering design. At present, the yielding strength in dowel-bearing capacity was determined by the 5% diameter offset proposed in ASTM D5764-97a [24], which has already been accepted. The yielding strength value of each specimen is displayed in Figure 12, and the average value of yielding strength of each group specimen is displayed in Table 1. Due to higher cost and more time needed for on-site testing, BS EN 1995-1-1 [27] and NDS-2015 [28] both gave the calculating formula for the yielding value of dowel-bearing strength perpendicular to grain. In the formula proposed in BS EN 1995-1-1 [27], the embedding strength was based on the bolt diameter and material density and is shown as the following formula:

$$f_c = \frac{0.082\,(1 - 0.01d)\rho_k}{k_{90}}. \quad (1)$$

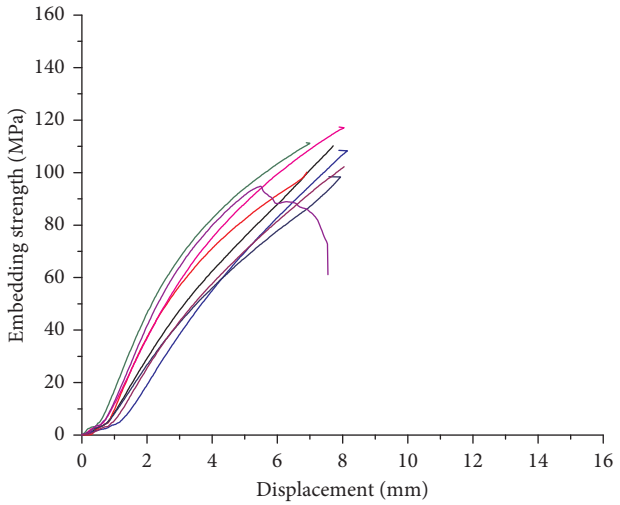

Figure 9: Strength-displacement curve of group H3.

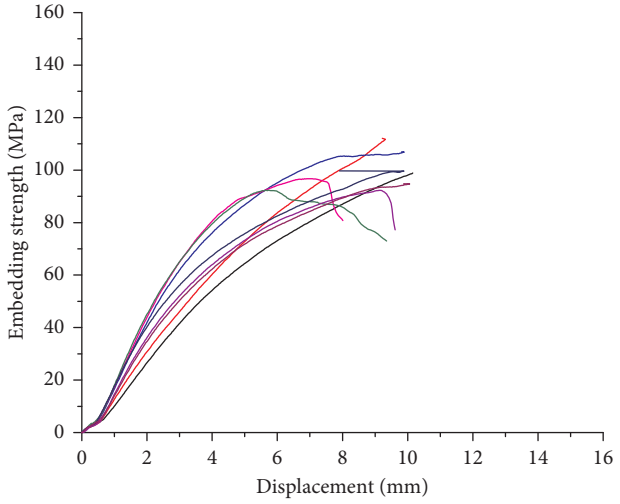

Figure 10: Strength-displacement curve of group H4.

For hardwoods,

$$k_{90} = 0.90 + 0.015d, \tag{2}$$

where f_c is the dowel-bearing strength perpendicular to grain (MPa), d is the bolt diameter (mm), and ρ_k is the density of wood (kg/m^3).

In NDS-2015 [28], the dowel-bearing strength perpendicular to grain also concerning with bolt diameter and wood density is given by the following formula:

$$F_e = \frac{6100G^{1.45}}{\sqrt{D}}, \tag{3}$$

where F_e is the dowel-bearing strength perpendicular to grain ((psi)^2), D is the bolt diameter (inch), and G is the relative density of wood.

For contrasting analysis of (1) easily, (3) was substituted to obtain the following formula:

$$f_e = \frac{212G^{1.45}}{\sqrt{D}}, \tag{4}$$

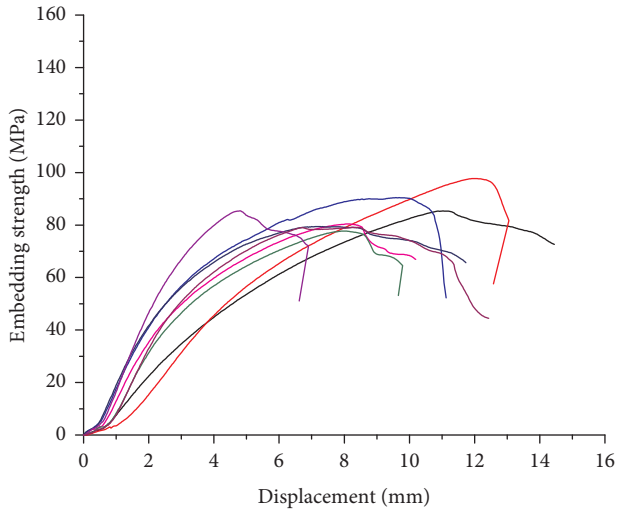

Figure 11: Strength-displacement curve of group H5.

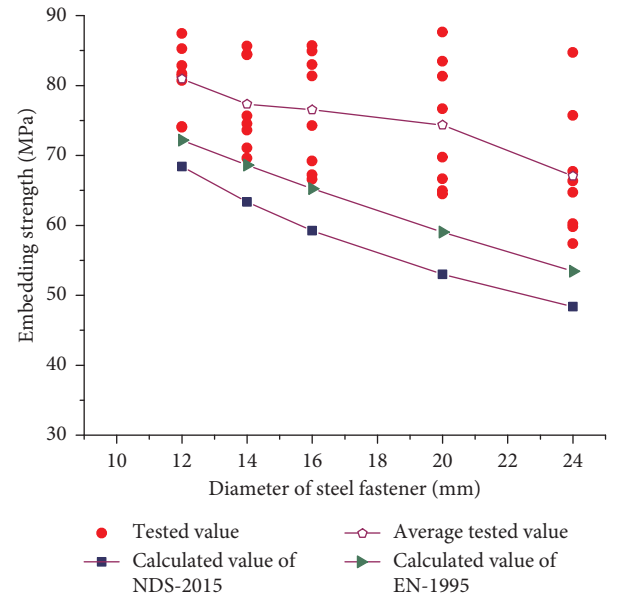

Figure 12: The comparison between the tested value and theoretical value.

where f_e is the dowel-bearing strength perpendicular to grain (MPa), D is the bolt diameter (mm), and G is the density of wood (g/cm^3).

The value of embedding strength in terms of (1) and (4) is shown in Table 1.

As shown in Table 1, the embedding strength value according to the formula is smaller when bigger bolt diameter was applied, which is in accord with the tendency of tested results. Moreover, the average bearing strength in terms of 5% bolt diameter offsetting is approximately the calculated value for small diameter bolt and is the obvious gap for big diameter bolt.

For PSB, the calculated value based on BS EN 1995-1-1 [27] is larger than that according to NDS-2015 [28] and approached the average tested result.

In Table 1 and Figure 12, the average tested values of 5 groups are all larger than the calculated values according to BS EN 1995-1-1 [27], which indicated that the dowel-bearing yielding strength of PSB perpendicular to grain can be obtained by using the formula proposed in BS EN 1995-1-1 [27].

4. Conclusions

Five group specimens in a total number of 40 were tested to investigate the mechanical behavior of embedding strength of PSB perpendicular to grain, and strength-displacement curves of each specimen were provided in this paper. According to the previous curve, the tested embedding yielding strength was obtained by the 5% bolt diameter offset; meanwhile, the calculated embedding strength in terms of the NDS-2015 15 and BS EN 1995-1-1 was provided. Some conclusions were obtained as following.

(1) The certain relationship between the embedding strength of PSB perpendicular to grain and bolt diameter was observed; the bigger the bolt diameter, the smaller the embedding strength.

(2) The mechanical properties of PSB is stable, and the variable coefficient of embedding strength adopted 5% bolt diameter offset is between 5.88% and 13.34%; moreover, the bigger the bolt diameter, the larger the variable coefficient.

(3) The average tested value of embedding yielding strength of PSB perpendicular to grain in accordance with the 5% bolt diameter is larger than the calculating value by using the formula proposed in NDS-2015 and BS EN 1995-1-1. So the method of using the calculating formula in BS EN 1995-1-1 or NDS-2015 to determine the embedding strength is feasible.

(4) The ratio between the tested ultimate strength and the yielding strength according to 5% bolt diameter offset decreased with the increase of bolt diameter.

Conflicts of Interest

The authors declare that they have no conflicts of interest.

Acknowledgments

The research was supported by the National Natural Science Foundation of China (nos. 51778299 and 51708049), the Project of Housing and Urban-Rural Development Ministry of China (no. 2014-K2-014), the Top-Notch Academic Programs Project of Jiangsu Higher Education Institutions (PPZY2015A041), the Science Foundation of Changzhou Institute of Technology (no. YN1615), and the Changzhou Sci & Tech Program (no. CJ20179043).

References

[1] R. H. Falk, "Wood as a sustainable building material," *Forest Products Journal*, vol. 59, no. 9, pp. 6–12, 2009.

[2] M. Mahdavi, P. L. Clouston, and S. R. Arwade, "Development of laminated bamboo lumber: review of processing, performance, and economical considerations," *Journal of Materials in Civil Engineering*, vol. 23, no. 7, pp. 1036–1042, 2011.

[3] M. Green and J. E. Karsh, *Tall Wood-the Case for Tall Wood Buildings*, Wood Enterprise Coalition, Vancouver, Canada, 2012.

[4] S. Rittironk, *Investigating Laminated Bamboo Lumbers Available Structural Material in Architectural Application*, Illinois Institute of Technology, Chicago, IL, USA, 2009.

[5] S. Amada, Y. Ichikawa, T. Munekata, Y. Nagase, and K. Shimizu, "Fiber texture and mechanical graded structure of bamboo," *Composites Part B: Engineering*, vol. 28, no. 1-2, pp. 13–20, 1997.

[6] A. Porras and A. Maranon, "Development and characterization of a laminate com-posite material from polylactic acid (PLA) and woven bamboo fabric," *Composites Part B: Engineering*, vol. 43, no. 7, pp. 2782–2788, 2012.

[7] W. Fuli, Z. Shao, and W. Yijun, "Mode II interlaminar fracture properties of Moso bamboo," *Composites Part B: Engineering*, vol. 44, no. 1, pp. 242–247, 2013.

[8] L. Tingju, J. Man, J. Zhongguo, H. David, W. Zeyong, and Z. Zuowan, "Effect of surface modification of bamboo cellulose fibers on mechanical properties of cellulose/epoxy composites," *Composites Part B: Engineering*, vol. 51, pp. 28–34, 2013.

[9] F. Correal Juan, "Mechanical properties of Colombian glued laminated bamboo," in *Proceedings of the 1st International Conference on Modern Bamboo Structures (ICBS'07)*, pp. 121–127, Changsha, China, October 2007.

[10] Y. Wei, S. X. Jiang, Q. F. Lv, Q. S. Zhang, L. B. Wang, and Z. T. Lv, "Flexural performance of glued laminated bamboo beams," *Advanced Materials Research*, vol. 168–170, pp. 1700–1703, 2010.

[11] H.-T. Li, Q.-S. Zhang, D.-S. Huang, and A. J. Deeks, "Compressive per-formance of laminated bamboo," *Composites Part B: Engineering*, vol. 54, pp. 319–328, 2013.

[12] S. Arijit, W. Daniel, and M. Skyler, "Structural performance of glued laminated bamboo beams," *Journal of Structural Engineering*, vol. 140, no. 1, p. 04013021, 2014.

[13] H.-T. Li, J.-W. Su, Q.-S. Zhang, A. J. Deeks, and D. Hui, "Mechanical performance of laminated bamboo column under axial compression," *Composites Part B: Engineering*, vol. 79, pp. 374–382, 2015.

[14] Z. Aiping, H. Dongsheng, L. Haitao, and S. Yi, "Hybrid approach to determine mechanical parameters of fibers and matrixes of bamboo," *Construction and Building Materials*, vol. 35, pp. 191–196, 2012.

[15] D. S. Huang, A. P. Zhou, and Y. L. Bian, "Experimental and analytical study on the nonlinear bending of parallel strand bamboo beams," *Construction and Building Materials*, vol. 44, pp. 585–592, 2013.

[16] D. S. Huang, Y. L. Bian, A. P. Zhou et al., "Experimental study on stress-strain relationships and failure mechanisms of parallel strand bamboo made from phyllostachys," *Construction and Building Materials*, vol. 77, pp. 130–138, 2015.

[17] D. S. Huang, Y. L. Bian, D. M. Huang et al., "An ultimate-state-based-model for inelastic analysis of intermediate slenderness PSB columns under eccentrically compressive load," *Construction and Building Materials*, vol. 94, pp. 306–314, 2015.

[18] D. R. Rammer, "Parallel-to-grain dowel-bearing strength of two Guatemalan hardwoods," *Forest Products Journal*, vol. 49, no. 6, pp. 77–87, 2014.

[19] D. R. Rammer and S. G. Winistorfer, "Effect of moisture content on dowel bearing strength," *Wood and Fiber Science*, vol. 33, no. 1, pp. 126–139, 2001.

[20] K. Sawata and M. Yasumura, "Determination of embedding strength of wood for dowel-type fasteners," *Journal of Wood Science*, vol. 48, no. 2, pp. 138–146, 2002.

[21] S. Franke and N. Magnière, "The embedment failure of european beech compared to Spruce wood and standards," *Materials and Joints in Timber Structures*, vol. 9, no. 1, pp. 221–229, 2014.

[22] M. Schweigler, T. K. Bader, G. Hochreiner, G. Unger, and J. Eberhardsteiner, "Load-to-grain angle dependence of the embedment behavior of dowel-type fasteners in laminated veneer lumber," *Construction and Building Materials*, vol. 126, pp. 1020–1033, 2016.

[23] N. A. B. Seri, M. F. B. Nurddin, and R. B. Hassan, "Dowel-bearing strength properties of glulam with and without glue line made of Mengkulang species," in *InCIEC 2015*, pp. 725–734, Springer, Berlin, Germany, 2016.

[24] American Society for Testing and Materials, *Standard Test Method for Evaluating Dowel–Bearing Strength of Wood and Wood-Based Products (ASTM D5764-97a)*, ASTM, West Conshohocken, PA, USA, 2013.

[25] American Society for Testing and Materials, "ASTM D2395 Standard test methods for specific gravity of wood and wood-based materials," in *Annual Book of ASTM Standard*, ASTM, West Conshohocken, PA, USA, 2002.

[26] American Society for Testing and Materials, *ASTM D143-09 Standard Test Methods for Small Clear Specimens of Timber*, ASTM, West Conshohocken, PA, USA, 2009.

[27] British Standards Institution, BS EN 1995-1-1, *Eurocode 5: Design of Timber Structures-Part 1-1: General-Common Rules and Rules for Buildings*, BSI, London, UK, 2004.

[28] American National Standards Institute, *NDS-2015 National Design Specification for Wood Construction*, American Forest and Paper Association, Washington, DC, USA, 2012.

Hindawi
Advances in Materials Science and Engineering
Volume 2018, Article ID 3258123, 10 pages
https://doi.org/10.1155/2018/3258123

Research Article

Investigation on the Sulfuric Acid Corrosion Mechanism for Concrete in Soaking Environment

Hongguang Min[1,2,3] **and Zhigang Song**[3]

[1]*Guangdong Provincial Key Laboratory of Durability for Marine Civil Engineering, College of Civil Engineering, Shenzhen University, 3688 Nanhai Avenue, Shenzhen 518060, China*
[2]*Shenzhen Graduate School, Harbin Institute of Technology, Shenzhen 518055, China*
[3]*Faculty of Civil Engineering and Mechanics, Kunming University of Science and Technology, 727 South Jingming Road, Kunming 650500, China*

Correspondence should be addressed to Hongguang Min; minhongguang@163.com

Received 23 January 2018; Accepted 31 March 2018; Published 7 May 2018

Academic Editor: Estokova Adriana

This paper chooses the apparent diffusion coefficient for OH^- (hydroxyl ion) for concrete as an index to evaluate the corrosion degree of concrete subjected to sulfuric acid. Based on the reaction boundary layer theory, a sulfuric acid corrosion model for concrete was established and verified through experiments. The experiment design and data processing of sulfuric acid corrosion tests for concrete were carried out using uniform test design and nonparametric regression. Effects of water-cement ratio and pH value are presented on the sulfuric acid corrosion mechanism for concrete. Test results show that when the pH value was 2.50, the sulfuric acid corrosion degree of concrete was the most serious. The boundary layer effect always existed in the sulfuric acid corrosion for concrete, and the corrosion process included rapid and stable corrosion stages. The apparent diffusion coefficient for OH^- for concrete increased with the decrease of pH value and the increase of water-cement ratio and cement proportion.

1. Introduction

Aggressive sulfuric acid is mainly derived from acid rain, industrial environment, and sewage treatment systems [1–4]; further, the physical and chemical reactions between aggressive sulfuric acid and cement hydration products are primary reasons for durability failure of concrete structures [5]. For example, the pH value of inner concrete decreases in a sulfuric acid corrosion environment, which leads to the destruction of the passive film on the surface of reinforcement steel bars, followed by severe steel bar corrosion. Previous studies have shown that water-cement ratio, pH value, type and proportion of cement, coarse aggregate content, mineral admixture, and other factors have important effects on the sulfuric acid corrosion mechanism for concrete [6–13]. In fact, these factors will affect the pore structures of concrete, and the change of pore structures will significantly affect the transport performance of concrete [14–17], which results in a decline in concrete resistance to sulfuric acid corrosion. Being different from the mechanism of sulfate attack on concrete [11, 12, 18, 19], the sulfuric acid corrosion mechanism for concrete is the result of a combined action of dissolved corrosion caused by hydrogen ion (H^+) and expanded corrosion caused by SO_4^{2-} (sulfate ion) [20]. This finding led Böhm et al. [21] to propose a moving boundary diffusion model, which can be used to predict sulfide corrosion rate for concrete. Böhm et al. [21] also studied the influencing factors of sulfuric acid corrosion rate. Based on this, Böhm et al. [22] and Jahani et al. [23] predicted sulfuric acid corrosion rate and corrosion layer thickness for concrete and cement mortar through applying the moving boundary diffusion model [21], which were also verified by experiments. Overall, the sulfuric acid corrosion mechanism for concrete is complicated. This mechanism has been studied by different researchers from different aspects; however, differences between these research results still

exist. Therefore, the prediction model for concrete corrosion due to sulfuric acid needs to be further studied.

Based on the theory of reaction boundary layer, this paper presents a sulfuric acid corrosion model for concrete combined with the authors' previous research results [24]. Thus, the apparent diffusion coefficient of OH^- (hydroxyl ion) for concrete was analyzed, and the corresponding theoretical formula was also put forward. Long-term soaking tests for concrete subjected to sulfuric acid corrosion were carried out for 150 days through applying uniform design and nonparametric regression. This study's observations on the effects of water-cement ratio and pH value on concrete sulfuric acid corrosion mechanism led to an apparent diffusion coefficient for OH^- for concrete. At length, the sulfuric acid corrosion model for concrete was verified by experiments.

2. Sulfuric Acid Corrosion Model for Concrete

$Ca(OH)_2$ (calcium hydroxide) in concrete dissolves in water to form the saturated $Ca(OH)_2$ solution, which produces Ca^{2+} (calcium ion) and OH^- by ionization. Because of the existence of concentration gradient, Ca^{2+} and OH^- diffuse into the soaking solution through the corrosion layer from the inner concrete. However, H^+ (hydrogen ion) and SO_4^{2-} diffuse into the inner concrete through the corrosion layer from the soaking solution under the action of concentration gradient thereby forming the reaction boundary layer. On the outer boundary of the reaction boundary layer, the OH^- concentration is zero, and the H^+ concentration is the concentration of the soaking solution H^+; however, on the inner boundary of the noncorrosion surface, the H^+ concentration is zero, and the OH^- concentration is the concentration found in the saturated $Ca(OH)_2$ solution. The sulfuric acid corrosion for concrete occurs in the reaction boundary layer, as shown in Figure 1.

In the process of sulfuric acid corrosion for concrete, OH^- diffuses from interior to exterior of concrete under the action of concentration gradient and reacts with H^+ in the soaking solution to form the reaction boundary layer. Only when the OH^- of the concrete surface has been consumed by H^+ in the soaking solution, the excess of H^+ continue to spread to the inner concrete in the concentration gradient effect and further react with OH^- inner concrete. Therefore, the whole process of sulfuric acid corrosion relies on the dissolution of $Ca(OH)_2$ out of concrete and consumption by H^+ in the soaking solution.

Sulfuric acid corrosion for concrete belongs to strong acid corrosion. Sulfuric acid reacts with $Ca(OH)_2$ in concrete, and the dissolution of generated soluble calcium salts causes the reaction process to continue and the alkalinity of concrete to decrease. Reactions occurring in the reaction boundary layer formed by the sulfuric acid corrosion for concrete can be represented as

$$Ca^{2+} + 2OH^- + 2H^+ + SO_4^{2-} = CaSO_4 + 2H_2O. \quad (1)$$

According to (1), the mole ratio of OH^- and H^+ is 1 : 1 in the reaction process, so the apparent diffusion coefficient for concrete is considered to be a constant. Assuming that the concentration change of OH^- in the reaction boundary layer is consistent with the diffusion process of homogeneous reaction; then the whole diffusion process can be expressed as

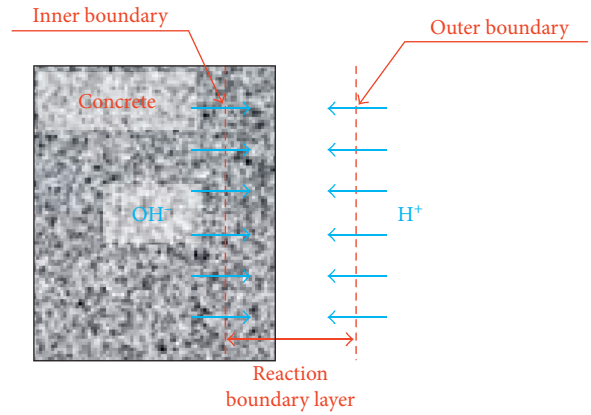

Figure 1: Reaction boundary layer of sulfuric acid corrosion on concrete.

$$\frac{\partial C_{OH^-}(x,\ t)}{\partial t} = D_{OH^-} \cdot \frac{\partial^2 C_{OH^-}(x,\ t)}{\partial x^2} - k \cdot C_{OH^-}(x,\ t) \cdot C_{H^+}(x,\ t), \quad (2)$$

where x is the distance of a point within the reaction boundary layer from the inner boundary (m), and t is the soaking time (s). k is the reaction rate constant for OH^- and H^+ ($L \cdot mol^{-1} \cdot s^{-1}$). Meanwhile, $C_{OH^-}(x,\ t)$ and $C_{H^+}(x,\ t)$ are the concentrations of OH^- and H^+ at location x and time t ($mol \cdot L^{-1}$), respectively. D_{OH^-} is the apparent diffusion coefficient for OH^- for concrete ($m^2 \cdot s^{-1}$).

Equation (3) gives the boundary conditions of (2) as

$$C_{OH^-}(0,\ t) = C_{OH^-};\ C_{OH^-}(\delta,\ t) = 0,$$
$$C_{H^+}(\delta,\ t) = C_{H^+};\ C_{H^+}(0,\ t) = 0, \quad (3)$$

where C_{OH^-} is the concentration of OH^- in the saturated $Ca(OH)_2$ solution ($mol \cdot L^{-1}$), C_{H^+} is the concentration of H^+ in the soaking solution ($mol \cdot L^{-1}$), and δ is the thickness of the reaction boundary layer (m).

Assuming that concentration distributions in the reaction boundary layer for OH^- and H^+ are satisfied, the following functions are derived as

$$C_{OH^-}(x,\ t) = C_{OH^-} \cdot \varphi(\theta);\ C_{H^+}(x,\ t) = C_{H^+} \cdot \psi(\theta),$$
$$\theta = \delta(t);\ \delta(0) = 0, \quad (4)$$

where $\varphi(\theta)$ and $\psi(\theta)$ are the shape functions of concentration distributions in the reaction boundary layer for OH^- and H^+, respectively. $\delta(t)$ is the thickness function of the reaction boundary layer.

Equations (3) and (4) show that $\varphi(\theta)$ and $\psi(\theta)$ must satisfy the following conditions as

$$\varphi(0) = 1;\ \varphi(1) = 0;\ \varphi'(1) = 0,$$
$$\psi(0) = 0;\ \psi(1) = 1;\ \psi'(0) = 0. \quad (5)$$

When combined with (2) and (4), the result can be shown as

$$\delta^{-1}(t)\cdot\int_0^1 -\theta\cdot\varphi'(\theta)\cdot d\theta\cdot\frac{d\delta(t)}{dt}=D_{OH^-}\cdot\delta^{-2}(t)\cdot\int_0^1\varphi''(\theta)\cdot d\theta-k\cdot C_{H^+}\cdot\int_0^1\varphi(\theta)\cdot\psi(\theta)\cdot d\theta, \quad (6)$$

which allows solving (6) as

$$\begin{aligned}\delta^2(t)&=N\cdot D_{OH^-}\cdot\left(k\cdot P\cdot C_{H^+}\right)^{-1}\\&\quad\cdot\left[1-\exp\left(-2k\cdot P\cdot C_{H^+}\cdot M^{-1}\cdot t\right)\right],\\M&=\int_0^1-\theta\cdot\varphi'(\theta)\cdot d\theta,\\N&=\int_0^1\varphi''(\theta)\cdot d\theta=\varphi'(\theta)\Big|_0^1=\varphi'(1)-\varphi'(0)=-\varphi'(0),\\P&=\int_0^1\varphi(\theta)\cdot\psi(\theta)\cdot d\theta.\end{aligned} \quad (7)$$

On the inner boundary within the reaction boundary layer, the relationship between the acid consumption rate of concrete and time can be expressed as

$$\begin{aligned}v_{H^+}(t)&=-S\cdot D_{OH^-}\cdot\frac{\partial C_{OH^-}(x,\ t)}{\partial x}\Big|_{x=0}\\&=-S\cdot D_{OH^-}\cdot C_{OH^-}\cdot\varphi'(0)\cdot\delta^{-1}(t),\end{aligned} \quad (8)$$

where S is the area of soaking surface (m^2), and $v_{H^+}(t)$ is the acid consumption rate of concrete, that is, H^+ consumption per unit time ($mol\cdot s^{-1}$).

Substituting (7) into (8) gives

$$\begin{aligned}v_{H^+}(t)&=A\cdot\left[1-\exp\left(-B\cdot t\right)\right]^{-1/2},\\A&=S\cdot C_{OH^-}\cdot\left(k\cdot N\cdot P\cdot D_{OH^-}\cdot C_{H^+}\right)^{1/2},\\B&=2k\cdot P\cdot C_{H^+}\cdot M^{-1}.\end{aligned} \quad (9)$$

Equation (9) shows that the acid consumption rate of concrete is relatively high in the initial reaction stage, decreases rapidly with the increase of reaction time, and will eventually become a constant, A. Hence, the whole process consists of two stages, that is, decline and stability. Then, the experimental study and theoretical analysis for concrete subjected to sulfuric acid corrosion can be carried as shown in Section 3.

3. Materials and Methods

3.1. Experimental Design and Specimen Preparation. The uniform test design method [25, 26] is a test design method that only considers the "uniform dispersion" of the test point in the test range. It is designed by the well-designed tables: the uniform design table. The uniform design table is usually represented by U_n (q^s), where U means uniform design, n means n tests, q indicates that every factor has q levels, and s indicates that the table has s columns, for example, U_8 (8^5), which means that 8 tests are required, each factor has 8 levels, the table has 5 columns, and a maximum of 5 factors. The biggest characteristic of uniform test design is that the number of tests required is usually equal to the level number of factors. When the test factors have the same level number, the uniform test design needs less tests than the orthogonal test design.

Considering the effects of the two factors of water-cement ratio and soaking solution's pH value on the sulfuric acid corrosion mechanism for concrete, both factors have eight levels (Table 1). Because this test is a problem of two factors and eight levels, enabling better test results with fewer test numbers, sulfuric acid corrosion tests for concrete were designed according to the uniform test design method, as shown in Table 2. Twenty-four concrete specimens were cast. The sizes were all 100 mm × 100 mm × 100 mm, and each kind of water-cement ratio consisted of three specimens. The continuous graded gravel of 5–16 mm was used as the coarse aggregate. The concrete mix proportions are in Table 3. Concrete specimens were taken out from the standard curing room after 28 days.

3.2. Sulfuric Acid Corrosion Tests for Concrete. Five surfaces of concrete specimens were sealed with paraffin, leaving only one surface as the exposed surface. Eight plastic boxes were used as the soaking pool, and three concrete specimens were placed into each soaking pool. In addition, the exposed surface of each concrete specimen was completely perpendicular to the bottom of the soaking pool. These specimens remained in their boxes and soaking for 150 days at room temperature, as shown in Figure 2.

The soaking solutions of sulfuric acid were prepared with different initial pH values by mixing the distilled water and concentrated sulfuric acid, and the volume of soaking solution of each group was always 10 L. The change of soaking solution's pH was measured by a portable pH meter in time, and then the soaking solution was titrated with sulfuric acid in time by a rubber head dropper and a cylinder so as to ensure the soaking solution's pH value was basically constant. At the same time, the liquid phase was stirred to ensure a uniform concentration of sulfuric acid throughout the volume of the liquid phase.

In the early stage of experiment, the soaking solution was titrated with sulfuric acid when the measured pH value was up to the titration pH value; however, in the final stage of experiment, even if the measured pH value was not up to the titration pH value, the soaking solution was still titrated with sulfuric acid to the initial pH value. Table 4 shows the titration pH value and titration sulfuric acid concentration. During the titration process, each titration time was recorded along with the amount of titration sulfuric acid, and the average acid consumption rate was obtained by dividing the amount of titration sulfuric acid at each interval based on the consecutive titration time periods.

4. Results and Discussion

4.1. Apparent Characteristics of Concrete Subjected to Sulfuric Acid Corrosion. After 150 days, the concrete specimens subjected to sulfuric acid corrosion were taken out with different water-cement ratios in the soaking solutions of different pH values. Figure 3 shows the apparent changes in

Table 1: Water-cement ratio and soaking solution's pH value.

Parameter	Level number							
	1	2	3	4	5	6	7	8
Water-cement ratio	0.70	0.65	0.60	0.55	0.50	0.45	0.40	0.35
pH value	4.00	3.70	3.40	3.10	2.80	2.50	2.20	2.00

Table 2: Uniform test design.

Parameter	Test number							
	1	2	3	4	5	6	7	8
Water-cement ratio	0.70	0.65	0.60	0.55	0.50	0.45	0.40	0.35
pH value	3.10	2.00	3.40	2.20	3.70	2.50	4.00	2.80

Table 3: Concrete mix proportions design ($kg \cdot m^{-3}$).

Material	Type	Water-cement ratio (w/c)							
		0.70	0.65	0.60	0.55	0.50	0.45	0.40	0.35
Water (w)	Tap water	210	210	210	210	210	210	215	168
Cement (c)	#425 OPC[1]	300	323	350	382	420	467	538	480
Fine aggregate (FA)	Artificial sand	765	739	676	665	618	586	528	532
Coarse aggregate (CA)	Gravel	1057	1063	1103	1085	1098	1089	1071	1131

[1]OPC represents ordinary Portland cement.

(a) (b)

Figure 2: Test layout for sulfuric acid corrosion on concrete: (a) specimens and (b) soaking pool.

the characteristics of concrete specimens. With the decrease of pH value, the color of each exposed surface of concrete specimen in turn was gray, yellow, and white. The gray surface indicated that the corrosion degree of the concrete specimen suffered sulfuric acid was light, and the color of the exposed surface was basically the same as the noncorrosion surface. The yellow surface revealed that the sulfuric acid corrosion degree was serious, and the surface of the concrete specimen had a loose yellow sand layer. The white surface shows that a large amount of $CaSO_4$ (calcium sulfate) was deposited on the concrete specimen surface. In the initial stage of the sulfuric acid corrosion of concrete, the reaction rate was very fast and a large amount of $CaSO_4$ was produced. At the same time, $CaSO_4$ blocked the surface pores of concrete specimen, which caused the corrosion reaction rate to gradually slow down, so the corrosion degree gradually decreased.

The sizes of concrete specimens were measured before and after sulfuric acid corrosion using a vernier caliper. These concrete specimen measurements of the average corrosion layer thicknesses' exposure to sulfuric acid after 150 days are shown in Figure 4. When the soaking solution's pH value was 2.50, the corrosion layer thickness was the largest, and the sulfuric acid corrosion degree was the most serious. When the soaking solution's pH value was between 2.50 and 4.00, with the decrease of pH value, the corrosion layer thickness increased, and the sulfuric acid corrosion degree became more and more serious. This may be because in the process of sulfuric acid corrosion for concrete, the formation rate of $CaSO_4$ was not much different from the dissolution rate, so the corrosion reaction continued into the concrete interior. However, the corrosion layer thickness decreased with the decrease of pH value when the soaking solution's pH value was between 2.00 and 2.50, leading to a progressively smaller sulfuric acid corrosion degree. This may be because the formation rate of $CaSO_4$ in the early corrosion reaction was far greater than its dissolution rate,

Table 4: Titration pH value and titration sulfuric acid concentration.

Test group	1	2	3	4	5	6	7	8
Water-cement ratio	0.40	0.50	0.60	0.70	0.35	0.45	0.55	0.65
Initial pH value	4.00	3.70	3.40	3.10	2.80	2.50	2.20	2.00
Titration pH value	5.00	4.00	3.60	3.30	3.00	2.70	2.30	2.10
Titration sulfuric acid concentration ($mol \cdot L^{-1}$)	0.125	0.125	0.125	0.125	0.125	0.500	0.500	0.500

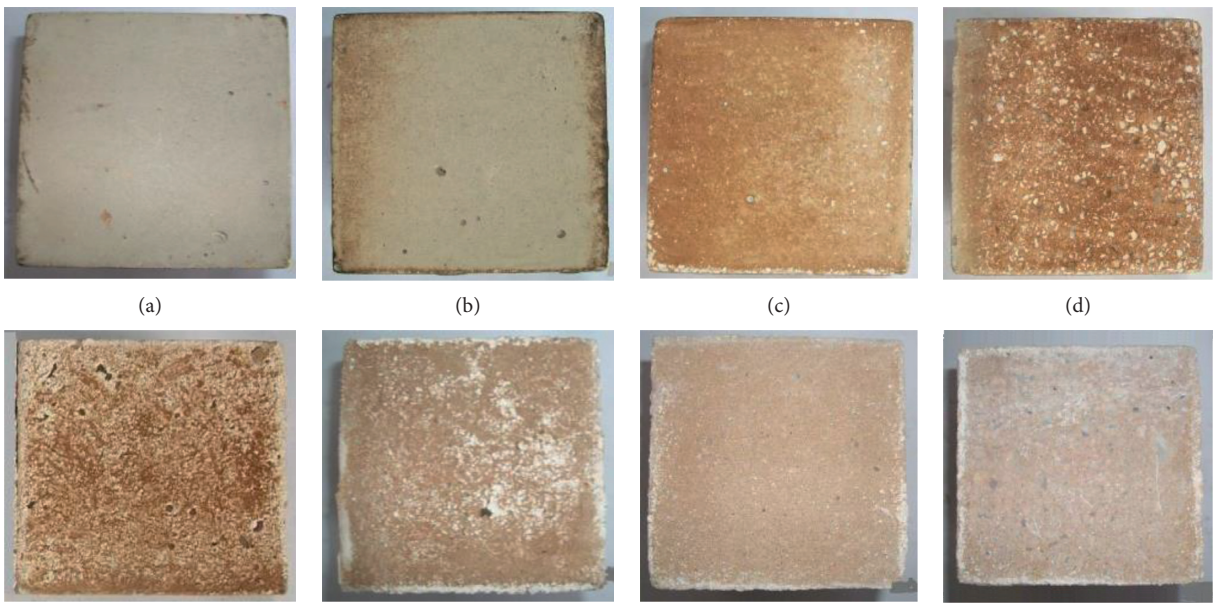

Figure 3: Apparent characteristics of concrete subjected to sulfuric acid corrosion after 150 days. (a) pH = 4.00, $w/c = 0.40$. (b) pH = 3.70, $w/c = 0.50$. (c) pH = 3.40, $w/c = 0.60$. (d) pH = 3.10, $w/c = 0.70$. (e) pH = 2.80, $w/c = 0.35$. (f) pH = 2.50, $w/c = 0.45$. (g) pH = 2.20, $w/c = 0.55$. (h) pH = 2.00, $w/c = 0.65$.

since the nondissolved $CaSO_4$ gradually deposited on concrete specimen surface, which blocked the surface pores and slowed down the corrosion reaction significantly.

4.2. Sulfuric Acid Corrosion Law for Concrete. According to the sulfuric acid corrosion tests for concrete, the acid consumption rate over time was measured as shown in Figure 5. The acid consumption rate of concrete in the early stage was relatively high, but it decreased rapidly and gradually stabilized with the corrosion reaction. The whole process consisted of two stages: the descending and stable periods. The cutoff point was approximately 800 hours. In addition, the lower the soaking solution's pH value was, the higher the initial acid consumption rate of concrete, leading to a greater sulfuric acid corrosion rate for concrete.

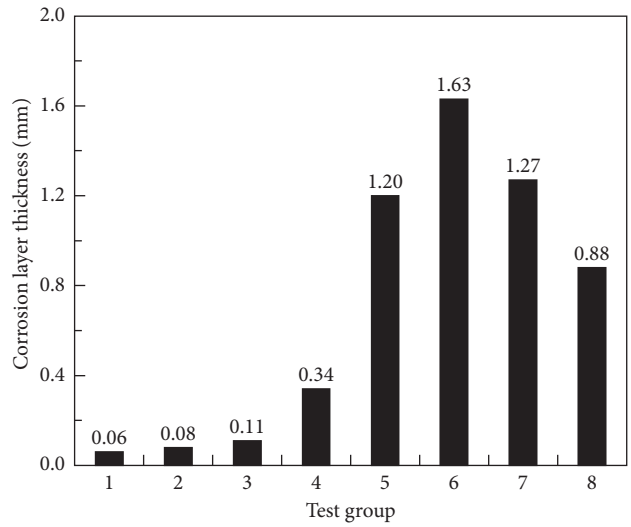

Figure 4: Corrosion layer thickness of concrete subjected to sulfuric acid corrosion after 150 days.

5. Verification of the Sulfuric Acid Corrosion Model and Determination of an Apparent Diffusion Coefficient for OH^- for Concrete

5.1. Verification of the Sulfuric Acid Corrosion Model for Concrete. To clearly show the variation law of the acid consumption rate of concrete over time, the measured data within 800 hours were fitted according to (9). The fitting parameters are seen in Table 5, and the fitting results are shown in Figure 6. Except for the last three groups of

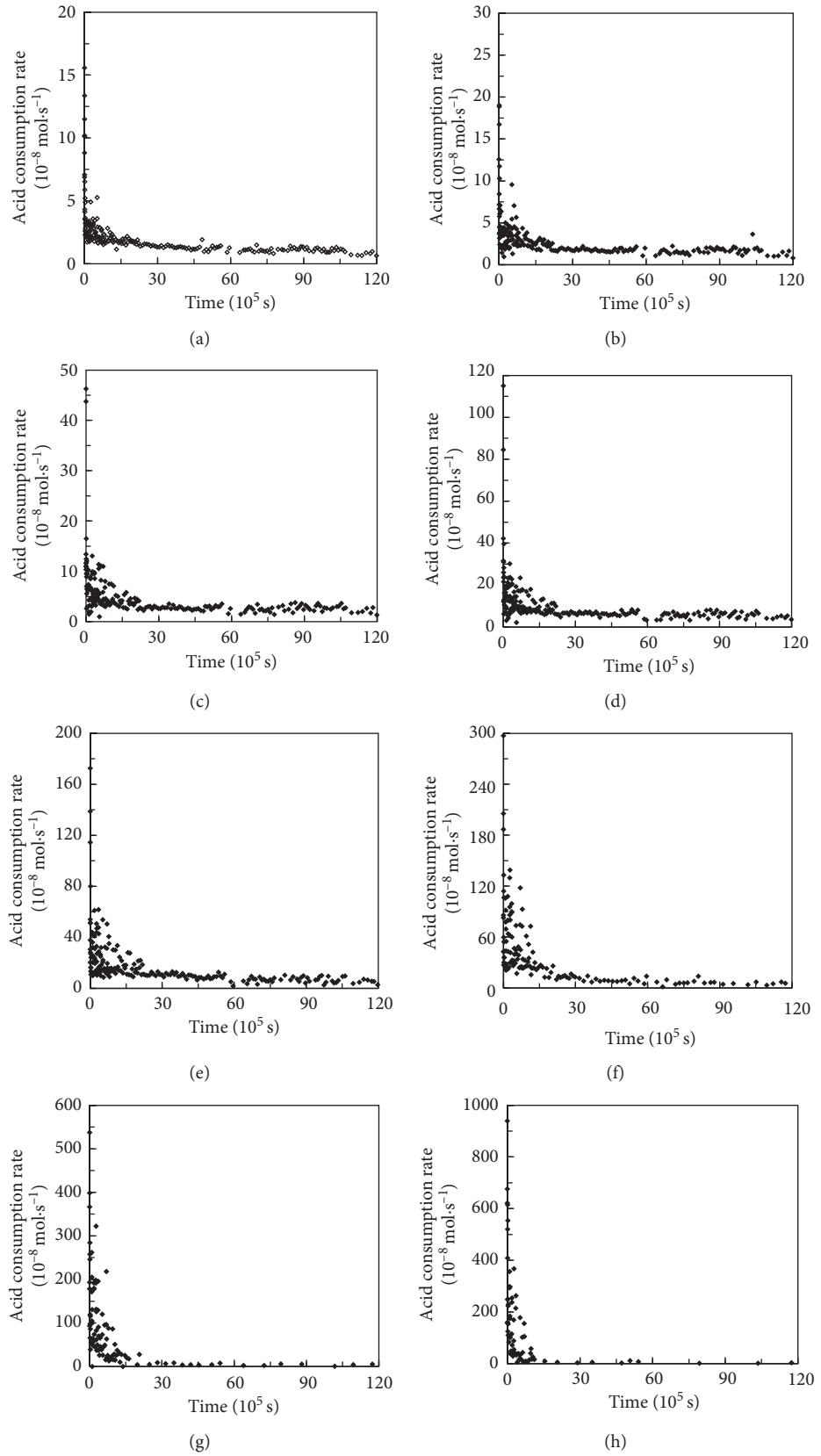

Figure 5: Relationship between the acid consumption rate and time. (a) pH = 4.00, $w/c = 0.40$. (b) pH = 3.70, $w/c = 0.50$. (c) pH = 3.40, $w/c = 0.60$. (d) pH = 3.10, $w/c = 0.70$. (e) pH = 2.80, $w/c = 0.35$. (f) pH = 2.50, $w/c = 0.45$. (g) pH = 2.20, $w/c = 0.55$. (h) pH = 2.00, $w/c = 0.65$.

experimental data, (9) gave all test specimens a higher fitting degree. The theoretical model can reflect the change law affecting the acid consumption rate over time, thereby verifying the accuracy of the theoretical model. When the soaking time was relatively long (200 hours), the measured values of the acid consumption rate were slightly lower than fitted values, and this trend was more obvious with the decrease of pH value in the soaking solution. This phenomenon is related to the flocculent $CaSO_4$ on the concrete surface, which is also called the boundary layer.

As the solubility of $CaSO_4$ decreases with the decrease of soaking solution pH value, the boundary layer thickness increases with the decrease of pH value. The presence of the boundary layer results in a decrease in the reaction rate, which slows down the formation rate of $CaSO_4$. At the same time, $CaSO_4$ is constantly dissolving out of the concrete to reduce the $CaSO_4$ concentration in the reaction boundary layer, resulting in the dissolution of the boundary layer, which increases the reaction rate. The deceleration or acceleration of the reaction rate caused by the formation or dissolution of the boundary layer will eventually reach a dynamic equilibrium.

5.2. Determination of an Apparent Diffusion Coefficient for OH^- for Concrete. Under a sulfuric acid corrosion environment, the dissolution of $Ca(OH)_2$ in concrete results in the change of concrete pore structures, which further results in the change of concrete's apparent diffusion coefficient. However, the apparent diffusion coefficient for concrete is difficult to measure directly, and then the formula for calculating the apparent diffusion coefficient for OH^- for concrete can be obtained by (9) as

$$D_{OH^-} = \frac{2A^2}{B \cdot S^2 \cdot C_{OH^-}{}^2 M \cdot N}. \tag{10}$$

Choosing a shape function which can satisfy (5) yields

$$\begin{aligned} \varphi(\theta) &= (1-\theta)^2, \\ \psi(\theta) &= \theta^2. \end{aligned} \tag{11}$$

Substituting (11) in (7) gives

$$\begin{aligned} M &= \frac{1}{3}, \\ N &= 2. \end{aligned} \tag{12}$$

Substituting (12) in (10) yields

$$D_{OH^-} = \frac{3A^2}{B \cdot S^2 \cdot C_{OH^-}{}^2}. \tag{13}$$

The total area S of the exposed surfaces of each group of concrete specimens was 0.03 m^2, and the concentration of OH^- in the saturated $Ca(OH)_2$ solution at 20°C was 0.045 $mol \cdot L^{-1}$; then, the apparent diffusion coefficients for OH^- for concrete were obtained by using Table 5 and (13), as shown in Figure 7. When the soaking solution's pH value was more than 2.50, the apparent diffusion coefficients for OH^- for concrete increased slowly with the decrease of pH value and then increased rapidly with the further decrease of pH value.

5.3. Effects of Water-Cement Ratio, Soaking Solution's pH Value, and Cement Proportion on the Apparent Diffusion Coefficient for OH^- for Concrete. Because the relationship was not directly determined between the apparent diffusion coefficient for OH^- for concrete and water-cement ratio, the soaking solution's pH value and cement proportion of $C/(C + FA + CA)$ required an analysis by ACE (alternating conditional expectation) regression [27] of nonparametric regression where x_1, x_2, x_3, and y are water-cement ratio, soaking solution's pH value, cement proportion, and $\ln(D_{OH^-} \times 10^{13})$, respectively. Searching for the transformation relations of $\varphi_1(x_1)$, $\varphi_2(x_2)$, $\varphi_3(x_3)$, and $\theta(y)$ which can satisfy the following mapping relation between input parameters of x_1, x_2, x_3, and function of y gave

$$\theta(y) = \varphi_1(x_1) + \varphi_2(x_2) + \varphi_3(x_3). \tag{14}$$

Thus, the function y was determined as

$$y = \theta^{-1}[\varphi_1(x_1) + \varphi_2(x_2) + \varphi_3(x_3)]. \tag{15}$$

The nonparametric regression analysis was performed using ACE. The fitting correlation coefficient was 0.9923, and the fitting effect was very good. Table 6 gives the values of each parameter before and after ACE regression, and (16) gives the mapping relations of $x_1 \sim \varphi_1(x_1)$, $x_2 \sim \varphi_2(x_2)$, $x_3 \sim \varphi_3(x_3)$, and $y \sim \theta(y)$ obtained using ACE. Figure 8 gives the relationship between the experimental and regression values for y, which is in good agreement with each other and has a positive proportion relationship. It can be seen from this that ACE has a very good practical value.

$$\begin{aligned} \varphi_1(x_1) &= 3.4610x_1 - 1.8173, \\ \varphi_2(x_2) &= -1.5847x_2 + 4.6946, \\ \varphi_3(x_3) &= 12.3549x_3 - 2.3583, \\ \theta(y) &= 0.3545y - 0.8446. \end{aligned} \tag{16}$$

Combined with (14) to (16) as

$$y = 9.76x_1 - 4.47x_2 + 34.85x_3 + 3.85. \tag{17}$$

Namely,

$$D_{OH^-} = 10^{-13} \times \exp\left(9.76\frac{w}{c} - 4.47\ \text{pH} + 34.85\frac{C}{C + FA + CA} + 3.85\right). \tag{18}$$

Equation (18) showed that when the pH value decreased, water-cement ratio and cement proportion increased; thus, the corrosion degree of concrete subjected to sulfuric acid increased in severity.

6. Conclusions

With the decrease of soaking solution's pH value, the color of the exposed concrete specimen surface changed from gray

Table 5: Fitting parameters.

Parameter	Test group							
	1	2	3	4	5	6	7	8
A (10^{-8} mol·s^{-1})	2.1938	2.9611	5.1368	11.2014	20.6806	42.8333	74.4444	100.8056
B (10^{-5} s^{-1})	8.2583	8.6528	13.1528	13.7472	14.4028	15.2111	12.2472	8.9056
R^2	0.9411	0.9520	0.8830	0.9157	0.8285	0.7160	0.5889	0.7013

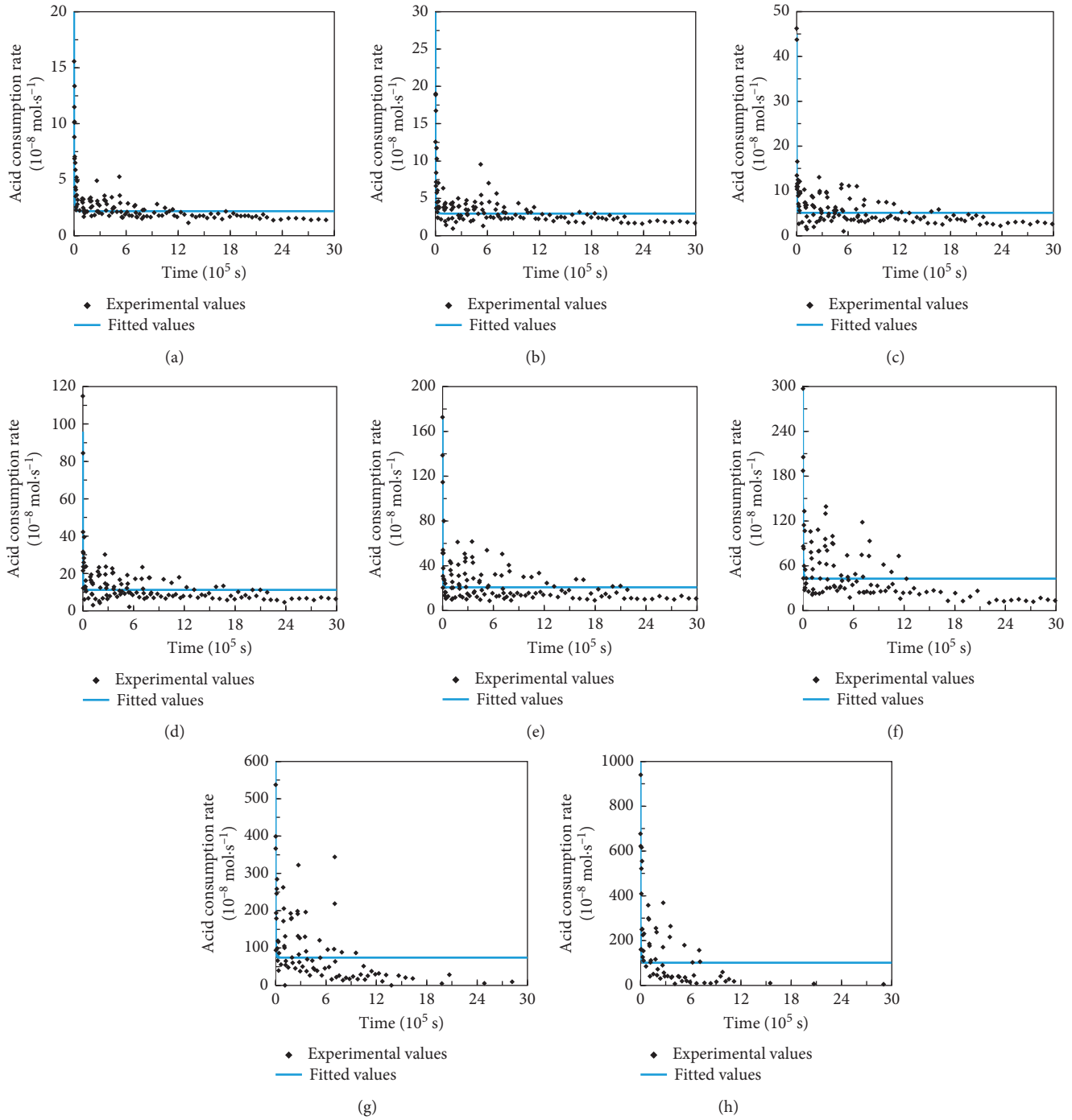

Figure 6: Comparison of the experimental and fitted values of acid consumption rate. (a) pH = 4.00, $w/c = 0.40$. (b) pH = 3.70, $w/c = 0.50$. (c) pH = 3.40, $w/c = 0.60$. (d) pH = 3.10, $w/c = 0.70$. (e) pH = 2.80, $w/c = 0.35$. (f) pH = 2.50, $w/c = 0.45$. (g) pH = 2.20, $w/c = 0.55$. (h) pH = 2.00, $w/c = 0.65$.

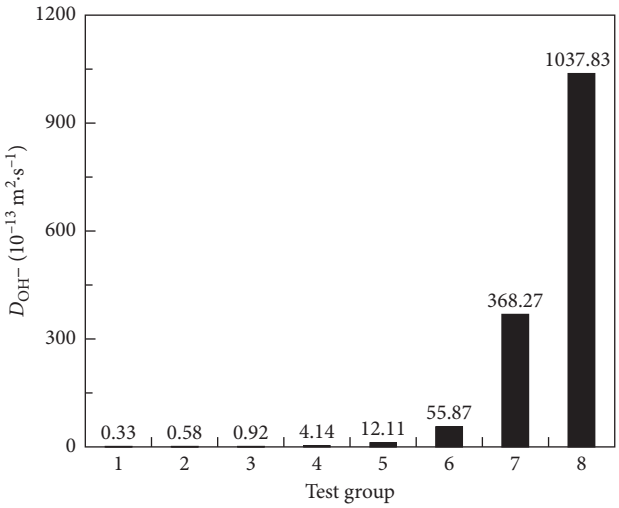

Figure 7: Apparent diffusion coefficient for OH^- for concrete.

Table 6: Values of each parameter before and after ACE regression.

Test group	x_1	$\varphi_1(x_1)$	x_2	$\varphi_2(x_2)$	x_3	$\varphi_3(x_3)$	y	$\theta(y)$
1	0.40	−0.4351	4.00	−1.5887	0.2516	0.7424	−1.0966	−1.2613
2	0.50	−0.0811	3.70	−1.1548	0.1966	0.0838	−0.5447	−1.0505
3	0.60	0.2589	3.40	−0.7209	0.1644	−0.3253	−0.0856	−0.8750
4	0.70	0.6036	3.10	−0.2655	0.1414	−0.6230	1.4195	−0.3164
5	0.35	−0.6082	2.80	0.2116	0.2240	0.4054	2.4942	0.0668
6	0.45	−0.2620	2.50	0.7093	0.2179	0.3361	4.0230	0.6052
7	0.55	0.0926	2.20	1.2307	0.1791	−0.1332	5.9088	1.2410
8	0.65	0.4313	2.00	1.5783	0.1520	−0.4864	6.9449	1.5903

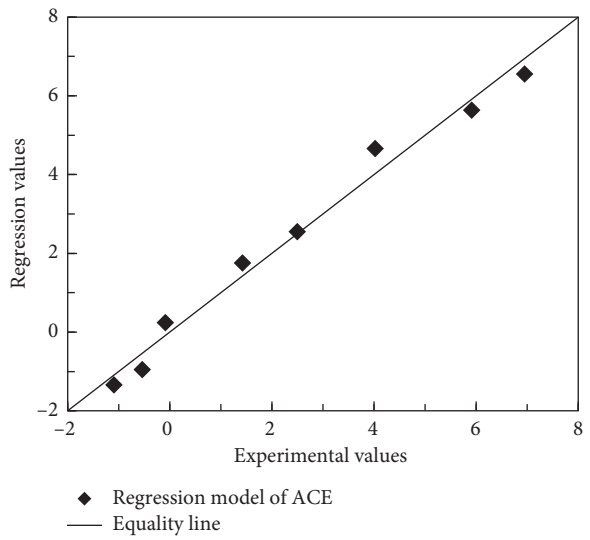

Figure 8: Comparison of the experimental and regression values for y.

to yellow and then to white. The corrosion layer thickness of the concrete specimen did not increase continuously with the decrease of pH value. When the soaking solution's pH value was 2.50, the corrosion layer thickness reached the maximum value, which means the sulfuric acid corrosion degree of concrete was the most serious.

A sulfuric acid corrosion model for concrete was established based on the reaction boundary layer theory and was solved by applying the separation of variables. Then, a theoretical formula for the acid consumption rate of concrete was obtained. The sulfuric acid corrosion process of concrete can be divided into two stages, namely, the rapid corrosion stage and the stable corrosion stage. Because of the effect of the boundary layer, the measured acid consumption rate of concrete was slightly lower than the theoretical value when the soaking time was relatively long. Through the sulfuric acid corrosion tests for concrete, the accuracy of the sulfuric acid corrosion model for concrete was verified. This model can be used to predict the sulfuric acid corrosion mechanism for concrete in practical engineering and to provide the foundation for steel corrosion prediction.

The sulfuric acid corrosion tests for concrete were planned using uniform design. The apparent diffusion coefficient for OH^- for concrete was chosen as the evaluation index for the sulfuric acid corrosion degree of concrete, and then the calculation formula was obtained through nonparametric regression. The results showed that the apparent diffusion coefficient for OH^- for concrete increased when the pH value decreased and the water-cement ratio and

cement proportion increased. The uniform design and nonparametric regression had a high efficiency in the experimental research and matched each other well, which was of great significance to this scientific research.

Data Availability

The data used to support the findings of this study are available from the corresponding author upon request.

Conflicts of Interest

The authors declare that they have no conflicts of interest.

Acknowledgments

This research was financially funded by the China Postdoctoral Science Foundation (2017M622789) and the National Natural Science Foundation of China (51078175).

References

[1] K. He, H. Yang, Z. B. Lu, F. F. Jia, E. P. Wang, and Q. X. Dong, "Effect of matrix modification on durability of cementitious composites in an acid rain environment," *Journal of Wuhan University of Technology–Materials Science Edition*, vol. 29, no. 3, pp. 498–503, 2014.

[2] M. P. Lavigne, A. Bertron, C. Botanch et al., "Innovative approach to simulating the biodeterioration of industrial cementitious products in sewer environment. Part II: validation on CAC and BFSC linings," *Cement and Concrete Research*, vol. 79, pp. 409–418, 2016.

[3] B. Huber, H. Hilbig, M. M. Mago, J. E. Drewes, and E. Müller, "Comparative analysis of biogenic and chemical sulfuric acid attack on hardened cement paste using laser ablation-ICP-MS," *Cement and Concrete Research*, vol. 87, pp. 14–21, 2016.

[4] N. De Belie, J. Monteny, A. Beeldens, E. Vincke, D. Van Gemert, and W. Verstraete, "Experimental research and prediction of the effect of chemical and biogenic sulfuric acid on different types of commercially produced concrete sewer pipes," *Cement and Concrete Research*, vol. 34, no. 12, pp. 2223–2236, 2004.

[5] P. K. Mehta, "Durability of concrete—fifty years of progress?," in *Proceeding of the 2nd International Conference on Concrete Durability ACI SP126–01*, pp. 1–32, Sapporo, Japan, 1991.

[6] Y. Yang, T. Ji, X. J. Lin, C. Y. Chen, and Z. X. Yang, "Biogenic sulfuric acid corrosion resistance of new artificial reef concrete," *Construction and Building Materials*, vol. 158, pp. 33–41, 2018.

[7] L. Gu, P. Visintin, and T. Bennett, "Evaluation of accelerated degradation test methods for cementitious composites subject to sulfuric acid attack, application to conventional and alkali-activated concretes," *Cement and Concrete Composites*, vol. 87, pp. 187–204, 2018.

[8] X. Li, Y. X. Lin, K. Lin, and T. Ji, "Study on the degradation mechanism of sulphoaluminate cement sea sand concrete eroded by biological sulfuric acid," *Construction and Building Materials*, vol. 157, pp. 331–336, 2017.

[9] E. Hewayde, M. Nehdi, E. Allouche, and G. Nakhla, "Effect of mixture design parameters and wetting-drying cycles on resistance of concrete to sulfuric acid attack," *Journal of Materials in Civil Engineering*, vol. 19, no. 2, pp. 155–163, 2007.

[10] Y. F. Fan, Z. Q. Hu, H. Y. Luan, D. W. Wang, and A. Chen, "A study of deterioration of reinforced concrete beams under various forms of simulated acid rain attack in the laboratory," *Structural Engineering and Mechanics*, vol. 52, no. 1, pp. 35–49, 2014.

[11] A. Grandclerc, P. Dangla, and M. Gueguen-Minerbe, "Modelling of the sulfuric acid attack on different types of cementitious materials," *Cement and Concrete Research*, vol. 105, pp. 126–133, 2018.

[12] J. Hill, E. A. Byars, J. H. Sharp, C. J. Lynsdale, J. C. Cripps, and Q. Zhou, "An experimental study of combined acid and sulfate attack of concrete," *Cement and Concrete Composites*, vol. 25, no. 8, pp. 997–1003, 2003.

[13] Z. T. Chang, X. J. Song, R. Munn, and M. Marosszeky, "Using limestone aggregates and different cements for enhancing resistance of concrete to sulphuric acid attack," *Cement and Concrete Research*, vol. 35, no. 8, pp. 1486–1494, 2006.

[14] H. G. Min, W. P. Zhang, and X. L. Gu, "Effects of load damage on moisture transport and relative humidity response in concrete," *Construction and Building Materials*, vol. 169, pp. 59–68, 2018.

[15] H. G. Min, W. P. Zhang, X. L. Gu, and R. Černý, "Coupled heat and moisture transport in damaged concrete under an atmospheric environment," *Construction and Building Materials*, vol. 143, pp. 607–620, 2017.

[16] W. P. Zhang, H. G. Min, and X. L. Gu, "Temperature response and moisture transport in damaged concrete under an atmospheric environment," *Construction and Building Materials*, vol. 123, pp. 290–299, 2016.

[17] W. P. Zhang, H. G. Min, X. L. Gu, Y. Xi, and Y. S. Xing, "Mesoscale model for thermal conductivity of concrete," *Construction and Building Materials*, vol. 98, pp. 8–16, 2015.

[18] S. Mirvalad and M. Nokken, "Studying thaumasite sulfate attack using compressive strength and ultrasonic pulse velocity," *Materials and Structures*, vol. 49, no. 10, pp. 4131–4146, 2016.

[19] M. O. Yusuf, "Performance of slag blended alkaline activated palm oil fuel ash mortar in sulfate environments," *Construction and Building Materials*, vol. 98, pp. 417–424, 2015.

[20] S. D. Xie, L. Qi, and D. Zhou, "Investigation of the effects of acid rain on the deterioration of cement concrete using accelerated tests established in laboratory," *Atmospheric Environment*, vol. 38, no. 27, pp. 4457–4466, 2004.

[21] M. Böhm, J. Devinny, F. Jahani, and G. Rosen, "On a moving-boundary system modeling corrosion in sewer pipes," *Applied Mathematics and Computation*, vol. 92, no. 2-3, pp. 247–269, 1998.

[22] M. Böhm, J. Devinny, F. Jahani, F. B. Mansfeld, I. G. Rosen, and C. Wang, "A moving boundary diffusion model for the corrosion of concrete wastewater systems: simulation and experimental validation," in *Proceedings of the American Control Conference*, pp. 1739–1743, San Diego, CA, USA, 1999.

[23] F. Jahani, J. Devinny, F. Mansfeld, and I. G. Rosen, "Investigations of sulfuric acid corrosion of concrete. I: modeling and chemical observations," *Journal of Environmental Engineering*, vol. 127, no. 7, pp. 572–579, 2001.

[24] Z. G. Song, X. S. Zhang, and H. G. Min, "Concentration boundary layer model of mortar corrosion by sulfuric acid," *Journal of Wuhan University of Technology–Materials Science Edition*, vol. 26, no. 3, pp. 527–532, 2011.

[25] K. T. Fang, *Uniform Design and Uniform Design Table*, Science Press, Beijing, China, 1994, in Chinese.

[26] K. T. Fang and C. X. Ma, *Orthogonal and Uniform Design of Experiments*, Science Press, Beijing, China, 2001, in Chinese.

[27] A. M. Hasofer and J. Qu, "Response surface modelling of monte carlo fire data," *Fire Safety Journal*, vol. 37, no. 8, pp. 772–784, 2002.

Hindawi
Advances in Materials Science and Engineering
Volume 2018, Article ID 6916258, 7 pages
https://doi.org/10.1155/2018/6916258

Research Article

Identification of Key Indicators for Sustainable Construction Materials

Humphrey Danso

Department of Construction and Wood Technology, University of Education Winneba, P.O. Box 1277, Kumasi, Ghana

Correspondence should be addressed to Humphrey Danso; dansohumphrey@yahoo.co.uk

Received 2 March 2018; Revised 26 March 2018; Accepted 10 April 2018; Published 26 April 2018

Academic Editor: Nadezda Stevulova

Studies on sustainable construction materials are on the rise with their environmental, social, and economic benefits. This study identifies the key indicators for measuring sustainable construction materials. The design used for the study was that of a survey which relied on a questionnaire with five-point Likert scale to generate data for the analysis. For this purpose, 25 indicators from the three dimensions (environmental, social, and economic) identified from the literature were presented to the respondents in a structured questionnaire, and responses were collected and analysed using SPSS. The study identified three key environmental indicators for measuring sustainable construction materials, and these indicators are human toxicity, climate change, and solid waste. Furthermore, adaptability, thermal comfort, local resources, and housing for all were identified as the four key social indicators for sustainable construction materials. In addition, maintenance cost, operational cost, initial cost, long-term savings, and life span were found to be the five key economic indicators for measuring sustainable construction materials. The study therefore suggests that these twelve indicators should be considered in future studies that seek to measure sustainable construction materials.

1. Introduction

The choice of construction materials has wide-reaching economic, environmental, and social consequence on any structure. The total cost of most structures depends greatly on the types of materials used. The energy consumption of any building has a significant relationship with the materials used for construction and the design of the building. Adaptability of some buildings by the society sometimes has bearing on the types of materials used. This therefore makes construction material an important factor in sustainable development. According to Ness et al. [1], sustainable development has been integrated into many aspects of the society in recent years. This has made the concept of sustainable development an important aspect of many industries worldwide [2]. According to Mailler [3], sustainability is an integrated concept, whereby environmental, social, and economic factors are interrelated. Sustainable development is a concept that is applicable in almost all fields of study and industry.

In the field of construction, sustainability is of great concern due to huge capital injunction and environmental factors coupled with societal adaptability. Construction materials and methodologies applied in building of structures have great influence in the sustainable development issues in the field of construction. Sustainable buildings take advantage of the natural resources available and depend on a "green" choice of materials [4]. According to Buildabroad [4], the availability of sustainable construction materials is on the rise, with new innovations and sourcing of materials that are not detrimental to the environment and are designed to enhance the energy efficiency of buildings. Sustainable construction materials are materials that are cost-effective and socially accepted and reduce negative environmental impacts, today and into the future during manufacturing and building structures. Peach [5] mentioned that sustainable construction materials include wool bricks, solar tiles, sustainable concrete, paper insulation, and triple-glazed windows. In low-income communities, earth-based technologies (such as rammed earth, compressed

Table 1: Some studies on the properties of sustainable construction materials produced with waste.

Material	Reference
Boron waste in soil bricks	[12]
Cassava peel in soil blocks	[13]
Coconut (coir) fibre in soil blocks	[14–17]
Coconut fibre in concrete	[18]
Waste paper in concrete	[19]
Waste paper in sandcrete blocks	[20]
Date palm in soil blocks	[21]
Flax (harakeke) in soil blocks	[22]
Hemp in concrete	[23]
Kenaf in soil blocks	[24]
Oil palm fibre in soil blocks	[25–27]
Pineapple leaves fibre in soil blocks	[28]
Plastic in soil blocks	[29–31]
Plastic in concrete	[32]
Sawdust in soil blocks	[33]
Scrap tire (crumb) rubber in soil blocks	[34, 35]
Seaweed fibre in soil blocks	[36]
Sheep wool in soil blocks	[37, 38]
Sisal fibre in soil blocks	[39]
Straw in soil blocks	[40–43]
Sugarcane bagasse ash in soil blocks	[44]
Sugarcane bagasse fibre in soil blocks	[14, 25]
Waste phosphogypsum and natural gypsum in soil blocks	[45]
Waste tea residue in soil bricks	[46]

earth blocks, and stabilised soil blocks) are the commonly used sustainable construction materials.

A number of studies [6–11] have reviewed the volume of literature in earth-based sustainable construction materials. Danso et al. [6] reviewed the existing published works on the effect of stabilisers (fibres and binders) on technical performance of soil blocks or bricks using parameters such as compressive strength, water absorption, and flexural strength. Delgado and Guerrero [7] also reviewed the state of use of the earth building in Spain which presented research organisations, modern projects carried out, and the existing manufacturers for compressed earth blocks, and also examined a pair of nonregulatory guides that could act as national reference documents. Hejazi et al. [8] reviewed the history, benefits, application, and possible executive problems of using different types of natural and/or synthetic fibres in soil reinforcement. Maniatidis and Walker [10] made a review of rammed earth construction by considering national codes, materials, structural design, construction, quality control, foundations, and maintenance. Pacheco-Torgal and Jalali [11] also reviewed some of the environmental benefits associated with earth construction including an overview about its past and present. They also included a review of economic issues, nonrenewable resource consumption, waste generation, energy consumption, carbon dioxide emissions, and indoor air quality.

The use of waste in producing sustainable construction materials is generating research interest in the last decade. Studies have investigated the properties of sustainable construction materials produced with waste in concrete or blocks. Table 1 outlines some of these studies and the types of sustainable construction materials they investigated.

It can be seen from Table 1 that some studies have investigated the properties of sustainable concrete with waste materials such as paper, plastic, and natural fibres. Earth-based construction materials have rather seen a large volume of research works. While rammed earth has also seen a number of studies into its properties, earth/soil blocks/bricks have recorded a massive investigation with different waste materials such as natural fibres, sawdust, scrap tire rubber, plastics, and animal wool fibres. All these studies contribute to the literature on sustainable construction materials.

Identifying and measuring the indicators for sustainable construction materials is relevant in placing construction material studies in the context of sustainable development. Danso [2] reviewed the general and relevant available indicators for measuring sustainable construction materials. However, there is lack of information on the most important sustainable indicators in relation with construction materials. This paper therefore identifies the key indicators for measuring sustainable construction materials.

2. Methodology

The design used for this study was that of a survey which relied on a questionnaire to generate data for the analysis. The questionnaire was developed, pretested to a sample of three experts in construction materials, and then modifications were made to obtain a more efficient instrument. A five-point Likert scale was used to measure the key indicators for sustainable construction materials. The Likert scale ranged from unimportant (1) to very important (5). Three main dimensions used are environmental, social, and economic. The environmental dimension consisted of eleven indicators, social dimension had eight indicators, and economic dimension had six indicators, making a total of 25 indicators. These indicators were adopted from the previous study [2] which reviewed the general and relevant available indicators for measuring sustainable construction materials. The indicators under their various dimensions are shown in Figure 1 which presents the hierarchical structure for construction material sustainability assessment. The questionnaire also asked the respondents to add any indicators they consider important and make any suggestions.

The population for the study was the professionals from the construction industry and academics who have researched and published in the area of construction and building materials. A purposive sampling technique was adopted to select the professional for data collection. The professionals were identified through their published materials (articles, books, and reports), and their email addresses noted. The questionnaire was designed with Adobe Acrobat Professional version 11, which made it easy to be emailed as an attachment to the respondents. In the email, the respondents were told to download, click preferred responses, save, and return by email. The questionnaire was administered to the construction professionals through their email addresses. After a month, a reminder was sent to those who have not responded. It must be noted that few emails

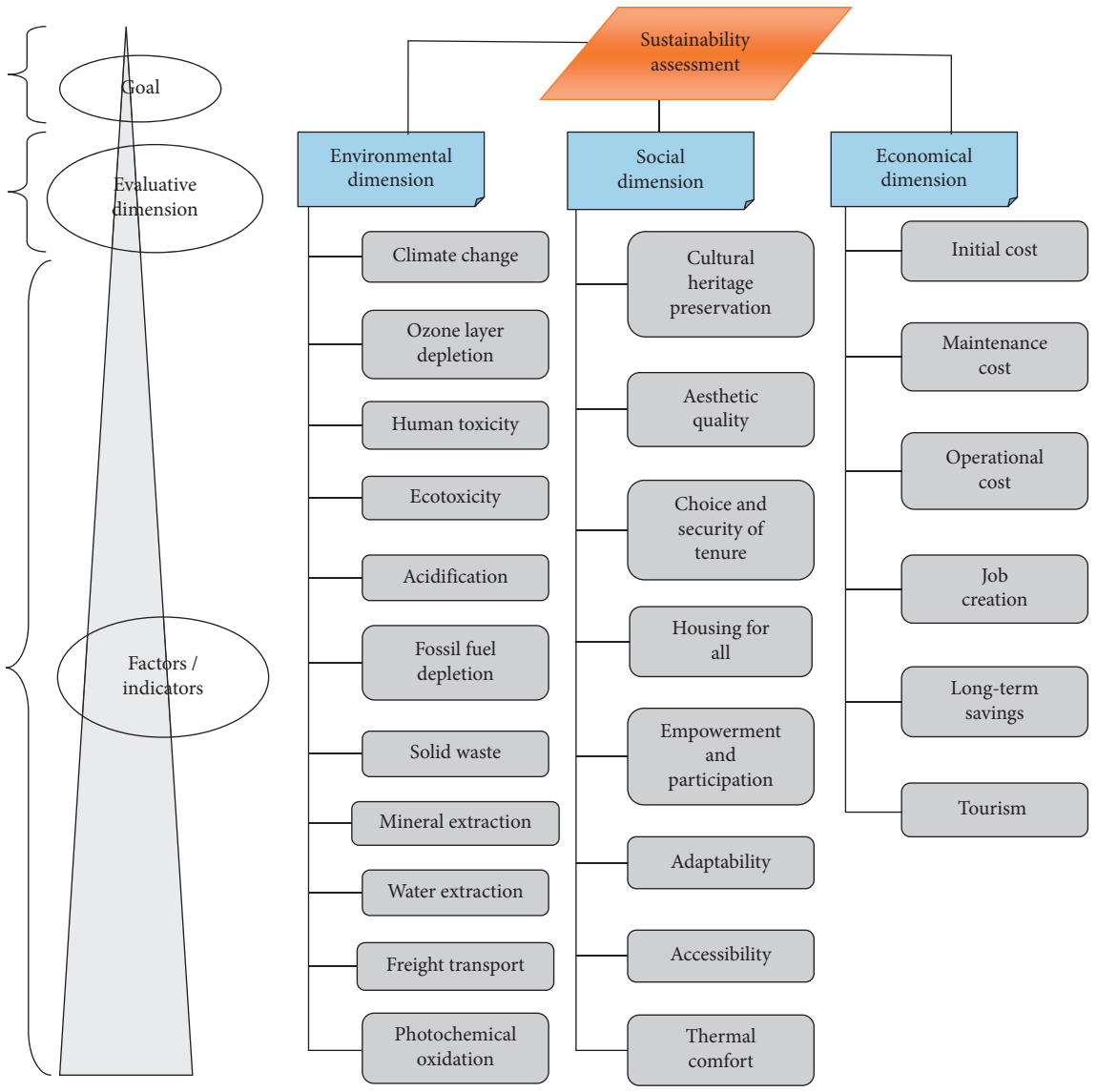

Figure 1: Hierarchical structure for construction material sustainability assessment [2].

were returned as error which might be due to invalid and wrong addresses.

The completed and returned questionnaires were downloaded, printed, and coded. The data obtained were analysed using the statistical package for social sciences (SPSS) version 22. The data from the questionnaire were inputted into SPSS and analysed by the use of descriptive statistics for obtaining the mean and standard deviation. In determining the key indicators for each dimension, a hypothesized mean of 4.000 and above was set as a critical cutoff point. It means that any indicator that recorded a mean of 4.000 or above was considered a key indicator, which the study identified as measuring sustainable construction materials. This represented the respondents' choice of indicators ranked between important and very important.

3. Results and Discussion

Out of the 115 questionnaires administered, 45 usable questionnaires were obtained, representing 39% response rate. Construct validity was also ensured by critically developing the indicators within an established theoretical framework. The Cronbach alpha reliability test for the items was above the recommended 0.7 [47]. From Table 2, all of the constructs have item loadings higher than the recommended 0.70. Data were analysed using descriptive analysis. The responses of the respondents are presented under three dimensions: (1) environmental, (2) social, and (3) economic.

3.1. Key Environmental Indicators. Table 3 presents the analysis of the environmental indicators of sustainable construction materials. The descriptive analysis shows that three items recorded mean values of 4.000 or more, which implies that the respondents rated the items between important and very important. The first ranked indicator for the environmental dimension is "human toxicity" with a mean value of 4.267. The following two indicators are "climate change" and "solid waste," both with a mean value of 4.000. The

Table 2: Item loading and construct reliability.

Dimension	Code	Indicators	Number of items	Cronbach alpha
Environmental	EN1	Climate change	11	0.734
	EN2	Ozone layer depletion		
	EN3	Human toxicity		
	EN4	Ecotoxicity		
	EN5	Acidification (acid deposit)		
	EN6	Fossil fuel depletion		
	EN7	Solid waste		
	EN8	Mineral extraction		
	EN9	Water extraction		
	EN10	Freight transport		
	EN11	Photochemical oxidation		
Social	SO1	Cultural heritage preservation	8	0.875
	SO2	Aesthetic quality		
	SO3	Choice and security of tenure		
	SO4	Housing for all		
	SO5	Empowerment and participation		
	SO6	Adaptability		
	SO7	Accessibility		
	SO8	Thermal comfort		
Economic	EC1	Initial cost	6	0.820
	EC2	Maintenance cost		
	EC3	Operational cost		
	EC4	Job creation		
	EC5	Long-term savings		
	EC6	Tourism		

Table 3: Descriptive statistics on environmental indicators ($n = 45$).

Indicator	$\overline{x}$	σ	R
Human toxicity	4.267*	1.009	1
Climate change	4.000*	1.108	2
Solid waste	4.000*	0.739	2
Ecotoxicity	3.933	0.780	3
Water extraction	3.867	0.815	4
Photochemical oxidation	3.800	1.057	5
Acidification	3.667	1.023	6
Fossil fuel depletion	3.667	1.023	6
Ozone layer depletion	3.667	1.087	6
Mineral extraction	3.600	0.963	7
Freight transport	3.000	0.826	8

*Key indicator, mean ≥ 4.000.

other environmental indicators (ecotoxicity, water extraction, photochemical oxidation, acidification, fossil fuel depletion, ozone layer depletion, mineral extraction, and freight transport) recorded values less than the hypothesized mean.

From the results, it can be seen that three indicators were identified as the key environmental sustainable construction materials. These indicators are human toxicity, climate change, and solid waste. Human toxicity aims to quantify the degree to which a particular substance causes damage to living organisms. Assessments of toxicity are based on guidelines for tolerable concentrations in air and water, tolerable daily intake, and acceptable daily intake for human toxicity [48]. Many of the chemicals used in the society have not undergone a risk assessment, and assessment techniques are still developing, something that manufacturers of construction products should also be aware of [48]. Issues relating to toxicity generate much debate in the construction industry, especially manufacturing of construction materials and their disposal after demolition. Users of construction materials should carefully review the material supplier's guidance and note any relevant regulations, codes, and standards appropriately. They should also consider the context and application within which the materials are to be used to ensure that industry-specific regulations or standards are complied with.

Climate change refers to the change in global temperature caused by the greenhouse effect by the release of "greenhouse gases" such as carbon dioxide by human activity. There is now scientific consensus that the increase in these emissions is having a noticeable effect on climate. Raised global temperature is expected to cause climatic disturbance, desertification, rising sea levels, and spread of disease [49]. Embodied carbon is the carbon dioxide (CO_2) or greenhouse gas (GHG) emissions associated with the manufacture and use of a product or service. For construction products, this means the CO_2 or GHG emissions associated with extraction, manufacturing, transporting, installing, maintaining, and disposing of construction materials and products [48].

Solid waste represents the environmental issues associated with the loss of resource implied by the final disposal of waste, and any waste that is disposed of in landfill or incinerated without energy recovery. The characterisation methodologies, for example, the Dutch EcoIndicator30 and the Swiss Ecopoints31, and the characterisation factors are based on the mass of solid waste [49]. Solid waste generated by construction materials is huge, from manufacturing of the materials, application of the materials, and disposal of the demolished structures.

3.2. Key Social Indicators. The analysis of the social indicators of sustainable construction materials can be seen in Table 4. The result indicates that four indicators were rated by the respondents as the key indicators within the theoretical mean of 4.000. "Adaptability" was the first ranked indicator with a mean value of 4.133. The second ranked indicator was "thermal comfort" with a mean value of 4.067. The next ranked indicators were "local resources" and "housing for all," both with a mean value of 4.000. Indicators such as cultural heritage, social value, choice and security of tenure, accessibility, empowerment and participation, and aesthetic quality had values less than the hypothetical mean.

Adaptable buildings are defined as "dynamic systems that carry the capacity to accommodate a set of evolving demands

Table 4: Descriptive statistics on social indicators ($n = 45$).

Indicator	$\overline{x}$	σ	R
Adaptability	4.133*	0.815	1
Thermal comfort	4.067*	0.939	2
Local resources	4.000*	0.977	3
Housing for all	4.000*	1.108	3
Cultural heritage	3.867	1.217	4
Social value	3.733	0.688	5
Choice and security of tenure	3.733	0.939	5
Accessibility	3.600	1.095	6
Empowerment and participation	3.600	1.156	6
Aesthetic quality	3.533	0.815	7

*Key indicator, mean ≥ 4.000.

Table 5: Descriptive statistics on economic indicators ($n = 45$).

Indicator	$\overline{x}$	σ	R
Maintenance cost	4.400*	0.889	1
Operational cost	4.400*	0.889	1
Initial cost	4.400*	0.889	1
Long-term savings	4.333*	0.879	2
Life span	4.067*	1.136	3
Job creation	3.667	1.087	4
Tourism	2.800	0.919	5

*Key indicator, mean ≥ 4.000.

regarding space, function, and components [50]". To ensure sustainability, building materials must build in adaptability to both its existing and new buildings. Buildings are more likely to be occupied and reused if they can be easily adapted to meet changing needs [51]. Buildings which are unable to adapt with such changing needs will become obsolete or require substantial refurbishment or demolition, where neither option may create a sustainable built environment [52].

Thermal comfort is the condition of mind which expresses satisfaction with the thermal environment [53], that is, the condition when someone is not feeling either too hot or too cold [54]. Building materials contribute greatly to thermal comfort of any structure. Adaptive thermal comfort broadens understanding of the human comfort zone by taking into account the ways that people's perceptions of their environment change based on seasonal expectations of temperature and humidity [55]. It is an undeniable fact (especially in warm climate areas) that houses built with local materials have cool room temperature particularly with houses built with soil or earth and thatches [56]. The consideration of thermal comforts is therefore important when selecting construction materials.

Local resources (materials) are usually available and affordable in most localities. Nature has provided mankind with some wonderful materials to build houses, and these materials require little processing or transporting and the costs are low [57]. It is important to identify and use locally manufactured and available materials (sand, stones, grass, thatches, clay, timber, clay bricks, and clay blocks) in providing houses especially in the developing countries in order to meet their housing demand [56].

"Housing for all" is a concept that describes the situation of ensuring that housing becomes affordable and available to every individual. Housing for all is therefore associated with affordable or low-cost housing. UN Habitat [58] defined affordable housing as a house that is adequate in quality and location and does not cost such that it prohibits its occupants from meeting other living costs and threatens their enjoyment of basic human rights. Low-cost housing on the other hand is a housing concept whose total cost for purchase or rent is deemed affordable for those in the median income bracket [59, 60]. The factors that contribute to housing for all include cost of materials, cost of labour, and cost of land, among others. The cost of construction materials constitutes between 60% and 70% of the cost of a building in developing countries [61]. Therefore, reduction of the material cost will invariably help in promoting housing for all.

3.3. Key Economic Indicators. Descriptive analysis of the economic indicators of sustainable construction materials is shown in Table 5. Five indicators were identified by the respondents as key economic factors of sustainable construction materials. These are maintenance cost, operational cost, initial cost, long-term savings, and life span, which recorded a mean value above 4.000 by the respondents. Indicators such as job creation and tourism obtained mean values below the hypothesized mean.

The maintenance cost of building components is the cost involved in the process of sustaining the performance of a building in accordance with the documented design and the operational needs. This process involves a set of activities that help in sustaining a building's components. Sahely et al. [62] opined that economic indicators such as operation and maintenance costs continue to play an important role in decision making as part of a larger set of indicators. Maintenance cost involves the cost of caring for the components of building to ensure reliability and prevention of failure.

The operational cost is the cost incurred in the day-to-day running or operation of the building. The operational cost includes mortgage payments, building insurance, taxes, maintenance and repair cost, and general and administrative expenses [54].

Initial costs are the costs that are incurred during the design and construction process. The initial cost of construction project includes the cost at the following stages of construction: planning, preliminary, design, and construction. The initial cost includes the cost of acquiring land and cost of materials for constructing the structures.

Long-term savings is critical in reducing the running cost of any structure. Construction materials and components with a long-term savings and low-maintenance effort reduce investments for maintenance, replacement, and renovation. While some sustainable materials may require greater upfront costs, they bring with them long-term savings due to reduced energy and transportation costs, as well as being beneficial for the environment in the long term [4].

4. Summary and Conclusion

The aim of this paper was to identify the key indicators for measuring sustainable construction materials. This study

was based on the three main dimensions of sustainable development, which are environmental, social, and economic. The study adopted 25 indicators from the literature out of which the respondents identified twelve (12) as key indicators for measuring sustainable construction materials. These include three key environmental indicators for measuring sustainable construction materials, which are human toxicity, climate change, and solid waste. Furthermore, adaptability, thermal comfort, local resources, and housing for all were identified as the four key social indicators for sustainable construction materials. In addition, maintenance cost, operational cost, initial cost, long-term savings, and life span were found to be the five key economic indicators for measuring sustainable construction materials. The study therefore suggests that these twelve indicators should be considered in future for any study that seeks to measure sustainable construction materials.

Data Availability

The data used to support the findings of this study are available from the corresponding author upon request.

Conflicts of Interest

The authors declare that they have no conflicts of interest.

References

[1] B. Ness, E. Urbel-Piirsalu, S. Anderberg, and L. Olsson, "Categorising tools for sustainability assessment," *Ecological Economics*, vol. 60, no. 3, pp. 498–508, 2007.

[2] H. Danso, "Dimensions and indicators for sustainable construction materials: a review," *Research and Development in Material Science*, vol. 3, no. 4, pp. 1–9, 2018.

[3] M. Mailler, "Sustainability assessment of an IAIA educational & networking forum," in *Proceedings of 28th Annual Conference of the International Association for Impact Assessment*, Perth, Australia, May 2008.

[4] Buildabroad, *Sustainable Materials: The Backbone of Any Sustainable Building Project*, 2017, https://buildabroad.org/2017/08/15/sustainable-materials.

[5] J. Peach, *Five Sustainable Building Materials that Could Transform Construction*, 2010, http://thisbigcity.net/five-sustainable-building-materials-that-could-transform-construction.

[6] H. Danso, B. Martinson, M. Ali, and C. Mant, "Performance characteristics of enhanced soil blocks: a quantitative review," *Building Research and Information*, vol. 43, no. 2, pp. 253–262, 2015.

[7] M. C. J. Delgado and I. C. Guerrero, "Earth building in Spain," *Construction and Building Materials*, vol. 20, no. 9, pp. 679–690, 2006.

[8] S. M. Hejazi, M. Sheikhzadeh, S. M. Abtahi, and A. Zadhoush, "A simple review of soil reinforcement by using natural and synthetic fibres," *Construction and Building Materials*, vol. 30, pp. 100–116, 2012.

[9] J. M. Khatib, *Sustainability of Construction Materials*, Woodhead Publishing, CRC Press, Cambridge, UK, 2009.

[10] V. Maniatidis and P. Walker, *A Review of Rammed Earth Construction*, University of Bath, Bath, UK, 2003.

[11] F. Pacheco-Torgal and S. Jalali, "Earth construction: lessons from the past for future eco-efficient construction," *Construction and Building Materials*, vol. 29, pp. 512–519, 2012.

[12] T. Kavas, "Use of boron waste as a fluxing agent in production of red mud brick," *Building and Environment*, vol. 41, no. 12, pp. 1779–1783, 2006.

[13] M. C. N. Villamizar, V. S. Araque, C. A. R. Reyes, and R. S. Silva, "Effect of the addition of coal-ash and cassava peels on the engineering properties of compressed earth blocks," *Construction and Building Materials*, vol. 36, pp. 276–286, 2012.

[14] H. Danso, B. Martinson, M. Ali, and J. B. Williams, "Effect of sugarcane bagasse fibre on the strength properties of soil blocks," in *Proceedings of 1st International Conference on Bio-based Building Materials*, Clermont-Ferrand, France, June 2015.

[15] B. Gaw and S. Zamora, *Soil Reinforcement with Natural Fibers for Low-Income Housing Communities*, MSc thesis, Worcester Polytechnic Institute, Worcester, MA, USA, 2011.

[16] J. I. Aguwa, "Study of coir reinforced laterite blocks for buildings," *Journal of Civil Engineering and Construction Technology*, vol. 4, pp. 110–115, 2013.

[17] M. G. Sreekumar and D. G. Nair, "Stabilized lateritic blocks reinforced with fibrous coir wastes," *International Journal of Sustainable Construction Engineering and Technology*, vol. 4, pp. 23–32, 2013.

[18] P. P. Yalley, *Use of Waste and Low Energy Materials in Construction*, Lambert Academic Publishing, Saarbrücken, Germany, 2012.

[19] I. I. Akinwumi, O. M. Olatunbosun, O. M. Olofinnade, and P. O. Awoyera, "Structural evaluation of lightweight concrete produced using waste newspaper and office paper," *Civil and Environmental Research*, vol. 6, pp. 160–167, 2014.

[20] H. Yun, H. Jung, and C. Choi, "Mechanical properties of papercrete containing waste paper," in *Proceedings of 18th International Conference on Composite Materials*, Jeju Province, Republic of Korea, August 2011.

[21] B. Taallah, A. Guettala, S. Guettala, and A. Kriker, "Mechanical properties and hygroscopicity behavior of compressed earth block filled by date palm fibers," *Construction and Building Materials*, vol. 59, pp. 161–168, 2014.

[22] T. M. Le and K. L. Pickering, "The potential of harakeke fibre as reinforcement in polymer matrix composites including modelling of long harakeke fibre composite strength," *Composites Part A: Applied Science and Manufacturing*, vol. 76, pp. 44–53, 2015.

[23] S. Elfordy, F. Lucas, F. Tancret, Y. Scudeller, and L. Goudet, "Mechanical and thermal properties of lime and hemp concrete ("hempcrete") manufactured by a projection process," *Construction and Building Materials*, vol. 22, no. 10, pp. 2116–2123, 2008.

[24] Y. Millogo, J. E. Aubert, E. Hamard, and J. C. Morel, "How properties of kenaf fibers from Burkina Faso contribute to the reinforcement of earth blocks," *Materials*, vol. 8, no. 5, pp. 2332–2345, 2015.

[25] H. Danso, D. B. Martinson, M. Ali, and J. Williams, "Effect of fibre aspect ratio on mechanical properties of soil building blocks," *Construction and Building Materials*, vol. 83, pp. 314–319, 2015.

[26] S. Ismail and Z. Yaacob, "Properties of laterite brick reinforced with oil palm empty fruit bunch fibres," *Pertanika Journal of Science and Technology*, vol. 19, pp. 33–43, 2011.

[27] S. M. Marandi, M. H. Bagheripour, R. Rahgozar, and H. Zare, "Strength and ductility of randomly distributed palm fibers

reinforced silty-sand soils," *American Journal of Applied Sciences*, vol. 5, no. 3, pp. 209–220, 2008.

[28] C. M. Chan, "Effect of natural fibers inclusion in clay bricks: physico-mechanical properties," *International Journal of Civil and Environmental Engineering*, vol. 3, pp. 51–57, 2011.

[29] P. P. Yalley and A. S. K. Kwan, "Use of waste and low energy materials in building block construction," in *Proceedings of 25th Conference on Passive and Low Energy Architecture (PLEA)*, Dublin, Ireland, June 2008.

[30] C. K. Subramaniaprasad, B. M. Abraham, and E. K. K. Nambiar, "Sorption characteristics of stabilised soil blocks embedded with waste plastic fibres," *Construction and Building Materials*, vol. 63, pp. 25–32, 2014.

[31] J. Cid-Falceto, F. R. Mazarrón, and I. Cañas, "Assessment of compressed earth blocks made in Spain: international durability tests," *Construction and Building Materials*, vol. 37, pp. 738–745, 2012.

[32] M. Raghatate Atul, "Use of plastic in a concrete to improve its properties," *International Journal of Advanced Engineering Research and Studies*, vol. 1, pp. 109–111, 2012.

[33] B. R. T. Vilane, "Assessment of stabilisation of adobes by confined compression tests," *Biosystems Engineering*, vol. 106, no. 4, pp. 551–558, 2010.

[34] S. Akbulut, S. Arasan, and E. Kalkan, "Modification of clayey soils using scrap tire rubber and synthetic fibers," *Applied Clay Science*, vol. 38, no. 1-2, pp. 23–32, 2007.

[35] P. Turgut and B. Yesilata, "Physico-mechanical and thermal performances of newly developed rubber-added bricks," *Energy and Buildings*, vol. 40, no. 5, pp. 679–688, 2008.

[36] M. Achenza and L. Fenu, "On earth stabilization with natural polymers for earth masonry construction," *Materials and Structures*, vol. 39, no. 1, pp. 21–27, 2006.

[37] F. Aymerich, L. Fenu, and P. Meloni, "Effect of reinforcing wool fibres on fracture and energy absorption properties of an earthen material," *Construction and Building Materials*, vol. 27, no. 1, pp. 66–72, 2012.

[38] C. Galán-Marín, C. Rivera-Gómez, and J. Petric, "Clay-based composite stabilised with natural polymer and fibre," *Construction and Building Materials*, vol. 24, no. 8, pp. 1462–1468, 2010.

[39] S. S. Namango and D. S. Madara, "Compressed earth blocks reinforced with sisal fibres," *Journal of Agricultural Pure Applied Science and Technology*, vol. 19, pp. 10–22, 2014.

[40] W. Quagliarini and S. Lenci, "The influence of natural stabilisers and natural fibres on the mechanical properties of ancient Roman adobe bricks," *Journal of Cultural Heritage*, vol. 11, no. 3, pp. 309–314, 2010.

[41] S. Yetgin, O. Cavdar, and A. Cavdar, "The effects of the fiber contents on the mechanic properties of the adobes," *Construction and Building Materials*, vol. 22, no. 3, pp. 222–227, 2008.

[42] F. Parisi, D. Asprone, L. Fenu, and A. Prota, "Experimental characterization of Italian composite adobe bricks reinforced with straw fibers," *Composite Structures*, vol. 122, pp. 300–307, 2015.

[43] A. Laborel-Préneron, J.-E. Aubert, C. Magniont, P. Maillard, and C. Poirier, "Effect of plant aggregates on mechanical properties of earth bricks," *American Society of Civil Engineers*, vol. 29, no. 12, p. 04017244, 2017.

[44] S. A. Lima, H. Varum, A. Sales, and V. F. Neto, "Analysis of the mechanical properties of compressed earth block masonry using the sugarcane bagasse ash," *Construction and Building Materials*, vol. 35, pp. 829–837, 2012.

[45] N. Degirmenci, "The using of waste phosphogypsum and natural gypsum in adobe stabilization," *Construction and Building Materials*, vol. 22, no. 6, pp. 1220–1224, 2008.

[46] I. Demir, "An investigation on the production of construction brick with processed waste tea," *Building and Environment*, vol. 41, no. 9, pp. 1274–1278, 2006.

[47] D. Straub, M. Boudreau, and D. Gefen, "Validation guidelines for IS positivist research," *Communications of the Association for Information Systems*, vol. 13, pp. 380–427, 2004.

[48] J. Anderson and J. Thornback, *A Guide to Understanding the Embodied Impacts of Construction Products*, Construction Products Association, London, UK, 2012.

[49] BRE, *Methodology for Environmental Profiles of Construction Products: Product Category Rules for Type III Environmental Product Declaration of Construction Products (Draft)*, 2007.

[50] Adaptable Futures, *Homepage of adaptable futures*, 2012, http://www.adaptablefutures.com.

[51] E. Annex, *Buildings–Adaptability, Durability and Materials*, 2015, http://democracy.york.gov.uk/documents/s4858/Annex%20E%20Sustainable%20Development.pdf.

[52] A. Manewa, M. Siriwardena, A. Ross, and U. Madanayake, "Adaptable Buildings for sustainable built environment," *Built Environment Project and Asset Management*, vol. 6, no. 2, pp. 139–158, 2016.

[53] BS EN ISO 7730, *Ergonomics of the thermal environment, Analytical determination and interpretation of thermal comfort using calculation of the PMV and PPD indices and local thermal comfort criteria*, 2005.

[54] Designing Buildings Wiki, *Thermal comfort in buildings*, 2016, https://www.designingbuildings.co.uk/wiki/Thermal_comfort_in_buildings.

[55] A. Ward, J. Boehland, and N. Malin, *Thermal Comfort and Building Management, BuildingGreen*, 2018, http://fmlink.com/articles/thermal-comfort-and-building-management.

[56] H. Danso, "Building houses with locally available materials in Ghana: benefits and problems," *International Journal of Science and Technology*, vol. 2, no. 2, pp. 225–231, 2013.

[57] GreenHomeBuilding, *Use Local Materials*, 2016, http://www.greenhomebuilding.com/localmaterials.htm.

[58] UN Habitat, *Affordable land and housing in Africa United Nations Human Settlement Programme*, 2011.

[59] B. Bhatta, "Analysis of urban growth and sprawl from remote sensing data," in *Advances in Geographic Information Science*, pp. 23–42, Springer, Berlin, Germany, 2010.

[60] H. Danso, *Use of agricultural waste fibres as enhancement of soil blocks for low-cost housing in Ghana*, Ph.D. thesis, School of Civil Engineering and Surveying, University of Portsmouth, 2015.

[61] H. Danso and D. Menu, "High cost of materials and land acquisition problems in the construction industry in Ghana," *International Journal of Research in Engineering and Applied Sciences*, vol. 3, no. 3, pp. 18–33, 2013.

[62] H. R. Sahely, C. A. Kennedy, and B. J. Adams, "Developing sustainability criteria for urban infrastructure systems," *Canadian Journal of Civil Engineering*, vol. 32, no. 1, pp. 72–85, 2005.

Hindawi
Advances in Materials Science and Engineering
Volume 2018, Article ID 4282181, 8 pages
https://doi.org/10.1155/2018/4282181

Research Article

Degradation of Roller-Compacted Concrete Subjected to Freeze-Thaw Cycles and Immersion in Potassium Acetate Solution

Wuman Zhang, Jingsong Zhang, Shuhang Chen, and Sheng Gong

Department of Civil and Engineering, School of Transportation Science and Engineering, Beihang University, Beijing 100191, China

Correspondence should be addressed to Wuman Zhang; wmzhang@buaa.edu.cn

Received 25 February 2018; Revised 19 March 2018; Accepted 2 April 2018; Published 15 April 2018

Academic Editor: Nadezda Stevulova

Two sets of roller-compacted concrete (RCC) samples cured for 28 days were subjected to freeze-thaw (F-T) cycles and immersion in laboratory conditions. F-T cycles in water and water-potassium acetate solution (50% by weight) were carried out and followed by the flexural impact test. The weight loss, the dynamic elastic modulus (E_d), the mechanical properties, and the residual strain of RCC were measured. The impact energy was calculated based on the final number of the impact test. The results show that the effect of F-T cycles in KAc solution on the weight loss and E_d of RCC is slight. E_d, the compressive strength, and the flexural strength of RCC with 250 F-T cycles in KAc solution decrease by 3.8%, 23%, and 36%, respectively. The content (by weight) of K^+ at the same depth of RCC specimens increases with the increase of F-T cycles. The impact energy of RCC specimens subjected to 250 F-T cycles in KAc solution decreases by nearly 30%. Microcracks occur and increase with the increase of F-T cycles in KAc solution. The compressive strength of RCC immersed in KAc solution decreases by 18.8% and 32.8% after 6 and 12 months. More attention should be paid to using KAc in practical engineering because both the freeze-thaw cycles and the complete immersion in KAc solution damage the mechanical properties of RCC.

1. Introduction

Roller-compacted concrete (RCC) is a zero-slump concrete compacted with vibratory and rubber-tired rollers [1]. RCC has been used in the construction of dams, pavements, and airport runways because of the lower cost and the easier placement operations [2–4]. RCC requires long-term stable performance when it is applied in airport runways because reconstruction causes a great impact on the air travel industry. Although the mechanical properties of RCC have been widely recognized, its frost resistance is still the focus in this field.

Piggott [5] found that the field performance of RCC was excellent in harsh environments, including northern U.S. states and Canada. The investigation showed that RCC with a reasonable mixture composition [6], casting and curing process [7, 8] had a good frost resistance. RCC also had better salt frost resistance when it was mixed with mineral admixtures [9]. Delatte and Storey [10] found that the freeze-thaw (F-T) durability of RCC mainly depended on the amount of cement paste and the water to cement ratio, but the degree of compaction had a less effect. However, the results reported by ACI Committee 325 [11] had shown that RCC mixtures were easy to damage by F-T cycles.

For RCC used at airport pavements in cold climates, potassium acetate (KAc) is being used as a deicer because of its high performance and aggressiveness. However, recent researches showed that KAc deicers could affect concrete durability through physical deterioration of concrete and chemical reaction between the KAc deicer and the hydration products of cement [12]. It has been suggested the deterioration of the airport runway may be related to the alkali-silica reaction between the hydration products of cement and KAc [9]. Julio-Betancourt [13] found that even without alkali-silica reactive aggregates, KAc deicers can cause degradation of strength, excessive expansion, and reduce resistance to freezing and thawing. It seems that investigations look to the KAc deicer as a problem, but given the varying results, the deterioration associated with the deicer is not completely understood.

Table 1: Mix proportions of RCC.

Water	Cement	Fine aggregate	Coarse aggregate	SP	AG
109	315	895	1207	2	0.023

The flexural strength and impact behavior are the most important parameters for RCC used in airport pavements. However, there is little research on the impact properties of RCC after F-T cycles in KAc solution. The effect of F-T cycles in KAc solution on the mechanical properties and impact resistance of RCC also needs to be elucidated. The main objective of this research focuses on the frost resistance and impact resistance of RCC exposed to the KAc deicer.

2. Materials and Experimental Process

2.1. Materials. Ordinary Portland cement (P.I 42.5), river sand with fineness modulus 2.61, coarse aggregate with sizes of 5–25 mm, microair 202 (AG), and polycarboxylate-based superplasticizer (SP) were used in this study. The mix proportions of RCC are listed in Table 1.

2.2. Experimental Procedure

2.2.1. Vebe Time Test. The Vebe method was used to measure the workability of RCC. This test method is a variation of the simple slump test and subjects the concrete to vibration after the slump cone removal. The small vibrating table operates at a fixed amplitude and frequency, and in the test, a plastic disc is placed in contact with the upper surface of the concrete. The test is completed when the lower surface of the disc has been completely coated with cement grout. The time is the measured parameter here. The Vebe time of fresh RCC is 28 s.

2.2.2. Specimen Preparation. The fresh mixture was poured into the prism molds in three layers. The dimensions of the mold are $100 \times 100 \times 400$ mm. A vibrating hammer was fixed on a 5 kg steel plate to apply the uniform rolling load. The rolling time of each layer was 30 seconds. After 24 h, the specimens were demolded and placed in the curing room for 28 days. The temperature was $20 \pm 2^{\circ}$C, and the relative humidity was 90%.

2.2.3. Strength of Specimens. Equations (1) and (2) were used to calculate the compressive strength, splitting tensile strength, and flexural strength.

$$f_c = \frac{F}{A}, \tag{1}$$

where f_c is the compressive strength (MPa), F is the maximum load (N), and A is the area of the cube loading face (mm).

$$f_f = \frac{Fl}{bh^2}, \tag{2}$$

where f_f is the flexural strength (MPa), F is the maximum load (N), l is the distance between the supporting rollers (mm), b is the width of the cross section (mm), and h is the height of the cross section (mm).

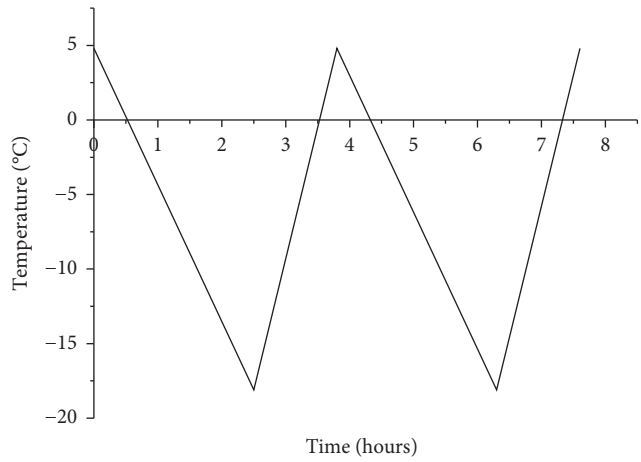

Figure 1: Temperature required by the standard of the specimen during the freeze-thaw cycles.

2.2.4. Freeze-Thaw Cycles and Immersion Test. Two sets of samples cured for 28 days were subjected to the following:

(a) F-T cycles, while samples were immersed in two different medias: water and 50% KAc solution (by weight).

(b) Laboratory conditions (RH 90%, $20 \pm 2^{\circ}$C), while samples were immersed in 50% KAc solution (by weight) for 6 and 12 months, respectively.

The F-T cycles were carried out according to GB-T50082-2009 [14]. A thermometer embedded at the center of the specimen was used to control the temperature. The maximum temperature and the minimum temperature are 5 ± 2 and $-18 \pm 2^{\circ}$C, respectively. Figure 1 shows the temperature of the specimen during the freeze-thaw cycles. The temperature curve was required by the standard. The real temperature of the sample itself can be different, depending, for example, on the properties of the sample and the accuracy of temperature sensors. Two different medias: water and 50% KAc solution (by weight) were used as the freezing medias. The total number of F-T cycles was 250.

The weight loss was calculated by the following equation:

$$\Delta W_n = \frac{W_0 - W_n}{W_0} \times 100, \tag{3}$$

where ΔW_n is the weight loss of the specimens at the nth freeze-thaw cycle (%), W_0 is the average weight of the concrete specimens before freeze-thaw cycles (kg), and W_n is the average weight of the concrete specimens at the nth freeze-thaw cycle (kg).

The DT-16-type dynamic modulus instrument was used to measure the relative dynamic modulus of elasticity. The relative dynamic modulus of elasticity was calculated by the following equation:

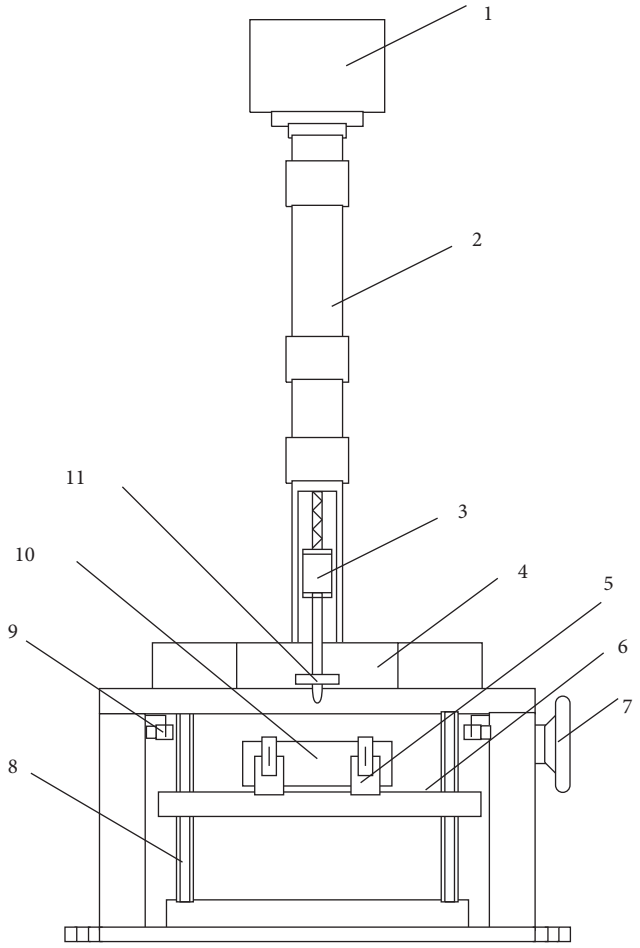

1. Lifting part.
2. Vertical guide pipe.
3. Release mechanism.
4. Part to prevent the second impact.
5. Holder.
6. Lifting pallet.
7. Lifting hand wheel.
8. Lead screw.
9. Optical signal tube.
10. Specimen.
11. Drop weight hammer.

Figure 2: The drop hammer impact testing machine.

$$E_d = \frac{W_i t_i^2}{W_1 t_1^2} \times 100, \quad (4)$$

where E_d is relative dynamic modulus of elasticity, W_1 is the initial weight of the specimen (kg), and W_i is the weight of a specimen after i times freeze-thaw cycles (kg). t_1 is the initial ultrasonic time of a specimen (s), and t_i is the ultrasonic time of a specimen after i times freeze-thaw cycles (s).

2.2.5. Flexural Impact Test. Figure 2 shows the drop hammer impact testing machine. It consists of two stiff constraints, which restrain the specimen from moving. It is capable of dropping a mass of 1.0–10.0 kg from height of up to 2.0 m above the target specimen. 3 kg and 0.3 m were used in this study. A steel cylindrical projectile with a 40 mm diameter is the head of the drop hammer. One part is designed to prevent the second impact. For each specimen, the side surface (2 mm from the top surface) and the bottom surface are bonded with a strain gauge, respectively. The strain was monitored by a high-speed data acquisition system. The impact energy is a constant value during the impact test. SZ120-100AA strain gauges were used to measure the strain [15, 16].

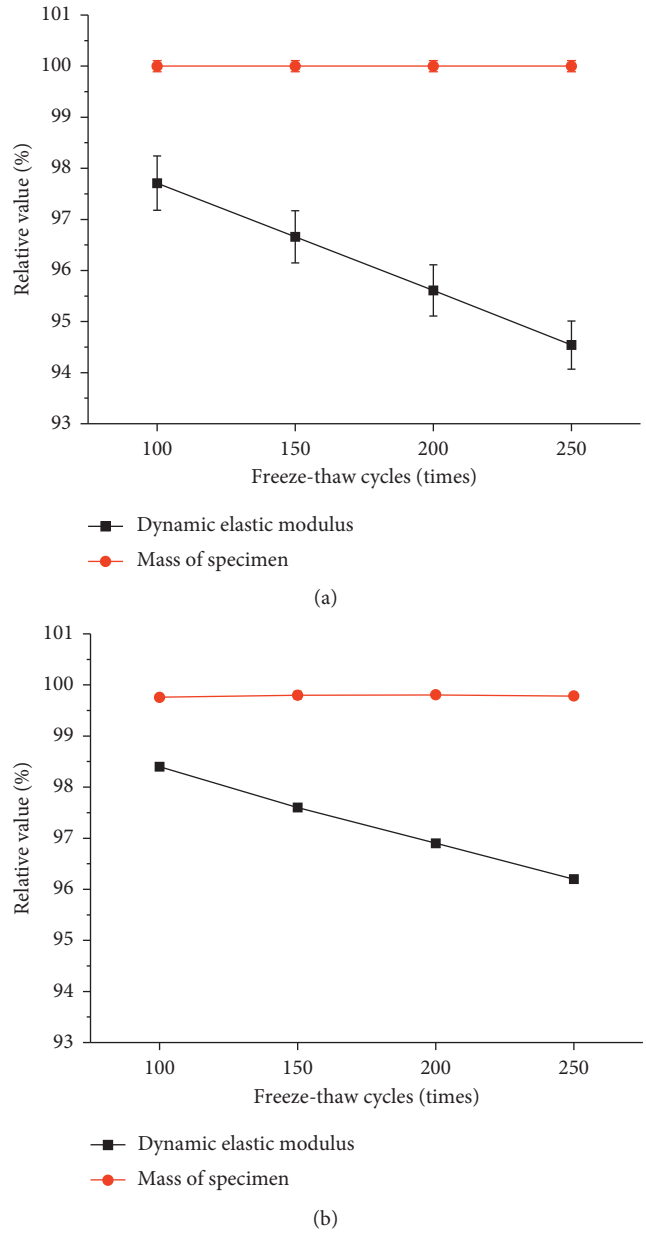

Figure 3: Relative weight loss and dynamic modulus of elasticity: (a) in water; (b) in KAc solution.

2.2.6. Microstructure and Element Content Analysis. The field emission scanning electron microscope (SEM, JSM-7500F) with energy dispersive X-ray analysis (EDX) was used to investigate the microstructures of the specimens. The samples for SEM analysis were soaked in anhydrous ethanol to stop hydration and dried at 60°C for 4 hours. The samples were coated with 20 nm gold before testing. The EDX was used to measure the element content of

Figure 4: Surface of the specimens subject to the F-T cycles in KAc solution: (a) 100; (b) 150; (c) 200; (d) 250.

samples. The resolution was 129.92 eV, and the measurement time was 50 s.

3. Results and Discussion

3.1. Freeze-Thaw Cycle Test

3.1.1. Weight Loss and Dynamic Modulus of Elasticity. The relative weight loss and the relative dynamic modulus of elasticity (E_d) of RCC with F-T cycles in water and KAc solution are shown in Figure 3. It clearly indicates that there is little change in weight of RCC with F-T cycles in water. Pigeon and Marchand [7], Andersson [17], and Marchand et al. [18] also obtained the similar results. The surface of the specimens with F-T cycles in KAc solution is shown in Figure 4. Based on Figures 3(b) and 4, the KAc deicer also caused no scaling or insignificant scaling in RCC. In the study from Wang et al. [19] and also Nanni [20], it was stated that KAc minor scaling might be related to alkali carbonation of concrete surface. However, Piggott [5] reported that the overall quality and properties of concrete and internal structure of concrete surface have an effect on the surface scaling. The preparation process of RCC may be another reason that the mass loss is not remarkable.

The F-T cycles in water or in KAc solution also have an insubstantial effect on E_d of RCC. E_d of RCC with 250 F-T cycles decreases by 5.5% and 3.8%, respectively. The loss of the elastic modulus of the RCC is less than that of normal concrete in the freeze-thaw test [21, 22]. This is probably due to the layering and the vibrating during the RCC specimen preparation which results in a higher surface strength.

3.1.2. Mechanical Properties of RCC. The compressive strength and the flexural strength of RCC cured for 28 days

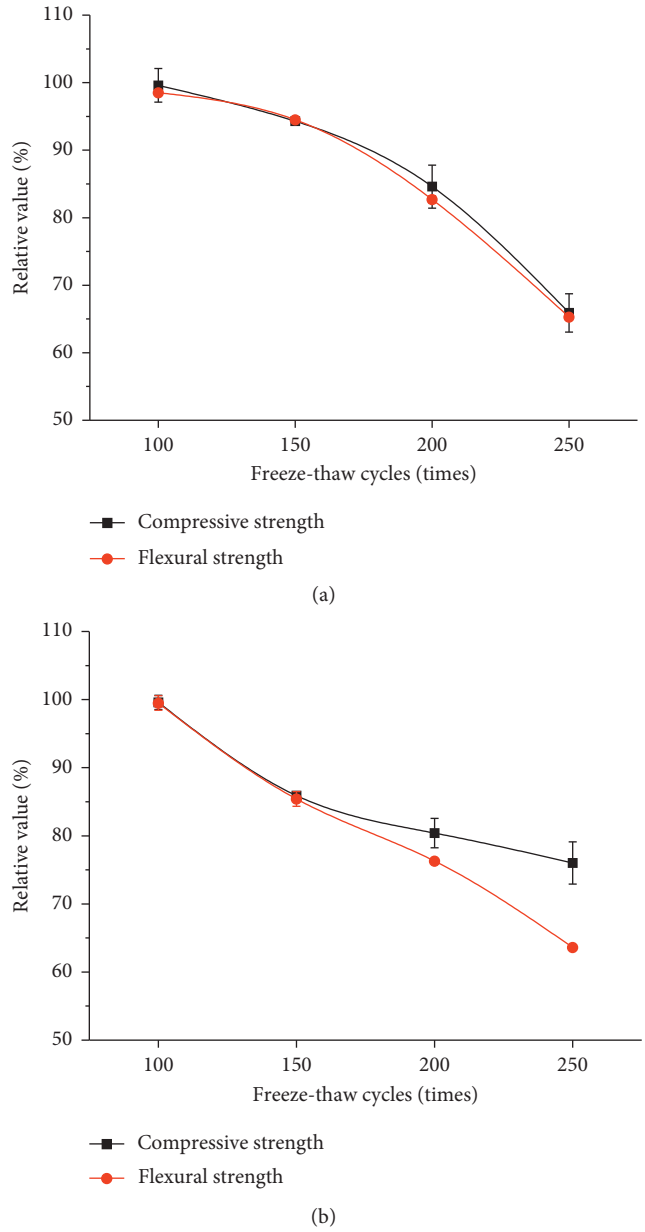

Figure 5: Relative compressive strength and flexural strength of RCC: (a) in water; (b) in KAc solution.

are 47.7 MPa and 9.0 MPa, respectively. Figure 5 shows the relative compressive strength and flexural strength of RCC subjected to F-T cycles in water and KAc solution. It can be seen that the F-T cycles in water or in KAc solution decrease both the compressive strength and the flexural strength of RCC. The compressive strength and the flexural strength are decreased by 33% when the RCC specimens are subjected to 250 F-T cycles in water. The results can be explained by the internal cracking caused by the expansion of water in concrete during F-T cycles.

250 F-T cycles in KAc solution decreases the compressive strength and the flexural strength of RCC by 23% and 36%, respectively. The strength loss can be explained by the traditional deterioration mechanism due to frost. In addition,

Table 2: The content of K^+ (by weight).

F-T cycles	100	150	200	250
Content of K^+ (%)	0.5	2.73	2.83	3.93

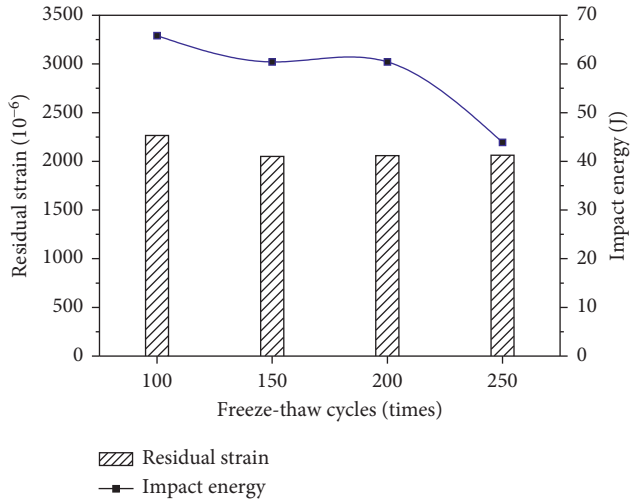

Figure 6: Residual strain and impact energy of RCC subjected to the F-T cycles in KAc solution.

it is postulated that KAc increases the level of saturation in concrete, possibly due to changes in surface tension and viscosity of pore water [13]. However, the decreasing trend in the compressive strength slowed. This is mainly attributed to the more penetration of KAc and the formation of an ettringite-like needle structure when the KAc deicer is used [19, 23]. The content (by weight) of K^+ at the same depth of the RCC specimens with the F-T cycles in KAc solution is shown in Table 2.

The deposition of ettringite seems to follow the appearance of cracks when F-T deterioration occurs. In the early stage, ettringite does not promote the propagation of existing cracks and cause new cracking in concrete. Cracks caused by frost damage will also give space for the crystallization of ettringite [24]. The filling and covering effect of ettringite on concrete crack could improve the compressive strength of concrete in early stage [25]. However, this filling action has slight effect on the flexural strength.

3.1.3. Impact Properties of RCC. Figure 6 shows the residual strain and impact energy of RCC subjected to the F-T cycles in KAc solution. It is clearly seen that the effect of the F-T cycles in KAc solution on the residual strain is slight. This is probably due to the damage of RCC under the impact loading is still a brittle fracture. In addition, the strain gauge bonded on the bottom surface of the specimen cannot record the strain when the specimen is broken into two sections. However, there is a decreasing trend in the impact energy of RCC, especially for the specimens subjected to 250 F-T cycles in KAc solution, and the impact energy decreases by nearly 30%. This result can be due to the decreasing action of the F-T cycles on the flexural strength of RCC.

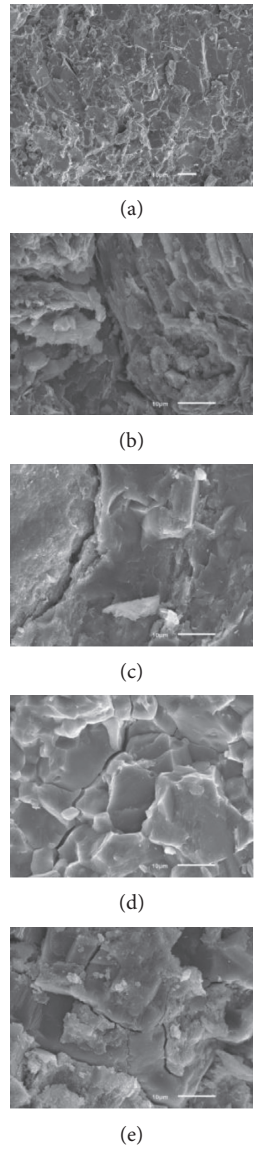

Figure 7: Microstructures of RCC without and with the F-T cycles in KAc solution: (a) 0; (b) 100; (c) 150; (d) 200; (e) 250.

3.1.4. Microstructures of RCC. In order to better understand the effect of the F-T cycles on the impact properties of RCC, the microstructures are observed and shown in Figure 7. Almost no microcrack occurs in the RCC matrix without the F-T cycles (Figure 7(a)). The F-T cycles will cause expansive pressure and osmotic pressure in concrete [26]. The surface spalling and internal cracking occur when the tensile stress produced by the two pressures exceeds the tensile strength of concrete. Therefore, microcracks occur and increase with the increase of the F-T cycles (Figures 7(b)–7(e)), which is consistent with the development of the strength of the specimens subjected to the F-T cycles in KAc solution.

3.2. Properties of RCC Immerged in KAc Solution. In order to determine whether the deicing fluid has a corrosive effect on the concrete, the specimens without the freeze-thaw cycles

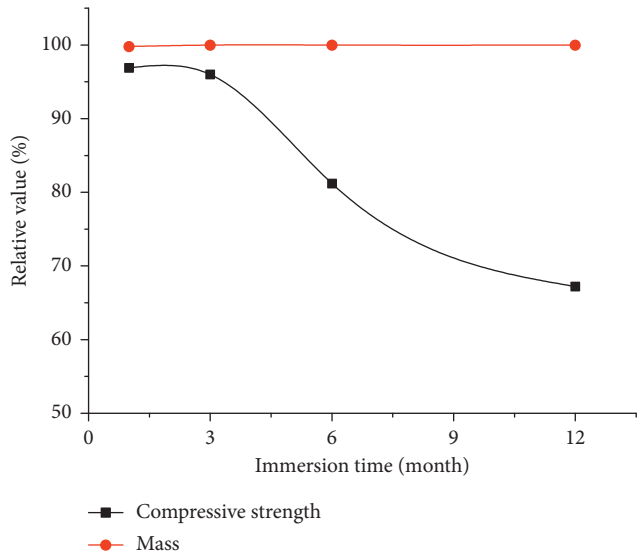

Figure 8: Relative mass and compressive strength of RCC immerged in KAc solution.

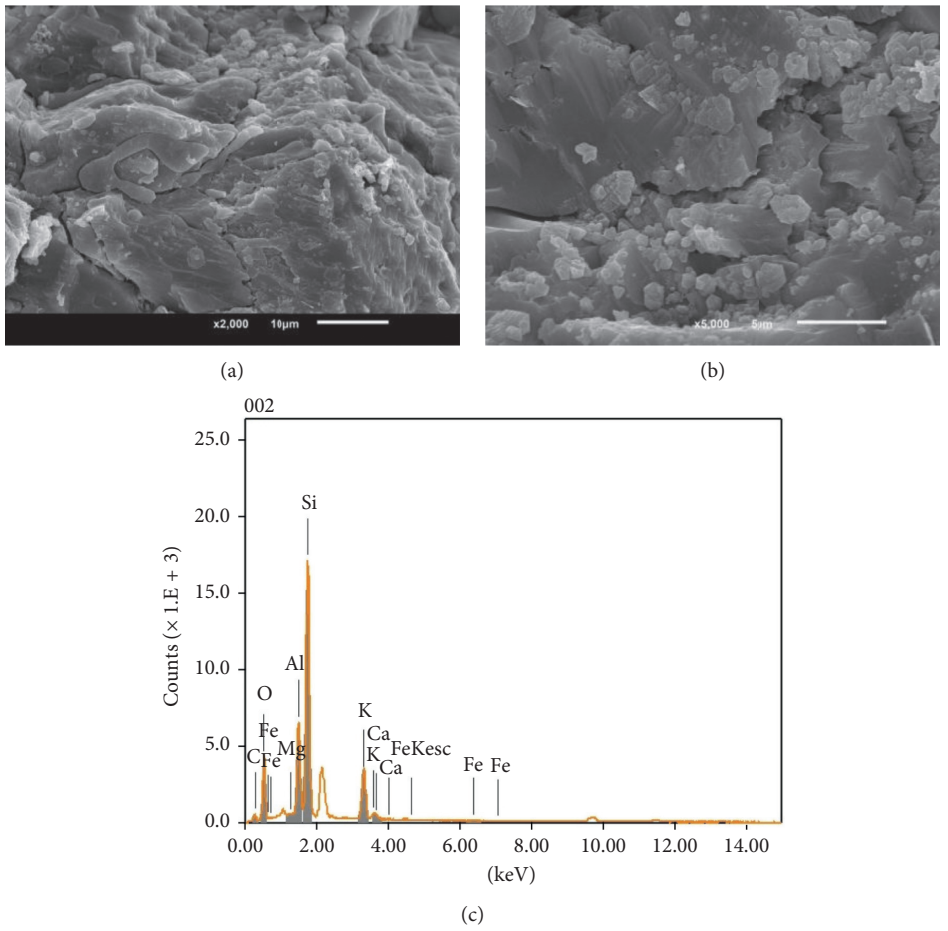

Figure 9: (a, b) Microstructures and (c) EDS of RCC immerged in KAc solution for 12 months.

are immersed in the KAc solution. The mass loss, the strength, and the microstructure of the specimens are measured. Figure 8 shows the mass and compressive strength of RCC immerged in KAc solution. It can be seen that the mass is almost unchanged after the RCC specimens are immersed in KAc solution for 12 months, which indicates that the complete immersion of the KAc solution does not cause the surface spalling. The compressive strength

has a smaller drop after 3 months of immersion. However, the compressive strength decreased by 18.8 and 32.8% after 6 and 12 months of complete immersion in KAc solution. The decrease of the compressive strength (32.8%) caused by 12-month immersion in KAc solution is very close to that (33%) of samples subjected to 250 F-T cycles in water. However, the decrease value is greater than that (23%) of samples subjected to 250 F-T cycles in KAc solution.

The microstructures and the energy dispersive spectrum (EDS) of RCC immerged in KAc solution for 12 months are shown in Figure 9. Comparing to the RCC matrix without the F-T cycles (Figure 7(a)), the microcracks were observed in the microstructure picture. In addition, the mass percentage of the K element in the new crystal is 5.58%, which indicates that more KAc solution has penetrated into the specimens subjected to 12 months of complete immersion in KAc solution. The osmosis pressure and the crystallization pressure of KAc solution may cause expansion and cracks in the RCC matrix, which decreases the compressive strength of specimens after a long-term contact with KAc solution.

3.3. Degradation Mechanism. The degradation mechanism of RCC subjected to the F-T cycles in KAc solution can be explained by the traditional theory due to frost. In addition to the pressure generated by osmosis and crystallization, KAc generally increases the saturation of the concrete and keeps concrete pores at or near the maximum fluid saturation, thereby increasing the risk of frost damage [13, 19].

Furthermore, KAc may induce alkali-silica reaction in the concrete-containing reactive aggregate, which causes expansion and cracks after a long-term contact. These cracks create channels for water and other solutions to penetrate into concrete and reduce freeze-thaw durability.

4. Conclusions

For the materials used and test methods applied, the following conclusions can be drawn:

(1) The effect of freeze-thaw cycles in KAc solution on the weight loss and the elastic modulus of RCC is slight. The elastic modulus of RCC with 250 freeze-thaw cycles decreases by 3.8%.

(2) 250 freeze-thaw cycles in KAc solution decrease the compressive strength and the flexural strength by 23% and 36%, respectively. The content (by weight) of K^+ at the same depth of RCC specimens increases with the increase of freeze-thaw cycles, which reduces the decreasing trend of the compressive strength caused by freeze-thaw cycles in KAc solution.

(3) The impact energy of RCC specimens subjected to 250 freeze-thaw cycles in KAc solution decreases by nearly 30%.

(4) Microcracks occur and increase with the increase of freeze-thaw cycles in KAc solution.

(5) The compressive strength of RCC without freeze-thaw cycles decreased by 18.8 and 32.8% after 6 and 12 months of complete immersion in KAc solution. The decrease of the compressive strength (32.8%) caused by 12 months immersion in KAc solution is greater than that (23%) of samples subjected to 250 F-T cycles in KAc solution.

(6) More attention should be paid to using KAc in practical engineering because both the freeze-thaw cycles and the complete immersion in KAc solution damage the mechanical properties of RCC. The decrease of mechanical properties of RCC used in airport runway will have serious effect on the flight safety. KAc solution should be replaced with a new type of harmless deicing fluid.

Data Availability

The datasets used during the current study are available from the corresponding author on reasonable request.

Conflicts of Interest

The authors declare that they have no conflicts of interest.

Acknowledgments

This research was supported by the National Natural Science Foundation of China (nos. 51378042 and 51678022) and the Fok Ying Tung Education Foundation (no. 132016).

References

[1] A. Mardani-Aghabaglou, Ö. Andiç-Çakir, and K. Ramyar, "Freeze-thaw resistance and transport properties of high-volume fly ash roller compacted concrete designed by maximum density method," *Cement and Concrete Composites*, vol. 37, no. 1, pp. 259–266, 2013.

[2] A. Yerramala and K. Ganesh Babu, "Transport properties of high volume fly ash roller compacted concrete," *Cement and Concrete Composites*, vol. 33, no. 10, pp. 1057–1062, 2011.

[3] P. W. Gao, S. X. Wu, P. H. Lin, Z. R. Wu, and M. S. Tang, "The characteristics of air void and frost resistance of RCC with fly ash and expansive agent," *Construction and Building Materials*, vol. 20, no. 8, pp. 586–590, 2006.

[4] M. Pigeon and V. M. Malhotra, "Frost-resistance of roller-compacted high-volume fly-ash concrete," *Journal of Materials in Civil Engineering*, vol. 7, no. 4, pp. 208–211, 1995.

[5] R. W. Piggott, *Roller Compacted Concrete Pavements—A Study of Long Term Performance*, Portland Cement Association, Skokie, IL, USA, R&D serial No. 2261, 1999.

[6] C. Hazaree, H. Ceylan, and K. Wang, "Influences of mixture composition on properties and freeze–thaw resistance of RCC," *Construction and Building Materials*, vol. 25, no. 1, pp. 313–319, 2011.

[7] M. Pigeon and J. Marchand, "Frost resistance of roller-compacted concrete," *Concrete International*, vol. 18, no. 7, pp. 22–26, 1996.

[8] C. Hazaree, P. Ramasamy, and W. P. David, "Roller-compacted concrete: a sustainable alternative," in *Green Building with Concrete-Sustainable Design and Construction*, G. M. Sabnis, Ed., pp. 129–180, CRC Press, Boca Raton, FL, USA, 2015.

[9] J. M. S. Silva, S. M. Cramer, M. A. Anderson, M. I. Tejedor, and J. F. Muñoz, "Concrete microstructural responses to the

interaction of natural microfines and potassium acetate based deicer," *Cement and Concrete Research*, vol. 55, pp. 69–78, 2014.

[10] N. Delatte and C. Storey, "Effects of density and mixture proportions on freeze–thaw durability of roller-compacted concrete pavement," *Transportation Research Record: Journal of the Transportation Research Board*, vol. 1914, pp. 45–52, 2005.

[11] ACI Committee, *State-of-the-Art Report on Roller-Compacted Concrete Pavements*, Vol. 32, ACI, Farmington, MI, USA, 1995.

[12] S. Ghajar-Khosravi, *Potassium Acetate Deicer and Concrete Durability*, University of Toronto, Toronto, ON, Canada, 2011.

[13] G. A. Julio-Betancourt, *Effect of De-Icer and Anti-Icer Chemicals on the Durability, Microstructure, and Properties of Cement-Based Materials*, University of Toronto, Toronto, ON, Canada, 2009.

[14] Ministry of Housing and Urban-Rural Development of People's Republic of China, *GB-T50082–2009, Standard for Test Methods of Long-Term Performance and Durability of Ordinary Concrete*, China Architecture & Building Press, Beijing, China, 2009, in Chinese.

[15] W. Zhang, S. Chen, N. Zhang, and Y. Zhou, "Low-velocity flexural impact response of steel fiber reinforced concrete subjected to freeze-thaw cycles in NaCl solution," *Construction and Building Materials*, vol. 101, pp. 522–526, 2015.

[16] W. Zhang, S. Chen, and Y. Liu, "Effect of weight and drop height of hammer on the flexural impact performance of fiber-reinforced concrete," *Construction and Building Materials*, vol. 140, pp. 31–35, 2017.

[17] R. Andersson, "Pavements of roller-compacted concrete-physical properties," *Nordic Concrete Research*, vol. 5, no. 11, pp. 7–17, 1986.

[18] J. Marchand, M. Pigeon, H. Isabelle, and J. Boisvert, "Freeze-thaw durability and deicer salt scaling resistance of roller compacted concrete pavements," in *Paul Klieger Symposium on Performance of Concrete*, pp. 217–236, SP 122-13, American Concrete Institute, Farmington Hills, MI, USA, 1990.

[19] K. Wang, D. E. Nelsen, and W. Nixon, "Damaging effects of deicing chemicals on concrete materials," *Cement and Concrete Composites*, vol. 28, no. 2, pp. 173–188, 2006.

[20] A. Nanni, "Curing of roller compacted concrete-strength development," *Journal of Transportation Engineering*, vol. 114, no. 6, pp. 684–694, 1988.

[21] Z. Wang, Q. Zeng, Y. Wu, L. Wang, Y. Yao, and K. Li, "Relative humidity and deterioration of concrete under freeze–thaw load," *Construction and Building Materials*, vol. 62, pp. 18–27, 2014.

[22] H. Cai and X. Liu, "Freeze-thaw durability of concrete: ice formation process in pores," *Cement and Concrete Research*, vol. 28, no. 9, pp. 1281–1287, 1998.

[23] C. Giebson, K. Seyfarth, and J. Stark, "Influence of acetate and formate-based deicers on ASR in airfield concrete pavements," *Cement and Concrete Research*, vol. 40, no. 4, pp. 537–545, 2010.

[24] Sulfate Task Group of Portland Cement Association, *Ettringite Formation and the Performance of Concrete*, 2001, http://www.cement.org/docs/default-source/fc_concrete_technology/is417-ettringite-formation-and-the-performance-of-concrete.pdf?sfvrsn=412.

[25] S. Ozaki and N. Sugata, "Long-erm durability of reinforced concrete submerged in the sea: concrete under severe conditions 2: environment and loading", in *Proceedings of the Second International Conference on Concrete Under Severe Conditions*, O. E. Gjørv, K. Sakai, and N. Banthia, Eds., pp. 448–457, CRC Press, Tromsø, Norway, June 1998.

[26] T. C. Powers, *Freezing Effects in Concrete*, Vol. 47, ACI Special Publication, Berkeley, CA, USA, 1975.

Hindawi
Advances in Materials Science and Engineering
Volume 2018, Article ID 6465136, 7 pages
https://doi.org/10.1155/2018/6465136

Research Article

Mechanical Behavior Analysis of Y-Type S-SRC Column in a Large-Space Vertical Hybrid Structure Using Local Fine Numerical Simulation Method

Jianguang Yue

College of Civil Engineering, Nanjing Tech University, Nanjing 211800, China

Correspondence should be addressed to Jianguang Yue; jgyue@njtech.edu.cn

Received 9 January 2018; Revised 7 March 2018; Accepted 11 March 2018; Published 2 April 2018

Academic Editor: Estokova Adriana

In a large spatial structure, normally the important members are of special type and are the safety key for the global structure. In order to study the mechanical behavior details of the local member, it is difficult for the common test method to realize the complex spatial loading state of the local member. Therefore, a local-fine finite element model was proposed and a large-space vertical hybrid structure was numerically simulated. The seismic responses of the global structure and the Y-type S-SRC column were analyzed under El Centro seismic motions with the peak acceleration of 35 gal and 220 gal. The numerical model was verified with the results of the seismic shaking table test of the structure model. The failure mechanism and stiffness damage evolution of the Y-type S-SRC column were analyzed. The calculated results agreed well with the test results. It indicates that the local-fine FEM could reflect the mechanical details of the local members in a large spatial structure.

1. Introduction

The spatial structures have been widely used in gymnasium, exhibition center, airport terminal, railway station, high-rise building, and bridge structures in China [1]. From the last century, some kinds of the spatial structures had been developed and researched deeply, including the thin-shell structure, cable structure, and space-truss structure. Till now, some modern spatial structures, such as the cable-membrane structure, beam string structure, and suspended-dome structure, will further promote the design theory and construction technique for the spatial structure system. Therefore, the mechanical performance of the complex structures and new members has become the research focus.

In this paper, the mechanism of a vertical hybrid structure of beam string roof and RC frame was analyzed. In this structure, a Y-type-steel steel-reinforced concrete column (Y-type S-SRC column) was used to strengthen the stiffness of the roof. The Y-type S-SRC column supports the roof by two slant steel pipe columns and transmits the loads to the ground by SRC column. Thus, the Y-type S-SRC column, which bears complex loads, is very important to ensure the safety of the roof and the whole structure. Lu [2] studied the seismic performance of this hybrid structure and analyzed the mechanical behavior of the Y-type S-SRC column through the static loading test. There are some similar experimental researches, for example, Fang et al. [3] studied the mechanical behavior of the steel-beam-SRC-column joint and RC-beam-circle-steel-pipe-column joint. Although the experiment is a good method to study the member's mechanical behavior, the actual loading and boundary conditions of the members are very difficult to be realized in the experiments for the limitations of experimental equipment. Therefore, there are some differences between the experiments and the realities of the load bearing states of the spatial member.

In a real structure, the loading and boundary conditions of the spatial member changes hand in hand with the responses of the whole structure. Similarly, in a finite element model of a structure, the mechanical responses of a member change synchronously with the global structure. It indicates that the FEM can simulate the loading and boundary conditions of the local member in a global structure. Obviously, it makes up some limitations of the test. Based on this understanding, this paper

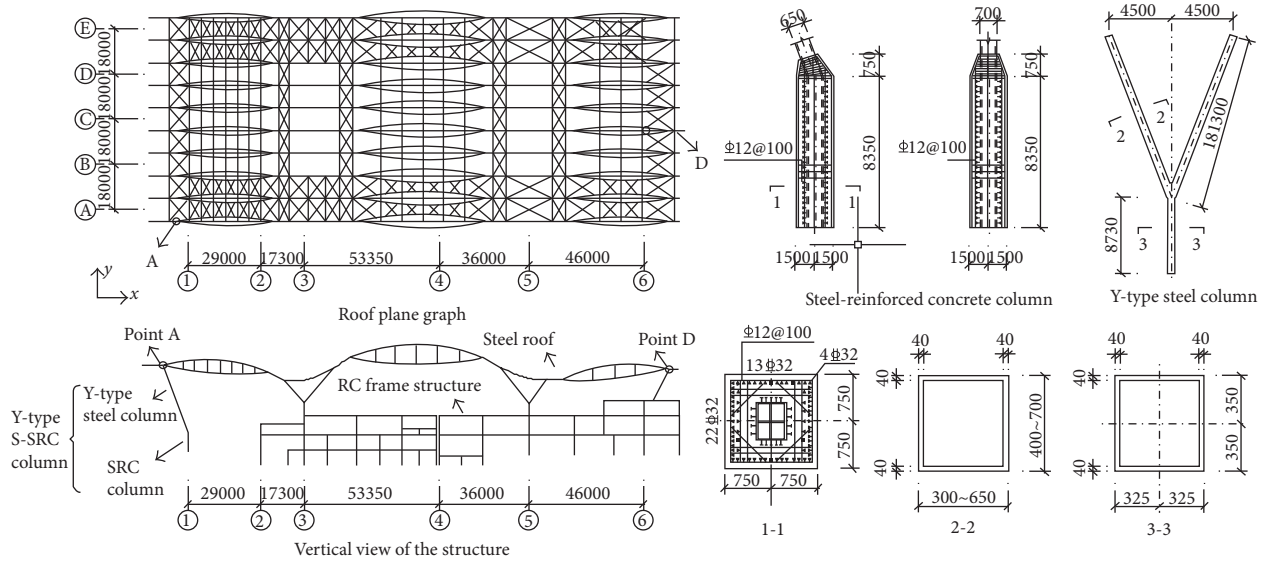

Figure 1: Draft of the structure and details of the Y-type S-SRC column.

studies the mechanical behavior of the Y-type S-SRC column by a local-fine finite element model. According to some experimental research results [2], the damage mechanism and stiffness damage of this type of column were analyzed in this paper.

2. The Vertical Hybrid Structure

This vertical hybrid structure (Figure 1), with the longitudinal span of 181.65 m and horizontal span of 64 m, consists of three-part continuous beam string roof and RC frame structure. The roof system includes the roof beams, box steel beams, I-type beams, and braces. At the axis 1 (Figure 1), the roof structure is supported by the Y-type S-SRC column. The top ends of the Y-type columns are hinged to the roof.

The details of the Y-type S-SRC column are shown in Figure 1. It consists of the Y-type steel tube and SRC column. The section width and height of the Y-type steel tube were 300–650 mm and 400–700 mm, respectively. The section of the SRC column was $1500 \times 1500\ mm^2$. The square section of the embedded steel tube was $650 \times 700\ mm^2$.

The cross-sectional width of the beam string was from 300 mm to 1622 mm and the height was from 768 mm to 2288 mm. The three spans of the continuous roof beam were 46.85 m, 89 m, and 46.85 m, respectively. The truss rod of the roof was the welded box tube with the width of 300 mm and height from 200 mm to 600 mm. The bottom chord of the roof was the cable steel rod with the diameter from 100 mm to 180 mm. The compressive strength of concrete was 19.1 MPa, and the elastic modulus of concrete was 32500 MPa. The yield strengths of steel reinforcements were 210 MPa, 300 MPa, and 360 MPa, respectively.

As shown in Figure 2, the seismic behavior of the global structure model with 1 : 35 geometric scale parameter was tested on the shaking table [4]. The three-directional waves of El Centro seismic motion were used as the input of the shaking table test. The ratio of the input waves in the x, y, and z directions was 1 : 0.85 : 0.65. Two case results of the test

Figure 2: Experimental model of the structure [2, 4].

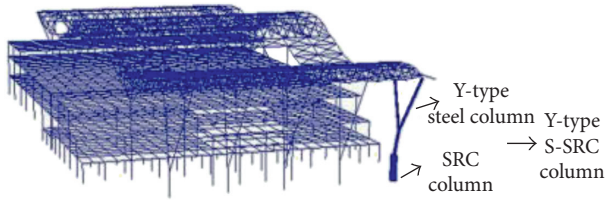

Figure 3: Finite element model.

[2, 4] were compared in this paper. In case 1, the value of peak acceleration of the input wave was 35 gal. In case 2, the value of peak acceleration of the seismic wave was 220 gal. More details about this experiment can be found in [2, 4].

3. Local-Fine FEM

There were a lot of members in the structure, so the global structure was better simulated by simple elements, such as beam elements and truss elements [5, 6]. In order to capture the mechanical details of the Y-type S-SRC column, the Y-type S-SRC column in axis 1 was simulated by the local-fine FEM (Figure 3).

In this local-fine FEM of the column (Figure 3), the steel tube was modeled by the S4R elements, and the steel

reinforcement was modeled by the T3D2 elements which were embedded in the concrete elements. The material behavior of steel was assumed as the ideal plastic-elastic model. The concrete was modeled by the C3D8R elements. The concrete behavior was described by the concrete plastic damage model in ABAQUS software [7]. The other SRC columns were simulated by the B31 elements, and the concrete material behavior was described by the smeared cracking constitutive model, in which the steel elements were coupled with the concrete elements. In the global structural FEM, the total element number was 71747 and the total number of nodes was 75285.

4. Material Behavior of the Confined Concrete

The material behavior of the concrete in the SRC column was described by the stress-strain relation for the confined concrete and the plastic damage model. According to the modified method of the yield criterion and flow rule [8, 9], the second invariant stress ratio of the tensile and compression meridian plane is 0.725, and the angle of dilatancy is 56.4°. Under monotonic loading, the stress-strain relation (Figure 4) of the confined concrete is described by the Mander model [10] as follows:

$$\sigma_c = \frac{f'_{cc}\lambda\left(\varepsilon'_c/\varepsilon'_{cc}\right)}{\lambda - 1 + \left(\varepsilon'_c/\varepsilon'_{cc}\right)^{\lambda}},$$
$$\lambda = \frac{E_c}{E_c - \left(f'_{cc}/\varepsilon'_{cc}\right)}, \tag{1}$$

where σ_c is the compressive stress of the concrete, f'_{cc} is the compression strength of the concrete, ε'_c is the compressive strain, and ε'_{cc} is the compressive strain corresponding with f'_{cc}. The elastic modulus of the concrete was calculated by the following equation:

$$E_c = 5000\sqrt{f'_c}. \tag{2}$$

The compression strain ε'_{cc} corresponding with f'_{cc} of the unconfined concrete is calculated by the following equations:

$$f'_{cc} = f'_c\left(-1.254 + 2.254\sqrt{1 + \frac{7.94f'_l}{f'_c}} - 2\frac{f'_l}{f'_c}\right),$$
$$\varepsilon'_{cc} = \varepsilon'_c\left(1 + 5\left(\frac{f'_{cc}}{f'_c} - 1\right)\right), \tag{3}$$
$$f'_l = \frac{1}{2}K_e\rho_s f_{yh},$$

and if the cross section is square,

$$K_e = \frac{\left(1 - \sum_i^n\left(\left(\omega'_i\right)^2/6b_cd_c\right)\right)\left(1 - s'/2b_c\right)\left(1 - s'/2d_c\right)}{1 - \rho_{cc}}, \tag{4}$$

where f'_l is the compressive transverse confined press of the core concrete, ε'_c is the compressive strain corresponding with the compressive strength f'_c of the concrete, f_{yh} is the yield strength of the longitudinal reinforcement, ρ_{cc} is the reinforcement ratio, n is the number of reinforcements, b_c is the separation distance of the stirrup in the direction of the section width, d_c is the

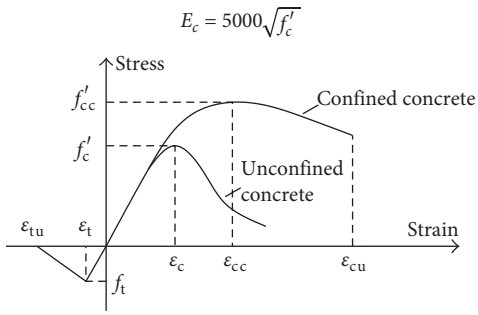

Figure 4: Stress-strain relations of the confined concrete.

Table 1: Comparisons of the structural dynamic behavior.

Mode	1 T (s)	2 T (s)	3 T (s)
Calculated	1.75	1.40	1.00
Test [2]	1.68	1.12	0.98

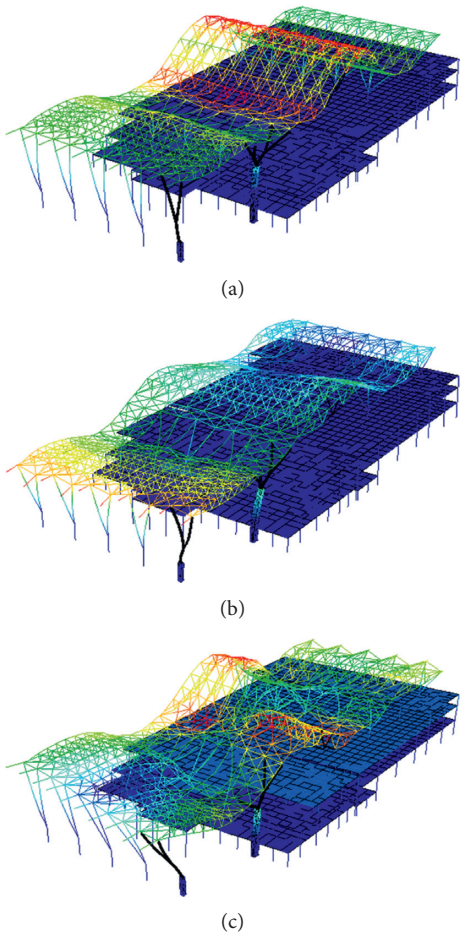

Figure 5: The calculated structural vibration modes. (a) The first vibration mode. (b) The second vibration mode. (c) The third vibration mode.

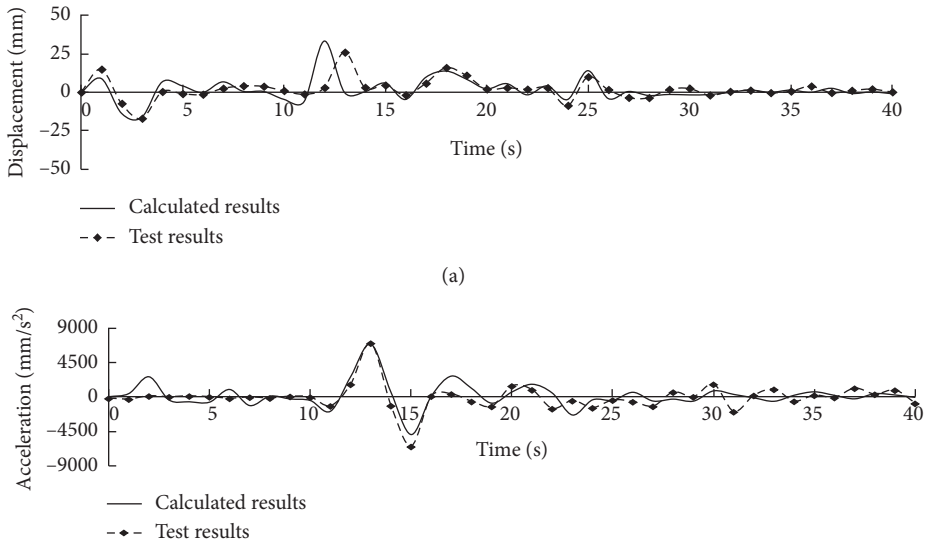

Figure 6: Comparisons of calculated and test results of case 2. (a) Displacement response of point D in the y direction. (b) Acceleration responses of point A in the y direction.

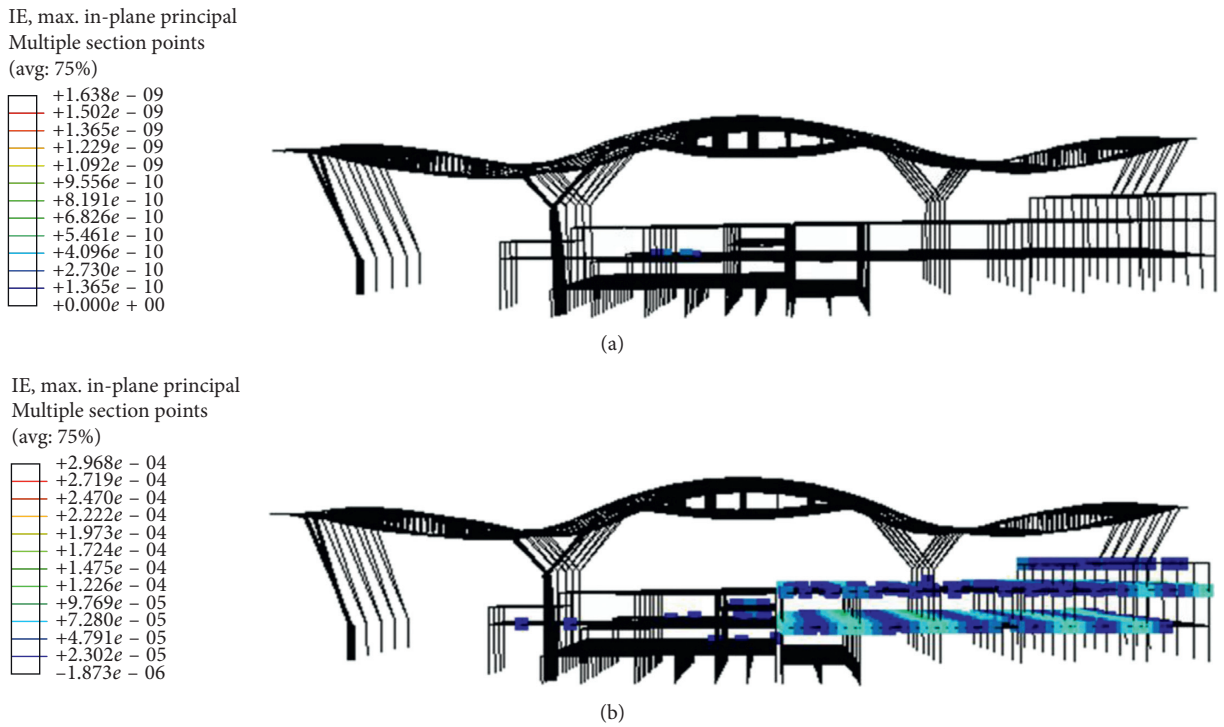

Figure 7: The damage states of the global structure: (a) case 1 and (b) case 2.

separation distance of stirrup in the direction of the section length, ρ_s is the stirrup ratio, s' is the clear space of the stirrup, and d_s is the separation distance of the stirrup on cross section.

5. Seismic Responses of the Local-Fine FEM

The calculated first three modes of the structure were compared with the test results in Table 1. The calculated first three vibration modes of the structure are shown in Figure 5. The first vibration mode is the translational motion of the global structure in the x direction. The second vibration mode is the translational motion in the y direction mixed with torsional motion of the global structure. The third vibration mode is the torsional motion of the roof. These characteristics of the vibration modes agree well with the test results [2, 4].

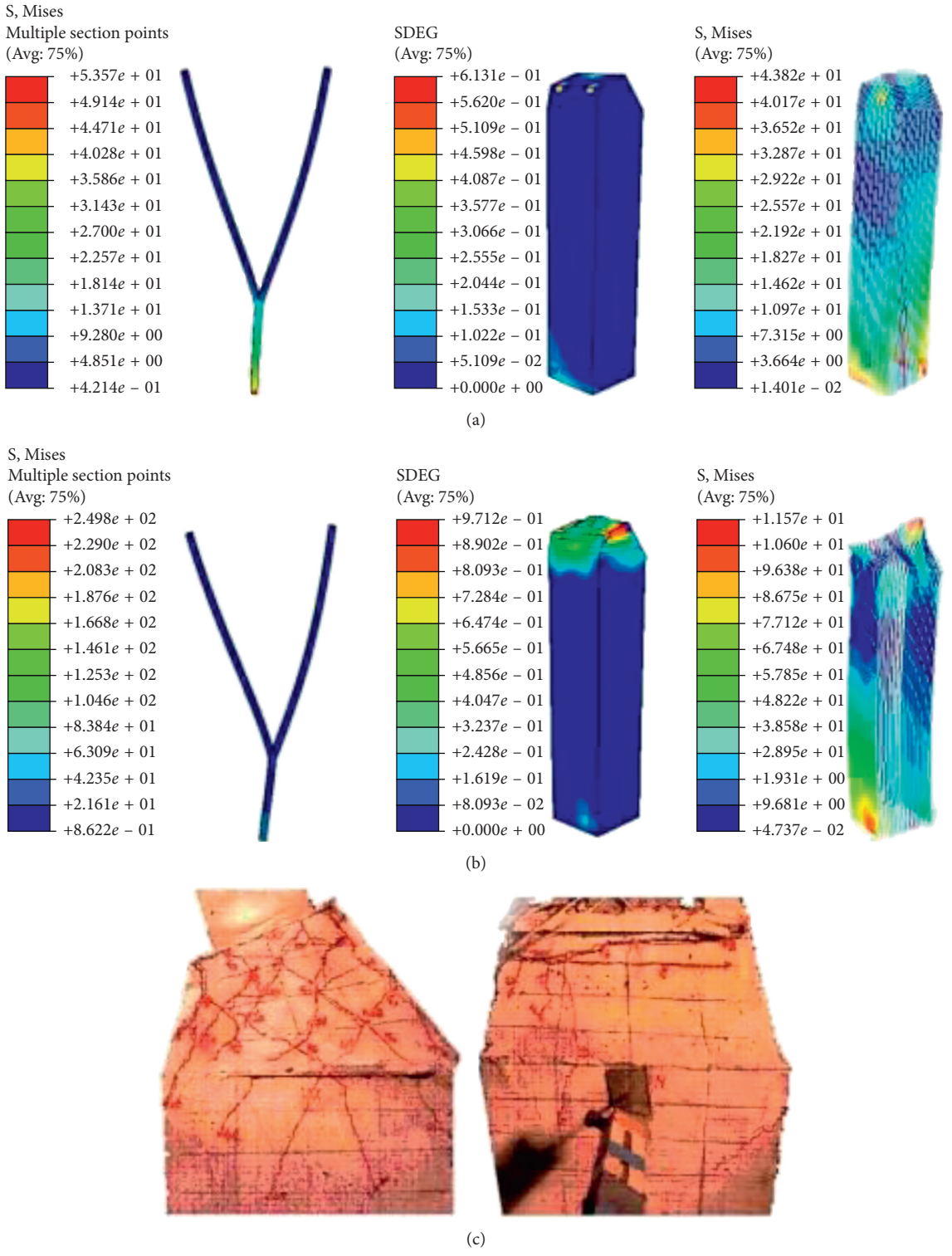

Figure 8: Damage comparisons. Calculated results in (a) case 1 and (b) case 2 and (c) test damage [2].

Under the seismic ground motion (El Centro seismic wave) with the peak acceleration of 220 gal, the calculated displacement responses of point D and acceleration responses of point A were compared, respectively, with test results as shown in Figure 6. The comparisons showed that the calculated results agreed well with the test results.

The global structural damage states can be described by the mechanical parameter plastic strain. Figure 7 shows the plastic strain distributions of the global structure in case 1 and case 2, respectively. In case 1 (Figure 7(a)), the damage mainly occurred at very few beams of the second floor of the RC frame structure, and the maximum plastic strain was

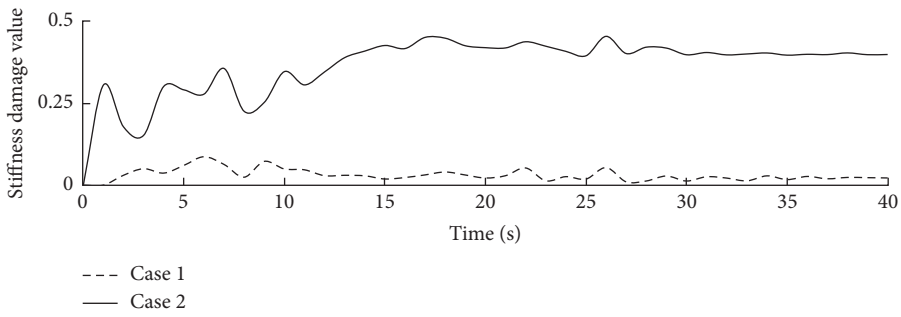

Figure 9: The stiffness damage evolutions of the SRC column.

about 1.638×10^{-9}. It indicates that the structure almost kept the elastic mechanical behavior global under the El Centro seismic motion with the peak acceleration of 35 gal. In case 2 (Figure 7(b)), the damage occurred at many beams of the second and third floors of the RC frame structure, and the maximum plastic strain was about 2.968×10^{-4}. It shows that the structure damaged seriously, but it probably did not collapse for almost all damages occurred at the beams of the RC frame.

6. Mechanical Behavior of Y-Type S-SRC Column

The Y-type S-SRC column was subjected to the forces from the roof by two connected points. The responses of the two points were very different under the same seismic motion. Based on the proposed local-fine FEM method, the mechanical behavior of the Y-type S-SRC column can be analyzed here. The calculated damage of the Y-type S-SRC column was compared with the test results as shown in Figure 8.

In case 1 (Figure 9), the concrete at the top and bottom ends of the SRC column damaged slightly, and the maximum damage value of concrete was 0.613. The maximum value of the von Mises stress of the steel column was 53.6 MPa at the bottom end. The maximum value of the von Mises stress of the longitudinal reinforcements was 43.8 MPa. It indicates that the column damaged slightly under the El Centro seismic wave with the peak acceleration of 35 gal.

In case 2 (Figure 9), the concrete at the top end of SRC column damaged seriously, the maximum value of the concrete damage was 0.971. The maximum value of the von Mises stress of the steel column was 249.8 MPa at the bottom end. The maximum value of the von Mises stress of the longitudinal reinforcements was 115.7 MPa. These calculated damage results agreed with the test results (Figure 9). According to the damage mode, the concrete at the top end of the SRC column could be strengthened by some structural measures in the actual engineering design.

The calculated stiffness damage evolutions of the SRC column in case 1 and case 2 were shown in Figure 9. In case 1, the maximum stiffness damage value of the SRC column was 0.05; thus, it means the SRC column damaged very slightly. In case 2, the maximum stiffness damage value of the SRC column was 0.45. It means the SRC column damaged seriously but not collapsed for concrete material damage that mainly occurred on the top end and the longitudinal reinforcement did not yield. These calculated results also agreed with the conclusion from the plastic strain analysis results of the global structure.

7. Conclusions

In this paper, the seismic responses of a large-space vertical hybrid structure and the mechanical behavior of the Y-type S-SRC column were analyzed based on the local-fine FEM. The calculated local damage results agreed with the test results and also the seismic responses of the global structure. However, the damage states of the Y-type S-SRC are related with the material strength, its configuration, and the global structure form. Another effected factor, that is, the second-order effect on the local mechanical details of the Y-type S-SRC column, was ignored in this paper. It shows that the proposed numerical simulation method can be used to study the mechanical behavior details of a local member of a large spatial structure.

Data Availability

The data used to support the findings of this study are available from the corresponding author upon request.

Conflicts of Interest

The author declares that there are no conflicts of interest.

Acknowledgments

The author acknowledges with thanks the support of the National Natural Science Foundation of China under the Grant no. 51778284 and the China Postdoctoral Science Foundation under the Grant no. 2016M591836.

References

[1] S. L. Dong, "Development and expectation of spatial structures in China," *Journal of Building Structures*, vol. 31, no. 6, pp. 38–51, 2010, in Chinese.

[2] X. L. Lu, *Shaking Table Test on Pudong International Airport Terminal 2 Building in Shanghai*, State Key Laboratory for Disaster Reduction in Civil Engineering of Tongji University, Shanghai, China, 2008, in Chinese.

[3] X. D. Fang, S. Y. Li, J. R. Qian, and R. Q. Yang, "Experimental research on seismic behavior of concrete filled steel tubular column-ring beam joint under cyclic loading," *Journal of Building Structures*, vol. 23, no. 6, pp. 10–18, 2002, in Chinese.

[4] X. L. Lu, F. Liu, and W. S. Lu, "Shaking table model test on Pudong International Airport Terminal 2 building in Shanghai," *Journal of Earthquake Engineering and Engineering Vibration*, vol. 29, no. 3, pp. 22–31, 2009, in Chinese.

[5] Z. X. Li, T. Q. Zhou, T. H. T. Chan, and Y. Yu, "Multi-scale numerical analysis on dynamic response and local damage in long-span bridges," *Engineering Structures*, vol. 29, no. 7, pp. 1507–1524, 2007.

[6] J. G. Yue, A. Fafitis, J. Qian, and T. Lei, "Application of 1D/3D finite elements coupling for structural nonlinear analysis," *Journal of Central South University of Technology*, vol. 18, no. 3, pp. 889–897, 2011.

[7] J. Lublinear, J. Oliver, S. Oller, and E. Oñate, "A plastic-damage model for concrete," *International Journal of Solids and Structures*, vol. 25, no. 3, pp. 299–329, 1989.

[8] T. Yu, J. G. Teng, Y. L. Wong, and S. L. Dong, "Finite element modeling of confined concrete-I: Drucker–Prager type," *Engineering Structures*, vol. 32, no. 3, pp. 665–679, 2010.

[9] T. Yu, J. G. Teng, Y. L. Wong, and S. L. Dong, "Finite element modeling of confined concrete-II: plastic-damage model," *Engineering Structures*, vol. 32, no. 3, pp. 680–691, 2010.

[10] J. B. Mander, M. J. N. Priestley, and R. Park, "Theoretical stress-strain model for confined concrete," *Journal of Structural Engineering*, vol. 114, no. 8, pp. 1804–1826, 1988.

Hindawi
Advances in Materials Science and Engineering
Volume 2018, Article ID 3063620, 14 pages
https://doi.org/10.1155/2018/3063620

Research Article

Preparation Parameter Analysis and Optimization of Sustainable Asphalt Binder Modified by Waste Rubber and Diatomite

Hanbing Liu, Mengsu Zhang, Yubo Jiao, and Liuxu Fu

College of Transportation, Jilin University, Changchun 130025, China

Correspondence should be addressed to Yubo Jiao; jiaoyb@jlu.edu.cn

Received 6 September 2017; Accepted 19 February 2018; Published 25 March 2018

Academic Editor: Estokova Adriana

In this study, crumb rubber and diatomite were used to modify asphalt binder. Wet process was adopted as a preparation method, and the corresponding preparation process was determined firstly. The effects of six preparation parameters (crumb rubber concentration, diatomite concentration, shear time, shear speed, shear temperature, and storing time) on properties of modified asphalt binder (penetration at 25°C, softening point, ductility, viscosity at 135°C, elastic recovery, and penetration index) were investigated, and multiresponse optimization was conducted using the response surface method. The results revealed that softening points, viscosity, elastic recovery, and penetration index increase, while penetration and ductility decrease with the increase of crumb rubber concentration. Softening points, viscosity, and penetration index increase, while penetration and ductility decrease with the increase of diatomite concentration, which presents little influence on elastic recovery of binder. Shear temperature presented significant effects on penetration, softening point, viscosity, and ductility. Shear speed, shear time, and storing time have similar effects on binder properties because of their similar mechanism of action. Based on the model obtained from the response surface method, optimized preparation parameters corresponding to specific criteria can be determined, which possess favorable accuracy compared with experimental results.

1. Introduction

Disposal of industrial wastes has become a critical problem in the world under the promotion of environmental management and mission of sustainable development [1, 2]. Millions of end-of-life tyres (ELTs) are generated each year due to the increasing number of vehicles, which have been regarded as one of the largest and most problematic waste polymeric materials with large quantity and durability [3]. Current researches have shown that crumb rubber (CR) derived from grinding of ELTs into asphalt modification can be an effective modifier for construction and maintenance of asphalt pavement [4]. For one thing, CR-modified asphalt and corresponding mixture possess favorable environmental benefits. Farina et al. [5] demonstrated the environmental results of recycled materials in bituminous mixtures for pavement wearing courses using life cycle assessment (LCA) methodology. Results reveal that the use of wearing course containing asphalt rubber obtained by the wet process presents significant benefits for energy saving, environmental impact, human health, preservation of ecosystems, and minimization of resource depletion. The reductions of the gross energy requirement and global warming potential range between 36% and 45% compared with standard paving solutions. Bartolozzi et al. [6] compared the environmental performances between rubberized asphalt pavement and the conventional one. Results show that the global environmental performances of the rubberized asphalt road are improved by 30–40%. La Rosa et al. [7] evaluated the environmental benefit of using recycled waste tyres in mixture with virgin rubber. It can be concluded that addition of ground tyre rubber (GTR) in styrene-isoprene-styrene (SIS) formulation considerably reduces the influences in terms of global warming potential, human toxicity, energy consumption, and so on. Yu et al. [8] evaluated the environmental burdens of plastic-rubber asphalt (PRA) mixture and styrene-butadiene-styrene (SBS) asphalt mixture by using a cradle-to-gate LCA model. The results revealed that PRA mixture is more environmental-friendly than SBS asphalt mixture. CR has been proved to be an effective modifier for virgin asphalt. Adding CR into asphalt

binder can improve its viscosity and elastic properties at high temperature, which can enhance the resistance ability to permanent deformation under traffic load. It can also increase the flexibility of asphalt binder at low temperature, thus making it more capable of resisting low temperature cracking [9–13]. Therefore, recycled ELTs have been widely used as a road-paving material in the world.

Diatomite is a naturally occurring, soft, siliceous sedimentary rock that can be easily crumbled into fine powder. The typical chemical components of diatomite are silica, alumina, and iron oxide [14]. Diatomite has been widely used as a asphalt modifier due to its low cost, large storage, and high absorptive ability [14–18]. The addition of diatomite into asphalt can improve its high temperature performance, storage stability, rutting resistance, and long-term aging resistance. Asphalt mastic modified by diatomite possesses more favorable high and medium temperature performances than that modified by limestone, hydrated lime, and fly ash [16]. However, diatomite-modified asphalt presents some drawbacks such as reducing the thermal conductivity and low temperature deformation ability of asphalt mixture [17]. In order to overcome this limitation, crumb rubber and diatomite can be used as a compound modifier for asphalt binder. Liu et al. [19] investigated the short-term aging properties of diatomite and crumb rubber compound–modified asphalt (DRA). The results revealed that DRA could combine the advantages of diatomite and crumb rubber and achieve better performance in short-term aging resistance than diatomite-modified asphalt (DA) and crumb rubber–modified asphalt (RA).

It is worth noting that different procedures and parameters can be applied to prepare crumb rubber and diatomite compound–modified asphalt binders [20]. The different preparation procedures and parameters can result in different interactions among crumb rubber, asphalt, and diatomite, thus affecting the properties of modified asphalt. But previous studies have rarely investigated the effect of preparation factors on the property of crumb rubber and diatomite compound–modified asphalt, and even the influences of preparation factors on properties of crumb rubber–modified asphalt and diatomite-modified asphalt are limited [20, 21].

In general, there are two kinds of production methods for crumb rubber–modified asphalt binder: the dry process and wet process [3, 22]. In the dry process, coarse crumb rubber is used to substitute a part of the mineral aggregate, which is suitable for producing asphalt mixture with favorable elasticity and anti-icing properties. In the wet process, crumb rubber and asphalt are mixed and allowed to react for a period that can take advantage of the benefits of both base ingredients. Crumb rubber–modified asphalt obtained through the wet process has spread worldwide and got much success by roads built in the past 30 years [3]. For the production of diatomite-modified asphalt, the wet process is the most widely used method. In the preparation of both crumb rubber–modified asphalt binder and diatomite-modified one, the device of high-speed mixing and shear stirring is usually adopted to obtain a homogeneous asphalt binder. The processing parameters including temperature, time, and speed determine the interaction condition, which is important for the properties of modified asphalt [23]. However, different preparation parameters were applied in recent researches. For the preparation of crumb rubber–modified asphalt, shear temperature 175°C, shear speed 5000 rpm, and shear time 40 min were adopted by Wang et al. [24]. Shear temperature 170–180°C, shear speed 5000 rpm, and shear time 5 min were used by Kedarisetty et al. [23]. In the research by Peralta et al. [25], asphalt rubber binder was heated at 180°C for 60 min and stirred at 230 rpm. For the preparation of diatomite-modified asphalt, the shear temperature is 150°C, shear speed is 3000 rpm, and shear time is 120 min in the research by Cong et al. [14]. The shear temperature is 150°C, shear speed is 4000 rpm, and shear time is 40 min in the research by Guo et al. [17]. The shear temperature is 160°C, shear speed is 5000 rpm, and shear time is 40 min in the research by Tan et al. [15]. As can be concluded from current researches, different preparation parameters were adopted. The effects of preparation parameters on properties of modified asphalt have not been demonstrated.

In this study, the preparation process for crumb rubber and diatomite compound–modified asphalt binder was determined. The effects of six kinds of preparation parameters (crumb rubber concentration, diatomite concentration, shear time, shear speed, shear temperature, and storing time) on properties of binder (penetration at 25°C, softening point, ductility, viscosity at 135°C, elastic recovery, and penetration index (PI)) were investigated using the response surface method (RSM). Relationships between preparation parameters and asphalt properties were obtained, and multiresponse optimization was conducted to determine the optimum preparation parameters corresponding to the satisfactory properties.

2. Materials and Methods

2.1. Raw Materials. Base asphalt AH-90 from Panjin Petrochemical Industry, crumb rubber particle from Changchun Yuxing Rubber Materials Co., Ltd., and diatomite produced by Changchun Diatomite Products Co., Ltd. were used in this study. The detailed properties for raw materials were given in [19].

2.2. Preparation of Crumb Rubber and Diatomite Compound–Modified Asphalt. The wet process was adopted to prepare the crumb rubber and diatomite compound–modified asphalt. A high-speed shear homogenizer (KRH-I, Shanghai Konmix Mechanical & Electrical Equipment Technology Co. Ltd., China) was employed, which can control its internal temperature through a heating device and oil bath. The preparation process mainly included three steps: heating of raw materials; shearing and mixing of asphalt, crumb rubber, and diatomite; and storing of modified asphalt binder. In this study, the influences of six important preparation parameters on compound-modified asphalt binder were investigated. They were content of crumb rubber by weight of the neat asphalt, content of diatomite by weight of the neat asphalt, shear temperature,

shear speed, shear time, and storing time. Contents of crumb rubber and diatomite are essential parameters affecting the properties of compound-modified asphalt. Shear speed, shear time, shear temperature, and storing time are key factors in the interaction process among asphalt, crumb rubber, and diatomite to achieve a homogeneous and stable modified binder. The adopted six preparation parameters have not been standardized in current researches, and the researchers have used various parameters. Based on previous research results and considering the workability of binder, the range for content of crumb rubber was 5–15%; it was 5–15% for content of diatomite, 160–190°C for shear temperature, 3000–6000 rpm for shear speed, 30–60 min for shear time, and 30–60 min for storing time in this study. Therefore, the detailed preparation process was determined as follows: firstly, neat asphalt, crumb rubber, and diatomite were separately heated in an oven at 140°C, and asphalt was at the fluid state that can be easily stirred. Secondly, the crumb rubber and diatomite were added into asphalt, which was placed into a shear homogenizer after preliminary mixing. Then, shear temperature and speed were set to the specific values; the blend of asphalt, crumb rubber, and diatomite was mixed and sheared for the specified shear time after the temperature of the blend reached the specified shear temperature. Finally, the blend was contained in the shear homogenizer to swell for the specified storing time. The crumb rubber and diatomite compound–modified asphalt binder was prepared for the tests.

2.3. Characterization Method. In order to evaluate the effects of content of crumb rubber, content of diatomite, shear temperature, shear speed, shear time, and storing time on asphalt properties, penetration, softening point, ductility, viscosity, elastic recovery, and penetration index (PI) were tested and investigated for compound-modified asphalt binder. Detailed illustrations for penetration, softening point, ductility, viscosity, and elastic recovery were conducted in [19].

The results obtained from penetration and softening point tests can be used to calculate the penetration index (PI). PI is an important property which is related to Van der Poel's monograph and useful to determine the stiffness of asphalt. PI was usually used for the classification of pure asphalt. However, it has been verified to be useful for polymer-modified ones [26]. PI can be calculated by the following classical approach [27]:

$$\mathrm{PI} = \frac{30}{1 + 50\left(\lg 800 - \lg P_{(25^{\circ}\mathrm{C},100\,\mathrm{g},5\,\mathrm{s})}/T_{\mathrm{R\&B}} - 25\right)} - 10, \quad (1)$$

where $P_{(25^{\circ}\mathrm{C},100\,\mathrm{g},5\,\mathrm{s})}$ is the penetration at 25°C and $T_{\mathrm{R\&B}}$ is the softening point temperature.

2.4. Response Surface Method. In order to analyze the effects of six preparation parameters (content of crumb rubber, content of diatomite, shear temperature, shear speed, shear time, and storing time) on the asphalt property, the response surface method (RSM) was utilized. The RSM is a group of mathematical and statistical techniques useful to design experiments. It can save cost and time by reducing the overall number of tests required [28, 29]. The RSM has been widely used in many areas to identify the effect of individual variables and interaction of different independent variables on the response [30–32]. An optimal quadratic model was used to determine the optimal condition of response:

$$y = \beta_0 + \sum_{i=1}^{k} \beta_i x_i + \sum_{i=1}^{k} \beta_{ii} x_i^2 + \sum_{i<j}^{k} \beta_{ij} x_i x_j + \varepsilon, \quad (2)$$

where y is the predicted response; x_i and x_j are the coded values of the preparation parameters; k is the number of independent variables; β_i is the linear effect of x_i; β_{ij} is the linear interaction between x_i and x_j; β_{ii} is the secondary effects of x_i; and ε is the random error.

In this study, the three level Box-Behnken design with six factors (content of crumb rubber, X_1; content of diatomite, X_2; shear time, X_3; shear speed, X_4; shear temperature, X_5; and storing time, X_6) was carried out. Actual and coded values of the independent variables are shown in Table 1. Combinations of X_1 (5%, 10%, 15%), X_2 (5%, 10%, 15%), X_3 (30, 45, 60 min), X_4 (3000, 4500, 6000 rpm), X_5 (160°C, 175°C, 190°C), and X_6 (30, 45, 60 min) were selected as independent variables. Penetration at 25°C, Y_1; softening point, Y_2; ductility at 15°C, Y_3; viscosity at 135°C, Y_4; elastic recovery at 25°C, Y_5; and penetration index (PI), Y_6 were adopted as the responses. The software Design-Expert 7.0 was adopted for the scheme design, model generating, statistical analysis, and optimization of the preparation parameters.

3. Results and Discussion

3.1. Experimental Scheme and ANOVA Results

3.1.1. Experimental Scheme. Experimental scheme for property analysis of compound-modified asphalt binder under the effect of preparation parameters was established based on the RSM. This scheme is composed of 54 experimental groups including 6 replicates at the central point, which is much less than a full test plan $3^6 = 729$. Three specimens are included in each group, and the corresponding average value is regarded as a representative one. The detailed experimental scheme and test results of responses are listed in Table 2. The relationships between independent variables and responses were analyzed by 3D response surface plots. A 3D plot is used to represent the dependent variables in function of two independent parameters, when other four variables are kept constant at level 0 in the code value. The interaction between independent variables can also be demonstrated in a 3D plot.

As can be seen from Table 2, the penetration ranged from 34.8 to 71.0 (0.1 mm). Softening point ranged from 46.8°C to 62.4°C. Ductility ranged from 141.0 to 379.7 mm. Viscosity ranged from 497.3 to 5752.0 mPa·s. Elastic recovery ranged from 21% to 63%. PI ranged from −1.5 to 0.83. According to these experimental ranges, the minimum and maximum values of penetration were obtained at Group

Table 1: Actual and coded values of the independent variables.

Coded value	Actual value					
	X_1 (%)	X_2 (%)	X_3 (min)	X_4 (rpm)	X_5 (°C)	X_6 (min)
−1	5	5	30	3000	160	30
0	10	10	45	4500	175	45
+1	15	15	60	6000	190	60

nos. 50 (X_1: 15%; X_2: 15%; X_3: 45 min; X_4: 3000 rpm; X_5: 175°C; and X_6: 45 min) and 46 (X_1: 5%; X_2: 5%; X_3: 45 min; X_4: 3000 rpm; X_5: 175°C; and X_6: 45 min), respectively. The minimum and maximum values of softening point were obtained at Group nos. 46 (X_1: 5%; X_2: 5%; X_3: 45 min; X_4: 3000 rpm; X_5: 175°C; and X_6: 45 min) and 50 (X_1: 15%; X_2: 15%; X_3: 45 min; X_4: 3000 rpm; X_5: 175°C; and X_6: 45 min), respectively. The minimum and maximum values of ductility were obtained at Group nos. 54 (X_1: 15%; X_2: 10%; X_3: 45 min; X_4: 3000 rpm; X_5: 160°C; and X_6: 45 min) and 14 (X_1: 15%; X_2: 5%; X_3: 45 min; X_4: 4500 rpm; X_5: 190°C; and X_6: 60 min), respectively. The minimum and maximum values of viscosity were obtained at Group nos. 46 (X_1: 5%; X_2: 5%; X_3: 45 min; X_4: 3000 rpm; X_5: 175°C; and X_6: 45 min) and 50 (X_1: 15%; X_2: 15%; X_3: 45 min; X_4: 3000 rpm; X_5: 175°C; and X_6: 45 min), respectively. The minimum and maximum values of elastic recovery were obtained at Group nos. 21 (X_1: 10%; X_2: 10%; X_3: 45 min; X_4: 4500 rpm; X_5: 190°C; and X_6: 60 min) and 50 (X_1: 15%; X_2: 15%; X_3: 45 min; X_4: 3000 rpm; X_5: 175°C; and X_6: 45 min), respectively. The minimum and maximum values of PI were obtained at Group nos. 49 (X_1: 15%; X_2: 5%; X_3: 45 min; X_4: 3000 rpm; X_5: 175°C; and X_6: 45 min) and 7 (X_1: 5%; X_2: 10%; X_3: 30 min; X_4: 4500 rpm; X_5: 175°C; and X_6: 60 min), respectively.

3.1.2. Analysis of Variance (ANOVA) Results for Quadratic Models and Independent Variables. Analysis of variance (ANOVA) was used to evaluate the statistical significance of independent parameters and interactions among them. The adequacy of the models constructed for penetration at 25°C, softening point, ductility at 15°C, viscosity at 135°C, elastic recovery at 25°C, and penetration index (PI) was checked by coefficient of determination (R^2), adjusted coefficient of determination (Adj. R^2), Adeq. precision, and Fisher's test value (F value). Models and factors were considered significant when $p < 0.01$. ANOVA results for quadratic models and independent variables are obtained and listed in Tables 3 and 4, respectively. The detailed explanations of results are given in Sections 3.2–3.7.

3.2. Penetration

3.2.1. Analysis of the Model for Penetration. The results of ANOVA for the penetration model indicated that the model possessed satisfactory levels of R^2 (0.90), Adj. R^2 (0.80), and Adeq. precision (11.014), which were significant at $p < 0.0001$. R^2 and Adj. R^2 values of the model were higher than 0.8, which revealed a close agreement between experimental results and predicted ones. Adeq. precision is the measure of the signal-to-noise ratio, and greater ratio than 4 is desirable. An Adeq. precision of 11.014 indicated that the model can be used to navigate the design space.

The second-order quadratic polynomial models were established based on the regression coefficients that were determined with the least squares method. Stepwise regression was used to identify the statistically significant variables. As can be seen from the ANOVA results of independent variables for the penetration model, the significant variables ($p < 0.05$) for the penetration model included X_1, X_2, X_5, X_{23}, X_{46}, X_{22}, X_{33}, and X_{44}.The reduced second-order model in terms of coded factors for penetration was obtained by removing the insignificant variables:

$$Y_1 = 43.81 - 6.69 \times X_1 - 4.97 \times X_2 + 5.17 \times X_5 + 3.10 \times X_{23} - 3.01 \times X_{46} + 2.87 \times X_{22} + 6.24 \times X_{33} + 6.22 \times X_{44}. \quad (3)$$

3.2.2. Effect of Preparation Parameters on Penetration. As shown in Table 4, the most significant linear variables on penetration include content of crumb rubber, content of diatomite, and shear temperature with $p < 0.0001$. Meanwhile, quadratic terms of shear time and shear speed present the most significant effect with $p < 0.0001$. The quadratic term of diatomite content has a significant effect with $p < 0.05$. Furthermore, the interaction terms of (diatomite content) ∗ (shear time) and (shear speed) ∗ (storing time) have significant effects on penetration with $p < 0.05$.

The relationships between preparation parameters and penetration were demonstrated in 3D response surface plots, which are shown in Figure 1. As can be seen from the figure, the penetration decreases with the increase of diatomite concentration and crumb rubber concentration. However, it increases with the increase of shear temperature. For the relationships of penetration with shear time, shear speed, and storing time, they present the trends of decreasing firstly and then increasing.

The interaction of crumb rubber and asphalt binder is essential for the performance of modified asphalt binder. Rubber particle swelling and significant absorption take place when rubber particles are added into heated asphalt binder. The polymer chains of rubber particles can absorb the lighter and solvating fractions of binder. Rubber particle size and shape are changed, and a gel-like structure is generated [3], which causes the reduction of penetration for asphalt binder.

Diatomite has a large specific area and good adsorption performance, which can effectively absorb the lower molecular group and lower polar aromatic molecular group for its mesoporous structure. The anchorage structure forms

Table 2: Experimental scheme with test results for property analysis of compound-modified asphalt binder.

Group number	Preparation parameters						Responses					
	X_1 (%)	X_2 (%)	X_3 (min)	X_4 (rpm)	X_5 (°C)	X_6 (min)	Y_1 (0.1 mm)	Y_2 (°C)	Y_3 (mm)	Y_4 (mPa·s)	Y_5 (%)	Y_6
1	5	10	45	6000	160	45	47.9	52.5	185.0	1343.3	33	−0.69
2	15	10	30	4500	175	30	47.5	56.2	218.3	2682.3	49	0.12
3	10	5	30	4500	190	45	67.7	50.5	339.5	1280.0	36	−0.33
4	15	5	45	6000	175	45	51.0	57.2	259.0	2865.0	58	0.50
5	10	15	45	4500	160	30	42.6	55.4	158.3	2098.0	36	−0.31
6	10	10	45	4500	175	45	44.8	53.3	203.3	1907.0	43	−0.66
7	5	10	30	4500	175	60	60.8	47.1	295.0	692.4	25	−1.50
8	10	10	45	4500	175	45	42.4	54.5	205.6	1919.0	44	−0.52
9	10	15	30	4500	190	45	50.6	54.8	294.3	1792.7	42	−0.04
10	10	10	45	4500	175	45	44.3	53.9	203.3	1907.0	43	−0.55
11	15	10	30	4500	175	60	51.4	55.1	244.0	1778.7	44	0.07
12	10	10	45	4500	175	45	43.6	53.9	204.5	1906.0	44	−0.58
13	10	5	45	4500	160	60	45.3	53.1	181.5	1833.3	42	−0.68
14	10	5	45	4500	190	60	55.0	51.0	379.7	1676.0	41	−0.73
15	10	10	30	3000	175	30	55.5	54.1	215.5	1844.7	34	0.03
16	5	10	30	4500	175	30	54.6	51.2	255.7	1140.7	25	−0.70
17	10	10	45	4500	175	45	43.1	54.1	204.9	1906.5	44	−0.57
18	10	15	60	4500	190	45	56.9	55.3	197.0	2017.0	51	0.36
19	10	5	30	4500	160	45	53.1	53.6	175.0	1402.0	40	−0.20
20	10	15	30	4500	160	45	41.8	55.9	171.0	2513.0	36	−0.24
21	10	10	30	3000	175	60	58.8	51.8	316.5	1301.7	21	−0.37
22	10	10	45	4500	175	45	44.8	53.3	203.3	1907.0	43	−0.66
23	10	5	60	4500	190	45	61.6	50.5	301.0	953.1	41	−0.58
24	5	5	45	6000	175	45	68.6	50.6	284.0	770.1	31	−0.27
25	15	10	45	6000	160	45	36.9	59.6	172.7	3821.0	54	0.24
26	10	5	60	4500	160	45	47.8	52.7	184.0	1034.0	46	−0.65
27	5	10	45	3000	160	45	54.6	50.7	219.3	880.4	27	−0.82
28	10	10	30	6000	175	60	53.8	54.2	231.0	2008.3	38	−0.02
29	10	15	45	4500	190	60	53.1	55.4	243.5	2109.0	53	0.21
30	15	10	60	4500	175	30	43.6	59.2	214.3	3675.7	57	0.54
31	5	15	45	6000	175	45	48.8	53.2	216.3	1356.0	29	−0.50
32	10	5	45	4500	190	30	56.8	51.4	341.3	1627.0	42	−0.55
33	10	10	60	6000	175	60	56.6	52.4	308.5	1930.3	47	−0.32
34	10	10	30	6000	175	30	57.9	52.2	354.3	1508.0	33	−0.31
35	5	10	45	3000	190	45	63.0	49.4	315.0	1188.0	32	−0.80
36	10	10	60	3000	175	30	53.3	54.0	269.5	2229.7	44	−0.09
37	10	15	60	4500	160	45	49.0	56.0	174.0	2430.0	42	0.15
38	10	15	45	4500	190	30	49.7	54.5	260.3	2054.0	46	−0.15
39	5	10	60	4500	175	60	49.9	50.9	249.0	913.4	34	−0.99
40	10	5	45	4500	160	30	49.2	53.3	197.7	1860.0	41	−0.44
41	5	15	45	3000	175	45	55.2	51.5	357.7	1202.7	15	−0.60
42	10	10	60	3000	175	60	60.3	50.9	329.0	774.4	25	−0.53
43	5	10	45	6000	190	45	59.3	49.9	314.5	704.8	30	−0.82
44	15	15	45	6000	175	45	37.1	60.4	191.7	4847.3	61	0.40
45	10	10	60	6000	175	30	66.3	49.5	348.0	1735.0	41	−0.65
46	5	5	45	3000	175	45	71.0	46.8	307.3	497.3	23	−1.21
47	15	10	45	3000	190	45	50.6	57.6	292.3	3509.0	54	0.57
48	15	10	45	6000	190	45	47.0	57.0	278.3	3539.0	60	0.26
49	15	5	45	3000	175	45	50.8	58.8	224.5	3724.3	55	0.83
50	15	15	45	3000	175	45	34.8	62.4	160.0	5752.0	63	0.64
51	10	15	45	4500	160	60	39.1	55.6	170.0	2198.7	32	−0.45
52	5	10	60	4500	175	30	58.4	49.1	309.5	765.9	23	−1.07
53	15	10	60	4500	175	60	40.6	59.5	198.7	4491.7	59	0.43
54	15	10	45	3000	160	45	40.2	59.3	141.0	3916.3	45	0.37

and the stiffening effect presents [33], which decrease the penetration of binder.

As for shear temperature, the interactions among asphalt, crumb rubber, and diatomite are strengthened with the increase of shear temperature. Rubber particle dissolution happens because of depolymerization and devulcanization, which break not only the polymer chains of rubber but also the crosslink bonds. Then, the swelling reaction is reduced,

Table 3: ANOVA results for quadratic models of modified asphalt properties.

Sources	R^2	Adj. R^2	Adeq. precision	F value	p value	Significant
Y_1	0.90	0.80	11.014	8.68	<0.0001	Yes
Y_2	0.95	0.90	17.854	18.37	<0.0001	Yes
Y_3	0.90	0.79	10.875	8.46	<0.0001	Yes
Y_4	0.94	0.87	13.392	13.94	<0.0001	Yes
Y_5	0.92	0.84	14.374	11.01	<0.0001	Yes
Y_6	0.93	0.85	14.466	12.00	<0.0001	Yes

Table 4: ANOVA results for independent variables.

Sources	Y_1		Y_2		Y_3		Y_4		Y_5		Y_6	
	F	p	F	p	F	p	F	p	F	p	F	p
X_1	74.86	<0.0001****	358.54	<0.0001****	26.1	<0.0001****	220.32	<0.0001****	279.97	<0.0001****	236.0	<0.0001****
X_2	41.34	<0.0001****	60.43	<0.0001****	17.3	0.0003***	23.60	<0.0001****	0.19	0.6701	15.2	0.0006***
X_3	0.26	0.6144	0.38	0.5416	0.0	0.8445	1.81	0.1899	19.69	0.0001****	0.0	0.9208
X_4	0.84	0.3668	0.07	0.7993	0.0	0.9755	0.03	0.8620	15.23	0.0006***	0.0	0.8415
X_5	44.66	<0.0001****	15.07	0.0006***	104.4	<0.0001****	1.66	0.2085	6.66	0.0159*	1.4	0.2500
X_6	0.33	0.5691	0.36	0.5541	0.0	0.9802	0.46	0.5041	0.24	0.6299	1.8	0.1901
X_{12}	0.27	0.6055	0.02	0.8832	2.0	0.1675	4.45	0.0448*	2.78	0.1077	1.4	0.2395
X_{13}	0.49	0.4923	3.59	0.0692	0.5	0.4847	8.96	0.0060**	2.33	0.1388	1.3	0.2606
X_{14}	0.98	0.3306	7.37	0.0116*	6.2	0.0197**	1.50	0.2312	0.35	0.5609	7.2	0.0125*
X_{15}	0.00	0.9454	0.02	0.8961	0.2	0.6962	0.08	0.7832	1.16	0.2905	0.4	0.5503
X_{16}	0.09	0.7717	0.26	0.6137	0.1	0.7023	0.03	0.8700	1.59	0.2184	1.1	0.3138
X_{23}	5.37	0.0286*	0.24	0.6252	0.6	0.4287	0.42	0.5223	0.14	0.7099	7.0	0.0134*
X_{24}	0.03	0.8562	0.71	0.4083	2.2	0.1461	0.02	0.8992	0.00	0.9543	1.8	0.1916
X_{25}	0.27	0.6110	2.23	0.1478	7.0	0.0137**	0.14	0.7147	11.70	0.0021**	3.4	0.0758
X_{26}	0.28	0.6017	0.31	0.5800	0.1	0.7374	0.01	0.9184	0.07	0.7989	1.3	0.2724
X_{34}	1.23	0.2783	1.33	0.2591	0.0	0.9543	0.05	0.8231	0.11	0.7442	0.4	0.5388
X_{35}	0.03	0.8635	0.18	0.6718	3.4	0.0782	0.07	0.7891	0.02	0.8861	0.2	0.6993
X_{36}	2.40	0.1332	2.93	0.0986	0.8	0.3941	0.36	0.5522	0.48	0.4967	1.1	0.3038
X_{45}	0.07	0.8001	0.53	0.4748	0.0	0.8845	0.41	0.5299	0.68	0.4156	0.3	0.5728
X_{46}	5.05	0.0334*	11.53	0.0022**	16.1	0.0005***	4.37	0.0466*	12.78	0.0014**	6.7	0.0158*
X_{56}	0.70	0.4095	0.03	0.8704	0.1	0.7497	0.00	0.9816	0.46	0.5027	1.0	0.3236
X_{11}	0.39	0.5398	7.87	0.0094**	0.4	0.5287	10.11	0.0038**	0.84	0.3692	3.6	0.0693
X_{22}	5.90	0.0223*	2.61	0.1183	0.9	0.3585	1.37	0.2530	0.10	0.7563	13.0	0.0013**
X_{33}	27.96	<0.0001****	3.72	0.0647	4.3	0.0471*	4.40	0.0458*	3.92	0.0585	5.1	0.0318*
X_{44}	27.76	<0.0001****	0.38	0.5442	23.2	<0.0001****	0.50	0.4840	5.90	0.0224*	13.0	0.0013**
X_{55}	0.29	0.5974	0.04	0.8452	0.0	0.8253	0.47	0.4968	0.09	0.7687	0.3	0.5725
X_{66}	1.71	0.2025	3.17	0.0869	11.8	0.0020**	0.10	0.7596	3.99	0.0562	0.8	0.3675

Note. $^{*}p \le 0.05$, $^{**}p \le 0.01$, $^{***}p \le 0.001$, and $^{****}p \le 0.0001$.

and the lighter fractions of binder increase. Therefore, the penetration increases with the increase of shear temperature.

Shear speed, shear time, and storing time present similar effects on penetration. At the early stage, rubber and diatomite particles are distributed more evenly in asphalt binder with the increase of shear speed, shear time, and storing time. The swelling effect is significant, and distances between particles are shortened. A gel-like structure and an anchorage structure are formed and strengthened. The penetration decreases. However, the crosslink bonds between particles are destroyed if the shear time and storing time are longer and the shear speed becomes higher, which increase the penetration of binder.

3.3. Softening Point

3.3.1. Analysis of the Model for Softening Point. The softening point model possessed satisfactory levels of R^2 (0.95), Adj. R^2 (0.90), and Adeq. precision (17.854), which were significant at $p < 0.0001$. R^2 and Adj. R^2 values of the model were higher than 0.8, which revealed a close agreement between experimental results and predicted ones. An Adeq. precision of 17.854 indicated that the model can be used to navigate the design space.

As can be seen from the ANOVA results of independent variables for the softening point model, the significant variables ($p < 0.05$) included X_1, X_2, X_5, X_{14}, X_{46}, and X_{11}. The reduced second-order model in terms of coded factors for softening point was obtained by removing the insignificant variables:

$$Y_2 = 53.83 + 4.15 \times X_1 + 1.70 \times X_2 - 0.85 \times X_5 - 0.73 \times X_{14} + 1.29 \times X_{46} + 0.94 \times X_{11}. \quad (4)$$

3.3.2. Effect of Preparation Parameters on Softening Point. As shown in Table 4, the most significant linear

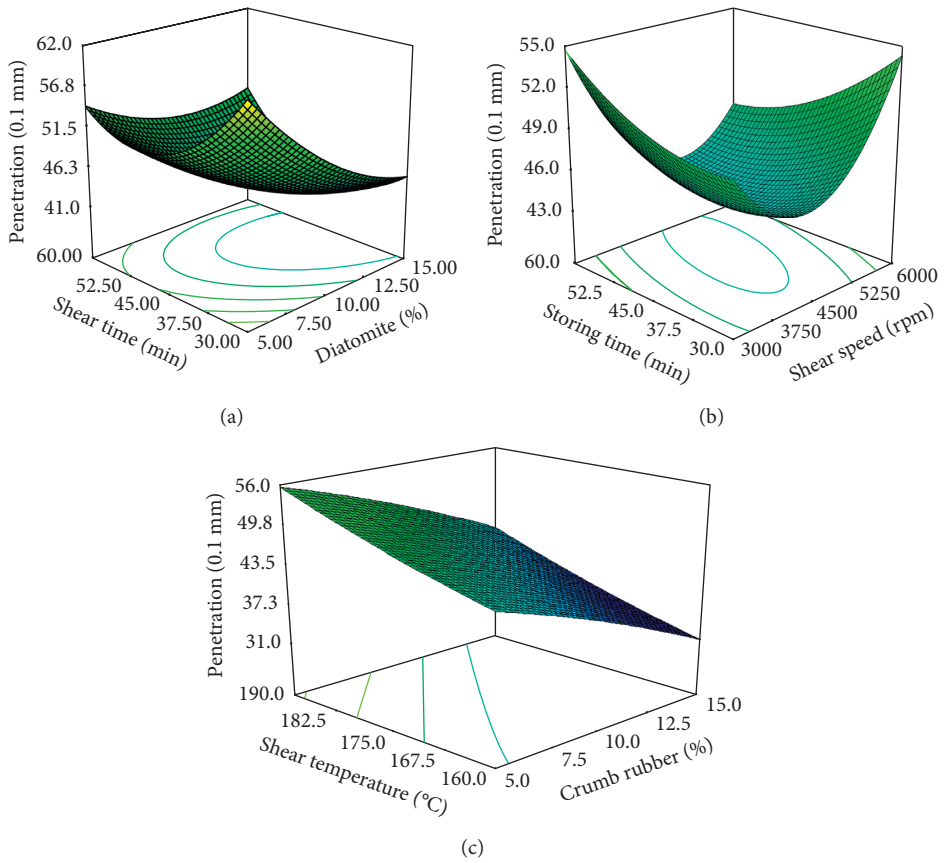

Figure 1: Response surface plots for the effect of preparation parameters on penetration. (a) Diatomite content ∗ shear time, (b) shear speed ∗ storing time, and (c) crumb rubber content ∗ shear temperature.

variables on softening point include content of crumb rubber and content of diatomite with $p < 0.0001$, followed by shear temperature with $p < 0.001$. Meanwhile, the quadratic term of crumb rubber content has a significant effect with $p < 0.01$. Furthermore, the interaction terms of (shear speed) ∗ (storing time) have significant effects on softening point with $p < 0.01$, followed by (crumb rubber content) ∗ (shear speed) with $p < 0.05$.

The softening points are applied to evaluate the high stability of modified asphalt binder. The higher the softening point is, the better the high susceptibility of asphalt is. The relationships between preparation parameters and softening point were demonstrated in 3D response surface plots, which are shown in Figure 2. As can be seen from the figure, the softening point increases with the increase of diatomite concentration and crumb rubber concentration. However, it decreases with the increase of shear temperature. For the relationships of the softening point with shear time, shear speed, and storing time, they present the trends of increasing firstly and then decreasing.

As discussed above, the polymer chains of rubber particles can absorb the lighter and solvating fractions of binder, and a gel-like structure is generated, which shortens the distances between particles and increases the softening point of binder. Diatomite can effectively absorb the lower molecular group and lower polar aromatic molecular group. The anchorage structure can improve the high temperature stability of asphalt binder with the increase of diatomite content. As for shear temperature, higher temperature will lead to the breakdown of polymer chains of rubber and crosslink bonds of binder. Therefore, the softening point increases with the increase of shear temperature. Shear speed, shear time, and storing time can strength the gel-like structure and anchorage structure of asphalt binder at the early stage, which make the softening point increase. However, the crosslink bonds between particles are destroyed if the shear time and storing time are longer and the shear speed becomes higher, which decrease the softening point of binder.

3.4. Ductility

3.4.1. Analysis of the Model for Ductility. The ductility model possessed satisfactory levels of R^2 (0.90), Adj. R^2 (0.79), and Adeq. precision (10.875), which were significant at $p < 0.0001$. R^2 value of the model was higher than 0.8 and Adj. R^2 value was highly close to 0.8, which revealed a close agreement between experimental results and predicted ones. An Adeq. precision of 10.875 indicated that the model can be used to navigate the design space.

As can be seen from the ANOVA results of independent variables for the ductility model, the significant variables

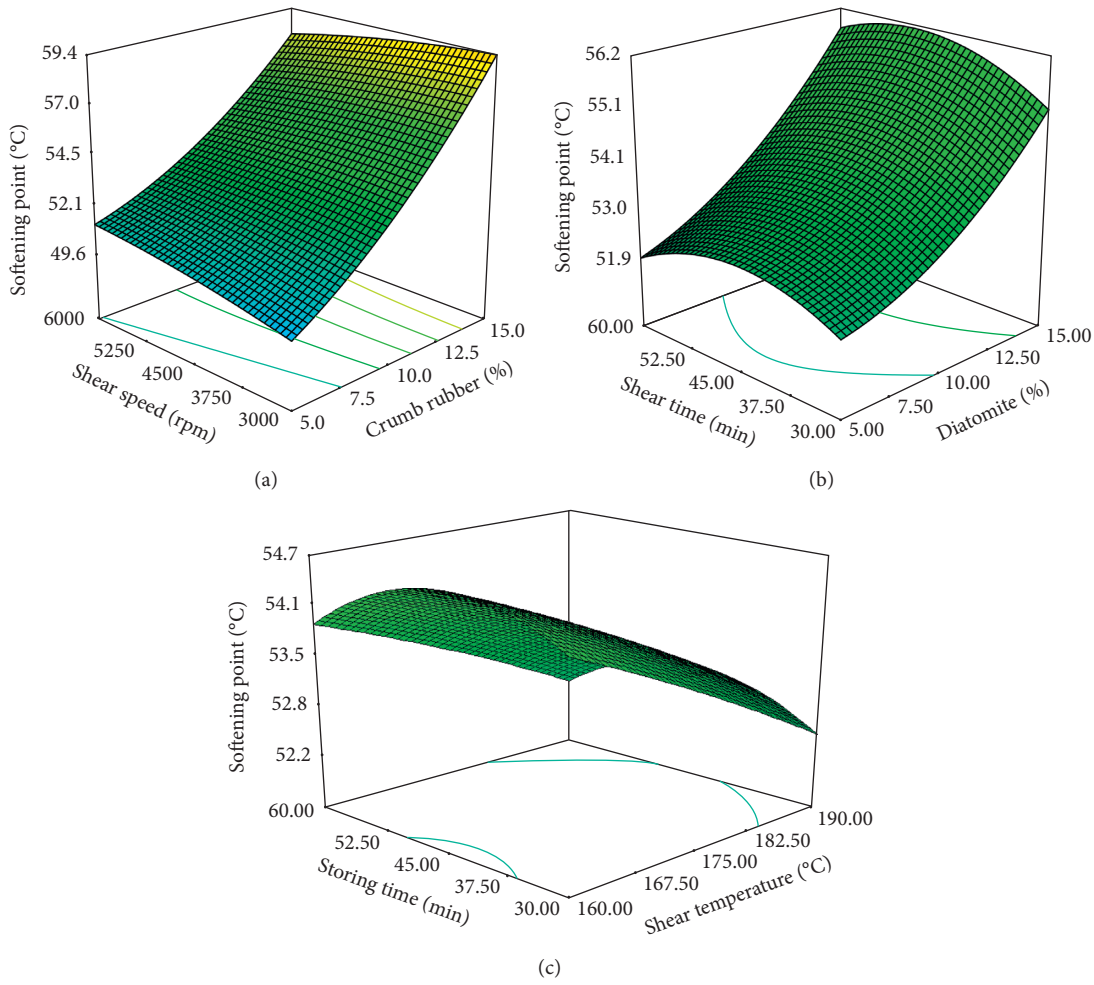

Figure 2: Response surface plots for the effect of preparation parameters on softening point. (a) Crumb rubber content ∗ shear speed, (b) diatomite content ∗ shear time, and (c) shear temperature ∗ storing time.

($p < 0.05$) included X_1, X_2, X_5, X_{14}, X_{25}, X_{46}, X_{33}, X_{44}, and X_{66}.The reduced second-order model in terms of coded factors for ductility was obtained by removing the insignificant variables:

$$Y_3 = 204.63 - 29.73 \times X_1 - 24.18 \times X_2 + 59.47 \times X_5 + 17.71 \times X_1 \times X_4 - 18.84 \times X_{25} - 40.42 \times X_{46} + 18.53 \times X_{33} + 42.80 \times X_{44} + 30.59 \times X_{66}. \quad (5)$$

3.4.2. Effect of Preparation Parameters on Ductility. As shown in Table 4, the most significant linear variables on ductility include content of crumb rubber and shear temperature with $p < 0.0001$, followed by content of diatomite with $p < 0.001$. Meanwhile, the quadratic term of shear speed has a significant effect with $p < 0.0001$, followed by storing time with $p < 0.001$ and shear time with $p < 0.05$. Furthermore, the interaction terms of (shear speed) ∗ (storing time) have significant effects on ductility with $p < 0.001$, followed by (crumb rubber content) ∗ (shear speed) and (diatomite content) ∗ (shear temperature) with $p < 0.01$.

Ductility can be used to reflect the low temperature performance of asphalt binder. The relationships between preparation parameters and ductility were demonstrated in 3D response surface plots, which are shown in Figure 3. As can be seen from the figure, the ductility increases with the increase of shear temperature. However, it decreases with the increase of diatomite concentration and crumb rubber concentration. For the relationships of ductility with shear time, shear speed, and storing time, they present the trends of decreasing firstly and then increasing.

The reasons lie in that addition of diatomite and crumb rubber can absorb the lighter fractions of the asphalt and result in large progressive increase of stiffness. The higher the stiffness is, the faster the failure stress reaches [16, 34]. Therefore, the elongation of compound-modified asphalt binder decreases. Another important reason is the stress concentration phenomenon occurring at the interface between the particle and asphalt. Therefore, the reduction of ductility does not indicate that the low temperature performance for crumb rubber and diatomite compound–modified asphalt is unsatisfactory. With the increase of shear temperature, viscosity toughness is reduced, resulting in the increase of

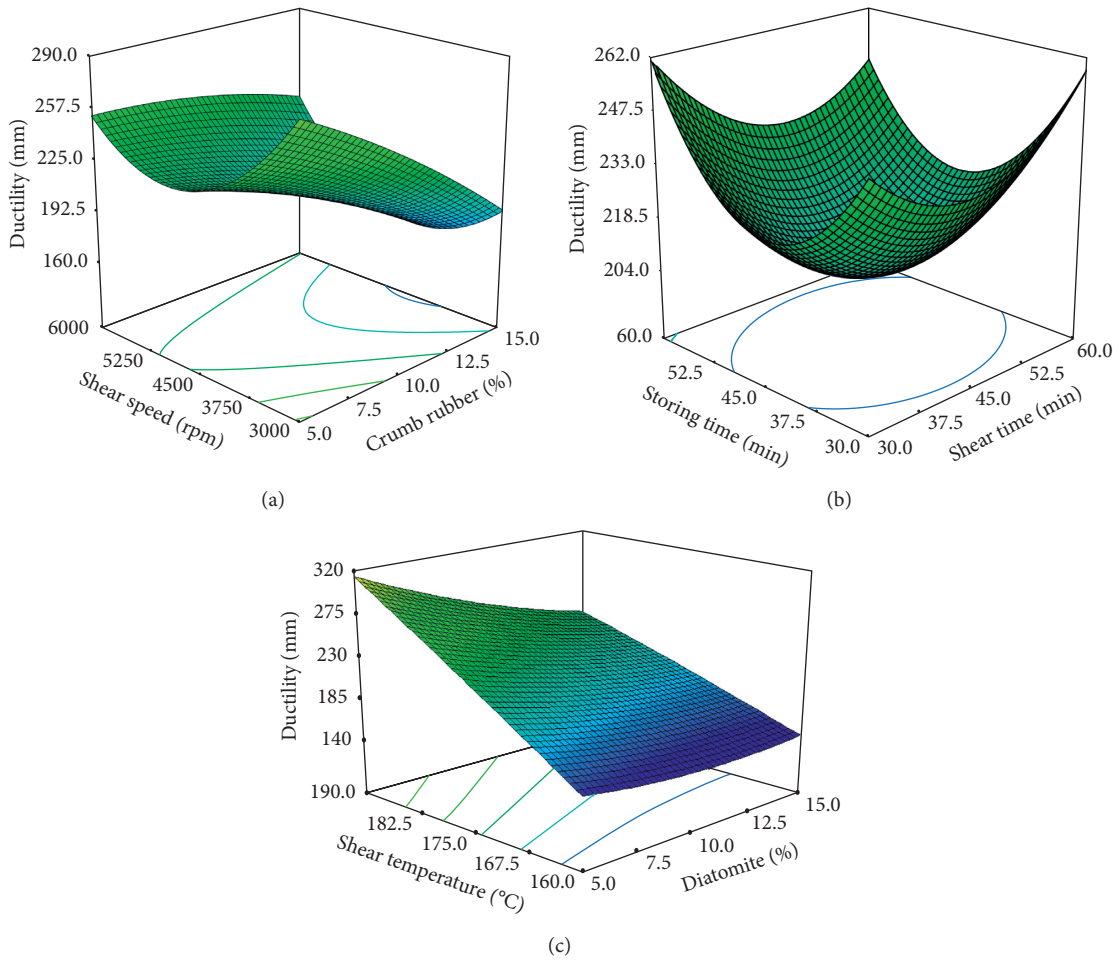

Figure 3: Response surface plots for the effect of preparation parameters on ductility. (a) Crumb rubber content ∗ shear speed, (b) storing time ∗ shear time, and (c) shear temperature ∗ diatomite content.

ductility. As for shear speed, shear time, and storing time, they can strength the gel-like structure and anchorage structure of asphalt and increase the stiffness of binder when their values are relatively lower. However, the stable structure will be destroyed when their values reach the critical points. Therefore, ductility decreases firstly and then increases with the increase of shear time, shear speed, and storing time.

3.5. Viscosity

3.5.1. Analysis of the Model for Viscosity. The viscosity model possessed satisfactory levels of R^2 (0.94), Adj. R^2 (0.87), and Adeq. precision (13.392), which were significant at $p < 0.0001$. R^2 and Adj. R^2 values of the model were higher than 0.8, which revealed a close agreement between experimental results and predicted ones. An Adeq. precision of 13.392 indicated that the model can be used to navigate the design space.

As can be seen from the ANOVA results of independent variables for the viscosity model, the significant variables ($p < 0.05$) included X_1, X_3, X_4, X_5, X_{25}, X_{46}, and X_{44}.The reduced second-order model in terms of coded factors for viscosity was obtained by removing the insignificant variables:

$$Y_4 = 1907.75 + 1381.14 \times X_1 + 125.24 \times X_3 - 16.34 \times X_4 - 120.2 \times X_5 - 42.11 \times X_{25} + 336.74 \times X_{46} + 100.93 \times X_{44}. \quad (6)$$

3.5.2. Effect of Preparation Parameters on Viscosity. As shown in Table 4, the most significant linear variables on viscosity include content of crumb rubber and shear time with $p \leq 0.0001$, followed by shear speed with $p < 0.001$ and shear temperature with $p < 0.05$. Meanwhile, the quadratic term of shear speed has a significant effect with $p < 0.05$. Furthermore, the interaction terms of (shear speed) ∗ (storing time) and (diatomite content) ∗ (shear temperature) have significant effects on viscosity with $p < 0.01$.

The relationships between preparation parameters and viscosity were demonstrated in 3D response surface plots, which are shown in Figure 4. As can be seen from the figure, the viscosities increase with the increase of diatomite concentration and crumb rubber concentration. However, they

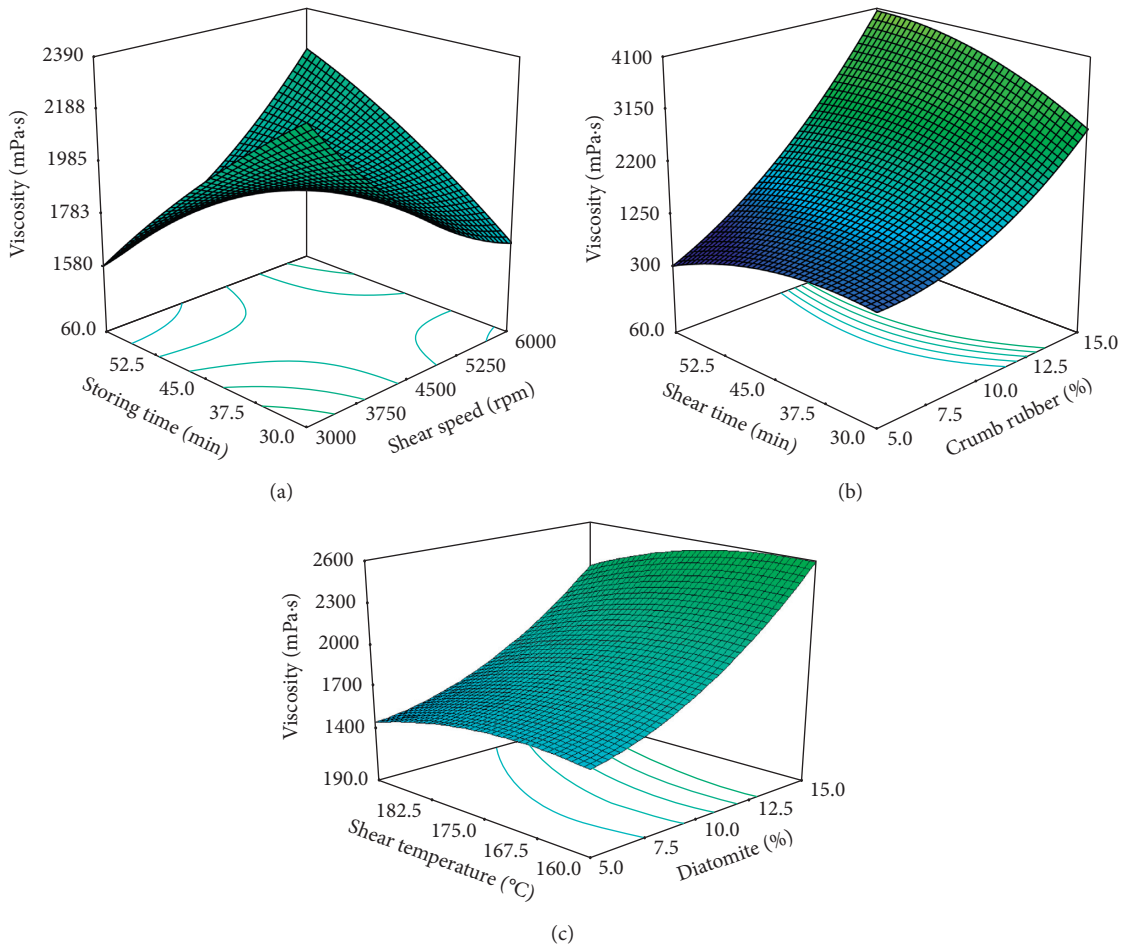

Figure 4: Response surface plots for the effect of preparation parameters on viscosity. (a) Storing time ∗ shear speed, (b) crumb rubber content ∗ shear time, and (c) shear temperature ∗ diatomite content.

present a declining trend with the increase of shear time, shear speed, shear temperature, and storing time.

This is because addition of diatomite and crumb rubber into asphalt can form a stable gel-like structure and an anchorage structure. The change in particle size and shape shortens the distances between particles, causing an increase in binder viscosity. If the values of shear temperature, shear speed, shear time, and storing time are too large, rubber particles will be broken down and dissolved into the liquid phase of binder. The crosslink bonds between particles will be destroyed, which will cause a reduction in binder viscosity.

3.6. Elastic Recovery

3.6.1. Analysis of the Model for Elastic Recovery. The elastic recovery model possessed satisfactory levels of R^2 (0.92), Adj. R^2 (0.84), and Adeq. precision (14.374), which were significant at $p < 0.0001$. R^2 and Adj. R^2 values of the model were higher than 0.8, which revealed a close agreement between experimental results and predicted ones. An Adeq. precision of 14.374 indicated that the model can be used to navigate the design space.

As can be seen from the ANOVA results of independent variables for the elastic recovery model, the significant variables ($p < 0.05$) included X_1, X_2, X_{12}, X_{13}, X_{46}, X_{11}, and X_{33}.The reduced second-order model in terms of coded factors for elastic recovery was obtained by removing the insignificant variables:

$$Y_5 = 43.40 + 13.92 \times X_1 + 0.36 \times X_2 + 2.40 \times X_{12} + 2.20 \times X_{13} + 5.15 \times X_{46} + 1.16 \times X_{11} - 2.51 \times X_{33}. \quad (7)$$

3.6.2. Effect of Preparation Parameters on Elastic Recovery. As shown in Table 4, the most significant linear variables on elastic recovery include content of crumb rubber and content of diatomite with $p < 0.0001$. Meanwhile, the quadratic term of crumb rubber concentration has a significant effect with $p < 0.01$, followed by shear speed with $p < 0.05$. Furthermore, the interaction terms of (crumb rubber concentration) ∗ (shear time) have significant effects on elastic recovery with $p < 0.01$, followed by (crumb rubber content) ∗ (diatomite content) and (shear speed) ∗ (storing time) with $p < 0.05$.

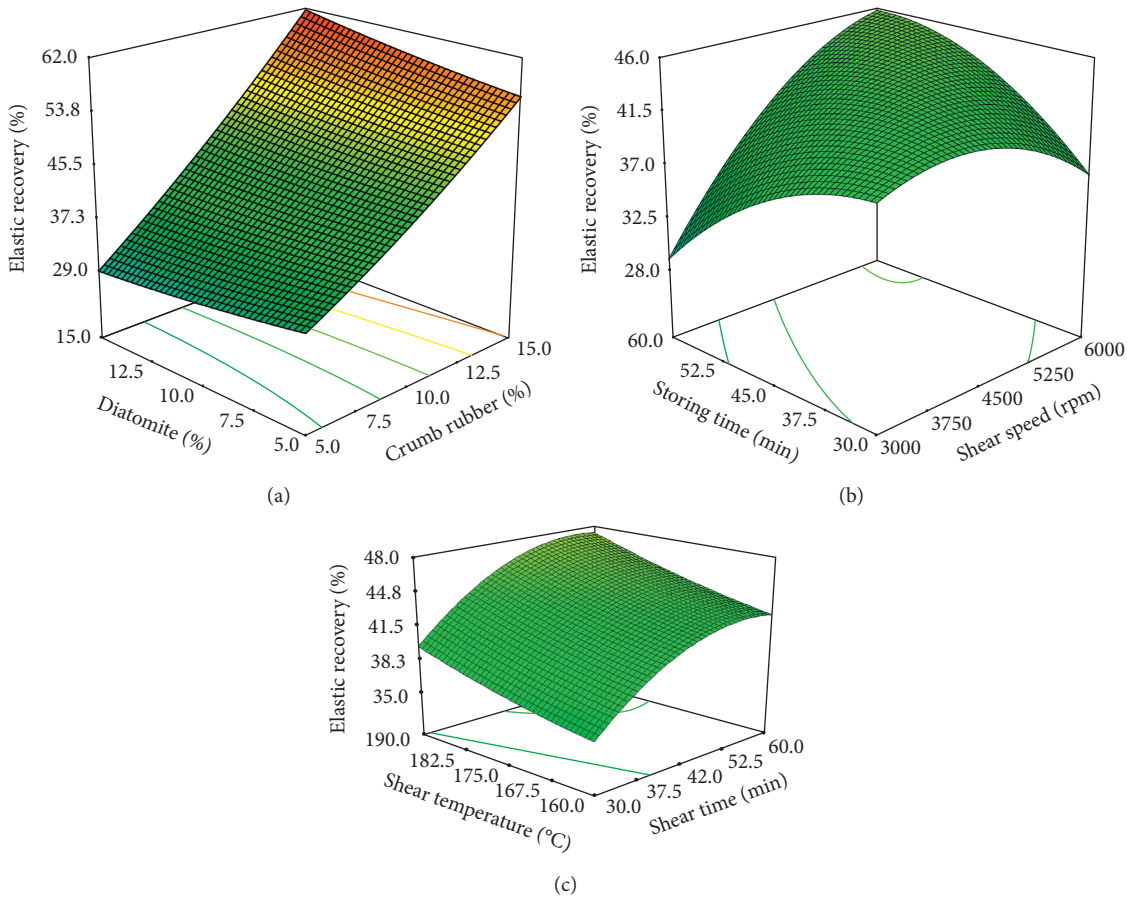

FIGURE 5: Response surface plots for the effect of preparation parameters on elastic recovery. (a) Crumb rubber content ∗ diatomite content, (b) storing time ∗ shear speed, and (c) shear temperature ∗ shear time.

The relationships between preparation parameters and elastic recovery were demonstrated in 3D response surface plots, which are shown in Figure 5. As can be seen from the figure, the elastic recovery increases with the increase of crumb rubber concentration and shear temperature. It increases with the increase of shear time and shear speed but at a decreasing rate. For the relationships of elastic recovery with storing time, they present the trend of increasing firstly and then decreasing slightly. Diatomite concentration can slightly increase the elastic recovery of binder. However, its effect is limited.

As can be seen from the results, the elastic recovery performance of the modified asphalt binder is mainly determined by crumb rubber concentration. The reasons lie in that crumb rubber possesses favorable elastic performance. Additions of crumb rubber into asphalt can strengthen the bonding effect of binder after swelling. The molecular force between particles is increased. Therefore, the ability of elastic recovery is improved. As for diatomite, it is a porous material without good elastic property. Its anchorage structure can enhance the elastic performance of binder to a certain extent. However, the effect is little.

3.7. Penetration Index (PI)

3.7.1. Analysis of the Model for PI. The PI model possessed satisfactory levels of R^2 (0.93), Adj. R^2 (0.85), and Adeq. precision (14.466), which were significant at $p < 0.0001$. R^2 and Adj. R^2 values of the model were higher than 0.8, which revealed a close agreement between experimental results and predicted ones. An Adeq. precision of 14.466 indicated that the model can be used to navigate the design space.

As can be seen from the ANOVA results of independent variables for the PI model, the significant variables ($p < 0.05$) included X_1, X_2, X_{14}, X_{23}, X_{46}, X_{22}, X_{33}, and X_{44}. The reduced second-order model in terms of coded factors for PI was obtained by removing the insignificant variables:

$$\begin{aligned} Y_6 = {} & -0.59 + 0.62 \times X_1 + 0.16 \times X_2 - 0.13 \times X_{14} \\ & + 0.19 \times X_{23} + 0.18 \times X_{46} + 0.22 \times X_{22} \\ & + 0.14 \times X_{33} + 0.22 \times X_{44}. \end{aligned} \quad (8)$$

3.7.2. Effect of Preparation Parameters on Penetration Index (PI). As shown in Table 4, the most significant linear variables on PI are content of crumb rubber with $p < 0.0001$, followed by content of diatomite with $p < 0.001$. Meanwhile, the quadratic term of diatomite concentration and shear speed has a significant effect with $p < 0.01$, followed by shear time with $p < 0.05$. Furthermore, the interaction terms of (crumb rubber concentration) ∗ (shear speed), (shear time) ∗ (diatomite content), and (shear speed) ∗ (storing time) have significant effects on PI with $p < 0.05$.

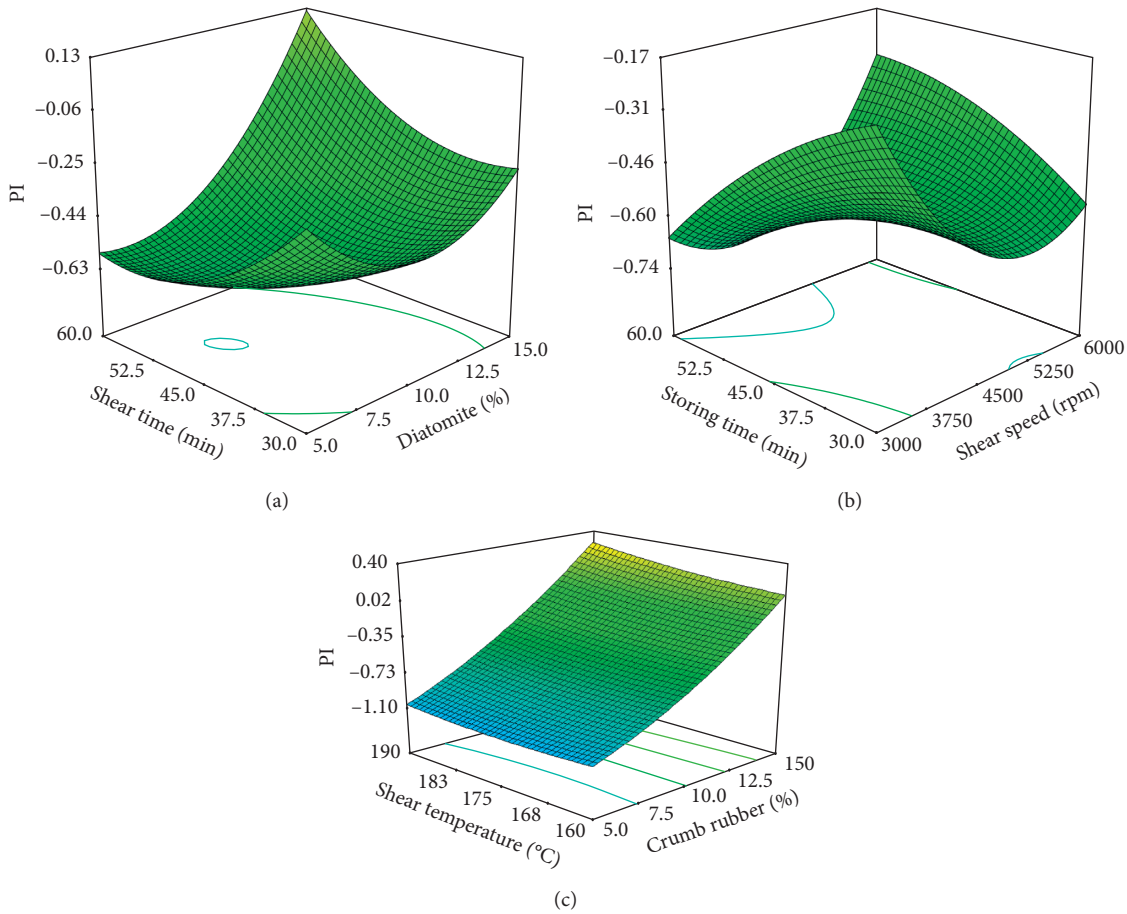

Figure 6: Response surface plots for the effect of preparation parameters on PI. (a) Shearing time ∗ diatomite content, (b) storing time ∗ shear speed, and (c) shear temperature ∗ crumb rubber content.

Table 5: Optimum preparation parameters and corresponding predicted and experimental results.

Factors	X_1	X_2	X_3	X_4	X_5
Optimum value	13.8	6.2	55	5300	183
Responses	Y_1	Y_2	Y_3	Y_4	Y_5
Predicted results	54.15	55.17	307.4	2708	67.63
Experimental results	54.96	54.56	296.6	2814	68.64
Relative error (%)	1.5	1.1	3.5	3.9	1.5

The relationships between preparation parameters and PI were demonstrated in 3D response surface plots, which are shown in Figure 6. As can be seen from the figure, the PI increases with the increase of crumb rubber concentration. It remains relatively stable before 8–10% of diatomite concentration and increases after that. The relationships of PI with shear speed and shear time present the trend of decreasing firstly and then increasing. PI increases with the increase of shear temperature with little amplitude.

The results reveal that addition of crumb rubber and diatomite into asphalt can effectively improve its temperature stability. This is mainly because of the gel-like structure and anchorage structure. As for shear time, shear speed, shear temperature, and swelling time, their influences on temperature stability of binder are lower than on diatomite concentration and crumb rubber concentration.

3.8. Multiresponse Optimization. Preparation parameters present different effects on properties of crumb rubber and diatomite compound–modified asphalt binder. In order to obtain the modified asphalt binder with satisfactory properties, multiresponse optimization is conducted using the RSM. Taking the modified asphalt used in the cold region, for example, the corresponding optimization criteria are determined according to JTG F40-2004 [35] and "*Guide for Design and Construction of Asphalt Rubber and Mixtures*" [36] in China. The optimization was carried out by maximizing the softening point, ductility, elastic recovery, and minimizing penetration, while the viscosity is between 1000 and 3000 mPa·s. Viscosity should not be too high because of the workability of modified asphalt binder. PI is not considered because it can be calculated based on penetration and softening point results according to (2). The optimization process is determined and listed in Table 5.

In order to verify the equations as well as the optimum data obtained by the RSM, experimental tests were conducted using the same preparation parameters listed in Table 5. The experimental results are obtained and also shown in

Table 5. As shown in this table, the predicted and experimental results possess favorable consistency.

4. Conclusions

In this paper, crumb rubber and diatomite compound–modified asphalt binder was prepared. The effects of preparation parameters on properties of modified asphalt binder were investigated, and multiresponse optimization was conducted using the response surface method. The following conclusions can be obtained:

(1) Response surface method is a suitable method for preparation parameter analysis and optimization of crumb rubber and diatomite compound–modified asphalt binder, which can effectively reduce the number of groups.

(2) Crumb rubber concentration presents significant effects on all of the asphalt properties used in this study. Softening points, viscosity, elastic recovery, and PI increase, while penetration and ductility decrease with the increase of crumb rubber concentration. It reveals that the addition of crumb rubber can improve the high temperature susceptibility, viscosity, and elastic recovery ability of binder.

(3) Diatomite concentration presents significant effects on all of the asphalt properties except elastic recovery. Softening points, viscosity, and PI increase, while penetration and ductility decrease with the increase of diatomite concentration, which presents little influence on elastic recovery of binder.

(4) Shear temperature presented significant effects on penetration, softening point, viscosity, and ductility. Shear speed, shear time, and storing time have similar effects on binder properties because of their similar mechanism of action.

(5) Based on the model obtained from the RSM, optimized preparation parameters corresponding to specific criteria can be determined, which possessed favorable accuracy compared with experimental results.

Investigation of other properties such as bending beam rheometer (BBR) and dynamic shear rheometer (DSR) tests of crumb rubber and diatomite compound–modified asphalt binder needs to be conducted in the near future.

Conflicts of Interest

The authors declare that they have no conflicts of interest.

Acknowledgments

The authors express their appreciation for the financial support of the National Natural Science Foundation of China under Grant no. 51408258; the China Postdoctoral Science Foundation funded projects (nos. 2014M560237 and 2015T80305); the Fundamental Research Funds for the Central Universities (JCKYQKJC06); and Science and Technology Development Program of Jilin Province.

References

[1] V. W. Y. Tam and C. M. Tam, "A review on the viable technology for construction waste recycling," *Resources, Conservation and Recycling*, vol. 47, no. 3, pp. 209–221, 2006.

[2] M. N. Amin, M. I. Khan, and M. U. Saleem, "Performance evaluation of asphalt modified with municipal wastes for sustainable pavement construction," *Sustainability*, vol. 8, no. 12, p. 949, 2016.

[3] D. L. Presti, "Recycled tyre rubber modified bitumens for road asphalt mixtures: a literature review," *Construction and Building Materials*, vol. 49, pp. 863–881, 2013.

[4] M. C. Zanetti, S. Fiore, B. Ruffino, E. Santagata, D. Dalmazzo, and M. Lanotte, "Characterization of crumb rubber from end-of-life tyres for paving applications," *Waste Management*, vol. 45, pp. 161–170, 2015.

[5] A. Farina, M. C. Zanetti, E. Santagata, and G. A. Blengini, "Life cycle assessment applied to bituminous mixtures containing recycled materials: crumb rubber and reclaimed asphalt pavement," *Resources, Conservation and Recycling*, vol. 117, pp. 204–212, 2017.

[6] I. Bartolozzi, S. Mavridou, F. Rizzi, and M. Frey, "Life cycle thinking in sustainable supply chains: the case of rubberized asphalt pavement," *Environmental Engineering and Management Journal*, vol. 14, no. 5, pp. 1203–1215, 2015.

[7] A. D. La Rosa, G. Recca, D. Carbone et al., "Environmental benefits of using ground tyre rubber in new pneumatic formulations: a life cycle assessment approach," *Proceedings of the Institution of Mechanical Engineers, Part L: Journal of Materials: Design and Applications*, vol. 229, no. 4, pp. 309–317, 2013.

[8] B. Yu, L. Jiao, F. Ni, and J. Yang, "Evaluation of plastic–rubber asphalt: engineering property and environmental concern," *Construction and Building Materials*, vol. 71, pp. 416–424, 2014.

[9] F. Moreno, M. Sol, J. Martín, M. Pérez, and M. C. Rubio, "The effect of crumb rubber modifier on the resistance of asphalt mixes to plastic deformation," *Materials and Design*, vol. 47, pp. 274–280, 2013.

[10] S. K. Palit, K. S. Reddy, and B. B. Pandey, "Laboratory evaluation of crumb rubber modified asphalt mixes," *Journal of Materials in Civil Engineering*, vol. 16, no. 1, pp. 45–53, 2004.

[11] O. Xu, F. Xiao, S. Han, S. N. Amirkhanian, and Z. Wang, "High temperature rheological properties of crumb rubber modified asphalt binders with various modifiers," *Construction and Building Materials*, vol. 112, pp. 49–58, 2016.

[12] K. L. N. N. Puga and R. C. Williams, "Low temperature performance of laboratory produced asphalt rubber (AR) mixes containing polyoctenamer," *Construction and Building Materials*, vol. 112, pp. 1046–1053, 2016.

[13] T. Wang, F. Xiao, S. Amirkhanian, W. Huang, and M. Zheng, "A review on low temperature performances of rubberized asphalt materials," *Construction and Building Materials*, vol. 145, pp. 483–505, 2017.

[14] P. Cong, S. Chen, and H. Chen, "Effects of diatomite on the properties of asphalt binder," *Construction and Building Materials*, vol. 30, pp. 495–499, 2012.

[15] Y. Tan, Z. Lei, and X. Zhou, "Investigation of low-temperature properties of diatomite-modified asphalt mixtures," *Construction and Building Materials*, vol. 36, pp. 787–795, 2012.

[16] Y. Cheng, J. Tao, Y. Jiao et al., "Influence of the properties of filler on high and medium temperature performances of asphalt mastic," *Construction and Building Materials*, vol. 118, pp. 268–275, 2016.

[17] Q. Guo, L. Li, Y. Cheng, Y. Jiao, and C. Xu, "Laboratory evaluation on performance of diatomite and glass fiber compound modified asphalt mixture," *Materials and Design*, vol. 66, pp. 51–59, 2015.

[18] P. Cong, N. Liu, Y. Tian, and Y. Zhang, "Effects of long-term aging on the properties of asphalt binder containing diatoms," *Construction and Building Materials*, vol. 123, pp. 534–540, 2016.

[19] H. Liu, L. Fu, Y. Jiao, J. Tao, and X. Wang, "Short-term aging effect on properties of sustainable pavement asphalts modified by waste rubber and diatomite," *Sustainability*, vol. 9, no. 12, p. 996, 2017.

[20] C. Fang, X. Qiao, R. Yu et al., "Influence of modification process parameters on the properties of crumb rubber/EVA modified asphalt," *Journal of Applied Polymer Science*, vol. 133, no. 27, 2016.

[21] H. Yu, Z. Leng, Z. Zhou, K. Shih, F. Xiao, and Z. Gao, "Optimization of preparation procedure of liquid warm mix additive modified asphalt rubber," *Journal of Cleaner Production*, vol. 141, pp. 336–345, 2017.

[22] X. Shu and B. Huang, "Recycling of waste tire rubber in asphalt and Portland cement concrete: an overview," *Construction and Building Materials*, vol. 67, pp. 217–224, 2014.

[23] S. Kedarisetty, K. P. Biligiri, and J. B. Sousa, "Advanced rheological characterization of reacted and activated rubber (RAR) modified asphalt binders," *Construction and Building Materials*, vol. 122, pp. 12–22, 2016.

[24] Q. Wang, S. Li, X. Wu, S. Wang, and C. Ouyang, "Weather aging resistance of different rubber modified asphalts," *Construction and Building Materials*, vol. 106, pp. 443–448, 2016.

[25] J. Peralta, H. M. Silva, L. Hilliou, A. V. Machado, J. Pais, and R. C. Williams, "Mutual changes in bitumen and rubber related to the production of asphalt rubber binders," *Construction and Building Materials*, vol. 36, pp. 557–565, 2012.

[26] J. C. Munera and E. A. Ossa, "Polymer modified bitumen: optimization and selection," *Materials and Design*, vol. 62, pp. 91–97, 2014.

[27] L. H. Li, *Road Engineering Materials*, China Communications Press, Beijing, China, 5th edition, 2010.

[28] M. L. Huang, Y. H. Hung, and Z. S. Yang, "Validation of a method using Taguchi, response surface, neural network, and genetic algorithm," *Measurement*, vol. 94, pp. 284–294, 2016.

[29] I. Kaymaz and C. A. McMahon, "A response surface method based on weighted regression for structural reliability analysis," *Probabilistic Engineering Mechanics*, vol. 20, no. 1, pp. 11–17, 2005.

[30] O. Rezaifar, M. Hasanzadeh, and M. Gholhaki, "Concrete made with hybrid blends of crumb rubber and metakaolin: optimization using response surface method," *Construction and Building Materials*, vol. 123, pp. 59–68, 2016.

[31] H. İ. Odabaş and I. Koca, "Application of response surface methodology for optimizing the recovery of phenolic compounds from hazelnut skin using different extraction methods," *Industrial Crops and Products*, vol. 91, pp. 114–124, 2016.

[32] M. H. Esfe, H. Hajmohammad, R. Moradi, and A. A. A. Arani, "Multi-objective optimization of cost and thermal performance of double walled carbon nanotubes/water nanofluids by NSGA-II using response surface method," *Applied Thermal Engineering*, vol. 112, pp. 1648–1657, 2017.

[33] Y. Song, J. Che, and Y. Zhang, "The interacting rule of diatomite and asphalt groups," *Petroleum Science and Technology*, vol. 29, no. 3, pp. 254–259, 2011.

[34] Y. Cheng, J. Tao, Y. Jiao, Q. Guo, and C. Li, "Influence of diatomite and mineral powder on thermal oxidative ageing properties of asphalt," *Advances in Materials Science and Engineering*, vol. 2015, Article ID 947834, 10 pages, 2015.

[35] JTG F40-2004, *Technical Specifications for Construction of Highway Asphalt Pavements*, Research Institute of Highway Ministry of Transport, Beijing, China, 2004, in Chinese.

[36] China Communications Press, *Guide for Design and Construction of Asphalt Rubber and Mixtures*, China Communications Press, Beijing, China, 2009, in Chinese.

Hindawi
Advances in Materials Science and Engineering
Volume 2018, Article ID 2172575, 8 pages
https://doi.org/10.1155/2018/2172575

Research Article

Construction Time of Three Wall Types Made of Locally Sourced Materials: A Comparative Study

Wojciech Drozd, Agnieszka Leśniak, and Sebastian Zaworski

Institute of Construction Management, Tadeusz Kościuszko Cracow University of Technology, Warszawska 24 St., 31-155 Kraków, Poland

Correspondence should be addressed to Wojciech Drozd; wdrozd@ztob.pk.edu.pl

Received 8 November 2017; Revised 22 January 2018; Accepted 4 February 2018; Published 19 March 2018

Academic Editor: Estokova Adriana

Similarly to any other industry, the construction sector puts emphasis on innovativeness, unconventional thinking, and alternative ideas. At present, when sustainable development, ecology, and awareness of people's impact on the environment grow in importance, low impact buildings can become an innovative alternative construction technology for the highly industrialized construction sector. The paper presents a comparative study of three walls made of available materials used locally, which can be classified as biosourced materials, in terms of construction time. The comparison of times necessary to make 1 m^2 of the wall allows us to decide which building technology is more advantageous in terms of the construction duration. A shorter construction time means lower labour costs and lower expenses for construction machines. In order to obtain answers to the questions posed, the authors made extensive searches of source data on the time-consuming building works which used locally sourced materials. Reference is made to "Temporary principles of erecting clay buildings" issued by the Institute of Housing Construction in Warsaw (Poland). Three types of walls made of locally sourced materials were studied: a wall made of clay blocks insulated with mineral wool boards, a wall made of clay compacted in formwork, and one insulated with mineral wool boards and wooden frame structure filled with straw bales and cladded with fibreboards. The layers have been chosen in such a manner that heat transfer coefficient values for the studied variants are as equal as possible (0.2 W/m^2 K), thus allowing a reliable comparative study.

1. Introduction

Modern material and technological solutions—concrete, steel, glass, and intelligent systems—have become the synonyms of modernity and luxury [1]. Buildings made of locally sourced materials are on the other extreme of modern construction. These solutions are based primarily on tradition and local, low-cost raw materials that do not require special treatment, which are readily available, such as soil, clay, straw, and sand. Human hands are the main building force, while the use of complicated techniques or expensive expertise is limited. Low impact buildings avoid complex technical solutions and support generally accessible raw materials. The construction market, dominated by giant construction companies, does not support the development of such solutions since they are not profitable. This makes it difficult to popularize such a building method on a large scale. Despite this, buildings made of locally sourced materials are becoming more common and perfectly fit into the idea of sustainable development.

The most important features of a building characterized by sustainable development can be described using four Rs: reduce, reuse, recycle, and recover [2]. Less material and energy are used to build such a building compared to conventional construction The materials used should be recycled and should allow for reuse after the end of the life of the building. Low impact buildings derive the materials from the surrounding environment. This supports local development and cultural independence of the region. Production of materials does not require high energy and high temperature processed and does not produce CO_2, so it consumes less energy needed to construct the building than conventional building construction. Transport of materials is only done locally [3]. And the structure itself is completely

biodegradable, and after the end of its life, it does not leave harmful waste, hard to break down by the environment. Building made of locally sourced materials allows for carrying out a lot of the work on one's own. It is available to all and creates local jobs [4].

Research in the field of natural building technologies is not numerous. Among them in paper [5] a comparison of the mechanical performance of structural elements built in three basic techniques, Earth block (adobe) masonry, rammed Earth, and cob, is presented. Up to present, few studies are available concerning the mechanical behaviour of straw bales in buildings. Such study is presented in [6] and aims at investigating the behaviour of straw bales and leads to recommendations for required bale densities. In [7], the viability of straw-bale construction has recently been investigated, in particular, its resistance to moisture. Similarly in [8], two options for the use of straw to fill envelop walls were investigated in the Andean Patagonian region: the direct use of straw bales, whether in whole or in halves, and the manufacturing of straw-clay blocks. All straw options analysed result in significantly better thermal performance than current choices of fired bricks or concrete blocks, which are commonly used in the region. In turn, in [9] was evaluated a straw-bale house located in Bavaria, Germany. The experimental work included compression tests, moisture content, thermal stability of bales, and pH. Reference [10] examines the use and accuracy of a moisture probe used in the walls of a straw-bale building. The measurements from a number of moisture probes placed in the walls of a case study straw-bale building over a 2-year period are presented. Similarly [11] concludes results from a study on moisture monitoring in straw-bale construction and includes the development of an empirical equation which relates the straw moisture content to surrounding microclimate relative humidity and temperature. Reference [12] presents results from a study on the thermal conductivity of some plaster materials that could be used for straw-bale buildings. Walls constructed in the straw-bale technology can boast excellent health qualities, which are difficult to obtain in traditional technologies [13].

Up until today, few studies are available concerning the time of construction of walls made of locally sourced materials. In this paper, the construction time of 1 m^2 of three types of walls built in these technologies was studied. The layers of the walls were chosen in such a manner that the heat transfer coefficient values for the studied variants are as equal as possible (0.2 W/m^2K), thus allowing a reliable comparative study:

(i) A wall made of clay blocks insulated with mineral wool boards

(ii) A wall made of clay compacted in formwork, insulated with mineral wool boards

(iii) A wooden frame structure filled with straw bales and cladded with fibreboards

Construction time allows us to tell which technology is more advantageous. In order to obtain answers to the questions posed, the authors made extensive searches of source data concerning the timing of building works using locally sourced materials. Literature does not actually present any time standards. The exception is "Temporary principles of erecting clay buildings" issued by the Institute of Housing Construction in Warsaw (Poland), which were used in the comparison.

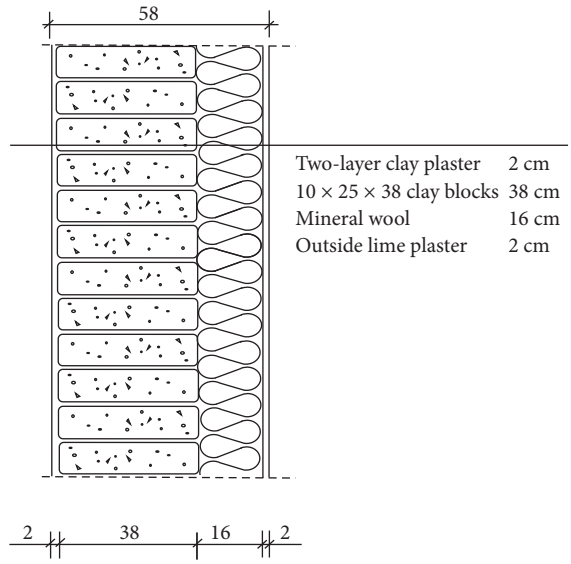

Figure 1: Cross section of the clay block wall.

2. Characteristics and Technical Parameters of Studied Walls

2.1. Wall Made of Clay Blocks Insulated with Mineral Wool Boards. The first studied structure was a wall made of 10 × 25 × 38 cm clay blocks insulated with mineral wool boards. The structural layer of the wall is 38 cm thick (Figure 1). On the outside, the wall will be insulated with 16 cm thick mineral wool boards and covered with lime plaster. On the inside, the wall will be covered with a two-layer clay plaster. Wood fibreboards have also been considered as insulation as more environmentally friendly, but this solution is presently too expensive to be compared with affordable EPS (expanded polystyrene).

2.2. Wall Made of Clay Compacted in Formwork, Insulated with Mineral Wool Boards. The other studied solution was the wall made of clay compacted in the formwork whose structural thickness was 30 cm (Figure 2). The formwork was demountable panels. The remaining wall layers were the same as in the clay block wall.

2.3. Wooden Frame Structure Filled with Straw Bales and Cladded with Fibreboards. The third variant was the wall made of small 31 × 41 × 70 cm straw bales placed in wooden frame structure (Figure 3). The frame structure will be erected in the timber-frame house technology where posts are made as frames, so-called ladders. The wooden frame skeleton will be cladded on both sides with 12-millimetre fibreboards for

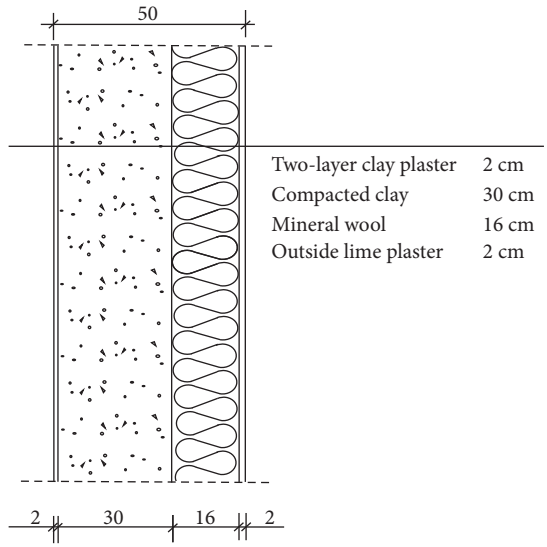

Figure 2: Cross section of the wall made of clay compacted in formwork.

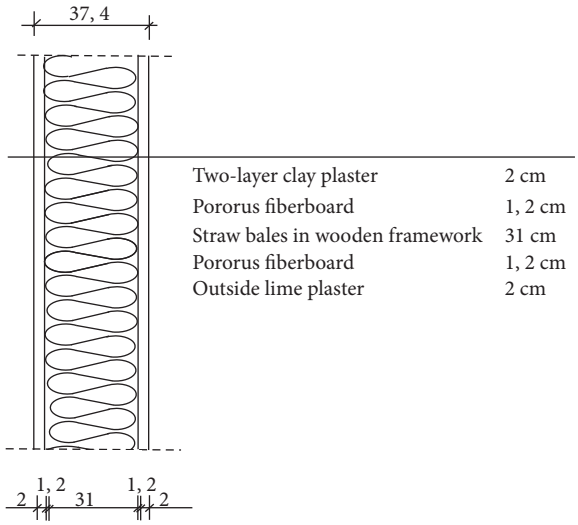

Figure 3: Cross section of the wall made in the straw-bale technology.

Table 1: Density and thermal conductivity of used materials.

	Material type	Density (kg/m^3)	Thermal conductivity λ (W/m K)
Insulation materials	Straw bales	100	0.073
	Porous fibreboard	300	0.060
	Mineral wool boards	160	0.037
Structural materials	Compacted clay and clay blocks	1800	0.900
	Pine wood	450	0.200
Materials	Lime plaster	1700	0.700
	Clay plaster	900	0.300

Source: own study, based on [14].

Table 2: Thermal properties of a clay block wall.

Layers	d (m)	λ (W/m K)	R (m^2 K/W)	U (W/m^2 K)
R_{si}			0.13	
Two-layer clay plaster	0.020	0.300	0.06666667	
Clay blocks	0.380	0.900	0.42222222	
Insulation: mineral wool	0.160	0.037	4.32432432	
Lime plaster	0.020	0.700	0.02857143	
R_{se}			0.04	
Total d	0.580	RT	5.012	0.200

Source: own study.

Table 3: Thermal properties of a compacted clay wall.

Layers	d (m)	λ (W/m K)	R (m^2 K/W)	U (W/m^2 K)
R_{si}			0.13	
Two-layer clay plaster	0.020	0.300	0.06666667	
Compacted clay	0.300	0.900	0.33333333	
Insulation: mineral wool	0.160	0.037	4.32432432	
Lime plaster	0.020	0.700	0.02857143	
R_{se}			0.04	
Total d	0.500	RT	4.923	0.203

Source: own study.

Table 4: Thermal properties of a straw-bale wall.

Layers	d (m)	λ (W/m K)	R (m^2 K/W)	U (W/m^2 K)
R_{si}			0.130	
Two-layer clay plaster	0.020	0.300	0.067	
Fibreboard	0.012	0.060	0.200	
Straw bales in frame structure	0.310	0.073	4.247	
Fibreboard	0.012	0.060	0.200	
Lime plaster	0.020	0.700	0.029	
R_{se}			0.040	
Total d	0.374	RT	4.912	0.204

Source: own study.

Table 5: Dependence of studied technologies on seasons and weather conditions.

Wall type	Works can be performed all year long	Works strongly dependent on weather conditions
Clay blocks	Yes	Yes
Compacted clay	No	Yes
Straw bale	No	Yes

Source: own study based on [14, 16, 17].

Table 6: Time necessary to make $10 \times 25 \times 38$ cm clay blocks.

Clay preparation difficulty	Compound preparation	Making of elements	Squaring of elements	Putting in trestles	Total time	Total time
			m-h/100 pcs			m-h/m^2
Medium-cohesion 801–1400 g/5 cm^2	2.52	5.82	0.42	0.50	9.26	$8.99 \times 0.38 = 3.42$
			m-h/m^3			
	2.45	5.65	0.41	0.49	8.99	

Source: own study.

Table 7: Time necessary to build the clay block wall (wall thickness 38 cm).

	Masonry works	Transport		Making of mortar	Auxiliary works	Total time
		Blocks	Mortar			
				m-h/m^3		
Ground floor	3.37	1.24	0.15	0.467	0.2	5.427
1st floor	3.37	1.88	0.20	0.467	0.21	6.127

Source: own study.

Table 8: Various works (wall thickness 38 cm).

Work	Unit	Time
Extra to the full wall for making corners	m-h/mb	0.23
Extra for making window reveals	m-h/mb	0.23

Source: own study.

Table 9: Time to make clay mortar for masonry works and plastering.

Making mortar with a machine	Manual sieving		Total time	Total time (per m^3 of the wall)	Total time (plaster)
	Sand	Clay			
	m-h/m^3			m-h/m^3	m-h/m^2
1.5	0.9	1.0	3.4	0.317	0.034

Source: own study.

good adhesion and improved thermal insulation. The wall will have a lime plaster on the outside and two-layer clay plaster on the inside.

3. Thermal Conductivity λ and Heat Transfer Coefficient U

Thermal conductivity λ (W/m K) is a measure of how well a material insulates the flow of heat. Porous, low-density materials have low thermal conductivity and hence are better insulators in comparison with denser materials.

While it is quite easy to obtain information on physical properties of typical construction materials, obtaining such information on locally sourced materials may prove a challenge.

The thermal conductivity of a straw bale and any other material depends on its compaction and moisture content. The values for straw bales in Table 1 are based on the studies conducted in November 2015 by the Building Research Institute in Warsaw (Poland) [15]. The study comprised evaluation of a $600 \times 600 \times 200$ mm straw bale, with density of about 100 kg/m^3.

The thermal conductivity of compacted clay, clay blocks, and clay plaster depends on the clay composition and used admixtures. Table 1 gives values for highly compacted (compacted clay and clay blocks) and medium-compacted clay (clay plaster).

The heat transfer coefficient "U" is a measure of how well a building enclosure transfers heat. The "U value" is expressed in W/(m^{2}K) and denotes how many watts of thermal energy pass through 1 m^2 of enclosure when the temperature difference between the inside and the outside is equal to 1 K. The lower the heat transfer coefficient is, the better the insulation properties a particular enclosure has.

The heat transfer coefficient is expressed by [3]

$$U = \frac{1}{R_T} \left(\mathrm{W}/\mathrm{m}^2\mathrm{K}\right), \tag{1}$$

where R_T is the total thermal resistance of a building partition, and total thermal resistance R_T for homogeneous partitions is described by the formula:

$$R_T = R_{si} + R_1 + R_2 + \cdots + R_n + R_{se} \left(\mathrm{W}/\mathrm{m}^2\mathrm{K}\right), \tag{2}$$

where R_{si} is the heat transfer resistance on the inner surface, $R_1 + R_2 + \cdots + R_n$ is the design thermal resistance of each layer, and R_{se} is the heat transfer resistance on the outer surface.

Thermal resistance of a homogeneous layer with thickness d is obtained from the following equation:

$$R = \frac{d}{\lambda} \left(\mathrm{m}^2\mathrm{K}/\mathrm{W}\right), \tag{3}$$

where d is the thickness of the material and λ is the design thermal conductivity of the material.

Tables 2–4 present the calculations of a heat transfer coefficient for the studied walls. The layers have been chosen in such a manner that the "U" values for the studied variants are as equal as possible, thus allowing a reliable comparative study.

Table 10: Time necessary to make inside clay plasters (1 layer).

Mortar making	Plastering	Transport	Additional works	Scaffolding	Extras	Total time
			m-h/m^2			
0.034	0.284	0.022	0.013	0.061	0.038	0.452

Source: own study.

Table 11: Time necessary to make 1 m^2 of the clay block wall.

Operation	Standard time	
	m-h/m^2	%
Making clay blocks	3.416	40
Making inside clay plasters	0.904	11
Erecting clay block wall	2.339	28
Thermal insulation: mineral wool boards	1.154	14
Making outside lime plasters	0.640	8
Total	8.453	100

Source: own study.

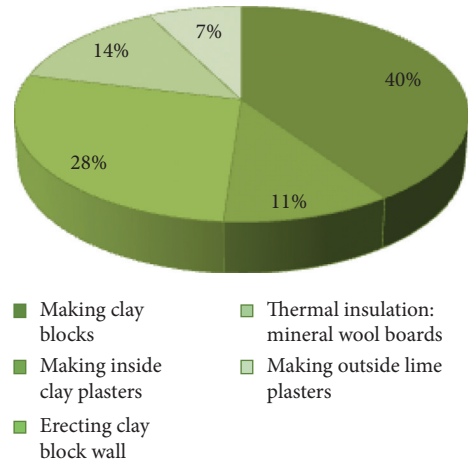

Figure 4: The percentage of the share of individual operations in making of 1 m^2 of the clay block wall.

4. Seasonality of Construction Works and Dependence on Weather Conditions

In temperate climate, the construction works and their effectiveness depend on the season and weather. Clay and straw are particularly sensitive to weather conditions and must be protected from water and subfreezing temperatures. After being put into the structure, the straw will be protected by the plaster, and clay must be protected from water at all times.

The construction works with locally sourced materials must be performed during a warm and relatively dry period, generally from late spring to early autumn. The works with conventional materials can be performed all year long if suitable precautions are taken, with exception of really low subfreezing temperatures. The exceptions among the locally sourced materials are dried clay blocks which also can be installed all year long if suitable precautions are taken.

In that area, conventional materials have a clear advantage over the alternative materials, although conventional materials must be protected from a long-term exposure to water and subfreezing temperatures. Such protection is however much simpler that in case of locally sourced materials.

Straw must not be wet when installed as it takes a long time to dry. Styrofoam, on the other hand, does not absorb water and is easy and quick to dry. Clay must be protected from precipitation at all times during the construction works by special roofing and by eaves when the building is in use. Dependence of studied technologies on seasons and weather conditions is given in Table 5.

5. Time of Making 1 m^2 of the Wall

5.1. Clay Block Wall. The study of time required to perform works in case of clay block walls refers to the "Temporary Principles of Erecting Clay Buildings" by the Institute of Housing Construction [16]. The standard times are expressed in m-h/m^3—man-hours per cubic metre of the clay block wall.

Standard times for making the clay blocks (Table 6) include maintenance of the storage yard for finished blocks, maintenance of machinery, tools, and fixtures, and squaring of the blocks and putting them in trestles. They do not, however, include storage yard levelling, construction of protective roofing, and excavation of drainage ditches.

Clay block walls are erected in the same manner as brick walls (Tables 7 and 8). The standard times include erecting walls using clay mortar, transport of blocks and mortar for a distance up to 20 m, and additional mortar mixing. The clay block walls are measured in m^3, and the openings in excess of 1 m^2 are subtracted from the wall volume.

Clay mortar should have the same composition as clay blocks (Table 9). The standard time for making clay mortar includes handling auxiliary materials at the distance of 10 m, mixing mortar with water, and operation and maintenance of machinery. The standard time does not include making a box for the mortar preparation and placement and relocation of machines used to make the mortar. The penultimate column of the Table 5 includes the time for making the mortar needed to erect 1 m^3 of the final clay block wall. The last column includes the time for preparing the mortar needed to make 1 m^2 of 1 cm thick plaster.

The clay plastering standard times include additional works: substrate wetting using a hose, surface scratching with a rake, application of plaster strips and skim coat and trowelling, and others (preparation and substrate cleaning) (Table 10). The clay plaster is made in layers, each 1 cm thick.

The time of making 1 m^2 thermal insulation using mineral wool boards has been taken from the Contractors Estimator KNR 33/2/4. The standard time for application of outside paster has been taken from the Contractors Estimator KNR 202/906/2.

Table 12: Time necessary to prepare the clay for compaction.

Clay preparation difficulty	Clay placement for mixing	Transport of admixtures	Processing with milling machine	Pouring into moulds	Total time
			m-h/m^3		
Medium-cohesion 801–1400 g/5 cm^2	0.51	0.52	0.08	0.35	1.46

Source: own study.

Table 13: Time necessary to make compacted clay walls.

	Formwork	Loading, transport, and unloading for formwork	Charge levelling	Compaction	Total time	Total time
		m-h/m^3				m-h/m^2
Ground floor	3.10	2.88	0.72	0.95	7.65	2.295
1st floor	3.38	2.92	0.75	0.95	8.00	2.40

Source: own study.

Table 14: Various works.

Various works	Unit of measure	Quantity
Placement of levelling layer under ceiling beams for load-bearing outside walls plus extra for more difficult formwork and compaction	m-h/m	1.00
Placement of levelling layer under ceiling beams for load-bearing inside walls plus extra for more difficult formwork and compaction	m-h/m	2.00
Placement of window templates, removal completion of works, plus extra for more difficult formwork and compaction		
Window templates above 0.5 m^2	m-h/pc	0.55
Window templates below 0.5 m^2	m-h/pc	0.40
Door templates above 0.5 m^2	m-h/pc	0.55

Source: own study.

Table 15: Time needed to build 1 m^2 of the compacted clay wall.

Operation	Standard time	
	m-h/m^2	%
Making inside clay plasters	0.904	15
Making compacted wall in formwork	3.248	55
Thermal insulation: mineral wool boards	1.154	19
Making outside lime plasters	0.604	11
Total	5.946	100

Source: own study.

The time to make 1 m^2 of the clay block wall (Table 11 and Figure 4) has been averaged due to various units of measure for intermediate operations (e.g., prefab lintels are expressed in m-h/m).

5.2. Compacted Clay Walls. The study of time required to make compacted clay walls also refers to the "Temporary Principles of Erecting Clay Buildings" by the Institute of Housing Construction [16]. The standard times are expressed in m-h/m^3—man-hours per cubic metre of the compacted clay wall.

Time to prepare the clay (Table 12) for compaction includes its mixing with cracking prevention admixtures and pouring into moulds after mixing. It does not include cutting of fibrous materials and protecting the materials from precipitation. The amount of prepared clay compound is measured in cubic metres. 1 m^3 of the compacted wall is an equivalent of about 1.55 m^3 of loose mixture.

Standard times for making compacted clay walls (Table 13) include transport of the mixture to the hoist at the distance of maximum 20 m, transport on the scaffolding at the distance of maximum 20 m, pouring into formwork, levelling of the poured layer, compaction, placement of window and door templates, and making of lime battens or placement of ceramic inserts. The standard times, however, do not include protecting the walls from weather conditions, making the insulation, handling of window and door templates, and making of the levelling layer as a cover for lintels (Table 14).

The unit of measure for walls in excess of 24 cm in thickness is m^3, and up to 24 cm in thickness is m^2. Openings larger than 1 m^2 should be subtracted from the wall volume.

The times of making the clay (Table 15 and Figure 5) mortar for inside plasters, mineral wall insulation, and outside plasters are identical as in case of the clay block wall. The time to make 1 m^2 of the compacted clay wall has been averaged due to various units of measure for intermediate operations (e.g., prefab lintels are expressed in m-h/m).

5.3. Straw-Bale Walls. The standard times for erecting walls in the straw-bale technology (Table 16 and Figure 6) have

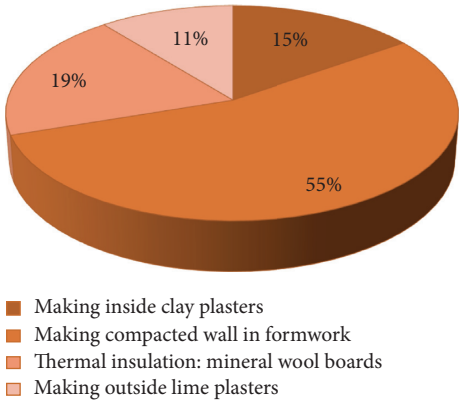

Figure 5: The percentage of the share of individual operations in making of 1 m^2 of the compacted clay wall.

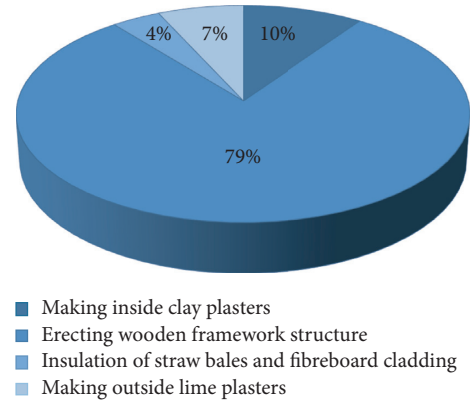

Figure 6: The percentage of the share of individual operations in making of 1 m^2 of the straw-bale wall.

Table 16: Time needed to build 1 m^2 of the straw-bale clay wall.

Operation	Standard time	
	m-h/m^2	%
Making inside clay plasters	0.904	10
Erecting wooden framework structure	7.437	79
Insulation of straw bales and fibreboard cladding	0.366	4
Making outside lime plasters	0.640	7
Total	9.347	100

Source: own study.

been taken from the Contractors Estimator. The amount of labour needed to fill the wooden structure with straw bales has been determined analogously to the Contractors Estimator's item 202/613/6. The standard times for making inside clay plasters are identical as for the clay walls.

The time to make 1 m^2 of the compacted clay wall has been averaged due to various units of measure for intermediate operations.

6. Conclusions

The comparison of times necessary to make 1 m^2 of the wall allows us to decide which construction technology is more advantageous in terms of construction duration. The small surfaces in the wall or surfaces with numerous windows and doors, as well as the drying time between Earth wall making and rendering operation, are calculated by additional time; therefore, they were not taken into account in this paper. The shorter construction time means lower labour costs and lesser expenses for construction machines.

In the case of investors, the construction time is an important measure of project success, as the shorter payback periods mean a quicker opportunity to reinvest or reuse financial resources.

The construction time is equally important for people building a home for themselves. It is a huge advantage for them to be able to perform the works in a favourable weather and to move in and use the house earlier.

The studies and Figure 7 allow us to draw the following conclusions:

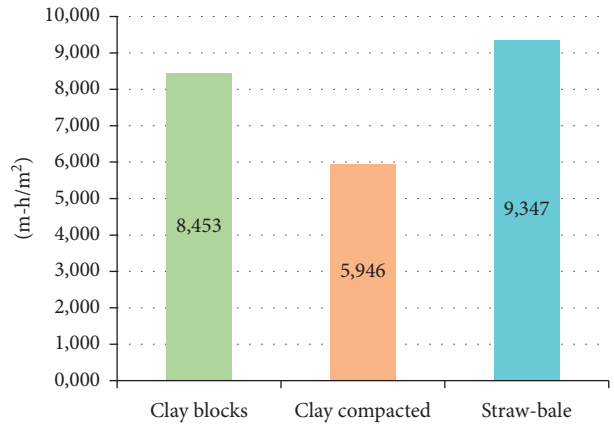

Figure 7: Time to make 1 m^2 of the wall in individual technologies.

(i) Compacted clay walls have the shortest wall erection time from among the studied natural building technologies.

(ii) Time to make 1 m^2 of the clay block wall is significantly longer as a result of a very time-consuming clay block preparation process. In the paper, it was assumed that blocks are made in-house, using mainly materials available free at the construction site.

(iii) The straw-bale technology had the worst results in the comparison. The factor which determines the long time needed to make 1 m^2 of the straw-bale wall is the necessity to erect the wooden framework structure.

(iv) Two-layer clay plaster can be an alternative to other contemporary inside wall finishing solutions.

Conflicts of Interest

The authors declare that they have no conflicts of interest.

References

[1] Law on Construction Products of 16 April 2004, Dz.U. 2004 No. 92 Item 881.

[2] W. Drozd, "Light clay straw bale solutions in the contemporary housing as an element of sustainable development. Selected issues," *E3S Web of Conferences*, vol. 10, p. 00016, 2016.
[3] PN-EN ISO 6946:2008, *Building Components and Building Elements*, 2008.
[4] BN–62/6738–01, *Masses of Cement—Clay Fillers*.
[5] L. Miccoli, U. Müller, and P. Fontana, "Mechanical behaviour of earthen materials: a comparison between earth block masonry, rammed earth and cob," *Construction and Building Materials*, vol. 61, pp. 327–339, 2014.
[6] T. Lecompte and A. Le Duigou, "Mechanics of straw bales for building applications," *Journal of Building Engineering*, vol. 9, pp. 84–90, 2017.
[7] J. Robinson, H. K. Aoun, and M. Davison, "Determining moisture levels in straw bale construction," *Procedia Engineering*, vol. 171, pp. 1526–1534, 2017.
[8] A. D. González, "Energy and carbon embodied in straw and clay wall blocks produced locally in the Andean Patagonia," *Energy and Buildings*, vol. 70, pp. 15–22, 2014.
[9] T. Ashour, H. Georg, and W. Wu, "Performance of straw bale wall: a case of study," *Energy and Buildings*, vol. 43, no. 8, pp. 1960–1967, 2011.
[10] S. Goodhew, R. Grffiths, and T. Woolley, "An investigation of the moisture content in the walls of a straw-bale building," *Building and Environment*, vol. 39, no. 12, pp. 1443–1451, 2004.
[11] M. Lawrence, A. Heath, and P. Walker, "Determining moisture levels in straw bale construction," *Construction and Building Materials*, vol. 23, no. 8, pp. 2763–2768, 2009.
[12] T. Ashour, H. Wieland, H. Georg, F. J. Bockisch, and W. Wu, "The influence of natural reinforcement fibres on insulation values of earth plaster for straw bale buildings," *Materials & Design*, vol. 31, no. 10, pp. 4676–4685, 2010.
[13] A. Leśniak and K. Zima, "Comparison of traditional and ecological wall systems using the AHP method," in *Proceedings of the 15th International Multidisciplinary Scientific GeoConference Surveying Geology and Mining Ecology Management (SGEM 2015)*, vol. 3, pp. 157–164, Albena, Bulgaria, June 2015.
[14] G. Minke and B. Krick, *Straw Cube Handbook*, Cohabitat Foundation, Łódź, Poland, 2015.
[15] Research ITB (Institute of Building Technology), *Study of the Heat Conduction Coefficient of Straw Cubes*, Report no. LFS00-02236/15/Z00NF, Institute of Building Technology, Warsaw, Poland, 2015.
[16] Institute of Housing Construction, *Temporary Principles of Erecting Clay Buildings*, Institute of Housing Construction, Warsaw, Poland, 1955.
[17] M. Zatylny, *Formal and Legal Conditions for Natural Construction in Europe and Poland with Particular Emphasis on the Use of Straw Cubes*, United Nations Development Program (UNDP), New York, NY, USA, 2013.

Hindawi
Advances in Materials Science and Engineering
Volume 2018, Article ID 6250941, 11 pages
https://doi.org/10.1155/2018/6250941

Research Article

Improvement of Mechanical Properties in Polypropylene- and Glass-Fibre-Reinforced Peach Shell Lightweight Concrete

Fan Wu,[1] Changwu Liu ,[1,2] Zhaofeng Diao,[2] Bo Feng,[2] Wei Sun,[2] Xiaolong Li,[2] and Shuang Zhao[2,3]

[1]*Institute of Disaster Management and Reconstruction, Sichuan University and The Hong Kong Polytechnic University, No. 1 Huanghe Road, Chengdu 610065, China*
[2]*College of Water Resource and Hydropower, Sichuan University, No. 24 South Section 1, Yihuan Road, Chengdu 610065, China*
[3]*China Yangtze Power Co., Ltd., China Three Gorges Corporation, No. 1 Construction Road, Yichang, China*

Correspondence should be addressed to Changwu Liu; liuchangwu@scu.edu.cn

Received 12 September 2017; Accepted 21 December 2017; Published 13 February 2018

Academic Editor: Nadezda Stevulova

The use of the polypropylene fibre and glass fibre with different volume fractions to improve the mechanical properties of peach shell lightweight concrete was investigated in this study. The volume fractions of 0.25%, 0.50%, and 0.75% were used for each fibre. The results showed that, as the polypropylene fibre and glass fibre were added into peach shell concrete, the density was reduced by up to 6.1% and the compressive strength, splitting tensile strength, and flexural strength were increased by 19.1%, 54.3%, and 38.6%, respectively. The highest compressive strength, splitting tensile strength, and flexural strength of 29.3 MPa, 2.87 MPa, and 3.09 MPa, respectively, were produced by peach shell concrete with 0.75% glass fibre. The results indicated that the incorporation of fibres significantly enhanced the postfailure toughness of peach shell concrete. It was found that the glass fibre was more effective than the polypropylene fibre in improving the mechanical properties of peach shell concrete. Although the incorporation of fibres slightly increased the water absorption and porosity, the type and content of fibres had no significant effect on water absorption and porosity. Therefore, the mechanical properties of peach shell lightweight concrete can be improved by adding polypropylene fibres and glass fibres.

1. Introduction

The use of agricultural or industrial wastes in concrete to replace the conventional raw material has achieved environmentally friendly and sustainable development by reducing the production costs of the raw material and contributing to waste disposal. The expanding extraction of conventional aggregates such as granite aggregate and sand in concrete production has caused serious environmental pollution problems [1]. The use of lightweight aggregates such as expanded clay, foamed slag, and natural pumice instead of conventional coarse aggregates can produce lightweight aggregate concrete (LWAC) [2]. LWAC has a lot of advantages including better fire resistance, heat insulation, sound absorption, and frost resistance [3]. Recently, the utilization of agricultural wastes such as coconut shell, oil palm shell, and apricot shell as a substitute for normal weight aggregates (NWAs) is gradually rising. On the other hand, the additional advantages of using agricultural wastes instead of normal aggregates to produce LWAC are to reduce environmental pollution and to deal with wastes [4]. Agricultural waste is rapidly storing in developing countries, and peach shell (PS) is the seed of peach fruits, which causes environmental problem around their cultivated areas. More than thousand tons of PS wastes need to be discharged each year in China. The lightweight and regenerative characteristic of PS compared to the NWAs can make PS as one of the potential lightweight aggregates and sustainable building materials in the production of LWAC. This could reduce the environmental pollution caused by PS and contribute to the reutilization of PS.

The improvement in the mechanical properties of LWAC depends on the oven-dried density, water-to-cement ratio, addition of other binder materials, aggregate content, and particle size [5, 6]. Previous studies showed that LWAC with higher compressive strength can be produced, but this concrete was prone to brittle and poor tensile strength due to the fact that the lightweight aggregate is usually weaker under tension [7, 8]. The tensile strength of LWAC is about one-tenth of its compressive strength [9]. The use of PS instead of NWA has a positive impact on density, and a reduction in density up to 30% can be achieved in the peach shell concrete (PSC). However, the splitting tensile and flexural strengths and modulus of elasticity (MOE) of PSC are lower than those of LWAC made of other lightweight aggregates such as pumice and expanded clay. The low tensile strength tends to cause significant tensile cracking to occur under lower tensile loads [10]. Hence, the improvement of the mechanical properties of PSC requires more attention.

Incorporation of fibres is an effective way to improve the mechanical properties of concrete, such as splitting tensile and flexural strengths and other related characteristics [11]. In fibre-reinforced concrete, the role of fibres is to improve the performance of concrete through the crack bridge effect of fibres and the fibre-cement-aggregate interfacial bond [5]. Previous research showed that fibre-reinforced concrete with two types of different fibres had better ductility, crack growth resistance, and impact resistance. In the composite fibre material system, the harder fibres enhance the first crack stress and ultimate strength, and the softer fibres control the crack propagation and increase the ductility [12]. Yap et al. [13] reported that oil palm shell lightweight concrete with 0.9% steel and 0.1% polypropylene (PP) fibres had better improvement in flexural toughness characteristics.

Although a lot of study works are ongoing on the addition of fibres in LWAC, there is only little literature on the incorporation of fibres in PSC. In order to make PSC like other LWAC applied to practical building structure elements such as sidewalks, parking lots, roadblocks, and partition walls, the mechanical properties and durability of PSC need to be further improved. The addition of fibres into PSC can make it as a ductile and sustainable building material. Commonly used fibres are the steel fibre, PP fibre, and nylon fibre, and there are few literatures available on the use of glass (G) fibres in LWAC. The main disadvantages of adding steel fibres to LWAC are a significant increase in density and reduced workability. The PP fibre is mainly used in concrete to enhance the ductility, toughness, and impact resistance, but do not expect them to improve the strength [12]. Mastali et al. [14] reported that adding G fibres led to a significant improvement in compressive strength, tensile strength, and impact resistance of G fibre-reinforced concrete. Compared to steel fibres, the advantage of adding PP fibres and G fibres to PSC is that the density is less than 2000 kg/m^3 and lower than the upper limit of the density set for LWAC. However, there are few literatures on the comparison of PP fibre- and G fibre-reinforced peach shell lightweight concrete.

The purpose of the present study is to investigate the influence of two types of fibres (PP fibre and G fibre) and each fibre at a volume fraction of 0.25%, 0.50%, and 0.75% on the mechanical properties of peach shell lightweight concrete. A comparison of the performance of PP fibre- and G fibre-reinforced peach shell lightweight concrete is investigated and reported, including workability, density, compressive strength, splitting tensile strength, flexural strength, modulus of elasticity, residual compressive strength, water absorption, and porosity. This work helps to expand the knowledge on the effect of PP fibres and G fibres with different contents on the mechanical properties of peach shell fibre-reinforced concrete (PSFRC).

2. Materials and Methods

2.1. Materials

2.1.1. Cement and Silica Fume. Type I 42.5 grade ordinary Portland cement was used in this study and obtained from a local cement company. The Blaine specific surface area and specific gravity are 3532 cm^2/g and 3.14 g/cm^3, respectively. In addition, silica fume (SF) was added in concrete as an additional mineral binder to improve the performance of concrete. SF content at 10% of the cement weight was used in all mixes.

2.1.2. Coarse and Fine Aggregates. Peach shell (PS) was used as an alternative coarse aggregate, and crushed pebble was used as a normal weight coarse aggregate. The density of PS is 63% lower than that of normal weight aggregates (NWAs), which is significant for reducing dead loads of building structures. River sand was used as a fine aggregate and obtained from a local sand company. The physical properties of the aggregates are shown in Table 1. PS was collected from a local peach plantation. Before using, they were washed to remove the residual dried peach pulp and the dust from the PS surface. Then, the dry PS was crushed by a crushing machine in the laboratory. Crushed PS was sieved with 4.75 mm and 9.5 mm sieves, respectively. Particles of size 4.75–9.5 mm were considered as coarse aggregates. Uncrushed and crushed PS and scanning electron microscopic (SEM) image at 5000 magnification times of crushed PS are shown in Figure 1. As can be seen from Figure 1, crushed PS has an irregular and rough surface, and the PS aggregate has a lot of circular porosity on the surface, and the diameter of the micropore is about 10–20 μm. Although a large number of porosity on the surface of PS reduces the density, it leads to the fact that PS has a higher water absorption compared to NWA. Therefore, PS was submerged in water for 24 h and kept in an internal saturated and surface dry condition before mixing.

2.1.3. Water and Superplasticizer. The water used in this study was normal tap water. A high-range naphthalene sulphonated superplasticizer (SP) was used in the study to increase the workability of fresh concrete. SP content at 1% of the cement weight was used in all mixes.

2.1.4. Fibres. Two different fibres used in this study are the (i) polypropylene (PP) fibre and (ii) glass (G) fibre. The properties of fibres are shown in Table 2.

Table 1: Physical properties of the aggregates.

Physical property	Coarse aggregate		Fine aggregate
	PS	NWA	River sand
Specific gravity (g/cm^3)	1.26	2.66	2.65
Fineness modulus	5	4.9	2.7
Bulk density (kg/m^3)	536	1449	1538
Water absorption (24 h) (%)	26.84	0.5	1.2
Aggregate impact value (%)	1.95	16.72	—
LA abrasion value (%)	6	25	—
Flakiness index (%)	48	24	—
Elongation index (%)	61	34	—
Grading			
Sieve size (mm)	Cumulative % by weight passing		
16	100		100
9.5	98.2		100
4.75	24.8		99
2.36	0		86
1.18	0		74.7
0.6	0		48.3
0.3	0		16.3
0.15	0		0

2.2. Mix Proportioning. The mix proportion of concretes is presented in Table 3. A total of six concrete mixes were prepared with different fibre contents, and a control mix without the addition of fibres was also produced for comparison purpose. The total amount of materials for all mixes was the same except in the case of two different fibres and three fibre volumes. The volume fractions of fibres were 0.25%, 0.50%, and 0.75%, respectively.

2.3. Specimen Preparation and Test Methods. The procedure of specimen preparation of peach shell fibre-reinforced concrete (PSFRC) was detailed as follows: firstly, PS and river sand were poured into a blender and dry mixed for 2 min. Then, fibres and cement and SF were added to the mixture and dry mixed for 1 min. Before the fibres were mixed, fibres were manually distributed. Following this, 60% water mixed with SP was added to the mixture and mixed for 3 min. Finally, 40% water was added to the mixture and mixed for 5 min. After mixing was complete, the slump test was carried out immediately, and then, the specimens were cast in oiled plastic moulds. All specimens were compacted by the vibrating table. Immediately after compaction, all specimens along with the moulds were covered by a plastic sheathing to prevent moisture evaporation. Specimens were removed from the moulds after 24 h. Finally, specimens were stored in a controlled room with a relative humidity of 95% ± 5% and a temperature of 20°C ± 2°C until the test age.

The workability of all mixes was measured by the slump test according to ASTM C143/C143M-12 (Figure 2). The density of all specimens was measured in accordance with ASTM C138. 100 mm cube specimens were used for the compressive strength test (BS EN12390-2:200 9 and BS EN12390-3:200 9) at the age of 3, 7, 28, and 56 days (Figure 2).

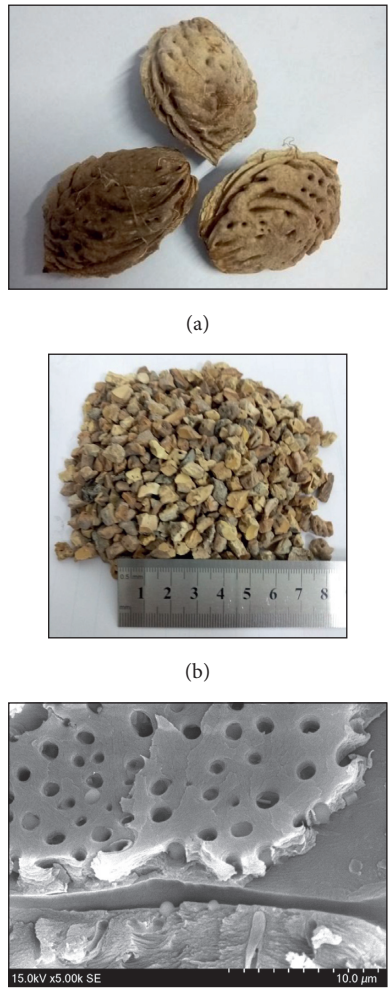

(a)

(b)

(c)

Figure 1: (a) Uncrushed PS, (b) crushed PS, and (c) SEM image of the crushed PS particle at 5000 magnification times.

The splitting tensile and flexural strengths and modulus of elasticity of all mixes were measured at the age of 28 days according to ASTM C496/C496M-11, ASTM C78-10, and ASTM C469-10 (Figure 2), respectively. The average value of at least three specimens is taken for each test result.

The water absorption test was carried out according to the procedures prescribed in ASTM C642. All specimens were oven-dried at 110 ± 5°C for not less than 24 h to remove moisture and achieve constant before testing. The specimens were then submerged in water for 24 h. The water absorption values of the specimen were calculated using the following formula:

$$\text{Water absorption } (\%) = \frac{M_2 - M_1}{M_1} \times 100, \quad (1)$$

where M_1 is the mass of the oven-dried specimen in air (g) and M_2 is the mass of the surface-dried specimen in air after immersion (g).

The porosity of all specimens was determined in accordance with ASTM C642. Absolute density is necessary to determine the total porosity by the method prescribed in ASTM C642; hence, the pycnometry method was applied for

Table 2: Properties of the PP fibre and G fibre.

Fibre		Fibre type	Length (mm)	Diameter (μm)	Specific gravity (g/cm^3)	Tensile strength (MPa)
PP	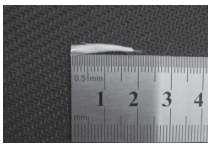	Monofilament	19	40	0.91	500
G	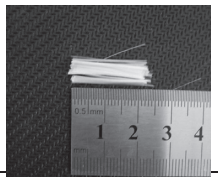	Monofilament	22	10	2.65	1200

Table 3: Mix proportion of concretes.

Mix code	Cement (kg/m^3)	SF (kg/m^3)	Water (kg/m^3)	Sand (kg/m^3)	SP (kg/m^3)	PS (kg/m^3)	PP fibre (%)	G fibre (%)
Control	550	55	180	780	5.5	360	0	0
PP25	550	55	180	780	5.5	360	0.25	0
PP50	550	55	180	780	5.5	360	0.50	0
PP75	550	55	180	780	5.5	360	0.75	0
G25	550	55	180	780	5.5	360	0	0.25
G50	550	55	180	780	5.5	360	0	0.50
G75	550	55	180	780	5.5	360	0	0.75

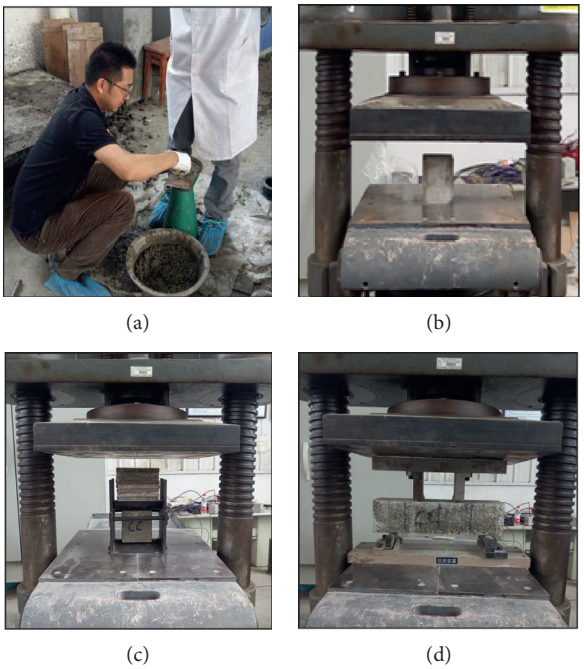

Figure 2: (a) Slump test, (b) compressive test, (c) splitting tensile test, and (d) flexural strength test.

the determination of absolute density. The total porosity and open porosity values of the specimen can be calculated by (2) and (3), respectively. The closed porosity volume can be obtained by subtracting the open porosity volume from the total porosity volume.

$$\text{Total porosity volume}\,(\%) = \frac{\rho_a - \rho_b}{\rho_a} \times 100, \tag{2}$$

where ρ_a is the absolute density of the specimen (g/cm^3) and ρ_b is the bulk density of the specimen (g/cm^3).

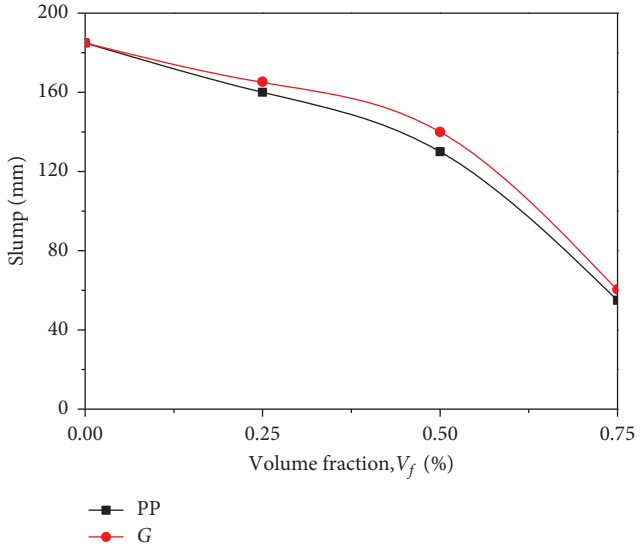

Figure 3: Relationship between the fibre content and slump value.

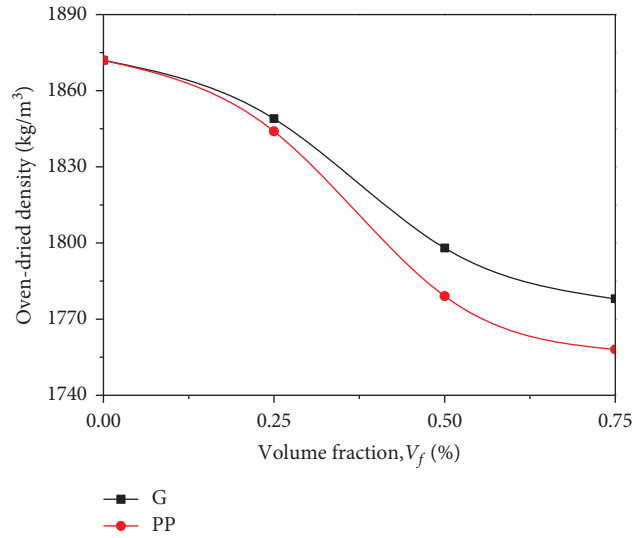

Figure 4: Relationship between the fibre content and oven-dried density.

$$\text{Open porosity volume}\,(\%) = \frac{M_3 - M_1}{M_3 - M_4} \times 100, \quad (3)$$

where M_1 is the mass of the oven-dried specimen in air (g); M_2 is the mass of the surface-dried specimen in air after immersion (g); M_3 is the mass of the surface-dried specimen in air after immersion and boiling (g); and M_4 is the apparent mass of the specimen in water after immersion and boiling (g).

3. Results and Discussion

3.1. Workability (Slump). Relationship between the fibre content and slump value is shown in Figure 3. Yew et al. [9] reported that the incorporation of different types of PP fibres in oil palm shell concrete caused a considerable decrease in the slump value. As expected, the results showed that the slump values of the fresh PSC with PP fibres and G fibres were reduced to 55 mm and 60 mm, respectively. The reason for this phenomenon can be explained by the fact that the fibre-cement paste interfacial bond in concrete restricts the dispersion and flow of the cement paste and improves the viscosity of the mixtures. With the increase in fibre volume fraction, the capability of the fibre-cement paste interfacial bond in concrete becomes stronger as more fibres absorb the cement paste to wrap around it. Therefore, the workability of concrete decreased as the fibre volume (V_f) increased from 0% to 0.75%. Mehta and Monteiro [15] reported that the LWAC with a slump value of 50–75 mm is similar to normal weight concrete with a 100–125 mm slump value. In the case of PSC, the slump value of PP fibre- and G fibre-reinforced PSC between 55 mm and 60 mm can easily be compacted.

Figure 3 also shows that the two types of fibres have an impact on the workability of concrete. For all V_f, the G fibre produced slightly higher slump values than the PP fibre. The increase in slump values at a range of 5–10 mm and the biggest difference between the G fibre and PP fibre were observed at $V_f = 0.50\%$, and the slump value of G50 was 7.8%

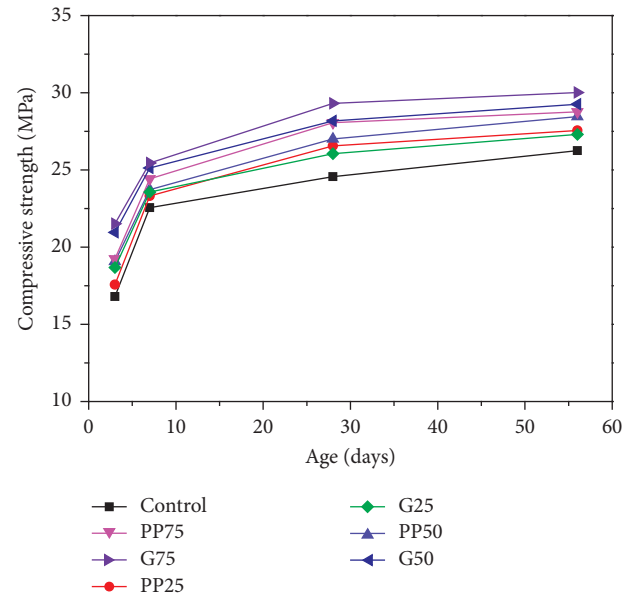

Figure 5: The development of the compressive strength of concretes.

higher than that of PP50. Song et al. [16] reported that the workability of fibres with a shorter length was lower than that of longer fibres. The shorter fibres have more surface area for the reinforcing fibre-cement paste bond [9]. Since the length of the G fibre is longer than that of the PP fibre and the surface of the G fibre is smoother, G fibres have lower effective surface area to develop a fibre-cement paste bond compared to PP fibres. Hence, the slump value of PSC incorporated with G fibres was slightly higher than that of PP fibres.

3.2. Density. Lightweight aggregate concrete (LWAC) is defined as concrete with a compressive strength of more than 15 MPa and an oven-dried density (ODD) in the range

Table 4: Compressive strength of concretes.

Mix	Compressive strength (MPa)				% increase in compressive strength (28 days)
	3 days	7 days	28 days	56 days	
Control	16.8 (68.3%)	22.6 (91.9%)	24.6	26.3 (106.9%)	—
PP25	17.6 (66.2%)	23.3 (87.6%)	26.6	27.6 (103.8%)	8.1
PP50	19.1 (70.7%)	23.7 (87.8%)	27.0	28.5 (105.6%)	9.8
PP75	19.2 (68.3%)	24.4 (86.8%)	28.1	28.8 (102.5%)	14.2
G25	18.7 (71.6%)	23.6 (90.4%)	26.1	27.3 (104.6%)	6.1
G50	21.0 (74.5%)	25.1 (89.0%)	28.2	29.3 (103.9%)	14.6
G75	21.5 (73.4%)	25.5 (87.0%)	29.3	30.2 (103.1%)	19.1

Note. Values in brackets denote the percentages of compressive strength to the corresponding 28-day compressive strength.

of 1600–2000 kg/m^3 [17]. Relationship between the fibre content and ODD is shown in Figure 4. The results showed that the ODD of all PSC ranged from 1758 kg/m^3 to 1872 kg/m^3 and fulfilled the requirement of LWAC because PS is about 63% lighter than NWA. The addition of PP fibres and G fibres in concrete reduced the ODD of PSC because fibres have a low specific gravity. When the volume fraction of PP fibres is added at percentages of 0.25%, 0.50%, and 0.75%, the ODD of these concretes decreased by 1.5%, 5.0%, and 6.1%, respectively, compared to the control mix.

Figure 4 also showed that the different types and volume fractions of fibres had an influence on the ODD of PSC. It was found that concrete with G fibres produced a slightly higher ODD than PP fibres, and the difference in the ODD of PSC is more significant as fibre volume fraction ranges from 0.25% to 0.75%. At $V_f = 0.75\%$, G75 had the lowest ODD of 1778 kg/m^3, and it was only 1.1% higher than PP75. It should be noted that although the specific gravity of PP fibres and G fibres is significantly different, its impact on the ODD of PSC is not obvious. However, compared to the density of approximately 2400 kg/m^3 for ordinary weight concrete, the ODD of PSC is reduced by about 26%, which is a significant reduction in the weight of concrete.

3.3. Compressive Strength. The development of the compressive strength of concretes up to 56 days is shown in Figure 5. The test results revealed that the compressive strength of all concretes increased as the curing age increased. As can be seen from Figure 5, there is a significant difference in the compressive strength between PSC containing different types and contents of fibres and control mix without any fibres. The enhancement of the ultimate compressive strength may be attributed to the fact that fibres arrest the growth of cracks due to the fibre-cement paste interfacial bond and the crack bridging effect of fibres [18].

The addition of PP fibres and G fibres had significantly increased the compressive strength of PSC at all ages, and the compressive strength increased as an increase in fibre content. The 28-day compressive strength of all mixes varied between 24.6 MPa and 29.3 MPa, which fulfilled the requirements for the strength and density of LWAC. It can be observed that compared to the control mix, the 28-day compressive strength of PP25, PP50, and PP75 increased by 8.1%, 9.8%, and 14.2%, respectively, and the 28-day compressive strength of G25, G50, and G75 increased by 6.1%, 14.6%, and 19.1%, respectively. Except for $V_f = 0.25\%$, the 28-day compressive strength of G fibre-reinforced PSC was slightly higher than that of PP fibre. This phenomenon indicated that the use of G fibre-reinforced PSC is a good choice.

Table 4 shows the compressive strength of concretes. All concretes attained approximately 66%–75% of compressive strength at 3 days and 87%–92% of compressive strength at 7 days. This indicated that all PSC developed high early compressive strength because the incorporation of SF increased the cohesiveness of cement paste and reduced the advance of microcracks, and eventually, the early compressive strength of PSC is increased. The addition of PP fibres and G fibres in concrete increased the 28-day compressive strength by about 6%–19%. At $V_f = 0.75\%$, G75 produced the highest 28-day compressive strength of 29.3 MPa, which is 19.1% higher than the control mix of 24.6 MPa. Although not every kind of lightweight aggregate is suitable for the production of LWAC, the results based on this study indicate that it is feasible to produce LWAC using PS as a lightweight aggregate.

Generally, the initiation and advance of cracks in concrete are due to the continuous increase in compressive loading. Since the tensile stress generated by the fibre is perpendicular to the crack propagation path, the debonding begins at the interface between the fibre and cement paste. Once the advancing cracks reach the fibre-cement paste interface, the stress concentration at the crack tip is released, and as a result, the development of the advancing crack is blunted and blocked. The fibre is like a bridge in this process that arrests the advancing cracks and consequently improves the strength of concretes [19, 20]. Therefore, the addition of PP fibres and G fibres enhanced the bonding of the fibre-cement paste interface and improved the compressive strength [16]. The compressive strength of G fibre-reinforced PSC is higher than that of PP fibre-reinforced PSC. This reason can be explained by the following: firstly, the tensile strength of G fibres in this study is 2.4 times that of PP fibres, and thus, compared to the PP fibre, the G fibre is easier to transfer higher tensile stress from a cracked fibre-cement interface to fibre. Secondly, under the same fibre volume fraction, the density of G fibre-reinforced PSC in this study is higher than that of PP fibre-reinforced PSC. Although the addition of fibres in this study reduced the density of PSC,

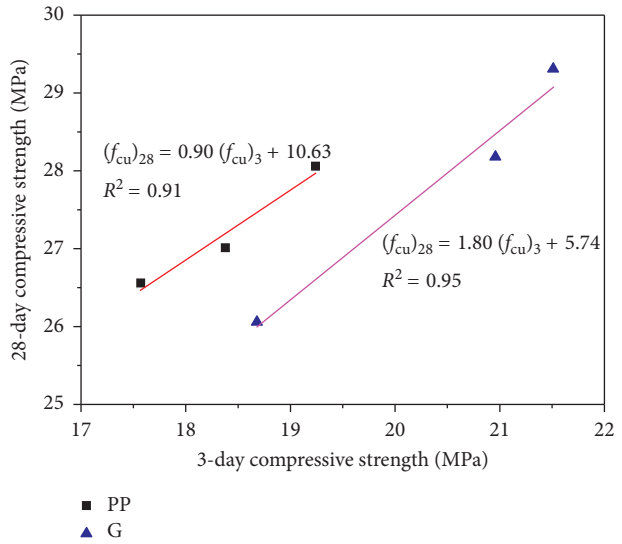

Figure 6: Relationship between 3-day and 28-day compressive strengths.

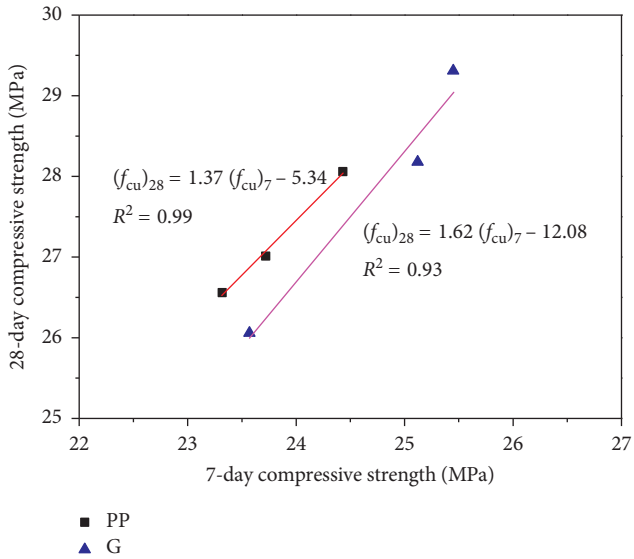

Figure 7: Relationship between 7-day and 28-day compressive strengths.

for normal weight concrete, the higher the density the higher the compressive strength. Thus, the compressive strength of higher density of G fibre-reinforced PSC is higher than that of PP fibre-reinforced PSC.

Due to the importance of knowing the 28-day compressive strength from the early age compressive strength, Figures 6 and 7 show the relationship between the 28-day compressive strength and compressive strength at early ages of 3 days and 7 days, respectively. As can be seen from Figures 6 and 7, there is a linear relationship with the high correlation coefficient between the 28-day compressive strength and the early compressive strength, and the 28-day compressive strength of PSC can be predicted by the early compressive strength.

3.4. Splitting Tensile and Flexural Strengths. Splitting tensile strength and flexural strength of all mixes are shown in Table 5. Comiloli et al. [21] reported that the incorporation of PP fibres in concrete can slightly enhance the flexural toughness of concrete. The fibre enhances the strength of concretes by the crack bridging effect and carrying part of load [12]. The results showed that the incorporation of PP fibres and G fibres in concrete increased both splitting tensile strength and flexural strength of PSC, and the more the fibre content, the higher the splitting tensile strength and flexural strength. The addition of PP fibres from 0.25% to 0.75% and glass fibres from 0.25% to 0.75% increased the splitting tensile strength up to 10.2%–36.6% and 7.5%–54.3%, respectively. Furthermore, the flexural strength of PP fibre- and G fibre-reinforced PSC was also improved. The flexural strength of PSC increased as an increase in fibre volume fraction. When the fibre volume fraction varies from 0.25% to 0.75%, the flexural strength for PP fibre and G fibre reinforced PSC increased by 6.7%–17.9% and 5.4%–38.6%, respectively. The advantage of PSC could be further explained based on Figure 8. From Figure 8, it was evident that the control concrete without

Table 5: Splitting tensile and flexural strengths and modulus of elasticity of concretes (28 days).

Mix	Splitting tensile strength (MPa)	Flexural strength (MPa)	Modulus of elasticity (GPa)
Control	1.86	2.23	8.71
PP25	2.05	2.38	9.63
PP50	2.15	2.50	10.15
PP75	2.54	2.63	10.85
G25	2.00	2.35	9.79
G50	2.52	2.69	10.75
G75	2.87	3.09	11.32

any fibres failed once the ultimate splitting tensile strength was reached due to low ductility. Furthermore, the fibre-reinforced PSC showed excellent crack arresting performance as the specimen was not broken into two pieces even after the failure load. This phenomenon attributed to the crack bridging effect of fibres, and fibres in concrete provide additional strength to the fibre-cement interfacial bond which carries a partial load.

Although the ODDs of PP75 and G75 were lower in this study, the splitting tensile strength and flexural strength of PP75 and G75 were higher than those of the control mix. Since the tensile stress of G fibres is greater than that of PP fibres, glass-fibre reinforced PSC produced a higher splitting tensile strength and flexural strength. At $V_f = 0.50\%$ and 0.75%, splitting tensile strength and flexural strength of PSC containing G fibres were found to be about 12.5%–13.0% and 7.6%–17.5%, respectively, and higher than those of PP fibres. Splitting tensile strength and flexural strength of G75 were 2.87 MPa and 3.09 MPa, respectively, which increased by 54.3% and 38.6%, respectively, compared to the control mix. Compared to the PP fibre, the higher tensile stress of the G fibre is more effective in transferring the tensile stress. At the

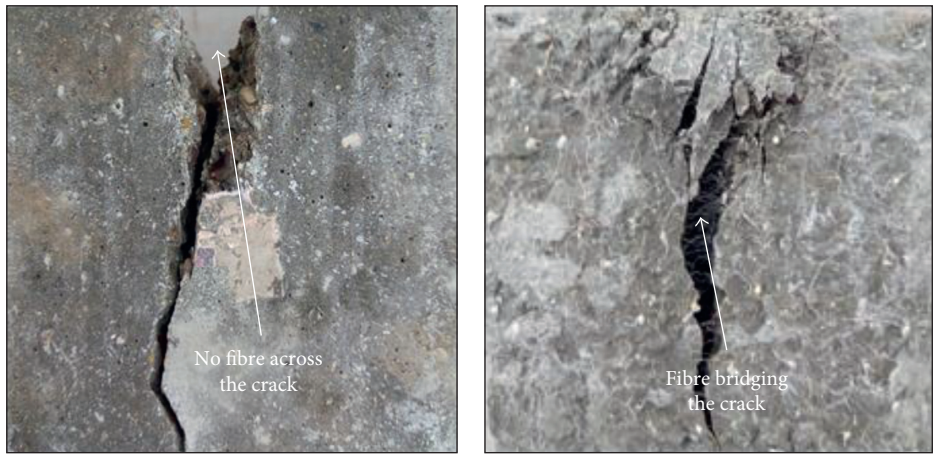

(a) (b)

Figure 8: Specimen after the splitting tensile test: (a) control concrete without fibres and (b) concrete containing fibres.

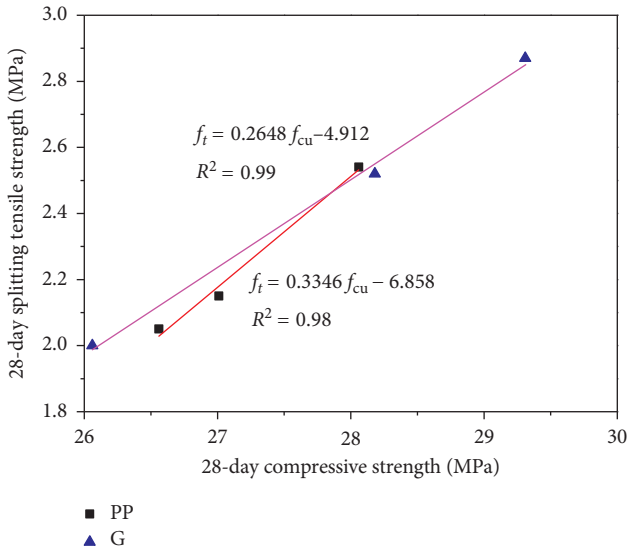

Figure 9: Relationship between the compressive strength and splitting tensile strength.

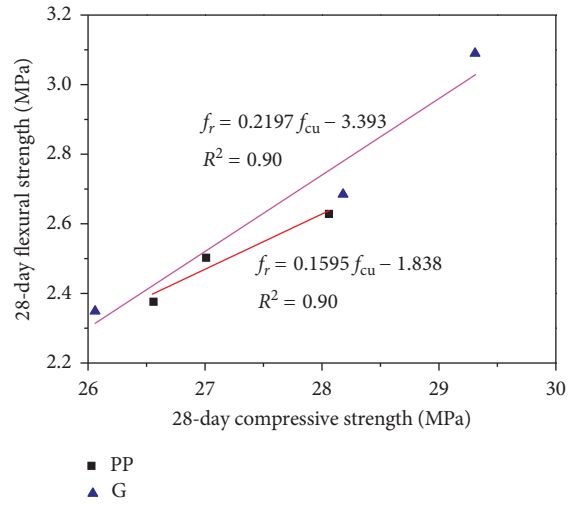

Figure 10: Relationship between the compressive strength and flexural strength.

same fibre volume fraction, the G fibre has a smaller diameter, leading to more fibres to join the cracks [22]. Due to the bridging effect of fibres, the stress concentration around cracks is reduced and the development of cracks is hindered. Eventually, the tensile strength of PSC is improved.

The relationship between the compressive strength and splitting tensile strength and flexural strength for PSC at 28 days is shown in Figures 9 and 10, respectively. As can be seen from Figures 9 and 10, the splitting tensile strength and flexural strength of PSFRC increase as an increase in compressive strength.

3.5. Modulus of Elasticity. Table 5 shows the modulus of elasticity (MOE) of all concretes, which ranges between 8.71 and 11.32 GPa. The control concrete in this study produced a minimum MOE of 8.71 GPa. The results showed that the types of G fibres and PP fibres had a significant effect on MOE. At $V_f = 0.25\%$, 0.50%, and 0.75%, the MOE of PP fibre- and G fibre-reinforced PSC increased by 10.6% and 12.4%, 16.5% and 23.4%, and 24.6% and 30.0%, respectively. The incorporation of fibres enhances the MOE of PSC because fibres arrest the initial cracks caused by shrinkage, and the crack bridging effect reduces the strain caused by the compression loading and consequently improves the MOE.

The MOE of PSFRC was found to depend on the fibre volume fraction, while the type of fibres had an insignificant influence on it. The volume fraction of G fibres increased from 0.25% to 0.75%, the MOE of G fibre-reinforced PSC increased by 15.6% from 9.79 GPa to 11.32 GPa, and the MOE of G fibre-reinforced PSC was 1.7%, 5.9%, and 4.3%, respectively, slightly higher than that of PP fibre.

Figure 11 shows the relationship between the compressive strength and MOE. As can be seen from Figure 11, there is a good relationship between the MOE and 28-day

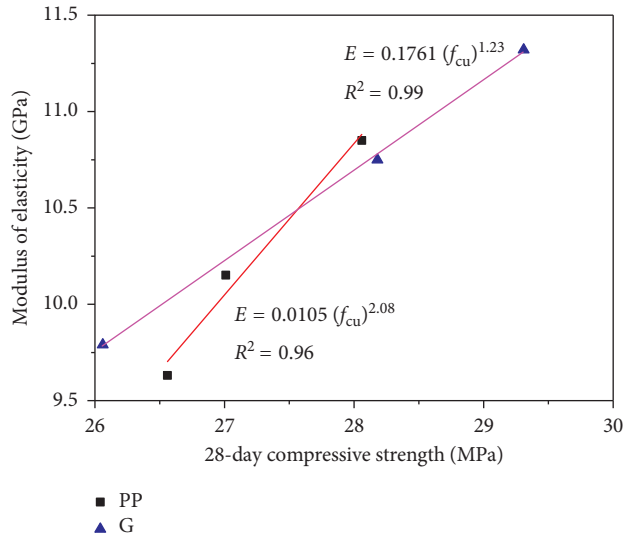

Figure 11: Relationship between the compressive strength and MOE.

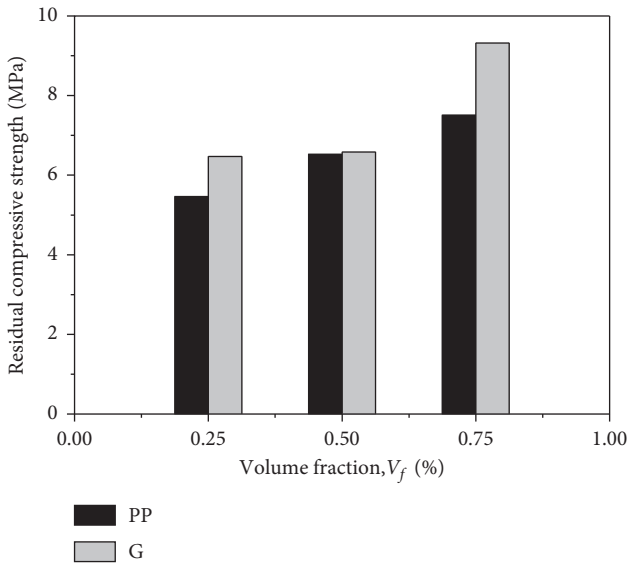

Figure 12: Residual compressive strength of concretes.

compressive strength of PSFRC, and the MOE of PP fibre-reinforced PSC and glass fibre-reinforced PSC can be predicted by the 28-day compressive strength, respectively.

3.6. Residual Compressive Strength. Residual compressive strength (RCS) can be used to evaluate the residual strength toughness of concretes. Figure 12 shows residual compressive strength of concretes. Because the crack bridging effect of fibres existed at two crack surfaces, in the fibre-reinforced concrete, additional loading forces are required for further growth of the crack. As expected, the incorporation of PP fibres and G fibres enhanced the residual strength toughness of PSC. The control concrete without any fibres had no RCS as the control concrete was immediately failed when the ultimate loading strength is reached. In addition, the more the fibre content, the higher the RCS value. At $V_f = 0.75\%$, PP fibre- and G fibre-reinforced PSC had the highest RCS value. It might be attributed to the crack bridging effect of fibres that existed at two crack surfaces, which can hinder further propagation of cracks, even after microcrack cracking. The results indicated that the influence of adding fibres on the improvement of postfailure toughness of PSC was very significant.

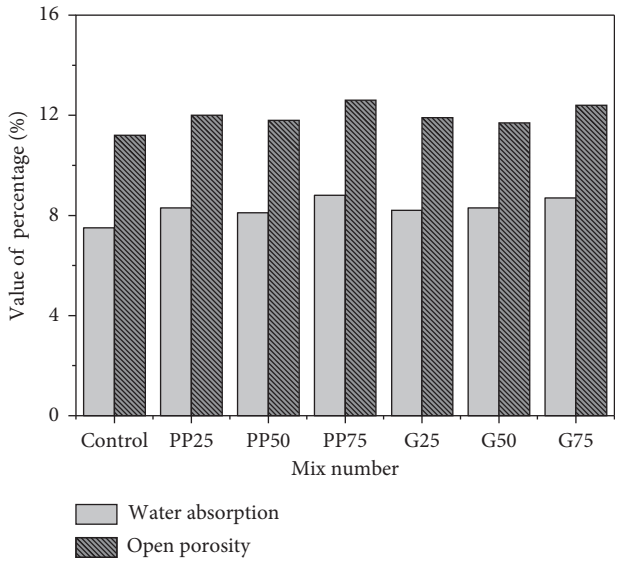

Figure 13: Percentage value of water absorption and open porosity of concretes.

3.7. Water Absorption and Porosity. Twenty-four-hour water absorption and open porosity for all mixes are shown in Figure 13. Lo et al. [23] studied that the water absorption of the lightweight aggregate affected the internal microstructure of the hardened mortar and the interfacial zone of concrete, and an increase in the water absorption of the lightweight aggregate resulted in an increase in the number of pores in the interfacial zone of concrete. Figure 13 clearly showed that the incorporation of fibres slightly increased the water absorption and open porosity of PSC, and the water absorption values of all concretes varied from 7.5% to 8.8%. However, the type and content of fibres had an insignificant effect on water absorption and open porosity, and the more the number of open pores, the higher the water absorption for all concretes. The addition of fibres might affect the number and area of micropores in PSC, which resulted in a small increase in water absorption and open porosity. Neville and Brooks [24] reported that although the water absorption cannot be used to determine the quality of concrete, the water absorption of most of the good-quality concretes usually is much lower than 10% by mass. It can be seen from Figure 13 that all concretes have less than 10% water absorption and meet the requirements of good concrete.

Total porosity and open porosity of concretes are shown in Figure 14. The result showed that the total porosity of PSC was between 15.1% and 16.5%, and the open porosity

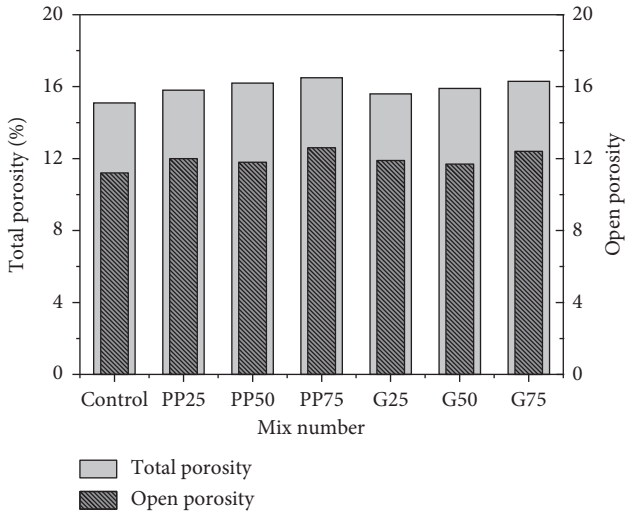

Figure 14: Total and open porosity of concretes.

varied from 11.2% to 12.6%. Furthermore, most of the total porosity in PSC was open porosity, and closed porosity accounted for a small portion of the total porosity because the surface of PS aggregates contains a lot of microscopic and connective pore structures. Results also showed that the type and content of fibres had an insignificant influence on the porosity of PSC, and the addition of fibres slightly increased the porosity of PSC. In addition, a slight increase in the total porosity was another reason that adding fibres reduced the density of PSC.

4. Conclusions

The influences of incorporating two types of fibres (polypropylene fibre and glass fibre) and different fibre volume fractions (0.25%, 0.5%, and 0.75%) on the mechanical properties of peach shell lightweight concrete have been investigated in this study. The following conclusions can be drawn based on the present study:

(1) The polypropylene fibre and glass fibre decrease the slump value of peach shell concrete. The slump values of the fresh peach shell concrete with polypropylene fibres and glass fibres are reduced to 55 mm and 60 mm, respectively. However, the concrete containing glass fibres produced slightly higher slump values than polypropylene fibres.

(2) The addition of polypropylene fibres and glass fibres reduces the oven-dried density of peach shell concrete. The oven-dried density of all concretes ranges from 1758 kg/m^3 to 1872 kg/m^3 and fulfills the requirement of lightweight aggregate concrete. In addition, the oven-dried density of peach shell concrete reduces with an increase in fibre content.

(3) All concretes have high early compressive strength. Polypropylene fibres and glass fibres significantly increase the compressive strength of peach shell concrete, and the compressive strength of peach shell concrete increases as an increase in fibre content. In addition, an increase in the 28-day compressive strength of peach shell concrete is about 6%–19%.

(4) The addition of polypropylene fibres and glass fibres in concrete increases the splitting tensile strength of peach shell concrete. Furthermore, the more the fibre content, the higher the splitting tensile strength. The addition of polypropylene fibres and glass fibres from 0.25% to 0.75% increases the splitting tensile strength up to 10.2%–36.6% and 7.5%–54.3%, respectively.

(5) The flexural strength of peach shell concrete increases as an increase in fibre volume fraction. The flexural strength for polypropylene fibres and glass fibres from 0.25% to 0.75% reinforced the peach shell concrete increase by 6.7%–17.9% and 5.4%–38.6%, respectively.

(6) The glass fibre-reinforced peach shell concrete produces a higher splitting tensile strength and flexural strength. At $V_f = 0.50\%$ and 0.75%, the splitting tensile strength and flexural strength of peach shell concrete containing glass fibres are found to be about 12.5%–13.0% and 7.6%–17.5%, respectively, and higher than those of polypropylene fibres.

(7) The effect of incorporating polypropylene fibres and glass fibres enhances the modulus of elasticity of peach shell concrete. Modulus of elasticity of all concretes ranges between 8.71 and 11.32 GPa. At $V_f = 0.25\%$, 0.50%, and 0.75%, the modulus of elasticity of polypropylene fibre- and glass fibre-reinforced peach shell concrete increases by 10.6% and 12.4%, 16.5% and 23.4%, and 24.6% and 30.0%, respectively.

(8) The control peach shell concrete produced no residual compressive strength. However, the addition of polypropylene fibres and glass fibres enhances the residual strength toughness of peach shell concrete. In addition, the higher the fibre volume content, the higher the residual compressive strength. At $V_f = 0.75\%$, the polypropylene fibre- and glass fibre-reinforced peach shell concrete have the highest residual compressive strength values and increase by 46% and 82%, respectively.

(9) The incorporation of fibres slightly increases the water absorption and porosity of peach shell concrete. However, the type and content of fibres have an insignificant effect on water absorption and porosity.

Conflicts of Interest

The authors declare that they have no conflicts of interest.

Acknowledgments

This work was financially supported by the Institute of Disaster Management and Reconstruction, Sichuan University-The Hong Kong Polytechnic University and College of Water Resource and Hydropower, Sichuan University. The authors

would also like to thank Dr. Ai Ting for her assistance in conducting some of the tests in this paper.

References

[1] A. Short and W. Kinniburgh, *Lightweight Concrete*, Applied Science Publishers, London, UK, 3rd edition, 1978.

[2] U. J. Alengaram, B. A. A. Muhit, and M. Z. Jumaat, "Utilization of oil palm kernel shell as lightweight aggregate in concrete-a review," *Construction and Building Materials*, vol. 38, pp. 161–172, 2013.

[3] P. Shafigh, M. Z. Jumaat, and H. Mahmud, "Mix design and mechanical properties of oil palm shell lightweight aggregate concrete: a review," *International Journal of Physical Sciences*, vol. 5, no. 14, pp. 2127–2134, 2010.

[4] E. Aguirre-Maldonado and F. Hernández-Olivares, "Study of fine mortar powder from different waste sources for recycled concrete production," in *Sustainable Development and Renovation in Architecture, Urbanism and Engineering*, pp. 253–262, Springer, Berlin, Germany, 2017.

[5] S. P. Yap, U. J. Alengaram, and M. Z. Jumaat, "Enhancement of mechanical properties in polypropylene- and nylon-fibre reinforced oil palm shell concrete," *Materials and Design*, vol. 49, pp. 1034–1041, 2013.

[6] M. K. Yew, H. Mahmud, B. C. Ang, and M. C. Yew, "Effects of heat treatment on oil palm shell coarse aggregates for high strength lightweight concrete," *Materials and Design*, vol. 54, pp. 702–707, 2014.

[7] U. J. Alengaram, M. Z. Jumaat, H. Mahmud, and S. M. Shirazi, "Effect of aggregate size and proportion on strength properties of palm kernel shell concrete," *International Journal of Physical Sciences*, vol. 5, no. 12, pp. 1848–1856, 2010.

[8] A. R. Khaloo and M. Sharifian, "Experimental investigation of low to high-strength steel fibre reinforced lightweight concrete under pure torsion," *Asian Journal of Civil Engineering*, vol. 6, no. 6, pp. 533–547, 2005.

[9] M. K. Yew, H. B. Mahmud, B. C. Ang, and M. C. Yew, "Influence of different types of polypropylene fibre on the mechanical properties of high-strength oil palm shell lightweight concrete," *Construction and Building Materials*, vol. 90, pp. 36–43, 2015.

[10] S. P. Yap, U. J. Alengaram, M. Z. Jumaat, and K. R. Khaw, "Torsional behaviour of steel fibre-reinforced oil palm shell concrete beams," *Materials and Design*, vol. 87, pp. 854–862, 2015.

[11] S. Hamoush, T. Abu-Lebdeh, and T. Cummins, "Deflection behaviour of concrete beams reinforced with PVA microfibres," *Construction and Building Materials*, vol. 24, no. 11, pp. 2285–2293, 2010.

[12] C. X. Qian and P. Stroeven, "Development of hybrid polypropylene-steel fibre reinforced concrete," *Cement and Concrete Research*, vol. 30, no. 1, pp. 63–69, 2000.

[13] S. P. Yap, C. H. Bu, U. J. Alengaram, K. H. Mo, and M. Z. Jumaat, "Flexural toughness characteristics of steel-polypropylene hybrid fibre-reinforced oil shell concrete," *Materials and Design*, vol. 57, pp. 625–659, 2014.

[14] M. Mastali, A. Dalvand, and A. R. Sattarifard, "The impact resistance and mechanical properties of reinforced self-compacting concrete with recycled glass fibre reinforced polymers," *Journal of Cleaner Production*, vol. 124, pp. 312–324, 2016.

[15] P. K. Mehta and P. J. M. Monteiro, *Concrete: Microstructure, Properties and Materials*, McGraw-Hill, New York, NY, USA, 3rd edition, 2006.

[16] P. S. Song, S. Hwang, and B. C. Sheu, "Strength properties of nylon- and polypropylene-fibre-reinforced concretes," *Cement and Concrete Research*, vol. 35, pp. 1546–1550, 2005.

[17] J. Newman and P. Owens, *Properties of Lightweight Concrete. Advanced Concrete Technology Set*, pp. 3–29, Butterworth-Heinemann, Oxford, UK, 2003.

[18] J. M. Gao, W. Sun, and K. Morino, "Mechanical properties of steel fibre-reinforced high-strength lightweight concrete," *Cement and Concrete Composites*, vol. 19, pp. 307–313, 1997.

[19] S. Kakooei, H. M. Akil, M. Jamshidi, and J. Rouhi, "The effects of polypropylene fibres on the properties of reinforced concrete structures," *Construction and Building Materials*, vol. 27, pp. 73–77, 2012.

[20] C. G. Han, Y. S. Hwang, S. H. Yang, and N. Gowripalan, "Performance of spalling resistance of high performance concrete with polypropylene fibre contents and lateral confinement," *Cement and Concrete Research*, vol. 35, no. 9, pp. 1747–1753, 2005.

[21] L. Comiloli, C. Failla, and G. A. Plizzari, "Steel and synthetic fibres for enhancing concrete toughness and shrinkage behaviour," in *Proceedings of International Conference Sustainable Construction Materials and Technologies*, pp. 231–240, Coventry, UK, 2007.

[22] N. Banthia and R. Gupta, "Influence of polypropylene fibre geometry on plastic shrinkage cracking in concrete," *Cement and Concrete Research*, vol. 36, no. 1, pp. 1263–1267, 2006.

[23] T. Y. Lo, H. Z. Cui, W. C. Tang, and W. M. Leung, "The effect of aggregate absorption on pore area at interfacial zone of lightweight concrete," *Construction and Building Materials*, vol. 22, no. 4, pp. 623–628, 2008.

[24] A. M. Neville and J. J. Brooks, *Concrete Technology*, Pearson Education Asia Pvt. Ltd., Malaysia, 2008.

Hindawi
Advances in Materials Science and Engineering
Volume 2018, Article ID 5271324, 15 pages
https://doi.org/10.1155/2018/5271324

Research Article

Evaluation of Carbonation Effects on Cement-Solidified Contaminated Soil Used in Road Subgrade

Yundong Zhou,[1,2,3] Lingling Pan,[4] Qiang Tang,[1,2,4] Yu Zhang,[4] Na Yang,[4] and Cong Lu[4]

[1]*Key Laboratory of Ministry of Education for Geomechanics and Embankment Engineering, Hohai University, Nanjing 210098, China*
[2]*Geotechnical Research Institute, Hohai University, Nanjing 210098, China*
[3]*Institute of Geotechnical Engineering, Nanjing University of Technology, Nanjing 210009, China*
[4]*School of Rail Transportation, Soochow University, Suzhou 215131, China*

Correspondence should be addressed to Qiang Tang; tangqiang@suda.edu.cn

Received 8 October 2017; Accepted 7 December 2017; Published 4 February 2018

Academic Editor: Estokova Adriana

Cement solidification/stabilization is widely used towards contaminated soil since it has a low price and significant improvement for the structural capacity of soil. To increase the usage of the solidified matrix, cement-solidified contaminated soil was used as road subgrade material. In this study, carbonation effect that reflected the durability on strength characteristics of cement-solidified contaminated soil and the settlement of pavement were evaluated through experimental and numerical analysis, respectively. According to results, compressive strengths of specimens with 1% Pb(II) under carbonation and standard curing range from 0.44 MPa to 1.17 MPa and 0.14 MPa to 2.67 MPa, respectively. The relatively low strengths were attributed to immobilization of heavy metal, which consumed part of SiO_2, Al_2O_3, and CaO components in the cement or kaolin and reduced the hydration and pozzolanic reaction materials. This phenomenon further decreased the strength of solidified soils. The carbonation depth of 1% Cu(II) or Zn(II) contaminated soils was 18 mm, which significantly increased with the increase of curing time and contamination concentration. Furthermore, the finite element calculation results showed that surface settlements decreased with the increase of modulus of subgrade and the distance away from the center. At the center, the pavement settlement was proportional to the level of traffic load.

1. Introduction

The development of industry and urbanization was accompanied with soil pollution, which attracts great attention in the recent years [1–4]. Heavy metal pollution in soils in various countries is summarized in Table 1. According to the site-investigation in Southern tailing area, France, the concentration of Pb(II) contained in soil reached around 9000 mg/kg, which was almost 281 times higher than that of natural soil [5]. Similarly, according to Seleznev and Yarmoshenko and CosKun et al., the soil in Turkey and Russia was also suffered with Pb(II) contamination [6, 7]. Besides, the concentration of Cu(II) in mining areas in Vietnam were founded as high as 1050 mg/kg [8]. In China, according to Zhang et al., the concentration of Cu(II) in Guangdong was founded as high as 4800 mg/kg [9]. Heavy metals are not only hazardous to the environment and public health but also lead to the degradation of mechanical properties of soils [10, 11]. Bochenek and Kurdowski found that the effect of solidification/stabilization of the waste is strongly related to the concentration of Pb(II) and Zn(II) [12]. The high concentration of heavy metals usually diminishes the solidification/stabilization of the waste.

Solidification/stabilization (S/S) is a commonly used remediation method towards heavy metal-contaminated soils. The S/S process is recognized by the U.S. Environmental Protection Agency (EPA) as the Best Demonstrated Available Technology (BDAT) for the land disposal of most toxic elements [10]. This method not only enhances the strength of soil effectively but also reduces the leaching of

Table 1: Heavy metal pollution of soils in various regions.

Country	Location	Metal content (mg/kg)						References
		Cr	Pb	Cu	Zn	Cd	Ni	
China	Guangdong	2600	150	4800	330	1.21	480	[9]
China	A rural area, Jianghan plain	253.8	4.88	64.6	—	20.3	589.5	[13]
Russia	Ekaterinburg	—	1027	370	—	—	663	[6]
France	Southern tailing area	—	9000	—	16,000	—	—	[5]
Turkey	73 places	830	968	167	165	1.7	249	[7]
Greece	Landfill site	172	93	356	344	18.8	66	[14]
Vietnam	Mining areas	135	—	1050	—	284	76.9	[8]
India	Nuggihalli, Karnataka	4863	84.1	153.6	—	—	1398	[15]
Background value in soil		133	31.8	41	114	0.314	58	[16]

heavy metals [11]. Numerous researchers have studied S/S process to immobilize heavy metal by means of various S/S agents such as cement, quicklime, hydrated lime, fly ash, and cement kiln dust [17, 18]. Cement is widely used in S/S due to its relative low price and significant improvement for the structural capacity of soil [19].

Conventionally, carbonation reaction of concrete is considered unfavorable, as it diminishes the durability of such materials, but for S/S system, this is different [20]. Exposure of S/S-treated waste to carbon dioxide resulted in physical and chemical transformations, which affected the long-term effectiveness of the S/S process. The microcracks were generated in the carbonated areas, which decreased the strength of concrete [21]. Gunning et al. demonstrated that accelerated carbonation could enhance the curing property of cement solidification and reduce the cost of disposal processes [22]. Although many studies investigated the carbonation reaction, its effects on the strength of contaminated soil that is solidified by cement still have not been systematically studied.

Road is the main transport infrastructure and an important stimulator to the economy. In order to meet the increasing demands in terms of axle loads and frequency of traffic, the entire road network demands a substantial amount of aggregates, bituminous, and cementitious binders [23]. Recently, with the increase of scarcity of raw materials, the road pavement industry is facing new challenges in terms of resources. Numerous laboratory studies and field trials have shown that recycled materials can totally or partially replace natural materials in road construction [24]. Brooks and Cetin confirmed that using 30% recycled demolition waste and cement kiln dust to strengthen the subgrade and to prepare the subbase helps reducing the overall thickness of the pavement [25]. Bennert et al. studied the performance of recycled concrete aggregate in base and subbase courses and concluded that a mixture of 25% of recycled concrete aggregates with 75% of natural aggregate has the same resilient response [26]. In China, contaminated soils in industrial sites including power plants and boiler plants which stabilized by cement were used as road materials for Shanghai, World Expo. Potential saving in raw materials and storage space made the use of solidified soil, an attractive alternative to highway engineers.

The solidified contaminated soil instead of raw material is used as subgrade material. In the field of practical engineering, due to the limitations of the construction environment, the contaminated soil is inevitably exposed to atmospheric carbon dioxide before strength formation. Carbon dioxide in the disposal environment enters into the pores of the contaminated soils during the curing period. Previous studies show that carbonation of S/S-treated material brings about physical and chemical transformations that can affect the long-term effectiveness of the S/S process [27]. Therefore, the simulation of the solidified contaminated soil after carbonation and the evaluation of its durability deserve to be studied.

In this paper, soils spiked with high levels of Pb(II), Zn(II), and Cu(II) contaminants were treated by cement as subgrade material. The objectives of this study are to systematically investigate the effects of carbonation on the strength of the cement-stabilized soils through the laboratory tests. The influence factors included the type and content of heavy metals, cement content, moisture content, and curing time. The mechanisms of Zn(II), Pb(II), and Cu(II) immobilization with cement are interpreted based on the results of X-ray diffraction (XRD), Inductive Coupled Plasma Emission Spectrometer (ICP), nitrogen adsorption measurement (N_2-BET), and scanning electron microscope (SEM) analysis. Subsequently, MIDAS/GTS finite element program is used to investigate the pavement settlements of application of solidified contaminated soil in subgrade. The final section summarizes the major findings of this study.

2. Materials and Methods

2.1. Raw Materials. The soils used in this study included one type of clay and one type of fine sand. The clay was commercial kaolin, obtained from Suzhou kaolin Co. Ltd., China. Commercial sand with diameters of approximately 1.0 mm was obtained from ShengFa Building Materials Co. Ltd., China. As the binder material, the commercially available OPC P·O42.5 was prepared, which consisted of 6%–15% active additive and 85%–94% cement. The natural moisture content of kaolin and sand was measured according to JIS A 1203. Grain size distribution of kaolin and sand was tested according to GB/T 50123-1999. Electrical

Table 2: Mixture composition of specimens.

No.	Heavy metal	Metal content (%)	Cement content (%)	Moisture content (%)
1	0	0	5	17
2	0	0	5	23
3	0	0	10	17
4	0	0	10	23
5	Pb	0.1	5	17
6	Pb	0.1	5	23
7	Pb	1	5	17
8	Pb	1	5	23
9	Pb	1	10	17
10	Pb	1	10	23
11	Zn	1	10	23
12	Cu	1	10	23

conductivity (EC) and pH of the kaolin and sand was measured by pH/EC meter (PH-2603, Lohand, China) following JGS 0212 and JGS 0211, respectively. The N_2-BET adsorption test was conducted to analyze specific surface area and average pore diameter of soil (NOVA2000e, Quantachrome, U.S.). The elemental and mineral composition of kaolin was analyzed by ICP-OES (Varian 720) and XRD (RAD-2B, Rigaku Corporation, Japan) correspondingly.

Firstly, soils and H_2O_2 were directly weighed inside the quartz vessels. The rotor was positioned inside the SRC system, which was previously filled with 120 mL of water and 5 mL of H_2SO_4. Secondly, the microwave heating procedure was operated as follows: 10 min of ramp and hold for 20 min at 250°C. After cooling down (65°C), the chamber was depressurized, and the resultant solution was diluted in volumetric flasks up to 25 mL. After that, the residue was carefully transferred into microwave digestion system to which 8 mL of a mixture of $20\%HNO_3 + 5\%HF + 5\%H_2O_2$ or $20\%HNO_3 + 0.4\%NH_4HF_2 + 5\%H_2O_2$ was added [28]. Finally, the vessel was closed and clamped within a support module and placed inside the microwave digestion system.

The heavy metal-contaminated soils were prepared artificially by adding $Pb(NO_3)_2$, $Zn(NO_3)_2{\cdot}6H_2O$, and $Cu(NO_3)_2$ (Analytical reagent, Sinopharm, China) as a source of pollutant. Zn(II) and Pb(II) were selected as the target heavy metals because they are commonly encountered in the contaminated sites worldwide, especially in China [29, 30]. The reason for choosing the source chemical in nitrate form was that the main chemical compositions of cement including Ca(II) and K(I) are very inert to react with nitrate anions. Besides, when compared to phosphate anions, nitrate anions have low sensitivity to the engineering characteristics of clay.

2.2. Specimen Preparation. Before the experiment, kaolin, cement, and sand samples were oven dried at 105°C for 24 hours (h) (101-A, Leao, China) and then cooled to room temperature in a desiccator [31, 32]. First of all, according to the ratio of sand/kaolin (7 : 3 by dry mass), samples were carried out and mixed manually for 4–5 minutes (min) in the vessel to achieve homogeneity. Second, cement was then added according to the ratios of cement/soils (5%/10%, on dry weight of soil basis), recorded as C5/C10. Third, based on the mixture proportion shown in Table 2, the heavy metal solutions were prepared artificially by adding $Pb(NO_3)_2$, $Zn(NO_3)_2{\cdot}6H_2O$, and $Cu(NO_3)_2$ (Analytical reagent, Sinopharm, China). After the mixing procedure, the mixture was transferred into a mold, which is 5 cm in diameter and 10 cm in height. At last, the specimens were extruded from the molds carefully with a hydraulic jack and were sealed with a polyethylene membrane to avoid severe dehydration.

After molding, partial samples were cured (≥95% humidity, 20 ± 2°C) for 1, 7, 14, and 28 days in a curing box (HBY-15B, Donghua, China). In addition, the rest of samples were placed in a carbonation testing apparatus (75 ± 5% humidity, 20 ± 2°C) containing CO_2 gas at the concentration of 20 ± 2% for 1, 7, 14, and 28 days. According to Pu and Unluer, the demolded samples were subjected to accelerated carbonation at 30 ± 2°C and 80 ± 5% RH under a CO_2 concentration of 10% for up to 28 days [33]. On the basis of Tang et al. (2017)'s research, the cement-fly ash mixtures were demoulded and placed in a carbonation testing apparatus containing CO_2 gas concentration of 20 ± 3%, relative humidity of 70 ± 2%, and temperature of 20 ± 2°C for 7, 14, and 28 days, which in accordance with the experimental scheme in this study [34]. In this study, the accelerated carbonation (CO_2 concentration of 20 ± 2%) was used to simulate the long-term effects of carbonation on the strength and leaching characteristics of cement-stabilized contaminated soils.

2.3. Compressive Strength Test. After curing, the unconfined compression tests were conducted as per ASTM D 2166-91 using a microcomputer-controlled electronic testing machine (LDS-50, Chenda, China), with a vertical displacement rate of 1 mm/min. The shape factor (height-to-diameter ratio) of the CPB specimens was 2.0. Total maximum loads were recorded, and the compressive strength was determined using the formula $q_u = F/A$, where q_u is the

compressive strength (MPa), F is the total maximum load (N), and A is the area of loaded surface (mm^2). Based on the accuracy of the experiment, all of these tests were conducted in replicate, and the average values were reported.

2.4. Carbonation Depth Test. The carbonated specimens were cut in half on the basis of splitting method, which were followed by removing residual powder. The freshly cut surfaces were sprayed with phenolphthalein, which turned pink where the pore solution exceeded pH 9, that is, where the matrix had not yet become carbonated [35]. As shown in Figure 1, the depth of carbonation L was measured at four different locations along four edges, and the average value was used to determine the extent of carbonation according to GB/T 50082-2009 [36]:

$$L = \frac{(L_1 + L_2 + L_3 + L_4)}{4}. \quad (1)$$

2.5. Numerical Simulation Model. Pavement is a multilayered structure composed of a concrete slab or an asphalt layer laid on a foundation system comprising various layers such as base and subgrade [37–43].

MIDAS/GTS finite element software was adopted to assess the structural capacity of pavement with the use of cement-solidified contaminated soil used in subgrade. The influences of subgrade modulus and vehicle load on the structural surface deflection were analyzed. In this paper, schematic plot of road structure is shown in Figure 2. The pavement structure is simplified as a two-dimensional (2D) axisymmetric plane strain case [44, 45].

In this model, the pavement length along the traffic direction was assumed infinite. The width of the subgrade was defined as 40 meters, while the road width was one-fourth of the subgrade. This setting was to eliminate the interference of boundary condition on the results. Besides, the depth of the model was 3 meters. The pavement structure comprised various layers including 18 cm asphalt layer, 40 cm cement treated base layer, and 242 cm cement-solidified contaminated soil layer. The details of the model (constitutive model, thickness, and basic properties of each layer) are shown in Table 3.

In pavement structure design, the axial load is usually assumed to be uniformly distributed on the contact area [46]. According to BZZ-100 standard axle load, axle load was 100 kN and contact pressure was 0.7 MPa. The contact area between tire and road surface was 0.134 m^2 in accordance with JTG D50-2006. The loading area was located at the center of the pavement illustrated in Figure 2, and the radius r_0 was 0.152 m. In order to eliminate the boundary effect, the bottom boundary was set to be completely fixed, and the side boundary was fixed in the lateral direction.

It is known that there is a correlation between modulus of cement-treated material and the strength of aggregate used [37]. Terashi et al. indicated that secant modulus (E50) had a linear correlation with q_u expressed by (2) [47]. Experimental findings according to Du et al. were that the dimensionless fitting parameter η varies in the range of

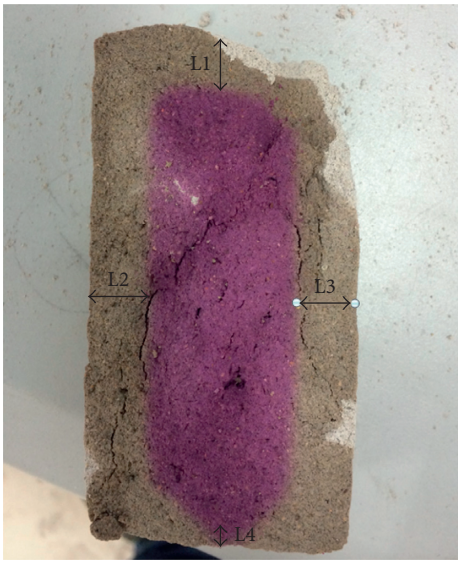

Figure 1: Carbonation depth of specimen.

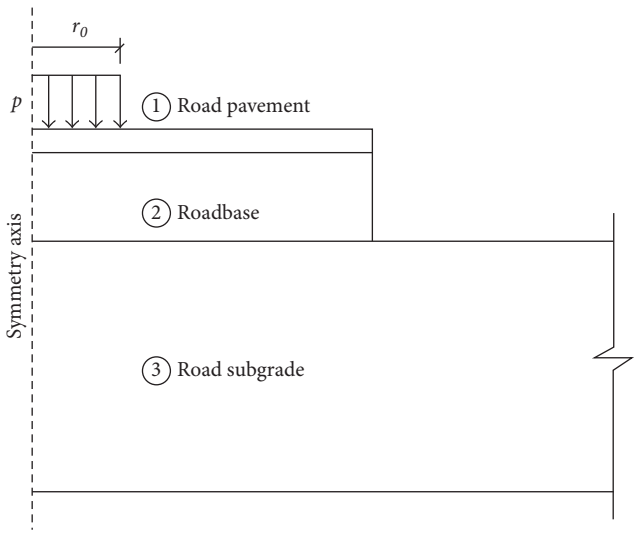

Figure 2: Schematic plot of road structure.

18 to 53, depending on heavy metal concentration and cement content [48]. Yang and Zhao investigated the relationship between deformation modulus (E_S) and modulus of elasticity (E), as shown in (3) and (4) [49]. Consequently, the elastic modulus of solidified contaminated soil was calculated based on (5).

$$E_{50} = \eta * q_u, \quad (2)$$

$$E_0 = \frac{(1+\mu)(1-2\mu)}{(1-\mu)} E_S, \quad (3)$$

$$E = (2.5 \sim 3.5) E_S, \quad (4)$$

$$E = (2.5 \sim 3.5) \frac{(1-\mu)}{(1+\mu)(1-2\mu)} E_0, \quad (5)$$

Table 3: Input parameters of finite element model.

Material	① Asphalt mixture	② Cement-steadied grit	③ Solidified contaminated soil
Constitutive model	Elasticity	Elasticity	Mohr–Coulomb
Thickness (m)	0.18	0.40	2.42
Bulk density (kN/m^3)	19.6	23.5	17.4
Elasticity modulus (MPa)	1400	500	30
Cohesive force (kPa)	/	/	24
Internal friction angle (°)	/	/	30
Poisson's ration	0.35	0.25	0.45

Table 4: Physical and mechanical properties of kaolin and sand.

Properties	Standard	Unit	Kaolin	Sand
Natural water content	JIS A 1203	%	2.90	0.39
pH	JGS 0211	—	4.70	7.50
EC	JGS 0212	mS/cm	0.42	0.06
Grain size distribution	GB/T50123-1999	—	—	—
Clay fraction (≤0.005 mm)	—	%	56.40	0.10
Silt fraction (0.075–0.005 mm)	—	%	18.80	2.98
Sand fraction (2–0.075 mm)	—	%	24.80	96.92
Correlation coefficient (R)	—	—	0.99	—
Specific surface area	—	m^2/g	29.41	—
Average pore size	—	nm	29.97	—
Total pore volume	—	cm^3/g	0.22	—

Table 5: Soil compounds identified by ICP.

Element	Unit	Concentration	Element	Unit	Concentration
Al	mg/kg	11,900.1	Na	mg/kg	3167.3
Ca	mg/kg	3024.41	Si	mg/kg	50,266.8
K	mg/kg	2303.5	Ti	mg/kg	3492.9
Fe	mg/kg	5520.2	Zn	mg/kg	344.76
Mg	mg/kg	171.02	Pb	mg/kg	116.99

where E_{50} is secant modulus (MPa); η is a dimensionless fitting parameter; according to Du et al. [48], values of η of uncontaminated soil, Pb0.1, and Pb1 are determined as 40, 28, and 18, respectively; E_0 is deformation modulus (MPa), according to Gong (2008), the deformation modulus was replaced by E_{50} [50]; μ is Poisson ratio; E_S is modulus of compressibility (MPa); and E is elastic modulus (MPa). The elastic modulus was applied to the numerical simulation in this paper.

3. Experimental Results and Discussion

3.1. Characterization of the Materials. The physical and chemical characteristics of soils are summarized in Table 4. As shown in Table 4, the moisture content of kaolin and sand are 2.90% and 0.39%, respectively. The pH value of kaolin is 4.70, which indicates its acid nature. The pH value of sand is 7.50, which is similar to the soil used in Du et al. [51]. EC values of kaolin and sand are 0.42 mS/cm and 0.06 mS/cm, respectively.

Concerning the N_2-BET adsorption tests, the correlation coefficient is 0.99, indicating that the obtained results are reliable. The specific surface area of kaolin used in this experiment is 29.41 m^2/g. In addition, the total pore volume and micropore aperture of kaolin are 0.22 cm^3/g and 29.97 nm, respectively. ICP results of kaolin and sand are presented in Table 5. Based on the XRD spectra shown in Figure 3, kaolin is mainly composed of kaolinite ($Al_2Si_2O_5(OH)_4$) and lizardite ($Mg_3Si_2O_5(OH)_4$), which are observed at $2\theta = 12.46^\circ$, 36.01°, and 24.97°. Considering the existence of Na(I) and Fe shown by ICP results, the characteristic peaks at $2\theta = 26.73$ and 20.43° indicate the presence of sodium phosphate hydrate ($Na_6P_6O_{18}{\cdot}6H_2O$) and iron silicon carbide (Fe-Si-C).

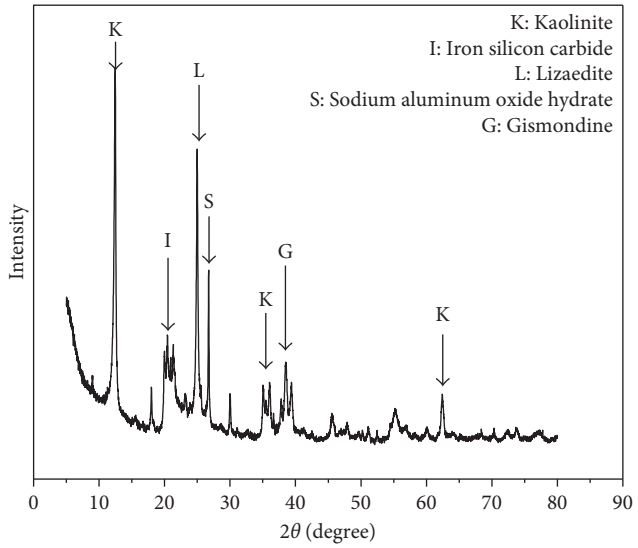

Figure 3: XRD analysis of kaolin.

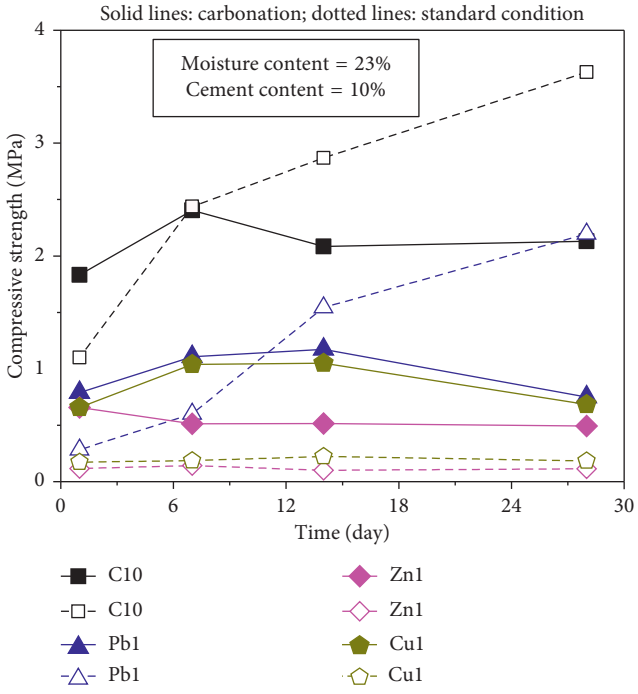

Figure 4: The unconfined compressive strength of solidified soil with different contaminations.

3.2. Compressive Strength Analysis. Figure 4 shows the variation in compressive strength values of the stabilized soils with different initial contamination species in which "C10" represent the uncontaminated soil with 10% cement content. The solid lines represent the carbonated specimens, while the dotted lines represent samples cured under standard conditions. As presented, initial contamination species have different effects on the compressive strength of stabilized soils. Under the standard curing condition, the uncontaminated soil after 1 day (d) of curing exhibits the highest compressive strength, which is 1.1 MPa. The strength of uncontaminated soil increases with curing time. As far as Pb(II) contaminated soil (Pb 1), the compressive strength is lower than that of clean soil during 28 days (d) curing periods. The compressive strength of Cu(II) or Zn(II) contaminated soil (Cu1/Zn1) shows no significant growth trend, which is only 5 percent of that of clean soil after 28 days (d) of curing. This is because the presence of Cu(II) or Zn(II) has a negative impact on the hydration reaction, which hinders the reactions of soils, cement, and contamination. Pb(II) exists mainly as Pb hydrate phases and Pb hydroxide ($Pb(OH)_2$) precipitated on the surface of calcium hydroxide ($Ca(OH)_2$) or calcium silicate hydrate (CSH). Compared to $Pb(OH)_2$, pyromorphite has a much lower solubility and a greater capacity to resist acid or alkaline attack [52, 53]. In addition, the solubility of $Zn_3(PO_4)_2{\cdot}4H_2O$ or $CaZn_2(PO_4)_2{\cdot}2H_2O$ is much lower than zinc hydroxide ($Zn(OH)_2$), which is the main product involved in the immobilization of Zn(II) with Portland cement [54].

Under carbonation condition, the compressive strength of soils with 1% Pb(II) or Cu(II) contamination increases slightly during the early stage (1–14 days), while decreases at the late stage (14–28 days). The typical SEM images for kaolin are shown in Figure 5. It is obvious that the microstructure of kaolin is sheet-shaped, whose specific surface area is 29.41 m^2/g. Therefore, CO_2 trends to enter the stabilized soil at the early stage due to the large pore size and total pore volume of kaolin. As a result, calcium carbonate hydrate promoted by CO_2 with heavy metal possesses high cementitious bonding strength and effectively fills soil macropores [55]. Carbonation mainly involves the primary hydration products: calcium silicate hydrate (CSH) and calcium hydroxide ($Ca(OH)_2$), which are converted to calcium carbonate ($CaCO_3$), according to the following stoichiometry [56]:

$$Ca^{2+} + 2(OH)^- + CO_2\,(aq) \rightarrow CaCO_3\,(s) + H_2O \qquad (6)$$

This assumption is based on the abundance of calcium ions in the pore water due to the dissolution of portlandite. The carbonation reaction is supported by calcium hydroxide that is generated by the decalcification of CSH gel after the original level of portlandite formed during depletion of ordinary Portland cement (OPC) hydration [57]:

$$x\mathrm{CaO}\cdot\mathrm{SiO_2}\cdot n\mathrm{H_2O} + y\mathrm{H_2O} \rightarrow (x-y)\mathrm{CaO}\cdot\mathrm{SiO_2}\cdot n\mathrm{H_2O} + y\mathrm{Ca(OH)_2} \qquad (7)$$

$$\mathrm{CSH} + \mathrm{HCO_3^-} \rightarrow \mathrm{CaCO_3} + \mathrm{SiO_2\,(gel)} + \mathrm{H_2O} \qquad (8)$$

Long-term attack by carbonic acid decomposes the CSH gel into calcium carbonate, acid-insoluble silica gel, and water. However, soil environment changes along with time, resulting in the decrease of compressive strength of stabilized soil.

Compared with carbonated specimens, the soil with 1% Pb(II) contamination cured under standard condition shows a higher compressive strength after 14 days of curing. This is

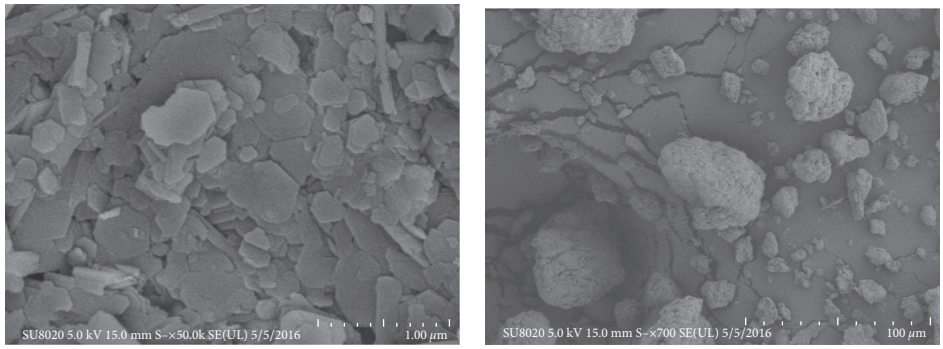

(a) (b)

Figure 5: SEM images of kaolin. (a) 1 μm. (b) 100 μm.

attributed to its constant hydration reaction. Other researchers have reported similar strength gains caused by carbonation during curing. They attributed this increase to the transformation of calcium hydroxide (the most abundant cement hydration product after CSH) to calcium carbonate with lower density, which grows into and fills the cement matrix pores [58]. Meanwhile, the hydration reactions of Cu(II) or Zn(II) contaminated soils are delayed, so that the Cu(II) or Zn(II) contaminated soils (Cu1 or Pb1) during 28 days (d) curing periods show lower compressive strengths than those of carbonated specimens.

The relationship between the compressive strength of stabilized soil and the concentration of heavy metal is presented in Figure 6. The notion, "C5," shown in Figure 6 represents the uncontaminated soil with 5% cement content. It is observed that the concentration of heavy metal has a remarkable effect on soil strength in both conditions. Under the standard curing condition, the compressive strengths of stabilized soils during 7–28 days (d) curing periods decline sharply when the concentration of Pb(II) increases from 0.1% to 1%. The strength of 0.1% Pb(II) contaminated soil is slightly lower than that of clean soil at the medium stage (7–14 days). At the same time, the soil with the concentration of 1% Pb(II) after 1 day (d) of curing exhibits the lowest strength, which is only 0.18 MPa. After carbonation, the specimens with 1% Pb(II) contamination declines from 0.97 MPa to 0.44 MPa at the late stage (14–28 days), which is more than twice of that uncontaminated soil. When the Pb(II) ions/soils ratio is small, the formation of lead oxide hydrate ($xPbO{\cdot}yH_2O$) will take place, which possess high cementitious bonding strength. As the Pb(II) concentration in soil increases, Pb(II) is bonded by OH^- in pore water, and the hydration reaction is incomplete [59]. This leads to the decrease in compressive strength associated with high heavy metal concentration.

The compressive strength values of the solidified soil with different cement contents are presented in Figure 7, in which "Pb1 C5" or "Pb1 C10" represent the 1% Pb(II) contaminated soil with 5% or 10% cement content. Under the standard curing condition, the specimens with 10% cement content show significantly higher strengths than those with lower cement content. As far as carbonated specimens, the soils exhibit higher compressive strengths

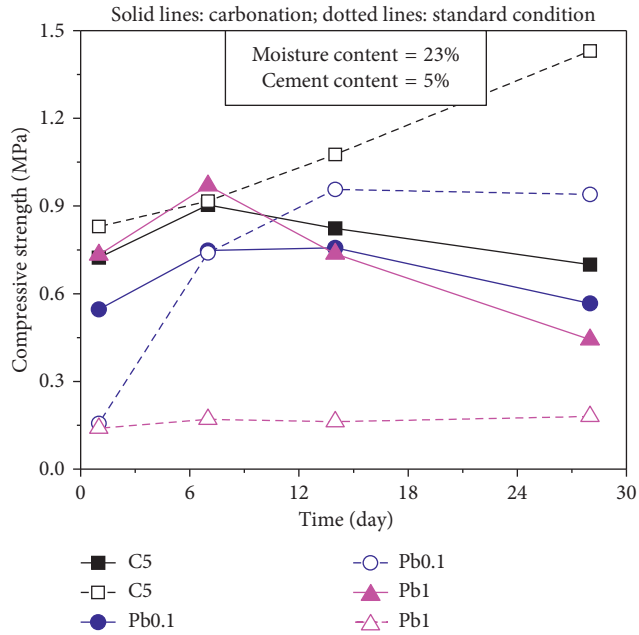

Figure 6: The unconfined compressive strength of solidified soil with different heavy metal contents.

during the early stage (1–14 days), while show lower strengths at the late stage (14–28 days). This phenomenon is due to the components of kaolin and cement. As shown in Table 5, the concentration of Si(II) element is measured as high as 50,266.8 mg/kg. The XRD analysis demonstrates that the concentrations of Al(III) and Ca(II) in kaolin are 11,900.1 mg/kg and 3024.4 mg/kg, respectively. Note that PbO is capable of reacting with both acid and base. As a result, the formation of silicate, aluminate, and plumbite will occur through the reaction of PbO with SiO_2, CaO, and Al_2O_3, respectively. When the cement/soils ratio is small, the immobilization of lead consumed large amounts of SiO_2, CaO, and Al_2O_3, which results in the decrease of the occurrence of hydration reaction and pozzolanic reaction [60, 61].

Figure 8 draws the relationship between strengths and the moisture contents. The notions, "17% or 23%," represent

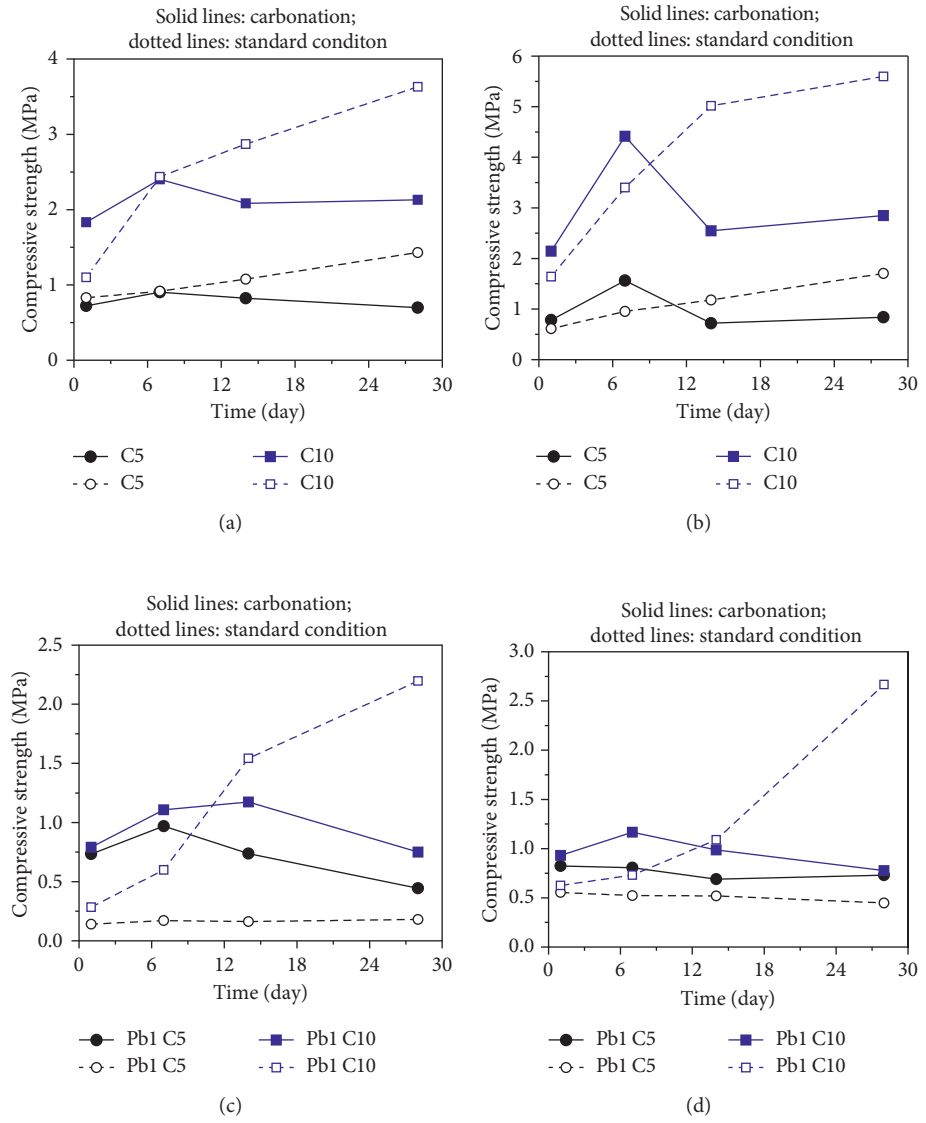

Figure 7: The unconfined compressive strength of solidified soil with different moisture contents. (a) Moisture content = 23%. (b) Moisture content = 17%. (c) Moisture content = 23%. (d) Moisture content = 17%.

the uncontaminated soil with 17% or 23% moisture content. Besides, "Pb1 17% or Pb1 23%" shown in Figure 8 indicates 1% Pb(II) contaminated soil with 17% or 23% moisture content. It shows that the specimens with 17% moisture content have higher compressive strengths than those with 23% moisture content in most cases in both standard and carbonation conditions. In this study, the agent has been able to react completely associated with relatively few cement.

Compared with samples cured under standard condition, the compressive strengths of carbonated specimens decline at the late stage (7–28 days). On one hand, cement hydration products are covered by carbonation precipitation generated by the precarbonation, which hinders the further occurrence of carbonation reaction and thereby decreases the strength of solidified soils. On the other hand, the decrease of pore volume of carbonated specimens also decreases the strength of solidified soil. This is because of the following reasons: (a) the increase of soil density, (b) the reduction of diffusion rate of carbon dioxide in the solidified soil, and (c) the decrease of carbonation reaction rate.

3.3. Carbonation Depth Analysis. The carbonation depth test results show that the depth of the cement-solidified soil is significantly enhanced with curing time. As shown in Figure 9, "M0" demonstrates the uncontaminated soil. The presence of heavy metal is beneficial to the carbonation depth of the solidified soil. At the moisture content of 23%, the depths of 1% Cu(II) or Zn(II) contaminated soils after 28 days (d) carbonation are 18 mm, which are 1.8 times higher than those of clean soils.

Figure 10 presents the relationship between carbonation depth and heavy metal concentrations. At the early stage (7–14 days), the carbonation depth of the specimens with

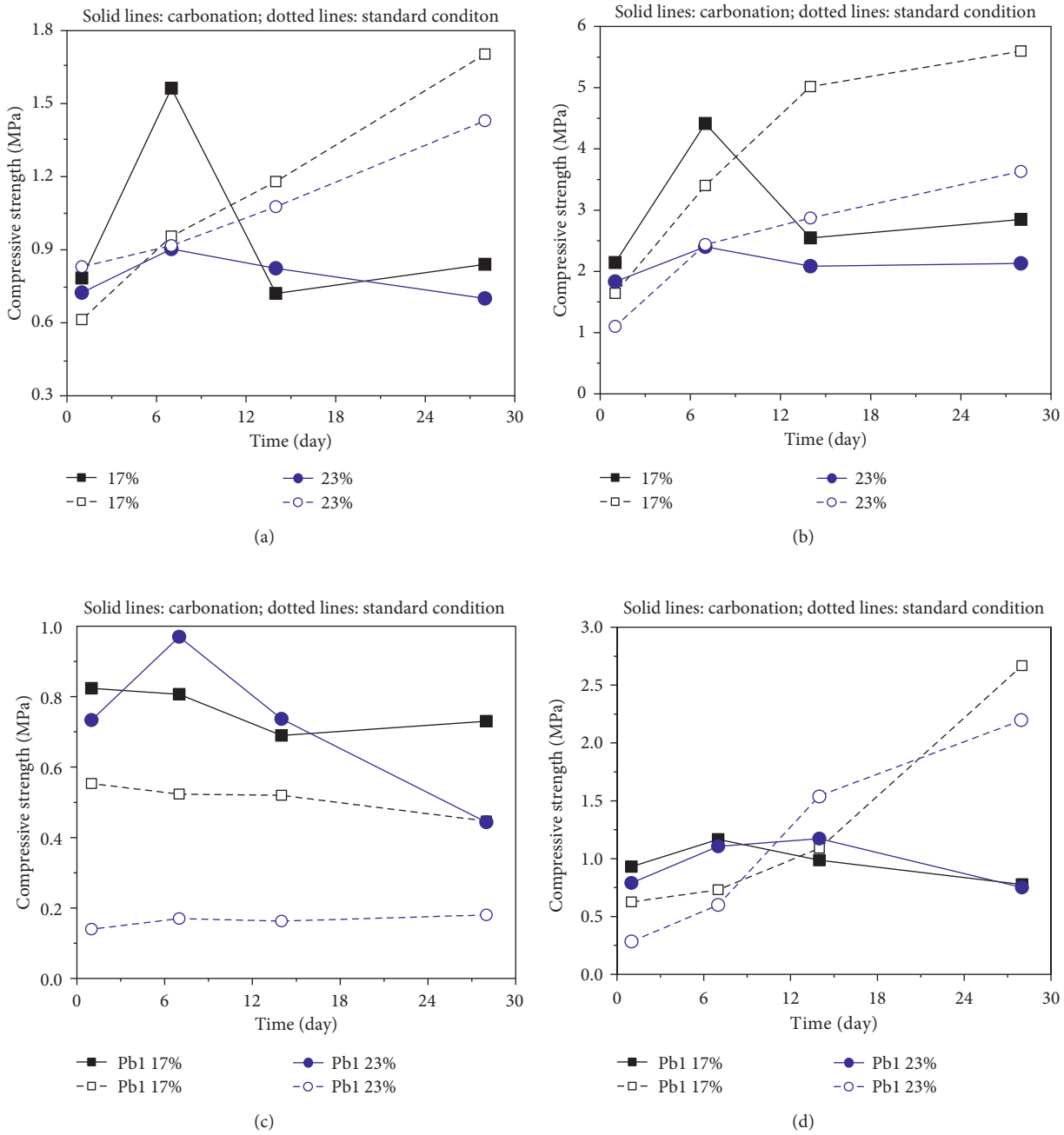

Figure 8: The unconfined compressive strength of solidified soil with different cement contents. (a) Cement content = 5%. (b) Cement content = 10%. (c) Cement content = 5%. (d) Cement content = 10%.

23% moisture content and 5% cement content grew rapidly with the increasing of heavy metal concentration. While in the late stage, immobilization of heavy metal consumed parts of SiO_2, Al_2O_3, and CaO components in the cement or kaolin, which reduces the hydration and pozzolanic reaction materials. That is why the carbonation reactions with high contamination concentration and 17% moisture content are lower than those with low concentration or clean soil.

Figure 11 demonstrates the carbonation depths of solidified soil under different cement contents. The density of soil and carbonation reaction rate is highly related with cement content. Under the same level of heavy metal concentration and curing time, the samples with 10% cement content show smaller carbonation depths than those with 5% cement content. Regarding the moisture content, the connectivity of the liquid phase in the solidified soil decreases due to the relative low moisture content, which leading to the increase of porosities of samples. This explains that the carbonation depths of specimens with 17% moisture content are higher than those with 23% moisture content.

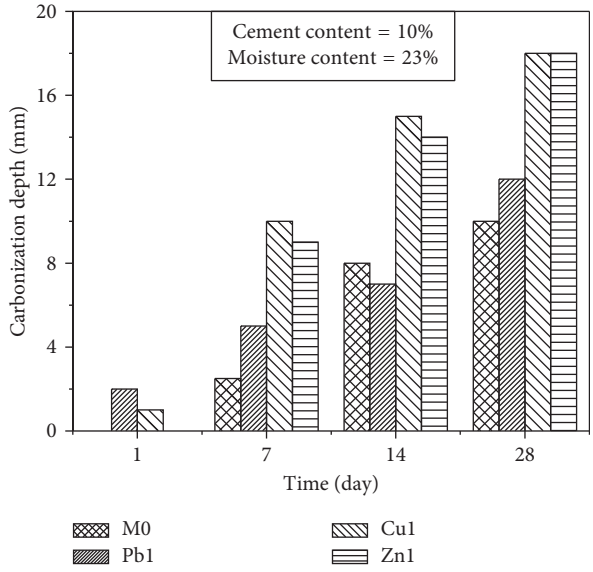

Figure 9: Carbonation depths of contaminated soil with different contaminations.

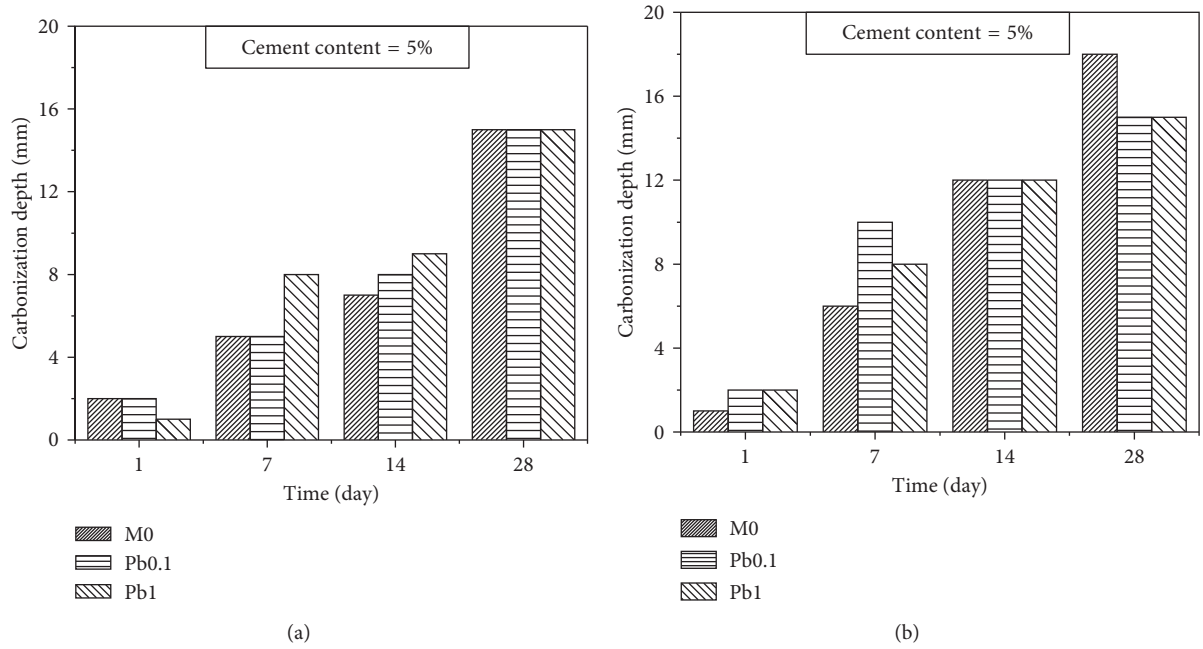

Figure 10: Carbonation depths of contaminated soil with different heavy metal contents. (a) Moisture content = 23%. (b) Moisture content = 17%.

4. Simulation Results and Analysis

This study uses the cement-solidified contaminated soil as road subgrade and explores the influences of subgrade modulus and vehicle load on pavement settlements.

4.1. Analysis of the Influence of Subgrade Modulus. The modulus of cement-treated material is a key mechanical factor to pavement design. Based on the experimental results, elasticity moduli of solidified soils under different conditions are shown in Table 6, in which the elasticity moduli of solidified Pb contaminated soil after 28 d curing under carbonation and standard condition range from 90.80 MPa to 210.28 MPa, from 36.87 MPa to 546.19 MPa, respectively. In this study, the elasticity moduli of subgrade are set from 50 MPa to 500 MPa.

Figure 12 shows the relationship between the elastic moduli of subgrade and the surface settlements of pavement. The surface settlement of the pavement decreases gradually with increasing of elastic modulus and the distance away from the load center. Comparing with

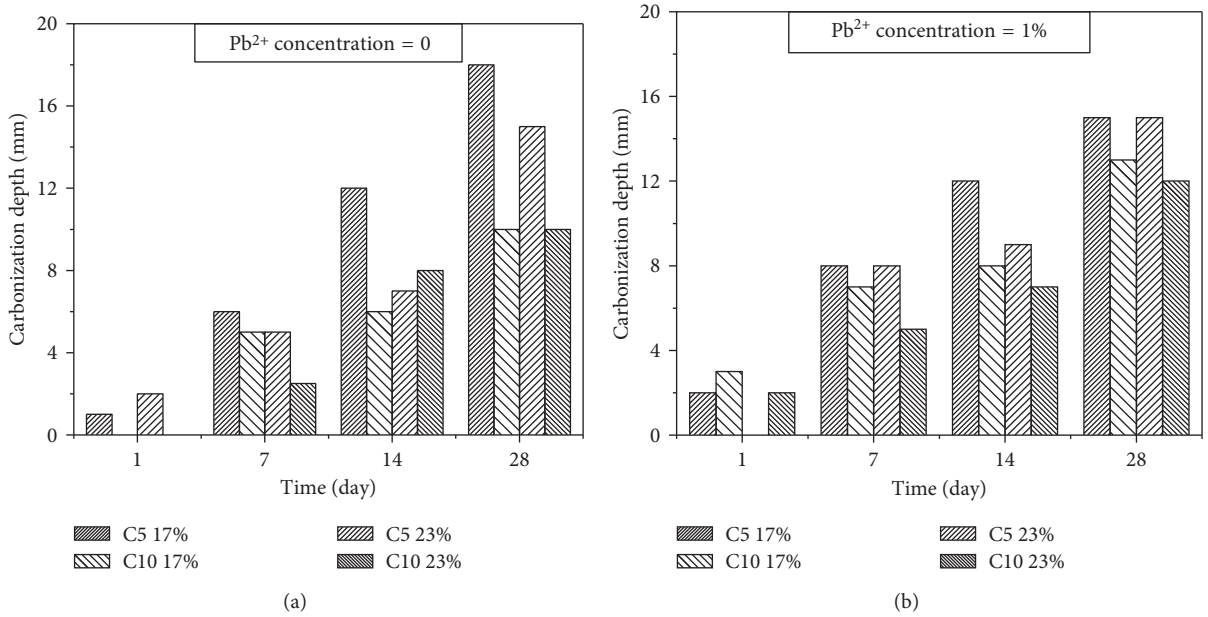

Figure 11: Carbonation depths of contaminated soil with different cement and moisture contents. (a) Pb^{2+} concentration = 0. (b) Pb^{2+} concentration = 1%.

Table 6: Elasticity moduli of solidified soils under different conditions.

Heavy metal content (%)	Cement content (%)	Moisture content (%)	E (MPa)							
			Carbonation (d)				Standard condition (d)			
			1	7	14	28	1	7	14	28
0	5	17	356.5	711.6	327.7	382.3	279.2	434.7	537.1	775.3
	5	23	329.2	411.2	374.7	318.6	377.8	417.2	490.1	650.9
	10	17	975.6	2008.8	1159.1	1295.7	748.0	1547.5	2283.4	2547.4
	10	23	834.5	1093.9	948.2	969.5	500.7	1109.1	1306.3	1652.2
Pb0.1	5	17	200.7	452.4	360.0	210.3	102.0	337.7	344.1	474.7
	5	23	174.2	238.4	241.1	180.5	49.9	235.8	304.8	299.5
Pb1	5	17	168.6	165.2	141.3	149.5	113.3	107.2	106.5	91.5
	5	23	150.2	198.7	150.9	90.8	28.7	34.8	33.3	36.9
	10	17	190.5	239.0	202.1	159.1	128.4	149.5	223.3	546.2
	10	23	161.8	226.7	240.3	153.6	58.0	122.9	316.1	449.9
Zn1	10	23	134.5	105.1	105.5	101.0	23.9	29.4	20.5	23.2
Cu1	10	23	134.5	213.0	215.1	140.0	35.5	38.2	45.7	37.6

the pavement settlements at the center, the settlements 2.5 m away from the center with elasticity moduli from 50 MPa to 500 MPa decline by 105.73%, 106.60%, 105.13%, and 104.62%, respectively, while the settlements at the edge decline by 109.92%, 103.77%, 102.56%, and 103.08%, respectively. Furthermore, along with the increase of elasticity moduli, surface settlements at the center decrease by 59.42%, 70.44%, and 75.24%, respectively. Thus, elasticity modulus plays a key role in the pavement settlement at the center.

4.2. Analysis of the Influence of Traffic Load. On the basis of BZZ-100 standard axle load, the vehicle loads are set to 0.7 MPa (standard axle load), 1.1 MPa (overload 50%), and 1.4 MPa (overload 100%). Such settings aim to investigate the influence of the traffic load.

The settlements of pavement with different traffic axle loads are presented in Figure 13. It is observed that traffic loads have a remarkable effect on the pavement settlements. With axle load increasing from 0.7 MPa to 1.4 MPa, the surface settlements at the center increase rapidly by 57.14% and 100%. It is indicated that the settlement at the centerline is linearly proportional to the axle load. In addition, the settlements of pavement have an inverse relationship with the distance away from the centerline. Compared with surface settlements at the center, the settlements 2.5 meter

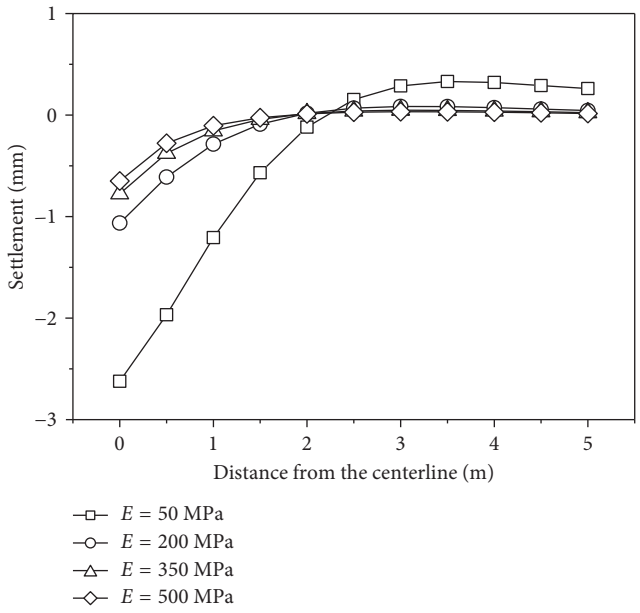

Figure 12: Settlements of the pavement with different subgrade moduli.

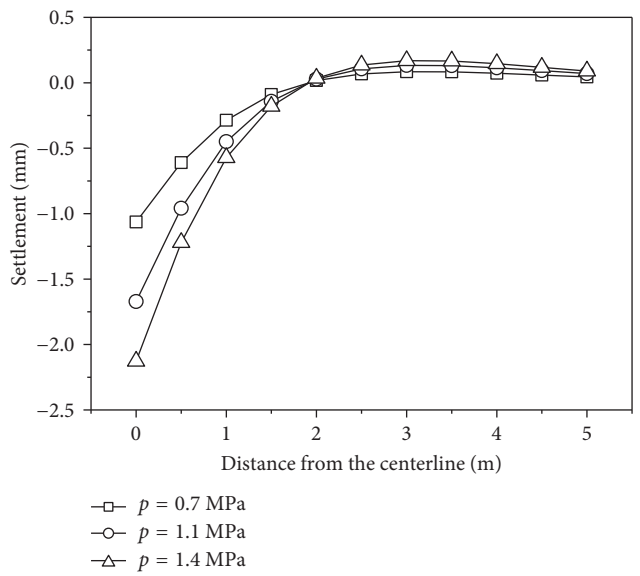

Figure 13: Settlements of the pavement with different axle loads.

away from the center with 0.7 MPa, 1.1 MPa, and 1.4 MPa decrease by 106.60%, 106.59%, and 106.57%, respectively. When the distance away from the center is more than 2.5 meter, traffic load is not the main factor affecting the pavement settlement.

5. Conclusions

This study evaluated the carbonation effects on strength and settlement of cement-solidified contaminated soil for the use of road subgrade. The major findings are summarized as follows:

(1) As far as initial contamination species, the compressive strengths of Cu(II) or Zn(II) contaminated soil (Cu1/Zn1) were lower than that of Pb(II) 1 and uncontaminated soil. Under both standard and carbonation conditions, compressive strengths of stabilized soils increased with curing time and declined sharply when the concentration of Pb(II) increased from 0 to 1%. Regarding moisture content, specimens with 17% moisture content showed higher strengths compared to those with 23% moisture content under both standard and carbonation conditions.

(2) The carbonation depth was significantly enhanced with curing time and contamination concentration. Under the same condition, the samples with 10% cement content had smaller carbonation depth compared with those with 5% cement content. In addition, the carbonation depths of specimens with 17% moisture content were higher than those with 23% moisture content.

(3) In the simulation, the surface settlements of the pavement decreased with the increase of elastic modulus and the distance away from the load center. Regarding traffic load, the settlement at the centerline was linearly proportional to the axle load. When the distance away from the center was more than 2.5 meter, traffic load was not a significant factor affecting the pavement settlement.

(4) Based on experimental and numerical analysis results, the strengths of the carbonated contaminated soil meet the standard of subgrade material, resulting in low settlement deformations. Therefore, the contaminated soils after carbonation possess long durability and carbonation resistance.

Nomenclature

S/S: Solidification/stabilization
XRD: X-ray diffraction
ICP: Inductive Coupled Plasma Emission Spectrometer
N_2-BET: Nitrogen adsorption measurement
SEM: Scanning electron microscope
EC: Electrical conductivity
C5: 5% cement content
C10: 10% cement content
17%: 17% moisture content
23%: 23% moisture content
Pb0.1: 0.1% Pb(II) contaminated soil
Pb1: 1% Pb(II) contaminated soil
Zn1: 1% Zn(II) contaminated soil
Cu1: 1% Cu(II) contaminated soil.

Conflicts of Interest

The authors declare that they have no conflicts of interest.

Acknowledgments

The research presented herein is supported by the National Nature Science Foundation of China (51708377), Natural Science Foundation of Jiangsu Province (BK20170339), China Postdoctoral Science Foundation funded project (2016M591756), Natural Science Fund for Colleges and Universities in Jiangsu Province (17KJB560008), Jiangsu Planned Projects for Postdoctoral Research Funds (1601175C), and project from Jiangsu Provincial Department of Housing and Urban-Rural Development (2016ZD18 and 2017ZD002). The research is also supported by Jiangsu Provincial Transport Bureau (2016T05).

References

[1] Q. Tang, X. W. Tang, M. M. Hu, Z. Z. Li, Y. M. Chen, and P. Lou, "Removal of Cd(II) from aqueous solution with activated Firmiana Simplex Leaf: behaviors and affecting factors," *Journal of Hazardous Materials*, vol. 79, no. 1–3, pp. 95–103, 2010.

[2] Q. Tang, T. Katsumi, T. Inui, and Z. Z. Li, "Membrane behavior of bentonite amended compacted clay," *Soils and Foundations*, vol. 54, no. 3, pp. 329–344, 2014.

[3] Q. Tang, HJ. Kim, K. Endo, T. Katsumi, and T. Inui, "Size effect on lysimeter test evaluating the properties of construction and demolition waste leachate," *Soils and Foundations*, vol. 55, no. 4, pp. 720–736, 2015.

[4] Q. Tang, T. Katsumi, T. Inui, and Z. Z. Li, "Membrane behavior of bentonite-amended compacted clay towards Zn(II) and Pb(II)," *Membrane Water Treatment*, vol. 6, no. 5, pp. 393–409, 2015.

[5] J. Escarré, C. Lefèbvre, S. Raboyeau et al., "Heavy metal concentration survey in soils and plants of the Les Malines Mining District (Southern France): implications for soil restoration," *Water, Air, & Soil Pollution*, vol. 216, no. 1–4, pp. 485–504, 2011.

[6] A. A. Seleznev and I. V. Yarmoshenko, "Study of urban puddle sediments for understanding heavy metal pollution in an urban environment," *Environmental Technology & Innovation*, vol. 1-2, pp. 1–7, 2014.

[7] M. CosKun, E. Steinnes, and M. Viladimirovna, "Heavy metal pollution of surface soil in the Thrace region, Turkey," *Environmental Monitoring and Assessment*, vol. 119, no. 1–3, pp. 545–556, 2006.

[8] N. T. H. Ha, M. Sakakibara, S. Sano, and M. T. Nhuan, "Uptake of metals and metalloids by plants growing in a lead–zinc mine area, Northern Vietnam," *Journal of Hazardous Materials*, vol. 186, no. 2-3, pp. 1384–1391, 2011.

[9] W. H. Zhang, W. U. Ying-Xin, and M. O. Simonnot, "Soil contamination due to e-waste disposal and recycling activities: a review with special focus on China," *Pedosphere*, vol. 22, no. 4, pp. 434–455, 2012.

[10] Q. Tang, Y. Liu, F. Gu, and T. Zhou, "Solidification/stabilization of fly ash from a municipal solid waste incineration facility using Portland cement," *Advances in Materials Science and Engineering*, vol. 2016, Article ID 7101243, 10 pages, 2016.

[11] Q. Tang, Y. Zhang, Y. F. Gao, and F. Gu, "Use of cement-chelated solidified MSWI fly ash for pavement material: mechanical and environmental evaluations," *Canadian Geotechnical Journal*, vol. 54, no. 11, pp. 1553–1566, 2017.

[12] A. Bochenek and W. Kurdowski, "Influence of zinc phase on the properties of Portland cement," *Cement Wapno Beton*, vol. 18, pp. 52–58, 2013.

[13] C. Gu, Y. Liu, D. B. Liu et al., "Distribution and ecological assessment of heavy metals in irrigation channel sediments in a typical rural area of south China," *Ecological Engineering*, vol. 90, pp. 466–472, 2016.

[14] A. Kasassi, P. Rakimbei, and A. Karagiannidis, "Soil contamination by heavy metals: measurements from a closed unlined landfill," *Bioresource Technology*, vol. 99, no. 18, pp. 8578–8584, 2008.

[15] A. K. Krishna, K. Rama Mohan, N. N. Murthy et al., "Assessment of heavy metal contamination in soils around chromite mining areas, Nuggihalli, Karnataka," *Environmental Earth Sciences*, vol. 70, no. 2, pp. 699–708, 2013.

[16] Ministry of Environmental Protection; Ministry of Land and Resources, *National Soil Pollution Survey Bulletin*, PRC, London, UK, 2014, http://www.zhb.gov.cn/gkml/hbb/qt/201404/t20140417_270670.htm.

[17] C. Vandecasteele, V. Dutré, D. Geysen, and G. Wauters, "Solidification/stabilisation of arsenic bearing fly ash from the metallurgical industry. Immobilisation mechanism of arsenic," *Waste Management*, vol. 22, no. 2, pp. 143–146, 2002.

[18] D. Dermatas, D. H. Moon, N. Menounou, X. Meng, and R. Hires, "An evaluation of arsenic release from monolithic solids using a modified semi-dynamic leaching test," *Journal of Hazardous Materials*, vol. 116, no. 1-2, pp. 25–38, 2004.

[19] F. Rosquoet, L. Thorel, J. Garnier, and Y. Canepa, "Lateral cyclic loading of sand-installed piles," *Soils and Foundations*, vol. 47, no. 5, pp. 821–832, 2007.

[20] W. Ashraf, "Carbonation of cement-based materials: challenges and opportunities," *Construction and Building Materials*, vol. 120, pp. 558–570, 2016.

[21] A. Fabbri, J. Corvisier, A. Schubnel, F. Brunet, B. Goffé, and G. Rimmele, "Effect of carbonation on the hydro-mechanical properties of Portland cements," *Cement and Concrete Research*, vol. 39, no. 12, pp. 1156–1163, 2009.

[22] P. J. Gunning, C. D. Hills, and P. J. Carey, "Accelerated carbonation treatment of industrial wastes," *Waste Management*, vol. 30, no. 6, pp. 1081–1090, 2010.

[23] L. D. Poulikakos, C. Papadaskalopoulou, B. Hofko et al., "Harvesting the unexplored potential of European waste materials for road construction," *Resources, Conservation and Recycling*, vol. 116, pp. 32–44, 2017.

[24] J. Jime´nez, J. Ayuso, and F. Agrela, "Use of mixed recycled aggregates with a low embodied energy from non-selected CDW in unpaved rural roads," *Construction and Building Materials*, vol. 34, pp. 34–43, 2012.

[25] R. M. Brooks and M. Cetin, "Application of construction demolition waste for improving performance of subgrade and subbase layers," *International Journal of Research and Reviews in Applied Sciences*, vol. 12, no. 3, p. 375, 2012.

[26] T. Bennert, W. Papp, A. Maher, and N. Gucunski, "Utilization of construction and demolition debris under traffic-type loading in base and subbase applications," *Transportation Research Record: Journal of the Transportation Research Board*, vol. 1714, pp. 33–39, 2000.

[27] A. C. Garrabrants, F. Sanchez, and D. S. Kosson, "Changes in constituent equilibrium leaching and pore water characteristics of a portland cement mortar as a result of carbonation," *Waste Management*, vol. 24, no. 1, pp. 19–36, 2004.

[28] M. V. B. Krishna, K. Chandrasekaran, S. Chakravarthy, and D. Karunasagar, "An integrated approach based on oxidative pyrolysis and microwave-assisted digestion for the multi-

elemental analysis of coal samples by ICP-based techniques," *Fuel*, vol. 158, pp. 770–778, 2015.

[29] Q. Tang, X. W. Tang, Z. Z. Li, Y. M. Chen, N. Y. Kou, and Z. F. Sun, "Adsorption and desorption behaviour of Pb(II) on a natural kaolin: equilibrium, kinetic and thermodynamic studies," *Journal of Chemical Technology & Biotechnology*, vol. 84, no. 9, pp. 1371–1380, 2009.

[30] Q. Tang, X. W. Tang, Z. Z. Li et al., "Zn(II) removal with activated firmiana simplex leaf: kinetics and equilibrium studies," *Journal of Environmental Engineering*, vol. 138, no. 2, pp. 190–199, 2012.

[31] Q. Tang, T. Katsumi, T. Inui, and Z. Z. Li, "Influence of pH on the membrane behavior of bentonite amended Fukakusa clay," *Separation and Purification Technology*, vol. 141, pp. 132–142, 2015.

[32] Q. Tang, W. Liu, H. Y. Wang, R. Cheng, and Y. F. Qian, "Membrane behavior of bentonite-amended Fukakusa clay under K, Na and Ca solutions," *Journal of Central South University*, vol. 23, no. 12, pp. 3122–3131, 2016.

[33] L. Pu and C. Unluer, "Investigation of carbonation depth and its influence on the performance and microstructure of MgO cement and PC mixes," *Construction & Building Materials*, vol. 120, pp. 349–363, 2016.

[34] Q. Tang, LL. Pan, Y. F. Gao et al., "Study on strength and environmental behaviors of solidified fly ash under carbonation effect," *Chinese Journal of Geotechnical Engineering*, 2017, http://kns.cnki.net/kcms/detail/32.1124.TU.20171029.1321.004.html.

[35] Rilem, "Measurement of hardened concrete carbonation depth," *Materials and Structures*, vol. 21, no. 6, pp. 453–455, 1998.

[36] X. Zha, H. Wang, P. Xie, C. Wang, P. Dangla, and J. Ye, "Leaching resistance of hazardous waste cement solidification after accelerated carbonation," *Cement and Concrete Composites*, vol. 72, pp. 125–132, 2016.

[37] L. Hu, J. Hao, and L. Wang, "Laboratory evaluation of cement treated aggregate containing crushed clay brick," *Journal of Traffic and Transportation Engineering*, vol. 1, no. 5, pp. 371–382, 2014.

[38] F. Gu, H. Sahin, X. Luo, R. Luo, and R. L. Lytton, "Estimation of resilient modulus of unbound aggregates using performance-related base course properties," *Journal of Materials in Civil Engineering*, vol. 27, no. 6, p. 04014188, 2014.

[39] F. Gu, Y. Zhang, C. V. Droddy, R. Luo, and R. L. Lytton, "Development of a new mechanistic empirical rutting model for unbound granular material," *Journal of Materials in Civil Engineering*, vol. 28, no. 8, p. 04016051, 2015.

[40] F. Gu, Y. Zhang, X. Luo, H. Sahin, and R. L. Lytton, "Characterization and prediction of permanent deformation properties of unbound granular materials for pavement ME design," *Construction and Building Materials*, vol. 155, pp. 584–592, 2017.

[41] F. Gu, X. Luo, R. C. West, A. J. Taylor, and N. D. Moore, "Energy-based crack initiation model for load-related top-down cracking in asphalt pavement," *Construction and Building Materials*, vol. 159, pp. 587–597, 2018.

[42] F. Gu, X. Luo, Y. Zhang, and R. L. Lytton, "Using overlay test to evaluate fracture properties of field-aged asphalt concrete," *Construction and Building Materials*, vol. 101, pp. 1059–1068, 2015.

[43] X. Luo, F. Gu, and R. L. Lytton, "Mechanistic composition-specific fatigue life of asphalt pavements," *Journal of Engineering Mechanics*, vol. 143, no. 12, p. 04017136, 2017.

[44] F. Gu, X. Luo, Y. Zhang, R. L. Lytton, and H. Sahin, "Modeling of unsaturated granular materials in flexible pavements," *E3S Web of Conferences*, vol. 9, p. 20002, 2016.

[45] F. Gu, X. Luo, R. Luo, R. L. Lytton, E. Y. Hajj, and R. V. Siddharthan, "Numerical modeling of geogrid-reinforced flexible pavement and corresponding validation using large-scale tank test," *Construction and Building Materials*, vol. 122, pp. 214–230, 2016.

[46] K. Himeno, T. Kamijima, T. Ikeda, and T. Abe, "Distribution of tire contact pressure of vehicles and its influence on pavement distress," in *Proceedings of Eighth International Conference on Asphalt Pavements*, Seattle, WA, USA, 1997.

[47] M. Terashi, H. Tanaka, T. Mitsumoto, Y. Niidome, and S. Homma, "Fundamentalproperties of lime and cement treated soils," *Report of the Port and Harbour Research Institute*, vol. 22, pp. 69–96, 1980.

[48] Y. J. Du, M. L. Wei, F. Jin, and Z. B. Liu, "Stress–strain relation and strength characteristics of cement treated zinc-contaminated clay," *Engineering Geology*, vol. 167, pp. 20–26, 2013.

[49] M. Yang and X. H. Zhao, "An approach for a single pile in layered soil," *Journal of Tongji University*, vol. 20, pp. 421–427, 1992.

[50] X. N. Gong, *Foundation Treatment Manual*, China Architecture and Building Press, Beijing, China, 3rd edition, 2008.

[51] Y. J. Du, M. L. Wei, K. R. Reddy, F. Jin, H. L. Wu, and Z. B. Liu, "New phosphate-based binder for stabilization of soils contaminated with heavy metals: leaching, strength and microstructure characterization," *Journal of Environmental Management*, vol. 146, pp. 179–188, 2014.

[52] S. Mignardi, A. Corami, and V. Ferrini, "Evaluation of the effectiveness of phosphate treatment for the remediation of mine waste soils contaminated with Cd, Cu, Pb, and Zn," *Chemosphere*, vol. 86, no. 4, pp. 354–360, 2012.

[53] A. Navarro, E. Cardellach, and M. Corbella, "Immobilization of Cu, Pb and Zn in mine-contaminated soils using reactive materials," *Journal of Hazardous Materials*, vol. 186, no. 2-3, pp. 1576–1585, 2011.

[54] P. Desogus, P. P. Manca, G. Orru, and A. Zucca, "Stabilization-solidification treatment of mine tailings using Portland cement, potassium dihydrogen phosphate and ferric chloride hexahydrate," *Minerals Engineering*, vol. 45, pp. 47–54, 2013.

[55] Y. J. Du, M. L. Wei, K. R. Reddy, and H. L. Wu, "Effect of carbonation on leachability, strength and microstructural characteristics of KMP binder stabilized Zn and Pb contaminated soils," *Chemosphere*, vol. 144, pp. 1033–1042, 2016.

[56] S. Bin Shafique, J. Walton, N. Gutierrez, R. Smith, and A. Tarquin, "Influence of carbonation on leaching of cementitious waste forms," *Journal of Environmental Engineering*, vol. 124, no. 5, pp. 463–467, 1998.

[57] C. Gervais, A. Garrabrants, F. Sanchez, and R. Barna, "The effects of carbonation and drying during intermittent leaching on the release of inorganic constituents from a cement-based matrix," *Cement and Concrete Research*, vol. 34, no. 1, pp. 119–131, 2004.

[58] M. F. Bertos, S. J. R. Simons, C. D. Hills, and P. J. Carey, "A review of accelerated carbonation technology in the treatment of cement-based materials and sequestration of CO_2," *Journal of Hazardous Materials*, vol. 112, no. 3, pp. 193–205, 2004.

[59] Q. Tang, J. M. Chu, Y. Wang, T. Zhou, and Y. Liu, "Characteristics and factors influencing Pb(II) desorption from a Chinese clay by citric acid," *Separation Science and Technology*, vol. 51, no. 17, pp. 2734–2743, 2016.

[60] Q. Tang, T. Zhou, F. Gu, Y. Wang, and J. M. Chu, "Removal of Cd(II) and Pb(II) from soil through desorption using citric acid: kinetic and equilibrium studies," *Journal of Central South University*, vol. 24, no. 9, pp. 1941–1952, 2017.

[61] Q. Tang, H. Y. Wang, X. W. Tang, and Y. Wang, "Removal of aqueous Ni(II) with carbonized leaf powder: kinetic and equilibrium studies," *Journal of Central South University*, vol. 23, no. 4, pp. 778–786, 2016.